Post-Tensioned Earthquake Damage Resistant Technologies for Accelerated Bridge Construction

Mustafa Mashal

A thesis submitted in partial fulfillment of the requirements for the degree of

Doctor of Philosophy

in

Civil Engineering

at the

University of Canterbury

Christchurch, New Zealand

October 2015

This thesis is dedicated to my parents

Kobra and Bashir Mashal

Abstract

Over the last few decades, Accelerated Bridge Construction (ABC) has been developed to answer the growing number of societal needs, as well as advancing the bridge practice. ABC offers faster bridge construction through prefabrication of the bridge substructure and superstructure elements in a factory, and the subsequent on-site assembly of the elements. In countries such as the United States, many of the state Departments of Transportation (DOTs) have developed ABC according to their own societal needs. There have been many applications of ABC in the United States, primarily in Texas, Utah, New Jersey, Florida, and Washington. However, application of ABC in regions with moderate-to-high seismicity requires in depth development, detailing consideration, experimental investigation, and analytical guidelines for the suitable connections between the precast members.

Over the last several years, two types of connections have been proposed for the prefabricated concrete bridge elements in seismic regions. The first type is called "emulative cast-in-place" which targets a similar seismic performance as that from a cast-in-place construction (e.g. formation of plastic hinges in the piers). This type of connection offers the advantage for prefabrication of the bridge elements which accelerates the bridge construction time. However, extensive damage to the bridge can be expected during a design level earthquake. Therefore, when referred in context of ABC, the emulative cast-in-place solution is called "ABC High Damage" in this research.

The second type of the proposed connections for ABC in seismic regions is a non-emulative solution called "Dissipative Controlled Rocking" (DCR). DCR connections combine unbonded post-tensioning tendons with external energy dissipaters between the precast members. The unbonded post-tensioning provides self centering for the bridge with dissipaters absorbing the seismic energy.

DCR connections are traditionally called "Hybrid" connections". They were primarily developed for multi-storey precast buildings in the late 1990s. Past observations from seismic performance of the precast buildings incorporating DCR connections, have shown minimal damage and business disruption in the structure following a major earthquake. Therefore, when DCR connections are used in ABC context, it can be called “ABC Low Damage”.

In this thesis, the use of emulative and DCR connections for ABC High Damage and ABC Low Damage has been thoroughly developed and experimentally tested. A series of quasi-static cyclic tests are performed on half-scale fully prefabricated cantilever and multi-column bridge piers. The specimens incorporate emulative and DCR connections between the precast elements. Several types of innovative dissipaters that can be used with DCR connections in ABC Low Damage, have been developed and experimentally validated. The design procedure, detailing consideration, construction technology, assembly sequence, experimental results, seismic performance, and analytical modeling, are presented for each type of ABC solutions discussed in the study. Qualitative and quantitative comparisons between the seismic performance of ABC High Damage and ABC Low Damage are also thoroughly presented.

The research concludes that ABC Low Damage offers the best seismic performance compared to ABC High Damage and cast-in-place solutions. The life-cycle cost analysis and seismic loss assessment for the above solutions are outside the scope this study. However, past research works on similar topics have shown that if the life-cycle cost of a bridge is considered, then the traditional cast-in-place, ABC High Damage, and ABC Low Damage solutions may result in similar total cost.

Acknowledgments

I would like to thank my primary supervisor, Associate Professor Alessandro Palermo, for his continuous support, guidance, encouragement, and supervision throughout my PhD program at the University of Canterbury.

I also would like to thank my co-supervisor, Dr. Allan Scott, for his support, and encouragement. I want to extend my sincere gratitude to my master degree supervisor, Professor Andre' Filiatrault of University at Buffalo - State University of New York, who encouraged me to study for a PhD in New Zealand and supported my doctoral application at the University of Canterbury. Similarly, I want to thank Professor Garth Thompson of the Kansas State University, and Associate Professor Gilberto Mosqueda of the University of California, San Diego, for serving as my referees for the University of Canterbury Doctoral Scholarship.

I am grateful of Dr. John Wood (John Wood Consulting Ltd.) for serving as my PhD internal examiner and also providing valuable input. At the same time, I would like to thank my PhD external examiner, Professor Jose Restrepo of the University of California, San Diego, for his useful comments.

I want to acknowledge the help provided by technical staff at the University of Canterbury with testing, especially Gavin Keats and Russell McConchie, without whom I would not have overcome the experimental challenges. A special thanks to fellow postgraduates and members of the Canterbury Bridge Team for their support. I want to express my thanks to Sam White and Michael Hobbs for their help with construction and testing of the specimens. Thanks to technical staff from Bradfords Precast Ltd. for their assistance and cooperation with the construction and delivery of the specimens.

I wish to acknowledge the University of Canterbury Doctoral Scholarship (2011-2014). I also wish to thank the New Zealand Natural Hazards Research Platform (NHRP) for

funding my PhD program as part of the project titled “Advanced Bridge Construction and Design for New Zealand” (ABCD), coordinated by Associate Professor Alessandro Palermo at the University of Canterbury (2011-2015).

I appreciate the continuous support provided by my family throughout my life, especially my parents, Kobra and Bashir Mashal, who have always been an inspirational source for me. I would like to thank my brother, Hanif Mashal, who has been on my side and helped me to overcome challenges in life. Thanks to my sisters, Negin Mashal, Nargis Mashal, and Nilofar Mashal, for their care and encouragement.

Last but not least, a special thanks to fiancée', Irene van Woerden, for her great companionship, love, and support during this PhD journey. I had the pleasure to spend time with her family during my stay in New Zealand. It was great to meet her parents (John and Jenny van Woerden), her brother (Tim van Woerden), and her grandparents (Hugo and Dorothy van Woerden). I look forward to the years to come as part of this family.

Table of Contents

Nomenclature

A	Cross-sectional area of the section
a	Equivalent concrete stress block depth
A_c	Area of circle segment in compression
A_{ex}	Area of the solid part section
A_{fuse}	Fused area of the grooved dissipater
A_h	Area enclosed by the hysteresis loop
A_{pt}	Cross-section area of post-tensioned tendon
A'_s	Area of compression reinforcement
A_s	Area of tension reinforcement / cross sectional area of confining shoe
A_{th}	Area of the threaded section of the bar
b	Armoring width / Height of column section
b_u	Width of the UFP plate
C	Damping coefficient
c	Neutral axis depth
$C(T_1)$	Elastic site hazard spectrum ordinate
C_c	Resultant concrete compression force
$C_d(T)$	Elastic 5% damped design acceleration
$C_h(T)$	Spectral shape factor

C_s	Compression steel force
d'	Depth to centroid of compression reinforcement
d	Diameter of the column
d_b	Diameter of the longitudinal rebar
d_{ex}	Diameter of the solid part of a grooved dissipater
d_{fuse}	Equivalent diameter of the grooved part in a grooved dissipater
d_i	Depth to centroid of tension steel reinforcement
$d_{pt,i}$	Depth to post-tensioned steel
d_s	Diameter of confined concrete
d_{th}	Diameter of the threaded grooved dissipater bar
D_u	Diameter of the UFP bend
e	Distance between the centroid of the section and post-tensioned tendons
E	Modulus of elasticity of steel
E_{pt}	Modulus of elasticity of tendons
f'_l	Effective lateral pressure
f'_c	Unconfined Concrete compressive strength
f'_{cc}	Confined concrete compressive strength
f_l	Lateral pressure from the armoring
F_m	Peak force of loop in a hysteresis
F_P	Plastic force
f_{pt}	Initial pre-tensioning force

f_{py}	Yield strength of pre-tensioned tendons
f'_s	Steel reinforcement compression stress
f_s	Steel reinforcement tension stress
$f_{sy,t}$	Yield strength of lateral reinforcement steel
F_U	Ultimate force
F_y	Yield force
f_y	Yield stress
f_{ye}	Effective yield stress of the rebar
f_{yh}	Yield strength of the armoring
g	Acceleration due to gravity
h	Armoring height
I_{cr}	Cracked moment of inertia
I_g	Gross moment of inertia
k_μ	Ductility factor
K_0	Initial Stiffness
k_e	Confinement effectiveness coefficient
L	Height of the column
L_{cant}	Distance from column face to point of beam contraflexure
L_{cb}	Height from top of the footing up to centerline of the cap beam
L_{ex}	Solid part between grooved and threaded parts in a bar
L_{fuse}	Fused length

L_p	Plastic hinge length
L_p	Plastic hinge length of the column
L_{sp}	Strain penetration length
$L_{sp,\ actual}$	Actual Strain penetration length
L_{th}	Threaded length of a grooved dissipater
l_{ub}	Unbonded length (tendons or reinforcing)
l'_{ub}	Unbonded length in dissipaters
M_{dec}	Decompression moment
M_N	Moment contribution from mild steel reinforcement or dissipaters
Mn	Nominal moment capacity
M_p	Plastic Moment
M_{pt}	Moment contribution from post-tensioned tendons
M_s	Moment contribution from axial loads
M_{tot}	Total moment capacity
M_y	Yield Moment
N	Axial load
n	Total number of gap openings along the unbonded tendon
N(T, D)	Near-fault factor
n_{pt}	Number of post-tensioned tendons
n_u	Number of UFPs
R	Confinement ratio

r	Post-yield stiffness factor / Ramberg-Osgood coefficient
R	Return Period factor
R_s	Return period factor for serviceability limit state
R_u	Return period factor for ultimate limit state
s'	Height of the shell
S_a	Spectral acceleration
S_d	Spectral displacement
SF	Scaling factor
S_P	Structural performance factor
t	Armoring thickness
T	Period
T_1	Fundamental period of the structure
T_{eff}	Effective period
T_{pt}	Tendon force
$T_{pt,\ initial}$	Initial post-tensioning load
T_s	Tension force of steel
t_u	Thickness of the UFP plate
V_b	Base shear force
Z	Zone factor / section modulus of the section
α	Unloading coefficient / Concrete stress block factor for strength
β	Force ratio / Concrete stress block factor for depth

Δ	Displacement or drift ratio
Δ_b	Deformation quantity used to control loading of the test specimen
Δ_{bm}	Value of deformation quantity corresponding to design storey drift
Δ_{by}	Value of deformation quantity at first significant yield of specimen
Δ_c	Total column displacement
δ_m	Peak displacement of loop in a hysteresis
Δ_p	Plastic displacement
Δ_{pt}	Elongation of the unbonded post-tensioned tendon
Δ_R	Performance point displacement
Δ_{Res}	Residual drift
Δ'_s	Elongation of the mild steel reinforcement in compression
Δ_s	Elongation of the mild steel reinforcement in tension
Δ_{sd}	Elongation of the mild steel bar at the design level drift in the structure
$\Delta_{tot\ (monolithic)}$	Total displacement of a monolithic beam
$\Delta_{tot\ (precast)}$	Total displacement of a precast beam
ΔT_{pt}	Increment of tendon load
Δ_u	Maximum displacement
Δ_y	First yield displacement
Δ_Y	Global yield displacement
ε_c	Compressive strain of concrete
ε_{max}	Maximum strain

$\varepsilon_{pt}(\theta)$	Increment of tendon strain at θ rotation
ε_r	Rupturing strain
ε'_s	Mild steel strain in compression
ε_s	Mild steel strain in tension
ε_{sul}	Cyclic strain at the maximum stress of longitudinal reinforcement
ε_{sut}	Strain at maximum stress of lateral reinforcement
ε_{us}	Uniform strain
ε_y	Yield strain
η	Spectral reduction factor
θ_{imp}	Imposed rigid rotation
θ_p	Plastic rotation
λ	Self-centering ratio / correction factor for elastic damping
μ	Displacement ductility
$\xi_{area\text{-}based}$	Area-based damping
$\xi_{el,\ tangent}$	Elastic tangent damping
ξ_{eq}	Equivalent time-history-calibrated damping
ξ_{hyst}	Hysteretic damping
ξ_{THA}	Equivalent Time-History Calibrated Damping ratio
ρ_{cc}	Ratio of the area of longitudinal reinforcement to the area of core section
ρ_{con}	Volume of confined concrete
ρ_s	Volumetric ratio of lateral reinforcement

σ_u	Ultimate stress
σ_y	Yield stress
ϕ_u	Ultimate curvature at the failure point
ϕ_y	Curvature at the first bar yield point
ϕ_Y	Curvature at the global yield point

1. INTRODUCTION AND SCOPE OF THE RESEARCH

1.1 Introduction

For the past several decades, the traditional construction method for concrete bridges has been the Cast-In-Place (CIP) construction. The CIP construction is commonly referred as "monolithic construction". In this type of construction, the bridge piers are constructed on-site at different stages. Although the initial cost for the monolithic construction of bridges has been proven lower, however, this type of construction can be a lengthy process, and hence requires more construction workers and resources on-site. Past experience has shown that monolithic construction of the highway bridges can result in severe traffic disruptions, especially in urban places where the traffic congestion was already very high.

The current widely practiced seismic design methodology for the monolithic construction relies on the bridge substructure system to respond ductile and inelastically during a major earthquake. This methodology aims to absorb the seismic energy in the predefined locations in a bridge substructure called “plastic hinge zones”. Formation of plastic hinges would result into yielding, buckling, and ultimately fracturing of the longitudinal rebars. It also causes spalling and crushing of the concrete (Kawashima, 2000, Priestley et al., 1996).

This methodology was originally developed by Professor Bob Park and Professor Tom Paulay at the University of Canterbury in the 1970s (Park and Paulay, 1975) and was further developed by Professor Nigel Priestley at the University of California, San Diego (Paulay and Priestley, 1992). It has been in practice since the late 1970s and has been introduced in many building codes around the world. Although it has prevented from the collapse of many bridges following a big earthquake, but in general the methodology targets the life safety and collapse prevention performance levels during a design level and maximum considered earthquake events, respectively. The bridge may suffer

extensive damage beyond repairability, can be left with residual displacement, and may not be functional after the earthquake (Christopoulos et al., 2002, Lee and Billington, 2011, Pampanin et al., 2003). Therefore, the downtime, repairing cost, residual displacement, and possible replacement, are the most undesirable aspects of the bridges designed according to this methodology.

In New Zealand, the traditional monolithic construction of bridges has been common among many bridge practitioners for the last several decades. During Canterbury Earthquakes, most of the bridges around the Christchurch city performed structurally well, but some critical bridges on the city's arterial routes had lost their functionality, and thus were closed for the emergency and public traffic (Palermo et al. (1), 2012, Wotherspoon et al., 2012, Palermo et al. (2), 2012). The bridges which suffered damage caused severe traffic disruptions for the public. A typical example is the bridge overpass on Moorhouse Avenue in Christchurch city which remained closed for more than one month following the February 22nd 2011 Christchurch Earthquake (Palermo and Mashal, 2012). Since then, the repair and replacement of several important bridges around the city have taken months and years.

Post-earthquake recovery of damaged bridges in New Zealand has resulted in significant traffic interruptions to such an extent that communities cannot reliably plan their travel timing. Nowadays, the basic demand from the communities is having durable and earthquake resilient infrastructure. Communities want long-term resilient bridge infrastructure with minimized maintenance costs following ordinary and extreme hazard conditions. At the same time, City Councils and asset managers demands include quick response, flexibility, and efficiency from the contractors and designers with minimum budget.

The Canterbury Earthquakes was a clear example of how the traditional monolithic construction targets only the initial lower construction cost, and following an earthquake only the life safety and collapse prevention of the bridge. However, given the current societal needs in many countries, we need to advance the bridge practice and add novel construction technology and seismic performance features, such as faster construction, limited traffic disruptions, and minimum downtime, repair, and residual displacement of the bridge following a major earthquake.

This thesis presents innovative solutions for faster construction of seismic resistant bridges, in particular development of appropriate connections between the precast elements of a bridge in high seismicity. The solutions are classified under High Damage and Low Damage connections. High Damage connections offer the advantage for prefabrication of the bridge elements. However, in terms of seismic performance, it targets similar seismic performance to that of a monolithic construction (e.g. formation of plastic hinges). This type of connections is sometimes referred as “Emulative Cast-In-Place" connections (Restrepo et al., 1995). Two types of High Damage connections, the grouted duct and member socket connections, were studied and experimentally tested for single and multi-column piers in this research.

The Low Damage connections are “Non-Emulative Cast-In-Place" connections that aim to localize all nonlinear deformation in a bridge structure at a fuse-type dissipater. The dissipater is designed to be easily replaced after an earthquake. This type of connections is also called "Jointed Ductile" connections (Priestley et al., 1999). In this thesis, the non-emulative connection is called “Dissipative Controlled Rocking” (DCR). This type of connection is developed to minimize earthquake damage and residual displacement in a bridge (Palermo, 2004, Palermo et al., 2005, 2007, 2008, and Marriott, 2009).

DCR connections, sometimes referred as “Hybrid PRESSS Connections” or just “Hybrid Connections”, combine unbonded post-tensioning tendons with external or internal dissipaters to provide self-centering and seismic energy dissipation in a bridge, respectively. The bridge will re-center, remain fully functional, and may suffer cosmetic to minor damage following a design level earthquake.

The main downside for DCR connections can be the initial construction cost due to addition of an extra construction phase for on-site post-tensioning of precast elements. The cost for the armoring of the connections and energy dissipaters can also contribute to the overall initial construction cost, but not to a considerable extent.

Low Damage or DCR connections offer the advantage for minimizing the repair work for a precast bridge during its lifetime serviceability. This could justify the higher initial construction cost of the low damage technologies for the infrastructure owners. DCR connections also eliminate the costs associated with the downtime and replacement of a bridge following a big earthquake.

Loss modeling can be a useful tool to find a balance between the initial construction cost, probability of the bridge suffering damage during its lifetime, delayed and limited functionality, penalty of the bridge damage, and the post-earthquake costs and downtime for the repair and replacement of the bridge. This type of modeling has previously been carried out for the low damage technologies (Bradley et al., 2010, Christopoulos et al., 2003, Dhakal and Mander, 2006, Lee and Billington, 2011, Mander et al., 2007, Marriott et al., 2009, Pampanin et al., 2003, Solberg et al., 2008, Uma et al., 2006, 2010).

Past studies on similar research have shown that when considering the life-cycle cost of a bridge which is composed of initial and lifetime maintenance expenditures, the total costs for the monolithic, High Damage, and Low Damage solutions may be similar and comparable to each other. The life-cycle cost analysis and seismic loss assessment for the above three solutions are outside the scope of the study here. They are recommended for future research, as presented in Section 7.5 in Chapter 7.

1.2 Accelerated Bridge Construction (ABC)

Lessons learned from the past earthquakes have shown that after taking a design level or maximum considered earthquake, a damaged bridge would require extensive repair work or possible replacement. In order to accelerate the on-site construction of the new bridge, an alternative construction technology to monolithic construction, has been recently proposed and developed. This technology offers the advantage for rapid construction by prefabricating the bridge substructure and superstructure elements in a factory, then transporting the precast elements to the construction site for assembly (Billington et al., 1999, Marsh et al., 2011). This technology is commonly known as "Accelerated Bridge Construction" or simply “ABC”.

ABC according to Federal Highway Administration (FHWA, 2013) is defined as “bridge construction that uses innovative planning, design, materials, and construction methods in a safe and cost-effective manner to reduce the onsite construction time that occurs when building new bridges or replacing and rehabilitating existing bridges.” It is important to mention that the reduced on-site construction time does not necessarily mean reducing the quality, instead, it implies to construct a cost-effective resilient bridge with increased safety and minimum traffic disruption (Ralls, 2014).

There are many advantages using ABC such as:

1. Limited disruption to traffic during construction, especially in populated areas
2. Fast project delivery
3. Cost savings related to the use of formwork
4. More accuracy in bridge elements due to their prefabrication
5. Better quality control of the materials used in the bridge elements
6. Lower machinery and equipment costs
7. Higher durability of the bridge elements
8. Reduced weight of the bridge structure
9. Higher level of safety
10. Less environmental impacts

Over the years, there have been plenty of examples for application of ABC in low seismicity as will be discussed in detail in Chapter 2. However, application of ABC in regions with moderate-to-high seismicity has been limited. This is due to uncertainty about the seismic performance of the connections between the precast elements. Lessons learned from the past earthquakes (Hawkins et al., 1994, Buckle, 1994) have shown specific vulnerability of precast connections in high seismicity.

Over the last few years, there have been primarily two types of connections proposed for ABC in seismic regions (Marsh et al., 2011). The first type of the connections is called “Emulative Cast-In-Place" or High Damage connections, as explained earlier. This type of connections when used in context for ABC, can be referred as “ABC High Damage”.

The second type of connections “Non-Emulative Cast-In-Place" include low damage seismic design technologies such as “Dissipative Controlled Rocking” (DCR), as introduced in the previous section. This type of connections aims to localize and minimize the damage in the bridge during a big earthquake. This type of connections

when used in context of ABC, can be referred as “ABC Low Damage”. The research in this thesis focuses on ABC High Damage and ABC Low Damage connections for the earthquake resilient design of prefabricated bridges.

Another type of connections which offer a compromise in terms of initial construction cost between ABC High Damage and ABC Low Damage, is called “ABC Controlled Damage” (White, 2014). ABC Controlled Damage connections use conventional reinforcing for the seismic energy dissipation, but offers self-centering of the bridge following an earthquake. Due to yielding of the longitudinal bars, there would be some damage to the connections. However, the extent of damage would be limited to certain regions of the structure which can be repaired without replacement of the whole bridge.

The repair strategy for ABC Controlled Damage will already be considered during the design phase of the bridge. Using this type of connections, the bridge will remain functional following a big earthquake. However, moderate repair work would be needed to reinstate the strength and ductility of the connections. This type of connections reduce the repair cost and downtime of the structure (compared to monolithic and ABC High Damage). ABC Controlled Damage is beyond the scope of this research. The design and repair strategies for ABC Controlled Damage was previously studied by White (2014) as part of the Advanced Bridge Construction and Design (ABCD) project at the University of Canterbury (2011-2015).

Table 1.1 presents a qualitative comparison of the different bridge construction practices described in this section. In Table 1.1, “red” color designates a high value, “orange” designates a moderate value, and “green” designates a low value.

Table 1.1. Comparison of different connection types for the bridge substructure system

		Low	Moderate	High
Monolithic	Material / Fabrication Cost			
	Construction Time			
	Repair Cost and Time			
ABC High Damage	Material / Fabrication Cost			
	Construction Time			
	Repair Cost and Time			
ABC Controlled Damage	Material / Fabrication Cost			
	Construction Time			
	Repair Cost and Time			
ABC Low Damage	Material / Fabrication Cost			
	Construction Time			
	Repair Cost and Time			

1.3 Research Motivation

In New Zealand, some of the bridge structures constructed between the 1920 up to 1950 need major retrofitting and possible replacement. This is due to their narrow width and poor approach highway alignments. The activities concerned with the maintenance, retrofitting, and frequent inspection of these bridges can cause severe traffic congestion and disruption for the public.

The New Zealand Transportation Agency (NZTA, 2010) project "Roads of National Significance" (RoNS) (2010-2020) identifies seven important state highways that are based around the five largest population centers in the country. These state highways are vital for the country's economic prosperity and require a considerable number of new bridge structures. The project is the largest of its kind in New Zealand history. It is an important part of the New Zealand government's National Infrastructure Plan (National Infrastructure Plan, 2010).

In the United States, approximately 210 million trips are taken daily across deficient bridges. Deficient bridges are composed of both structurally deficient and functionality obsoletes bridges. Most of these deficient bridges are in the immediate urge of repairs and replacements. The number of structurally deficient bridges was put at 66,749 which makes up one-third of the total bridge decking in the country. (ASCE Report Card for America's Infrastructure, 2013).

Past experience of ABC in countries like the United States, has shown that using ABC in a very populated urban center or in a particular location critical for the traffic network could reduce the construction time by 60 to 70% (Palermo and Mashal, 2012).

In today's world, we are moving towards new societal needs that aim to limit business and traffic disruptions following an earthquake. Therefore, preserving the functionality of a bridge structure after a design level or Maximum Considered Earthquake (MCE) event, is a further objective that the research community is currently investigating.

In order to save lives and protect the economy, it is vital that bridges remain drivable and functional following a natural disaster. Furthermore, since bridges are commonly exposed to the environment around them, the community would feel safer and less vulnerable if bridges preserve their integrity during a seismic event. A bridge does not only link people, but also embodies the advancements in civil engineering which will be clearly visible to the citizens.

Accelerated construction techniques, use of high performance and durable materials, and advanced earthquake technology, are the key elements for the next generation of bridges around the world. By using improved materials and better construction technologies, we can extended the serviceability life of new bridges to a hundred years with minimal maintenance costs (Palermo and Mashal, 2012).

The research community has always been aware of the challenges that our communities are facing nowadays. In countries like the United States, the research community, practitioners, and end users, are beginning to merge their expertise together to solve some of these challenges. For example, in 2002 the American Association of State Highway Transportation Officials (AASHTO) in collaboration with several research institutes and universities, started a strategic bridge plan which aims to improve the

construction and performance of bridges in different aspects (AASHTO Strategic Plan, 2005). One of the proposed solutions has been to have more coordination and involvement of the research community with the Departments of Transportation (DOTs), contractors, and designers.

In case of New Zealand, the development of innovative technologies combined with high performance materials are not solely sufficient. It needs a long term vision and strategy plan which should involve all related parties such as New Zealand Transportation Agency (NZTA), KiwiRail, key city councils (Auckland, Wellington, Christchurch, Hamilton, and Dunedin), contractors, practitioners, and more importantly researchers.

1.4 Novelty of the Research

In comparison to previous research on ABC, there are several novelty aspects in the study here which are discussed in below.

1. A very comprehensive study and literature review on ABC from some of the world's leading nations in the field of bridge engineering are presented. This includes the state-of-the-art research on ABC in seismic regions from renowned researchers until 2015. This is explained in Chapter 2.

2. The study discusses the development, detailing considerations, and experimental testing of several types of emulative connections for ABC in high seismic regions. Most of the previous research on emulative connections have been limited to testing of a particular connection in a cantilever column only. In the research here, the performance of emulative connections is not only tested for cantilever columns, but also for the combination of two different types of emulative connections in a precast bent. This is presented in Chapter 3.

3. The research provides details on invention of new metallic dissipaters for seismic protection of structural and non-structural components. The concepts for a variety of bracing type and min plug and play devices are developed. Most of the concepts are validated through experimental testing of several prototypes. The University of Canterbury has filed for a United States Provisional Patent to protect this invention due to its viable commercial aspect. This is discussed in Chapter 4.

4. The thesis include development, detailing, and experimental testing of precast multi-column pier support (bent) with Dissipative Controlled Rocking (DCR) connections. Past research programs on ABC with DCR connections have mainly tested a variety of DCR connections for simple cantilever columns. The study here experimentally investigates the use of DCR connections in a bent. Several new aspects of detailing and energy dissipation mechanisms are introduced. Some of the innovative dissipaters from Chapter 4 are tested in the bent for an enhanced seismic performance of the structure. This is presented in Chapter 5.

5. The study present simplified analytical models which are calibrated against the experimental results to predict the response of ABC with emulative and DCR connections. The models utilize existing theoretical models, spreadsheets, and commercial software packages. Most of the past analytical research have used research oriented software packages to model and predict the response of ABC. In this research, the use of commercial software packages for simplified modeling aims to provide easy and reliable modeling tools for the practitioners to predict the seismic response of ABC.

1.5 Scope and Objectives of the Research

The scope of the research in this study is development of cost-competitive and seismic resistant concrete bridge substructure systems which feature important aspects such as rapid construction, improved quality, durability, and lower life-time maintenance.

There mainly two objectives in this thesis:

1. Development of earthquake resistant bridge systems which feature higher speed of construction, enhanced seismic performance, and lower post-earthquake repair costs. This includes below sub-objectives:

    - Development of design procedures, detailing considerations, construction technology, and assembly sequence for earthquake resilient prefabricated bridge piers (ABC High Damage and ABC Low Damage).

    - Development of innovative dissipaters that can be used with ABC High Damage and ABC Low Damage solutions for a better seismic performance.

    - Experimental testing to confirm the seismic performance of ABC High Damage, Innovative Dissipaters, and ABC Low Damage.

    - Development and refinement of simplified analytical modeling to validate and predict the response of the solutions developed and tested in this research.

    - Improvement of existing technologies for High Damage and DCR connections.

2. Utilizing experimental results and observations from testing, qualitative and quantitative comparisons of seismic performance between ABC High Damage and ABC Low Damage.

1.6 Thesis Structure

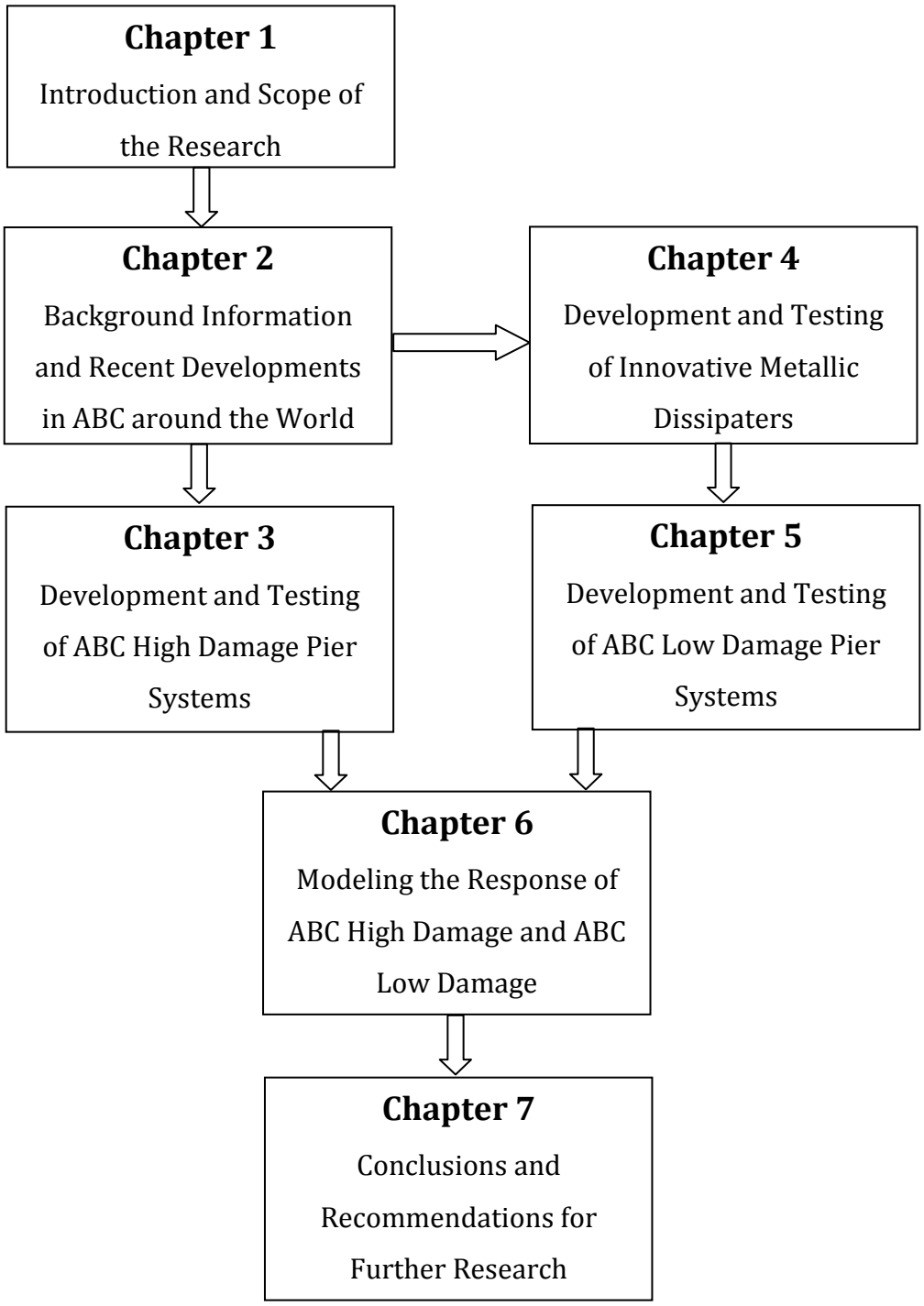

Figure 1.1: Thesis Structure

1.7 Overview

Chapter 1 provides an introduction of the research. In this Chapter, the research motivation, scope, and objectives of the thesis are discussed.

Chapter 2 presents an extensive background information and literature review on Accelerated Bridge Construction (ABC). A detailed review of the past and recent ABC applications is presented. This Chapter also provides a summary of prefabrication technologies in some of the world leading nations in bridge practice. It further explains the latest developments and the state-of-the-art research on ABC connections in high seismicity in countries such as the United States, Taiwan, and New Zealand.

Chapter 3 discusses the development of emulative cast-in-place solution for Accelerated Bridge Construction (ABC High Damage). This Chapter focuses on two types of bridge substructure systems, the cantilever and multi-column pier support systems, for typical highway bridges in New Zealand. In the first part of Chapter 3, four half-scale cantilever columns are developed and tested under uni and bi-directional quasi-static cyclic loading protocols. In the second part of the Chapter, a half-scale multi-column bent is developed for uni-directional quasi-static cyclic testing. Detailed information on the design procedure, detailing considerations, construction technology, assembly sequence, experimental testing, and results, are presented for each specimen.

Chapter 4 presents the development of innovative dissipaters for seismic protection of structures. This chapter focuses on the invention, construction, and experimental testing of several dissipaters that can be used with ABC Low Damage, as well as for the low damage construction of building structures. The innovative dissipaters include bracing types and mini plug and play devices. There are many novel features incorporated in these dissipaters such as cost-effectiveness, minimal low cycle fatigue, and multi-seismic performance. Some the features in the dissipaters are not integrated in the available metallic dissipaters in the market. Due to innovative nature, the University of Canterbury has filed for a United States Provisional Patent Application (Keats, Palermo, and Mashal) to protect the intellectual property in this Chapter.

Chapter 5 presents the development of non-emulative solution for Accelerated Bridge Construction (ABC Low Damage). A half-scale multi-column bent (similar to that in

Chapter 3) is developed for quasi-static cyclic testing. Key detailing and dissipater arrangements are investigated experimentally for the rocking bent. Some of the innovative dissipaters from Chapter 4 are tested in the bent for a superior seismic performance. This Chapter provides useful information on the design procedure, construction technology, and assembly sequence of the precast elements for ABC Low Damage. It presents an experimental parametric study on the capacity and self-centering of the bent under variable levels of post-tensioning. Observations and results from the experimental testing are thoroughly presented. Chapter 5 also presents qualitative and quantitative comparisons between ABC High Damage and ABC Low Damage. Observations from the extent of damage during testing are used to present a qualitative comparison between the two solutions. At the same time, experimental results and plots are utilized to provide a quantitative comparison for the seismic performance.

Chapter 6 presents simplified analytical tools for macro-modeling of ABC High Damage, Innovative Dissipaters, and ABC Low Damage. Existing analytical models are refined to capture and predict the response of the systems tested in this research to a good level of accuracy.

Chapter 8 summarizes the results from the experimental and analytical investigations. It also provides recommendation for a range of relevant topics for further research.

1.8 Bibliography

1. AASHTO Highway Subcommittee on Bridges and Structures (2005). AASHTO Strategic Plan for Bridge Engineering, Washington, D.C., United States.

2. Billington, S. L., Barnes, R. W., and Breen, J. E. (1999). A Precast Segmental Substructure System for Standard Bridges. Journal of Precast/Prestressed Concrete Institute, 44(4):56-73.

3. Bradley, B., Cubrinovski, M., Dhakal, R., and MacRae, G. (2010). Probabilistic Seismic Performance and Loss Assessment of a Bridge-Foundation-Soil System. Soil Dynamics and Earthquake Engineering, 30(5):395-411.

4. Buckle, I. G. (1994). The Northridge, California Earthquake of January 17, 1994: Performance of Highway Bridges. National Centre for Earthquake Engineering Research (NCEER), Technical Report 0008 1994, University at Buffalo (SUNY), New York, United States.

5. Christopoulos, C., Filiatrault, A., Uang, C., and Folz, B. (2002). Post-tensioned Energy Dissipating Connections for Moment-Resisting Steel Frames. Journal of Structural Engineering, 128(9):1111-1120.

6. Christopoulos, C., Pampanin, S., and Priestley, M. J. N. (2003). Performance-Based Seismic Response of Frame Structures including Residual Deformations. Part I: Single-Degree of Freedom Systems. Journal of Earthquake Engineering, 7(1):97-118.

7. Dhakal, R. and Mander, J. (2006). Financial Risk Assessment Methodology for Natural Hazards. Bulletin of the New Zealand Society for Earthquake Engineering (NZSEE), 39(2): 91-105.

8. Federal Highway Administration (2013). http://www.fhwa.dot.gov/bridge/abc/

9. Hawkins, N., Wood, S., and Stanton, J. (1994). Performance of Parking Garages in the 1994 Northridge Earthquake. American Society of Civil Engineers Structures Congress, Boston, Massachusetts, United States.

10. Kawashima, K. (2000). Seismic Design and Retrofit of Bridges. Bulletin of the New Zealand Society for Earthquake Engineering (NZSEE), 33(3):265-285.

11. Keats, G., Palermo, A., and Mashal, M. Energy Dissipation Device. United States Provisional Patent Application: 61/149,199. Filing Date April 17 2015.

12. Lee, W. K. and Billington, S. L. (2011). Performance-Based Earthquake Engineering Assessment of a Self-Centering, Post-Tensioned Concrete Bridge System. Earthquake Engineering and Structural Dynamics, 40(8):887-902.

13. Mander, J., Dhakal, R., Mashiko, N., and Solberg, K. (2007). Incremental Dynamic Analysis Applied to Seismic Financial Risk Assessment of Bridges. Engineering Structures, 29(10):2662-2672.

14. Marriott, D. (2009). The Development of High-Performance Post-Tensioned Rocking Systems for the Seismic Design of Structures. PhD Thesis, University of Canterbury, New Zealand.

15. Marriott, D., Pampanin, S., Bull, D., and Palermo, A. (2009). A Probabilistic Seismic Loss Assessment of Advanced Post-tensioned Precast Bridge Systems. Proceedings of New Zealand Society for Earthquake Engineering (NZSEE) Conference, Christchurch, New Zealand.

16. Marsh, M. L., Wenli, M., Garrett, B. E., Stanton, J. F., Eberhard, M. O., and Weinert, M. D. (2011). Application of Accelerated Bridge Construction Connections in Moderate-to-High Seismic Regions. National Cooperative Highway Research Program, Report 698, Washington D.C., United States.

17. National Infrastructure Plan (2010). New Zealand Government. http://www.infrastructure.govt.nz/plan

18. New Zealand Transport Agency (2010). Roads of National Significance (RoNs)-Economic Assessments Review. http://www.nzta.govt.nz/network/rons/

19. Palermo, A. (2004). The Use of Controlled Rocking In the Seismic Design of Bridges. PhD Thesis, Politecnico Di Milano (Technical University of Milan), Milan, Italy.

20. Palermo, A. and Mashal M. (2012). Accelerated Bridge Construction and Seismic Damage Resistant Technology: A New Zealand Challenge. Bulletin of the New Zealand Society for Earthquake Engineering, 45(3): 123-134.

21. Palermo, A. and Pampanin, S. (2008). Enhanced Seismic Performance of Hybrid Bridge Systems: Comparison with Traditional Monolithic Solutions. Journal of Earthquake Engineering, 12(8):1267-1295.

22. Palermo, A., Kivell, A., Wotherspoon, L., Hogan, L. S., Yashinsky, M., Bruneau, M., and Camnasio, E. (2012). Overview of Bridge Performance during the 2011 Christchurch Earthquake. Proceedings of the Sixth International Conference on Bridge Maintenance, Safety, and Management, Stresa, Italy.

23. Palermo, A., Pampanin, S., and Calvi, G. M. (2005). Concept and Development of Hybrid Solutions for Seismic Resistant Bridge Systems. Journal of Earthquake Engineering, 9(6):899-921.

24. Palermo, A., Pampanin, S., and Marriott, D. (2007). Design, Modeling, and Experimental Response of Seismic Resistant Bridge Piers with Post-tensioned Dissipating Connections. Journal of Structural Engineering, 133(11):1648-1661.

25. Palermo, A., Wotherspoon, L., Hogan, L. S., Heux, M. L., Camnasio, E., and Brando, M. (2012). Seismic Performance of Concrete Bridge during Canterbury Earthquakes. Proceedings of the American Society of Civil Engineering Structures Congress, Chicago, Illinois, United States.

26. Pampanin, S., Christopoulos, C., and Priestley, M. J. N. (2003). Performance-Based Seismic Response of Frame Structures Including Residual Deformations. Part II: Multi-Degree of Freedom Systems. Journal of Earthquake Engineering, 7(1):119-147.

27. Park, R. and Paulay, T. (1975). Reinforced Concrete Structures. John Wiley and Sons Incorporation, New Jersey, United States.

28. Paulay, T. and Priestley, M. J. N. (1992). Seismic Design of Reinforced Concrete and Masonry Buildings. John Wiley and Sons Incorporation, New Jersey, United States.

29. Priestley, M. J. N., Seible, F., and Calvi, G. (1996). Seismic Design and Retrofit of Bridges. John Wiley and Sons Incorporation, New Jersey, United States.

30. Priestley, M. J. N., Sritharan, S., Conley, J. R., and Pampanin, S. (1999). Preliminary Results and Conclusions from the PRESSS Five-Story Precast Concrete Test Building. Precast/Prestressed Concrete Institute Journal, 44(6):42-67.

31. Ralls, M. L. (2014). History of ABC Implementation in U.S. Proceedings of the National Accelerated Bridge Construction Conference, 3-10, Miami, United States.

32. Restrepo, J. I., Park, R., and Buchanan, A. H. (1995). Tests on Connections of Earthquake Resisting Precast Reinforced Concrete Perimeter Frames of Buildings. PCI Journal, 40(1):44-61.

33. Solberg, K., Dhakal, R., Mander, J., and Bradley, B. (2008). Computational and Rapid Expected Annual Loss Estimation Methodologies for Structures. Earthquake Engineering and Structural Dynamics, 37(1):81-101.

34. Uma, S. R., Pampanin, S., and Christopoulos, C. (2006). A Probabilistic Framework for Performance-based Seismic Assessment of Structures Considering Residual Deformations. Proceedings of the First European Conference on Earthquake Engineering and Seismology, Geneva, Switzerland.

35. Uma, S. R., Pampanin, S., and Christopoulos, C. (2010). Development of Probabilistic Framework for Performance-Based Seismic Assessment of Structures Considering Residual Deformations. Journal of Earthquake Engineering, 14(7):1092-1111.

36. White, S. (2014). Controlled Damage Rocking Systems for Accelerated Bridge Construction. Master Thesis, University of Canterbury, Christchurch, New Zealand.

37. Wotherspoon, L., Hogan, L. S., Palermo, A., Heux, M. L., Bruneau, M., and Anagnostopoulou, M. (2012). Performance of Bridges during the 2010 Darfield Earthquake. Proceedings of the Sixth International Conference on Bridge Maintenance, Safety, and Management, Stresa, Italy.

2. BACKGROUND INFORMATION AND RECENT DEVELOPMENTS IN ABC AROUND THE WORLD

2.1 Introduction

In the first part of this Chapter, an introduction to common substructure systems for concrete bridges is provided. A history of the development and application of Accelerated Bridge Construction (ABC) in several world leading countries in field of bridge engineering is also explained in detail.

In the second part of the Chapter, the state-of-the-art research on ABC in seismic regions are discussed. This includes past research works into ABC and the on-going efforts for enhancing the performance of ABC in moderate-to-high seismicity.

In the third part of the Chapter, a history of the pioneered seismic technologies in New Zealand is presented. This part aims to provide an overview of how some of these technologies were previously applied in the bridges which had put New Zealand at the forefront of earthquake engineering back in the days.

In summary, the main objectives of this Chapter are as follows:

1. An overview of the development, past application, and advances in research on enhancing the performance of ABC in seismic regions.

2. Based on the first objective, identifying the trends and areas where more research work is necessary.

3. Using the technologies pioneered in New Zealand to enhance the performance of ABC in seismic regions.

2.1.1 Classification of Substructure Systems for Concrete Bridges

A bridge structure is composed of substructure and superstructure elements. The superstructure system includes the deck, girders, and other structural or non-structural components. The substructure system supports the weight of superstructure and is composed of foundations, piers, abutments, and cap beam. The substructure resists the gravity and service loads transferred from the superstructure. It also provides seismic force resisting system for the whole structure.

In many countries around the world, construction of the superstructure system for the short-to-medium span (up to 30 meters) concrete bridges has already been shifted from cast-in-place construction to precast. However, the monolithic or cast-in-place construction of the substructure system is still the preferred method of construction among many nations around the world (Palermo and Mashal, 2012).

Recently, there has been significant push in the industry and academia towards precasting of the substructure elements in countries such as the United States, New Zealand, Japan, Taiwan, and some European countries. These are discussed in detail in the subsequent sections. Generally, the substructure system is classified under cast-in-place or precast construction, as explained in the following sections.

2.1.1.1 Cast-In-Place Substructures

Cast-in-place substructures also known as monolithic systems are widely used for all types of bridges, regardless of the bridge dimensions (span lengths and pier heights). The use of cast-in-place formwork for the standard column shapes (circular or rectangular) has been proven to be cost effective. However, it does not offer any flexibility for changing the column shapes due to some economical reasons. Most of the old concrete bridges around the world have cast-in-place substructure systems (Billington et al., 2001). Figure 2.1 shows a typical highway bridge in the United States with monolithic substructure system.

Figure 2.1. Typical cast-in-place substructure in Texas, after Billington et al. (2001)

Billington et al. (2001) discusses many alternative cast-in-place substructure systems for bridges with the common precast pre-tensioned superstructure system, such as individual columns, walls, hammerhead, and multi-column piers (Figure 2.2).

For the individual columns the superstructure can be segmental, trapezoidal box girders, or U-beams. This type of substructure system provides many benefits, such as reducing the number of the individual supports which contributes to the visibility through the bridge.

Wall substructures are commonly used in rivers. A disadvantage of this type of the substructure system is that it may block the visibility through a bridge from many angles.

Hammerhead piers can be T-shaped single-column bents. They are recommended for the narrow bridges where visibility through the bridge is required. They can be partially or fully integrated with the superstructure or can be located underneath the superstructure system.

Multi-column piers are very common for wide bridges, and are very economical for any bridge width. The bents can be skewed or straight with the axis of the bridge.

Figure 2.2 shows a variety of the substructure systems commonly in use in many countries around the world.

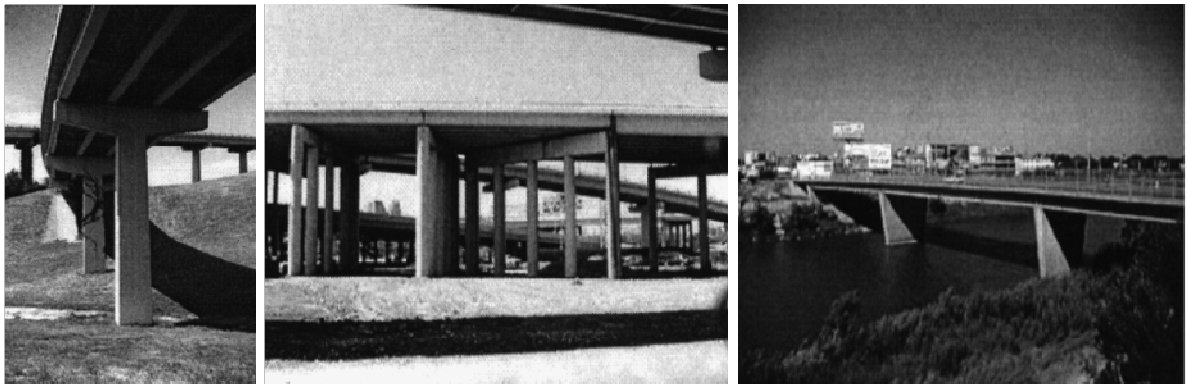

(a) **(b)** **(c)**

Figure 2.2. Bridge pier types: (a) Hammerhead (b) Multi-column (c) Wall, after Billington et al. (2001)

2.1.1.2 Precast Substructures

In the past, bridge precast components were intended primarily for the superstructure elements in bridges with short-to-moderate spans. The popular precast superstructure systems include girders of I-shape, T-shape, U-shape, and segmental box sections. From these precast sections, the technology for the precast segmental box construction has always been advancing. Over the years, there has been plenty of construction methodologies developed for it.

Precast substructure system in a bridge offers many advantages. These include application of the advanced technologies and materials, or alternatives for a combination of precasting and high performance materials for a faster construction and increased durability of the bridge structure.

There are a number of factors that need to be considered for the development of a precast substructure system. This includes, but is not limited to cost competiveness, appropriately sized sections that can be fabricated in the existing precast plants, improved durability, matching the design specifications, and sections that would be applicable to different types of projects.

Recent study by Billington et al. (2001) seeks to achieve a better standardization of the precast segmental substructure system in the United States. The study aims to optimize the shape of segments and the construction sequence for the bridge piers, as shown in Figure 2.3.

It is important to note that the overall cost of a bridge with precast substructure must not exceed the cost of a bridge with cast-in-place substructure system. Therefore, precasting of bridge substructure system can be very feasible when there are a large number of structural elements with regular sections to be cast. This offers the advantage for using the mould repeatedly in a prefabrication yard. Therefore, reducing the prefabrication cost.

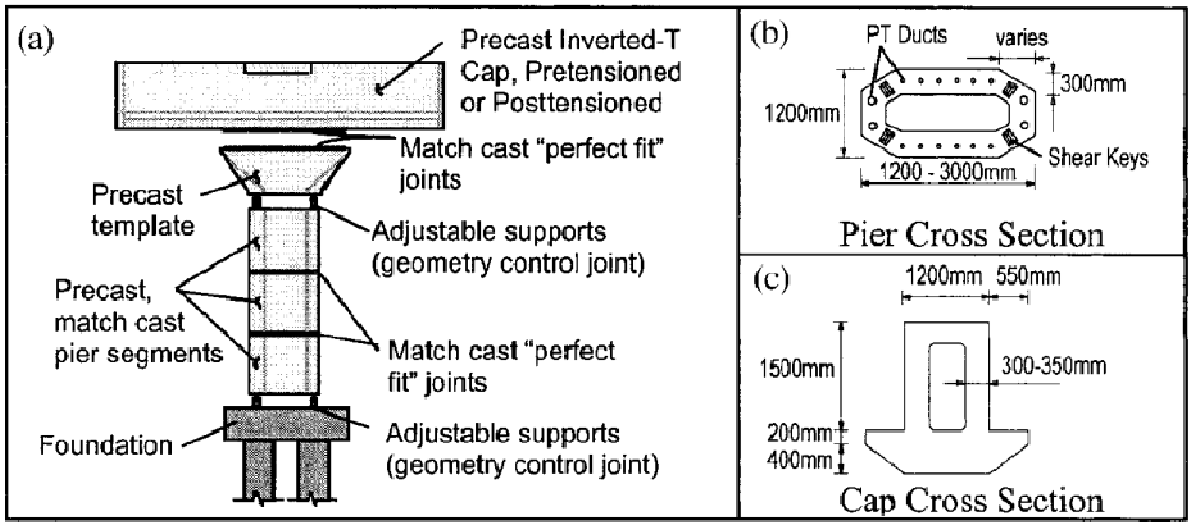

Figure 2.3. Elements of a precast segmental pier, after Billington et al. (2001)

Although there have been previous applications of the precast substructure for the bridge piers in countries such as the United States, however, it has been limited to regions with low seismicity (Stanton et al., 1992). The Loma Prieta Earthquake in 1989 and the Northridge Earthquake in 1994 highlighted unexpected high vulnerability of precast concrete structures in general (Buckle, 1994, Hawkins et al., 1994). For these bridges, the deck unseating and deck to pier fastener connection failures were the main causes of many bridge collapses.

As a consequence, in Europe, new versions of building codes have penalized precast concrete structural systems through a more conservative reduction factor for ductility (Eurocode 8, 2004). Bridge substructures are normally designed for column sway mechanism under lateral loading. This means that there is little redundancy in the system compared to buildings (such as beam sway mechanism). Resilient connections are important between the precast elements for the ductility needed for the bridge in seismic regions. Therefore, a comprehensive study into strength and ductility of precast

connections is vital before implementation of the precast substructure systems in regions with moderate-to-high seismicity.

For building structures, structural designers have accepted the compromise to have partially prefabricated elements combined with some cast-in-place connections. The connections are designed and constructed in such a way to emulate the cast-in-place or monolithic behavior (as discussed previously in Chapter 1). This type of connections has the advantage for reducing construction time and achieving similar levels of ductility as that can be expected of a cast-in-place construction.

Nowadays the latest technologies in structural engineering are moving toward "Mechanized Systems", also called as "Dissipative Fuses". These fuses are in the shape of high-tech linkages or seismic devices which absorb most of the earthquake energy transferred to the structure. The Dissipative Fuses reduce the damage to its minimum in the structural members which indeed eliminates any post-earthquake disruption in the structure. Greater social demands and needs will gradually cause the practitioners and contractors to abandon the concept for the emulative cast-in-place technology and move toward the technology for Dissipative Fuses, Priestley et al., (1999) and Pampanin et al., (2010) (buildings), Marriott (2009), Palermo (2004), Palermo et al., (2005), and Palermo and Mashal (2012) (bridges).

2.2 History of Development and Implementation of ABC

Over the last few decades, the United States, Europe, Japan, Taiwan, and New Zealand have interpreted and developed ABC in their contexts based on the societal needs. These are discussed in detail in the following sections.

2.2.1 United States

Following the rapid advancement of the transportation network in the second half of the twentieth century, the technology for innovative seismic-proof bridge design and construction has been changing its shape throughout the country. In the last three decades, the Transportation Research Board (TRB) has administered sponsorship of research for many state Departments of Transportation (DOTs) for the advancement of ABC research. Ralls (2014) presents a history of the development and implementation of ABC in the United States. A brief list of the research programs from the beginning is summarized and presented as follows.

2.2.1.1 Transportation Research Board (TRB) National Cooperative Highway Research Program (NCHRP)

The first NCHRP Synthesis Report on Prefabricated Bridge Elements and System (PBES) was published in 1985 (NCHRP, 1985). The report proposed prefabricated superstructure systems such as prestressed concrete I-beam, precast and prestressed box beam, precast and prestressed channel, and precast slab span for highway bridges. The main objective of this research was to use prefabricated elements to reduce the cost and to accelerate the construction time of a bridge.

After nearly two decades, a second synthesis report on PBES was published in 2003 (NCHRP, 2003). The main focus of this report was to gather existing information on the use of innovative PBES, repair and replacement of bridges, on-site construction time, traffic disruptions, and environmental impact. During 1985 until 2003, new systems were developed for prefabrication of both substructure and superstructures systems. The motives behind using PBES were aligned with the advantages that ABC offers, as discussed in Chapter 1.

2.2.1.2 TRB Task Force on Accelerating Innovation in the Highway Industry

Following publication of TRB Special Report 249 (1996) "Building Momentum for Change", effort towards a national accelerated construction initiative started. The report recommended establishment of a strategic discussion to promote accelerated construction for the highway infrastructure which also included bridges. The report also contributed in creation of the TRB Task Force on Accelerating Innovation in the Highway Industry (A5T60) in 1999 (FHWA, 2005).

In 2000, the A5T60 organized a two-day workshop in Washington D.C. to investigate the associated issues with accelerating highway construction. In 2002, the A5T60 along with AASHTO Technology Implementation Group (TIG), and FHWA sponsored Accelerated Construction Technology Transfer (ACTT) workshops in the states of Indiana and Pennsylvania. All three workshops turned to be a great success. This led AASHTO TIG and FHWA to sponsor ACTT workshops in more than 25 states around the country. In these workshops, ACTT process was discussed and applied to a particular project. A team of national bridge professionals and local agency experts from a multidisciplinary background were evaluating all design and construction aspects of the project, from contracting phase to design and then the subsequent construction.

2.2.1.3 AASHTO Technology Implementation Group (TIG)

The American Association of State Highway and Transportation Officials Technology Implementation Group (AASHTO TIG) was originally created in 2000. It consisted of state DOTs and Federal Highway Administration (FHWA) managers. The formation of TIG was intended to identify and support the implementation of several ready-to-use ABC technologies every year. The AASHTO TIG proposed precast concrete bent caps to be implemented around the country. It also created a Lead State Team which was composed of bridge practitioners from DOTs, FHWA, and the industry for a wider implementation of precast bents in construction of bridges nationwide.

2.2.1.4 TRB Second Strategic Highway Research Program

This program was authorized by the United States Congress in 2005. This was a short term research program with objectives such as investigation of factors causing the highway crashes and traffic congestion. Several ABC products were developed and

published. The most important product was the toolkit for the "Innovative Bridge Design for Rapid Renewal" (SHRP2, 2013). The toolkit included important information such as standard design details, specifications, guidelines, and design examples.

2.2.1.5 AASHTO/FHWA/TRB International Scan on PBES

This program was sponsored by AASHTO, FHWA, and TRB. The objective of the program was to do a research scan on PBES in Japan and Europe (FHWA, 2005). The project had some recommendations for application of innovative technologies as follows:

- Movement Systems: Self-propelled modular transporters and bridge installation
- Superstructure Systems: Inverted T-beam with composite cast-in-place topping, prefabricated concrete decks (partial and full depth), U-shaped segments
- Substructure Systems: Sumitomo Precast form for resisting Earthquakes and for Rapid Construction (SPER System)

2.2.1.6 FHWA Highways for LIFE (HfL) Program

This program was funded by the United States Congress in 2005. The term "LIFE" stands for "Longer-lasting highway infrastructure using Innovations to accomplish the Fast construction of Efficient and safe highways and bridges". The objectives of this program were to improve construction safety, to reduce traffic congestion and disruption during the construction, and improve the quality of highway infrastructure.

Between 2006 up to 2012, the HfL program funded construction of several bridges using ABC technologies. These technologies included several types of modular decked beams, precast abutments, precast piers, superstructure replacement, and lateral slide technologies.

Overall, the constant and frequent research have led to production of useful documents such as FHWA Report IF-09-10 (FHWA, 2009) "Connection Details for Prefabricated Bridge Elements and Systems" and NCHRP Report 698 (Marsh et al., 2011) "Application of Accelerated Bridge Construction connection in Moderate-to-High Seismic Regions". The NCHRP Report 681 (Restrepo et al., 2011) "Development of Precast Bent Caps for

Seismic Regions" is another example of recent efforts for advancing ABC as part of HfL Program.

2.2.1.7 AASHTO/TRB United States Domestic Scan Program

In 2007, AASHTO member states funded NCHRP Project 20-68A "The United States Domestic Scan Program" (2007-2015). This program manages the implementation of the domestic technology on a particular technical topic. The scan topics are selected by AASHTO and NCHRP based on suggestions from the DOTS and FHWA. The domestic scans have provided valuable input to address topics that can advance the application of ABC. Examples include "Best Practices in Accelerated Construction Techniques" (Blanchard et al., 2009) and "Best Practices Regarding Performance of ABC Connections in Bridge Subjected to Multi-Hazard and Extreme Events" (Kapur et al., 2012).

2.2.1.8 FHWA Every Day Counts Initiative

FHWA started its "Every Day Counts" (EDC) initiative in 2009. The goals for this program were to quickly categorize and apply market-ready innovations in highway infrastructure. Since beginning of EDC, it has helped with the development and construction of a large number of projects incorporating ABC technologies.

For example, in 2011-2012 more than one thousand bridges were constructed using an accelerated type of construction such as PBES technology. In 2011, FHWA founded the Center for Accelerating Innovation (CAI) to offer national management on implementing transportation innovations. Currently, CAI also includes the EDC initiative and products from the HfL program.

2.2.1.9 ABC University Transportation Center

ABC-University Transportation Center (ABC-UTC) was established in 2013 through funding from the Research and Innovative Technology Administration, under the Department of Transportation. ABC-UTC is located at the Florida International University and is in association with the Iowa State University and the University of Nevada at Reno. Current research programs at ABC-UTC include precast bridge railing, seismic connection details, and gathering of ABC projects and research into databases which could be accessible for bridge practitioners.

2.2.1.10 Caltrans and AASHTO Strategic Plan (2005-2015)

The California Department of Transportation (Caltrans) and AASHTO have a broad picture for improvement of ABC technologies as part of the AASHTO Strategic Plan (AASHTO, 2005). Caltrans has adopted ABC as an element of the Accelerated Project Delivery (APD) which has many benefits such as leading to expedited capital improvement, and improving the state's economy.

The NCHRP Report 20-73 "Accelerating Transportation Program and Project Delivery: Conception to Completion" (Keck et al., 2010) is one of the recently accomplished projects in the United States. The NCHRP and a number of DOTs in the United States have been funding research projects to enhance the seismic performance of the connections for ABC.

One of the complementary research works towards the widespread implementation of ABC in regions with moderate-to-high seismicity has been to investigate the connections between the precast elements. This included connections between the column to foundation and the girder to bent cap (TRB, 2010).

Caltrans has been one of the most active DOTs in the United States for the development of ABC technologies in seismic regions. It has developed a strategic research plan for the next decade. The plan initially focuses on the connections between the foundation to substructure and substructure to superstructure. It further aims to understand the seismic performance of the existing ABC connections which are currently used for ABC in non seismic areas. Caltrans is currently sponsoring workshops with consulting engineers, fabricators, erectors, transporters, and general contractors, in order to engage the industries to improve the construction cost and quality of new precast components (Chung et al., 2008).

2.2.1.11 Recent Applications of ABC in the United States

There have been many examples of ABC in the United States by state DOTs. This section provides a summary of the highlighted projects where ABC was used for construction of the bridge substructure and superstructure systems. It is important to mention that most of these bridges were primarily located in low seismicity.

Recent examples from the Texas DOT include the Pierce Elevated Freeway Bridge Replacement project and the Louetta Road Overpass (Billington et al., 1999). The piers were precast segmental columns which were assembled on-site.

Other examples of the recent precast concrete piers in the United States are the Seven Mile Bridge, Sunshine Skyway Bridge, and John T. Collinson Rail Bridge, all in the State of Florida, Vaina-Enon Bridge in the State of Virginia, Linn Cove Viaduct "Vail Pass" (Figure 2.4a and Figure 2.4b) in the State of Colorado, Segmental Piers of State Highway 183 (Figure 2.4c) in the State of Texas, Victory Bridge in the State of New Jersey, US 6 Bridge over Keg Creek in the State of Iowa, and I-84 Bridge over Dingle Ridge Road in the State of New York . Figure 2.4 through 2.9 show recent applications of ABC in the United States.

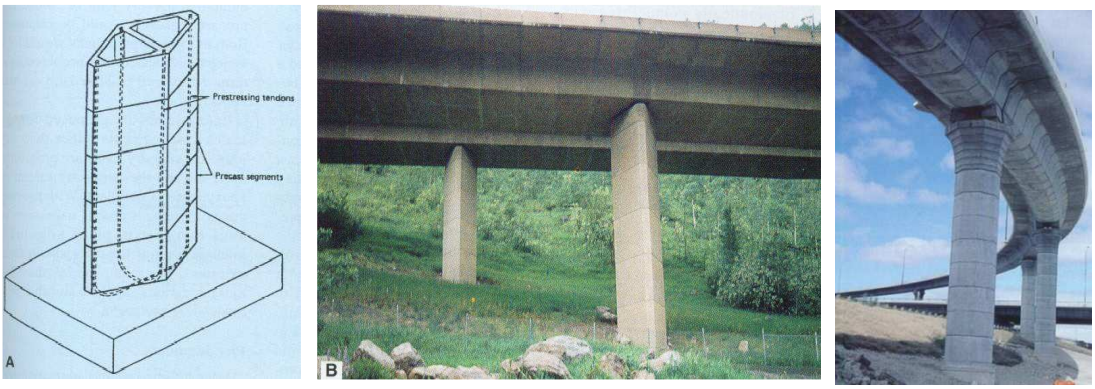

(a) **(b)** **(c)**

Figure 2.4. (a & b) Precast segmental piers of the Vail Pass in Colorado (c) State Highway 183 in Austin, Texas, after Billington et al. (1999)

Figure 2.5 shows the replacement of I-287 Viaduct over the Saw Mill River Parkway in the State of New York. The piers were precast post-tensioned to accelerate the construction. After a cost and benefit analysis, this solution was concluded to be fast and cost-effective for this multiple span viaduct. There was a shear key located between the pier segments to transfer shear forces. Joints between the segments were sealed using epoxy adhesive. Post-Tensioned rods were tied in the cast-in-place foundation and were running through the segments. Spliced couplers were used to connect the post-tensioning rod at different levels up the height of the piers. Upon assembly of all segments, the entire pier which consisted of several segments was post-tensioned and secured (FHWA, 2009).

Figure 2.5. Replacement of I-287 Viaduct (courtesy of New York DOT)

In the last few years, most of ABC projects in California were completed in less than 5 months. As an example, the I-40 Marble Wash Bridge was replaced by the precast girders in only 28 days in 2007 (Figure 2.6).

Figure 2.6. Replacement of I-40 Marble Wash Bridge (courtesy of Caltrans)

In Florida, the Edison Bridge (Figure 2.7) is one of the examples of ABC. The bridge was constructed using precast H-shaped columns and U-shaped cap beams. These shapes were selected to reduce weight of the substructure. The column to footing and column to cap beam connections consisted of steel grouted reinforcing bar splicer system. The splicers were oversized (13 mm) to accommodate construction tolerances. After the construction, the labor and insurance costs were well less than the conventional cast-in-place construction due to a reduced construction time on the water (FHWA, 2009).

Figure 2.7. Edison Bridge, after FHWA (2009)

In Texas, the replacement of the Lake Ray Hubbard Bridge on State Highway 66 in 2000 incorporated ABC technology. Piers were cast-in-place concrete columns supporting a precast cap beam (Figure 2.8). The column to cap beam connection was grouted ducts. Standard post-tensioning ducts were installed in the cap beam during prefabrication (Figure 2.9a). The ducts ran from the bottom to the top of the cap beam. While lowering the cab beam on the columns, a worker guided the column bars into the ducts. Steel shims were used to level the cap beam.

Another example of ABC in Texas is the replacement of Lake Belton Bridge on State Highway 36 in 2004 (Figure 2.9). The bridge superstructure consisted of prestressed U-beams (Figure 2.9c). The substructure was twin cast-in-place columns supporting a precast hammerhead cap (Figure 2.9d). The column to cap connection was grouted duct connection. The procedure for placing the precast cap beam on the columns (Figure 2.9a and Figure 2.9b) was similar to that used in construction of Lake Ray Hubbard Bridge (Figure 2.8b).

(a) (b) (c)

Figure 2.8. Lake Ray Hubbard Bridge: (a) Grouting ducts in the cap beam at the prefabrication yard (b & c) Placing the precast bent cap, after FHWA (2009)

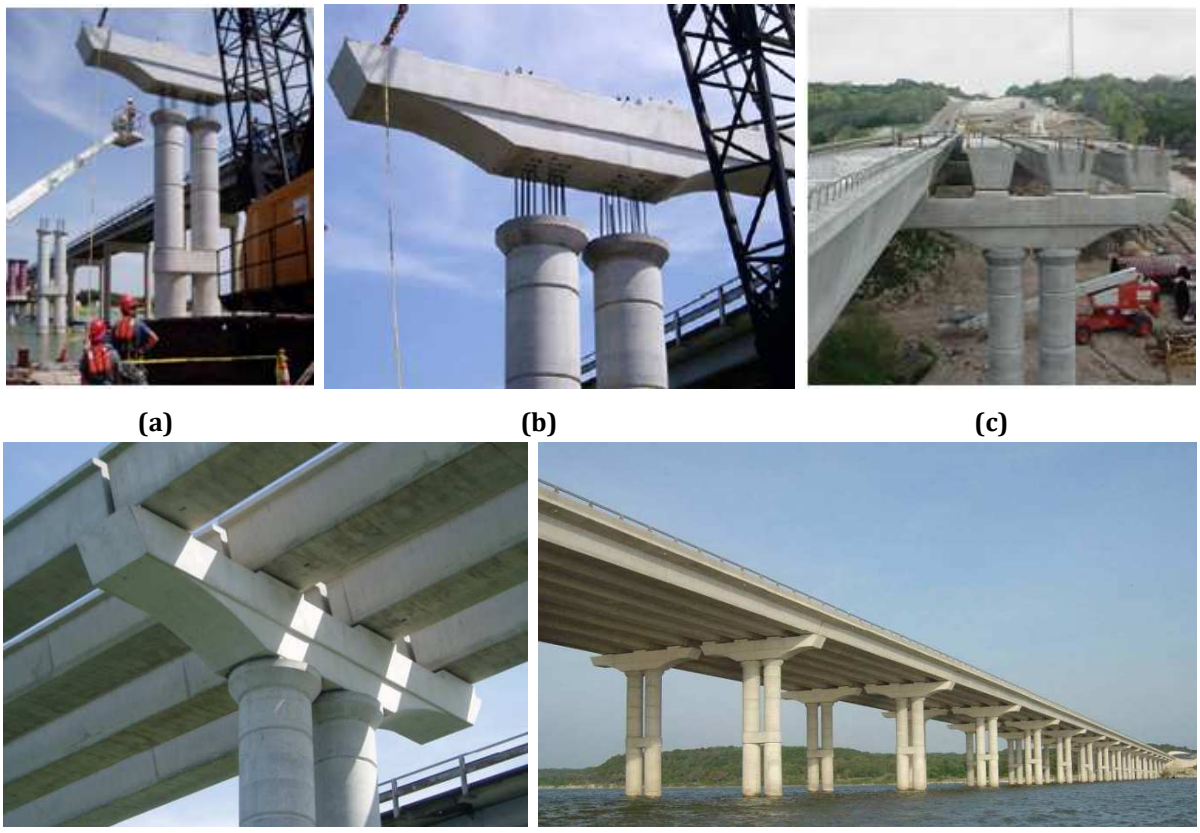

(a) (b) (c)

(d) (e)

Figure 2.9. Lake Belton Bridge Replacement: (a) Placing the precast bent cap (b) Aligning the column rebars in the ducts (c) U-Shaped prestressed beam over the precast cap (d & e) Completed bridge, after FHWA (2009)

2.2.2 Europe

In general, ABC in Europe has not had any significant innovative technology for the bridge substructure systems in seismic areas. Low damage seismic protective systems primarily include seismic isolation of bridge superstructure system. This solution has been growing very rapidly. Significant efforts have been and are under way to make seismic isolation technology more cost-efficient, compared to cast-in-place construction (Palermo and Mashal, 2012).

In Europe, ABC has mainly been limited to the decking systems or the superstructure elements in a bridge. The most common decking systems are the steel-composite deck with the precast concrete panels (partial or full depth). The panels are connected through studs to the steel beams. This technology reduces construction time and weight of the superstructure (FHWA, 2005). A summary on the prefabrication of bridge elements and systems in some leading European countries are discussed below.

2.2.2.1 The Netherlands and Belgium

Prefabrication of bridges is common in the Netherlands and Belgium. One of the most evolving technologies in these countries has been the development of moving systems (Figure 2.10). These systems move bridge components from the prefabrication yard to their final position. The moving systems include methods such as driving, lifting, pushing or pulling, skidding or sliding (Figure 2.10a), and pivoting.

One of the most popular methods has been driving the prefabricated bridge to its final location using the Self-Propelled Modular Transporters (SPMTs), as shown in Figure 2.10b and Figure 2.10c.

The SPMTS can drive and lift prefabricated bridge components by a computer-controlled modular transporter system. The axles and wheels are designed to support a maximum weight of 33 tons in addition to the transporter weight. The wheels can pivot 360 degrees which gives the freedom of movement in all horizontal directions for the transporter (Figure 2.11). The SPMTs can be driven in steeper grades (8 percent). It can be coupled with additional units in the longitudinal and lateral directions to transport bigger and wider prefabricated elements with all units being driven by one driver (FHWA, 2005).

(a) **(b)** **(c)**

Figure 2.10. (a) Sliding a bridge to its final position (b &c) Moving large bridges using SPMTs, after FHWA (2005)

(a) **(b)**

(c) **(d)**

Figure 2.11. Movement capability of an SPMT in all horizontal directions (FHWA, 2005)

2.2.2.2 Germany

The importance of accelerating construction on the federal controlled access highways in Germany (Autobahns) is well accepted. This is due to daily growing traffic volume on the Autobahns. During the bidding process, the contractors are encouraged to shorten the construction times, than those given by the client.

The Federal Highway Research Institute (BASt) is working under the Ministry of Transport to improve the safety, economy, and operational efficiency of the road network in the country. One of BASt objectives for enhancing the bridge infrastructure has been development of environmentally friendly technologies which also offer advantage for the reduced weight. Latest research on the concrete bridges at BASt includes use of exchangeable pre-and post-tensioned cables and high-strength self-consolidating concrete (FHWA, 2005).

A General Circular to the Principal Road Construction Authorities in Germany was issued in 1993. This limited the use of prefabricated, prestressed concrete components only to bridges with single span with less than 35 m in length. Furthermore, monolithic connections between the precast elements and continuity in the longitudinal direction for multi-span bridges were required by the authorities.

In Germany, prefabrication of bridge components was historically limited to only pedestrian bridges. However, recently bridge practitioners have developed design and construction practices which can be utilized for the prefabrication of superstructure components. This includes using cast-in-place concrete decks to make an integral connection between the precast girders to pier cap. This provides longitudinal and transverse continuity for the bridge (Figure 2.12). In this case, the piers are cast-in-place concrete. To construct an integral connection between the beams and cap, beams are temporarily propped first (Figure 2.12a), then the end beams are encased in the cap using cast-in-place concrete. Sometimes it is also common to provide longitudinal post-tensioning tendons over the pier cap for a better continuity (FHWA, 2005).

(a) **(b)**

Figure 2.12. (a) Precast beams are temporarily propped (b) Precast, prestressed concrete beams with integral connection (FHWA, 2005)

In general, the use of prefabricated concrete elements in Germany is limited to situations where a reduced construction time is needed, traffic disruption needs to be minimized, or there is not sufficient space for the formwork. Data from bridge construction in Germany shows that the total cost for the precast concrete bridges is 25 percent more than cast-in-place bridges.

The bridge industry is currently planning to use high-strength self-consolidating lightweight concrete (up to 100 MPa), in beams and bridge decks. For the superstructure elements, partial-depth concrete decks which are prefabricated on steel

or precast concrete beams are a common bridge practice (Figure 2.13). In this type of prefabricated decks, the beams are connected to the prefabricated deck through welded studs (Figure 2.13a). This type of deck system also eliminates the need for an additional formwork for a cast-in-place concrete topping on-site (Figure 2.13b).

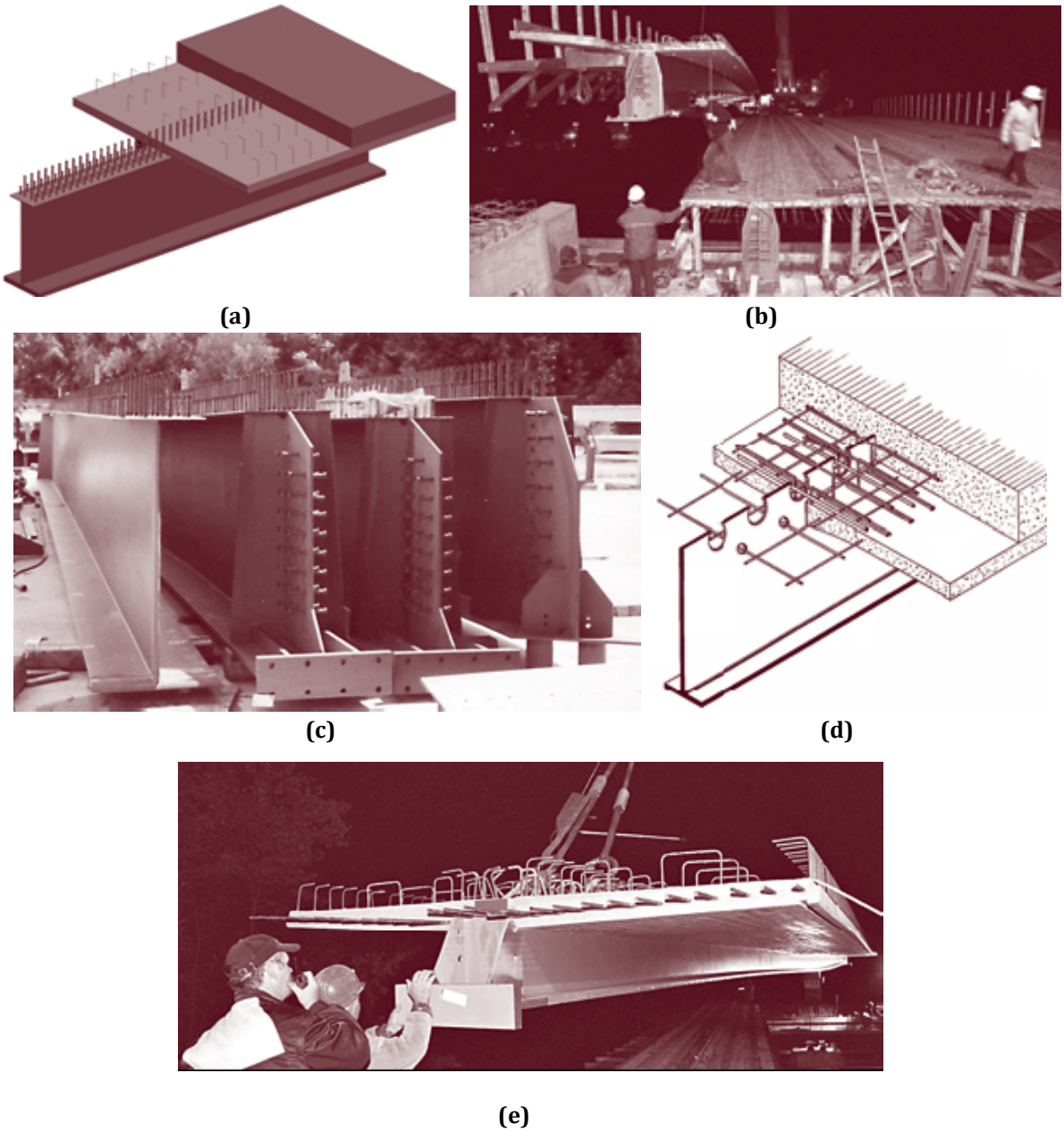

Figure 2.13. Prefabricated partial-depth concrete deck on steel beams (FHWA, 2005)

2.2.2.3 France

The Laboratoire Central des Ponts et Chaussées (LCPC) is a government owned institute that is working under the Ministries of Public Works and Research. The LCPC mainly carries out below tasks:

- Maintains and develops existing infrastructure
- Ensures road user safety
- Mitigates the environmental impacts of the infrastructure during its service life to better control natural hazards
- Optimizes civil engineering structures
- Promotes the introduction of new materials and technologies in civil engineering

In France, the main owners of the road bridges have a priority list of features based on the relative importance for a bridge. Typically, the construction time has the least priority on the list. Prefabrication of bridge elements started after World War Two. Each bridge in France has different dimensions. This means that there are no standardized section sizes for the prefabricated elements.

Pre- and post-tensioning of the bridge superstructure elements is common. Cast-in-place concrete slabs are commonly used for typical pre-tensioned concrete bridges with short spans (less than 30 m). Like Germany, integral connections between the beams and cap and providing continuity for the bridge by placing a cast-in-place diaphragm are also common bridge practices.

A common system for the precast superstructure system for 6-25 m span bridges has been the “Poutre Dalle System”. This system is consisted of shallow, precast, prestressed concrete inverted T-beams, as shown in Figure 2.14. The beams are lined up next to each other and are connected together through a longitudinal joint. The longitudinal joint is made by overlapping the 180 degrees hooks that protrude from the sides of the webs (Figure 2.14c). A cast-in-place concrete diaphragm is then poured on top to provide continuity for the structure.

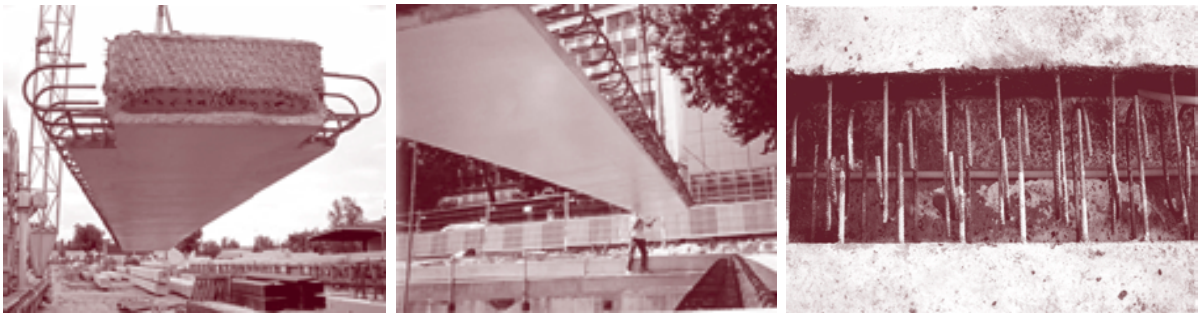

(a) **(b)** **(c)**

Figure 2.14. (a & b) Poutre Dalle System (c) Longitudinal joint with overlapping hooks, after FHWA (2005)

Other popular deck systems include the Dalle Preflex System and the Full-Depth Precast Concrete Deck Panels. The Dalle Preflex System is similar to Poutre Dalle System, however, it uses steel I-beams with beams bottom flanges embedded in a prestressed concrete slab, as shown in Figure 2.15. The units are connected to each other through hooked bars which are running through the beams steel web. Additional longitudinal and transverse reinforcements are provided before pouring a cast-in-place slab.

(a) **(b)**

Figure 2.15. Dalle Preflex System: (a) Single I-beam (b) Double I-beam (FHWA, 2005)

For Full-Depth Precast Concrete Deck Panels, the panels are match cast, epoxied together, and are post-tensioned in the longitudinal direction. Reinforcing bars are extending from the sides of a panel which are then overlapped with the adjacent panel to provide continuity (Figure 2.16a and Figure 2.16b). The panels have pocket holes which are left during the prefabrication. This allows the studs to be welded to the steel beams (Figure 2.16a and Figure 2.16c). The panels are supported on the continuous elastomeric pads. The panels are then grouted to the steel beams through the stud pocket described earlier. The pockets are then filled with concrete.

(a) **(b)** **(c)**

Figure 2.15. Full-Depth Precast Deck Panels: (a) Panels placed next to each other (b) Adjacent panel reinforcing overlapping (c) Panel pocket holes (FHWA, 2005)

In summary, currently bridge practitioners in France are more focusing on the development and use of ultra-high performance concrete (more than 150 MPa in compressive strength) for more durable bridge elements. There have been several examples of using this type of concrete for highway bridges around the country.

2.2.3 Japan

Highways in Japan are managed by the Japanese Highway Public Corporation (JHC) which is owned by the government. JHC responsibilities include construction and operation of the expressways, ordinary roads, and parking facilities. Using rapid construction techniques for the infrastructure projects have high priority in Japan. This is due to reasons such as high project costs and labor, lack of skilled labor due to retirements, traffic disruptions, construction quality, and work zone safety. Japan is gradually lacking more skilled labor for the cast-in-place construction. Therefore, a reduction in number of skilled labors and higher labor costs have led for the development of prefabricated the bridge components (FHWA, 2005).

The precasting technologies in Japan are mostly developed for the superstructure elements. The most popular and recently implemented systems include precast prestressed segmented concrete constant-depth box girders (Figure 2.16 and Figure 2.17), full-depth prefabricated concrete decks (Figure 2.18), hybrid steel-concrete deck systems (Figure 2.19), and orthotropic steel decks.

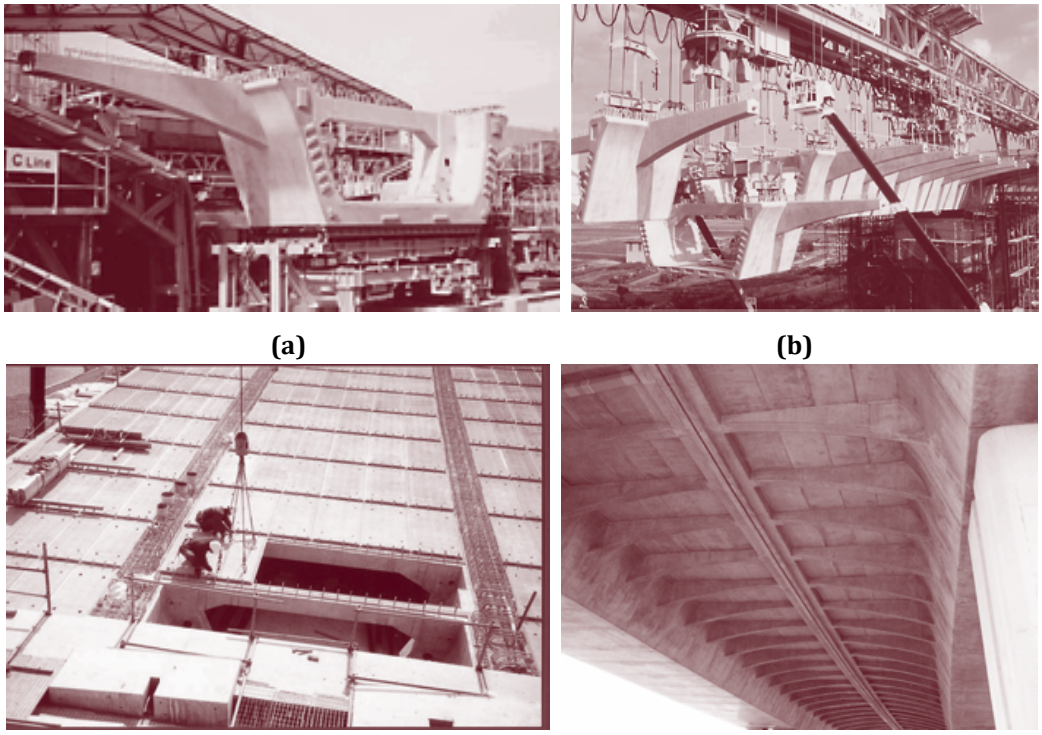

(a) (b)

(c) (d)

Figure 2.16. Precast concrete box girder bridges in Furukawa Viaduct (FHWA, 2005)

Figure 2.17. Precast, prestressed segmented concrete constant-depth girders in Anjo Viaduct (FHWA, 2005)

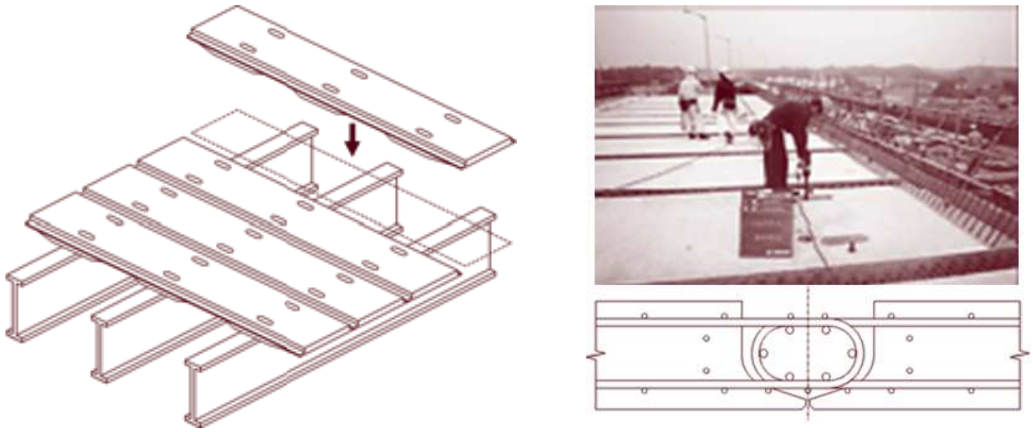

(a) (b)

Figure 2.18. Full-depth prefabricated concrete decks, transversely pre-tensioned: (a) Placing panels (b) Longitudinal joints between the panels, after FHWA (2005)

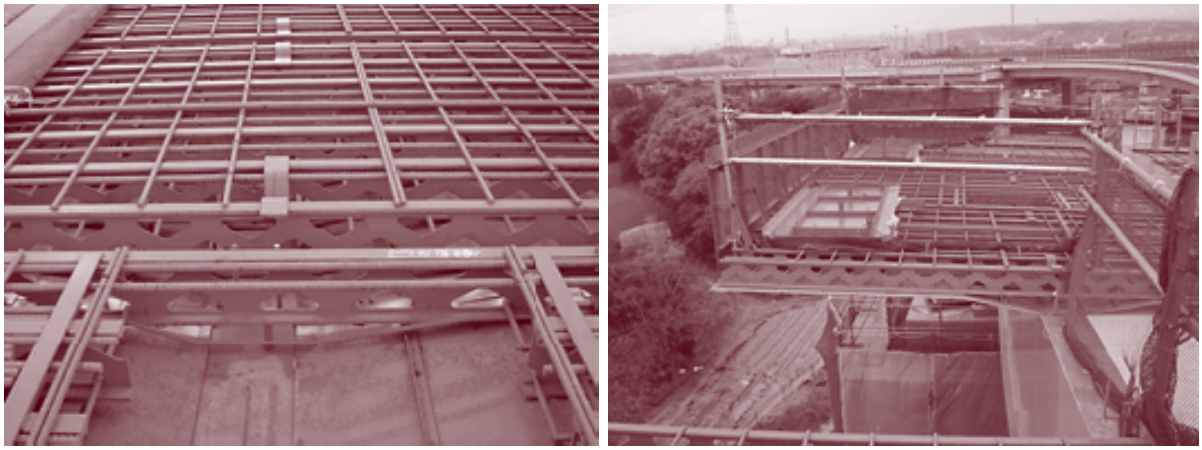

Figure 2.19. Hybrid steel-concrete deck (FHWA, 2005)

The Mitsuki Bashi Method (Three-Month Bridge) is a rapid construction technique for bridges in urban environment in Japan. This method was developed by Mitsui Engineering and Shipbuilding Co Ltd. The bridge components in this system include steel hull footing, steel bridge pier and cap, and a steel box girder superstructure, as shown in Figure 2.20.

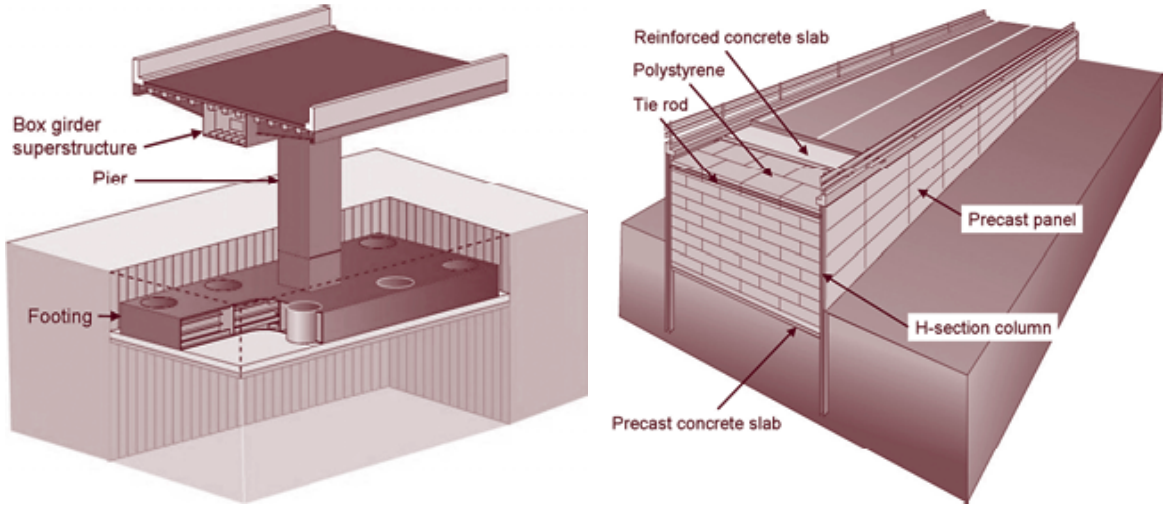

(a) **(b)**

Figure 2.20. Mitsuki Bashi Method: (a) Construction of substructure and superstructure systems (b) Construction of the bridge approaches (FHWA, 2005)

The estimation for the shortest construction time using this method is about 3.5 months for a 400 m crossover. The construction sequence for this system is as follows:

1. Excavating the ground for footing and placing the steel hull footing. The footing comes with a short pier and holes for the piles. This allows driving the piles while steel pier and cap are installed
2. Pouring concrete in the hull to fill the foundations
3. Assembling the main span offsite and then transporting it to the construction site
4. Constructing the bridge approaches as shown in Figure 2.20 (b)
    A. Columns with H-section are driven on the side of the final approach
    B. Soil with the identical dead weight as the approach portion is excavated
    C. A precast concrete slab is placed around the columns in the excavated portion
    D. Installment of expanded polystyrene above the slab and placement of the precast panels between the columns
    E. Construction of a concrete slab and riding surface on top

Another recently developed accelerating construction method in Japan is the Sumitomo Precast form for resisting Earthquakes and for Rapid construction (SPER). This method was developed by Sumitomo Mitsui Construction Company for short and tall bridge piers in seismic regions. In this methodology, the 100 mm thick stay-in-place precast concrete panels are initially used as the formwork, then they are subsequently utilized as the structural elements (FHWA, 2005). For construction of short solid piers, the concrete panels comprised of pre-installed cross ties (Figure 2.21a and 2.21b) are used as the exterior formwork. The segments sit on top of each other and are connected through epoxy joints. After assembly is finished, the segments are filled with cast-in-place concrete to generate a solid section.

For construction of tall hollow pier sections (Figure 2.21c), two forms (inner and outer) are used to make a hollow section, as shown in Figure 2.21d. The hollow sections are made on site using two channel-shaped sections to reduce weight (Figure 2.21d and Figure 2.21e). Longitudinal and transverse rebars are placed before the concrete is cast.

(a)

(b)

(c)

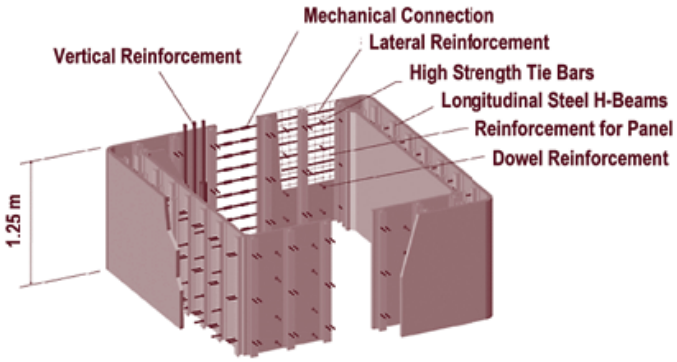

(d)

(e)

Figure 2.21. SPER Method: (a & b) Precast panels for solid short piers (c) Tall hollow piers (d & e) Segment detailing for tall hollow piers, after FHWA (2005)

This type of methodology recommends using high-strength concrete and reinforcing bars to facilitate the on-site construction and to prevent from the rebar congestion. The methodology incorporates special details to safely transfer the gravity and lateral loads through the elements along the load paths.

Overall, the SPER Method is a semi-prefabricated technology, which allows a reduction of 60-70% in the construction time when compared to a conventional cast-in-place construction. Most of the savings in construction time comes from the elimination of formwork and reduction in placement time of the rebars (FHWA, 2005).

A similar concept to SPER Method was proposed and tested in the United States at the State University of New York at Buffalo (Marson and Bruneau, 2004). The technology is using steel tubes for the formwork and subsequently as the structural shells. The shells and the cast-in-place concrete infill are designed and detailed to develop a composite action. The seismic performance of this composite system is similar to a conventional cast-in-place construction (e.g. formation of plastic hinges).

In summary, Japan shares similar trends in use of prefabricated substructure elements as some European countries. Precast segmented bridge piers are not very popular. In 2005, there were only four bridges for which the SPER method was used.

2.2.4 Taiwan

In Taiwan, the most popular prefabricated substructure system has been the segmental bridge piers. This type of system has already been used in several bridges around the country. However, the bridges are designed to respond elastically during a design level earthquake. This means the pier sections had to be significantly large (Figure 2.22).

Examples of the prefabricated segmental piers in Taiwan include the Chang-Shou Bridge and the Yu-Le Bridge, as shown in Figure 2.23a and Figure 2.23b, respectively. Both bridges were constructed in 1987. The concrete segments were hollow sections and sit on top of each other. After assembly of the segments, steel bars were used as the unbonded post-tensioning to hold the segments together. The segmental substructures were designed to respond elastically during a design level earthquake. Following the 1999 Chi-Chi Earthquake, there was no damage observed to these bridge piers (Chang et al., 2012).

Figure 2.22. Prefabricated segmental piers, after Chang et al. (2012)

(a) **(b)**

Figure 2.23. Prefabricated segmental piers in Taiwan: (a) Chang-Shou Bridge (b) Yu-Le Bridge (Ou et al., 2012)

Recently, there have been some applications of precast bent system in Taiwan. This includes the Neihu MRT project in Taipei in 2007. The bridge components consisted of precast caps, U-shaped girders, and precast box girder segments (Figure 2.25). The piers were cast-in-place concrete (Figure 2.24a). The column to cap connection comprised of an internal circular shear key and on-site welded connection around the interface (Figure 2.24b). A fatigue testing under the gravity loads on a similar hammerhead specimen was carried out at the National Center for Research on Earthquake Engineering (NCREE) in Taipei. There was no damage to the specimen and the column to cap connection (Figure 2.24c).

In summary, there have been several applications of ABC in Taiwan in the last few decades. More research programs are currently under way to develop cost competitive and earthquake resilient prefabricated segmental substructure systems. Further details on the state-of-the-art research on ABC in Taiwan are provided in Section 2.3.2.

(a) (b) (c)

Figure 2.24. Neihu MRT: (a) Lowering the precast cap, internal shear key is visible (b) On-site welding of the connection (c) Fatigue testing at the NCREE (Chang et al., 2012)

(a) (b)

Figure 2.25. Neihu MRT precast girders: (a) U-shaped (b) Box segments

2.2.5 New Zealand

Currently, the state highway network in New Zealand includes about 11,000 kilometers of roads, more than 4,000 bridges, and a large number of culverts. The combined length of the bridges on the state highway network is over 140 kilometers. Reinforced concrete bridges and culverts make up more than 80% of the combined length and almost 75% of the bridges (Palermo and Mashal, 2012). In New Zealand, the cast-in-place concrete construction is used twice as much as the precast concrete. Recently, the use of precast concrete is constantly growing around the country. Most of the old reinforced concrete and timber bridges constructed between 1930 up to 1950 are being replaced with new bridges incorporating precast concrete decking systems. An example of where this is happening is the city of Christchurch, as documented in "A City of Bridges" (Ince, 1998).

History of precasting bridge superstructure in New Zealand goes back to the 1970's. Back then, the Ministry of Works (MOW) published several standard precast girder sections, such as twin hollow-core, I-beam, and U-shaped, for short span bridges around the country. The main objectives behind precasting of the superstructure elements were cost saving in design time and the use of standard moulds by prefabricators (Gray et al., 2003).

A survey from the precast prestressed bridge beam manufacturers was conducted in early 2000's. Data included 102 newly constructed bridges with precast superstructure systems which consisted of double hollow-core, single hollow-core, I-beam and U-shaped with deck slab, gull wing, and spaced box sections. The survey indicated the popularity of double hollow-core bridge deck around the country. This was due to flexibility in design and economic savings associated with this type of section.

The single hollow-core was popular in some northern parts of New Zealand's South Island and central parts of the North Island. The I-beam and U-shaped girders were common for longer span bridges. The single rectangular cell box section which is a variation to double hollow-core, was widely used in the North Island on Route PJK in Tauranga (Gray et al., 2003). Figure 2.26 presents a summary of the survey. The total production length of all types of sections were 61,400 meters. The percentages are based on linear meters of each beam type.

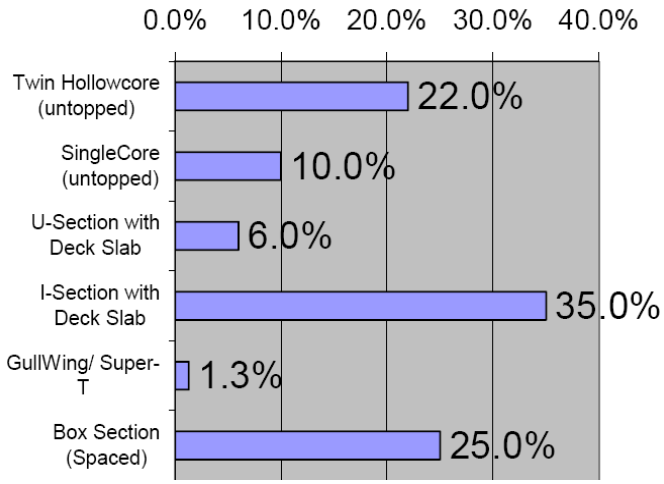

Figure 2.26. Summary of beam types produced in New Zealand, after Gray et al. (2003)

Nowadays, New Zealand bridges with short span lengths (15-30 m) are typically constructed using precast decks which can be either continuous or simply supported, and cast-in-place concrete substructure (piers and foundations). If a strict functional requirement leads to a bridge span greater than 30 m, a reinforced concrete solution which uses a cantilevered or launched construction technology becomes the primary and preferred method of construction. Figure 2.27 shows a typical example of bridge with precast deck and cast-in-place piers in New Zealand.

(a) **(b)**

Figure 2.27. Typical New Zealand bridge practice: (a) cast-in-place substructure and precast superstructure (b) Typical completed bridge (Palermo and Mashal, 2012)

In 2008, the New Zealand Transportation Agency (NZTA) published an updated report on "Standard Precast Concrete Beams" (NZTA Report 364, 2008). This report primarily includes four types of precast superstructure systems for short-to-medium span

bridges. A summary of the precast deck systems from the NZTA Report 364 (2008) is presented in Figure 2.28 to Figure 2.31.

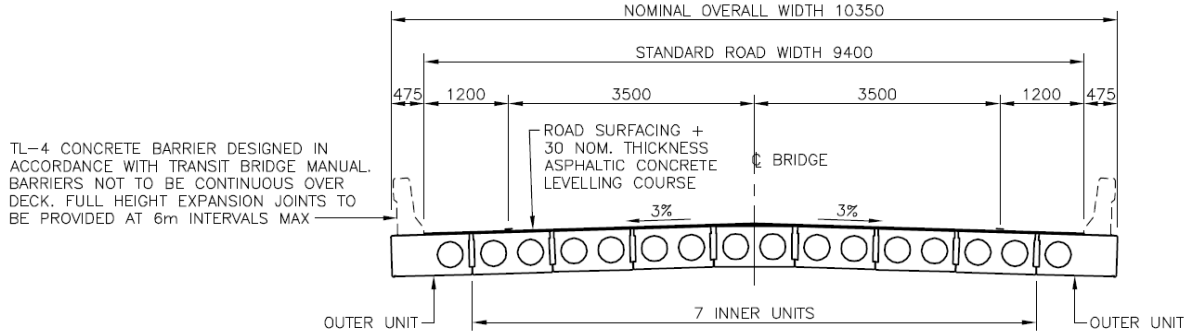

Figure 2.28. Double hollow-core precast deck (up to 14 m span)

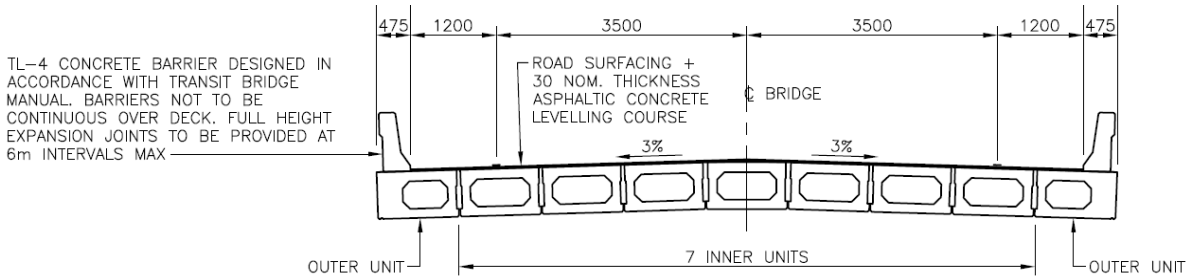

Figure 2.29. Single hollow-core precast deck (up to 22.5-25 m span)

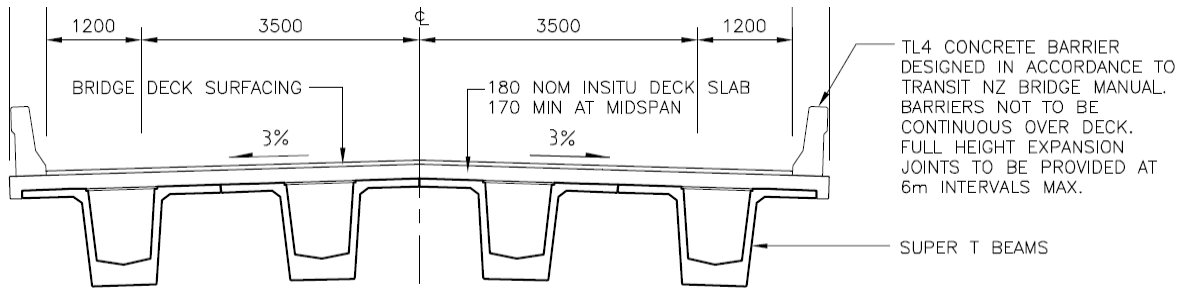

Figure 2.30. Super T-section precast deck (up to 30 m span)

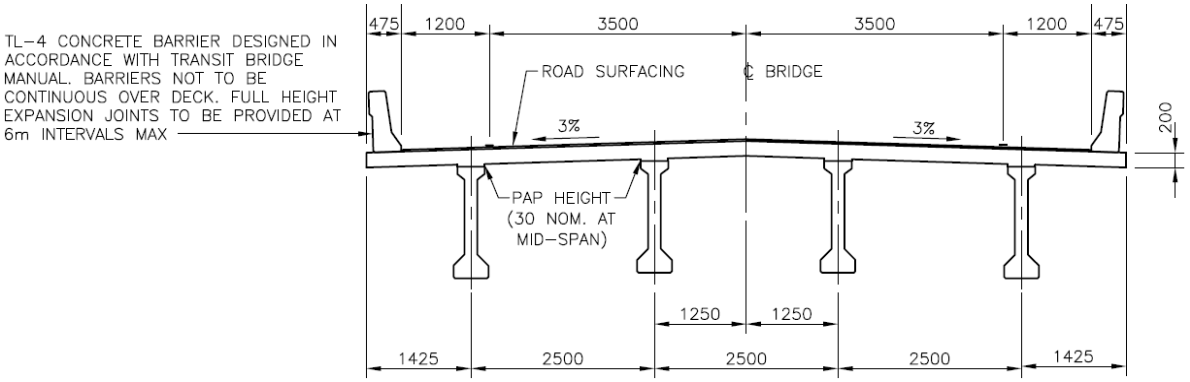

Figure 2.31. I-section precast deck (up to 24 m span)

In summary, the bridge substructures in New Zealand are mainly dominated by conventional cast-in- place concrete. Despite growing market size in the country, there have not been sufficient prefabrication facilities developed for precasting of the piers.

New Zealand bridge practitioners feel more confident to adopt a cast-in-place (monolithic) substructure which accepts damage and post-earthquake repair costs following a seismic event. The NZTA Bridge Manual Third Edition (NZTA, 2013) presents ductility values (μ) and locations of plastic hinges in the piers as part of seismic design procedure for monolithic bridges with different substructure configurations, as shown in Figure 2.32. The NZTA Bridge Manual briefly mentions other solutions for seismic design of earthquake resistant bridges such as bridges with rocking foundations and use of dissipative devices.

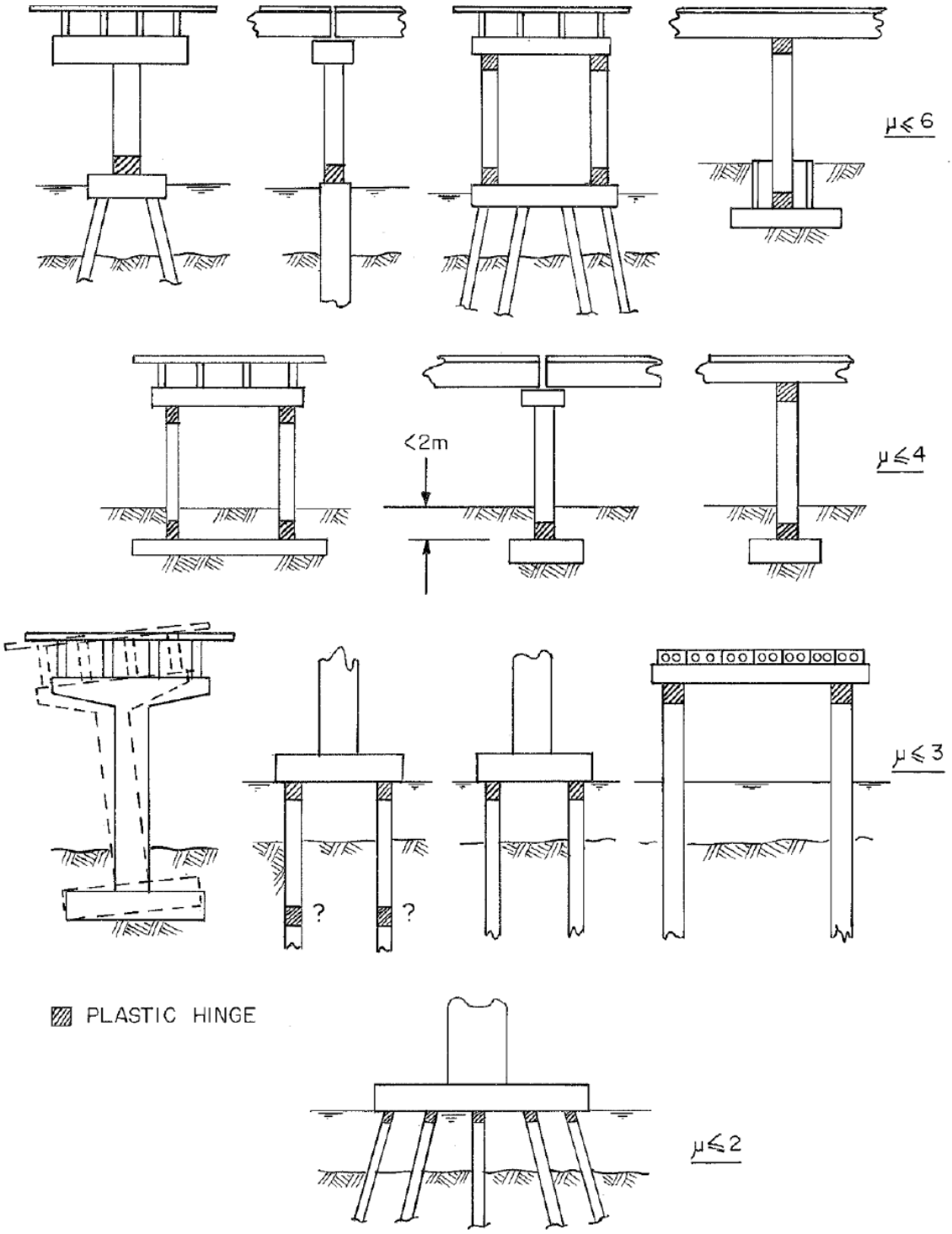

Figure 2.32. Location of plastic hinges and the corresponding maximum allowable values for displacement ductility factors (μ) for various bridge substructure systems, after NZTA Bridge Manual (2013)

2.3 State-of-the-Art Research on ABC in Seismic Regions

Over the last twenty years, there have been many research studies on ABC in seismic regions. In particular, these studies were conducted in the United States, Japan, Taiwan, and New Zealand. The studies have been focusing on the development of earthquake resilient connections between the prefabricated concrete elements. This includes connections between the precast members for both buildings and bridges in high seismicity. A summary of the recent research on ABC in seismic regions from around the world are presented in the following sections.

2.3.1 Emulative Cast-In-Place Connections

Marsh et al. (2011) presents a summary of the connections that can be used for ABC in moderate-to-high seismic regions. Some of these connections are developed to emulate the seismic performance from a monolithic connection such as formation of plastic hinges (Park and Paulay, 1975). In Chapter 1, this solution was named "ABC High Damage". A brief description of each connection is presented here.

2.3.1.1 Bar Coupler Connections

This type of emulative cast-in-place connection is used to splice two rebars at their end points. The coupler allows the axial force to be transferred from one bar to the other which makes it function similar to a welded butt splice. In this type of connection, the transfer of tension is more critical. There have been different types of couplers developed over the past years. Examples includes threaded sleeve, headed bars with separate sleeves, external clamping screws, and grouted sleeve, as shown in Figure 2.33.

Bar couplers can be used in locations such as footing to column, splices between the column segments or cap beam segments, and column to cap beam connections. From all types of coupler bars available in the market, the grouted sleeve connections are widely used in bridges in the state of Utah in the United States. The state of Utah has been known to have moderate-to-high seismic regions. Grouted Sleeve connections are part of the standard Utah Department of Transportation (UDOT) precast substructure details. The UDOT Precast Substructure Elements Manual (UDOT, 2010) and Precast Piers and Footings (UDOT, 2009) provide details on the use of grouted sleeve connections.

A recent example for the application of grouted splice sleeves in the United States is the Edison Bridge in the State of Florida (Figure 2.7). Grouted sleeve connections are also widely used in buildings throughout the United States. However, the couplers ability to sustain inelastic cyclic deformations has not been fully investigated yet.

More details on bar coupler connection can be found in Paulson (1991), Fouad et al. (2006), Culmo (2009), and Bromenschenkel (2010). However, additional research is needed to document drift capacity, influence of coupler on bar strain distribution, and coupler's location and orientation on inelastic performance. Caltrans ABC Strategic Plan (Chung et al., 2008) Phase-I includes further research into grouted splice sleeve connections. The solutions will be focusing on emulative cast-in-place technologies which accept damage in the piers during an earthquake. The research work will include characterization of the ultimate behavior and performance of the coupler bar connections in high seismicity.

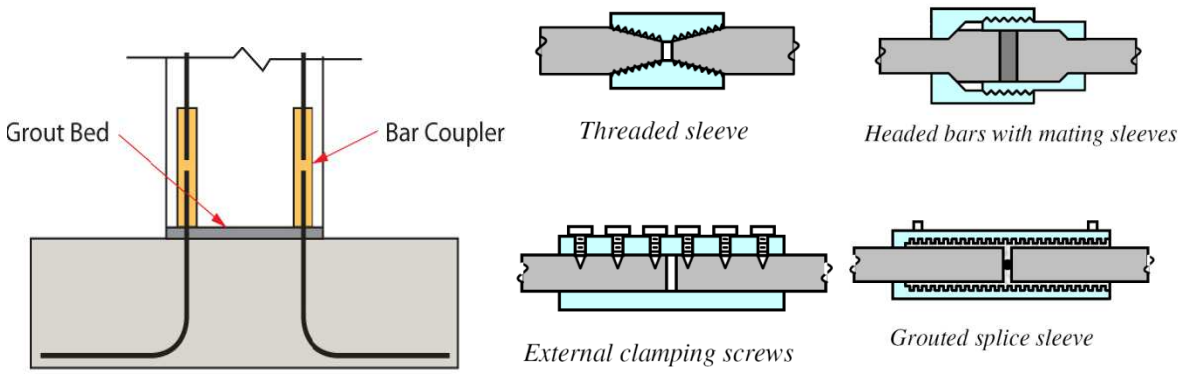

Figure 2.33. Bar coupler connections (Marsh et al., 2011)

2.3.1.2 Grouted Duct Connections

In this type of emulative cast-in-place connection, the starter bars from one member is extended into the ducts which are placed during the prefabrication inside the second member, as shown in Figure 2.34a. The ducts are later fully grouted using high-strength mortar to secure the connection between the precast members. Once the grout is hardened, it confines the bars inside the ducts. The load transfer mechanism in grouted duct connection is different from the coupler bars, as discussed before. In grouted duct connection, the force is transferred from the starter bars to the surrounding concrete and to the longitudinal bars lap-splice outside the duct.

Grouted duct connection can be used for pile to pile cap, spread footing or pile cap to pile, column to cap beam, and for splices between the column cap beam segments. The grouted duct connection has already been used in non-seismic and seismic regions (Figure 2.34d). The Utah DOT is currently developing standard connection details between the prefabricated elements. One of the connections includes the grouted duct for the column to footing and column to cap connections (Figure 2.34e). There is a significant amount of research done on this type of connections. Past research works include Matsumoto et al. (2001), Brenes et al. (2006), Riva (2006), Culmo (2009), Pang et al. (2008, 2010), Haraldsson et al. (2011), and Restrepo et al. (2011).

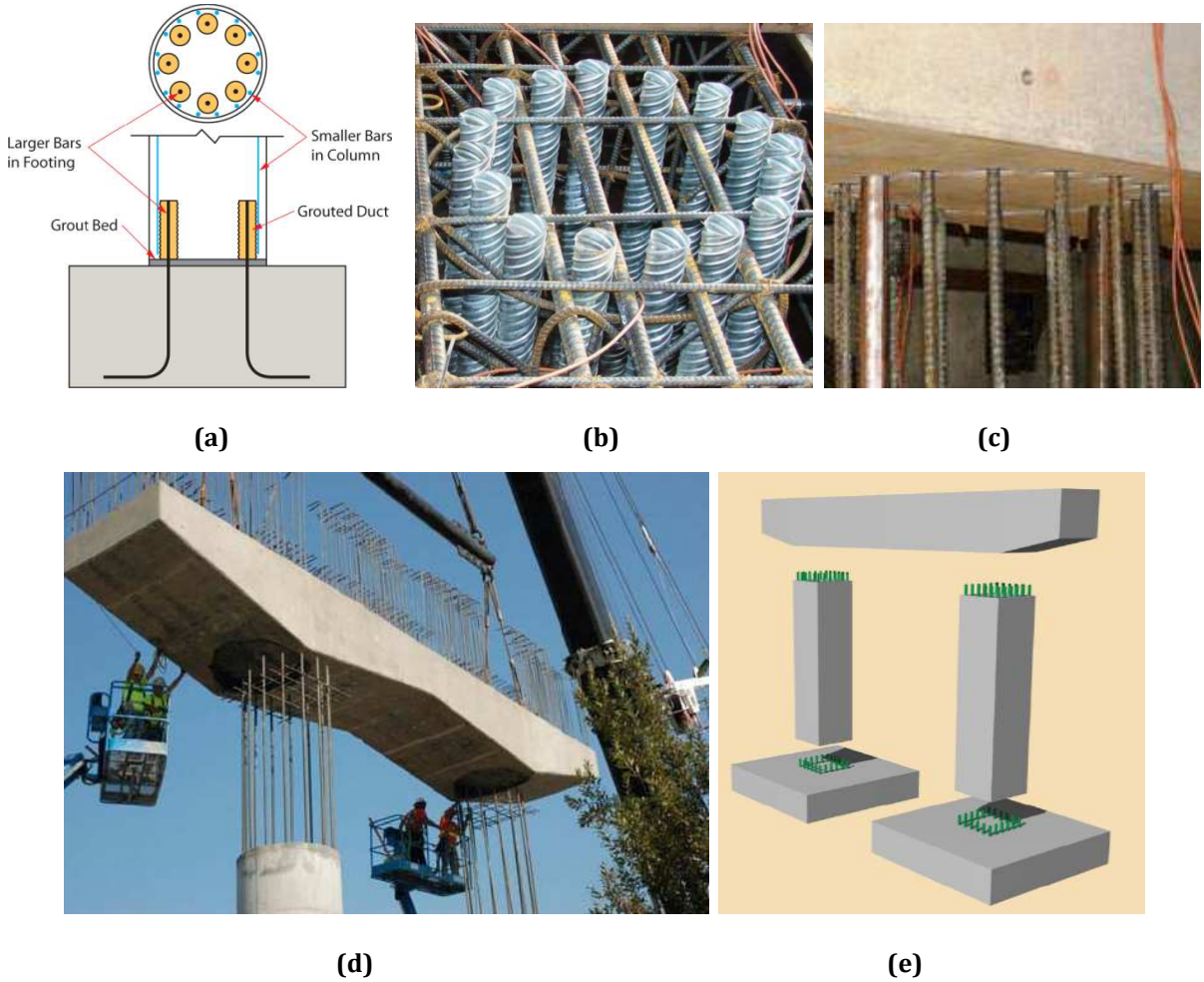

(a) **(b)** **(c)**

(d) **(e)**

Figure 2.34. (a) Typical grouted duct connection (b) Ducts left inside the member at the prefabrication yard (c) Guiding starter bars from one precast member to other (d) Grouted duct lower stage cap erection for Washington DOT, SR 520/SR 202 Bridge (e) UDOT concept for grouted duct connections in a precast bent, after Marsh et al. (2011) and Matsumoto (2009)

The grouted duct connection has also been a common construction technique for connection of precast panel to footing connections in New Zealand (Palermo and Mashal, 2012). However, most of these applications have been limited by using the grouted duct connection at the capacity protected zones in a structure. Therefore, use of grouted duct connection in the plastic hinging zones of a structure in high seismicity has been limited.

Caltrans Strategic Plan (Chung et al., 2008) Phase-I includes more research into grouted duct connections. More research on grouted duct connections is needed to document issues such as influence of duct size and effects of location of duct on anchorage length and cyclic performance, lap splicing response under cyclic loading, duct materials, off-center and group pull-out effects, and reinforcing bedding layer.

2.3.1.3 Pocket connections

This type of emulative cast-in-place connection can be constructed by extending out bars from column or pile and inserting them into a preformed pocket inside the other precast member, as shown in Figure 2.35. Grout or concrete closure pour is then used to secure the connection.

Pocket connections can be used in locations such as column to cap beam, footing to column, and pile to pile cap connections. Past research on the pocket connections showed good performance of the connection and their potential applications in seismic regions. The downside of the pocket connections is the additional curing time which makes it less attractive for an accelerated construction. Perhaps, this can be prevented by using especial type of grout or concrete which strengthens rapidly.

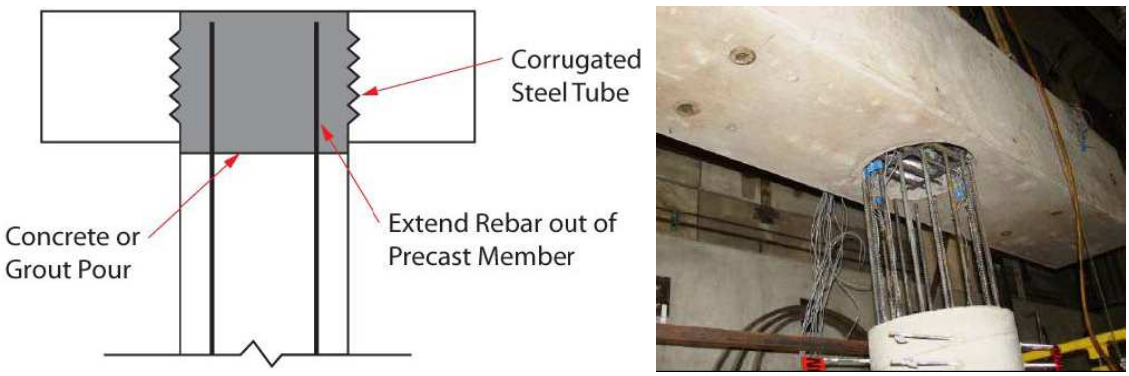

Figure 2.35. Pocket connection, column to cap beam (Marsh et al., 2011)

More details on this type of connections can be found in Matsumoto (2009), Restrepo et al. (2011), and Karapiperis et al. (2010). However, further experimental work is needed to develop design specification, joint behavior, and performance limit states.

2.3.1.4 Member Socket Connections

The member socket is another type of emulative cast-in-place connection which is formed by embedding a precast element inside another element. The second element can be either precast or cast-in-place concrete. If both elements are precast, then the connection is secured using a grout or concrete closure pour in the preformed socket (Figure 2.36a). The other solution is to have the second element cast around the first one, as shown in Figure 2.36b.

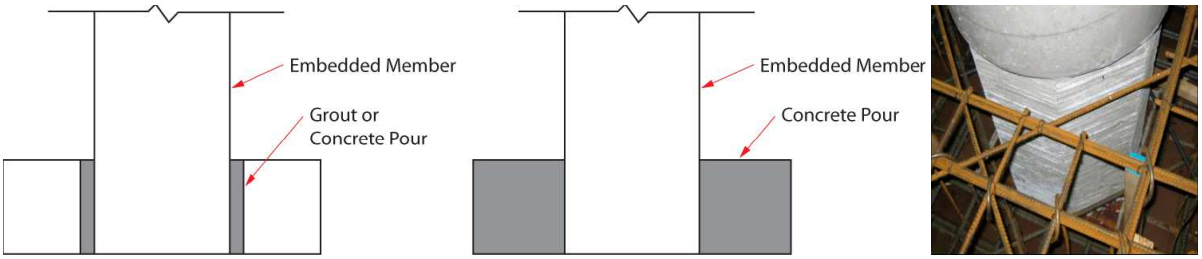

(a) **(b)** **(c)**

Figure 2.36. Member socket connection: (a) Precast column and footing (b & c) Precast column and cast-in-place concrete tested at the University of Washington, Seattle (Marsh et al., 2011 and Haraldsson et al., 2011)

This type of connection can be used for footing to column, column to cap beam, and pile to pile cap connections. Recently, this type of connection was used for footing to column connection of a precast bent on Interstate Highway 5 in the State of Washington (Figure 2.37). The connection was previously investigated and experimentally tested by Haraldsson et al. (2011) at the University of Washington, Seattle (Figure 2.36c). More details on the socket connection can be found in Riva (2006).

Another type of member socket connection includes the Concrete-Filled Steel Tubes (CFST). Past research on CFST include Marson and Bruneau (2004), Kingsley (2005), Zhu et al. (2006), Nelson et al. (2008), Roeder et al. (2009), and Culmo (2009). Additional experimental and analytical modeling is required to develop load transfer mechanisms in the socket, construction tolerances, durability, and design guidelines.

(a) **(b)** **(c)**

(d) **(e)**

Figure 2.37. Member socket connection on I-5 in the State of Washington: (a) Bent connections(b & c) Precast column and cast-in-place footing (d) Column to cap grouted duct connection (e) Completed bridge, after Haraldsson et al. (2013) and FHWA (2012)

2.3.1.5 Cast-In-Place Connections

The cast-in-place connections are sometimes referred as "Integral Connections". They are used to form joints between the precast elements at the superstructure level. This type of connection is used in the integral cap beam or at the diaphragm to girder connection for steel and concrete composite bridge structures. The integral connection used to be constructed using traditional cast-in-place methods. However, for ABC the connections may require use of steel or precast concrete stay-in-place formwork. The formwork can be filled later with reinforced concrete which integrates different bridge components in the joint region.

Figure 2.38a shows an example of the cast-in-place integral cap beam that supports the concrete girders with a lower stage cap beam. The construction sequence for creating an integral connection is to first construct the lower stage cap beam, then infill it later after erection of the superstructure. The connection provides continuity for the longitudinal positive and negative moment during seismic loading. In ABC, the lower

stage of the cap beam can be precast. This is possible by using any of the emulative connections described earlier. Figure 2.38b shows an example of a precast lower stage cap for San Mateo Bridge in the State of California.

Integral connection can be used in locations such as, pile to pile cap, spread footing or pile cap to column. This type of connection presents potential application for connections of columns, cap beam, and bridge superstructure.

(a) **(b)**

Figure 2.38. (a) Integral connection with precast girders (b) San Mateo Bridge precast girders, the upper stage form was built on-site (Marsh et al., 2011)

More details on this type of connections can be found in Sritharan et al. (1999, 2001), Holombo et al. (2000), Sritharan (2005), NCHRP Report 681 (Restrepo et al., 2011), Bromenschenkel (2010), Snyder and Sritharan (2010a, 2010b), and Sritharan et al. (2014). It should be noted that integral connection was not specifically developed for ABC. Therefore, it requires re-detailing since the cap for ABC in seismic regions is a capacity protected element.

2.3.2 Semi-Emulative Cast-In-Place Connections

The recent work by Ou et al. (2012) proposes a new type of precast concrete segmental pier for ABC in seismic regions. The lower region of the segmental column is Cast-In-Place (CIP) construction while the upper portion is unbonded post-tensioned precast concrete segments, as shown in Figure 2.40a. In this type of construction, initially a rebar cage for the CIP region of the column is provided on top of the foundation cage, as shown in Figure 2.39. The cage uses U-shaped loop steel ducts for the post-tensioning

tendons. While casting the foundations, the lower portion of the cage is also cast. Subsequently, formwork is placed around the CIP region of the column and the first precast segment (S1) is positioned on top of the rebar cage. The segment will be supported by the steel brackets which are located on top of the formwork. The upper part of the rebar cage is extended into a recess which is located in the bottom of the first segment. Finally, the formwork for CIP region and the hollow (recess) core of the segment are filled with CIP concrete. Precast segments are assembled on top of each other with the unbonded post-tensioning running through the duct inside the segments. After positioning the last precast segment, the segmental column is post-tensioned to secure the segments.

A tall segmental column (Figure 2.40c and Figure 2.40d) was constructed and experimentally tested. The specimen was detailed such that under a design level lateral loading, the lower cast-in-place region of the column forms a plastic hinging mechanism. The height of the cast-in-place region is selected such that it simulates a conventional plastic hinge mechanism, as shown in Figure 2.40a and Figure 2.40b. The upper precast segments are designed to remain elastic .

Experimental results from quasi-static testing showed great ductility and energy dissipation for the segmental column (Figure 2.41e). The CIP region of the column developed a plastic hinging mechanism. Figure 2.41a through 2.41d presents damage progression in the specimen at different drift ratios.

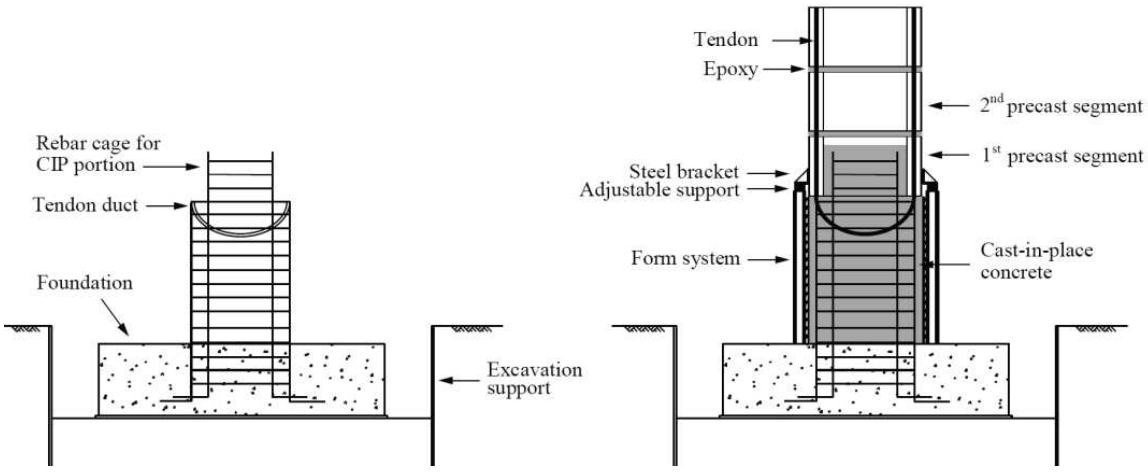

Figure 2.39. Joint construction technique for the precast segmental column

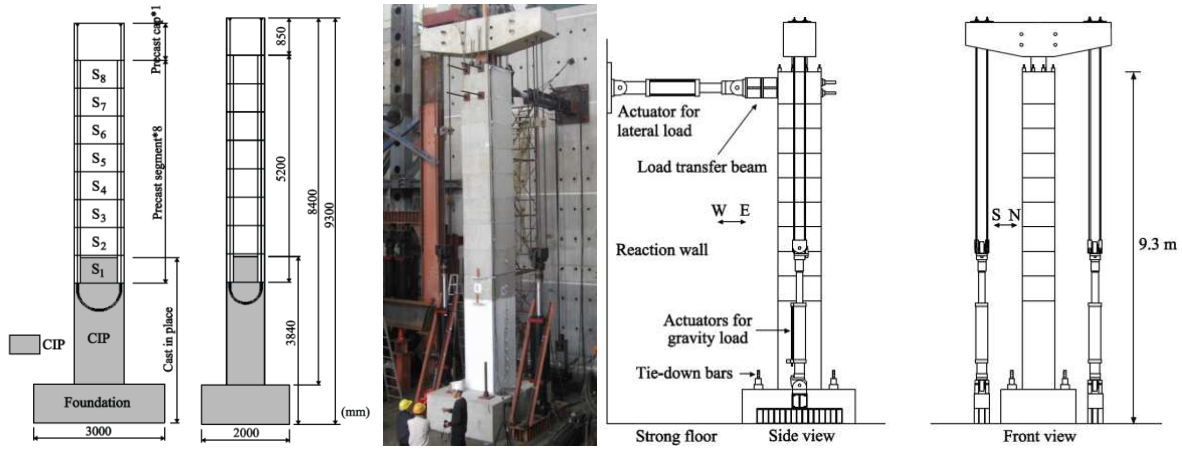

(a) (b) (c) (d)

Figure 2.40. Precast segmental pier (a) Section view (b) Elevation view (c) Assembled column in the lab (d) Test setup, after Ou et al. (2012)

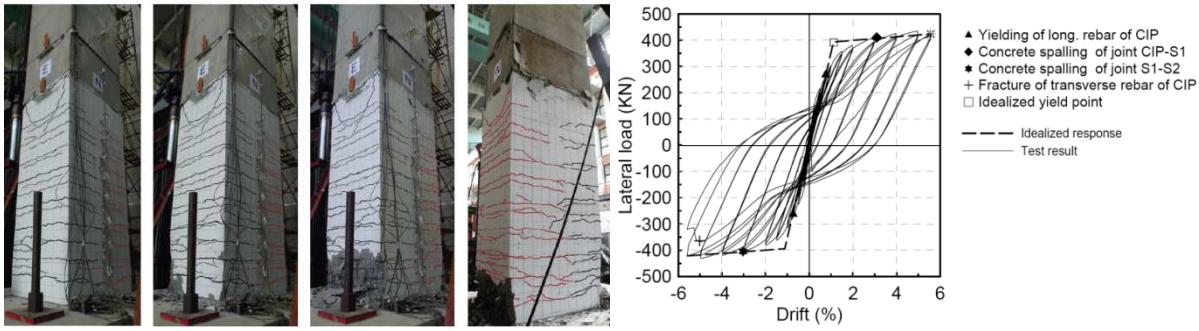

(a) (b) (c) (d) (e)

Figure 2.41. Testing observation and results (a) Cracks at 3% drift (b) Concrete spalling near the base at 5% drift (c) Fracture of the stirrups and buckling of longitudinal bars at 5.6% (d) Concrete spalling around the corners of the first segment (e) Force-drift hysteresis showing performance limit states on an idealized bilinear backbone curve

In summary, the semi-emulative cast-in-place solution provides the advantage for prefabrication of the segments. The unbonded post-tensioning through the segments also provides self-centering of the segments following a big earthquake. However, since the design philosophy here is based on limiting the damage only to the CIP region of the column, residual drift and extensive damage at the plastic hinging zones are the downsides of this type of solution. For a real life bridge with this technology, the bridge may remain drivable, but with a delayed functionality following a design level earthquake. The repair work may require the whole replacement of the bridge for the long-term service and resilience.

2.3.3 Non-Emulative Cast-In-Place Connections

This type of connections includes the rocking pier systems and emerging technologies. The history and recent developments on the rocking pier systems and emerging technologies, are discussed in detail as follows.

2.3.3.1 Rocking Pier Systems

The history of rocking structures goes back to ancient Roman times. Historical structures such as piers of marble columns in Acropolis and Delphi in ancient Greece incorporated rocking segmental sections (Pampanin et al., 2010).

The concept for pure rocking was initially introduced by Housner (1963). A pure rocking motion results in a negative stiffness of the system which elongates the natural period of the structure. Therefore, it provides a sort of seismic isolation for the structure which allows the structure to deflect, rather than restraining the displacement and rotation at the critical joints. Pure rocking does not provide any supplementary dissipation in the system, apart from that resulting from the inherent and contact damping. Therefore, it can be simply thought as having a non-linear spring hysteresis, unless there are other sources of supplementary dissipation in the system. Since the development of pure rocking, a number of bridges were designed and constructed using this technology.

Beck and Skinner (1974) adopted the rocking concept for the seismic design of the South Rangitikei Viaduct in the North Island of New Zealand (Figure 2.42a). The Viaduct was constructed in 1981. The Rangitikei Viaduct is the fourth highest and second longest railway viaduct in New Zealand. The Viaduct is 315 m long with 78 m high piers. It is an impressive all-concrete structure with twin-shafted vertical piers carrying a continuous prestressed hollow box superstructure of six spans.

The Viaduct is an example of isolation through controlled base-uplift during a transverse rocking action. When an earthquake occurs, the pier bases can lift up to 130 mm to allow energy and pressure to shift from one pier leg to the other. The rocking action is supplemented with energy dissipation through the use of large torsional energy dissipaters which are located at the base of the piers (Figure 2.42b and Figure

2.42c). This system avoids formation of plastic hinges in the bridge piers under a big earthquake while it provides self-centering of the bridge through gravity loads.

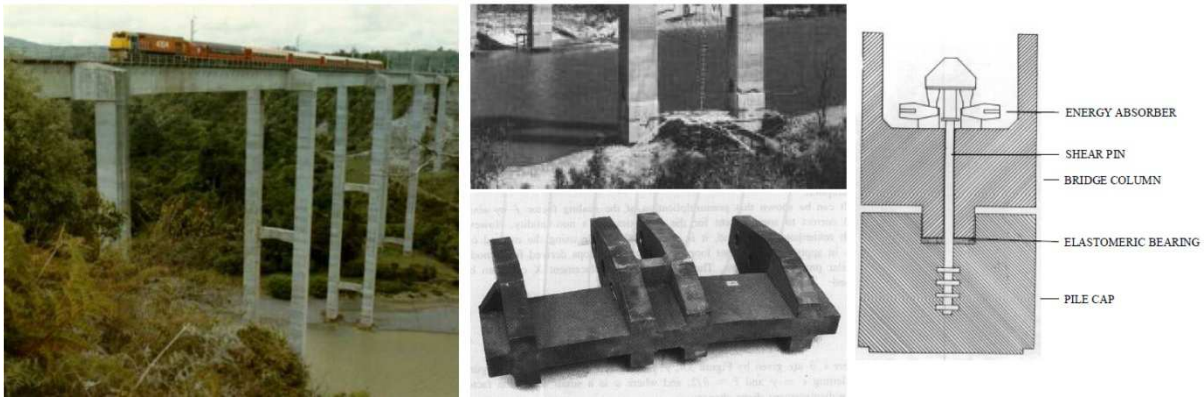

(a) **(b)** **(c)**

Figure 2.42. (a) Rangitikei Viaduct in New Zealand (b) Torsional-beam dissipater with transverse loading arms used at the base of the piers (c) Schematic for the stepping piers, after Beck and Skinner (1974)

Mander and Cheng (1997) based on the concept for "Damage Avoidance Design", proposed a modular type precast bridge construction system in seismic regions. In this concept, the bridge is free to rock under the lateral loading. The piers incorporate special detailing to eliminate the damage during an earthquake.

One option in this system is to add unbonded post-tensioning to increase the moment capacity and self-centering of the piers, however, it is not a requirement. The damping in the system relies on the impact alone during rocking. Another option to increase the contact damping is to add a rubber interface under the piers. In order to investigate the seismic performance for such a system, experimental testing was carried out on a nearly full-scale pier specimen, as shown in Figure 2.43. As expected under the lateral loading, the pier started rocking and behaved in an elastic fashion with minimal damage and strength degradation (Figure 2.43a and Figure 2.43b).

Force-displacement hysteresis plots for the rocking and rocking combined with post-tensioning cases are shown in Figure 2.43c and Figure 2.43d, respectively. A numerical model to capture the seismic performance of the system was also proposed which was in good agreement with the experimental results.

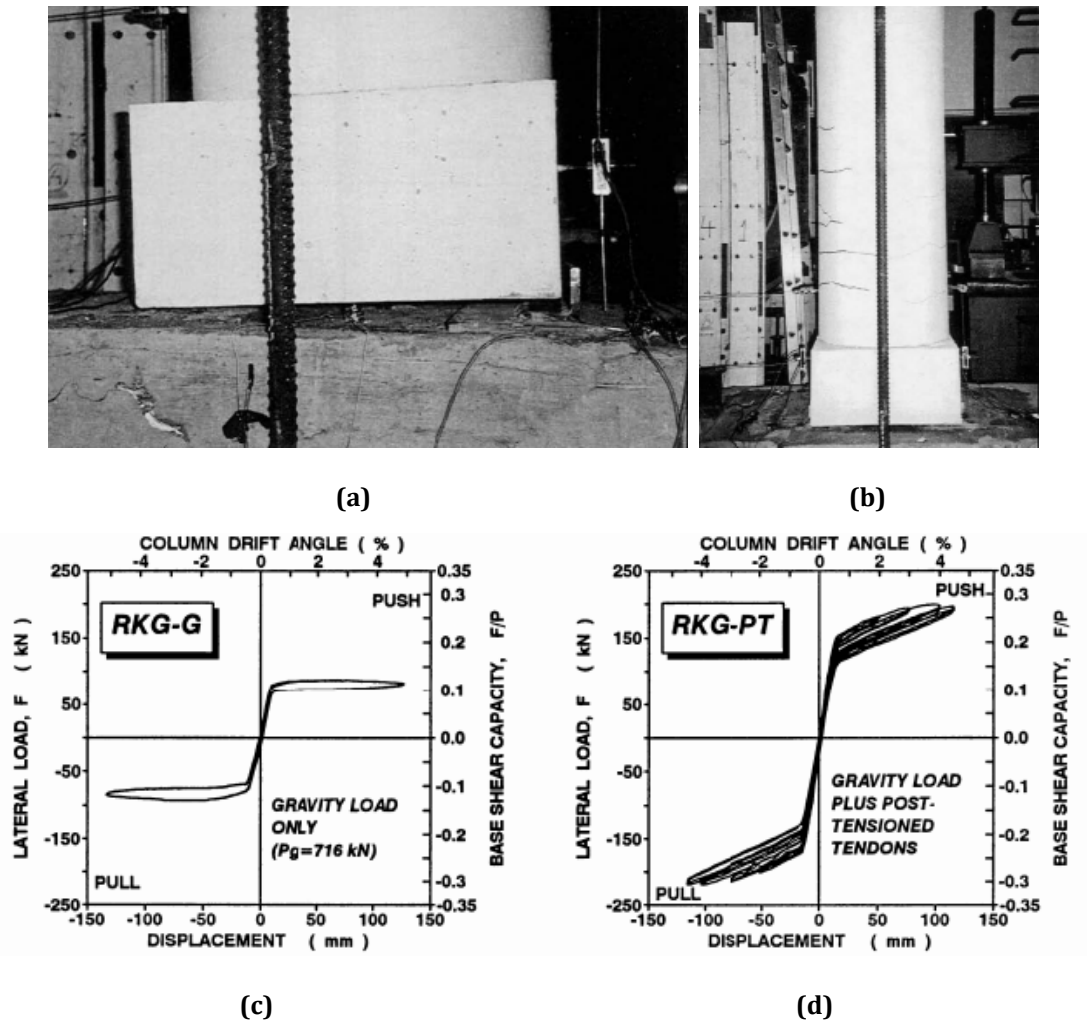

Figure 2.43. Precast rocking column concept from Mander and Cheng (1997): (a) Rocking of the column under the lateral loading (b) Minor cracking to the pier (c) Force-displacement hysteresis under gravity alone (d) Force-displacement hysteresis under gravity plus the unbonded post-tensioning

Hewes and Priestley (2002) experimentally studied the seismic performance of a precast segmental bridge column with unbonded post-tensioning and no supplemental dissipation. The specimens included two circular segmental columns with high aspect ratio and two other specimens with low aspect ratio. The first segment where the rocking interface was located underneath was jacketed for a better concrete confinement. Experimental investigations showed that with lower initial post-tensioning force, all specimens performed well. The specimens were able to accommodate large nonlinear drifts (4.0%) without considerable strength degradation. Results from testing of specimens with higher initial post-tensioning force showed that the specimen with the thicker steel jacketing for the first segment achieved larger drift

(6%) compared to the other ones. There was little strength degradation and in general, the damage was limited to minor concrete crushing at the base of the pier.

Another type of rocking system is called “hybrid”. The hybrid concept was initially developed for the building frames. The development of hybrid system for buildings was part of a joint United States-Japan research program titled “PREcast Seismic Structural Systems” (PRESSS), coordinated by the University of California, San Diego (Priestley, 1991, 1996, Priestley et al., 1999, Stanton et al., 1991, 1997, Stone et al., 1995). In the United States the term “hybrid” describes the use of two reinforcing materials. A hybrid connection is comprised of unbonded post-tensioned tendons with mild steel reinforcement or any other type of energy dissipating devices. Hybrid connections aim to replace plastic hinges in a structure.

In hybrid connections, the joint between the precast members are expected to open during an earthquake. Hybrid connections can be used in locations such as footing to column, splices for column segments or cap beam segments, and column to cap beam. In a typical hybrid connection, the member displacement is designed to have concentrated rotation at the joint. In case of an earthquake, the members are capacity protected elements which means minimal plastic deformation and damage to the elements. The tendons are designed to remain elastic and are able to elongate evenly along their full lengths. Therefore, they provide re-centering capacity to the system with minimum to zero residual drift following a design level earthquake. The energy dissipaters are intended to absorb the seismic energy. The combined response of the system results into a “flag-shaped” hysteresis loop, as shown in Figure 2.44.

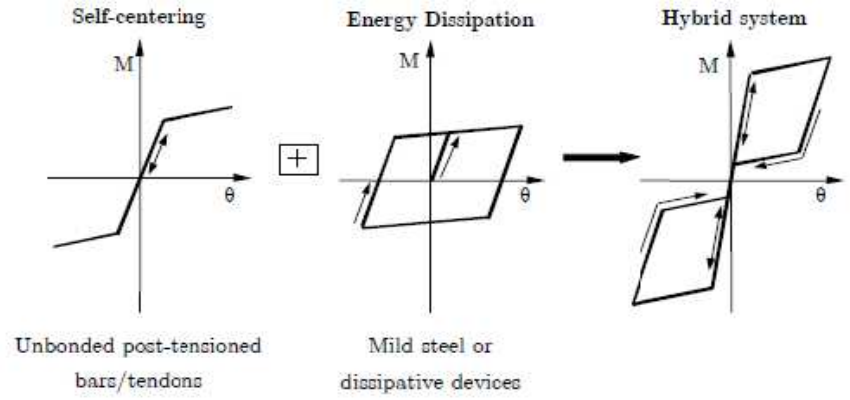

Figure 2.44. Flag-shaped hysteresis of a typical hybrid connection (Priestley et al., 1999)

Further research into hybrid connections for the frame and wall systems were conducted by Kurama (1997), Kurama et al. (1999), Restrepo et al. (2001). Recently, guidelines for the design of hybrid connections in PRESSS buildings were published in the PRESSS Design Handbook (Pampanin et al., 2010).

The concept for hybrid connection between the precast members was successively extended to precast bridges by Palermo (2004), Stanton et al. (2005), and Palermo et al. (2005, 2007, and 2008). The concept of "Dissipative Controlled Rocking" (DCR) is an equivalent term for the hybrid connection between the precast elements of a bridge. It is called DCR since the rocking motion can become energy dissipative through the use of dissipative linkages (reinforcing bars, mild steel dissipaters, or mechanical dissipative devices) which are positioned at the rocking interfaces. A typical DCR connection activates when an earthquake occurs. The connection provides self-centering plus energy dissipation for the structure. This technology reduces the damage in the substructure and superstructure of a bridge during an earthquake. It also preserves the functionality of the bridge following the earthquake. The only sacrificial elements in this type of technology are the dissipative devices which can be easily replaced.

The Kobe Earthquake in 1995 showed that self-centering is an important design consideration to preserve the structural integrity of a bridge following a big earthquake. In fact, several bridge piers which were designed in compliance with the building codes suffered extensive damage with large permanent displacements beyond the reparability extent. As a consequence, the Japanese seismic codes introduced an additional design check on the residual drift of the bridge piers (Palermo and Mashal, 2012). Studies by the Japanese scientists such as Kawashima (2002) concluded that the use of post-tensioning could be an efficient way to drastically reduce the residual drift in the bridge piers after a big earthquake.

Palermo (2004) adapted a Direct Displacement-Based Design (DDBD) procedure for the controlled rocking bridge systems which was successively refined by Marriott (2009). Study carried out by Palermo et al. (2005) highlights the benefits of DCR technology in a bridge compared to the conventional ductile cast-in-place construction. In Figure 2.45 both bridges are designed with the similar moment capacities. For the rocking system (Figure 2.45b) there is no damage to the structural members with similar maximum

displacement to that of the monolithic bridge. However, the bridge with DCR solution has zero residual displacement following an earthquake compared to the monolithic one (Figure 2.45a).

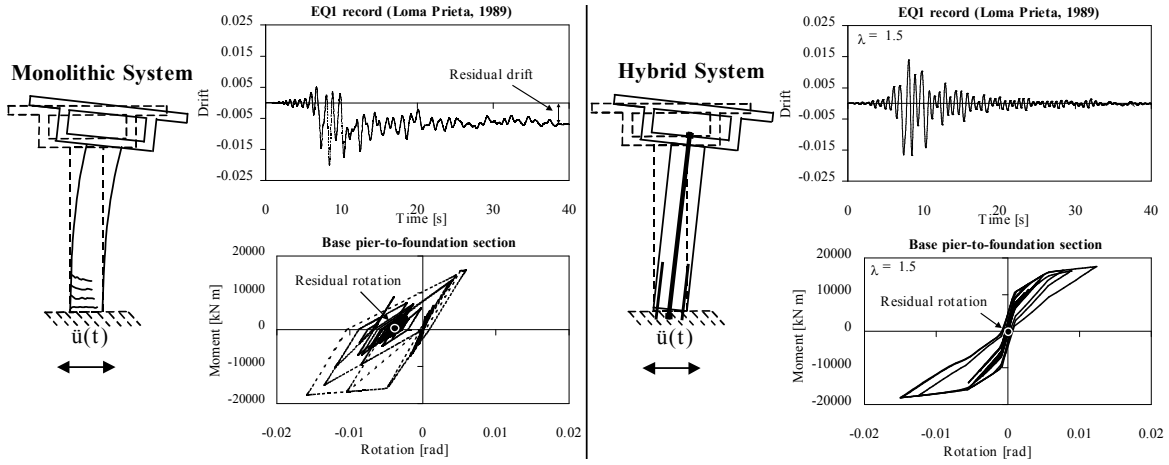

(a) **(b)**

Figure 2.45. Seismic performance comparison between the hybrid and monolithic bridge piers, after Palermo et al. (2005)

For a DCR connection, the total moment capacity of a rocking joint (M_{tot}) is sum of the moment contributions from the unbonded post-tensioning (M_{pt}), axial load (M_N), and the energy dissipaters (M_s), as presented in Equation 2.1.

$$M_{tot} = M_{pt} + M_N + M_s \tag{2.1}$$

The self-centering ratio (λ) is a parameter which controls the overall energy dissipation and self-centering behavior in a DCR connection, as presented in Equation 2.2 below.

$$\lambda = \frac{M_{pt} + M_N}{M_s} \tag{2.2}$$

The New Zealand Concrete Standards (NZS 3101, 2006) and PRESSS Design Handbook (Pampanin et al., 2010) recommend values between 1.15 to 1.5 for the self-centering ratio to be adopted during design of a DCR connection. Past studies have shown that an adequate level of self-centering and energy dissipation can be achieved for a DCR connection using above range of values for λ.

Further investigations into use of unbonded post-tensioning for the segmented bridge piers with and without supplemental dissipation devices, were carried out by Christopoulos (2004), Billington and Yoon (2004), Solberg et al. (2006), Ou et al. (2007), Marriott (2009), Yen and Aref (2010), Sideris et al. (2010), Guerrini et al. (2012), Davis et al. (2012), and Thonstad et al. (2014). Results from these research investigations have demonstrated that controlled rocking technology can drastically minimize the damage in the piers while providing self-centering and limiting the dissipation capacity in one or more critical rocking interfaces. A summary of the several recent research investigations are presented below.

Christopoulos (2004) studied the dynamic behavior of single degree of freedom flag-shaped hysteretic systems. The research investigated systems with different values of λ from post-tensioning only ($\lambda = \infty$) to elastoplastic systems ($\lambda = 0$). The study concluded that the flag-shaped hysteretic systems with adequate energy dissipation can sustain similar maximum displacement demand during an earthquake as that of a conventional monolithic system. Even though the flag-shaped hysteretic systems can dissipate at most half of the seismic energy per cycle as that of an elastoplastic system.

Billington and Yoon (2004) presented a solution where ductile fiber-reinforced cement-based composites (DFRCC), simply referred as fiber-reinforced concrete here, was used at the plastic hinging zones of an unbonded post-tensioned segmental precast pier (Figure 2.46). The idea was to distribute damage throughout a segment constructed of DFRCC. There was no reinforcing rebars running through the joint between the segments. This was adopted as it can provide a faster construction method on-site.

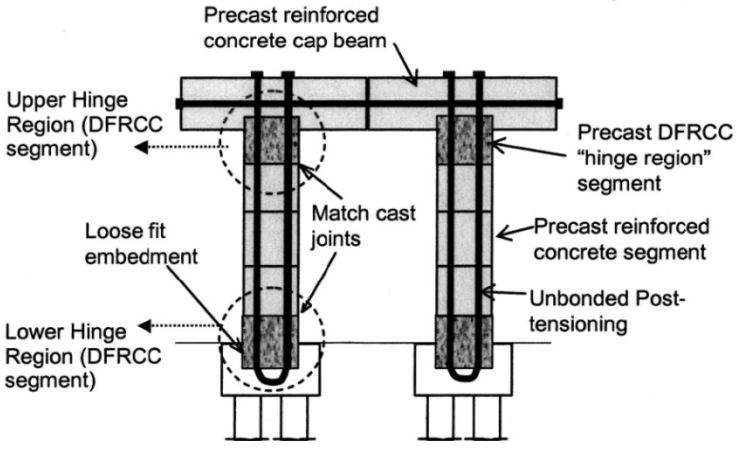

Figure 2.46. Concept for segmentally precast bridge piers by Billington and Yoon (2004)

Several scaled specimens (1/6th of a typical bridge pier) with both normal concrete and fiber-reinforced were constructed for experimental testing. All specimens sustained a drift level of 9% before the unbonded post-tensioning tendons yielded. The residual displacements were in order of less than 1%. It was shown that the fiber-reinforced concrete specimens dissipated more energy through finer distributed cracking up the height of the segment compared to the specimens constructed with normal concrete. The fiber-reinforced concrete specimens also performed well under the high compressive loads without any steel jacketing for the cover confinement.

Solberg et al. (2006) studied the seismic performance of highway bridge piers incorporating the Damage Avoidance Design (DAD) which is a similar concept as DCR under bi-directional loading. The specimens were 1/3rd scaled bridge columns. The DAD specimen was a circular pier with a square shoe block. The shoe block was made of high strength concrete mix with 1% crimped-steel fibers per weight, but no external armoring. The longitudinal rebars of the pier were welded to the rebars from the shoe block to make a monolithic connection between the elements. For a better confinement of the connection, the welded rebars were hand-wrapped in wire ropes, as shown in Figure 2.47a and Figure 2.47b.

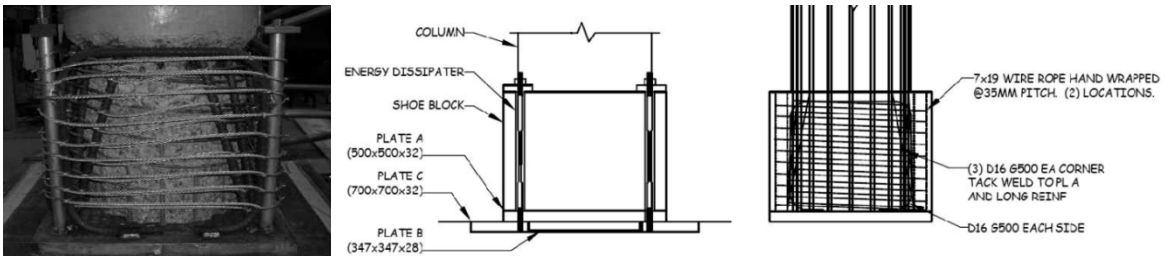

(a) **(b)**

Figure 2.47. (a) Reinforced shoe block with hand-wrapped wires around (b) Design details of the shoe block for the DAD specimen, after Solberg et al. (2006)

The DAD specimen was tested under bi-directional quasi dynamic loading using a 10,000 kN DARTEC machine (Figure 2.48a). An identical conventional ductile specimen to DAD was also constructed and tested as a benchmark for comparison of seismic response. There was minor damage to the shoe block in the DAD specimen which was tested up to 5.5% drift. The rocking of the shoe block was obvious during the testing, as shown in Figure 2.48b. The damage to the shoe block was limited to minor concrete crushing at the corners which was caused by the concentrated axial loads during higher

drifts (Figure 2.48c). It was concluded that the use of fiber-reinforced concrete and adequate confinement were effective to limit the damage to the shoe block. Due to the rocking mechanism for the DAD specimen, there was no residual displacement and strength degradation during testing. A comparison of the hysteresis response between the DAD pier and conventional ductile pier is presented in Figure 2.49.

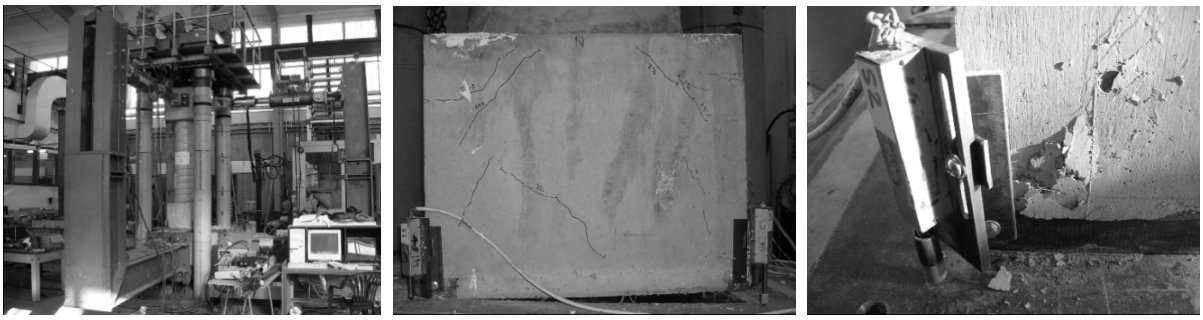

(a) **(b)** **(c)**

Figure 2.48. (a)Testing apparatus (b) Shoe block rocking at 3% drift (c) Local crushing at the shoe block corner, after Solberg et al. (2006)

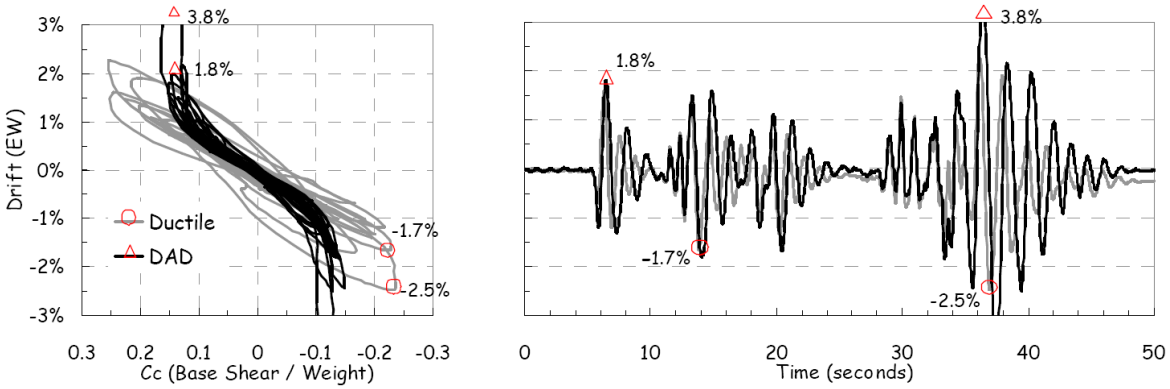

Figure 2.49. Experimental plots for a comparison between the conventional ductile pier and the DAD pier subjected to El Centro Earthquake (Solberg et al., 2006)

Findings from the research showed that the bridge owners will have a 90% confidence that the DAD pier will not be damaged under a design level earthquake. This means that the bridge will be open for the traffic with no delayed functionality. It was also concluded that for a Maximum Considered Earthquake (MCE), there would be 50% confidence that the pier will not collapse. From a comparison of the data for the DAD pier to that of conventional ductile specimen, it was shown that similar levels of confidence can be expected from the conventional cast-in-place construction. However, the conventional construction may suffer extensive damage during a design level earthquake.

Marriott (2009) studied the seismic response of DCR connections for precast bridge piers with the internal and external sources of energy dissipation, as shown in Figure 2.50. The experimental investigations included testing on several 1/3rd scaled bridge piers. The testing consisted of uni and bi-directional quasi static loading. A benchmark conventional ductile pier was also tested to compare the testing results.

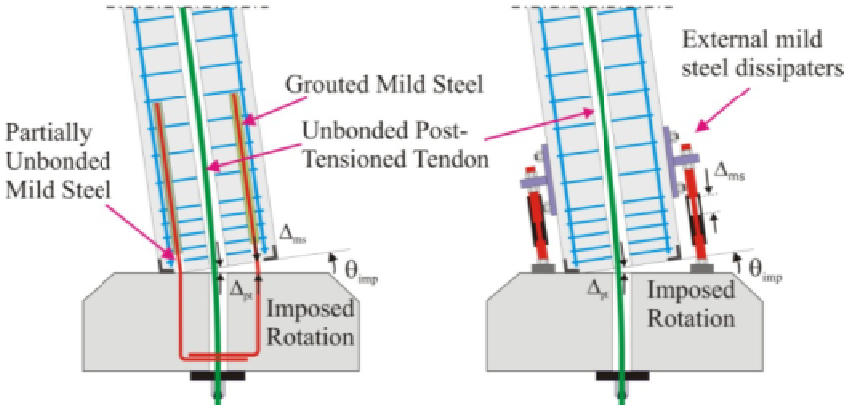

(a) **(b)**

Figure 2.50. DCR connections: (a) Internally grouted dissipaters (b) Externally mounted dissipaters, after Marriott (2009)

For the DCR pier with internal dissipation, mild steel bars were grouted into ducts inside the precast pier, as shown in Figure 2.50a. The mild steel rebars were unbonded for over a certain length to prevent premature yielding under small seismic loads, as well as distributing deformation over a longer length of the rebars.

Several types of detailing were tested. In one case, the starter bars were threaded into the foundation concrete inserts and were fused over a length of 50 mm, as shown in Figure 2.51c. The bars were fused by reducing the diameter of the bar over a certain length to concentrate the inelastic deformation to that portion of the bar. The precast column had ducts to house the unbonded post-tensioning tendons and the foundation starter bars (Figure 2.51b). Shear transfer across the rocking joint was relied on the dowel action of the mild steel rebars plus an internal shear key. The hemispherical internal shear key was intended to provide more self-centering of the pier and to prevent from sliding. The hemispherical internal shear key was located at the center of the rocking interface, as shown in Figure 2.51c. To provide sufficient confinement for the base of the rocking column, steel angles of 2 mm wall thickness were cast around the perimeter of the pier (Figure 2.51b). The steel angle was intended to prevent from

crushing of the cover concrete under concentrated compressive stresses when the column starts rocking. After lowering down the concrete column on the foundation, the starter bars were grouted inside the ducts (Figure 2.51d).

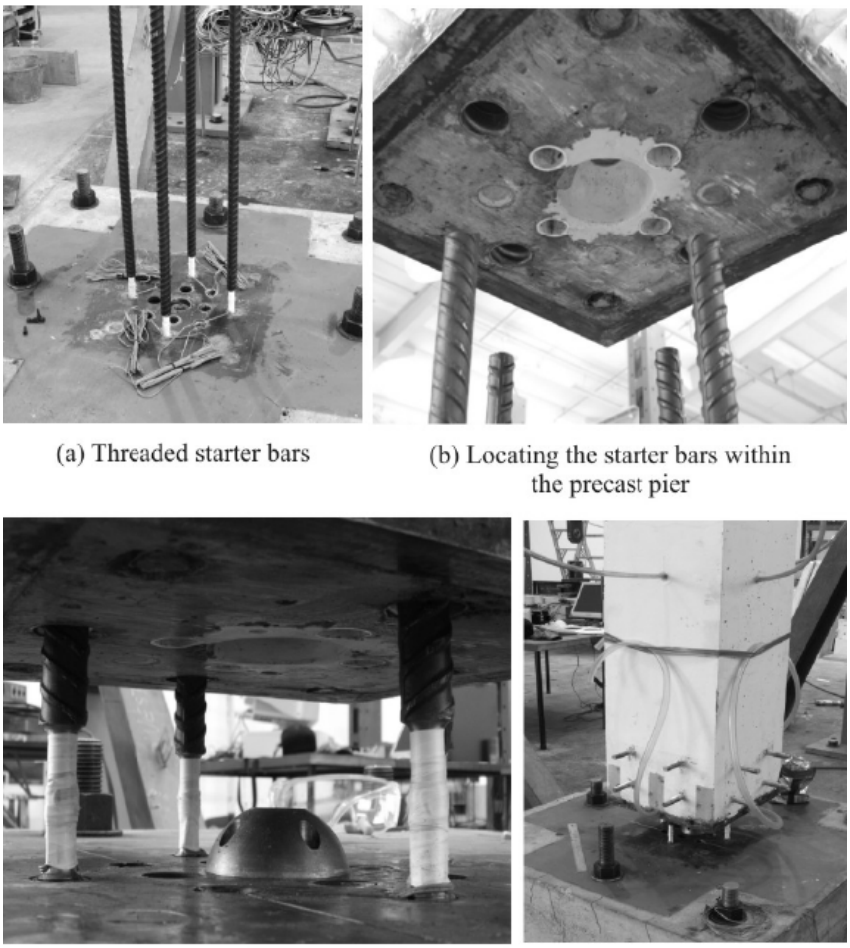

(a) Threaded starter bars

(b) Locating the starter bars within the precast pier

(c) & (d) Lowering the precast pier onto the foundation

Figure 2.51. DCR connection with internal dissipaters, after Marriott (2009)

Following quasi-static cyclic testing, there was no major damage to the precast column with DCR connection. Some flexural cracking occurred up the height of the column with some superficial spalling of the concrete at the rocking interface, as shown in Figure 2.52a and Figure 2.52b. The specimen had less than 1% residual drift at the end of testing. Observations from testing of the ductile monolithic column showed extensive cracking and spalling at the plastic hinge zone of the column. In contrast, the DCR connection with internal source of energy dissipation had a very stable response with good energy dissipation capacity. Also, there was less strength degradation in the rocking column under cyclic loading. A force-displacement hysteresis is presented in Figure 2.52c.

(a) **(b)** **(c)**

Figure 2.52. Testing results from the DCR connection with internal dissipaters: (a & b) Superficial spalling of the cover (b) Force-displacement hysteresis, after Marriott (2009)

In general, a DCR connection with internal source of energy dissipation is fast to construct and cost-effective. However, following an earthquake, it is difficult to inspect the rebars. Therefore, the repairs might be complicated due to the location of the dissipation source inside the columns (Marsh et al., 2011).

An alternative to internal dissipaters in a DCR connection is to use external dissipaters. A concept for this was presented earlier in Figure 2.50a. In this case, the external dissipaters are introduced at the column to foundation rocking connection. The dissipaters are attached to the outside face of the pier at one end and are fixed to the foundation in the other end. There is a wide range of dissipaters and devices that can be used as external source of energy dissipation. These include mini plug and play devices such as mini Buckling Restrained Braces (BRB) which can be made easily from the mild steel rods (Palermo et al., 2007), or alternatively other types of metallic, viscous, and friction dissipaters which will be discussed in Chapter 4.

Marriott (2009) studied the response of a cantilever bridge pier with DCR connection and external source of dissipation. The pier was identical to the one discussed before in Figure 2.51. However, in this case external dissipaters were attached at the rocking interface between the precast column and the foundation. A typical external dissipater used by Marriott (2009) was made of a mild steel rod which was fused over a certain length and confined inside a steel tube. Epoxy was injected inside the dissipater to fill the gap between the rod and the tube. Also it aimed to prevent from buckling of the mild steel rod when the dissipater is in compression (Figure 2.53b). The ends of the mild

steel rod were threaded to provide anchoring points, as shown in Figure 2.53a and Figure 2.53b.

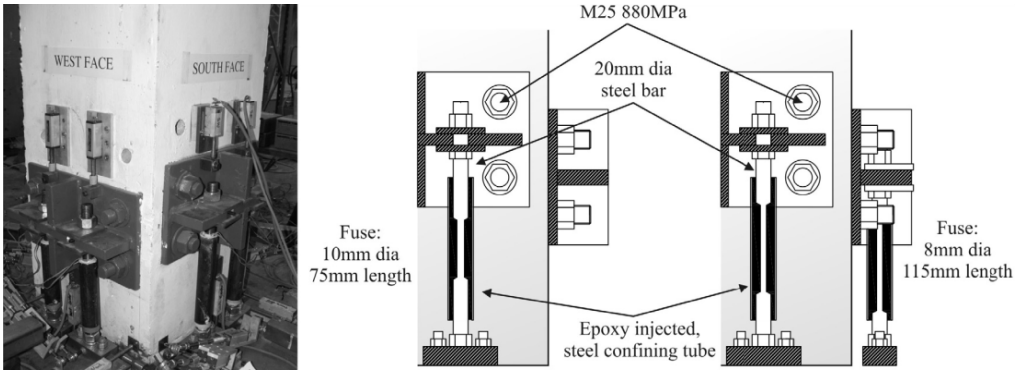

(a) **(b)**

Figure 2.53. DCR connection with external dissipaters, after Marriott (2009)

Testing results under quasi-static cyclic loading showed that the DCR connection with the mini BRB external dissipaters had the most stable hysteresis response of all other solutions tested, including the one with internal dissipaters, as shown in Figure 2.54c. The precast column suffered only flexural hairline cracking. There was no slip at the steel brackets in the column which maximized the efficiency of the external dissipaters. There was no yielding of the tendons or rupturing of the dissipaters up to 3.5% drift. Following testing, there was zero residual displacement in the column, as can be seen from the force-displacement hysteresis plot of Figure 2.54c.

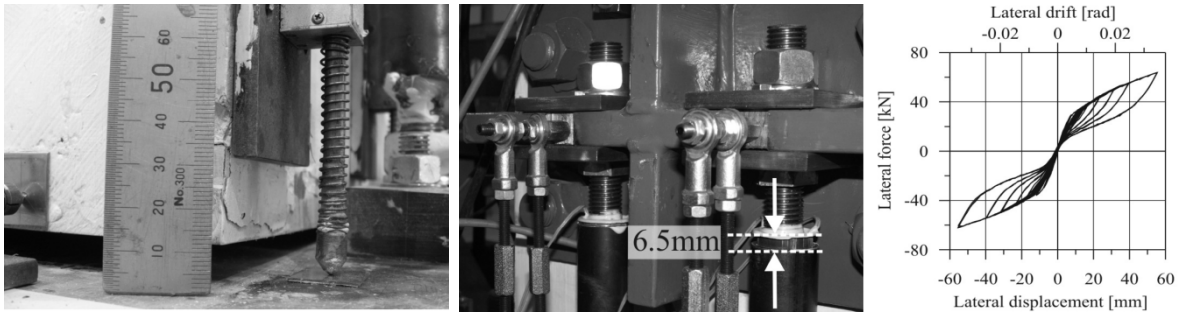

(a) **(b)** **(c)**

Figure 2.54. Testing results from the DCR connection with internal dissipaters: (a) Uplift of the rocking column (b) Extension of the external dissipaters during rocking (c) Force-displacement hysteresis, after Marriott (2009)

In summary, using external dissipaters in a DCR connection offers many advantages such as easy installation, inspectability, replaceability, minimum on-site grouting, better self-centering, and minimum repairs after a big earthquake.

Another recent experimental investigation into rocking connections was shake table and quasi static testing of a half-scale fully precast segmental bridge by Sideris et al. (2010, 2012). The project was funded by the Federal Highway Administration (FHWA) at the University at Buffalo - State University of New York. The research investigated the concept of hybrid sliding-rocking (HSR) for the post-tensioned segmental bridge piers. In HSR system, the pier segments consist of HSR joints combined with unbonded post-tensioned tendons. The research studied two types of HSR members. The first type was HSR with slip-critical joints and linear post-tensioning geometry (HSR-SC), as shown in Figure 2.55a. The second type was HSR with the rocking-critical joints and nonlinear post-tensioning geometry (HSR-RC), as shown in Figure 2.55c. The half-scale specimen incorporated HSR-RC superstructure and two single-column HSR-SC piers, as shown in Figure 2.55.

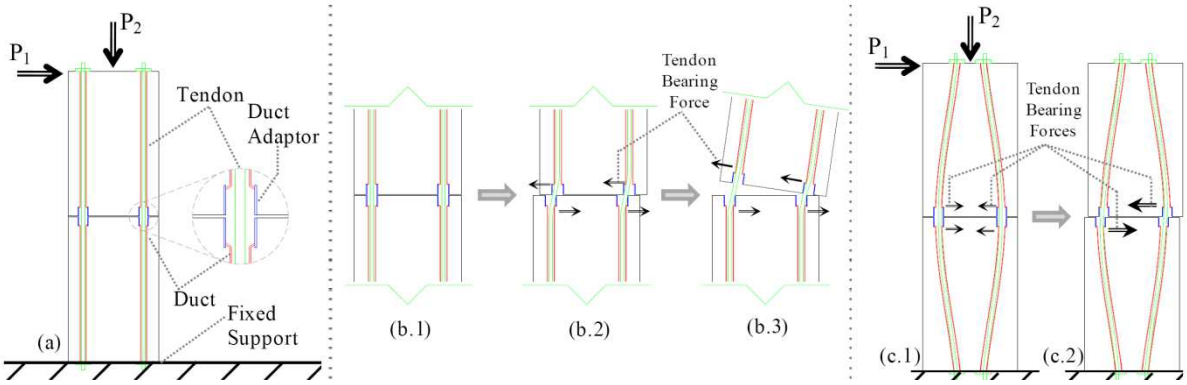

Figure 2.55. (a) Benchmark configuration (b) Slip-critical HSR joint: (b.1) Un-deformed configuration (b.2)Siding capacity reached (b.3) Rocking response following the sliding (c) Benchmark configuration with nonlinear PT geometry: (c.1) Un-deformed configuration (c.2) Response against sliding, after Sideris et al. (2012)

First phase of testing included extensive series of shake table tests (around 150) on the bridge specimen (Figure 2.56a). The second phase of testing consisted of quasi-static cyclic testing on a single pier, as shown in Figure 2.56b. A force-displacement plot of the quasi-static cyclic response is presented in Figure 2.56c.

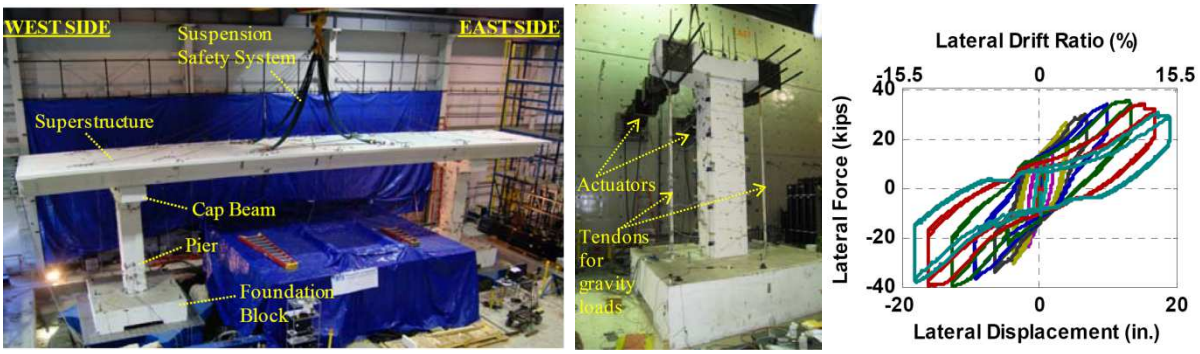

(a) **(b)** **(c)**

Figure 2.56. (a) Precast concrete segmental bridge specimen, mounted on the two shake tables in testing lab at the University at Buffalo (b) HSR-SC pier joint under quasi-static cyclic loading (c) Force-displacement hysteresis , after Sideris et al. (2012)

Research concluded that HSR-SC piers have substantial energy dissipation capacity, large values of ductility, and moderate self-centering capacity. After testing, the specimen suffered moderate damage. The damage included crushing of the concrete at the column to footing rocking joint and concrete spalling in areas closer to the HSR joints. The superstructure had lower energy dissipation, but higher self-centering capacity. It suffered minor damage.

Guerrini et al. (2012) proposed an innovative technology for precast bridges with hybrid connections in high seismic regions. The research was supported by the California Department of Transportation (Caltrans) at the University of California, San Diego. The technology consisted of precast concrete piers with hybrid connection at the rocking interfaces, as shown in Figure 2.57a. The concrete column was sandwiched by dual steel shells extending up its full height. The outer steel shell was intended as a substitute to the longitudinal and transverse reinforcement in the column. The inner shell was intended to prevent concrete implosion (Figure 2.57b).

Unbonded post-tensioning tendons were intended to provide self-centering capacity for the column. The energy dissipation mechanisms were in the form of internal and external mild steel dissipaters, as shown in Figure 2.58 and Figure 2.59, respectively. This was similar to the solution investigated by Marriott (2009). Another novelty in this research was introduction of rubber and disc bearings on top of the column to control yielding of post-tensioning (Figure 2.58c and Figure 2.59c). The stiffness of the bearings was selected such that if during higher drifts the post-tensioning is close to its yield

point, then the bearings will be compressed to protect the post-tensioning bars. Therefore, the post-tensioning force will not be increased with further displacement.

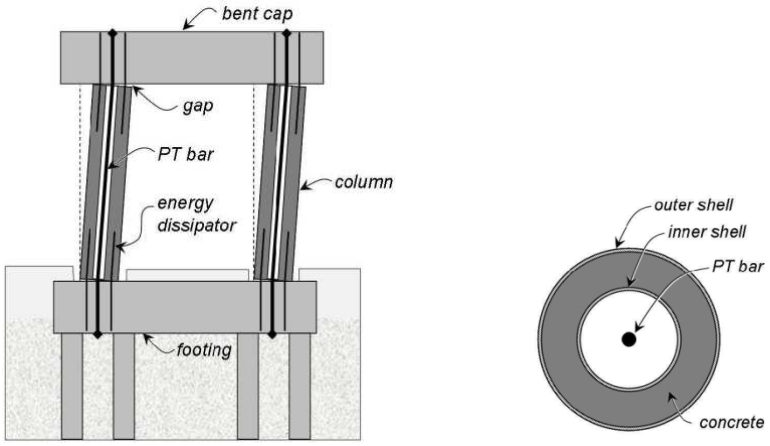

(a) **(b)**

Figure 2.57. (a) Proposed bent system (b) Pier cross-section (Guerrini et al. 2012)

(a) **(b)** **(c)**

Figure 2.58. DCR with internal dissipaters (a) Column base cross-section (b) Starter bars with unbonded length, but not fused (c) Disc bearings above the load stub

(a) **(b)** **(c)**

Figure 2.59. DCR with external dissipaters (a) Column base cross-section (b) Mini BRBs attached around the DCR connection(c) Rubber bearings above load stub

The specimens were tested under quasi-static cyclic loading. For the DCR specimen with internal dissipaters, the mortar bed at the rocking interface started crushing during 3%

drift cycles. It had extensive damage during 7.5% drift cycles. This resulted in loss of stiffness and reduced self-centering capacity, as can be seen from the force-drift hysteresis plot in Figure 2.61a. There was also damage to concrete and permanent deformation of the steel shells due to lateral expansion of the concrete (Figure 2.60a).

For the column with external dissipaters, the mini BRBs started buckling at their end connections during 3% drift cycles (Figure 2.60b). This resulted in loss of stiffness, as can be seen from the hysteresis in Figure 2.61b. The mortar bed started crushing during 3% drift cycles which caused an abrupt change in stiffness of the system. This followed by extensive crushing of the mortar bed during 5% drift cycles. This caused considerable loss of stiffness and self-centering capacity in the system (Figure 2.61b). The dissipaters ultimately fractured during 7.5% drift cycles. Following testing, the distortion and damage to the energy dissipaters were extensive (Figure 2.60b).

(a) **(b)**

Figure 2.60. (a) Damage to concrete and steel shell for DCR with internal dissipaters (b) Damage to dissipaters and mortar bed for DCR with external dissipaters

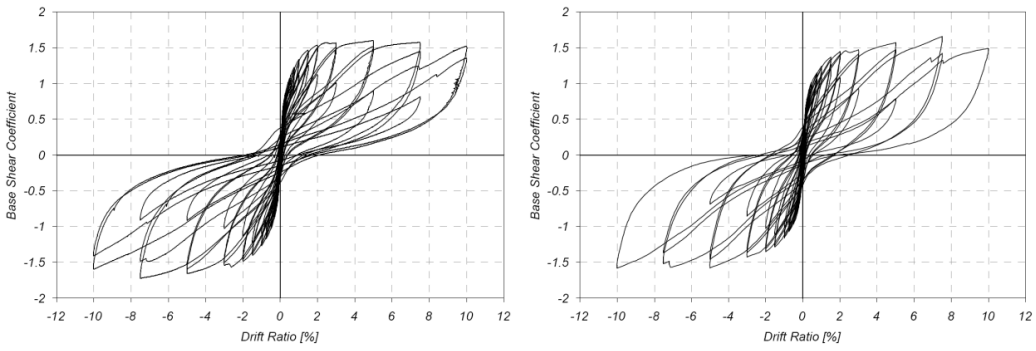

(a) **(b)**

Figure 2.61. Force-displacement plots: (a) Internal dissipaters (b) External dissipaters

Davis et al. (2012) proposed the concept for a dissipative controlled rocking bridge using unbonded pre-tensioned strands inside the columns. The research was supported

by the State of California at the University of Washington in Seattle through the Transportation Systems Research Program of the Pacific Earthquake Engineering Research Center (PEER).

In this concept, there are no post-tensioning tendons in a DCR connection. However, unbonded prestressing strands are positioned inside the column during the prefabrication. This system is illustrated in Figure 2.62a. In this system, the column to footing connection is a member socket connection while the column to cap connection is a grouted duct connection. Similar to a DCR connection, internal mild steel rebars are provided at the crack plane where rocking is expected for energy dissipation. This type of hybrid connection is intended to result in a similar flag-shape hysteresis as that can be expected of a DCR connection with unbonded post-tensioning and internal or external dissipaters.

Several specimens were tested under quasi-static cyclic loading. The performance of each specimen was compared against a conventional ductile pier benchmark. The pre-tensioned specimens achieved similar moment capacity. Following 10% drift cycles, there was less than 1% residual drift in the piers. However, despite good self-centering, the columns experienced extensive spalling, bar buckling, and bar rupture at relatively lower drifts. The dissipated energy was also lower than that of a ductile concrete pier.

This concept was later refined by Eberhard et al. (2014) at the University of Washington, Seattle. To prevent damage to the concrete and rebars, the original concept was modified using Hybrid Fiber Reinforced Concrete (HyFRC) shells at the rocking interfaces, as illustrated in Figure 2.62b. The HyFRC shells were intended to provide confinement for the concrete, delay bar buckling, and enhance the column ductility. A similar specimen to that tested previously by Davis et al. (2012) was constructed using HyFRC at the plastic hinging zone.

Results from quasi-static cyclic loading showed that HyFRC shell was effective to limit the spalling to the concrete. However, it did not significantly delay bar buckling and bar fracture. Figure 2.63 presents a comparison of the moment-drift plots between a conventional concrete and a HyFRC constructed rocking connection.

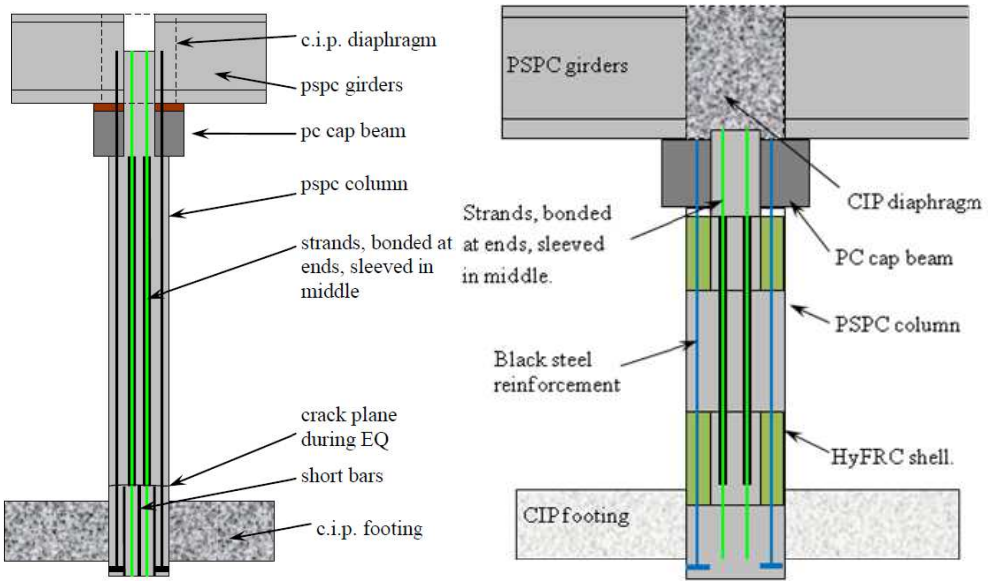

(a) **(b)**

Figure 2.62. Pre-tensioned bridge bent system: (a) Concept by Davis et al. (2012) (b) Modified concept by Eberhard et al. (2014)

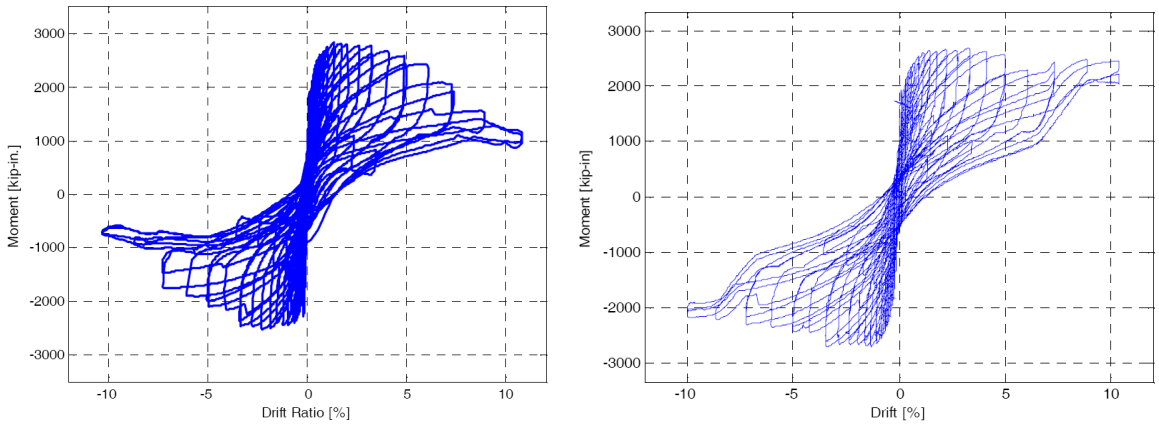

(a) **(b)**

Figure 2.63. Moment-drift plots for rocking joint constructed of: (a) Conventional concrete (b) HyFRC, after Eberhard et al. (2014)

Recently, White (2014) experimentally investigated the performance of Controlled Damage Connections for ABC in high seismicity. The research was part of the same project (ABCD) as the one in this thesis. The project "Advanced Bridge Construction and Design" (ABCD) at the University of Canterbury is a nationally funded research program through the New Zealand Natural Hazards Research Platform (2011-2015).

ABC Controlled Damage was briefly introduced earlier in Chapter 1. Controlled Damage Connections are based on the concept of DCR or hybrid connections. Controlled Damage

connections aim to limit damage in the bridge substructure while providing self-centering to minimize the residual displacement following a big earthquake. This means that the bridge would be drivable and open for the traffic with no delayed functionality. However, minor to moderate repair work would be necessary to reinstate the strength and ductility capacity of the pier after the earthquake. The repair strategies are normally considered at the design stage of the bridge. This would allow a rapid post-earthquake damage repair which in return minimizes traffic disruption and repair costs.

Two types of Controlled Damage Connections (CDC) were tested for half-scale precast cantilever bridge specimens. The first type featured CDC with Member Socket Connection (MSC) for the column to foundation connection (Figure 2.64d). In this type of connection, unbonded post-tensioning tendons are added to a typical MSC (as discussed in Section 2.3.1.4) to minimize the residual displacement of the pier after an earthquake. During the prefabrication, threaded anchors are cast into the precast components (Figure 2.64b and Figure 2.64c). These anchors are later used for mounting of the external dissipaters as a repair mechanism for the pier, as shown in Figure 2.65. The longitudinal rebars at the column to footing interface are taped (unbonded) over a certain length (Figure 2.64b). This is intended to encourage initiation of the rocking from the column to footing interface.

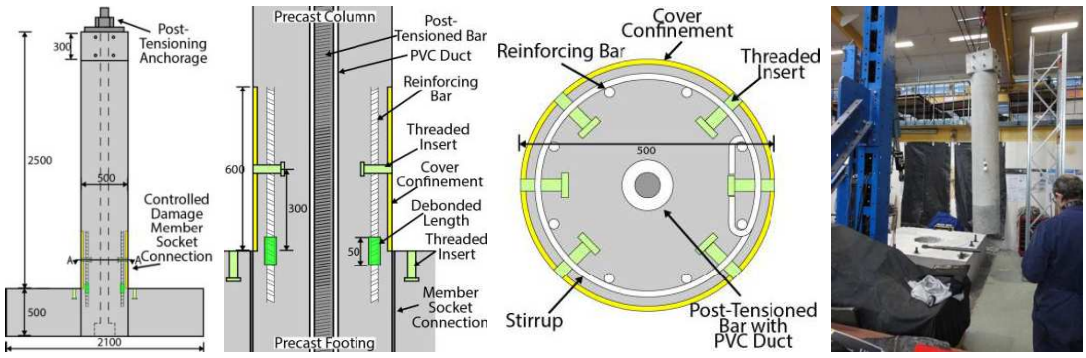

(a) **(b)** **(c)** **(d)**

Figure 2.64. Controlled Damage MSC: (a) Column specimen (b) Column to foundation connection detailing (c) Column base cross-section (d) Placement of the column

The repair strategy for the Controlled Damage Member Socket Connection (CD-MSC) is presented in Figure 2.65. In Figure 2.65a and Figure 2.65d, the mini BRB dissipaters shown for the repair are a novel type of dissipaters, known as the Grooved Bar Dissipater. It is a superior generation of the mini BRBs used for the DCR connection in

the past research investigations (Gurerrini et al., 2012, Marriott, 2009, and Sarti et al., 2013). More information on Grooved Bar Dissipaters are presented in Chapter 4.

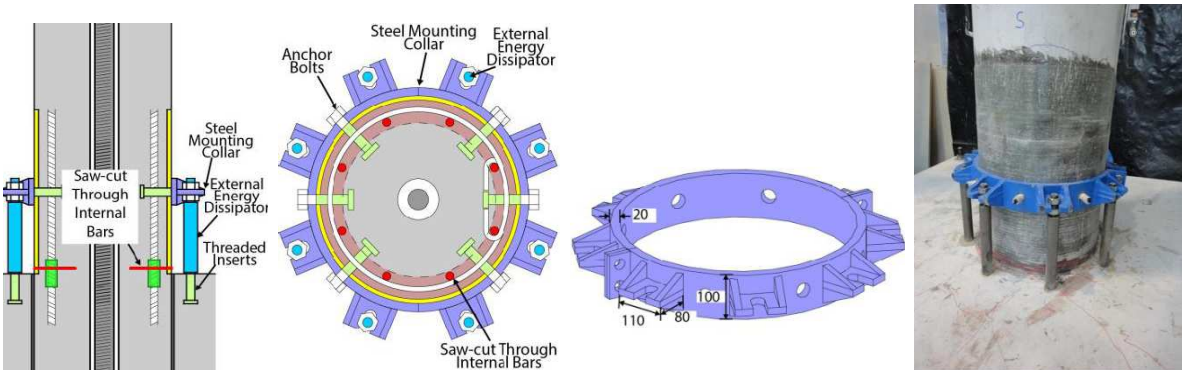

(a) **(b)** **(c)** **(d)**

Figure 2.65. Repair strategy for CD-MSC: (a) Mounting of external dissipaters (b) Column cross-section after repair (c) Dissipater mounting collar (d) Column after the repair

Experimental results from quasi-static bi-directional testing of the column with Controlled Damage MSC showed a stable force-displacement hysteresis (Figure 2.66a). There was no concrete spalling up to 3.25% drift cycles. Following testing, the column was repaired with a strategy described earlier (Figure 2.65). The repaired specimen was tested under the same loading as the benchmark column. Although, there was some slip observed in the collar during testing which was caused by a poor detailing. However, the repaired column performed well with good self-centering and energy dissipation capacity.

Figure 2.66b presents the force-displacement hysteresis for the repaired column. From a comparison of the plots in Figure 2.66, it is clear that the column capacity and ductility was reinstated following the repair strategy.

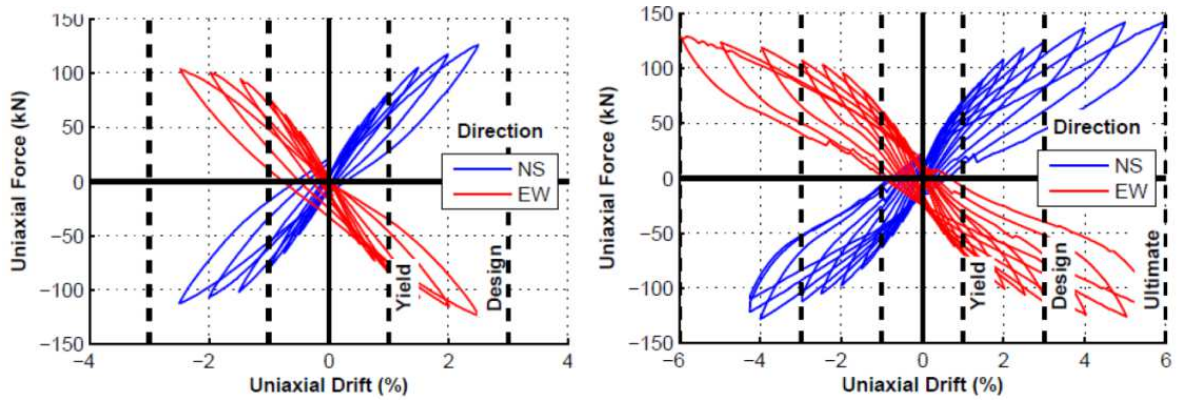

(a) (b)

Figure 2.66. Force-displacement hysteresis CD-MSC: (a) Original column (b) After repair

A second type of Controlled Damage Connection investigated by White (2014) was the Controlled Damage Coupled Bar Connection (CD-CBC), as shown in Figure 2.67a. In this type of connection, replaceable segments of the column longitudinal bars are located in a recess at the plastic hinging zone of the column (Figure 2.67b and Figure 2.68a). Couplers are used to connect the replaceable segments to the permanent reinforcements of the foundation and the column. Steel armoring is provided around the column base and top of foundation to prevent crushing of the concrete during rocking. The replaceable rebar segments are taped for a better ductility, as shown in Figure 2.68b. Stirrups are provided around the rebar segments (Figure 2.68b) and a formwork is placed around the connection. The connection is then filled with cast-in-place concrete. Once the concrete hardens, the formwork is removed (Figure 2.68c). The construction sequence for the CD-CBC is illustrated in Figure 2.69.

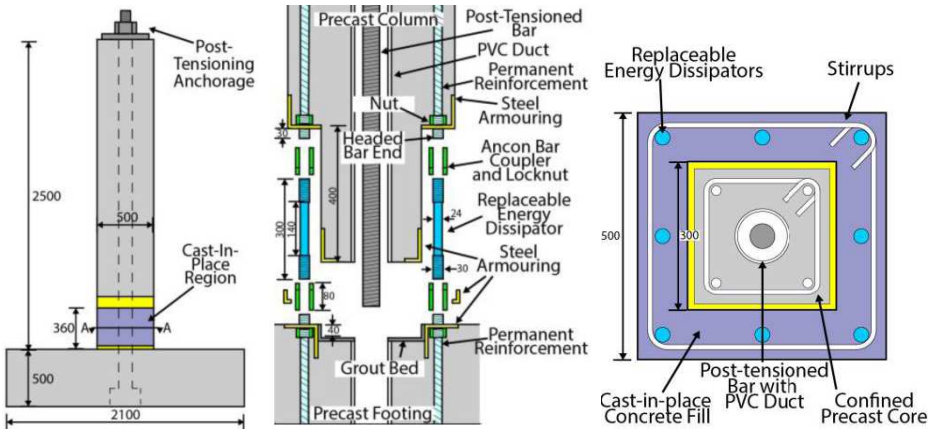

(a) (b) (c)

Figure 2.67. Controlled Damage CBC: (a) Column specimen (b) Column to foundation connection detailing (c) Column base cross-section

(a) **(b)** **(c)**

Figure 2.68. Controlled Damage CBC Construction: (a) Dissipaters and couplers (b) Placement of the column (c) Formwork removed, completed pier

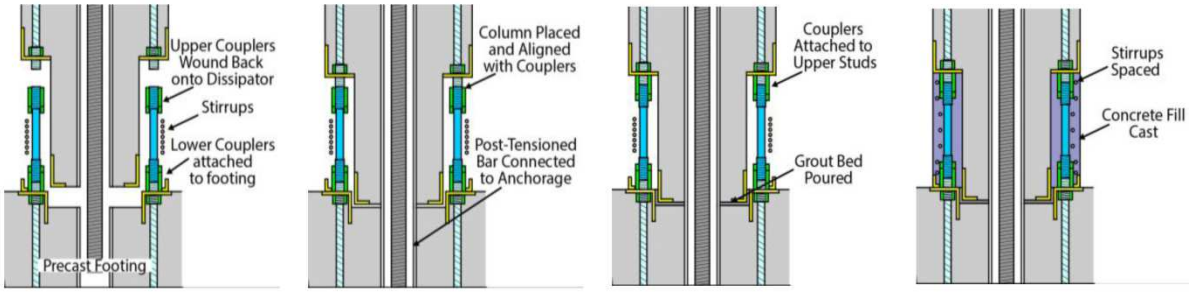

Step 1 **Step 2** **Step 3** **Step 4**

Figure 2.69. Controlled Damage CBC Construction sequence

The repair strategy for CD-CBC includes replacment of the rebar segments. This would require the perimeter concrete around the connection to be removed. The concrete column core with unbonded post-tensiong running through it would provide support for the gravity loads. Figure 2.70 presents the repair strategy for CD-CBC step by step.

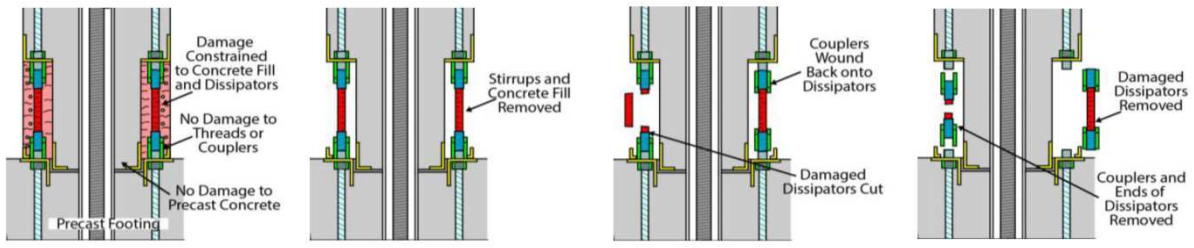

Step 1 **Step 2** **Step 3** **Step 4**

Figure 2.70. Controlled Damage CBC repair strategy

Experimental results from quasi-static bi-directional testing of the column with CD-CBC showed a stable force-displacement hysteresis (Figure 2.71a). Despite the flag-shaped response of the column not being very obvious compared to CD-MSC, the column behaved well. There was an unintended bonding of the column core to the foundation.

This restrained the rocking of the joint to a certain limit, and thus decreased the self-centering capacity of the connection. During the repair process, some limited buckling of the rebar segments was observed. The repaired column was tested under the same loading as the benchmark column. From a comparison of the force-displacement hysteresis plots for the original and repaired column, it is clear that the column capacity and ductility were reinstated following the repair strategy, as presented in Figure 2.71. It should be noted that the New Zealand Concrete Standards (NZS 3101, 2006) prohibits use of couplers in the plastic hinging zones. This has been due to uncertainties in performance of the couplers under cyclic loading. However, in this research, there was no damage to the couplers and they behaved well under the cyclic loading.

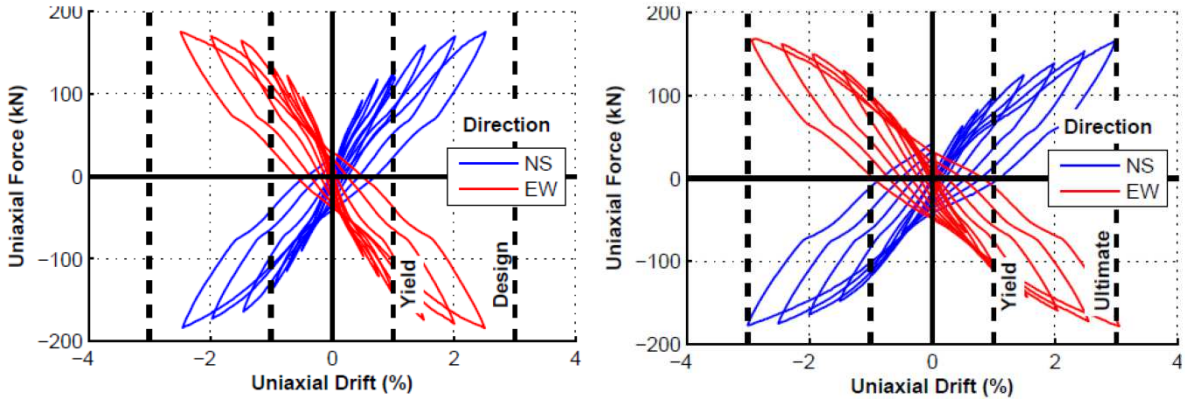

(a) **(b)**

Figure 2.71. Force-displacement hysteresis CD-CBC: (a) Original column (b) After repair

The study by White (2014) concluded that both types of Controlled Damage Connections showed good potential for ABC in seismic regions. The ABC Controlled Damage will generally have a slightly higher initial construction cost compared to conventional ductile cast-in-place construction. The increase in the initial construction cost is associated with the inclusion of the components such as unbonded post-tensioning, armoring, and energy dissipaters. However, given the better performance of Controlled Damage Connections, and straightforward cost-effective repair strategy that does not require the replacement of the bridge, the overall life cycle cost of the bridge could be comparable to a conventional ductile construction. The repair strategies developed for ABC Controlled Damage eliminates all type of uncertainty about the residual strength and ductility of the pier.

In summary, ABC Controlled Damage offers advantages such as improving post-earthquake serviceability and relatively simple repair options. This makes the technology a good competitor to the conventional ductile cast-in-place construction in seismic regions.

2.3.3.2. Emerging Materials and Technologies for ABC in Seismic Regions

Marsh et al. (2011) presents several types of emerging materials and technologies which are proposed for ABC in seismic regions. Most of these materials and technologies are at an early stage of development. Examples include Rotational Elastomeric Bearings (REB) and Special Energy-Dissipating Bar Systems.

Rotational Elastomeric Bearings can be used in locations where concentrated deformation is expected in the structure. These locations include foundation to column and column to cap beam regions. Motaref et al. (2010) experimentally studied the response of a precast segmental pier with REB at the column base (Figure 2.72). Testing results showed great displacement capacity of the connection compared to other emulative and hybrid connections. This type of connection was also effective in reducing the moment from the pier entering the foundation for a given column drift.

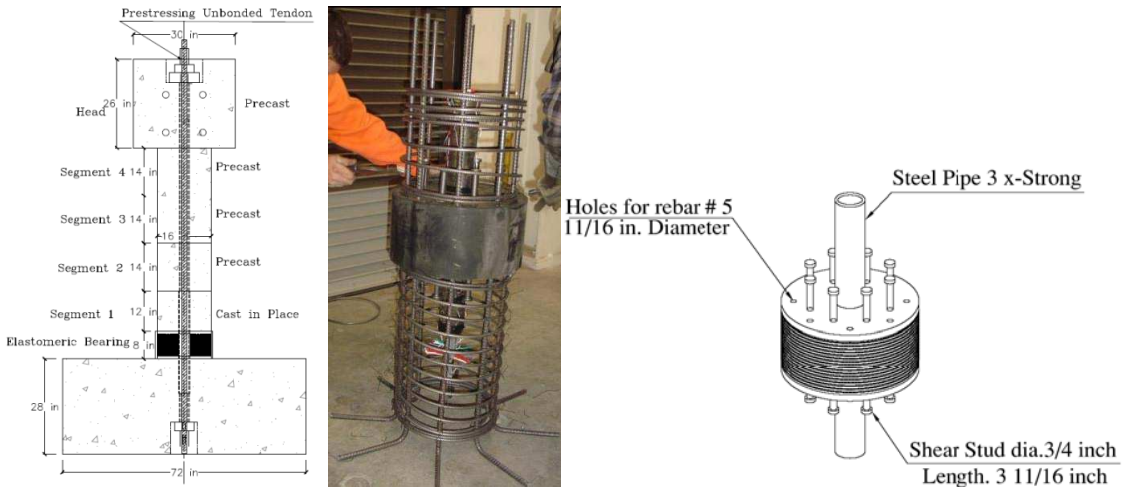

(a) **(b)** **(c)**

Figure 2.72. (a) Specimen with REB connection for testing (b) Elastomeric bearing energy-dissipating bars at column base (c) REB, after Motaref et al. (2010)

Special Energy-Dissipating Bar Systems include Nickel-Titanium (NiTi) alloy bars and other Shape Memory Alloys (SMAs). These are relatively new technologies for the earthquake protection of structures. These systems are known for their super-elasticity

(self-centering feature) and temperature-related properties. There has been some analytical and experimental testing on SMAs and their potential applications at the plastic hinging zones in a structure. Findings are discussed in DesRoches et al. (2004), Youssef et al. (2008), Roh and Reinhorn (2010), Saiidi et al. (2006, 2009), and Varela and Saiidi (2014).

A two-dimensional stress-strain curve for a typical SMA bar is presented in Figure 2.73a. The temperature dependency, deformation, and shape memory behavior of NiTi SMAs are illustrated in a three-dimensional stress-strain diagram in Figure 2.73b.

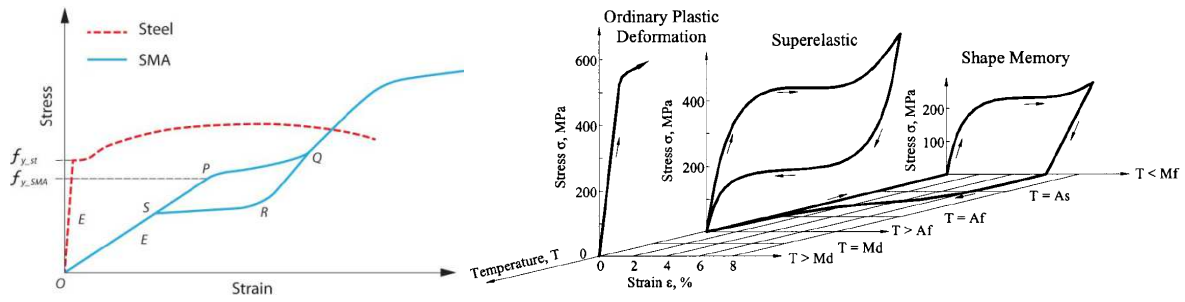

(a) **(b)**

Figure 2.73. (a) Two-dimensional stress-strain behavior of a SMA bar versus steel, after Youssef et al. (2008) (b) Three-dimensional stress-strain temperature diagram, after DesRoches et al. (2004)

In summary, emerging materials and technologies show promise for the future applications of these technologies for ABC in seismic regions. Despite offering some unique advantages, the cost for some of these technologies can be very high, even when compared against the DCR connections. From the construction risk perspective, materials such as the SMA bars and REBs pose a high risk. This is due to lack of construction detailing. Extensive research efforts are required before applying them with ABC in seismic regions (Marsh et al., 2011).

2.4 History of Seismic Technologies in New Zealand

This section presents a summary of low damage bridge technologies developed over the years in New Zealand. The development and application of cost-effective energy dissipation devices in New Zealand go back to the 1970s. Back then, New Zealand was one of the pioneers for the development and application of advanced seismic technologies around the world. Some of the technologies developed for the seismic protection of bridges and buildings included dissipative connections and devices which absorb seismic energy.

Among the pioneers, a well known scientist was Dr. Bill Robinson (1938-2011) who invented the lead extrusion damper in the mid 1970s. This was followed by his invention of the Lead-Rubber Bearings (LRBs) at the laboratories of New Zealand Department of Scientific and Industrial Research (DSIR) in 1974 (Skinner et al., 1993).

Another well respected pioneer was Dr. Ivan Skinner (1923-2014). Skinner's contributions included the development of cost-effective innovative devices and energy dissipaters. His famous innovative torsional beam damper (Figure 2.74g) to absorb seismic energy was used in the construction of the world's first rocking bridge (South Rangitikei Viaduct) in 1981. The Rangitikei Viaduct is a clear example of one of the first bridges constructed with low damage seismic technologies around the world, as discussed previously in Section 2.3.3.1.

Figure 2.74 presents several types of energy dissipation devices made of LRBs, steel plates, and lead extrusion invented by Robinson and Skinner. According to Robinson (1995), there were 50 base isolated road and rail bridges in New Zealand in 1995. From these bridges, 40 of them used lead-rubber bearings for isolation, 1 used lead-rubber bearing and lead extrusion dampers, 2 had rubber bearings and lead extrusion dampers, and 7 were with rubber bearing and flexural steel dissipaters.

Following the 1994 Northridge Earthquake in the United States and the 1995 Kobe Earthquake in Japan, the use of lead-rubber bearings for seismic protection of the bridges and buildings in the United States and Japan had tremendously increased. Unfortunately, most of the seismic isolation and dissipative devices developed in New Zealand during 1970 to 1980 have not been significantly used in the current New

Zealand bridge practice. For example, in 2005 there were only 48 highway bridges and one Railway Bridge in the country which were base isolated (Kelly et al., 2010). This corresponded to less than 1% of the bridge road network in New Zealand.

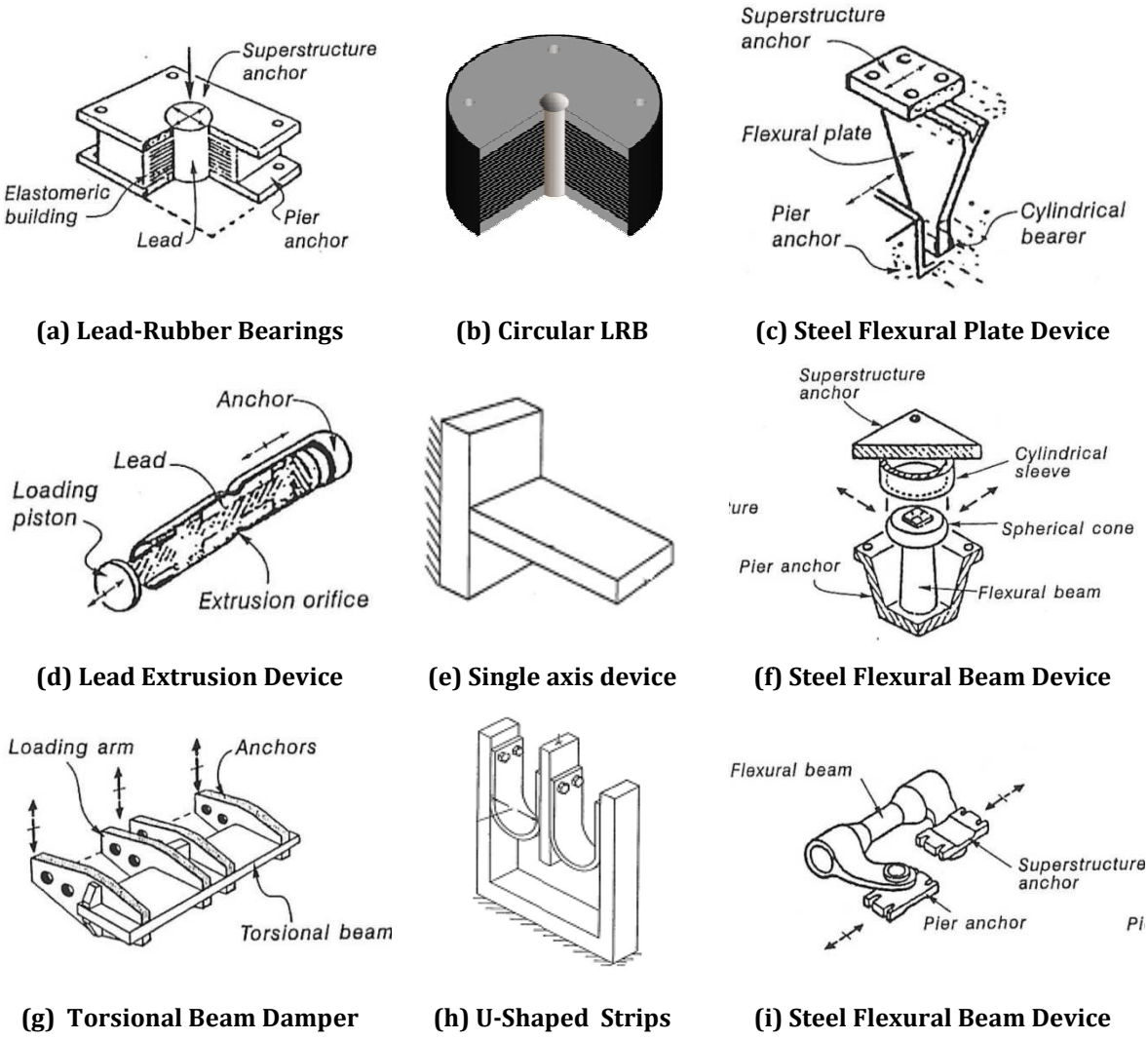

(a) Lead-Rubber Bearings **(b) Circular LRB** **(c) Steel Flexural Plate Device**

(d) Lead Extrusion Device **(e) Single axis device** **(f) Steel Flexural Beam Device**

(g) Torsional Beam Damper **(h) U-Shaped Strips** **(i) Steel Flexural Beam Device**

Figure 2.74. Mechanical Energy Dissipating Devices invented by Bill Robinson and Ivan Skinner at the DSIR, after Skinner et al. (1993)

From the dissipaters shown in Figure 2.74, the lead-rubber bearings (Figure 2.74a), the lead extrusion device (Figure 2.74d), and the torsional beam damper (Figure 2.74g), have already been used in seismic protection of bridges. The single axis dampers (Figure 2.74h), steel flexural plate device (Figure 2.74c), and the U-shaped strips (UFPs) (Figure 2.74h), have been used in buildings, but not in bridges (Kelly et al., 2010, Pampanin et al., 2011).

The UFPs have already been implemented to a number of low damage concrete and timber buildings around New Zealand which incorporated DCR connections. The Southern Cross Hospital in Christchurch which remained undamaged during Canterbury Earthquakes is one of the examples (Pampanin et al., 2011).

The application of U-shaped strips also known as U-Shaped Flexural Plates (UFPs) (Kelly et al., 1972) in the coupled rocking walls was investigated by Iqbal et al. (2010) and Pampanin et al. (2011). Recently, Baird et al. (2014) carried out experimental and numerical study of UFPs. During an earthquake, the UFPs are activated following a vertical relative sliding of the rocking wall panels respect to each other (Figure 2.75b). A sample UFP and its force-displacement response under quasi-static cyclic loading are shown in Figure 2.75a and Figure 2.75c, respectively.

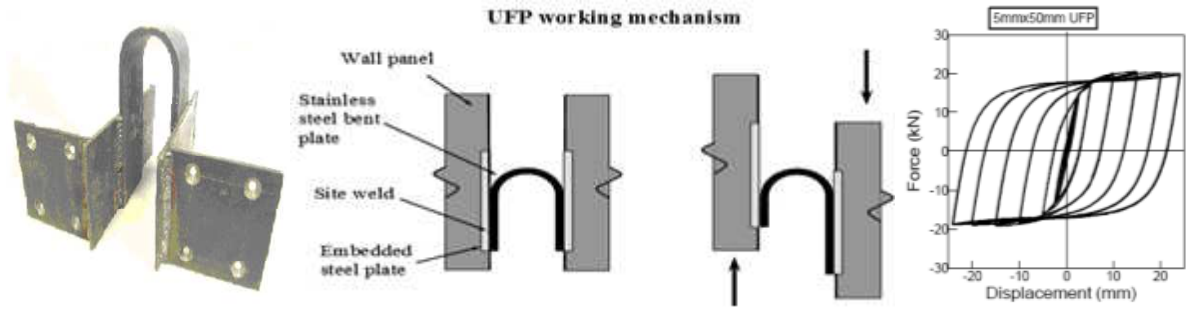

(a) **(b)** **(c)**

Figure 2.75. (a) A typical UFP, mounted between the steel plates for installation in rocking timber wall panels (b) UFP working mechanism (c) Force-displacement hysteresis, after Iqbal (2010)

UFPs offer great advantages such as cost-effectiveness, balanced response under tension and compression loading, minimal low-cycle fatigue, and less degradation under cyclic loading. Some of these features are not included in the available metallic dissipaters in the market. The UFPs have great potential of application in ABC in seismic regions. Therefore, it has been of a particular interest in this research to further develop a solution that can use UFPs with DCR connections for ABC Low Damage, as will be discussed in detail in Chapter 4.

2.5 Conclusions

There are many advantages associated with Accelerated Bridge Construction (ABC). These advantages include faster construction, minimal disruption to traffic and communities around the bridge site, better quality control, reduced maintenance requirements, less labor and equipment on-site, improved work zone safety, and less environmental impacts. Most of these advantages are not featured in the conventional monolithic construction of bridges.

In the last several years, primarily in the United States, the State DOTs, FHWA, and AASHTO, have been very active for sponsoring research into development of concepts for ABC in moderate-to-high seismic regions. The researchers in the United States, Taiwan, and New Zealand, are currently working on the new methodologies for improving seismic performance of the connections for ABC. Several types of connections have been proposed and investigated. The connections can be classified under emulative cast-in-place, semi-emulative cast-in-place, and non-emulative cast-in-place.

Caltrans ABC Strategic Plan (Chung et al., 2008) aims to improve the existing technologies for ABC and develop low damage solutions. For example, under the emulative cast-in-place connections, the grouted duct connections and splice sleeve couplers have already been in practice for buildings. Caltrans has included these connections for further research in the first phase of their ABC Strategic Plan. The future research will investigate the implementation of these connections for ABC in seismic zones. These connections are currently manufactured by a number of companies around the world and are available in the market. They are shown to be suitable for prefabricated bridge elements. The revision of the guidelines, standards, and specifications for these connections, do not appear to be major issues for Caltrans.

The second phase of Caltrans ABC Strategic Plan focuses on the structural systems which incorporate non-emulative cast-in-place connections for a low damage seismic design. The low damage systems are intended to minimize and eliminate damage in the precast bridge elements through dissipation of seismic energy in the connections. At the same time, this type of systems provides self-centering capacity for the whole bridge.

The low damage systems include the hybrid or DCR connections between the precast members. The DCR connections offer great seismic performance benefits. Past research programs have shown great promise for using DCR connections for the low damage seismic design of the prefabricated structures. DCR connections have been applied to many concrete, steel, and timber buildings worldwide, but as yet not to any bridges. There is a common concern among the bridge practitioners for the potential higher costs associated with DCR connections for ABC. The higher costs include the addition of a construction phase for unbonded post-tensioning which has to be weighed against the benefits for self-centering capacity.

Past research by Palermo (2004) and Marriott et al. (2008) into DCR technology have confirmed the feasibility of the technology without necessarily increasing the total costs respect to a conventional ductile cast-in-place pier. Recent findings from the loss modeling analyses have confirmed the benefits of an ABC Low Damage technology. The research showed that if a bridge incorporating the conventional ductile cast-in-place construction is located on an important arterial route of a big city, and there are limited detour options available, the loss due to the bridge downtime might exceed the cost of the bridge replacement following a big earthquake.

Based on current market trends in New Zealand, the damage resistant bridge technology using DCR connections should mainly target precast bridges with low-to-moderate span length (up to 30 m). Alternative construction systems using DCR connections for medium-to-long span precast bridges (more than 30 m) will be a future market trend. For the application of ABC Low Damage in New Zealand, suitable standards and guidelines on the precast segmental and non-segmental bridge substructure systems would need to be developed. This could be a similar task as what was developed by NZTA for the precast deck systems (NZTA Report 364, 2008).

The development of guidelines and detailing for the precast substructure systems in New Zealand would need to be based on the bridge span length, pier geometry, construction limits (e.g. cost-effectiveness, crane limits etc), and functional requirements. Another task is the development of guidelines for various configurations of the precast substructure systems (e.g. single or multi-column piers), as well as for each precast decking systems of NZTA Report 364. The guidelines should include

recommendation on location of rocking interfaces in a variety of substructure configurations under the seismic design criteria. The development of appropriate design procedure, detailing, and construction of DCR connections for bridges would be another crucial task.

2.6 Research Motivations

As described throughout this Chapter, there have been many types of solutions proposed for ABC in seismic regions. Most of these solutions are developed for emulative cast-in-place connections. There have been only a few large-scale testing carried out to validate their suitability for ABC in seismic regions. This type of solution accepts damage in the bridge substructure system during an earthquake.

Non-emulative cast-in-place connections have been developed with the aim to limit damage in the substructure system. There has been some research investigations on the development and testing of appropriate non-emulative connections. However, most of the studies have shown some type of damage to the connections which would need minor to moderate repairs (e.g. replacement of dissipaters, repairing flexural cracks in the column) following an earthquake. For a damage free substructure system which eliminates the need for replacement of the dissipaters, avoids cracking to the columns, and incorporates full self-centering, there has not been many research investigations done yet. Therefore, the research in this thesis aims to fill the aforementioned existing gaps in both types of technologies (emulative and non-emulative) through experimental and analytical investigations. These technologies have been investigated for short-to-medium span bridges in the context of New Zealand. New energy dissipation devices with superior seismic performance have been proposed, and their application in ABC has been validated through large scale-testing.

New Zealand has always been a world-leader for pioneering ground-breaking seismic design concepts and dissipative devices. The introduction of capacity design philosophy for seismic design of reinforced concrete structures was a revolutionary step in design of structures in earthquake prone areas (Park and Paulay, 1975). The research work by Professor Bob Park (1933-2004) and Professor Tom Paulay (1923-2009) at the University of Canterbury had immediately benefited the New Zealand bridge standards, design process, and construction technology in the 1970s. However, despite a

flourishing past, the amount of research work in the field of bridge engineering in New Zealand has significantly decreased over the last 10 to 15 years, as also cited in Kotze (2009). The New Zealand bridge community appears to live in the legacy of the past and a strategic research vision for the next two decades is still missing.

The research here is a starting point for the development of the next generation of bridge systems in New Zealand. The research aims to revive the low damage seismic design concepts using energy dissipaters invented by Bill Robinson (1938-2011) and Ivan Skinner (1923-2014) during 1970-1980s in New Zealand. These technologies have been modernized and thoroughly tested to meet the growing expectations of bridge owners and the society. For a proper implementation of these novel seismic technologies, bridge engineering communities such as NZTA, KiwiRail, City Councils, and bridge practitioners, should keep constant interactions with the researchers involved in the field of bridge engineering.

The research in this thesis is part of a national research project titled “Advanced Bridge Construction and Design for New Zealand” (ABCD). The project is funded by the Natural Hazards Research Platform under the New Zealand Ministry of Science and Innovation (2011-2015). The program is coordinated by Associate Professor Alessandro Palermo at the University of Canterbury. As part of the ABCD project, further research studies on the development of DCR connections for the superstructure system (Chegini and Palermo, 2014) and durability of emulative and DCR connections (Andisheh et al., 2014), are currently underway at the University of Canterbury.

2.7 Bibliography

1. AASHTO Highway Subcommittee on Bridges and Structures (2005). AASHTO Strategic Plan for Bridge Engineering. AASHTO, Washington, D.C., United States.

2. Accelerated Construction Technology Transfer (ACTT) (2005). "How to" Guide for State Highway Agencies. United States Department of Transportation, Federal Highway Administration (FHWA), Washington, D.C., United States.

3. Andisheh, K., Scott, A., and Palermo, A. (2014). Preliminary Estimation of Reduction Factors In Mechanical Properties Of Steel Reinforcement Due To Pitting Simulated Corrosion. Proceedings of New Zealand Society for Earthquake Engineering Conference, Auckland, New Zealand.

4. Beck, J. L. and Skinner, R. I. (1974). The Seismic Response of a Reinforced Concrete Bridge Pier Designed to Step. International Journal of Earthquake Engineering and Structural Dynamics, 2(4):343-358.

5. Billington, S. L., Barnes, R. W., and Breen, J. E. (1999). A Precast Segmental Substructure System for Standard Bridges. Journal of Precast and Prestressed Concrete Institute, 44(4):56-73.

6. Billington, S.L., and Yoon, J.K. (2004). Cyclic Response of Unbonded Post-Tensioned Precast Columns with Ductile Fiber-Reinforced Concrete. Journal of Bridge Engineering, 9(4):353-363.

7. Billington, S.L., Barnes, R.W., Breen, J.E. (2001). Alternative substructure systems for standard highway bridges. ASCE Journal of Bridge Engineering, 6(2): 87-94.

8. Blanchard, B. A., Schexnayder, C. J., Bohuslav, T. R., DeWitt, S. D., Schneider, C., Raymond, G. Anderson, S., and Sheffield, R., (2009). Best Practices in Accelerated Construction Techniques, NCHRP Project 20-68A, Scan 07-02. Transportation Research Board, National Research Council, Washington, D.C., United States.

9. Brenes, F., Wood, S., and Kreger, M. (2006). Anchorage Requirements for Grouted Vertical-Duct Connectors in Precast Bent Cap Systems, Report No. 0-4176-S. Center for Transportation Research, the University of Texas at Austin, Texas, United States.

10. Bromenschenkel, R. (2010). Caltrans Next Generation Bridge. Proceedings of 26th US-Japan Bridge Engineering Workshop, New Orleans, Louisiana., United States.

11. Bruneau, M., and Marson, J. (2004). Seismic Design of Concrete-Filled Circular Steel Bridge Piers. Journal of Bridge Engineering, 9(1):24-34.

12. Buckle, I. G. (1994). The Northridge, California Earthquake of January 17, 1994: Performance of Highway Bridges, Technical Report 0008 1994. National Centre for Earthquake Engineering Research (NCEER), Buffalo, New York, United States.

13. Change, K. C., Tsai, M. S., Ou, Y. C., Wang, P. H., and Lee G. C. (2012). Research and Application of Precast Segmental Concrete Bridge Columns in Regions of High Seismicity. Proceedings of 6th International Conference on Bridge Maintenance, Safety, and Management (IABMAS), Stresa, Italy.

14. Chegini, Z., and Palermo, A. (2014). Investigation of The Behavior of Small-Scale Bridge Models Using Shake Table Tests. Proceedings of New Zealand Society for Earthquake Engineering Conference, Auckland, New Zealand.

15. Christopoulos, C. (2004). Frequency Response of Flag-Shaped Single Degree-of-Freedom Hysteretic Systems. Journal of Engineering Mechanics, 130(8):894-903.

16. Chung, P. C., Wolfe, R. W., and Fang, J. Q., (2008). Caltrans Accelerated Bridge Construction (ABC) Initiative. California Department of Transportation (Caltrans), Sacramento, California, United States.

17. Culmo, M. (2009). Connection Details for Prefabricated Bridge Elements and Systems, Report No. FHWA-IF-09-010. Federal Highway Administration, Office of Bridge Technology, Washington, D.C., United States.

18. Davis, P. M., Janes, T. M., Eberhard, M. O., and Stanton, J. F. (2012). Unbonded Pre-Tensioned Columns for Bridges in Seismic Regions, PEER Report 2012/04. Pacific Earthquake Engineering Research (PEER) Center, University of California, Berkeley, California, United States.

19. DesRoches, R., McCormick, J., and Delemont, M. (2004). Cyclic Properties of Superelastic Shape Memory Alloy Wires and Bars. Journal of Structural Engineering, 130(1):38-46.

20. Eberhard, M. O., Stanton, J. F., Haraldsson, O. S. Finnsson, G., Davis, P. M., and Schoettler, M. J. (2014). Development of a Bridge Bent System for Rapid Construction and Enhanced Seismic Performance. Proceedings of 10th United States National Conference on Earthquake Engineering, Anchorage, Alaska, United States.

21. Eurocode 8 (2004). Design of Structures for Earthquake Resistance.

22. Federal Highway Administration (2005). Prefabricated Bridge Elements and Systems in Japan and Europe, Report FHWA-PL-05-003. FHWA, Washington, D.C., United States.

23. Federal Highway Administration (2009). Connection Details for Prefabricated Bridge Elements and Systems, Report FHWA-IF-09-010. FHWA, Washington, D.C., United States.

24. Fouad, F. H., Hamby, D., Rizk, T., and Stafford, E. L. (2006). Prefabricated Precast Concrete Bridge System for the State of Alabama. University Transportation Center for Alabama, Tuscaloosa, Alabama, United States.

25. Gray, A., Gaby, P., Brown, G., Kirkcaldie, D., Cato, R., and Sweetman, P. (2003). New Zealand Precast Concrete Bridge Beams Stage 1 - Research and Identify Proposed Standard Beam Shapes and Spans. Transfund New Zealand, Wellington, New Zealand.

26. Guerrini, G., Restrepo, J. I., Massari, M., and Vervelidis, A. (2012). Self-Centering Precast Concrete Dual-Shell Steel Columns. Proceedings of 15th World Conference on Earthquake Engineering, Lisbon, Portugal.

27. Haraladsson, O., Stanton, J. F., and Eberhard, M. O. (2011). Laboratory Tests of Column-to-Footing Socket Connections, Report No. FHWA-HIF-13-039. Federal Highway Administration, Office of Bridge Technology, Washington, D.C., United States.

28. Haraldsson, O. S., Janes, T. M., Eberhard, M. O., and Stanton, J. F. (2013). Seismic Resistance of Socket Connection between Footing and Precast Column. Journal of Bridge Engineering, 18(9):910-919.

29. Hawkins, N., Wood, S., and Stanton, J. (1994). Performance of Parking Garages in the 1994 Northridge Earthquake. American Society of Civil Engineers Structures Congress, Boston, Massachusetts, United States.

30. Hewes, J. T., and Priestley, M. J. N. (2002). Seismic Design and Performance of Precast Concrete Segmental Bridge Columns, Report No. SSRP-2001/25. California Department of Transportation, Sacramento, California, United States.

31. Holombo, J., Priestley, M. J. N., and Seible, F. (2000). Continuity of Precast Prestressed Spliced-Girder Bridges under Seismic Loads. Precast/Prestressed Concrete Institute Journal, 45(2):40–63.

32. Housner, G. W. (1963). The Behavior of Inverted Pendulum Structures during Earthquakes. Bulletin of the Seismological Society of America, 53(2):403-417.

33. Ince, J. A. (1998). A City of Bridges. Christchurch City Council, New Zealand.

34. Iqbal, A., Pampanin, S., Palermo, A., Buchanan, A. (2010). Seismic response of post-tensioned timber walls. Proceedings of 14th European Conference on Earthquake Engineering. Skopie-Ohrid, Republic of Macedonia.

35. Kapur, J., Keever, M., Yen, W. P., Sletten, J., Dekelbab, W., Tobias, D., Bardow, A., and Saiidi, M. S., (2012). Best Practices Regarding Performance of ABC Connections in Bridges Subjected to Multi-hazard and Extreme Events, NCHRP Project 20-68A, Scan 11-02. Transportation Research Board, National Research Council, Washington, D.C., United States.

36. Karapiperis, D., Lykidis, G., Savvopoulos, G. C., Khaled, E. S., and Loukakis, K. (2010). Combined Effort. Civil Engineering, 80(7):74–85.

37. Kawashima, K. (2002). Seismic Design of Concrete Bridges. Proceeding of the first fib Congress. Osaka, Japan.

38. Keck, D., Patel, H., Scolaro, A. J., Block, A., and Ryan, C. (2010). Accelerating Transportation Project and Program Delivery: Conception to Completion, NCHRP Report 662. Transportation Research Board, National Research Council, Washington, D.C., United States.

39. Kelly, J. M., Skinner, R. I., and Heine, A. J. (1972). Mechanisms of Energy Absorption in Special Devices for use in Earthquake Resistant Structures. Bulletin of the New Zealand Society for Earthquake Engineering, 5(3).

40. Kelly, T., Skinner, I., and Robinson, W.H. (2010). Seismic Isolation for Designers and Structural Engineers. National Information Centre of Earthquake Engineering (NICEE), Kanpur, India.

41. Kingsley, A. M. (2005). Experimental and Analytical Investigation of Embedded Column Base Connections for Concrete Filled High Strength Steel Tubes. Master's Thesis, University of Washington, Seattle, Washington, United States.

42. Kotze, R. (2009). The Future of Concrete Bridges. Contrafed 33(1), New Zealand.

43. Kurama, Y. (1997). Seismic Analysis, Behavior, and Design of Unbonded Post-Tensioned Precast Concrete Walls. PhD thesis, Lehigh University, Bethlehem, Pennsylvania, United States.

44. Kurama, Y. C., Sause, R., Pessiki, S., and Lu, L. (1999). Lateral Load Behavior and Seismic Design of Unbonded Post-Tensioned Precast Concrete Walls. PCI Journal, 96(4).

45. Mander, J., and Cheng, C. T. (1997). Seismic Resistance of Bridge Piers Based on Damage Avoidance Design, Technical Report NCEER-97-0014. University at Buffalo (SUNY), New York, United States.

46. Marriott, D. (2009). The Development of High-Performance Post-Tensioned Rocking Systems for the Seismic Design of Structures. PhD Thesis, University of Canterbury, Christchurch, New Zealand.

47. Marriott, D., Pampanin, S., Bull, D., and Palermo, A. (2009). A Probabilistic Seismic Loss Assessment of Advanced Post-tensioned Precast Bridge Systems. Proceedings of New Zealand Society for Earthquake Engineering (NZSEE) Conference, Christchurch, New Zealand.

48. Marsh, M. L., Wenli, M., Garrett, B. E., Stanton, J. F., Eberhard, M. O., and Weinert, M. D. (2011). Application of Accelerated Bridge Construction Connections in Moderate-to-High Seismic Regions, NCHRP Report 698. TRB, National Research Council, Washington, D.C., United States.

49. Marson, J., and Bruneau, M. (2004). Cyclic Testing of Concrete-Filled Circular Steel Bridge Piers Having Encased Fixed-Based Detail. Journal of Bridge Engineering, 9(1):14–23.

50. Matsumoto, E. E. (2009). Emulative Precast Bent Cap Connections for Seismic Regions: Grouted Duct and Cap Pocket Test Results, Report ECS-CSUS-2009-05. California State University at Sacramento, California, United States.

51. Matsumoto, E. E., Waggoner, M. C., Sumen, G., Kreger, M. E., Wood, S. L., and Breen, J. E. (2001). Development of a Precast Bent Cap System, Report 1748-2. Center of Transportation Research, the University of Texas at Austin, Texas, United States.

52. Motaref, S., Saiidi, M. S., and Sanders, D. (2010). Experimental Study of Precast Bridge Columns with Built-in Elastomer. Journal of the Transportation Research Board (2202):109-116.

53. National Cooperative Highway Research Program (NCHRP) Synthesis of Highway Practice 119 (1985). Prefabricated Bridge Elements and Systems, Transportation Research Board (TRB), National Research Council, Washington, D.C., United States.

54. NCHRP Synthesis 324 (2003). Prefabricated Bridge Elements and Systems to Limit Traffic Disruption during Construction. Transportation Research Board, National Research Council, Washington, D.C., United States.

55. Nelson, M., Lai, Y. C., and Fam, A. (2008). Moment Connection of Concrete-Filled Fiber Reinforced Polymer Tubes by Direct Embedment into Footings. Advances in Structural Engineering, 11(5):537–547.

56. New Zealand Standards (NZS) (2006). The Design of Concrete Structures, NZS 3101. Wellington, New Zealand.

57. New Zealand Transport Agency (2008). Standard Precast Concrete Bridge Beams, Report No. NZTA 364. Wellington, New Zealand.

58. New Zealand Transport Agency (2013). Bridge Manual, Third Edition. Wellington, New Zealand.

59. Ou, Y. C., Chiewanichakorn, M., Aref, A. J., Lee, G. C. (2007). Seismic Performance of Segmental Precast Unbonded Post-tensioned Concrete Bridge Columns. Journal of Structural Engineering. 133(11) 1636-1647.

60. Ou, Y. C., Tsai, M. S., Oktavianus, Y., and Chang, K.C. (2012). Cyclic Testing Of a Tall Precast Segmental Concrete Bridge Column with a Cast-In-Place Plastic Hinge Region. Proceedings of 6th International Conference on Bridge Maintenance, Safety, and Management (IABMAS), Stresa, Italy.

61. Palermo, A. (2004). The Use of Controlled Rocking In the Seismic Design of Bridges. PhD Thesis, Politecnico Di Milano (Technical University of Milan), Italy.

62. Palermo, A. and Mashal M. (2012). Accelerated Bridge Construction and Seismic Damage Resistant Technology: A New Zealand Challenge. Bulletin of the New Zealand Society for Earthquake Engineering, 45(3): 123-134.

63. Palermo, A. and Pampanin, S. (2008). Enhanced Seismic Performance of Hybrid Bridge Systems: Comparison with Traditional Monolithic Solutions. Journal of Earthquake Engineering, 12(8):1267-1295.

64. Palermo, A., Pampanin, S., and Calvi, G. M. (2005). Concept and Development of Hybrid Solutions for Seismic Resistant Bridge Systems. Journal of Earthquake Engineering, 9(6):899-921.

65. Palermo, A., Pampanin, S., and Marriott, D. (2007). Design, Modeling, and Experimental Response of Seismic Resistant Bridge Piers with Post-tensioned Dissipating Connections. Journal of Structural Engineering, 133(11):1 648-1661.

66. Pampanin, S., Kam W., Haverland, G., Gardiner, S. (2011). Expectation Meets Reality: Seismic Performance of Post-Tensioned Precast Concrete Southern Cross Endoscopy Building during the 22nd Feb 2011 Christchurch Earthquake. Proceedings of New Zealand Concrete Industry Conference, Rotorua, New Zealand.

67. Pampanin, S., Marriot, D., and Palermo, A. (2010). PRESSS Design Handbook. New Zealand Concrete Society (NZCS) Incorporation, Auckland, New Zealand.

68. Pang, J. B. K., Eberhard, M. O., and Stanton, J. F. (2010). Large-Bar Connection for Precast Bridge Bents in Seismic Regions. Journal of Bridge Engineering, 15(3):231-239.

69. Pang, J., Steuck, K., Cohagen, L., Eberhard, M., and Stanton, J. (2008). Rapidly Constructible Large-Bar Precast Bridge-Bent Seismic Connection, Report No. WA-RD 684.2. Washington State Transportation Center (TRAC), Washington, United States.

70. Park, R. and Paulay, T. (1975). Reinforced Concrete Structures. John Wiley and Sons, Incorporation, New Jersey, United States.

71. Paulson, C., and Hanson, J. M. (1991). Fatigue Behavior of Welded and Mechanical Splices in Reinforcing Steel, NCHRP Project 10-35 Final Report. Transportation Research Board, National Research Council, Washington, D.C., United States.

72. Priestley, M. J. N. (1991). Overview of PRESSS Research Program. Precast/Prestressed Concrete Institute Journal, 36(4):50-57.

73. Priestley, M. J. N. (1996). PRESSS Program - Current Status and Proposed Plans for Phase III. Precast/Prestressed Concrete Institute Journal, 41(2):22-40.

74. Priestley, M. J. N., Sritharan, S., Conley, J. R., and Pampanin, S. (1999). Preliminary Results and Conclusions from the PRESSS Five-Story Precast Concrete Test Building. Precast/Prestressed Concrete Institute Journal, 44(6):42-67.

75. Ralls, M. L. (2014). History of ABC Implementation in U.S. Proceedings of National Accelerated Bridge Construction, 3-10, Miami, United States.

76. Restrepo, J. I., Mander, J., and Holden, T. J. (2001). New Generation of Structural Systems for Earthquake Resistance. Proceedings of New Zealand Society for Earthquake Engineering (NZSEE) Conference, Wairakei, New Zealand.

77. Restrepo, J. I., Tobolski, M. J., and Matsumoto, E. E. (2011). Development of a Precast Bent Cap System for Seismic Regions, NCHRP Report 681. Transportation Research Board, National Research Council, Washington, D.C., United States.

78. Riva, P. (2006). Seismic Behavior of Precast Column-to-Foundation Grouted Sleeve Connections. Proceedings of International Conference on Advances in Engineering Structures, 121-128, Waterloo, Canada.

79. Robinson, W. H. (1995). Seismic Isolation, the New Zealand Experience. American Society of Mechanical Engineering, New York, United States.

80. Roeder, C. W., Lehman, D. E., and Thody, R. (2009). Composite Action in CFT Components and Connections. AISC Engineering Journal, 47(4):229–242.

81. Roh, H., and Reinhorn, A. M. (2010). Hysteretic Behavior of Precast Segmental Bridge Piers with Superelastic Shape Memory Alloy Bars. Engineering Structures, 32(10): 3394–3403.

82. Saiidi, M. S., and Wang, H. (2006). Exploratory Study of Seismic Response of Concrete Columns with Shape Memory Alloys Reinforcements. ACI Structural Journal, 103(3):435-442.

83. Saiidi, M. S., O'Brien, M., and Mahmoud, S. (2009). Cyclic Response of Concrete Bridge Columns using Superelastic Nitinol and Bendable Concrete. ACI Structural Journal, 106(1):69–77.

84. Sarti, F., Smith, T., Palermo, A., Bonardi, D., and Carradine, D. M. (2013). Experimental And Analytical Study of Replaceable Buckling-Restrained Fuse-Type (BRF) Mild Steel Dissipaters. Proceedings of New Zealand Society for Earthquake Engineering Conference, Wellington, New Zealand.

85. Sideris, P., Anagnostopoulou, M., Aref, A., and Filiatrault, A. (2010). Seismic Performance of Precast Segmental Bridges. Proceedings of 9th United States National and 10th Canadian Conference on Earthquake Engineering: Reaching Beyond Borders, Toronto, Canada.

86. Sideris, P., Aref, A. J., and Filiatrault, A. (2012). Hybrid Sliding-Rocking Post-Tensioned Segmental Bridges: Large-Scale Quasi-Static and Shake Table Testing. Proceedings of 15th World Conference on Earthquake Engineering, Lisbon, Portugal.

87. Skinner, I., Robinson, W. H., and McVerry, G. H. (1993). An Introduction to Seismic Isolation. John Wiley & Sons, New York, United States.

88. Snyder, R., and Sritharan, S. (2010a). Caltrans Project 05-0160-Seismic Performance of an I-Girder to Inverted-T Bent Cap Connection: A Summary of the Horizontal Load Test of the Inverted-T Test Unit. Iowa State University, Ames, Iowa, United States.

89. Snyder, R., and Sritharan, S. (2010b). Caltrans Project 05-0160—Seismic Performance of an I-Girder to Inverted-T Bent Cap Connection: A Summary of the Vertical Load Test of the Inverted-T Test Unit. Iowa State University, Ames, Iowa, United States.

90. Solberg, K., Dhakal, R., Mander, J., and Mashiko, N. (2006). Performance of a Damage Protected Highway Bridge Pier Subjected to Bi-directional Earthquake Attack. Journal of Structural Engineering, 135(5):469-478.

91. Special Report 249 (1996). Building Momentum for Change: Creating a Strategic Forum for Innovation in Highway Infrastructure. Transportation Research Board, National Research Council, Washington, D.C., United States.

92. Sritharan, S., Priestley, M. J. N., and Seible, F. (1999). Enhancing Seismic Performance of Bridge Cap Beam-to-Column Joints using Prestressing. Precast/Prestressed Concrete Institute Journal (PCI), 44(4): 74–91.

93. Sritharan, S., Priestley, M. J. N., and Seible, F. (2001). Seismic Design and Experimental Verification of Concrete Multiple Bents. American Concrete Institute (ACI) Structural Journal, 98(3):335–346.

94. Sritharan, S., Vander Werff, J., Abendroth, R. E., Wassef, W. G., and Greimann, L. F. (2005). Seismic Behavior of a Concrete/Steel Integral Bridge Pier System. Journal of Structural Engineering, 131(7):1083–1094.

95. Sritharan, S., Werff, J. V., Peggar, R., and Bromenschenkel, R. (2014). Seismic Performance of Precast Grider-to-Cap Beam Connections Designed for ABC. Proceedings of National Accelerated Bridge Construction Conference, 313-322, Miami, United States.

96. Stanton, J. F., Wacker, J. M., Hieber, D. G., and Eberhard, M. O. (2005). Design of Precast Concrete Piers for Rapid Bridge Construction in Seismic Regions. Washington State Transportation Center (TRAC), University of Washington, Seattle, Washington, United States.

97. Stanton, J., Hawkins, N., and Eberhard, M. (1992). Seismic Connections for Precast Concrete Structures. Proceedings of 10th World Conference on Earthquake Engineering, 4403-4403, Madrid, Spain.

98. Stanton, J., Hicks, T., and Hawkins, N. (1991). PRESSS Project 1.3 - Connection Classification and Evaluation. PCI Journal, 36(5):62-71.

99. Stanton, J., Stone, W. C., and Cheok, G. S. (1997). Hybrid Reinforced Precast Frame for Seismic Regions. PCI Journal, 42(2):20-32.

100. Stone, W. C., Cheok, G. S., and Stanton, J. F. (1995). Performance of Hybrid Moment Resisting Precast Beam-Column Concrete Connections Subjected to Cyclic Loading. ACI Structural Journal, 91(2):229-249.

101. Strategic Highway Research program (SHRP2) (2013). Innovative Bridge Designs for Rapid Renewal - ABC Toolkit. Transportation Research Board, National Research Council, Washington, D.C., United States.

102. Thonstad, T., Haraldsson, O. S., Stanton, J. F., and Eberhard, M. O. (2014). An ABC Bridge Bent That Self-Centers After an Earthquake. Proceedings of National Accelerated Bridge Conference, 630-639, Miami, United States.

103. Utah Department of Transportation (2009). Precast Piers and Footings. UDOT, Salt Lake City, Utah, United States.

104. Utah Department of Transportation (2010). Precast Substructure Elements Manual. UDOT, Salt Lake City, Utah, United States.

105. Varela, S., and Saiidi, M. S. (2014). Damage-Free Earthquake-Resistant Deconstructible Columns for ABC. Proceedings of National Accelerated Bridge Conference, 620-629, Miami, United States.

106. White, S. (2014). Controlled Damage Rocking Systems for Accelerated Bridge Construction. Master Thesis, University of Canterbury, Christchurch, New Zealand.

107. Yen, W.P., Aref, A. (2010). Development of Accelerated Bridge Construction Detail for Seismic Regions. University at Buffalo (SUNY), New York, United States.

108. Youssef, M. A., Alam, M. S., and Nehdi, M. (2008). Experimental Investigation on the Seismic Behavior of Beam-Column Joints Reinforced with Superelastic Shape Memory Alloys. Journal of Earthquake Engineering, 12(7):1205–1222.

109. Zhu, Z., Ahmad, I., and Mirmiran, A. (2006). Seismic Performance of Concrete-Filled FRP Tube Columns for Bridge Substructure. Journal of Bridge Engineering, 11(3):359–370.

3. DEVELOPMENT AND TESTING OF ABC HIGH DAMAGE PIER SYSTEM

3.1 Introduction

This Chapter presents the development and testing of precast segmental cantilever and multi-column bridge pier systems. Two types of emulative Cast-In-Place (CIP) connections, the Grouted Duct Connection (GDC) and Member Socket Connection (MSC), for precast elements were experimentally tested. These connections were previously introduced in Chapter 2 under emulative CIP connections for ABC. Emulative CIP connections target similar seismic performance to that of monolithic construction (e.g. formation of plastic hinges). Therefore, given the extent of damage in the connections following a design level earthquake, the emulative connections are titled "ABC High Damage" or simply High Damage (HD) connections.

In the first phase of testing, four half-scale precast cantilever segmental columns were constructed and tested. Two specimens featured GDC for the column to footing and segment to segment connections. The other two specimens incorporated MSC for the column to footing and GDC between the segments. Using observation of seismic performance and testing results from the first specimen, some detailing improvements for GDC were incorporated in the design and construction of subsequent specimens.

In the second phase of testing, a half-scale fully precast multi-column pier (bent) was constructed and tested. The columns were not segmental in this specimen. The column to footing connection was MSC while the column to cap beam connection was GDC.

Testing results and observation from the second phase of testing are used for the seismic evaluation and assessment of an identical specimen, but with Dissipative

Controlled Rocking (DCR) connections in the third phase of testing. This will be discussed under ABC Low Damage in Chapter 5.

In summary, the main objectives of this Chapter are as follows:

1. Presenting design procedure and detailing considerations for ABC High Damage pier systems (cantilever and multi-column).

2. Discussing construction technologies and assembly procedures for ABC High Damage pier systems.

3. Investigating seismic performance of ABC High Damage with two types of emulative cast-in-place connections (grouted duct and member socket connections). This objective is achieved through development and experimental testing of several half-scale cantilever columns under uni and bi-directional quasi-static cyclic loading.

4. Following testing of columns with member socket connections to their failure points, investigation of sliding resistance of the column stubs under vertical loads. This objective is attained through carrying out punching shear (pull through) testing on the footing blocks of cantilever columns with member socket connections.

5. Investigating seismic response of a multi-column pier (bent) which incorporates a combination of grouted duct and member socket connections for the column to cap beam and column to footing connections, respectively. This objective is achieved through development and testing of a half-scale bent under uni-directional quasi-static testing.

3.2 ABC High Damage: Cantilever Segmental Pier System

Four half-scale segmental piers were developed using High Damage (HD) connections between the precast components. The HD connections tested include the Grouted Duct Connection (GDC) and Member Socket Connection (MSC). Two specimens (HDS1 and HDS2) were with the square cross-sections. The other two (HDC1 and HDC2) were circular sections. A summary of the specimens with their connection types and loading protocol are presented in Table 3.1.

Table 3.1. Summary of the test specimens

Specimen	Connection Type		Section Shape	Quasi-Static Testing Protocol
	Column to Foundation	Segment to Segment		
HDS1	GDC	GDC	Square	Uniaxial
HDS2	GDC	GDC	Square	Biaxial
HDC1	MSC	GDC	Circular	Uniaxial
HDC2	MSC	GDC	Circular	Biaxial

Figure 3.1 presents a general schematic for the HD specimens. The prototype structure, testing arrangement, design procedure, detailing considerations, construction technology, assembly sequence, and testing results for each HD column, are presented accordingly.

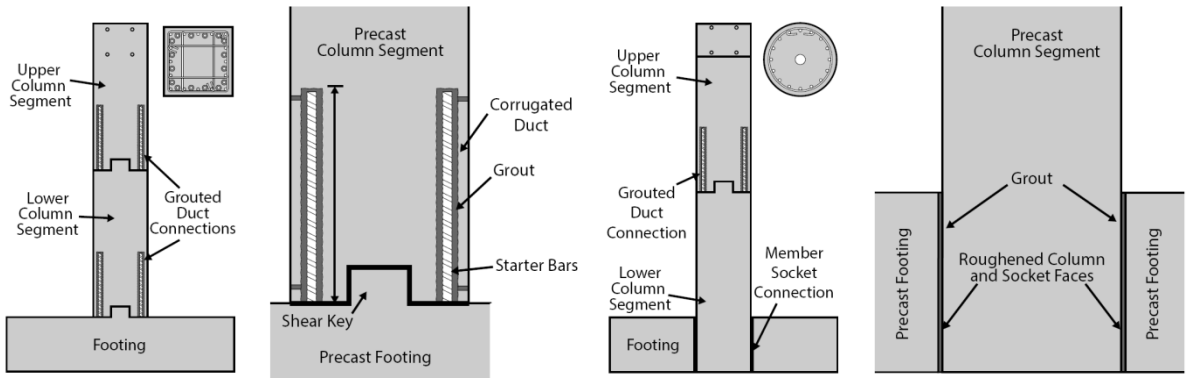

(a) HDS1 and HDS2 **(b) GDC** **(c) HDC1 and HDC2** **(d) MSC**

Figure 3.1. Schematic of High Damage columns and their connections

3.2.1 Prototype Structure

The prototype structure was developed based on a hammerhead pier for a typical highway bridge in New Zealand, as shown in Figure 3.2. The bridge has six spans of equal length. Each span is 12 m which gives a total length of 72 m for the bridge. The height from the column to footing connection up to the center of mass of the bridge is taken to be 5 m. The overall width of the bridge is taken as 10.4 m.

The superstructure is consisted of a double hollow-core deck according to NZTA 364 Report (NZTA, 2008). As explained in Chapter 2, the double hollow-core deck is one of the most popular superstructure systems for the short span bridges in New Zealand.

The bridge is assumed to be located on non-liquefiable soils. During development of the prototypes, no specific design for the footings was considered. The base connections are taken to be fully fixed with no soil-structure interaction taken into account. The footing system shown in Figure 3.2 for the prototype structure is only indicative.

There was no consideration given for the service loads on the bridge in combination with the earthquake loads, except the gravity loads resulting from the dead load of the superstructure and self-weight of the substructure elements (cap beam and pier).

A Force-Based Design (FBD) approach was used for the earthquake loading of the prototype structure. This was based on the seismic loading criteria from New Zealand Bridge Manual Second Edition (NZTA, 2003) and New Zealand Standards 1170.5 “Structural Design Actions-Earthquake Actions” (NZS, 2004). It should be noted that the third edition for the New Zealand Bridge Manual (NZTA, 2013) was published after the design of the prototype here. The updated Manual contains several amendments under the seismic loading criteria for design of bridges. This edition of the Manual was subsequently used for the development of the prototype for the multi-column pier system in the second and third phase of testing.

The reason behind using a force-based design approach was due to its compliancy with the current building codes in New Zealand. The force-based design is widely known and practiced for the design of bridges in New Zealand. Recently, an alternative Displacement Based Design (DBD) was developed by Priestley et al. (2007) to replace

the current force-based design methodology. The displacement based design is utilizing displacement limits for a structure which is very useful especially for the design of rocking type structures. Since 2007, the displacement based design has been incorporated in several building codes in the United States (Caltrans, 2013) and Australia (Austroads, 2012), for the design of bridges. In New Zealand, a displacement based design approach is currently sought for the future editions of the Bridge Manual.

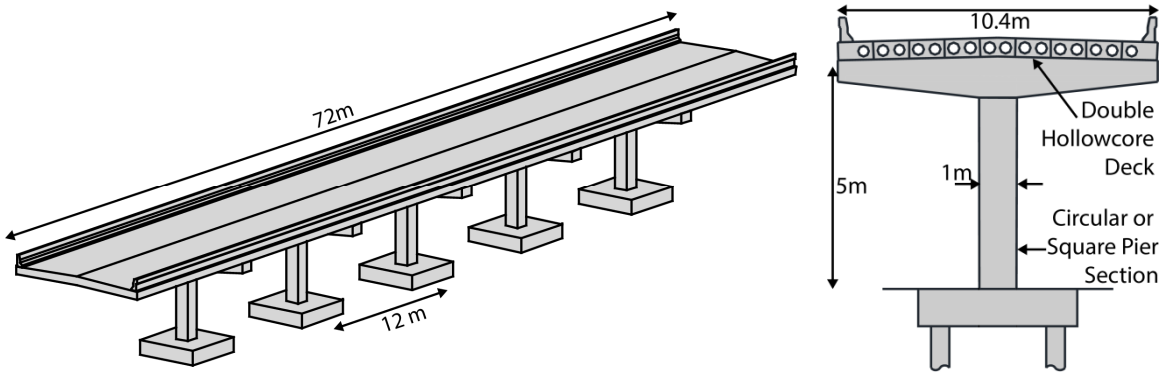

(a) Longitudinal view **(b) Elevation view**

Figure 3.2. Prototype Bridge

Table 3.2 presents a summary of the seismic parameters selected for the prototype bridge in accordance with NZS 1170.5 and NZTA Bridge Manual 2nd Edition. More details on the methodology for calculating lateral loads in accordance with NZS 1170.5 can be found in Section A.1 of Appendix A. In Table 3.2, the design gravity and design lateral loads are scaled down by 4 for the half-scale specimens. The scaling factor 4 is the reduction factor in the cross-sectional area of the half-scale specimens. This means that for the full-scale column shown in Figure 3.2b, the cross-sectional area of the column would be 4 times greater than the cross-sectional area of its half-scale column.

Table 3.2. Summary of the force-based design parameters

Seismic Hazard Factor, Z	0.3
Soil Class	C (Shallow Soils)
Return Period, T_R	1000 Years
Return Period Factor, R	1.3
Near Fault Factor, N	1
Assumed Ductility, μ	3
Structural Performance Factor, S_p	0.7
Fundamental Natural Period, T	0.4 sec
Design Lateral Load, V	680 kN
Scaled Lateral Load, V_{scaled}	170 kN
Design Gravity Load, W	1800 kN
Scaled Gravity Load, W_{scaled}	450 kN
Seismic Coefficient (V_{scaled}/W_{scaled})	0.38

3.2.2 Testing Arrangement

This section provides information on testing arrangement for the HD specimens. The uniaxial testing corresponds to seismic loading of the bridge pier in the transverse direction. This means that the lateral loads in the longitudinal direction of the bridge are resisted by the abutments. For testing this was represented by using a lateral ram with 400 kN capacity acting on one of the horizontal directions (North-South) on the specimen. The ram was attached to a reaction steel braced frame.

The biaxial testing corresponds to seismic loading of the piers in both horizontal directions. In this case, the piers are the main seismic force resisting system for the bridge. During testing, this case was represented by using two rams perpendicular to each other in the North-South and East-West directions. Both rams were identical with 400 kN capacity, and were attached to reaction steel braced frames. In order to prevent from out-of -plane movements in the reactions frames, the frames were also braced in the transverse directions.

Gravity loads on a half-scale column was simulated using an unbonded post-tensioned bar running through a duct at the center of the column, and fixed mechanically at the bottom of footing and top of the column. Using a hydraulic jack on top of the column, the bar was stressed to a force level corresponding to the scaled gravity load (W_{scaled}), as presented in Table 3.2. There was a load cell (axial actuator) along the load path for the post-tensioned bar to monitor the force levels (axial load on the column) during testing. The gravity load was being held constant (to within approximately ±5%) during testing.

A 400 x 400 x 50 mm steel plate was put between the load cell and top of the column to distribute the bar stress over a larger area on top of the column. In this case, as column displaces, the post-tensioned bar will be stretched more. Therefore, it increases the axial force on the column. In order to prevent from such a scenario, the hydraulic jack was being regulated throughout the tests, in order to keep the axial force on the column close to the scaled gravity load.

Figure 3.3 and Figure 3.4 illustrate testing setup for the uniaxial and biaxial loading, respectively. It should be noted that the uniaxial testing arrangement for HDS1 was identical to HDC1. Similarly, the biaxial testing setup for HDS2 was identical to HDC2.

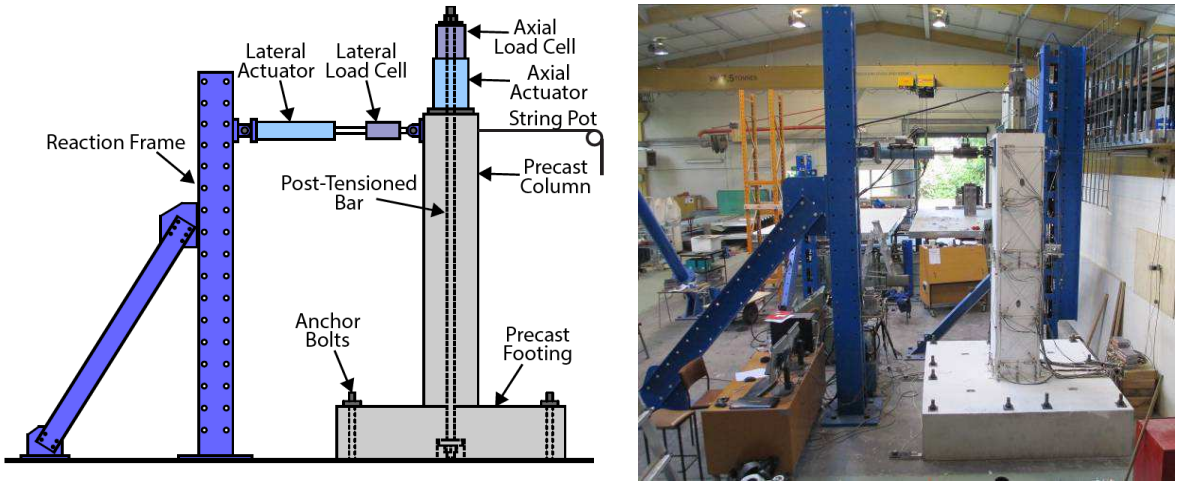

(a) In-plane elevation view **(b) Typical pier under testing**

Figure 3.3. Uniaxial testing setup

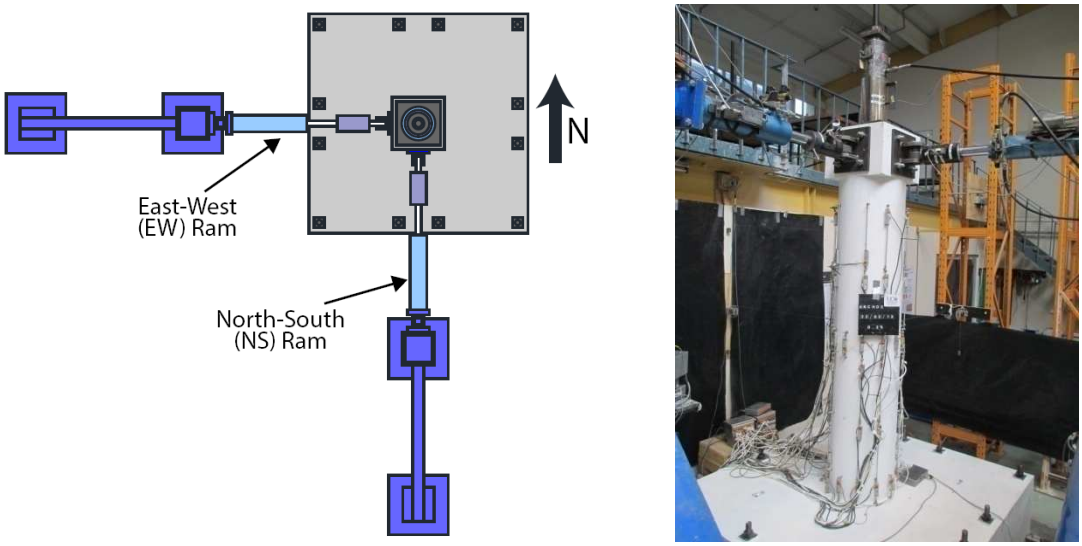

(a) Plane view **(b) Typical pier under testing**

Figure 3.4. Biaxial testing setup

3.2.2.1 Uniaxial Loading Protocol

The uniaxial testing consisted of unidirectional quasi-static cyclic loading with increasing displacements. The input loading sequence at each drift ratio on a test specimen was consisted of three cycles of loading at the corresponding drift ratio, followed by a smaller cycle with a half amplitude of the drift ratio as the one for the previous three cycles. There was an increasing factor of 1.2 to 1.5 between the consecutive drift ratios. Each uniaxial cycle comprised of a push and pull in the North-South (NS) direction on the test specimen. This type of loading protocol was adopted from the ACI recommendations (ACI Innovation Task Group 1, 2001). The uniaxial quasi-static cyclic loading is plotted in Figure 3.5.

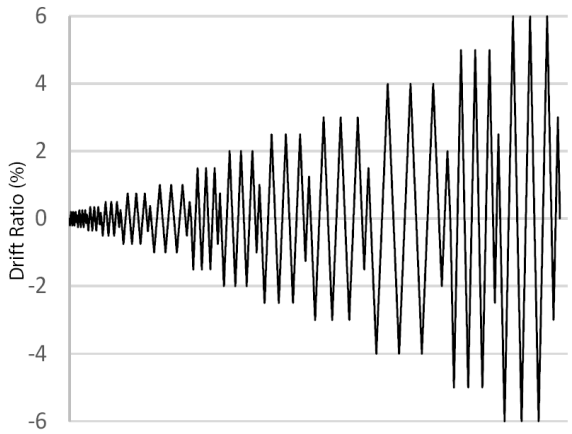

Figure 3.5. Uniaxial drift input

3.2.2.2 Biaxial Loading Protocol

The biaxial testing comprised of bi-directional quasi-static cyclic loading. It incorporated the same drift amplitude ratios as the ones used in uniaxial testing. For each drift cycle, there was a uniaxial push and pull in the East-West (EW) direction which was followed by another uniaxial push and pull in the NS direction. Following that, the two horizontal rams were loading the specimen simultaneously in both directions which was resulting in a clover shaped drift path, as shown in Figure 3.6a. Using a clover shape protocol is a conservative approach as bridge piers generally are not subjected to 100% load demands in both horizontal directions simultaneously. In a normal bridge pier, it is very likely that demand in the transverse direction governs the design of the piers compared to the longitudinal direction. Generally, the superstructure transfers the loads to the abutments in the longitudinal direction, (NZTA, 2013)

To explain the clover shape loading, Figure 3.6b illustrates the drift amplitude in each horizontal direction (x and y) on a polar curve plot. The radius (r) at a given point in the clover loading can be expressed in terms of the angle (θ). In this instance, it can be seen that $r(\theta) = R\,Sin(2\theta)$, where R is the resultant drift, as shown on the polar curve plot in Figure 3.6b. The "x" (NS direction) and "y" (EW direction) coordinates can be shown in terms of their components on the corresponding axes as $x(\theta) = r(\theta)\,Cos(\theta)$ and $y(\theta) = r(\theta)\,Sin(\theta)$, respectively. It can be calculated that the maximum drift in the x and y axes occur at $\theta = 35^0$ and $\theta = 55^0$, respectively. This means that the maximum resultant drift (R) occurs at $\theta = 45^0$. Similar to uniaxial testing, one complete biaxial cycle was applied to the test specimen at an input drift ratio. This means there were three negative and positive excursions of both rams (NS and EW) during that input drift ratio.

The loading regime described here for the biaxial testing, was based on that used by Marriott (2009). It is important to note that the drift ratios shown in Figure 3.7 for the biaxial input were inputted to each NS and EW rams. During the clover loading, the resultant drift ratio of the specimen under testing was larger (1.3 times bigger) than the input drift ratio of each ram. As an example for an input 4% drift ratio loading, the column will undergo a peak resultant drift of 1.3 x 4% = 5.2% during the clover stage.

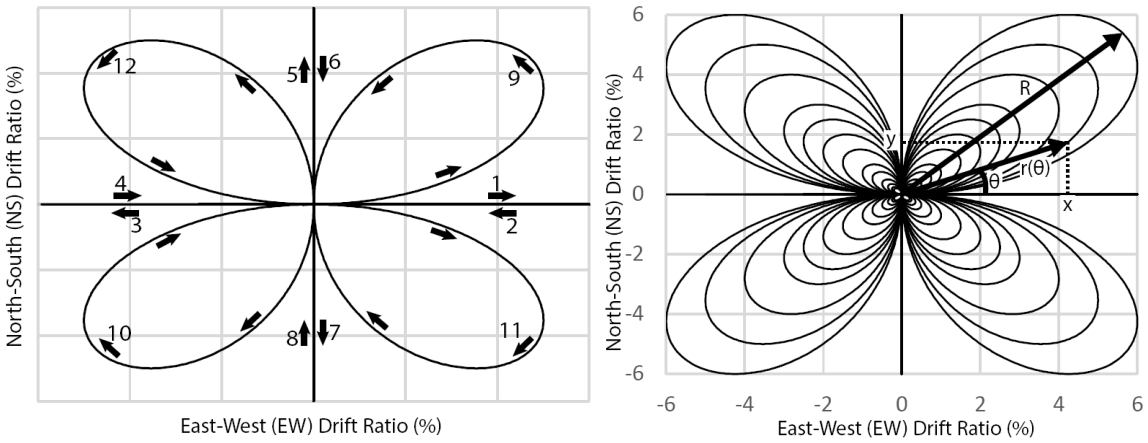

(a) Loading sequence **(b) Drift input for clover stage**

Figure 3.6. Biaxial testing loading

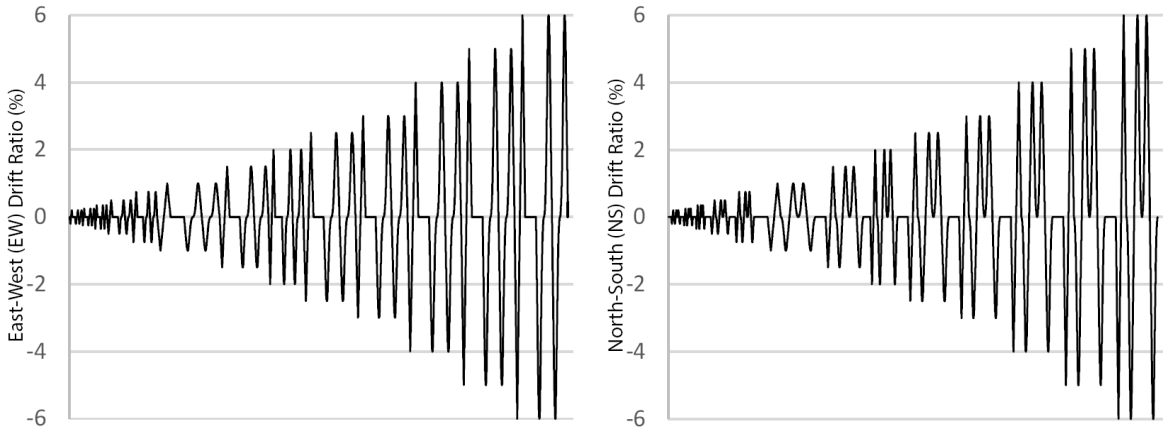

(a) Drift input for EW ram **(b) Drift input for NS ram**

Figure 3.7. Biaxial testing loading

3.2.2.3 Data Acquisition System

The data acquisition system was designed to gather and record all necessary information from the instruments attached on the specimen during testing. Two computer systems were used, the controller system and the logger system.

The controller system comprised of a computer where the testing software was installed. The drift input files were uploaded to the software which was setting up displacement targets for the horizontal actuators. The loads in the actuators were also being controlled through a safety button in the software. The controller system was designed to start or stop testing at any drift ratio from an input file. This was necessary

as the cracks were being measured and marked when the specimen was at its maximum displacement (peak drift ratio in the input file).

The logger system comprised of a separate computer which was intended to record the data from the instruments mounted on the specimen and the load cells at each step during testing. Each instrument was calibrated to a channel in the logger computer. There was a trigger set for the logger system which was designed to get a reading from all instruments mounted on the specimen, then transferring the data to the logger computer at a rate of approximately 10 readings per second. The data was then stored in a file automatically in the computer. Some of the instrumentations used during testing for measuring different parameters are discussed below.

3.2.2.3.1 Lateral Displacement

Lateral displacement in the specimen under testing was measured using rotary string potentiometers (rotary pots) which were mounted on an adjacent wall which was independent of the reaction frame. Additional rotary pots were installed to measure the displacement of the reaction frame and elongation or contraction of the rams at each step of loading.

3.2.2.3.2 Lateral and Axial Loads

Lateral and axial loads were measured using load cells which were mounted along the load paths in each direction. Two 500 kN load cells were used for the horizontal rams (400 kN capacity) while a 1000 kN load cell was used on top of the column for the axial loads from the unbonded post-tensioned bar, as shown in Figure 3.3 and Figure 3.4.

3.2.2.3.3. Structure Deformation

Flexural and shear deformations of a column under testing were measured using vertical, horizontal, and diagonal array of rod end potentiometers (pots). The pots were mounted on the faces of column and were measuring displacements with four digits accuracy. The data from the pots were then used to locate the neutral axis depth up the height of the column sections at each step of loading. Once the neutral axis is known, the moment-curvature and other useful plots were easily constructed.

Figure 3.8 presents a typical external instrumentation of the column. Plenty of pots were installed on the specimen in case some of the pots break up during testing or do not record data. During biaxial testing, the number of pots was even increased for a better collection of data from the deformation and response of the column. Several spring pots were mounted between the footing and strong floor to monitor any sliding of the footing during testing, as shown in Figure 3.8c and Figure 3.8d.

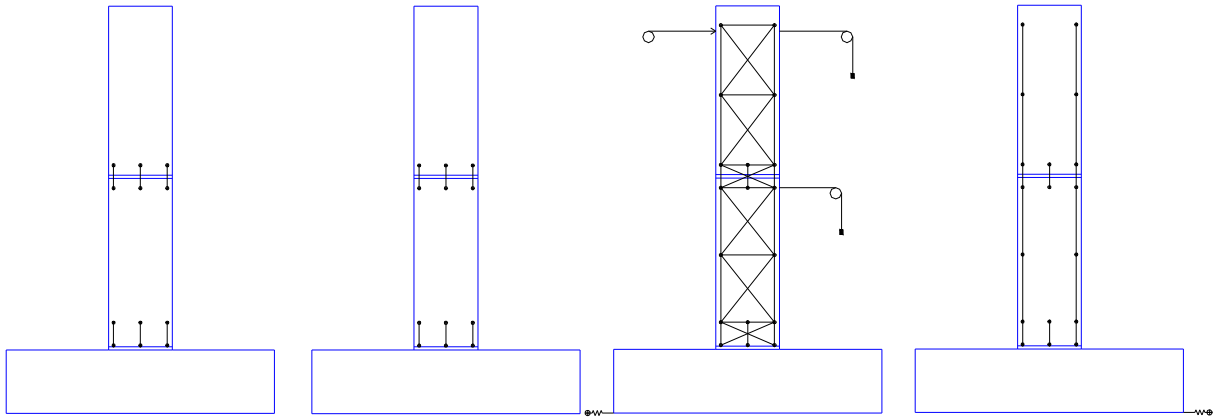

(a) North face **(b) South face** **(c) East face** **(d) West face**

(e) North face **(f) South face** **(g) East face** **(h) West face**

Figure 3.8. Typical instrumentation of a column under testing

3.2.2.3.4. Strain Gauges

Strain gauges were installed on the reinforcing bars of each column component before pouring concrete at the prefabrication yard. Strain gauges were located at the expected plastic hinging regions in the column. This included column to footing and segment to segment connections. They were intended to record longitudinal reinforcing bar deformation during testing.

The process of installing strain gauges on the reinforcing bars is presented in Figure 3.9. Strain gauges had very delicate wires coming out of the columns. The wires were later plugged into a strain gauge box to transfer the data from the specimen during testing. Strain gauges carried a high risk of being broken during the precasting of the components at the prefabrication yard. Proper caution was paid to the extent possible to not damage them when pouring concrete. It should be noted that in this research, strain gauges were used as a secondary source of instrumentation for recording the experimental data during testing. The primarily source of instrumentation was relied on the external pots attached on the faces of the column in the lab.

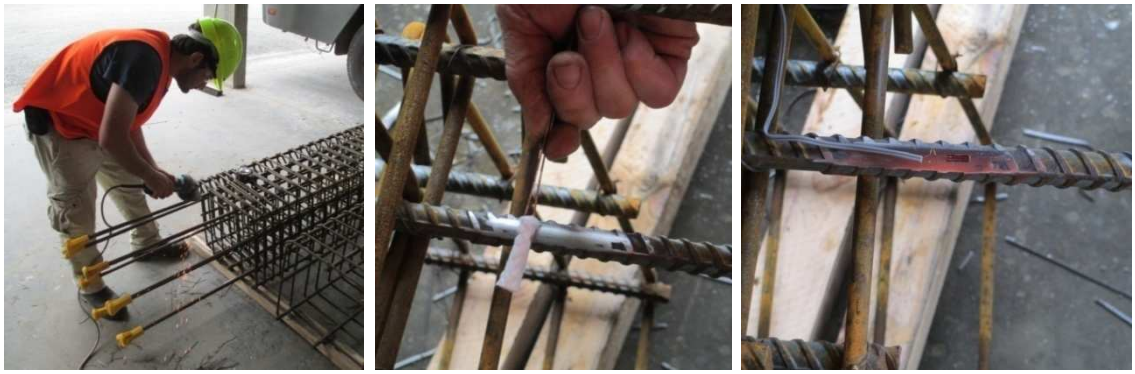

(a) Grinding face of rebar **(b) Cleaning with Acetone** **(c) Strain gauge is glued on rebar**

(d) Wax coat for water proofing **(e) Wrapping rubber tape** **(f) Installed strain gauges on rebars**

Figure 3.9. Typical installation process for strain gauges on reinforcing bars

3.2.3 Material Characterization and Properties

The primary materials for the construction and assembly of the specimens included concrete, reinforcing bars, and high strength grout. During the construction and assembly process, several samples were taken from each material to make sure they are compliant with the specified strength and properties selected during the design stage. A summary of the material characterization is presented as follows.

3.2.3.1 Concrete Slump Testing and Samples

All specimens in this thesis were prefabricated at the Bradfords Precast Ltd. in Ashburton, New Zealand. The concrete was supplied by Ashburton Contracting Ltd. (ACL) which was located less than 5 km from the prefabrication yard. The ACL had an automatically operated concrete batch plant which selected the aggregate, cement, sand, and water proportions based on the specified concrete strength. Once the concrete was mixed in a truck mixer and was ready for delivery, an amount of the mixed concrete which was sufficient for filling three standard cylinder moulds and slump testing was poured in a wheel barrow (Figure 3.10b). For every concrete mixer truck, a slump testing was being carried out at the ACL before delivery of the concrete to the Bradfords prefabricated yard for pouring of the specimen components (footing and segments).

The procedure for the slump testing was adopted from the ASTM C143/C143M-12 "Standard Test Method for Slump of Hydraulic-Cement Concrete" (ASTM, 2012). The slump limits were set according to Table 6.3.1 of the ACI 211-91 "Standard Practice for Selecting Proportions for Normal, Heavy weight, and Mass Concrete" (ACI, 1991). The minimum slump was specified to be 25 mm for all components. The maximum slumps were 75 mm for the foundations and 100 mm for the beams and columns.

Following the on-site slump testing, three standard concrete cylinder moulds (100 mm diameter and 200 mm height) were filled with concrete from each truck mixer for each component of the specimen. The procedure for taking concrete samples, was in accordance with ASTM C31/C31M-12 "Standard Practice for Making and Curing Concrete Test Specimens in the Field" (ASTM, 2012). After a day, the samples were taken out of their moulds and soaked in a tub filled with fresh water. The samples were then transferred to the University and were stored inside a fog room until the testing day. Figure 3.10 presents photos for the concrete slump testing and sampling procedure.

(a) Concrete Truck Mixer at ACL

(b) Pouring concrete for on-site testing

(c) Slump test with the cone and rod

(d) Removing the cone gently

(d) Potting the rod on top of the cone

(e) Measuring the concrete slump

(f) Moulds for the concrete samples

(g) Concrete cylinders soaked in a tub

Figure 3.10. Slump testing and concrete sampling at the concrete plant

3.2.3.2. Reinforcing Bar Tension Strength

The grade of reinforcing bars for all specimens and their components was specified as Grade 500E (seismic) according to AS/NZS 4671 (NZS, 2001). Plain bars were used for the transverse reinforcing of the columns. All other rebars were deformed bars. This type of reinforcing rebars should have a yield stress of over 500 MPa but lower than 600 MPa, uniform elongation of more than 10% (strain), and tensile ratio (tensile strength divided by yield strength) of between 1.15 to 1.4.

Rebar samples with different diameters, were taken from the supplier bundles for a tensile testing. The rebar testing was done under a 1000 kN Avery Universal Testing Machine (UTM), as shown in Figure 3.11. The samples were 500 mm long with 300 mm of engaged length during testing (Figure 3.11b). A standard strain pot was installed at the mid-height of the sample to measure the elongation during testing (Figure 3.11b). The testing was based on ASTM A370-05 "Standard Test Method and Definitions for Mechanical Testing of Steel Products" (ASTM, 2005).

(a) Reinforcing bar samples

(b) Rebar under UTM

(c & d) Fractured rebars with different diameters

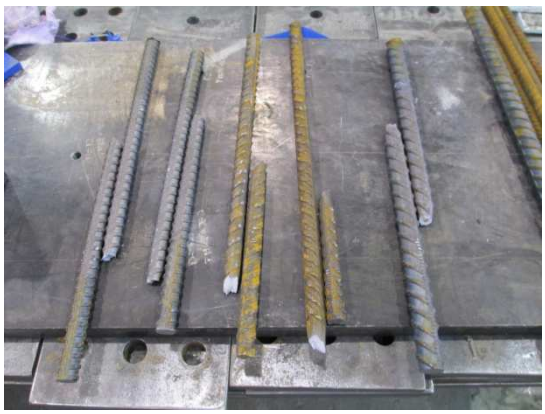

(e) Samples after fracture

Figure 3.11. Rebar tensile testing photos

An average of the actual yielding strength for the samples was calculated and is presented in Table 3.3. A typical strain-stress curve for a rebar is shown in Figure 3.12.

Table 3.3 Summary of the actual rebar yielding strength in MPa

Rebars	HDS1	HDS2	HDC1	HDC2
Longitudinal	516	516	516	516
Transverse	556	556	556	556

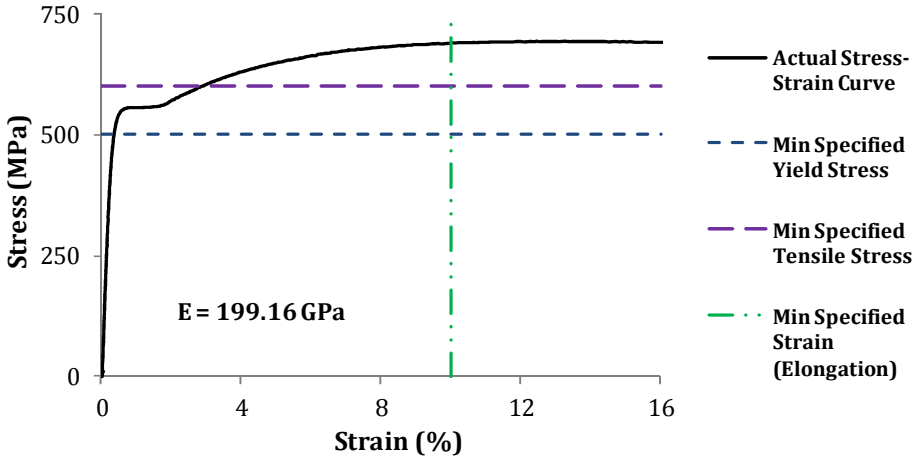

Figure 3.12. Actual Stress-Strain Curve for a 10 mm diameter rebar sample (Grade 500E)

3.2.3.3 Concrete Compressive Strength

The specified minimum concrete compressive strength for all specimen components was 40 MPa at 28 days. The concrete samples were tested under a 1000 kN Concrete Compression Test Machine at 28 days and on the testing day of each specimen, as shown in Figure 3.13. The compression testing of the samples was carried out to assure that the average compressive strength is bigger than the minimum specified strength during pouring.

The compressive testing of the concrete cylinders was in accordance with ASTM C39/C39M-05 "Standard Test Method for Compressive Strength of Cylindrical Concrete Specimens" (ASTM, 2005). An average of compressive strength for the samples was calculated. Table 3.4 presents average concrete compressive strength for each component (column and footing) on the testing day of the specimen. It should be noted that the results from any concrete cylinder which had a premature failure such as

failure due to loading surface roughness or shear was not taken into account while calculating the final average compressive strength.

(a) Compression Test Machine (b) Concrete sample (c) Tested samples, cone failure visible

Figure 3.13. Concrete cylinder compression testing photos

Table 3.4. Summary of the average concrete compressive strength in MPa

Elements	HDS1	HDS2	HDC1	HDC2
Footing	59	51	43	44
Column	60	51	54	45

3.2.3.4 High-Strength Grout Compressive Strength

The specified minimum compressive strength for the grout in the grouted duct and member socket connections was 38 MPa at 28 days. Sika Grout 215 was used for the grouted duct connections and Sika Grout 212 for the member socket connections. The difference between Sika 212 and 215 is in the size of the cement particles. In Sika 215 the cements particles are a bit finer which makes it more attractive for grouting of smaller ducts. In terms of compressive strength, Sika 215 grout has comparable strength to Sika 212. The strengths normally depend on the quantity of mixing water. More details can be found in Sika manufacture data sheets (Sika Group, 2015).

Grout samples were taken during assembly of each specimen. The cylinder sample was 50 mm in diameter and 100 mm in height. The samples were tested under a 1000 kN Compression Test Machine on the testing day for each column specimen. In general, the sampling and testing procedure was in accordance with ASTM C1019-05 “Standard Test Method for Sampling and Testing Grout” (ASTM, 2005). Table 3.5 presents average compressive strength of the grout on the testing day of each specimen.

Table 3.5. Summary of the average grout compressive strength in MPa

Connection type	HDS1	HDS2	HDC1	HDC2
Grouted Duct Connection	64.5	53	51	44
Member Socket Connection	-	-	59	42

3.2.3.5 Unbonded Post-Tensioned Bar

As explained in Section 3.2.2, an unbonded post-tensioned bar was used to simulate the gravity loads on the half-scale specimens. This bar was a Hot Rolled Macalloy 1030 Post-Tensioning System Bar (Macalloy, 2011) with 40 mm nominal diameter. Table 3.6 presents a summary of the mechanical properties for the 1030 Macalloy bar.

Table 3.6. Summary of the mechnical properties for the 1030 Macalloy bar

Minimum Elongation (%)	Modulus of Elasticity (GPA)	Nominal 0.1% Proof Stress (Yielding) (MPa)	Nominal Ultimate Tensile Strength (MPa)
6	170	835	1030

3.2.4 Grouted Duct Connection (GDC)

Grouted Duct Connection (GDC) was previously introduced and explained in detail in Chapter 2. As a summary, GDC is an emulative cast-in-place connection in which the starter bars from one member are extended into the ducts which are placed inside the second member during prefabrication. Following assembly of the elements, high-strength mortar is pumped inside the ducts to secure the connection (Marsh et al. 2011).

In the first phase of testing here, GDC was used for the connection of the column to foundation and segment to segment, as presented earlier in Table 3.1. Some important detailing considerations for GDC are as follows.

3.2.4.1 Detailing Considerations

HDS1 and HDS2 featured GDC as the primary connections (column to footing). At the same time, GDC was used for the segment to segment connections in all columns (HDS1,

HDS2, HDC1, and HDC2). Design of columns will be presented in Section 3.2.6 later. This section presents some general important detailing considerations for.

The internal actions in GDC under vertical and lateral loadings are illustrated in Figure 3.14a and Figure 3.14b, respectively. The shear transfer mechanism across GDC relies on combination of several resisting parameters. This includes friction and bond in the grouted interface, dowel action of the starter bars, and the internal shear key. For simplicity in design process, it was assumed that all shear forces are transferred through the internal shear key. Figure 3.14c presents internal actions in a shear key used in GDC. In this research, the shear key was designed according to NZS 3101 "The Design of Concrete Structures" (NZS, 2006). The shear key was treated as a corbel and designed in accordance with the principals of shear friction from NZS 3101.

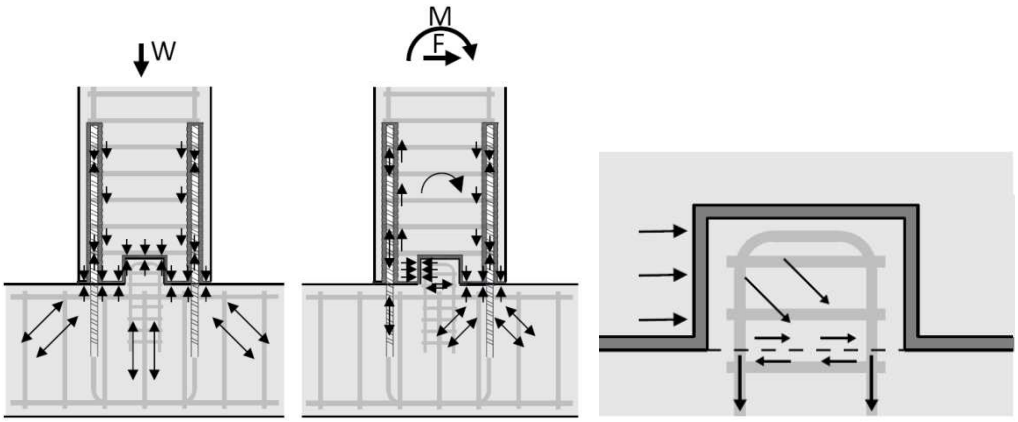

(a) Vertical loads **(b) Lateral loads** **(c) Shear key under lateral loads**

Figure 3.14. Internal actions in Grouted Duct Connections (GDCs)

The bond mechanism in the corrugated steel ducts is shown in Figure 3.15a. The corrugated steel ducts provide a load path for the tension loads in the column to be transferred to the starter bars which are extending out of the foundation into the ducts. The loads are transferred in the ducts through bearing of the deformation of the corrugated steel ducts and reinforcing bars against the surrounding grout and concrete.

Brenes et al. (2006) and Raynor et al. (2002) showed that a small quantity of stress can be transferred through chemical adhesion and friction which exist between the steel duct and the surrounding concrete and grout. The study showed that using corrugated steel ducts is more effective in terms of transferring the stresses compared to plain plastic or steel ducts. Corrugations of the ducts increase the interlock between the

grout, concrete, and starter bars. This would enhance the ultimate bond strength in GDC. Therefore, in this research the corrugated steel ducts were used in all GDCs. More details on the effects of duct size and materials in GDC can be found in Brenes et al. (2006) and Pang et al. (2010).

In GDC, the starter bars are confined by the surrounding grout and the corrugated ducts. This provides enhanced bond strength for the starter bars which fully transfer the stresses in a shorter development length of the starter bars when compared to rebars used in a conventional cast-in-place construction (Brenes et al., 2006). This means that due to duct confinement a shorter development length, can be used for the starter bars. Brenes et al. (2006) provides detailed explanation and expressions to calculate this length. It is a common practice to allow an additional 75 mm length of the starter bar in the grouting duct. The upper 75 mm of the grout normally has high water-cement ratio and low strength. This is sometimes called "bleeding effects". Therefore, this length should be avoided when calculating the required development length of a starter bar inside the grouting duct.

In the study here, it was decided to allow full development length of the starter bars similar to what specified for rebars in cast-in-place construction and calculated in accordance with NZS 3101 (NZS, 2006). A reason behind this decision was to show that in case the quality of on-site grouting materials does not match the specified strength for various reasons, then there is a redundancy in the system. This redundancy comes from a longer development length in the starter bars which also includes the bleeding effects. Therefore, it provides a better safety margin on any pulling-out effects in the starter bars. Another reason was to show how to emulate the cast-in-place construction.

The increased bond strength of the starter bars inside the corrugated ducts leads to a shorter strain penetration length at the GDC interface. When the column is displaced laterally, the crack at the column to footing interface will start opening. Opening of this crack will lead the starter bars to carry tension loads over a shorter strain penetration length. This means, a shortened length in a starter bar will have to accommodate the total deformation of the bar. The consequence of this would be strain concentrations in the bar at the interface connection (Raynor et al., 2002). This phenomenon is shown in Figure 3.15b by Line A. Strain concentration in the starter bars is undesirable since it

can reduce the ultimate drift capacity of the column which means reduced ductility capacity of the bar and eventually the column. Strain concentrations can also make the starter bars susceptible to low-cycle fatigue failure due to a reduced number of loading cycles up to the failure point (Coffin, 1954, Mander et al., 1994, Manson, 1953, Stanton et al., 2005).

The effects of leaving an unbonded length of the longitudinal rebars in the concrete columns were previously studied by Kawashima et al. (2001).The study showed that an unbonded length of the longitudinal rebars in the plastic hinging zones of the reinforced concrete columns can significantly increase the ultimate drift capacity, and thus enhancing the overall column ductility. Leaving an unbonded length of the starter bars in GDC at the column to footing connection can eliminate the effects of strain concentrations at the interface. The unbonded length of the rebar will provide a longer length where the total deformation of the rebar can be distributed. This is shown in Figure 3.15b by Line B. The study by Kawashima et al. (2001) also suggested that reinforced concrete column with an unbonded length of the rebars in their plastic hinges had suffered less spalling of the concrete compared to columns with no unbonded length.

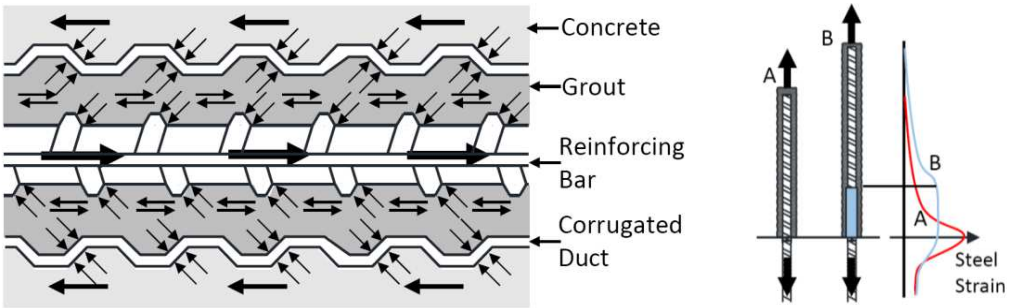

(a) Bond mechanism in grouted duct **(b) Effect of unbonded length**

Figure 3.15. Bond mechanism and strain penetration effects in GDC

The unbonded length also increases the yield drift of the column. However, past studies (Kawashima et al., 2001) have shown that this increase is less than the increase in the ultimate drift capacity. This means that the column with an unbonded length of the rebars can sustain higher levels of displacement ductility near or at the failure point of the column. In order to calculate the required unbonded length of the rebars in the plastic hinges, the following procedure was adopted. The plastic hinge length (L_P) of a

conventional monolithic column can be approximated using Equation 3.1 from Priestley et al. (2007).

$$L_P = 0.08L_{cant} + L_{sp,actual} \quad (3.1)$$

In Equation 3.1, L_{cant} is the distance from the top of footing to the point of contraflexure in the column. $L_{sp,\,actual}$ is the actual strain penetration length of the rebar (above and under footing surface). Using the expression proposed by Paulay and Priestley (1992), the L_{sp} for a conventional column can be calculated using Equation 3.2.

$$L_{sp} = 0.022 f_y d_b \quad (3.2)$$

Where in Equation 3.2, d_b denotes the longitudinal bar diameter and f_y is the yielding strength of the rebar. The unbonded length of the starter bars confined inside the grouted ducts was estimated from testing of the first specimen (HDS1) with GDC. In HDS1, there was no debonding of the starter bars at the interface connection. In this case, the plastic hinge length of the column at the base was observed to be approximately half of the height of the square column section. Inputting this value in Equation 3.1 for L_p gives an estimate for the actual strain penetration length ($L_{sp,\,actual}$) of the starter bars inside the grouted ducts. The required unbonded length (l_{ub}) of the confined starter bars to emulate a conventional monolithic column plastic hinge length can be calculated using Equation 3.3.

$$l_{ub} = L_{sp} - L_{sp,actual} \quad (3.3)$$

The unbonded length calculated using this methodology was incorporated in the design and construction of HDS2 as will be discussed in the subsequent sections.

Another accurate method for calculation of the required unbonded length is to treat the column to footing GDC interface as a rocking connection according PRESSS Design Handbook (Pampanin et al., 2010), refer to Section 4.4.1 in Chapter 4. In this methodology, the strain in a rebar is limited to less than 5%, then the required unbonded length can be calculated using the expressions presented in the Handbook.

A combination of armoring and unbonded length can be used in GDC for an enhanced performance. The armoring at the base of the column will provide external confinement

to limit crushing of the unconfined (cover) concrete when column displaces laterally. Crushing of the cover concrete can result in a loss of stiffness in the column, as well as reduced energy dissipation. It also leads to buckling of the longitudinal rebars at higher drifts. The armoring can be provided in terms of steel shoe or jacketing.

The armoring at the base of the column can lead to an enhanced performance for the column, especially at higher drift ratios where buckling of the starter bars can be eliminated when the column section is under compression. Currently there is lack of specific hand calculation methodologies to design the armoring requirement. However, complex analysis such as Finite Element Methodology (FEM) could be an alternative method. As an approximate hand calculation methodology, the armoring can be designed using the concrete confinement model by Mander et al. (1988). Using Equation 3.4, a confinement ratio (R) can be targeted as below.

$$\frac{f'_{cc}}{f'_{c}} = R \tag{3.4}$$

Where in Equation 3.4, f'_{cc} is the confined concrete compressive strength and f'_c is the compressive strength of the unconfined concrete. f'_{cc} is calculated from Equation 3.5.

$$f'_{cc} = f'_c \left(-1.254 + 2.254 \sqrt{1 + \frac{7.94 f'_l}{f'_c}} - 2\frac{f'_l}{f'_c} \right) \tag{3.5}$$

In Equation 3.5, f'_l is the effective lateral pressure from the armoring which can be calculated from Equation 3.6 below.

$$f'_l = k_e \, f_l \tag{3.6}$$

In Equation 3.6, f'_l is the effective lateral pressure calculated according to Mander et al. (1988). f_l is the lateral pressure from the armoring (Equation 3.7).

$$f_l = \frac{A_S f_y}{h \, b} \tag{3.7}$$

Where h and b parameters are shown in Figure 3.16 for a typical square armoring. A_s can be calculated from Equation 3.8.

$$A_s = 2\,ht \tag{3.8}$$

Rearranging Equation 3.7 by inputting A_s from Equation 3.8 and solving for the armoring thickness (t), as presented in Equation 3.9.

$$t = \frac{b f_l}{2\,f_y} \tag{3.9}$$

From Equation 3.9, the required armoring thickness (t) can be calculated based on the assumed confinement ratio (R) at the beginning of the process. It should be noted that as presented in Equation 3.9, the calculated expression for t is independent of the armoring height (h). Therefore, it is recommended that a sufficient height for the armoring should be selected to limit the damage in the plastic hinges.

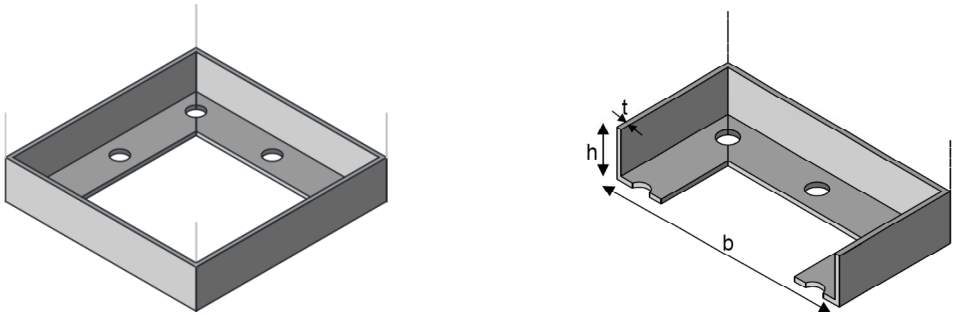

(a) Drilled holes in armoring are for starter bars **(b) Armoring parameters**

Figure 3.16. Typical base armoring for a square section column with GDC

3.2.5 Member Socket Connection (MSC)

Member Socket Connection (MSC) was explained in Chapter 2. As a summary, MSC is an emulative cast-in-place connection which can be formed by embedding a precast element inside another element. The second element can be either precast or cast-in-place concrete. If both elements are precast, then the connection is secured using a grout or concrete closure pour in the preformed socket. The other solution is to have the second element cast around the first one on-site (Marsh et al. 2011).

This type of connection was used for the column to footing connection in two specimens (HDC1 and HDC2), refer to Table 3.1. Some important detailing considerations for MSC are explained as follows.

3.2.5.1 Detailing Considerations

The connection details in a MSC are different from that of a conventional cast-in-place system. The most important difference is that there are no bars crossing the column to footing interface. Vertical loads are resisted by the shear friction without reinforcing crossing across the roughened surface of the column and socket. It is important to note that roughening of the concrete surface in this study is intended for a better bond with the grout, rather than a primary design aspect for this type of connection. Another difference is that generally the longitudinal column rebars are not bent out at the bottom. Instead the bars are left straight with foot inserts (headed anchors) at the ends (Haraldsson et al., 2013).

The headed anchors can be used when the development length of the column longitudinal rebars inside the socket are shorter than the values specified for the development length of the conventional cast-in-place columns in the building codes. This gives the advantage of not necessarily increasing the socket depth for the development length purposes. Use of straight bars also offer several important advantages such as simple transportation or handling and reduced hazards posed by the protruding bars. Straight bars with headed anchors at ends offer a more direct transfer of the rebar forces compared to bent-out bars, as shown in Figure 3.17c.

A strut and tie model proposed by Haraldsson et al. (2013) for MSC is illustrated in Figure 3.17a. As it can be seen in Figure 3.17b, if a headed bar details is used, the diagonal strut force of the column is transferred to the column rebars through a node which comprised of three compression strut. Therefore, the force transfer in this case is dependent on the direct bearing. In contrary, in a conventional bent-out bar detail, forces are transferred through the bond to the curved part of the rebar.

In general, the important detailing considerations for MSC are the depth of the socket, column diameter, and the relative size of the socket to column diameter. The socket depth needs to be sufficient for a safe transfer of loads from the column to the footing. The axial loads which need to be transferred through a MSC include the weight of the piers, superstructure, and any vertical intertial loads during a vertical excitation.

In MSC, shear and bearing loads are transferred through the grouted interface between the column and footing. Vertical forces from the structure induce shear forces in the socket, as shown in Figure 3.18a. These vertical forces include the axial loads discussed in the previous paragraph. In addition to vertical loads, Osanai et al. (1996) showed that lateral loads also generate shear forces in the grouted interface of the socket, as shown in Figure 3.18b.

The bearing stresses are induced in the socket under the lateral loading, as shown in Figure 3.18c. As it can be observed, in addition to compressive stresses in the radial direction, there are hoop tensile stresses around the socket which are perpendicular to the compressive bearing stresses. As the tensile capacity of concrete is negligible, the hoop stresses can cause radial cracking near and around the socket which would extend to the perimeter of the footing. In order to prevent from the radial cracking of the footing, circular hoop bars or straight bars can be provided on top and bottom layers of the reinforcing bars in the footing. For a maximum efficiency, the rebars should be orientated tangentially to the hoop stresses. These bars do not have to go through the column, as the column stub has its own stirrups and is confined inside the socket.

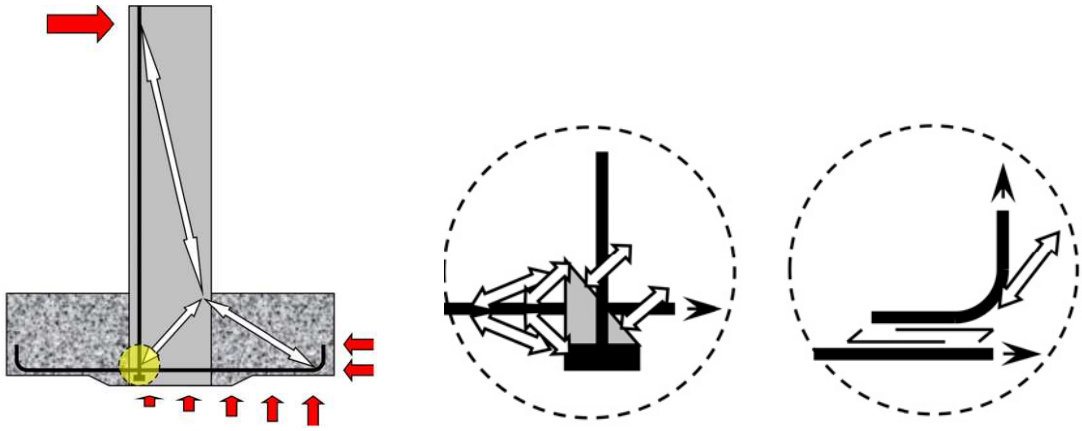

(a) Global strut and tie model **(b) Headed bar detail** **(c) Bent-out bar detail**

Figure 3.17. Strut and tie model for MSC, after Haraldsson et al. (2013)

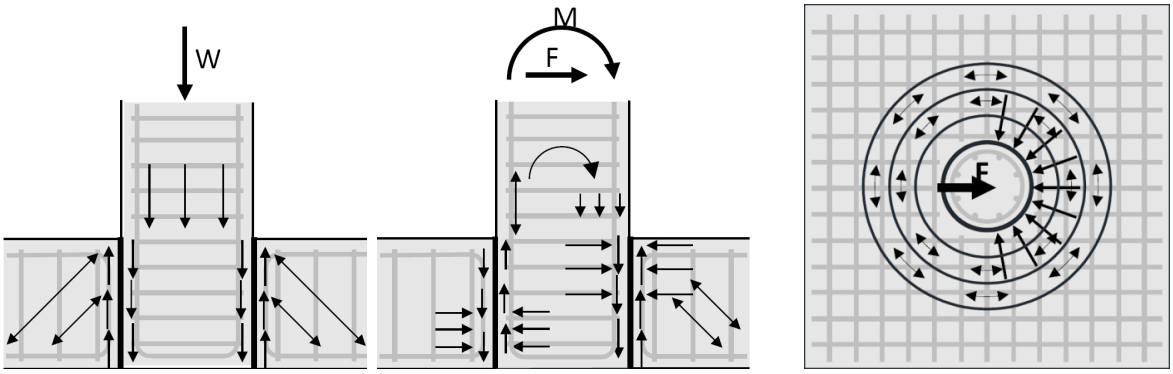

(a) Vertical loads **(b) Lateral loads** **(c) Hoop stresses**

Figure 3.18. Load transfer mechanism and internal actions in MSCs

Under vertical loading, if the socket depth is insufficient, it can lead to a shear failure of the grouted interface. The reason behind this type of failure is the insufficiency of area in the socket walls where shear forces can be transferred safely. This type of shear failure in the socket is likely to be a punching shear failure (pull through) in which the column may slip through the footing (Marsh et al., 2011). In most cases the column base area is considerably smaller than the area of footing or pile cap underneath. This means if the column slips through the socket, the vertical loads transferred through the column will produce significantly higher stresses which can puncture the soil underneath, and therefore results in soil failure underneath which supports the structure. White (2014) presented a simple comparison on the effects of socket depth on the transfer of vertical loads for a circular column, as illustrated in Figure 3.19.

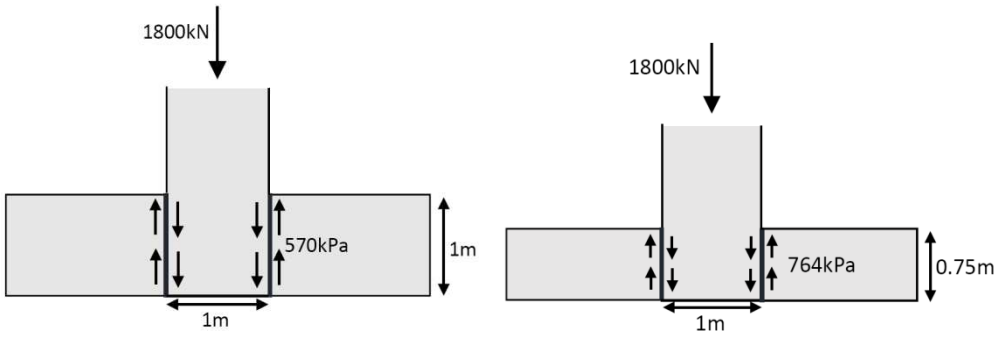

(a) 1 m deep socket **(b) 0.75 m deep socket**

Figure 3.19. Effect of socket depth on shear stresses in the grouted interface for a circular column under vertical loads (White, 2014)

Under lateral loads, bearing stresses in the grouted interface of the socket form a load couple, as shown in Figure 3.20. In this instance, the deeper the socket depth is

(distance between the load couple), the smaller the bearing stresses would be. Insufficient socket depth under lateral loads can result in crushing of the grout at the interface. White (2014) showed that if assuming that bearing stresses are distributed over a 20% depth of the socket at the top and bottom fibers, a reduction of 25% in socket depth can lead to a 60% increase in bearing stresses (Figure 3.20).

In this thesis, it was found that keeping a ratio of one to one between the socket depth and the column diameter was sufficient to transfer all vertical and lateral loads safely from the column to the footing through MSC. However, it is suggested here that further research would be necessary to quantify the appropriate socket depths for various column shapes and cross-sections such as square, rectangle, octagonal etc.

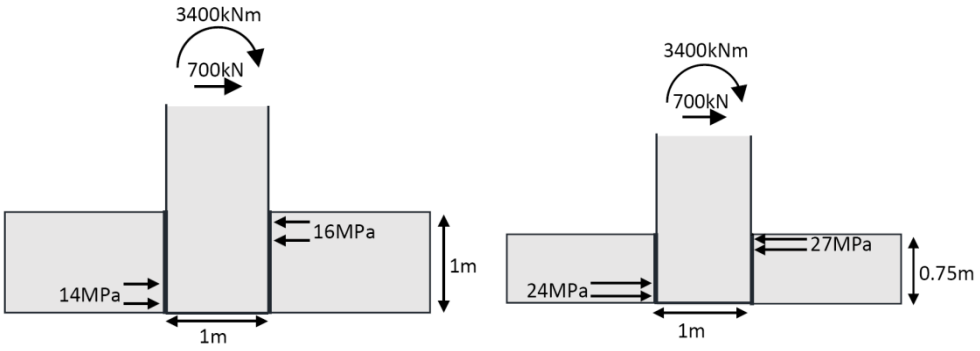

(a) 1 m deep socket **(b) 0.75 m deep socket**

Figure 3.20. Effect of socket depth on shear stresses in the grouted interface for a circular column under lateral loads (White, 2014)

Figure 3.17 presents two alternatives if insufficient socket depth is available (Marsh et al., 2011 and White, 2014). The first one is a partial socket can be used instead of a full depth one, as shown in Figure 3.21a. In this instance, the socket does not extend all the way through the footing. The second alternative is to use a shear key in the socket for the connection of the column to footing, as shown in Figure 3.21b. It should be noted that an increase in column diameter and socket depth will reduce the internal actions in MSC. This is because it will provide a larger surface area around the socket for the transfer of loads.

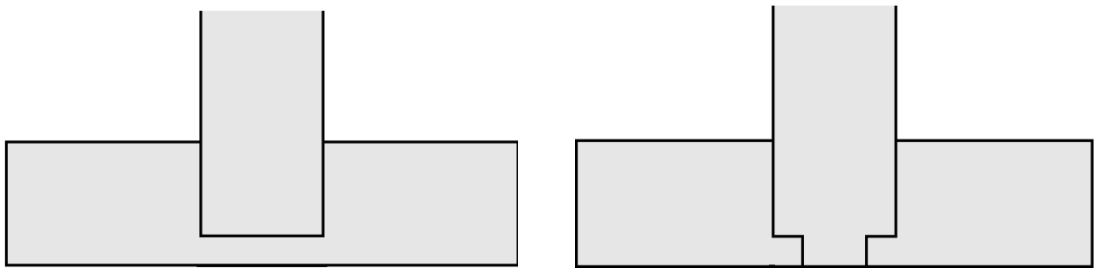

(a) Partial socket **(b) Shear key socket**

Figure 3.21. Alternative socket details, after Marsh et al. (2011) and White (2014)

Another important consideration for MSC is the gap between the column stub and footing socket wall. The gap would need to be sufficient to allow for the construction tolerances when assembling the precast elements, as well as flow of the grout when grouting the joint. If the gap is left too large, it will reduce the effectiveness of the grouted interface inside the socket when transferring shear forces from the column into the socket (Osanai et al., 1996).

In this research, it was found that a 10 mm gap between the column stub and socket wall was sufficient to accommodate the construction tolerances and flow of the grout for the columns with 500 mm diameter. However, larger gaps maybe required for the columns with other shapes and sizes to accommodate the on-site construction tolerances. Therefore, further research is required to quantify the maximum gap width that would not reduce the effectiveness of the connection for transferring loads. This is out of the scope of this thesis.

3.2.6 Design, Construction, and Assembly of ABC High Damage Columns

3.2.6.1 HDS1 and HDS2

Grouted Duct Connection (GDC) was used for the column to footing and segment to segment connections. Each specimen consisted of three precast elements. The elements included lower and upper segments of the column and a footing block. The columns were designed according to NZS 3101 (NZS, 2006) for the design loads presented for the half-scale columns in Table 3.2.

For HDS1, the lower segment of the column consisted of 16-YD16 longitudinal rebars. The upper segment had 8-YD16 rebars due to a reduced moment demand. 16-YD16

starter bars were extending out of the footing into grouting ducts of the lower segment. Similarly, 8-YD16 starter bars were extending out of the lower segment into the upper segment. To provide shear, confinement, and anti-buckling capacity in the plastic hinging zones of the column, transverse reinforcement in terms of YD10 stirrups spaced at 50 mm were used. The stirrups spacing was 100 mm above the plastic hinge regions. Corrugated galvanized steel ducts were placed inside the lower and upper segments to house the starter bars from the footing and upper segment, respectively. The grouting ducts were 40 mm in internal diameter and 750 mm long. All corrugated steel ducts used in this research had a wall thickness of 0.3 mm.

There was a 70 mm diameter duct located at the center of the column segments and the footing. This duct was intended to house the unbonded post-tensioned bar which was used to apply axial force on the column specimen during testing. It is important to mention that in an actual bridge pier similar to HDS1, there will not be any unbonded post-tensioned bar located at the center of the column or footing. Therefore, there will be no need of leaving a central duct during prefabrication.

The footing was designed to be a capacity protected element. A 2.1 m square footing with 500 mm depth was used. Footing reinforcements consisted of double layers of YD16 bars spaced at 150 mm. There were 12 galvanized steel ducts extending up the height and distributed around the perimeter of the footing. The ducts were 50 mm in internal diameter and were intended to house 38 mm diameter hold-down bolts which were securing the footing block to the strong floor during testing in the lab. A small cubical recess at the center of the bottom face of the footing was left to provide room for the mechanical anchorage of the unbonded post-tensioned bar. It should be noted that in an actual bridge pier, there will be no need of leaving ducts for the hold-down bolts or any recess to house the mechanical anchorage of the unbonded post-tensioned bar.

150 x 250 x 250 cubical shear keys were provided at the column to footing and segment to segment connections. Cubical recesses with slightly larger sizes (10 mm) were provided at the bottom of the segments to house the shear keys. Although the shear force can be resisted through the dowel action in the starter bars, however, in this study it was preferred that shear keys transfer all shear loads across the interface. In this instance, the dowel action of the starter bars for resisting shear forces can be neglected.

In this case, the starter bars are intended to dissipate energy in flexural action only. The shear keys were designed using the principals of shear friction according to NZS 3101 (NZS, 2006). Use of shear keys can prevent from excessive shear degradation in the connection during cyclic loading. In past research studies, the shear friction and the dowel action of rebars were relied on to transfer the shear forces across the interface of a grouted duct connection (Marsh et al., 2011).

For HDS1, there was not any armoring provided at the base of the column or unbonded length of the starter bars at the column to footing interface. Figure 3.22 presents reinforcing details for HDS1. A full set of technical drawings for HDS1 can be found in Section B.1 of Appendix B.

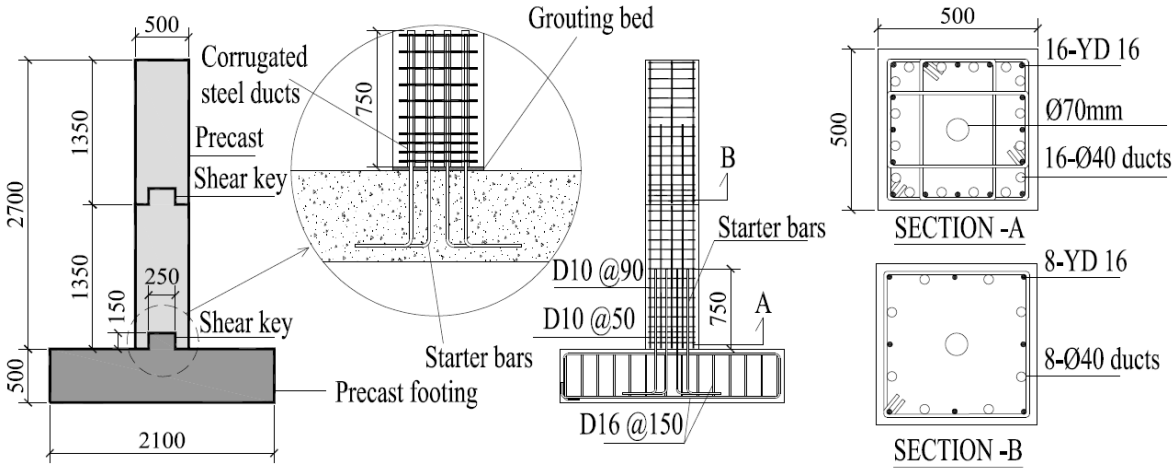

Figure 3.22. HDS1 section and details

All specimens were constructed out at a commercial prefabrication yard. Rebars were supplied by another manufacturer and were already bent-out and cut-off according to rebar schedule. All cages were tied at the prefabrication yard (Figure 3.23).

Before pouring the footing, a foam block was used to form a recess at the base of the footing to house the mechanical fixings for the unbonded post-tensioned bar later, as shown in Figure 3.24a.

(a) Rebar bundles bent-out and cut-off

(b) Tied cages for the segments and footing

(c) Cages transported to their formwork

(d) Footing cage being adjusted inside formwork

Figure 3.23. HDS1 construction photos

Plywood formworks were used for the column segments and footing. Corrugated steel grouting ducts were tied to the cages according to construction drawings (Figure 3.24c). Plastic breather tubes were installed in the grouting ducts prior to tying them in the cages (Figure 3.24b). These tubes were left for grouting of the precast segments later.

To ensure a good alignment of the starter bars at the connection interfaces, plywood templates were used at the ends of the segment before pouring concrete (Figure 3.24c and Figure 3.24d). An adequate number of lifters were placed inside the segments and footing during prefabrication. The lifters were designed to handle the weight of the elements, as well as any dynamic effects caused during lifting. After pouring the segments, the top surface of the elements was smoothened using a Hand Darby, as shown in Figure 3.24h. Following precasting stage, the completed elements were loaded on back of a trailer and transported to the lab for assembly and testing (Figure 3.25).

(a) Foam block visible at base of footing

(b) Corrugated duct with breather tubes

(c) Template plywood at the ends

(d) Corrugated ducts tied and aligned

(e) Pouring the segments

(f) Pouring the footing shear key

(g) Column segments after pouring

(h) Footing block after pouring

Figure 3.24. HDS1 construction photos

(a) Completed footing block

(b) Column segments, side lifters visible

(b) Footing block loaded on the trailer

(c) Column segments secured on the trailer

Figure 3.25. HDS1 elements completed and ready for delivery to the lab

After the elements for HDS1 were delivered in the lab, the next steps included assembly of the column, instrumentation, and experimental testing. Hold-down bolts were wound into the floor holes. The footing was lifted by the lab crane and was lowered down on the hold-down bolts. The footing was temporarily propped at approximately 500 mm higher than the strong floor level by using plywood planks underneath. The fixing for the unbonded post-tensioned bar (Macalloy bar) was inserted inside the recess at the bottom face of the footing. The fixing consisted of a washer (50 mm thick) and a nut. The timber planks were then removed and the footing was lowered down on the floor. The bolts were secured using washer and nuts on top of the footing (Figure 3.26a).

Given the maximum clearance height for the lab crane as 4 m, it was not possible to run a full length of the Macalloy bar (3 m) through the duct at the center of the footing. This would have not left any room for placing the lower column segment on top of the footing later. Therefore, a piece of Macalloy bar (1.5 m long) was cut-off and run through the footing central duct and was wound to the bar fixing underneath.

The lower column segment was lifted and lowered on top of the footing (Figure 3.26b). The footing starter bars and the central Macalloy bar were aligned and guided inside their respective ducts in the lower column segment. Steel shims and packers were used between the footing and lower column segment interface. The shims were intended to perform two jobs. Firstly, when adjusting the verticality of the column, shims and packers can be very useful. Secondly, they were leaving a gap of approximately 25 mm at the column to footing interface which was left for a grouting bed made of Sika 212.

After positioning the shims, the lower column segment was lifted again and a foam torus with a bead of silicone caulk were placed around the footing shear key. This detail was used to seal the central duct in order to avoid leakage of grout when pumping the grout inside the ducts. A similar detail was used for the segment to segment connection, as shown in Figure 3.26c and 3.26d.

A grouting bed was placed on top of the footing around the column spot and the column segment was lowered. This displaced some excess grout from around the grouting bed. It should be noted that shims and grouting bed would not be necessary if match casting is used during prefabrication. In that instance, a thin layer of epoxy would be sufficient at the connection interfaces. Following assembly of the column to footing connection, a bar coupler was used to splice the Macalloy bar on top of the lower segment, as can be seen in Figure 3.27d. The upper segment was placed on top of the lower segment and similar procedure as that for column to footing connection was repeated for the segment to segment assembly (Figure 3.26e and Figure 3.26f).

It is important to mention that during the assembly process when aligning the starter bars into the grouting ducts, some misalignment issues had to be resolved. As presented by Marsh et al. (2011), misalignment of the starter bars can be a potential construction risk for the grouted duct connections. This would need to be considered during the design and prefabrication. Mitigation methods may include frequent alignment inspections of the ducts during the prefabrication of the components. Another alternative is to provide adequate construction and assembly tolerances through enlarging the duct diameter. The study in this thesis showed that a 34 mm tolerance in the grouting ducts would be sufficient to eliminate any misalignment issues of the starter bars during the assembly process.

(a) Footing block positioned **(b) Column to footing interface** **(c) Foam torus**

(d) Silicone caulk around the central duct **(e) Upper segment placed** **(f) Segments assembled**

Figure 3.26. HDS1 assembly photos

Following assembly of the elements, the next step was securing the starter bars inside the ducts by pumping high strength grout into the ducts. Initially plastic fill were installed in all ducts. There were two fill tubes for each grouting duct. One tube was located close to the bottom of the duct and the other near the top, as shown in Figure 3.27b. The gaps around the fill tubes were sealed using silicone caulk.

The grouting ducts in both segments were initially filled with water and flushed. This gives three advantages. Firstly, flushing of the ducts can remove any debris and help with the smooth flow of the grout. Secondly, it can indicate any leakage around the grouting bed or segments. Thirdly, if the quantity of the filled water is measured, it can provide an accurate estimate of the volume of grout required to fill the ducts and space around the shear key. During the water filling process, any leaks were stopped using water proofing mortar. Grouting mix was then pumped into the bottom fill tubes and was allowed to fill the grouting ducts and flow upwards out of the top fill tubes. The pumping continued until it was visible that the grout was flowing out of the all top fill tubes. At this stage, all fill tubes were sealed and the fresh grout was left to cure for at

least 7 days before testing the specimen. The grouting sequence is shown in Figure 3.27. Figure 3.28 presents photos from the grouting process.

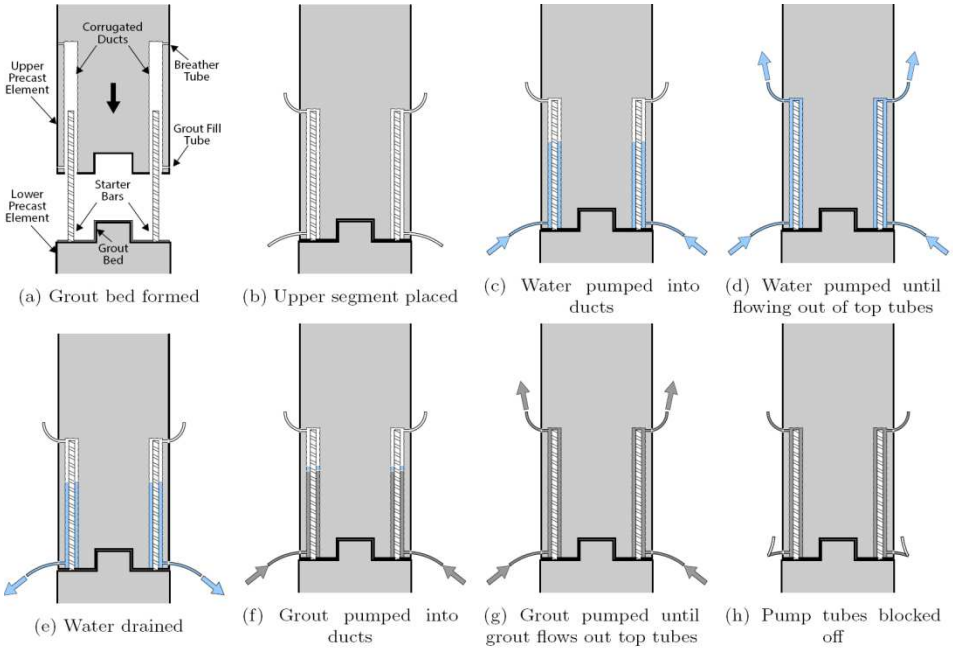

Figure 3.27. Grouting sequence, after White (2014)

(a) Water into ducts **(b) Top segment fill tubes** **(c) Water proofing mortar for leaks**

(d) Mixing grout **(e) Grout poured in a pump** **(f) Pumping the grout into the ducts**

Figure 3.28. HDS1 grouting photos

After 3 days, the fill tubes were removed and the breather holes were patched using epoxy, as shown in Figure 3.29a. The column was subsequently painted in white color. For the connection of the horizontal ram swivel to the column, four high-strength threaded rods (25 mm in diameter) were drilled and epoxied inside the column, as shown in Figure 3.29c. The column was fully instrumented and the horizontal ram was attached (Figure 3.29d).

(a) Patched holes (b) First paint coat (c) Epoxied rods for swivel (d) Instrumented column

Figure 3.29. HDS1 completed and ready for testing

For HDS2, the column dimensions and reinforcing details were identical to HDS1. However, there were two detailing improvements incorporated in HDS2. Firstly, armoring was provided at the base of the column to provide confinement for the cover concrete which would limit spalling. The armoring was made of 100 x 100 x 5 Angle, as shown in Figure 3.30b. The armoring had 30 mm diameter drilled holes to for the starter bars from the footing. There were no studs connecting the armoring to the concrete core. It was simply inserted at the base of the column cage and formwork before pouring the concrete at the prefabrication yard, as shown in Figure 3.31b.

The armoring was designed according to the procedure explained in Section 3.2.4.1 for a targeted confinement ratio ($R = 1.3$). This gave $f'_l = 1.925\ MPa$, the confinement effectiveness coefficient (k_e) was equal to 0.831 for the half-scale square column. The minimum required armoring wall thickness (t) from Equation 3.9 was calculated to be 2 mm. A 5 mm thick angle was instead used for extra confinement.

The second detailing improvement was leaving 120 mm unbonded (taped) length in the starter bars at the column to footing interface, as shown in Figure 3.32a. This was intended to eliminate the strain concentration effects at the interface for an enhanced

ductility of the column, as previously explained in Section 3.2.4.1. Normal duct tape was used to wrap the 120 mm length of the starter bars. However, when considering the durability of the connection, it is better to use Denso Tape instead which is a corrosion resistant tape. The 120 mm unbonded length was calculated based on the observation from the testing of HDS1 in which there was debonding of starter bars at the column to footing interface.

Testing results from HDS1 showed a plastic hinge length (L_p) of approximately half the height of the column cross-section ($L_p = 250\ mm$). Inputting this value into Equation 3.1 with $L_{cant} = 2500\ mm$ (height from the top of the footing to the center line of the horizontal ram) and solving for $L_{sp,\ actual}$ (actual strain penetration length) would give $L_{sp,\ actual} = 50\ mm$ for HDS1. At the same time, using Equation 3.2, the strain penetration length (L_{sp}) for an equivalent conventional ductile monolithic column could be calculated as $L_{sp} = 176\ mm$. Utilizing Equation 3.3, the required unbonded length (l_{ub}) could be calculated as approximately 120 mm.

Figure 3.30 illustrates the detailing improvements for HDS2. A full set of technical drawings for HDS2 can be found in Section B.1 of Appendix B. Figure 3.31 presents construction photos for HDS2. Photos from the completed components of HDS2 and assembled specimen are shown in Figure 3.32. The assembly and grouting procedure for HDS2 was identical to that of HDS1.

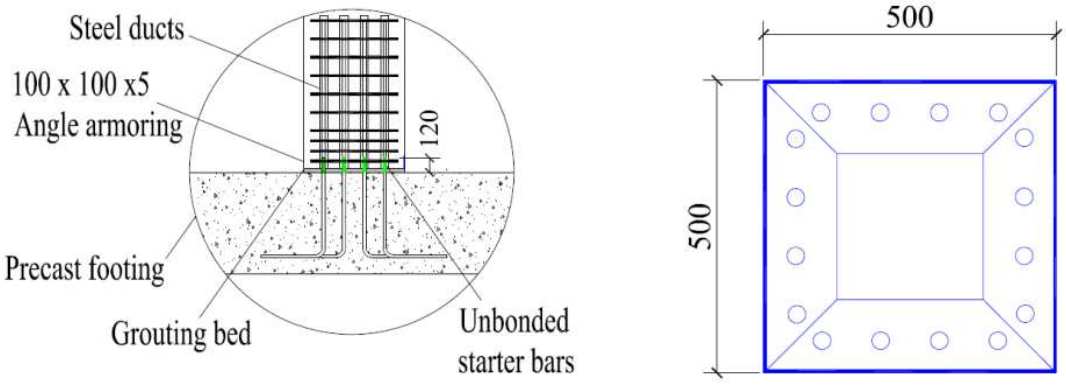

(a) Column to footing detail **(b) Armoring detail**

Figure 3.30. HDS2 detailing improvements

(a) Pouring the lower segment (b) Armoring visible at the base (c) Completed precast elements

Figure 3.31. HDS2 construction photos

(a) Lower segment base (b) Upper segment base (c) Deboned footing starter bars

(d) Footing block positioned (e) Lower segment (f) Upper segment (g) Completed column

Figure 3.32. HDS2 assembly photos

3.2.6.2 HDC1 and HDC2

Member Socket Connection (MSC) was used for the column to footing connection. The segment to segment connection was Grouted Duct Connection (GDC). Similar to HDS1 and HDS2, the column consisted of three precast elements. This included the footing block, lower column segment, and upper column segment. The circular column was designed according to NZS 3101 (NZS, 2006) for the same design load as that of HDS1 and HDS2, refer to Table 3.2.

For HDC1, the lower segment of the column consisted of 16-YD16 straight longitudinal rebars. The upper segment had 8-YD16 rebars due to reduced moment demand. There was no headed bar (foot inserts) used for the lower segment rebars inside the socket. The development length from NZS 3101 for a conventional ductile cast-in-place column was calculated to be approximately 500 mm. Given the 500 mm height of the lower column segment stub inside the socket for HDC1, there was no need of bent-out longitudinal rebars or foot inserts. In this case, the column stub will be confined in the footing socket which means even a shorter development length would be sufficient for MSC compared to a conventional monolithic column. Further research would be required to quantify the development length of the column rebars in a MSC, if the foot inserts or compliance with a conventional monolithic column approaches are not used.

To provide shear, confinement, and anti-buckling capacity in the plastic hinging zones of the column, transverse reinforcement in terms of YD10 hoops spaced at 50 mm were used. The hoops spacing was 90 mm above the plastic hinge regions. Corrugated galvanized steel ducts were placed inside the upper segment to house the starter bars from the lower segment. The grouting ducts were 40 mm in diameter and 750 mm long.

Similar to HDS1 and HDS2, there was a 70 mm diameter duct located at the center of the column segments. This duct was intended to house the unbonded post-tensioned bar to apply axial force on the column during testing. A cubical recess at the bottom face of the lower column segment was left to provide mechanical anchorage for the unbonded post-tensioned bar.

The footing was designed to be a capacity protected element. A 2.1 m square footing with 500 mm depth was used. The footing was reinforced with double layers of YD16

bars spaced at 150 mm. There was a socket at the center of the footing with 500 mm depth and 520 mm diameter. The socket walls and concrete surface from the portion of the column inside the socket (stub) were roughened during the prefabrication process. The roughened surface was made by lubricating the formworks with a retarding agent before casting the concrete. After the formwork is removed (generally 1-2 days after casting), pressure washer is used to expose the aggregate on the concrete surface. The retardant can be This was intended to provide a strong bond between the grout interface and the precast surfaces. Similar to HDS1 and HDS2, galvanized steel ducts left for the hold-down bolts around the perimeter of the footing.

The shear key at the segment to segment connection was designed to transfer all shear loads across the interface. In this instance, the dowel action of the starter bars for shear resistance was neglected. The shear keys were designed as corbels in accordance with the empirical design procedure for corbels and brackets in NZS 3101 (NZS, 2006). In this methodology, reinforcing bars are designed using the principals of shear-friction.

Figure 3.33 presents reinforcing details for HDC1. A full set of technical drawings for HDC1 and HDC2 can be found in Section B.2 of Appendix B. The reinforcing and construction details for HDC1 and HDC2 were exactly identical. HDC1 was intended for uniaxial testing while HDC2 for biaxial testing.

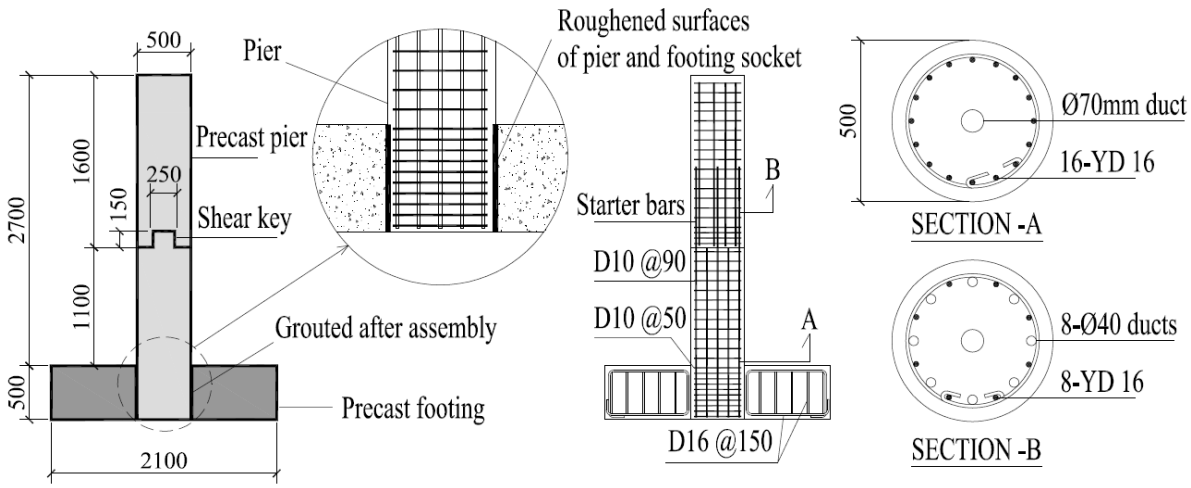

Figure 3.33. HDC1 and HDC2 section and details

The footing socket was made using a plastic cylinder at the center of the footing. For a roughened surface of the socket, retarding agent was applied around the plastic

cylinder before casting the footing (Figure 3.34d). Figure 3.34 presents construction photos of HDC1 and HDC2.

(a) Footing cage with central socket

(b) Tied cages for the segments and footings

(c) Retarding agent for roughened surface

(d) Footing with socket in the formwork

Figure 3.34. HDC1 and HDC2 construction photos

For construction of the circular segments, steel casing was used (Figure 3.35a). Each column segment was cast separately (Figure 3.35h and Figure 3.35i). The cages for the column segments were secured inside the metal formworks. Plywood templates were used for the lower and upper segments to ensure good alignment of the starter bars into the grouting ducts at the segment to segment connection, as shown in Figure 3.35b.

After closing the formworks, each segment had to be poured vertically. The formworks were then lifted up by a crane and were lowered on to the pouring platform (Figure 3.35d). After securing the formworks, concrete from a mixer truck was filled inside a container which was then lifted up by a crane to the pouring platform (Figure 3.36a).

Figure 3.35 and Figure 3.36 present photos from construction of HDC1 and HDC2.

(a) Metal formwork for the segments (b) Securing the cage (c) Closing the casing

(d) Casing lifted up (e) Moving the casing (f) Pouring platform (g) Lowering the casing

(h) Upper segments ready for pouring (i) Lower segments ready for pouring

Figure 3.35. HDC1 and HDC2 construction photos




(a) Filling concrete **(b & c) Moving the container to platform** **(d) Pouring the segments**


(e) Upper segments poured **(f) Lower segments poured, shear key visible**

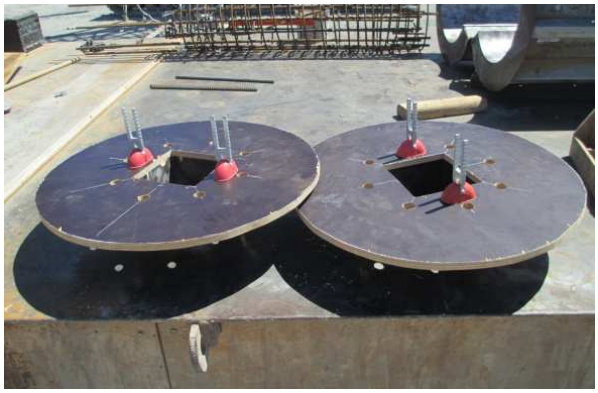


(g) Plywood template for lower segments **(h) Templates positioned, shear keys poured**

Figure 3.36. HDC1 and HDC2 construction photos

Completed elements for HDC1 and HDC2 are shown in Figure 3.37. After the elements arrived in the lab, the next step was assembling the column. Hold-down bolts were wound in the strong floor. Two rings of foam torus, one inside the socket and one outside along with some bead of silicone caulk were left at the center of the footing spot (Figure 3.38a). The inner ring was intended to seal the area around the recess at the base of the column stub so when grouting the MSC, the grout will not flow into the anchorage area of the post-tensioned bar inside the recess. The outer ring had slightly

bigger diameter than the socket. It was expected to prevent from the flow of the grout underneath the footing. The footing was then lowered on the bolts and was secured.

(a) Precast elements, roughened stub

(b) Footing socket, roughened walls

(c) Lower segment base with fixing recess

(d) Upper segment base with shear key recess

Figure 3.37. HDC1 and HDC2 elements completed and ready for delivery to the lab

The upper column segment was put on top of the lower segment with a Macalloy bar running through the central duct (Figure 3.38c). Similar to HDS1 and HDS2, the starter bars from the lower segment were aligned and guided into the ducts of the upper segment. The whole column was then inserted into the footing socket (Figure 3.38d). It should be noted that this type of assembly was appropriate due to constraints in the lab environment. In an actual bridge, there will be no Macalloy bar running through the column. Therefore, the assembly process would include assembly of the lower segment inside the socket, and then placement of the upper segments on top of each other.

For the column to footing member socket connection, small wooden wedges were used to center the column and adjust the verticality (Figure 3.38i). Steel shims were used to align the top segment. Following this, the upper segment was lifted and a grout bed was

poured on top of the lower segment (Figure 3.38f). Once the upper segment was lowered again, it displaced any excess grout from the grouting bed (Figure 3.38g). The grouting bed thickness and materials was similar to what used for HDS1 and HDS2.

(a) Foam torus under footing **(b) Footing block placed** **(c) Column ready** **(d) MSC assembly**

(e) Column inserted **(f) Grouting bed and lower segment** **(g) Segment to segment connection**

Figure 3.38. HDC1 assembly photos

After assembly of the segment to segment connection, the column to footing MSC was ready to be grouted. Fresh water was sprayed into the socket walls and column stub. This was done to prepare a saturated surface condition around the joint. High strength grout was mixed in a bucket and poured into the grouting interface using a scoop (Figure 3.39a and Figure 3.39b). In order to avoid any air voids inside the grouting interface, a thin strip of metal was used to agitate the grout (Figure 3.39c). Pouring of the grout combined with agitation was continued until the annulus was completely filled.

The small wooden wedges were not removed for a few hours until the grout had started to cure. Once the grout had gained some strength, the wooden wedges were carefully removed without damaging the grout interface. Any voids left after the removal of the wooden blocks were subsequently filled with fresh grout.

The last step was pumping the grout inside the ducts and the space around the shear key at the segment to segment connection, as shown in Figure 3.39d through Figure 3.39f. The grouting procedure was identical to that explained for HDS1 and HDS2 in Section 3.2.6.1 which was illustrated in Figure 3.27 previously. Figure 3.39g shows the completed and instrumented column. The assembly and grouting process for HDC2 was identical to that of HDC1.

(a) Grout mixed for MSC

(b) Pouring the grout, wedges visible

(c) Agitating the grout

(d) Grout in the pump

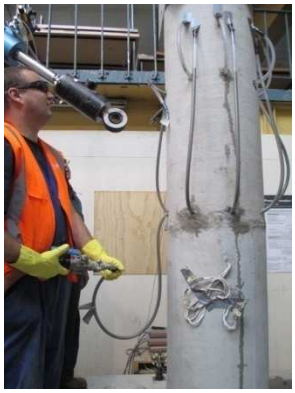

(e) Pumping the grout

(f) Sealing the fill tubes

(g) completed column

Figure 3.39. HDC1 assembly and grouting photos

3.2.7 Testing Results and Performance Evaluation

3.2.7.1 HDS1

HDS1 was tested under uniaxial loading. During 0.35% drift ratio, minor flexural cracks occurred in the grouting bed at the base of the column. The cracks were marked on the column and measured in size at the peak drift of each drift ratio throughout testing.

During 0.5% drift ratio, more cracks appeared throughout the segments. Most of the cracks remained less than 0.4 mm in width with the density of the cracks increasing during larger drift ratios. Bigger cracks which indicated considerable deformation were concentrated near the column to footing grouting bed. During 3% drift ratio, there was a 7 mm gap opening at the column to footing interface (Figure 3.40a). There was also 1.5 mm gap opening at the segment to segment interface (Figure 3.40b). However, there was no spalling at this location and the gap opening remained under 2 mm until the end of testing (5% drift ratio). Few hairline diagonal cracks were observed close to the column to footing and segment to segment connections. Spalling of the concrete and deterioration of the bottom grouting bed initiated during 3% drift ratio (Figure 3.40c) which corresponded to the Ultimate Limit State (ULS) performance level.

During 4% drift ratio, the extent of spalling increased significantly with spalling being concentrated to a height of approximately 200 mm above top face of the footing. First starter bar rupturing at the column to footing connection occurred during the first cycle of 5% drift ratio when the column was close to its peak drift. At the end of testing, the spalling height increased to 250 mm. This was mainly located on the northern and southern corners and faces of the column. After removing the loose concrete, buckling of starter bars was obvious on both faces, as shown in Figure 3.41.

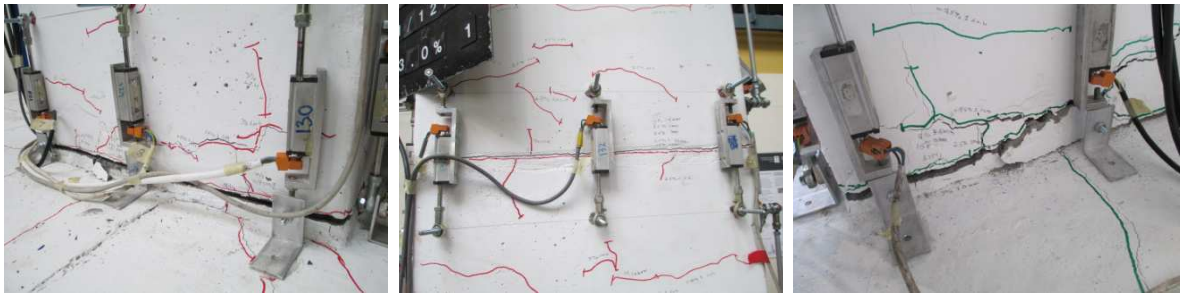

(a) 7 mm gap opening at bottom (b) 1.5 mm gap opening at top (c) Spalling at bottom GDC

Figure 3.40. HDS1 at 3% drift ratio

(a) Northern face spalling **(b) Northern face, buckling and fracture of rebars**

(c) Southern face spalling **(d) Southern face, buckling and fracture of rebars**

Figure 3.41. HDS1 column to footing connection at the end of testing (5% drift ratio)

Table 3.7 presents crack sizes for each interface connection at different drift ratios during testing. Figure 3.42 presents photos from the damage progression to HDS1 at different drift ratios during testing. The photos were taken at the end of each drift ratio.

Table 3.7. Summary of the maximum crack widths measured during HDS1 testing

	Drift Ratios (%)							
	0.35	**0.5**	**1.0**	**1.5**	**2.5**	**3**	**4**	**5**
Column to Footing (mm)	<0.4	0.4	1	2	5	7	10	Spall
Segment to Segment (mm)	<0.4	0.4	0.5	0.5	1	1.5	2	2

(a) Testing start **(b) End of 0.5% drift ratio** **(c) End of 1.5% drift ratio**

(d) End of 3.0% drift ratio **(e) End of 4.0% drift ratio** **(f) End of 5.0% drift ratio**

Figure 3.42. Damage progression in HDS1 during testing

There were also some hairline cracks in the footing (Figure 3.43). The cracks were originating from the GDC and propagating towards the perimeter of the footing in a radial manner. The cracks remained less than 0.4 mm in size throughout testing.

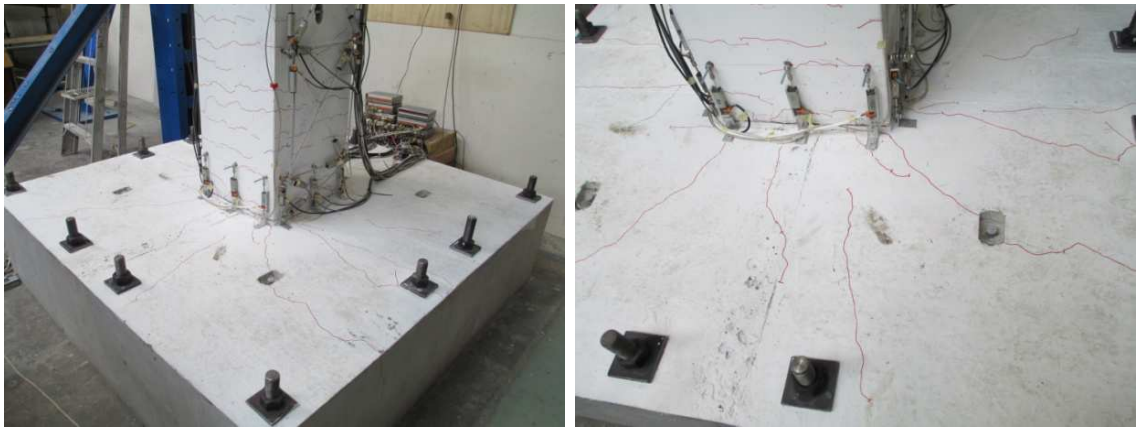

(a) Radial hairline cracking in the footing block **(b) Close-up view or radial cracking**

Figure 3.43. Radial hairline cracking to HDS1 footing block

The force-drift hysteresis for HDS1 is shown in Figure 3.44. It can be observed that the column yielded at a drift ratio of 0.75%. Given the spalling initiation (ULS performance limit) at 3%, the displacement ductility at ULS was 4. At the column failure point (rupturing of rebars at 5%), the displacement ductility was over 6. As can be seen from the load-drift hysteresis, there were large residual displacements in the column after the column yielded. The residual displacement of the column was more than 50% of the peak drift ratio during 4% and 5% drift ratio cycles.

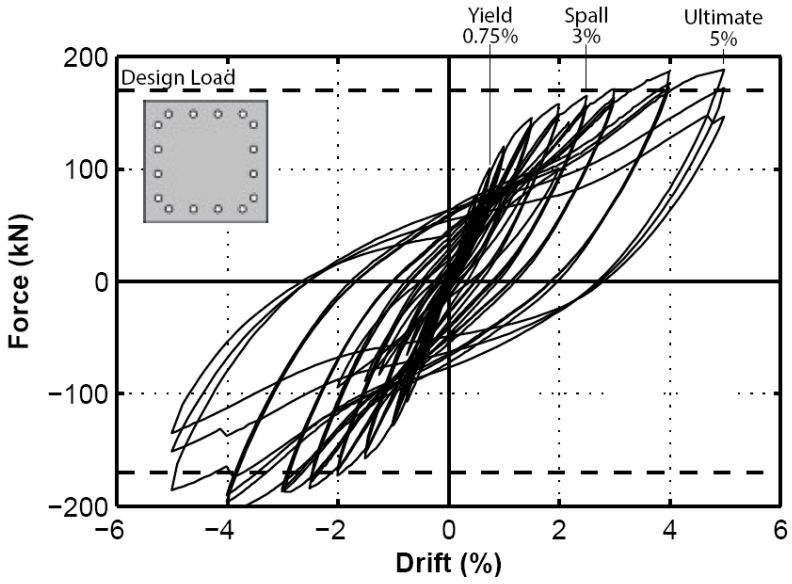

Figure 3.44. HDS1 force-drift hysteresis

The curvature was measured using the instruments available at the testing lab (externally attached potentiometers) which were located at the plastic hinging zones. An alternative method could be to place several marks (dots) on the specimen before

testing, then capturing the movements of dots using a high speed camera as the specimen is being pulled or pushed. Other methods may include use of advanced sensors and instruments which could provide an improved measurement of the curvature. The moment-curvature plot for HDS1 is shown in Figure 3.45. From Figure 3.44 and Figure 3.45, the column capacity was reduced significantly following the bar rupturing during 5% drift ratio.

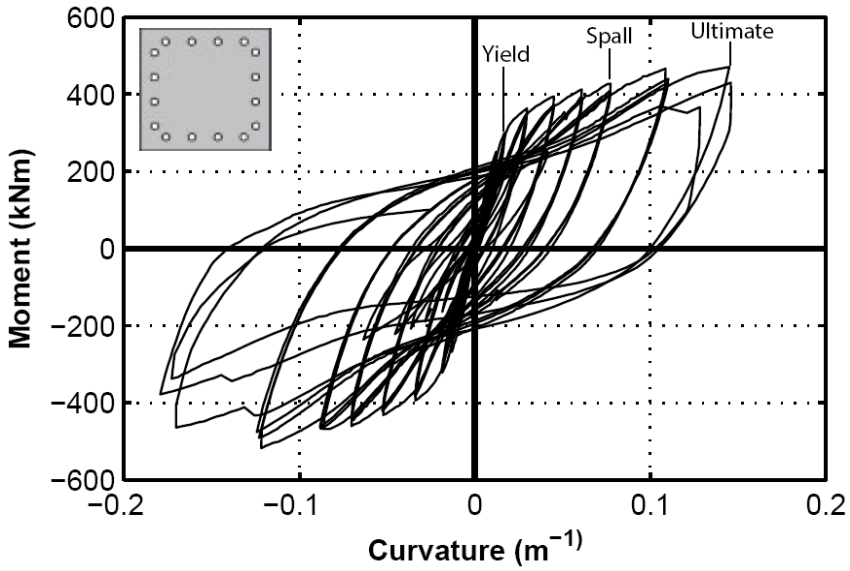

Figure 3.45. HDS1 moment-curvature hysteresis

From Figure 3.44, the column maximum lateral load was 205 kN which corresponded to a moment capacity of 510 kNm. This load is bigger than the column design lateral load of 170 kN in accordance with Table 3.2 for the half-scale specimen.

During testing as the column displaced, there was very little increase in the post-tensioned bar which was used to apply axial loads on the column. This indicated that the bar may have been fully bonded across the interface. Following testing and disassembly of the column, it was found that during pumping of the grout inside the ducts at the column to footing interface, some grout had leaked inside the central duct and the post-tensioned Macalloy bar was fully bonded across the interface. This was thought due to insufficiency of the foam torus and some beads of silicone caulk left around the footing shear key before pumping the grout inside the ducts. However, similar detail was used for the segment to segment connection, but there was no bonding of the post-tensioned bar at this location.

The interpretation of the bonded post-tensioned Macalloy bar is that the bar was applying axial load only on the top of the upper segment with no axial load being transferred to the footing. The bonded Macalloy bar was acting like a bonded reinforcing bar located at the center of the lower segment section. The increase in the lateral load of the column (205 kN) following ULS was caused by this error. Similarly, the increase in post-stiffness in the hysteresis plots shown in Figure 3.44 was caused by the bonded Macalloy bar. The bonded Macalloy bar affected only the capacity of the section, but not the overall ductility of the system as longitudinal bar rupturing was achieved at 5% drift.

The curvature distribution up the height of the column at peak of each drift ratio is plotted in Figure 3.46. As it can be seen, the curvature level was increasing at the column to footing and segment to segment connections with further applied drifts. Testing results showed that inelastic deformation of the starter bars occurred at both interfaces. Although majority of nonlinear deformation happened at the column to footing interface, however, having an extra plastic hinge at the segment to segment interface increased the total energy dissipation capacity of the column. This had also led to an increase in the ultimate drift capacity of the column since the inelastic deformation was distributed between the two connections. However, during larger drifts, majority of damage and gap opening were concentrated at the bottom interface.

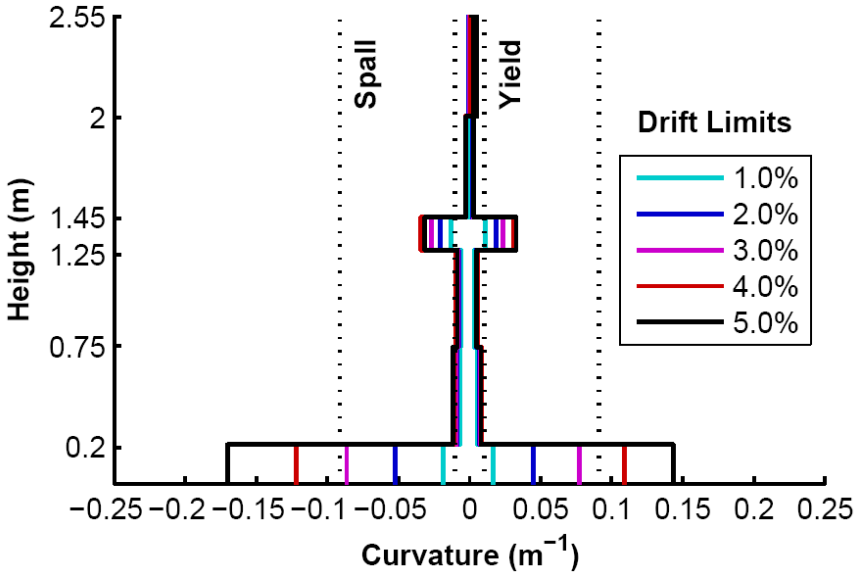

Figure 3.46. HDS1 curvature distribution (NS direction)

As it can be observed from Figure 3.46, there were two plastic hinges in the column. However, most of the nonlinear deformation occurred at the bottom plastic hinge. This was spread over 200 mm height of the column from the base. As explained earlier, observations from testing suggested a plastic hinge length of 250 mm (half the height of the column cross-section) where concrete spalling had extended through. This shows a good correlation with the experimental results. In Figure 3.46, it is also clear that as expected the column regions outside the plastic hinges remained elastic.

It should be noted that the data from the strain gauges were not utilized for all four columns (HDS1, HDS2, HDC1, and HDC2) in this research. Most of the strain gauges were broken during precasting of the columns. This issue was already forecasted ahead of prefabrication and testing of the specimens. Therefore, a large number of high-precision potentiometers were installed externally on all faces of the column to provide the necessary data and information about the performance of the column during testing. This eliminated the needs for strain gauges data during testing.

The area-based damping ($\xi_{area\text{-}based}$) for HDS1 is plotted against increasing displacement ductility (μ) in Figure 3.47. The area-based damping was calculated from the enclosed areas of the force-drift hysteresis from Jacobsen (1930) in Equation 3.10 below.

$$\xi_{area-based} = \frac{A_h}{2\pi F_m \delta_m} \tag{3.10}$$

In Equation 3.10, A_h is the area enclosed by the hysteresis loop, F_m is the peak force of the loop, and δ_m is the peak displacement of the loop.

According to Priestley et al. (2007), a correction factor needs to be applied to the area-based damping in order to convert it to an equivalent time-history-calibrated (THA, ξ_{THA}), hysteretic damping (ξ_{hyst}), as presented in Equation 3.11. This step is necessary for representing the area-based damping in terms of hysteretic damping which then would represent the damped response of the structure following a nonlinear dynamic analysis (THA). More information can be found in Priestley et al. (2007).

$$Correction\ Factor = \frac{\xi_{THA}}{\xi_{area-based}} = -0.018\xi_{area-based} + (0.0875\mu + 0.723) \tag{3.11}$$

Using Equation 3.11, the corrected area-based damping (hysteretic damping, ξ_{hyst}) is presented in Equation 3.12.

$$\xi_{hyst} = \xi_{area-based}\,[-0.018\,\xi_{area-based} + (0.0875\mu + 0.723)] \quad (3.12)$$

The corrected area-based damping curve from the experimental data, is plotted against the displacement ductility in Figure 3.47. For a comparison, theoretical hysteretic damping curves for the hysteretic models of conventional monolithic systems such as Takeda-Fat (e.g. reinforced concrete beam) and Takeda-Thin (e.g. reinforced concrete column) based on Dwairi-Kowalsky damping rule (Dwairi et al., 2007) and in accordance with Priestley et al. (2007) were also plotted alongside the experimental hysteretic damping. For the theoretical damping curves, it was assumed that the system had an effective period ($T_{eff} \geq 1\ sec$).

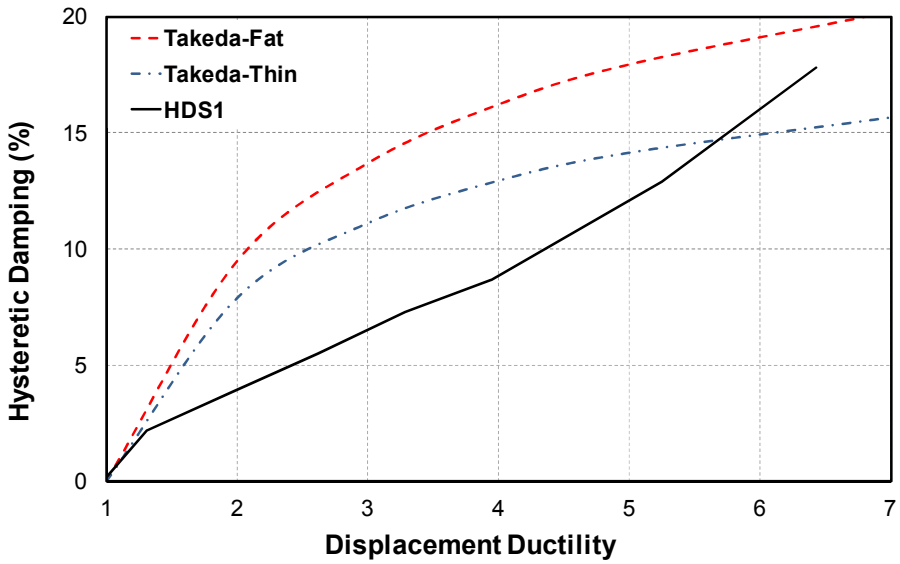

Figure 3.47. HDS1 corrected area-based hysteretic damping (ξ_{hyst})

In Figure 3.47, the hysteretic damping and displacement ductility from the experimental testing shows a relatively linear trend between each other. According to Figure 3.47, the hysteretic damping is lower than that of a Takeda-Thin model up to a ductility of just over 5.5. For ductilities beyond this value, the experimental hysteretic damping curve is located between the Takeda-Fat and Takeda-Thin models. The experimental hysteretic damping curve attained a value of 18% at the failure point of the column.

The seismic performance of HDS1 was evaluated using the displacement-based assessment methodology, as outlined in Marriott (2009) in accordance with Priestley et

al. (2007). In this methodology, the Acceleration Displacement Response Spectrum (ADRS) curves along with the damping relationship developed previously are utilized to assess the performance of the column under various seismic hazard levels. The force-drift hysteresis is normalized to match the units of the ADRS curves. This can be simply done by dividing the applied lateral force by the column design axial load.

In the first step, the normalized force-drift hysteresis from the experimental testing is plotted. The elastic design spectrum is constructed for different seismic hazard levels in accordance with NZS 1170.5 (NZS, 2004). The hazard levels selected here were based on the return periods of 25 years ($R = 0.25$), 1000 years ($R = 1.3$), and 2500 years ($R = 1.8$) which correspond to the Serviceability Limit State (SLS), Ultimate Limit State (ULS), and Maximum Considered Earthquake (MCE) limit states, respectively. Other seismic parameters were identical to those assumed during the design of the column, refer to Table 3.2.

The elastic design spectrum is converted into ADRS using the methodology presented in Priestley et al. (2007) and PRESSS Design Handbook (Pampanin et al., 2010) which is based on an assumed sinusoidal harmonic oscillation theory. The spectral displacement (S_d) in accordance with this methodology can be calculated for every spectral period (T), as given in Equation 3.13. In this Equation, $C_d(T)$ is the elastic 5% damped design acceleration calculated according to NZS 1170.5, and g is the acceleration due to gravity ($g = 9.81\ m/sec^2$). The ADRS curves are graphed on the same plot as the normalized backbone curve from the force-drift hysteresis. It should be noted that the spectral displacement for each ADRS curve was divided by 2 to account for the half-scale size of the column.

$$S_d = \frac{C_d(T)\ g\ T^2}{4\pi^2} \tag{3.13}$$

In the second step, an ADRS curve (demand) is compared against the first loading cycle from the experimental response (capacity). The intersection point between the two curves is called the “performance point”. The displacement $\Delta_{R(i)}$ is noted (Figure 3.48a).

In the third step, $\Delta_{R(i)}$ is used to define the area-based damping of the system from the experimental results $\xi_{R(i)}$, as shown in Figure 3.48b. In the next stage, $\xi_{R(i)}$ is converted

to an equivalent time-history-calibrated damping (ξ_{eq}) using Equation 3.19. Following this, the spectral reduction factor (η) is calculated in accordance with Equation 3.14.

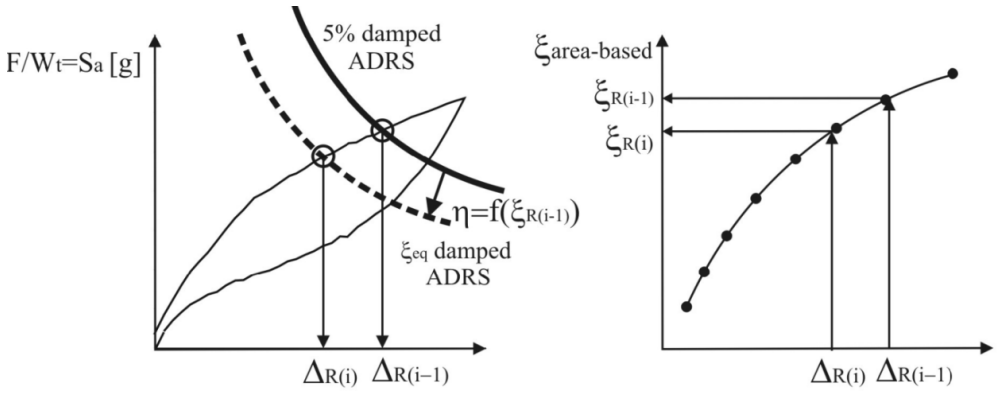

(a) ADRS domain **(b) Displacement-ductility relationship**

Figure 3.48. Evaluation of the performance point, after Marriott (2009)

$$\eta = \sqrt{\frac{0.07}{0.02 + \xi_{eq}}} \tag{3.14}$$

The reduction factor (η) can be shown as a ratio between the spectral acceleration (S_a) with (ξ) percent damping and the spectral acceleration with 5% damping, as presented in Equation 3.15. Similarly, η can be defined in terms of the ratio between the spectral displacements, as presented in Equation 3.16.

$$\eta = \frac{S_a(T,\xi)}{S_a(T,5\%)} \tag{3.15}$$

$$\eta = \frac{S_d(T,\xi)}{S_d(T,5\%)} \tag{3.16}$$

Appropriate values of reduction factor (η) for near-field earthquakes is outside the scope of the research here. As presented in Table 3.2 parameters, the near-fault factor was taken equal to 1.0 for the prototype structure which means only far-field earthquakes are considered. Boomer and Mendis (2004) and Faccioli et al. (2004) present appropriate reduction factors for near-field ground motions.

In the fourth step, the ADRS demand curve is reduced (dampened) by applying the reduction factor (η). The performance point which defines the displacement Δ_R is updated. The procedure is repeated until a convergence is found for Δ_R.

The Equivalent Viscous Damping (EVD, ξ_{eq}) is the sum of the corrected area-based hysteretic damping (ξ_{hyst}) and the elastic tangent damping ($\xi_{el,\ tangent}$), as shown in Equation 3.17. Past studies have shown that a tangent stiffness proportional damping model can be a better representation of the elastic damping (Priestley et al., 2007).

$$\xi_{eq} = \xi_{hyst} + \xi_{el,tangent} \tag{3.17}$$

A single-degree-of-freedom (SDOF) model is normally used as a substitute structure for the Direct Displacement-Based Design (DDBD) of structures. In this instance, correction factors are applied to convert the elastic damping (secant stiffness, $\xi_{el,\ secant}$) of the structure to a tangent stiffness proportional model (tangent stiffness, $\xi_{el,\ tangent}$), as presented in Equation 3.18.

$$\xi_{el,tangent} = \mu^{\lambda}\xi_{el,secant} \tag{3.18}$$

In Equation 3.18, μ is the system displacement ductility and $\xi_{el,\ secant}$ is normally equal to 5% for reinforced concrete structure. In this Equation, λ is a correction factor which equals to -0.378 for monolithic columns (Takeda-Thin), -0.313 for monolithic beams (Takeda-Fat), and -0.430 for post-tensioned rocking system (Flag-Shaped). By substituting ξ_{hyst} and $\xi_{el,\ tangent}$ from Equation 3.12 and Equation 3.18 into Equation 3.17, Equation 3.19 presents the expression for EVD (ξ_{eq}) which incorporates all time-history and tangent stiffness calibrations.

$$\xi_{eq} = 5\%\mu^{\lambda} + \xi_{area-based}\,[-0.018\,\xi_{area-based} + (0.0875\mu + 0.723)] \tag{3.19}$$

The expression in Equation 3.19 is primarily intended for far-field ground motions. Further research is needed to calculate ξ_{eq} for impulsive near-field earthquakes. Using the displacement-based assessment methodology presented earlier, Figure 3.49 presents the ADRS plot for HDS1. In Figure 3.49, the expected performance of the column under each hazard level is represented by crosses on the graph. When constructing the demand curves, the Structural Performance Factor (S_p) was taken to be 1.0 according to Marriott (2009). From the ADRS plot, the column will reach a peak drift of 0.2% under a SLS event. This is well below the yielding point of the column (0.75%) which means the column will remain elastic during a SLS event from NZS 1170.5. The column will have a peak drift ratio of 2.4% under a ULS earthquake. This is slightly

lower than the assumed 3% drift ratio during the design. The reason behind this was the higher post-yield stiffness of the column which occurred due to bonding of the post-tensioned Macalloy bar during construction. This error has influenced the peak drift ratio for a ULS event. If the Macalloy bar was not grouted and remained fully unbonded, the column would have had lower post-yielding stiffness. This would have caused a ULS event to generate a drift ratio close to the design drift ratio (3%) of the column, as obtained for HDC1 in Section 3.2.7.3. According to Figure 3.49, a MCE level earthquake will generate a peak drift ratio of 3.8% in the column.

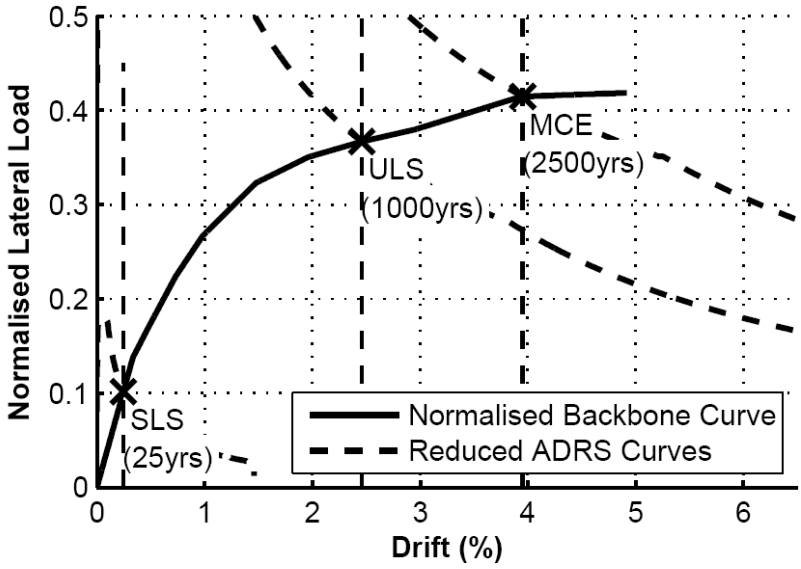

Figure 3.49. HDS1 ADRS plot

The energy dissipated per each loop of each drift ratio cycle is presented in Figure 3.50. In this Figure, the cumulative dissipated energy during testing is also plotted on the secondary axis of the graph. The dissipated energy was calculated using a numerical integration of the area enclosed inside the hysteresis loop for each first three cycles at each drift ratio. The cumulative dissipated energy is the sum of the energy dissipated in the three cycles at each drift ratio.

From Figure 3.50, it can be seen that the first cycle of loading at each drift ratio dissipates the maximum energy. The amount of energy dissipated is decreased in the second and third cycles. The reason behind the reduction in the subsequent cycles of each drift ratio is the strength degradation of the column under cyclic loading. This is very obvious in the cycles during 5% drift ratio where extensive concrete spalling, starter bar buckling, and rupturing had occurred.

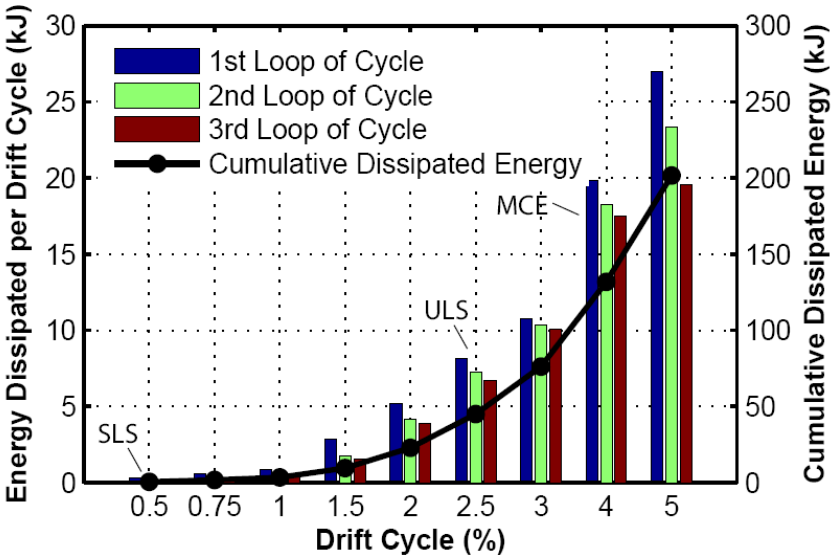

Figure 3.50. HDS1 dissipated energy (per cycle and cumulative)

3.2.7.2 HDS2

HDS1 was tested under biaxial loading. Despite a more demanding biaxial loading, the column performed similar to HDS1. At 0.25% drift ratio, minor flexural cracking appeared in the column with similar distribution as HDS1.

The base armoring was very effective to limit the spalling and damage to the cover concrete. However, during 2.5% drift ratio which corresponded to 3.25% resultant drift ratio (ULS performance level), minor to moderate spalling occurred in the corners of the column, near the column to footing interface, as shown in Figure 3.51c and Figure 3.51d. The spalling was due to biaxial clover loading of the specimen where the whole column was pivoted at one corner at the peak drift. This caused higher compressive stresses concentrated at the pivoted corner which had resulted in concrete spalling.

The gap opening at the column to footing interface was measured to be 12 mm at the peak of 2.5% drift ratio (Figure 3.51a). There was also 2 mm gap opening at the segment to segment interface during 3% drift ratio (Figure 3.51b). Deterioration and flaking of the bottom grouting bed initiated during 2.5% drift ratio (Figure 3.51a). The ULS performance of the specimen was similar to that for HDS1. Although HDS1 was tested under a less demanding uniaxial loading compared to biaxial loading.

As expected, the largest crack was located at the column to footing interface where there was a 120 mm unbonded length of the starter bars left during the construction.

Most of the other cracks, apart from those at the column to footing and segment to segment interfaces, remained less than 0.4 mm in width. There was no signs of spalling at this location and the gap opening remained under 2.5 mm until the end of testing, as shown in Figure 3.52e. Few hairline diagonal cracks were observed at the column to footing and segment to segment connections.

During 5% drift ratio (7% resultant drift ratio), the bottom crack size was measured o be 32 mm (Figure 3.52a). First starter bar ruptured during 5% drift ratio (6.5% resultant drift ratio, MCE performance level). The grouted bed was completely crushed at this point (Figure 3.52b). The bar rupturing point was significantly larger than that of HDS1. This proved that the debonding of the starter bars at the column to footing connection was very effective to increase the ultimate drift capacity of the column. During testing, there was no obvious signs of buckling of the starter bars. It appeared that the external armoring had prevented from excessive buckling of the rebars. However, some buckling of the starter bars was observed upon the disassembly which had occurred in the parallel direction to the faces of the column.

Following testing, spalling in the corners of the column at the column to footing connection had occurred up to a height of 250 mm from the top face of the footing, as shown in Figure 3.52c and Figure 3.52d.

Table 3.8 presents crack sizes for each interface connection at different drift ratios during testing. Figure 3.53 presents photos from the damage progression to HDS2 at different drift ratios during testing. The photos were taken at the end of each drift ratio.

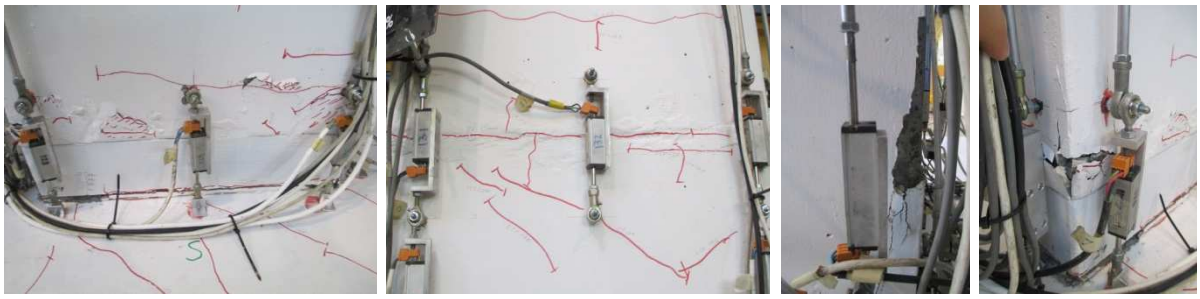

(a) 12mm gap opening at base (b) 1.5 mm gap opening at top (c & d) Spalling in the base corners

Figure 3.51. HDS2 at 2.5% drift ratio (3.25% resultant drift ratio)

(a) 32 mm Gap opening at base at peak 5% drift

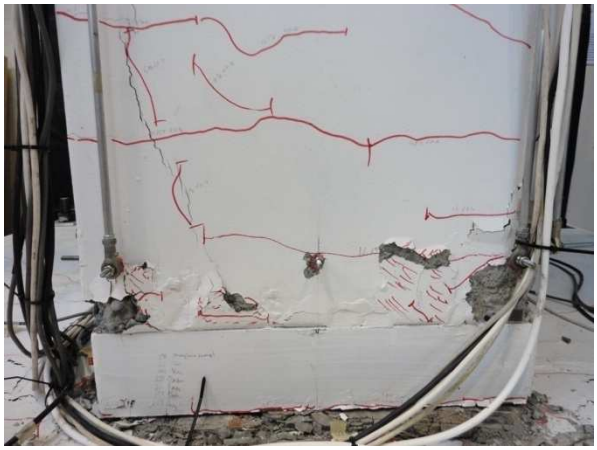

(b) Crushed grouting bed

(c &d) Extent of spalling at the end of testing

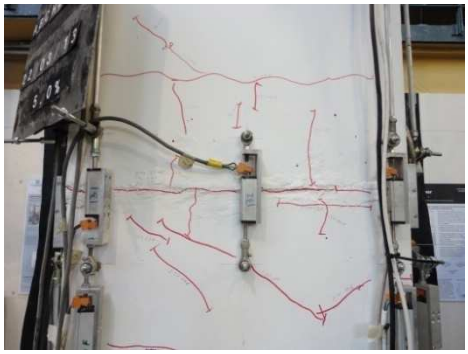

(d) Extent of damage at top GDC

Figure 3.52. HDS2 column to footing connection (7% resultant drift ratio)

Table 3.8. Summary of the maximum crack widths measured during HDS2 testing

	Resultant Drift Ratios (%)							
	0.5	**0.7**	**1.4**	**2.1**	**3.5**	**4.2**	**5.7**	**7**
	Uniaxial Drift Ratios (%)							
	0.35	**0.5**	**1.0**	**1.5**	**2.5**	**3**	**4**	**5**
Column to Footing (mm)	0.4	1	2	5	12	14	17	32
Segment to Segment (mm)	<0.4	<0.4	0.4	1	1.5	1.5	2	2.5

Similar to HDS1, there were some hairline cracks in the footing (Figure 3.54). The cracks were originating from the GDC and propagating towards the perimeter of the footing in a radial manner. The cracks remained less than 0.4 mm in width throughout testing.

(a) Testing start

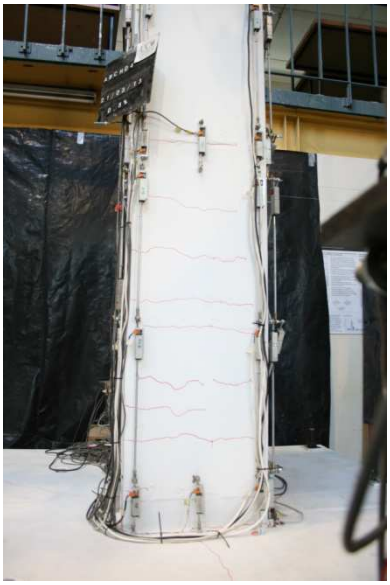

(b) End of 0.5% drift ratio

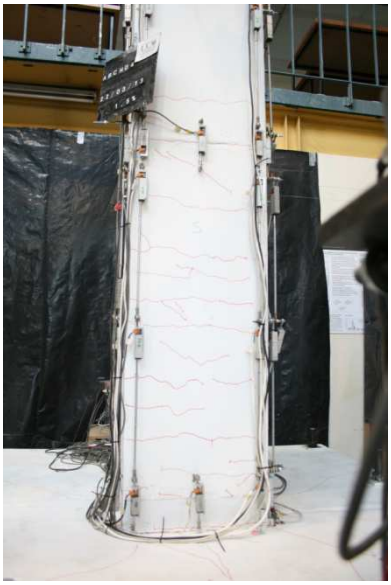

(c) End of 1.5% drift ratio

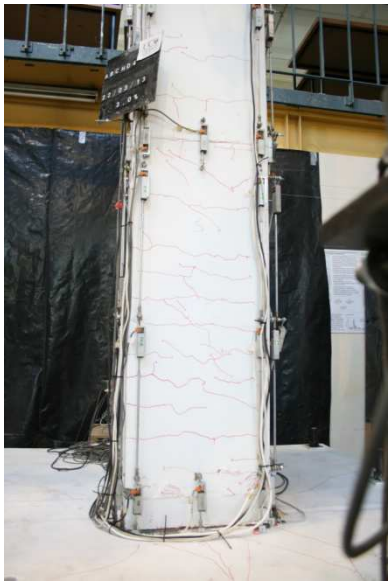

(d) End of 3.0% drift ratio

(e) End of 4.0% drift ratio

(f) End of 3.0% drift ratio

Figure 3.53. Damage progression in HDS2 during testing

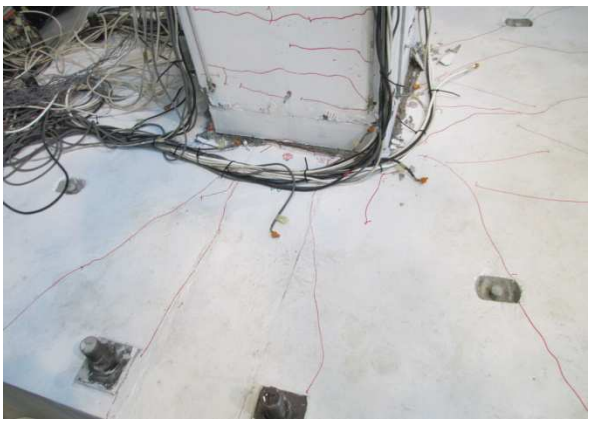

Figure 3.54. Radial hairline cracking to HDS2 footing block

The force-drift hysteresis plots for HDS2 are shown in Figure 3.55. The uniaxial response is shown in Figure 3.55a at each drift ratio. The biaxial response is shown in Figure 3.55b which presents the force-drift hysteresis during the clover stage of loading at each drift ratio. The resultant force (F_{rslt}) and displacement (Δ_{rslt}) of the column at the clover stage can be found using Equation 3.20 and Equation 3.21, respectively. Based on the clover quadrant, the resultant force and displacement hysteresis are plotted in their respective quadrants, as shown in Figure 3.55b.

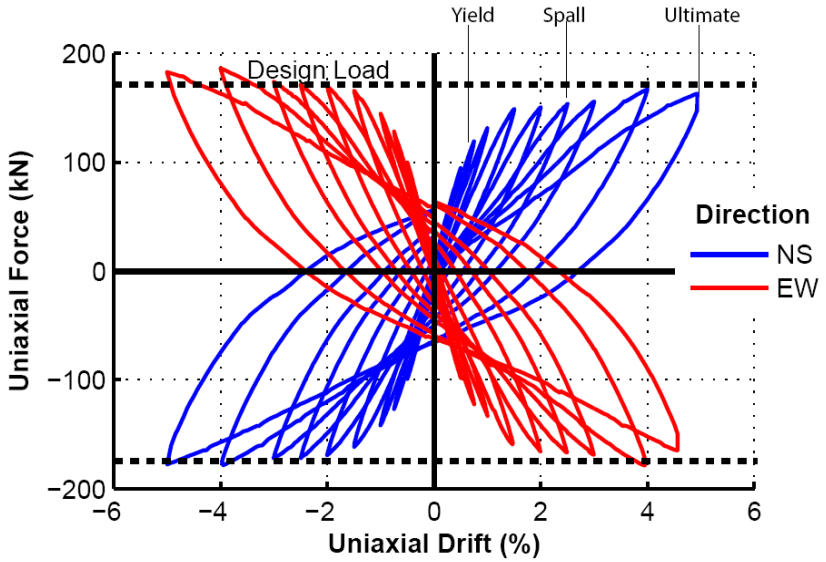

(a) Uniaxial force-drift hysteresis

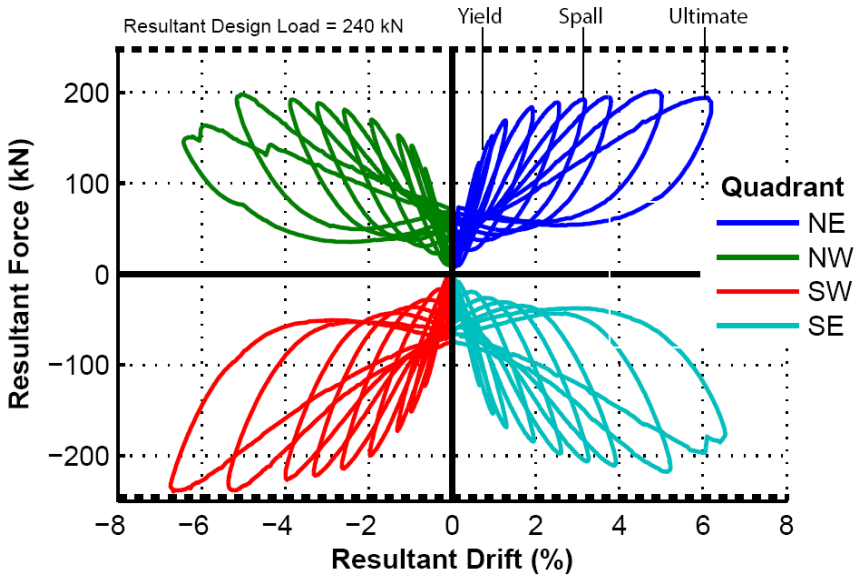

(b) Biaxial (resultant) force-drift hysteresis

Figure 3.55. HDS2 force-drift hysteresis plots

$$F_{rslt} = \sqrt{F_{NS}^2 + F_{EW}^2} \tag{3.20}$$

$$\Delta_{rslt} = \sqrt{\Delta_{NS}^2 + \Delta_{EW}^2} \tag{3.21}$$

From Figure 3.55b, it can be seen that HDS2 column attained a peak resultant lateral load of 240 kN in the third quadrant. Although the column was subjected to a much severe biaxial loading, however, the strength degradation in the column occurred only during the last cycle of 5% drift ratio (7% resultant drift ratio). The column base armoring was effective in limiting the strength degradation which can be caused by spalling of the concrete around the column base. The column force was approximatley 20% higher during the South-West (SW) clover stage when compared to the other three clovers. This was thought to be due to a slight asymmetry in the construction of the column.

The curvature distribution up the height of the column at peak of each drift ratio in the NS and EW directions are plotted in Figure 3.56a and 3.56b, respectively. Similar to HDS1, inelastic deformation of the starter bars occurred at both interfaces. Majority of the nonlinear deformation happened at the column to footing interface. This can be supported by the observed crack opening at different drift ratios, as presented in Table 3.8. As it can be observed from Figure 3.56a and Figure 3.56b, most of the nonlinear deformation happened at the bottom 200 mm height of the column which shows a good correlation between the observed damage and crack opening at the column bottom plastic hinge during testing.

Similar to HDS1, the spalling height in the corners of the column suggested a plastic hinge length of 250 mm (half the height of the column cross-section). The plastic hinge length was measured using a measuring tape following testing. Further research is needed on measuring the actual plastic hinge length for the types of connections tested in this research.

In Figure 3.56a and Figure 3.56b, it is also clear that as expected the column regions outside the plastic hinges remained essentially elastic.

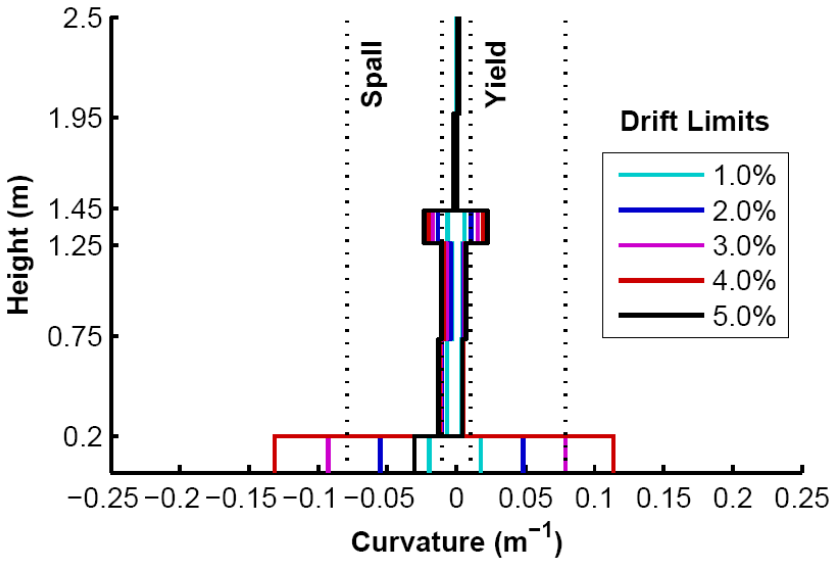

(a) Curvature distribution (NS)

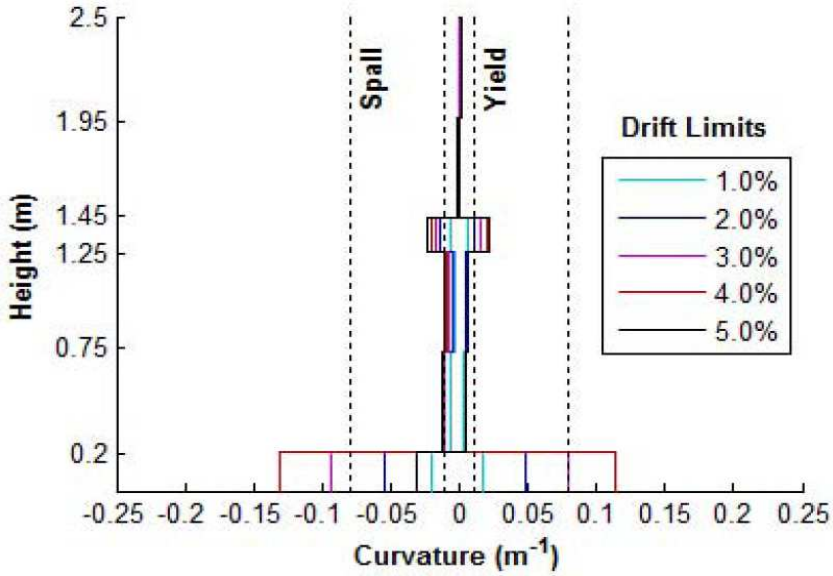

(b) Curvature distribution (EW)

Figure 3.56. HDS2 curvature distribution plots

Using the same procedure as that used for HDS1, the corrected area-based damping (hysteretic damping) was calculated. This was done by considering the uniaxial loading stage in the EW direction (Figure 3.55a) for each drift ratio. Results showed that HDS2 achieved a peak hysteretic damping of 13% at the failure point (Figure 3.57). This was lower compared to HDS1. This was due to an increased yield displacement in HDS2 (due to debonding of the starter bars) which in return decreased the displacement ductility for a given drift ratio. This reduced the hysteretic and elastic damping.

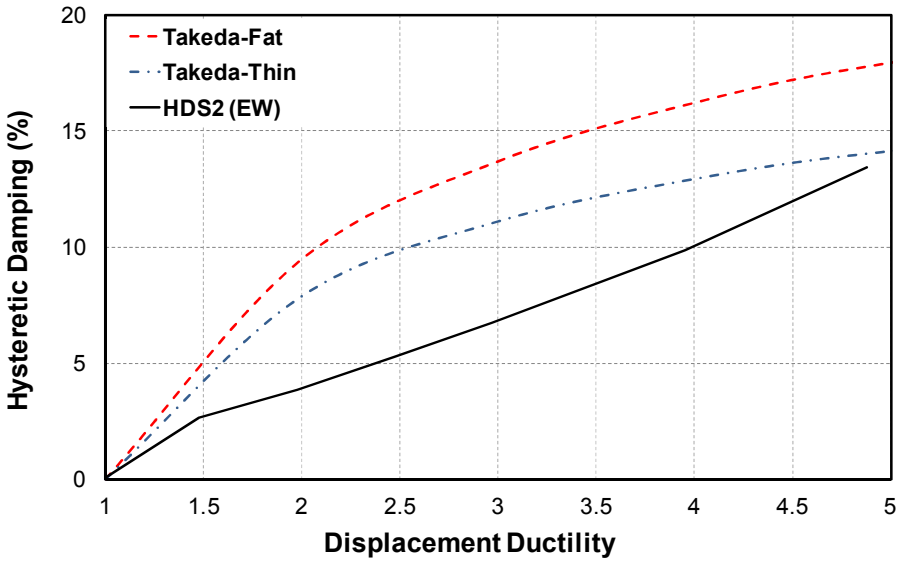

Figure 3.57. HDS2 corrected area-based hysteretic damping (ξ_{hyst}) in the EW direction

The performance evaluation procedure for the ADRS analysis was identical to that presented for HDS1 previously. As shown in Figure 3.58, a SLS event will produce 0.3% drift ratio which is lower than the column yielding point (Figure 3.55a). The ULS and MCE events will generate 2.2% and 3.8 drift ratios, respectively. Comparing these values and the corresponding limit states to those for HDS1, it can be observed that they are very close to each other. It should be noted that the increased initial stiffness of HDS2 (Figure 3.58) compared to that of HDS1 (Figure 3.49) is due to debonding of the starter bars and the column base armoring which resulted in less distributed cracking up the height of the column.

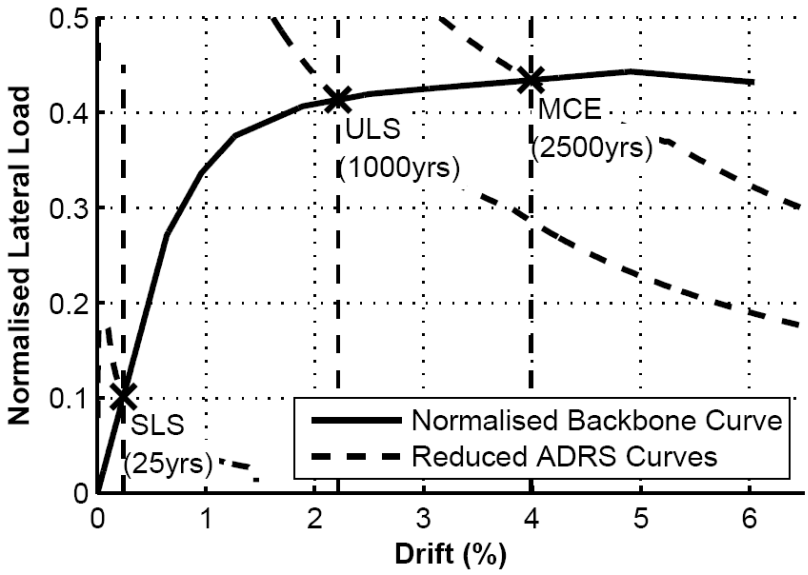

Figure 3.58. HDS2 ADRS plot

Figure 3.59 presents the dissipated energy plots for HDS2. In this plot, the energy dissipated during uniaxial (NS and EW directions) and biaxial (four clover stage) cycles of loading are shown separately for each drift ratio. As it can be seen, for the smaller drift ratios, there is a little difference in the quantity of energy dissipated during each drift loop. However, during higher drift ratios, the difference is more obvious with the SE and NW clovers showing considerable reduction in dissipated energy when compared against the cycles from the smaller drift ratios. This is an indication of strength degradation in the column during the higher drift ratios.

When comparing the cycles from all four clovers and uniaxial loadings, it is also obvious that the SW clover has a slightly higher level of energy dissipation. Although it can be expected that given the loading sequence, the SW clover loop should have less energy dissipation than the NE clover loop, but as explained earlier, the higher strength of the column was obvious during the SW clover loading, as shown in Figure 3.55b. This had caused the SW clover loop to have a slightly larger energy dissipation.

When comparing the cumulative dissipated energy for HDS2 to that of HDS1, it is almost exactly double. This can be expected as the equivalent uniaxial drift input was applied to both lateral rams during biaxial testing.

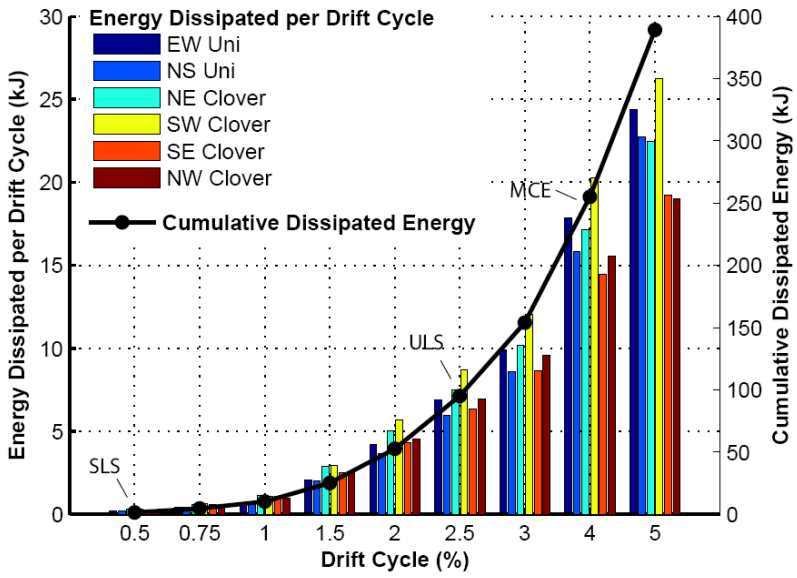

Figure 3.59. HDS2 dissipated energy (per cycle and cumulative)

3.2.7.3 HDC1

HDC1 was tested under uniaxial loading. At 0.25% drift ratio, minor flexural cracks initiated in the column. The cracking continued up the height of the column throughout testing. Majority of the cracks consisted of hairline cracking which were closed once the lateral force in the ram was released.

The cracking distribution was similar to that of HDS1. However, in HDC1 there was a wider distribution of big cracks at the base of the column. This indicated a larger plastic hinge length in the column (Figure 3.60a) where the nonlinear deformation was concentrated. The plastic hinge length was measured to be approximately equal to the diameter of the column section. According to NZS 3101 (NZS, 2006), similar plastic hinge length would be expected from a ductile monolithic column.

Spalling of the cover concrete at the base of the column started during the 3% drift ratio (ULS performance level), as shown in Figure 3.60a. There was also 2 mm gap opening at the segment to segment interface during 3% drift ratio. However, there was no signs of spalling at this location (Figure 3.60b) and the gap opening remained under 2.5 mm until the end of testing (6% drift ratio). Few hairline diagonal cracks were observed near the column to footing and segment to segment connections.

The spalling continued further with increasing applied drift ratios. The lateral actuator hit the stroke limit in pulling during the 6% drift ratio. At this stage, a displacement of 130 mm (5.2% drift ratio) could be achieved in pulling in the South direction, but a displacement of 150 mm (6%) in pushing in the North direction.

Some column longitudinal bar buckling was observed during the larger drift ratios (Figure 3.61b). First bar rupture occurred during the second cycle of the peak displacement at 6% drift ratio (Figure 3.61b). This corresponded to MCE performance level. Since the bar rupture occurred during the second cycle, it was obvious that the low-cycle fatigue was the main cause behind the bar failure. The bar buckling may have also contributed to the fracture.

At the end of testing, the spalling height at the base of column was measured to be 500 mm from the top of the footing (Figure 3.61a). The spalling occurred mainly on the

northern and southern sides of the column, as shown in Figure 3.61c and Figure 3.61d, respectively.

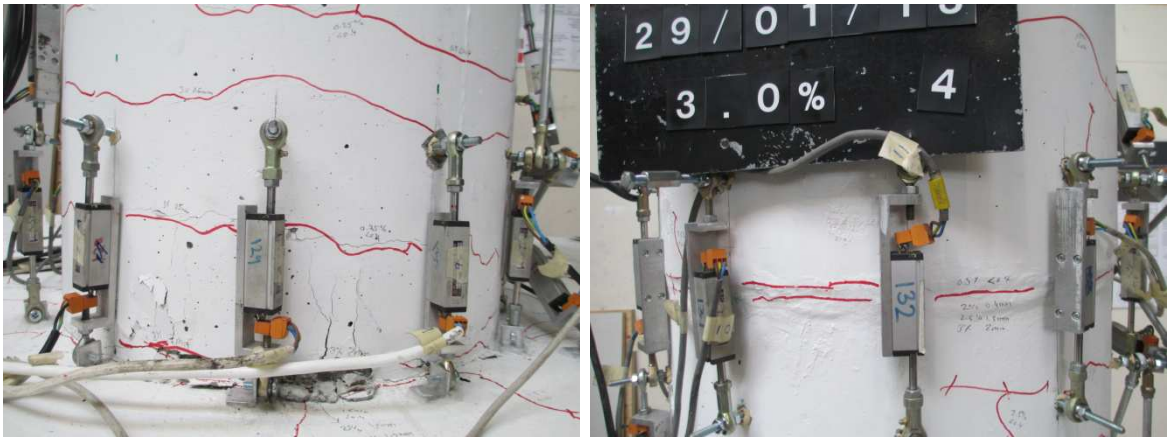

(a) Spalling at the column to footing MSC **(b) 2 mm gap opening at the segment to segment**

Figure 3.60. HDC1 at 3% drift ratio

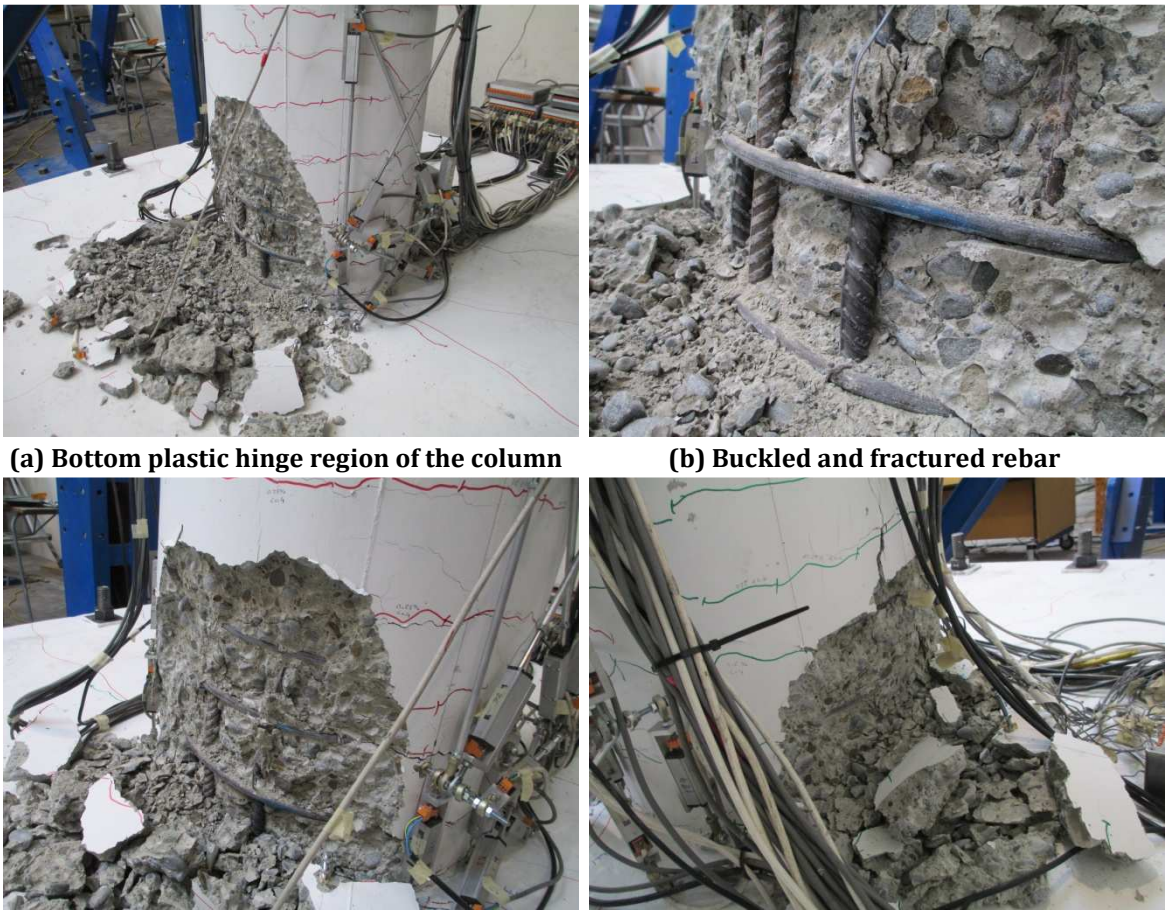

(a) Bottom plastic hinge region of the column **(b) Buckled and fractured rebar**

(c) Southern face spalling **(d) Northern face spalling**

Figure 3.61. HDC1 column to footing connection at the end of testing (5% drift ratio)

Table 3.9 presents crack sizes for each interface connection at different drift ratios during testing. Figure 3.62 presents photos from the damage progression to HDC1 at different drift ratios during testing. The photos were taken at the end of each drift ratio.

Table 3.9. Summary of the maximum crack widths measured during HDC1 testing

	Drift Ratios (%)							
	0.35	**0.5**	**1.0**	**1.5**	**2.5**	**3**	**4**	**5**
Column to Footing (mm)	<0.4	0.4	0.6	1	1.5	Spall	Spall	Spall
Segment to Segment (mm)	<0.4	<0.4	0.4	0.4	1.5	2	2.5	2.5

(a) Testing start **(b) End of 0.5% drift ratio** **(c) End of 1.5% drift ratio**

(d) End of 4.0% drift ratio **(e) End of 5.0% drift ratio** **(f) End of 6.0% drift ratio**

Figure 3.62. Damage progression in HDC1 during testing

There were also some hairline cracks in the footing (Figure 3.63). The cracks were originating from the MSC and propagating towards the perimeter of the footing in a radial manner. The cracks remained of less than 0.4 mm width throughout testing.

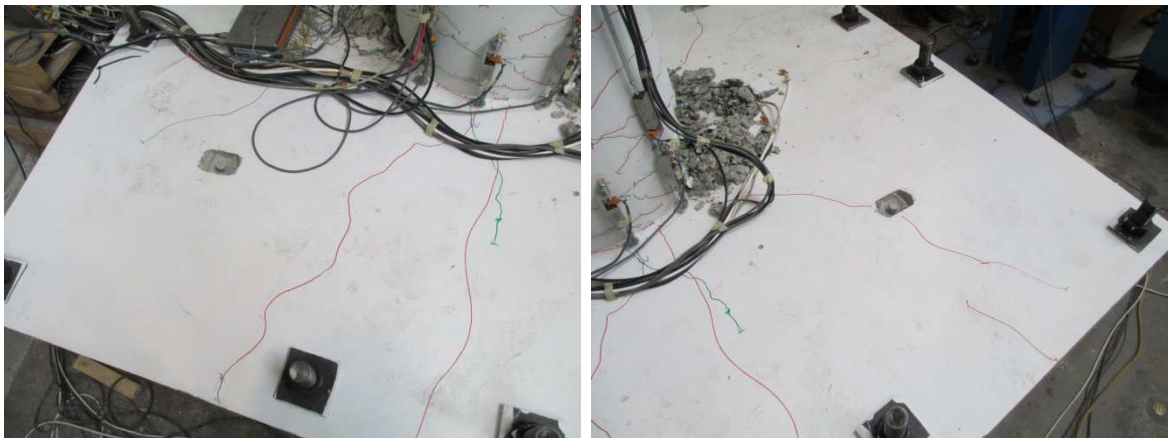

Figure 3.63. Radial hairline cracking to HDC1 footing block

The force-drift hysteresis for HDC1 is shown in Figure 3.64. The column peak lateral load was 150 kN. Since similar longitudinal reinforcing detail (16-YD16) was used for all cantilever columns in this study, the columns with circular sections would have had a lower moment capacity compared to those with square sections. The design lateral load of 170 kN from Table 3.2 can be reduced by a factor to calculate the design lateral load for columns with circular sections. This factor can be calculated from the ratio between the moment capacity of the column with circular section (375 kNm, refer to Figure 6.8a in Chapter 6) and the column with square section (439 kNm, refer to Figure 6.5a in Chapter 6). Using this methodology, the reduction factor was calculated to be 0.854. The reduced design lateral load for columns with circular sections is therefore 145 kN.

As shown in Figure 3.64, the post-yield stiffness of the column is significantly lower than that of HDS1. This indicated that the unbonded post-tensioned Macalloy bar performed as intended for simulating axial load on the column.

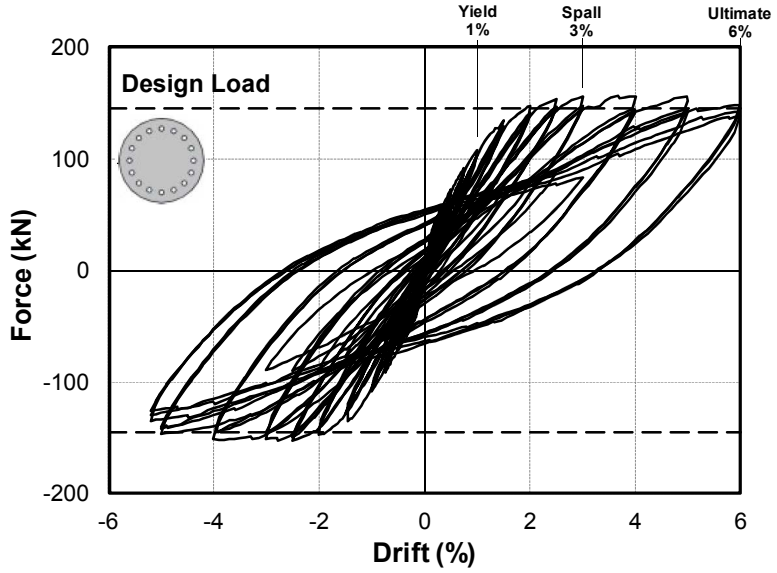

Figure 3.64. HDC1 force-drift hysteresis

From Figure 3.64, it can be observed that the column yield drift was 1%. Given the spalling initiation (ULS performance limit) at 3%, the displacement ductility at ULS was 3. At the column failure point (rupturing of the rebars at 6%), the displacement ductility was 6. As can be seen from the load-drift hysteresis, there was large residual displacement in the column after the column yielded. The residual displacement of the column was more than 50% of the peak drift ratio during 5% and 6% drift ratio cycles. The moment-curvature plot for HDC1 is shown in Figure 3.65.

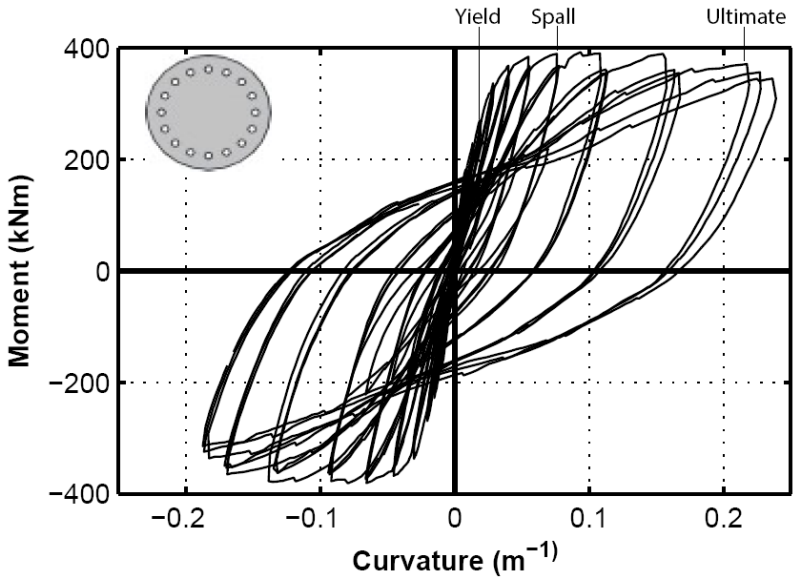

Figure 3.65. HDC1 moment-curvature hysteresis

The curvature distribution up the height of the column at peak of each drift ratio is plotted in Figure 3.66. Similar to HDS1, the curvature level was increasing at the column to footing and segment to segment connections with further applied drift ratios.

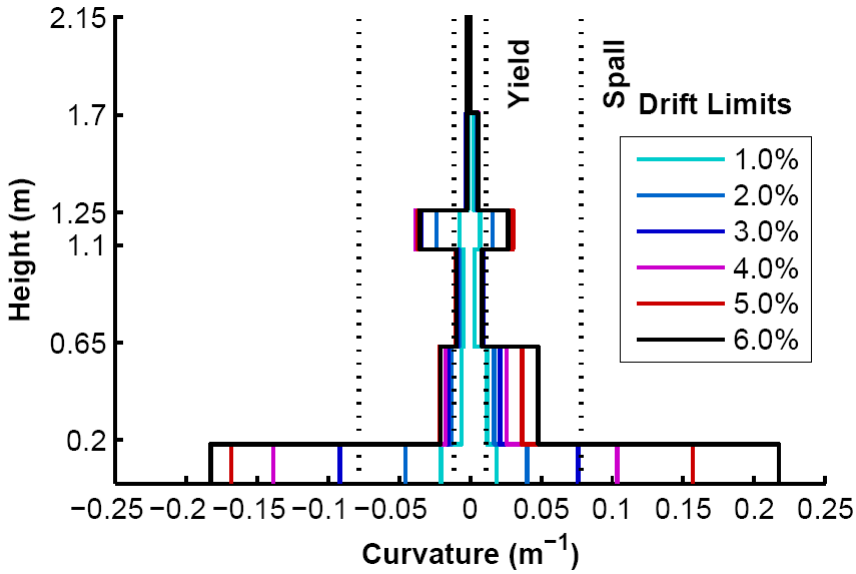

Figure 3.66. HDC1 curvature distribution (NS direction)

The second array of pots from the base of the column was located between heights of 200 mm to 650 mm from the top of footing. The pots showed higher values of curvature than those observed in HDS1 and HDS2. This indicated that the plastic hinge zone at the column to footing connection had extended further up the height of the column (Figure 3.66). This was also in agreement with the observed plastic hinge length of 500 mm during testing.

The corrected area-based damping (hysteretic damping) plots for HDC1, is shown in Figure 3.67. Similar to HDS1 and HDS2, there was a relatively linear relationship between the hysteretic damping and the displacement ductility. The column achieved a hysteretic damping of 17% at the failure point. This was similar to that of HDS1. According to Figure 3.67, the experimental hysteretic damping curve for HDC1 was lower than a theoretical Takeda-Thin up to a displacement ductility of just under 5.5. Following that, the curve located between the Takeda-Thin and Takeda-Fat curves (Figure 3.67).

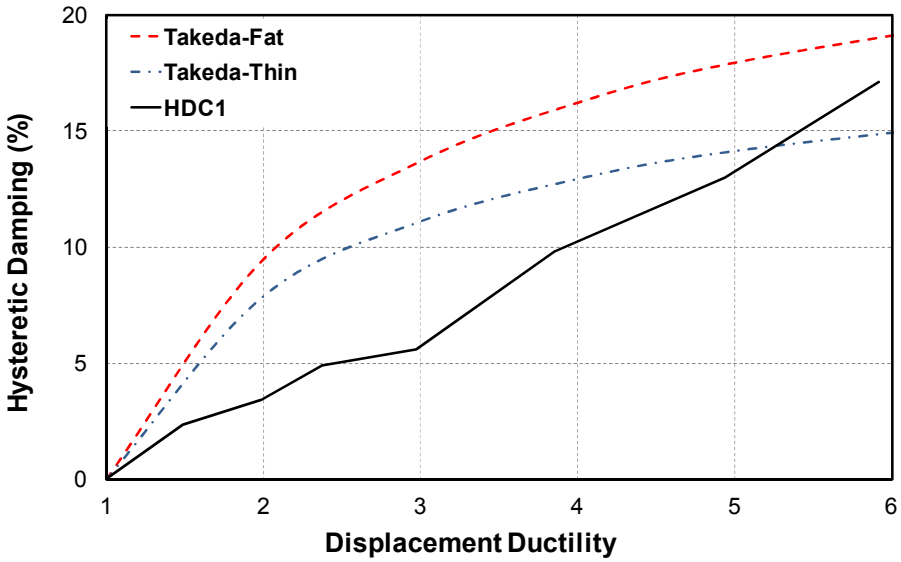

Figure 3.67. HDC1 corrected area-based hysteretic damping (ξ_{hyst})

The ADRS plot for HDC1 is presented in Figure 3.68. The observed lower post-yield stiffness in the column, resulted into higher levels of drift ratios for the ULS and MCE level earthquakes. According to Figure 3.68, a ULS earthquake will generate just under 3% drift ratio. This is almost exactly the drift ratio that was adopted during the force-based design of the prototype structure. This means that good assumptions were made during the design process of the column. From Figure 3.68, a MCE event will generate 4.8% drift ratio in the structure which is almost 1.6 times greater than ULS drift level.

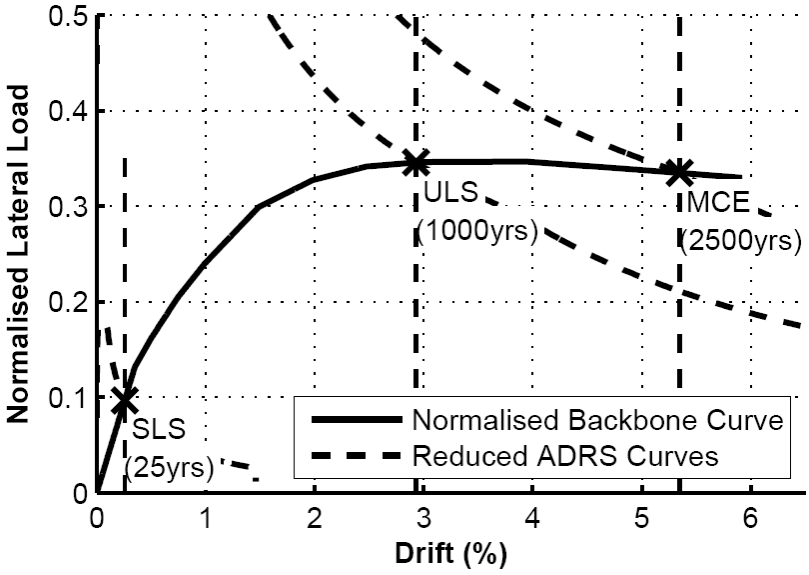

Figure 3.68. HDC1 ADRS plot

The energy dissipated per each cycle of each drift ratio for HDC1 is presented in Figure 3.69. By comparing the cumulative dissipated energy for HDC1 at 5% drift ratio to that of HDS1, the column had less amount of energy dissipated. However, since HDC1 reached an ultimate drift ratio of 6% before failure, in contrast to HDS1 which achieved 5% only, it can be stated that the column had more energy dissipation in total to that of overall HDS1.

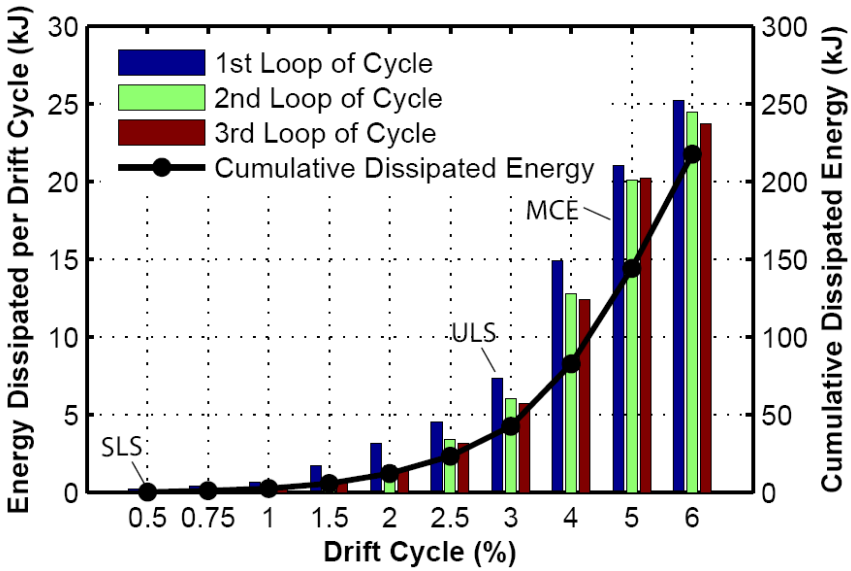

Figure 3.69. HDC1 dissipated energy (per cycle and cumulative)

3.2.7.4 HDC2

HDC2 was tested under biaxial loading. At 0.2% drift ratio, minor flexural cracks initiated in the column. The cracking distribution was similar to that of HDC1, with increased drift ratios, more cracks appeared up the full height of the column throughout testing. Majority of the cracks consisted of hairline cracking which were closed once the lateral force in the rams was removed.

Spalling of the cover concrete at the base of the column started during the 2.5% drift ratio (3.25% resultant drift ratio, ULS performance level), as shown in Figure 3.70a. There was also 2 mm gap opening at the segment to segment interface during 2.5% drift ratio. However, there was no signs of spalling at this location (Figure 3.70b) and the gap opening remained under 3 mm until the end of testing (5% drift ratio). Few hairline diagonal cracks were observed in the vicinity of column to footing and segment to segment connections.

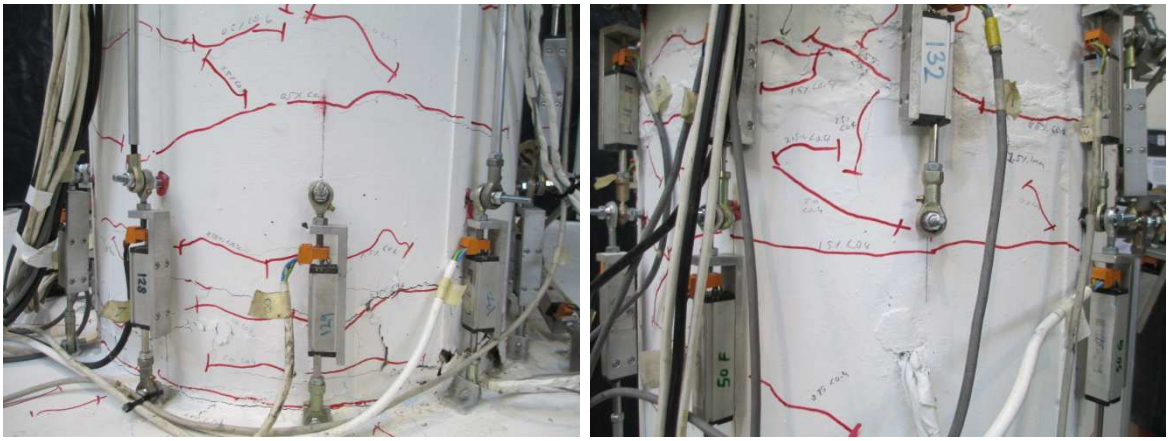

(a) Spalling at the column to footing MSC **(b) 2 mm gap opening at the segment to segment**

Figure 3.70. HDC2 at 2.5% drift ratio (3.25% resultant drift ratio)

The concrete spalling was significant during the 3% drift ratio (4.2% resultant drift ratio). The spalling continued further with the increasing applied drift ratios. The lateral actuator in the East-West direction hit the stroke limit during the 5% drift ratio. At this stage, a full 6% actuator excursion could not be achieved. Some considerable column longitudinal bar buckling was observed during the larger drift ratios (5% and 6%), as shown in Figure 3.71c. First bar rupture occurred during the 6% drift ratio when the column entered the clover loading stage (Figure 3.71d). This corresponded to MCE performance level.

At the end of testing, the spalling height at the base of column was measured to be 500 mm from the top of the footing. Due to severe biaxial loading, the spalling in HDC2 was more extensive compared to that observed in HDC1. The spalling occurred all around the base of the column, as shown Figure 3.71a and Figure 3.71b.

(a) Bottom plastic hinge region of the column

(b) Extent of spalling around the column

(c) Buckled rebars

(d) Ruptured rebar

Figure 3.71. HDC2 column to footing connection at the end of testing (6% drift ratio)

Table 3.10 presents crack sizes for each interface connection during testing.

Table 3.10. Summary of the maximum crack widths measured during HDC2 testing

	Resultant Drift Ratios (%)							
	0.5	**0.7**	**1.4**	**2.1**	**3.5**	**4.2**	**5.7**	**7**
	Uniaxial Drift Ratios (%)							
	0.35	**0.5**	**1.0**	**1.5**	**2.5**	**3**	**4**	**5**
Column to Footing (mm)	<0.4	0.4	1	1.5	2.5	Spall	Spall	Spall
Segment to Segment (mm)	<0.4	<0.4	0.4	1	2	2.5	3	3

Figure 3.72 presents photos from the progression of damage to HDC2 during testing. There were some hairline cracks in the footing similar to that of HDC1.

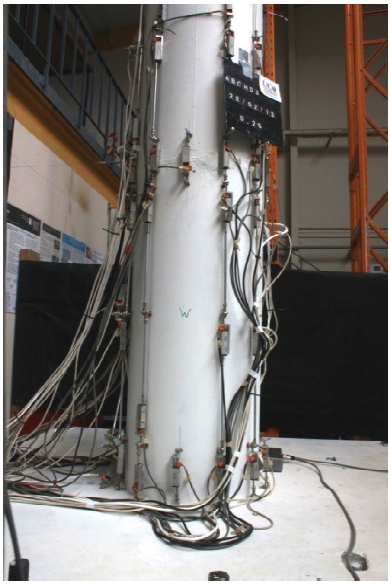

(a) Testing start

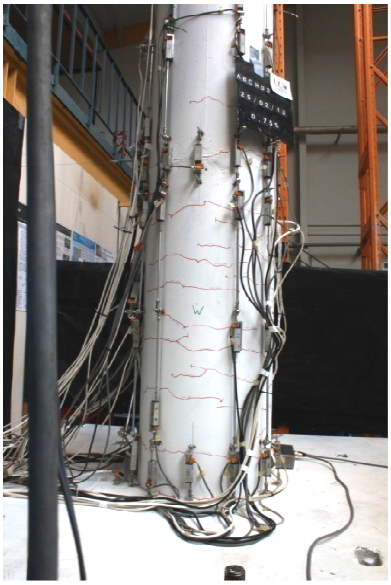

(b) End of 0.75% drift ratio

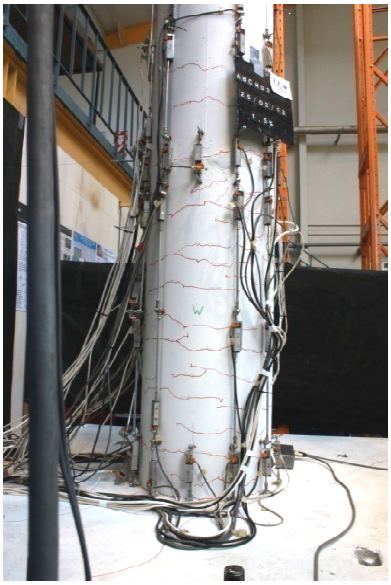

(c) End of 1.5% drift ratio

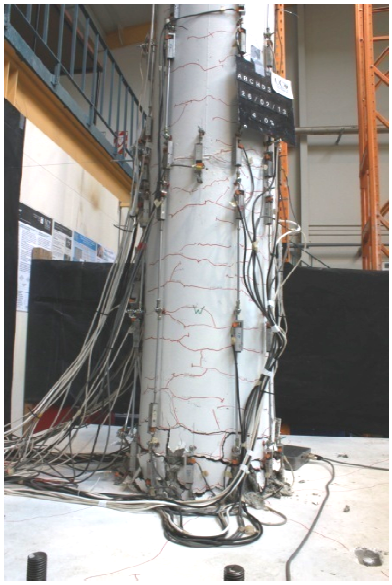

(d) End of 4.0% drift ratio

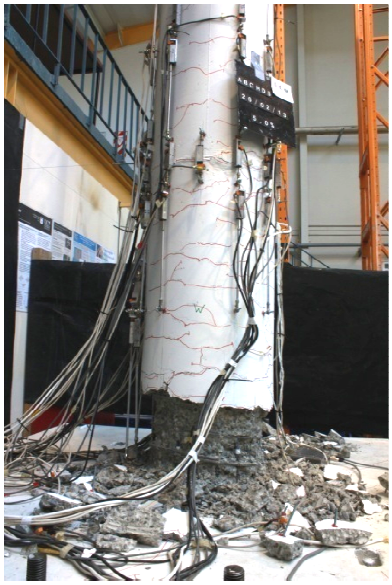

(e) End of 5.0% drift ratio

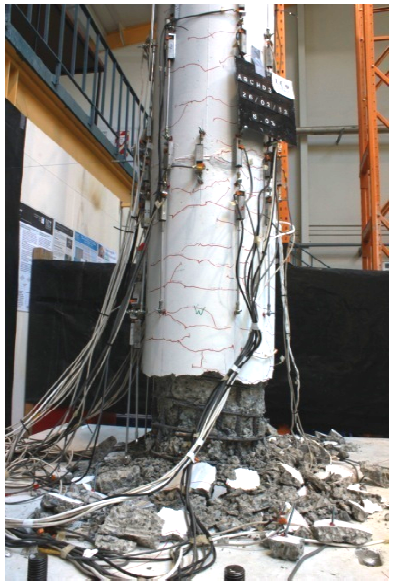

(f) End of 6.0% drift ratio

Figure 3.72. Damage progression in HDC2 during testing

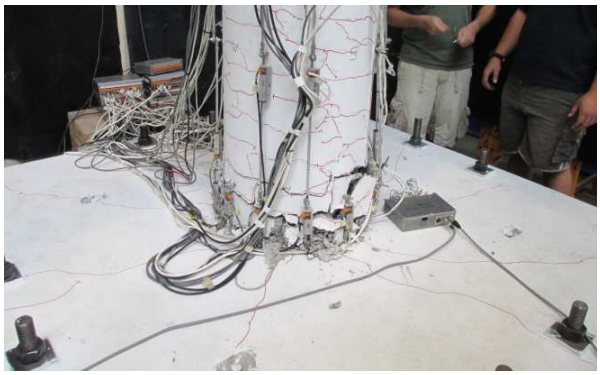

Figure 3.73. Radial hairline cracking to HDC2 footing block

The uniaxial and biaxial force-drift hysteresis plots for HDC2 are shown in Figure 3.74a and Figure 3.74b, respectively. The peak lateral load of the column was 155 kN which is slightly higher than the design lateral load of 145 kN. The strength degradation in the column started during 3% drift ratio compared to 5% drift ratio in HDC1. Due to severe and more demanding biaxial loading, the column had greater spalling around the base which contributed to more strength degradation in HDC2.

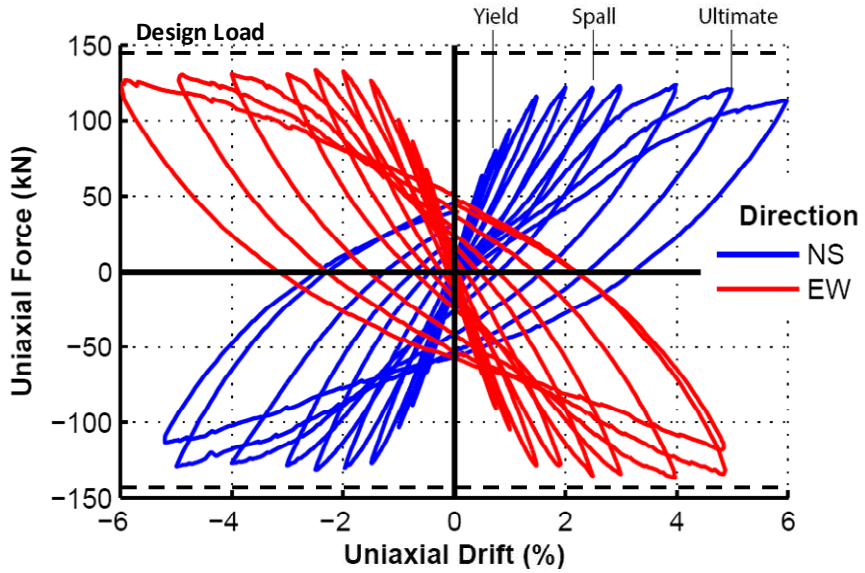

(a) Uniaxial force-drift hysteresis

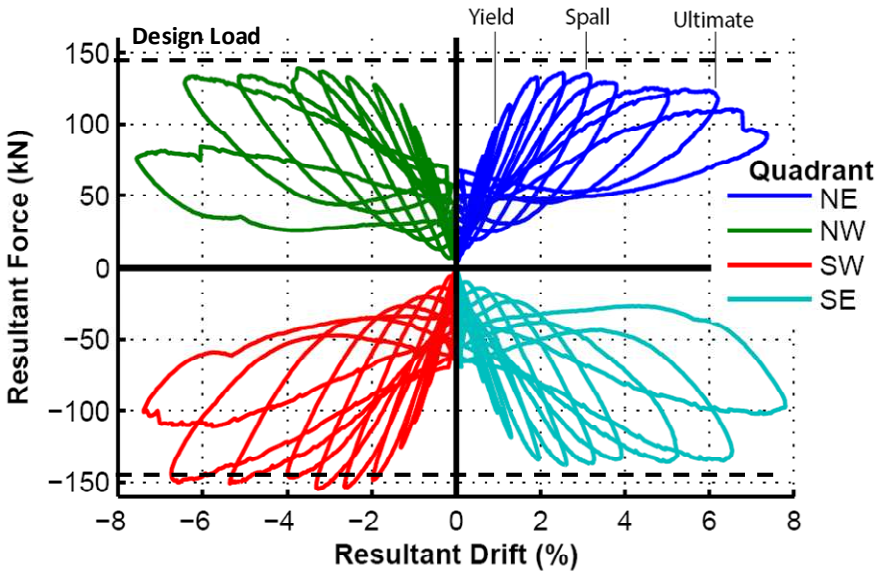

(b) Biaxial (resultant) force-drift hysteresis

Figure 3.74. HDC2 force-drift hysteresis plots

The curvature distribution up the height of the column at peak of each drift ratio in the NS and EW directions are plotted in Figure 3.75a and 3.75b, respectively. Similar to HDC1, inelastic deformation of the starter bars occurred at both interfaces. Majority of the nonlinear deformation happened at the column to footing interface. This can be supported by the observed crack opening and spalling at different drift ratios, as presented in Table 3.10.

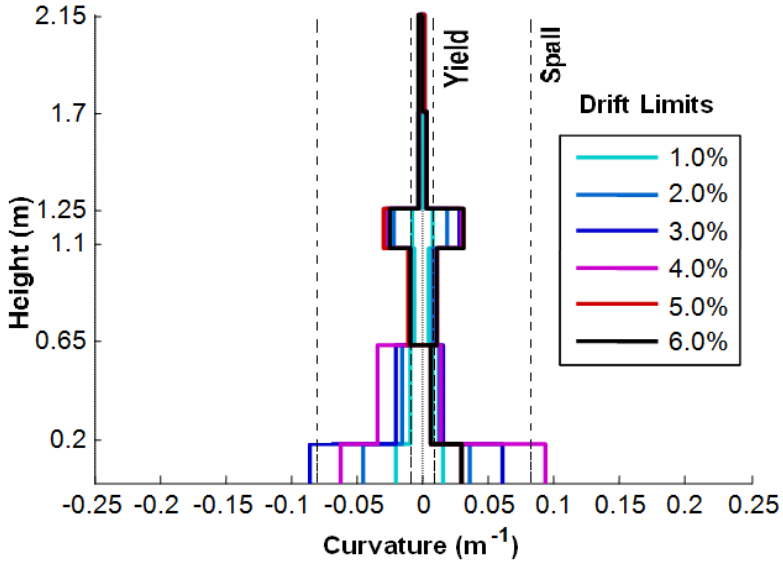

(a) Curvature distribution (NS)

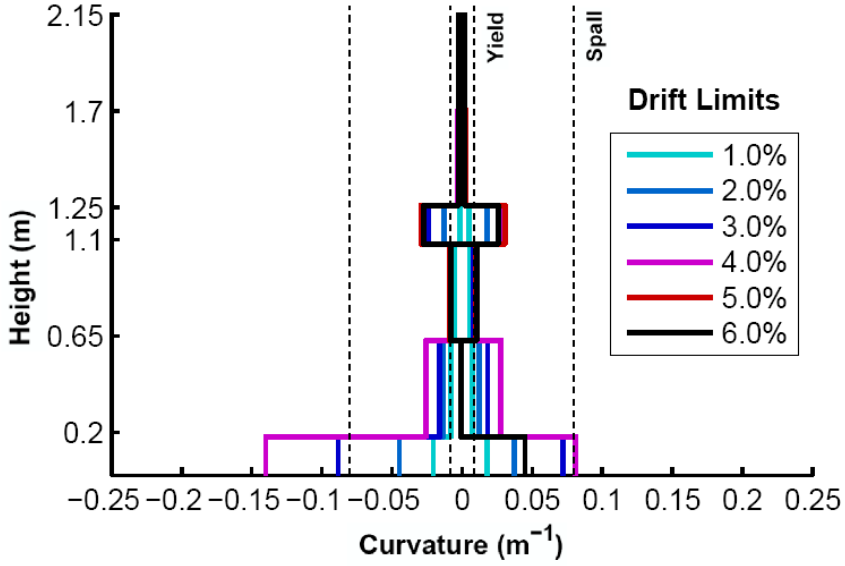

(b) Curvature distribution (EW)

Figure 3.75. HDC2 curvature distribution plots

As it can be observed from Figure 3.75a and Figure 3.75b, similar to HDC1, the plastic hinge zone at the column to footing connection had extended further up the height of the column. This was also in agreement with the observed plastic hinge length of 500 mm during testing. The asymmetry at the bottom plastic hinge in Figure 3.75a could have been due to some asymmetry in the construction of the column and its strength under bi-directional loading (Figure 3.74b).

Using the same procedure as that used for HDS2, the biaxial corrected area-based damping (hysteretic damping) was calculated for HDC2, as shown in Figure 3.76. Despite higher strength degradation under biaxial testing compared to other previously tested column, HDC2 showed a good level of energy dissipation capacity. The column reached an ultimate hysteretic damping of 17%. This is similar to that of HDC1 which was tested under uniaxial loading. It is important to note that in Figure 3.76, the damping values were calculated based on the uniaxial hysteresis loops. Given the less strength degradation of the column under uniaxial loading compared to the degradation under biaxial loading loops, this had resulted into larger damping values.

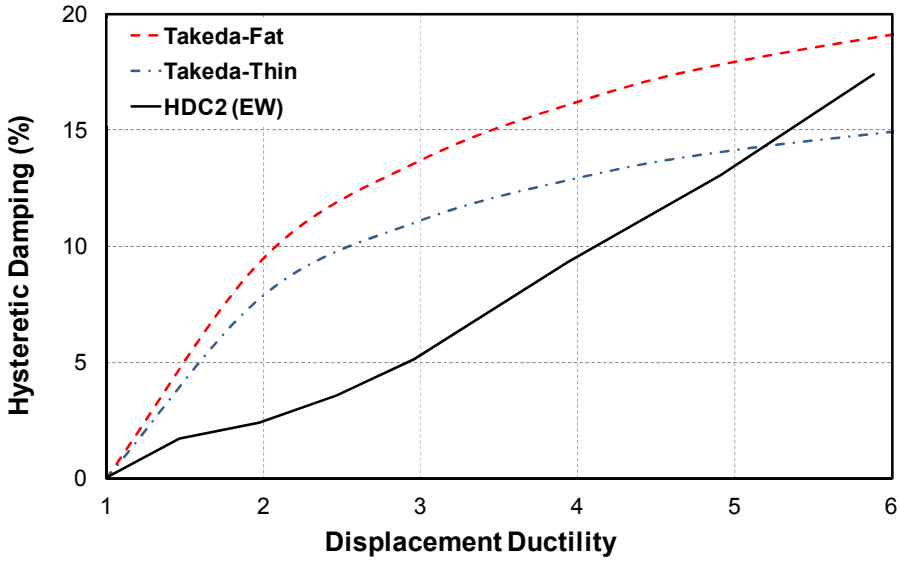

Figure 3.76. HDC2 corrected area-based hysteretic damping (ξ_{hyst}) in the EW direction

According to ADRS plot in Figure 3.77, a SLS event will produce just under 0.5% drift ratio in the structure which is lower than column yielding point (Figure 3.74). A ULS and MCE event will generate 2.8% and 5.7% drift ratios, respectively. Comparing these values with their corresponding limit states to those of HDC1 (uniaxial testing), it can be

noted that a MCE event generates higher drift in HDC2 compared to that of HDC1 (4.8%). This was due to higher strength degradation in HDC2 under biaxial loading.

Figure 3.78 presents the dissipated energy for HDC2. The higher level of strength degradation in the column can also be seen from the reduction in the dissipated energy during higher drift ratios. When comparing the cumulative dissipated energy for HDC2 (375 kJ) to that of HDC1 (225 kJ), it is approximately 1.6 times greater. In testing of HDS2, the dissipated energy was 2 times greater than that for HDS1. Since there was no confinement armoring in HDC2, there was more strength degradation in the column compared to that in HDS2.

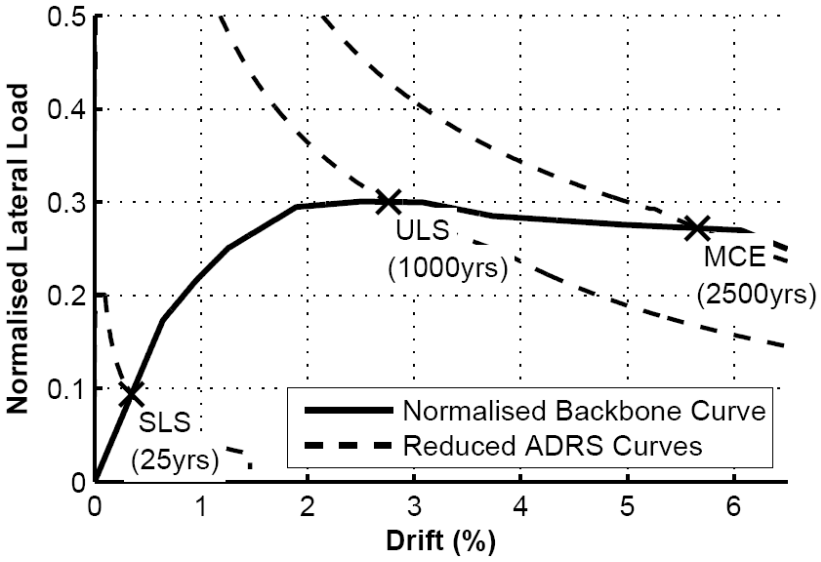

Figure 3.77. HDC2 ADRS plot

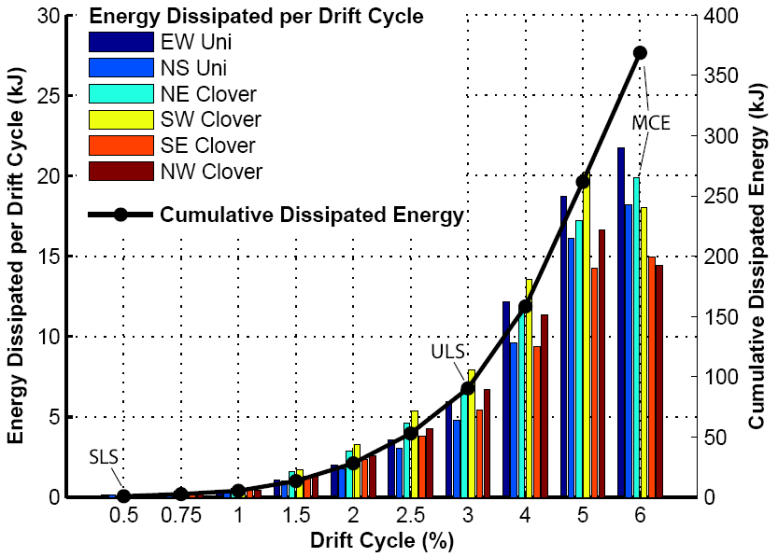

Figure 3.78. HDC2 dissipated energy (per cycle and cumulative)

3.2.7.5 Punching Shear Tests (HDC1 and HDC2)

After finishing testing on HDC1 and HDC2 specimens, it was decided to ensure the gravity load carrying capacity of the grouted interface of the member socket connection. As previously shown in Figure 3.18a of Section 3.2.5.1, under gravity loads an inadequate strength of the grout in MSC may lead to a situation where the column is sliding inside the socket and puncturing the soil underneath. In order to ensure the sufficient residual capacity of the grouting interface following a severe cyclic loading, punching shear (pull through) tests were carried out on the footing blocks of HDC1 and HDC2 to ensure that sufficient resistance is left in the connection for gravity loads.

The punching shear testing procedure was identical for both specimens. The HDC1 column was cut off from the top of the footing. Figure 3.79c illustrates arrangement for the punching shear testing.

(a) Hold-down bolts and I beams

(b) Hydraulic jack under the column stub

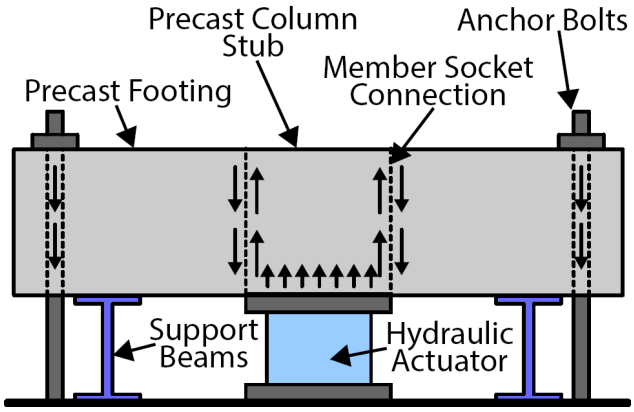

(c) Punching shear testing arrangement

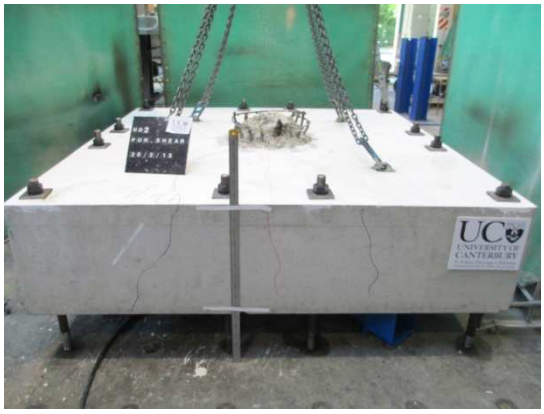

(d) Footing under punching shear testing

Figure 3.79. Punching shear testing setup of MSC

For punching shear test, twelve hold-down bolts were wound in the floor holes (Figure 3.79a). The footing was lowered on the hold-down bolts and placed on several blocks made of steel I-beams. The bolts were tightened which restrained the footing from any vertical or horizontal movement. A hydraulic cylinder with a capacity of 2567 kN was placed underneath the column stub (Figure 3.79b). The cylinder started pushing the column stub upwards. The vertical movement of the column stub was being measured by using a laser line and an attached ruler on one of the four sides of the footing (Figure 3.79d). At the same time, high resolution photos were being taken throughout testing.

There was considerable radial cracks in the footing which were originating from near the socket and propagating away towards the perimeter of the footing (Figure 3.80a and Figure 3.80b). Existing radial cracking around the socket reached 0.4 mm in size.

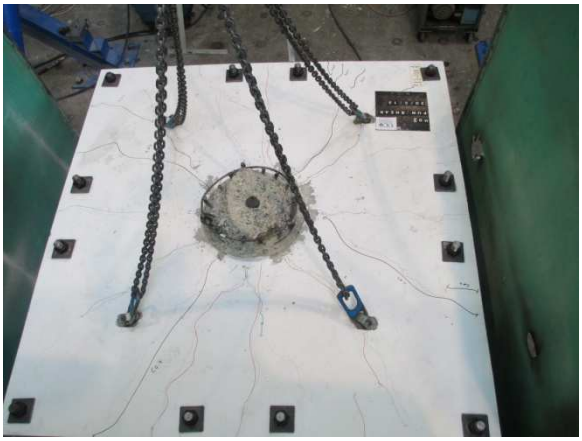

(a) Radial cracking of the footing

(b) Cracks originating around the socket

(c) No sliding of the column stub

(d) Bottom face of the column stub

Figure 3.80. Punching shear testing of MSC

During testing, the bending of the 500 mm thick footing block was visible from all four sides. After reaching a force level of 1350 kN which corresponded to 3 times of the

column design gravity load (450 kN, refer to Table 3.2), the testing was stopped. This was due to limits on the capacity of the floor holes and hold-down bolts. There was no apparent signs of slipping of the column stub out of the socket up to this point, as can be seen in Figure 3.80c.

Similar testing was carried out on the footing block of HDC2. The results were identical. It was concluded that sufficient resistance of the grouted interface will remain in the socket, even after severe biaxial cyclic loading of the column to its failure point. This means that there was not any substantial grout degradation in the MSC due to cyclic loading of the column to the failure point.

3.2.7.6 Comparison of Results: Grouted Duct vs. Member Socket

Figure 3.81 and Figure 3.82 present experimental plots for the Grouted Duct Connection (GDC) and Member Socket Connection (MSC) under uniaxial testing.

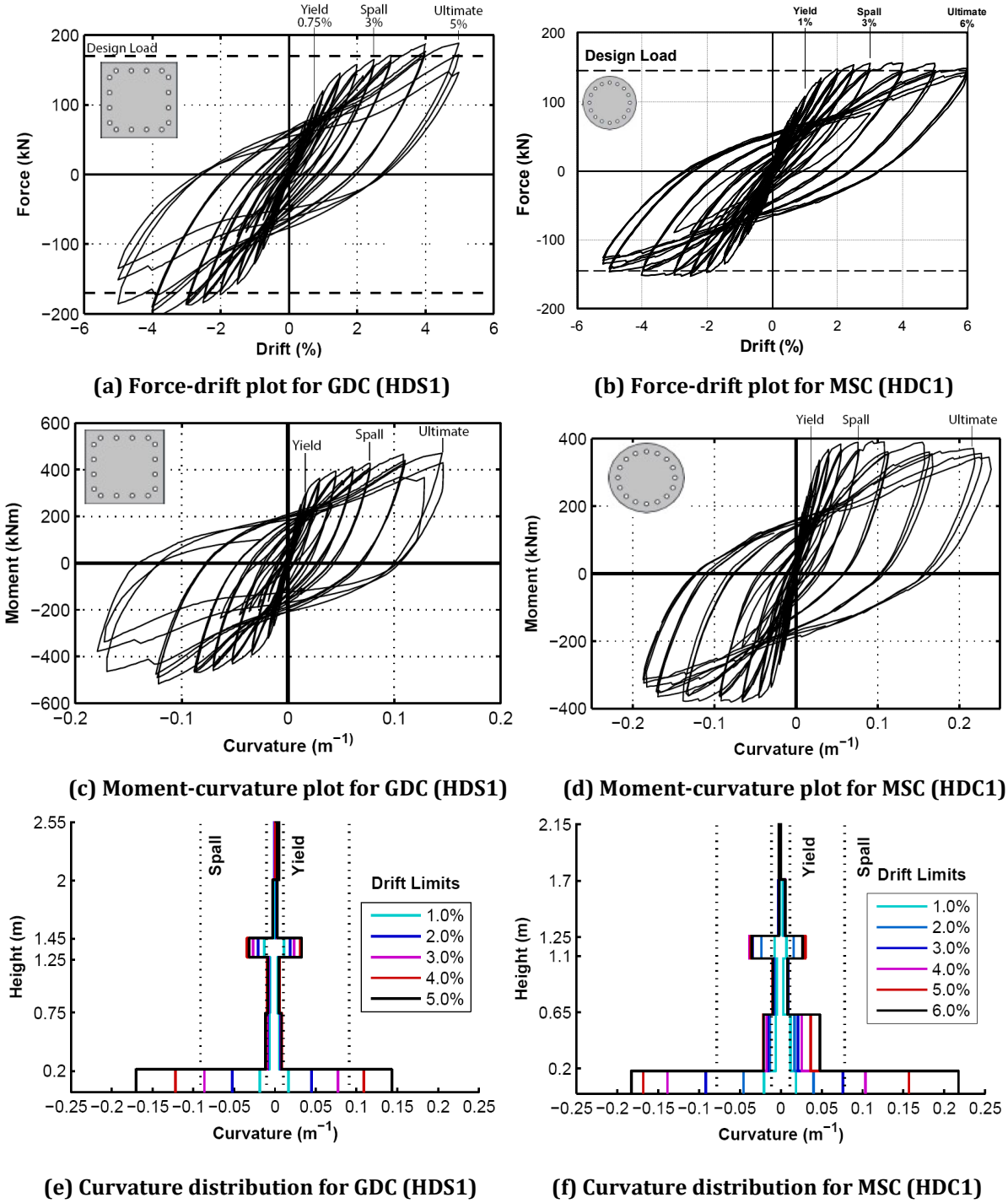

(a) Force-drift plot for GDC (HDS1) **(b) Force-drift plot for MSC (HDC1)**

(c) Moment-curvature plot for GDC (HDS1) **(d) Moment-curvature plot for MSC (HDC1)**

(e) Curvature distribution for GDC (HDS1) **(f) Curvature distribution for MSC (HDC1)**

Figure 3.81. Comparison of experimental plots for GDC and MSC under uniaxial testing

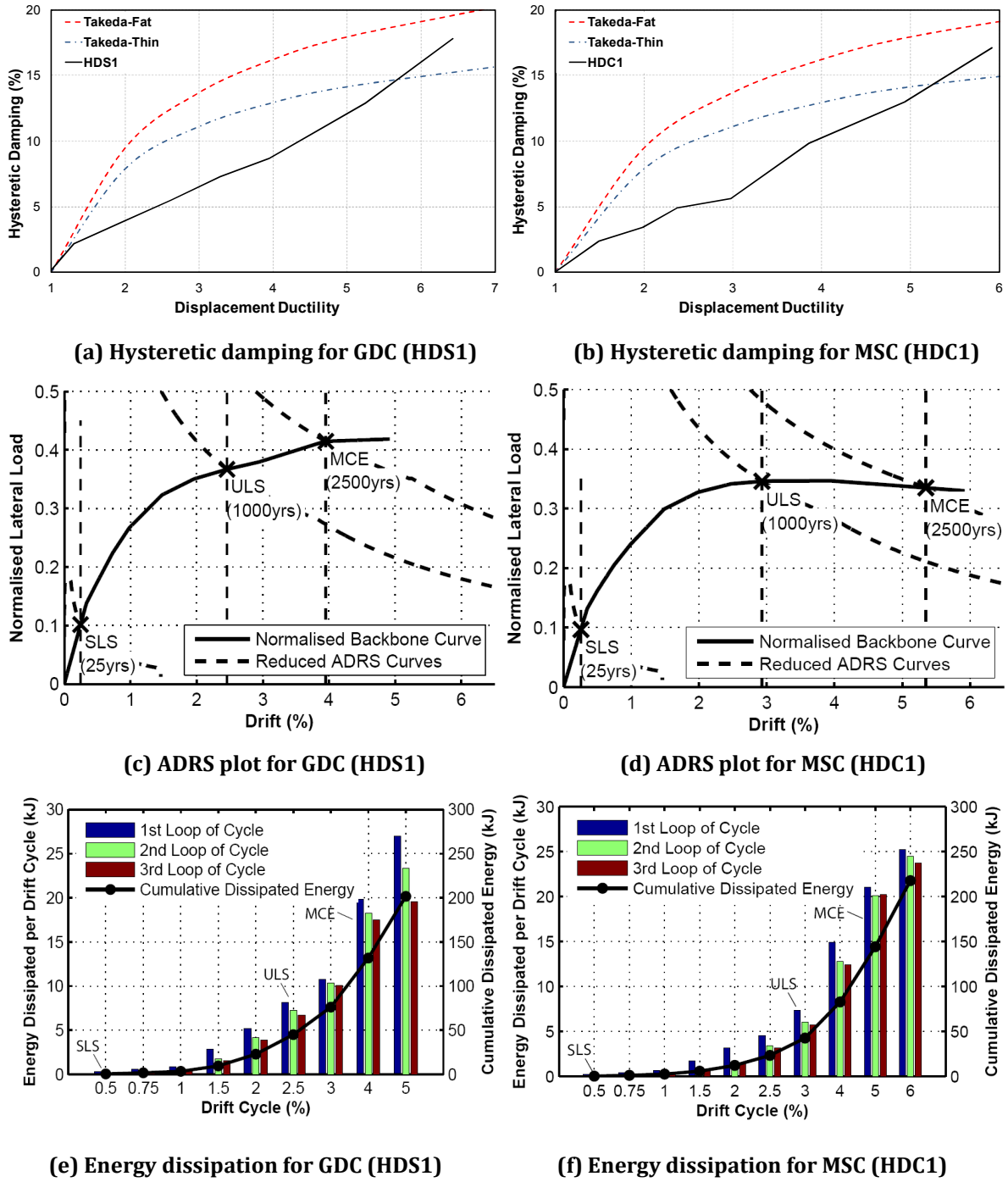

(a) Hysteretic damping for GDC (HDS1) **(b) Hysteretic damping for MSC (HDC1)**

(c) ADRS plot for GDC (HDS1) **(d) ADRS plot for MSC (HDC1)**

(e) Energy dissipation for GDC (HDS1) **(f) Energy dissipation for MSC (HDC1)**

Figure 3.82. Comparison of experimental plots for GDC and MSC under uniaxial testing

Figure 3.83 and Figure 3.84 present experimental plots for GDC and MSC under biaxial testing.

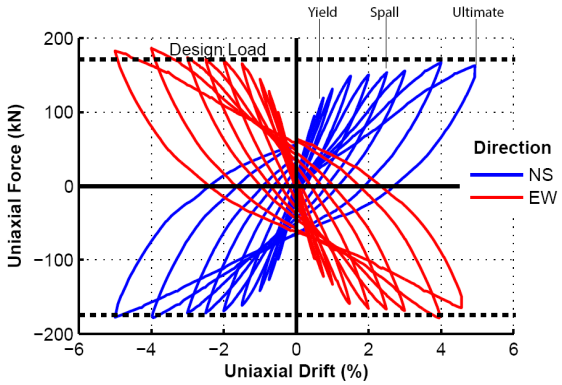

(a) Force-drift plot for GDC (HDS2, uniaxial)

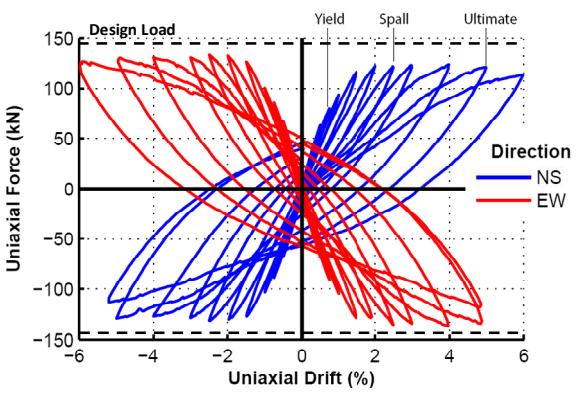

(b) Force-drift plot for MSC (HDC2, uniaxial)

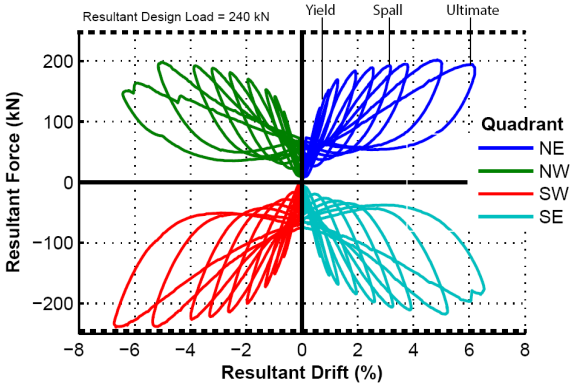

(c) Moment-curvature for GDC (HDS2, resultant)

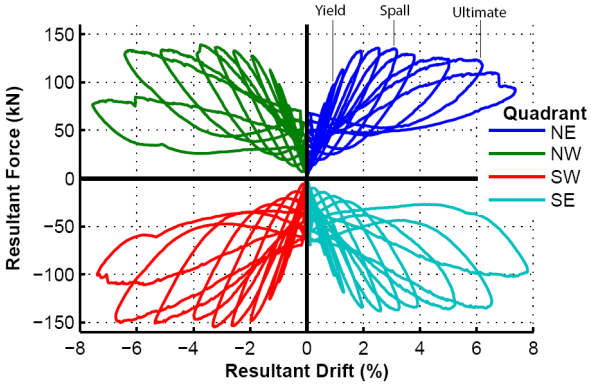

(d) Moment-curvature for MSC (HDC2, resultant)

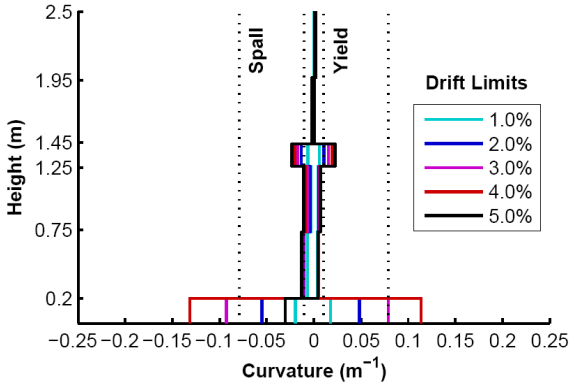

(e) Curvature distribution for GDC (HDS2, NS)

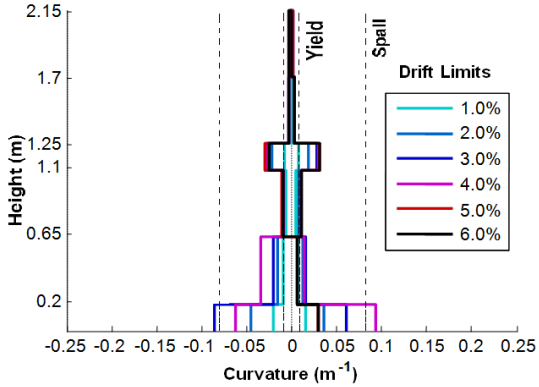

(f) Curvature distribution for MSC (HDC2, NS)

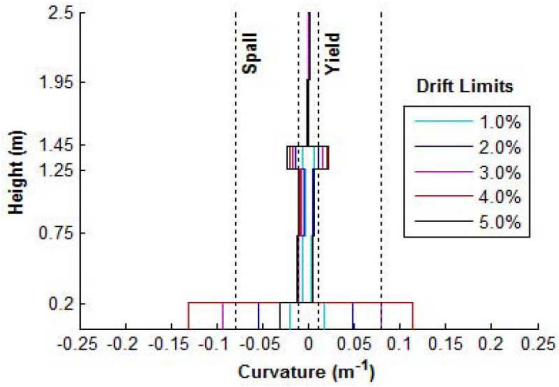

(g) Curvature distribution for GDC (HDS2, EW)

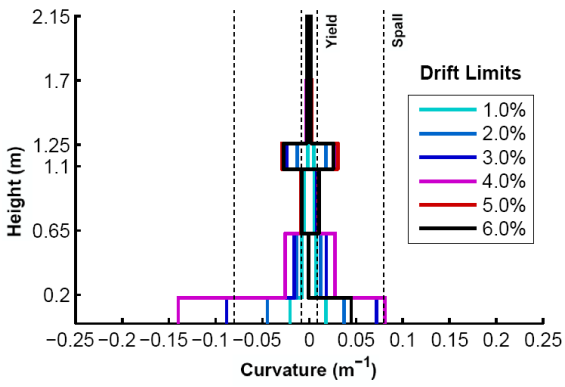

(h) Curvature distribution for MSC (HDC2, EW)

Figure 3.83. Comparison of experimental plots for GDC and MSC under biaxial testing

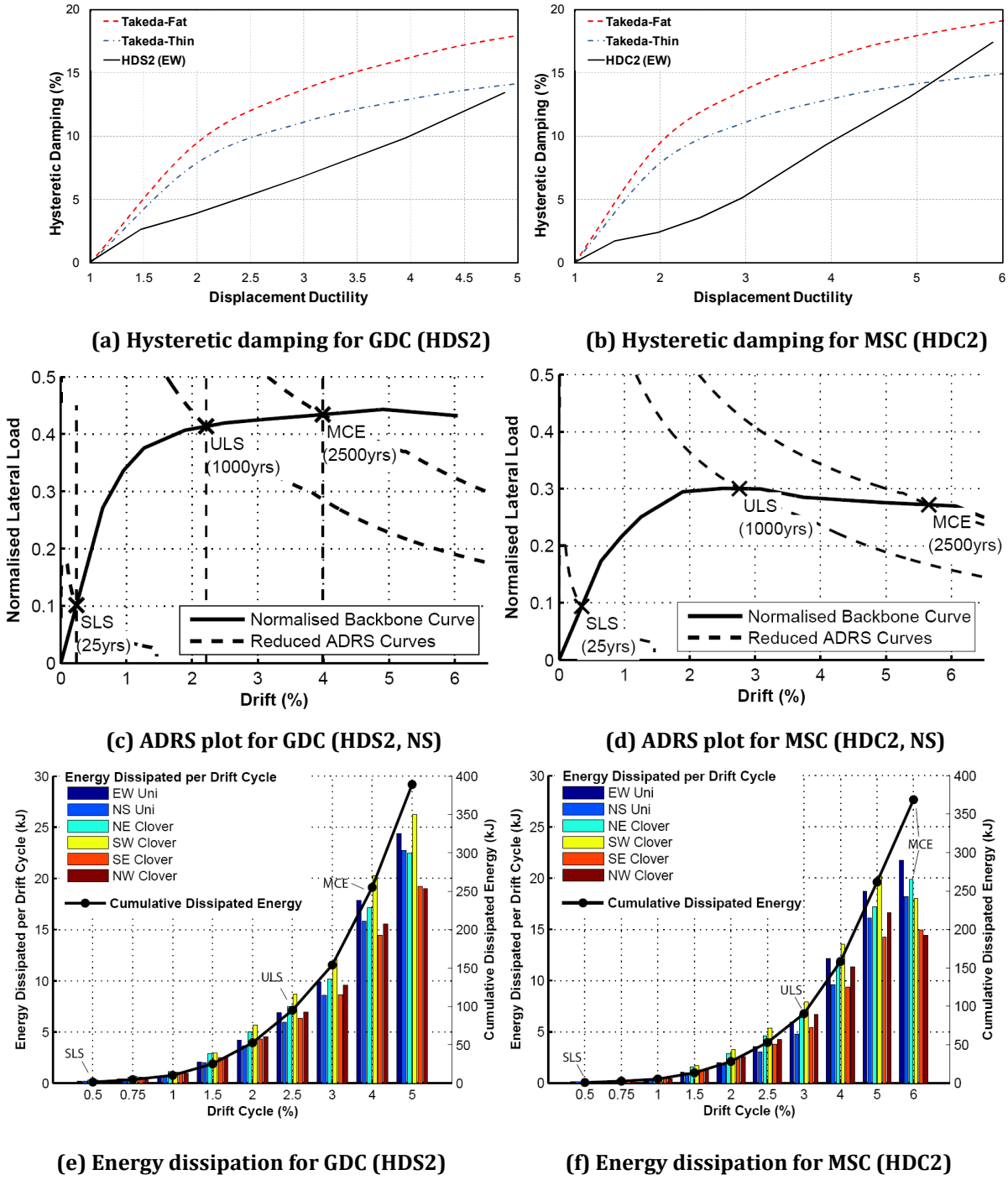

(a) Hysteretic damping for GDC (HDS2) **(b) Hysteretic damping for MSC (HDC2)**

(c) ADRS plot for GDC (HDS2, NS) **(d) ADRS plot for MSC (HDC2, NS)**

(e) Energy dissipation for GDC (HDS2) **(f) Energy dissipation for MSC (HDC2)**

Figure 3.84. Comparison of experimental plots for GDC and MSC under biaxial testing

Figure 3.85 presents plots for comparision of the hysteretic damping between GDC and MSC under uniaxial and biaxial testing. The plots for comparison of energy dissipation are shown in Figure 3.86.

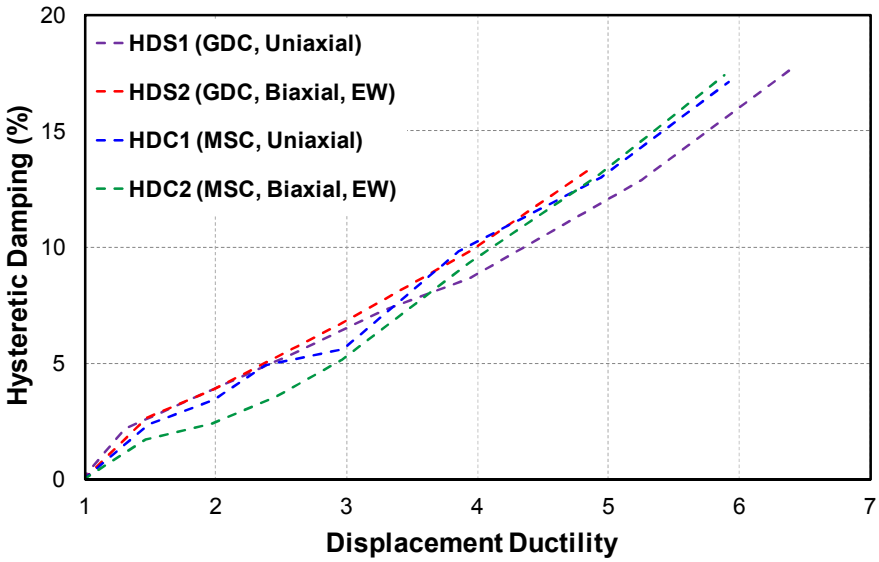

Figure 3.85. Comparison of hysteretic damping for GDC and MSC

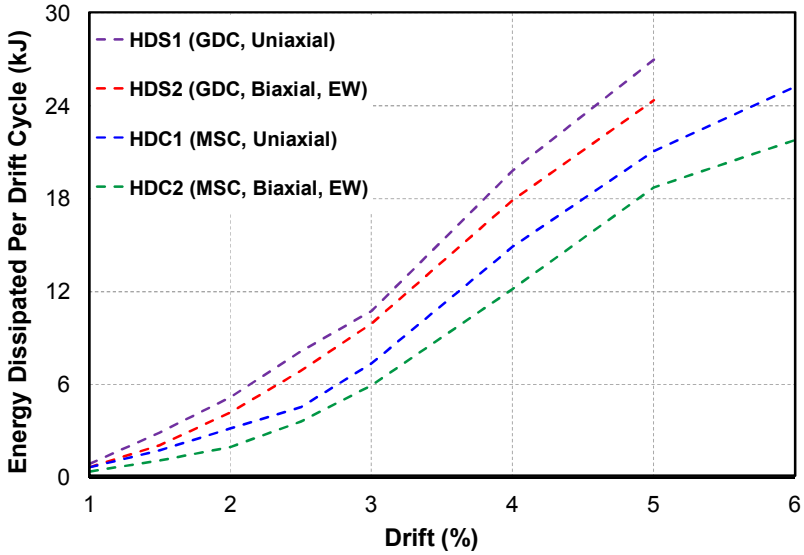

(a) Energy dissipation per drift cycle

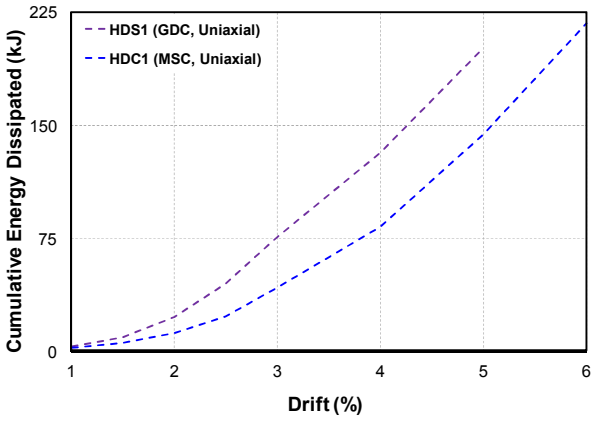

(b) Cumulative energy dissipation (uniaxial)

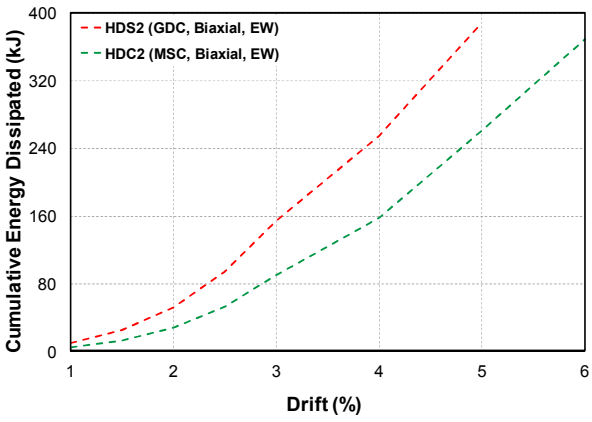

(c) Cumulative energy dissipation (biaxial)

Figure 3.86. Comparison of energy dissipation for GDC and MSC

A summary of the ADRS results for the cantilever columns with GDC and MSC is presented in Table 3.11.

Table 3.11. Summary of ADRS results for the cantilever columns

Testing	Specimen	Primary Connection Type	SLS Drift (%)	ULS Drift (%)	MCE Drift (%)
			25 yr	1000 yr	2500 yr
Uniaxial	HDS1	Grouted Duct	0.2	2.4	3.8
	HDC1	Member Socket	0.25	3	4.8
Biaxial	HDS2	Grouted Duct	0.3	2.2	3.8
	HDC2	Member Socket	0.5	2.8	5.7

3.2.8 Summary of the Connection Testing Results

3.2.8.1 HDS1

- The column featured grouted duct connection for the column to footing and segment to segment connections.
- The column was tested under uniaxial cyclic loading.
- There was no armoring provided at the base of the column.
- There was no unbonded length of the starter bars left at the column to footing interface.
- The ultimate drift capacity of the column was 5% before the first starter bar ruptured.
- Hairline cracking started during 0.35% drift ratio, the cracking was distributed up the height of the column.
- Spalling of the cover concrete initiated during 3% drift ratio, the spalling height was measured to be 250 mm (half height of the column cross-section) at the end of testing.

- There was a 7 mm gap opening at the base of the column during 3% drift ratio (ULS performance level).
- Starter bars started buckling during bigger drift ratios (4% onwards) which may have also contributed in low-cycle fatigue failure of the starter bars.
- There was some gap opening at the segment to segment grouted duct connection. However, this was considerably smaller than the gap opening at the column to footing interface during larger drift ratios.
- Based on the experimental observations, the presence of a second hinge at the segment to segment connection had enhanced the seismic performance of the cantilever column.

3.2.8.2 HDS2

- The column incorporated grouted duct connection for the column to footing and segment to segment connections.
- The column section and reinforcement details were identical to HDS1.
- The column was tested under biaxial cyclic loading.
- There was base armoring of the column at the column to footing connection.
- There was a 120 mm unbonded (taped) length of the starter bars left at the column to footing interface.
- Armoring proved to very effective in limiting the spalling around the base of the column, minor spalling occurred only in the corners of the column due to higher compressive loads during clover stage loading of the column.
- Armoring also prevented buckling of the starter bars towards the outside face of the column to some extent. Upon disassembly there was some buckling and twisting of the rebars observed at the column to footing interface, but this was thought to be due to a more demanding loading (bi-directional).

- The unbonded length of the starter bars was very effective in distributing the inelastic deformation in the rebars. This diminished the chances of any low-cycle fatigue failure. It also prevented from any strain concentration effects at the column to footing interface. The unbonded length of the starter bars had increased the ultimate drift capacity of the column by at least 30%.

- Bar rupturing occurred during 7% resultant drift ratio which is considerably higher (30%) than that of HDS1. The ultimate displacement of the column was comparable to those observed in testing of HDC1 and HDC2.

- Other observations from the performance of the column such cracking distribution and spalling height etc, were similar to those observed in HDS1.

- Figure 3.87 presents a comparison of the observed damage between HDS1 and HDS2 by the end of testing (MCE performance level).

(a) HDS1 at 5% drift ratio **(b) HDS2 at 7% resultant drift ratio**

Figure 3.87. Comparison between the observed damage in HDS1 and HDS2

3.2.8.3 HDC1

- The column incorporated member socket connection for the column to footing and grouted duct for the segment to segment connections.
- The column was tested under uniaxial cyclic loading.
- The column ultimate drift capacity was 6% before first rebar rupturing occurred.
- The hairline cracks started during the 0.25% drift ratio. The cracking distribution was similar to what observed in testing of HDS1 and HDS2. Larger cracks were located at the base of the column. Instead of a single gap opening, there were multiple big cracks at the plastic hinge zone.
- Spalling initiated during the 3% drift ratio, the spalling height was measured to be 500 mm (diameter of the column section) at the end of testing.
- Bar buckling occurred during larger drift ratios (4% onwards).
- Some gap opening at the segment to segment connection occurred.

3.2.8.4 HDC2

- The column section and reinforcement details were identical to HDC1.
- The column was tested under biaxial cyclic loading.
- The column behaved similar to HDC1. The cracking, spalling, and bar failure drift ratios were similar to those observed during testing of HDC1.
- The spalling level was much more severe compared to HDC1. This was due to a more demanding biaxial loading. The height of spalling was similar to that of HDC1.
- Figure 3.88 presents a comparison of the observed damage between HDC1 and HDC2 at the end of testing (MCE performance level).

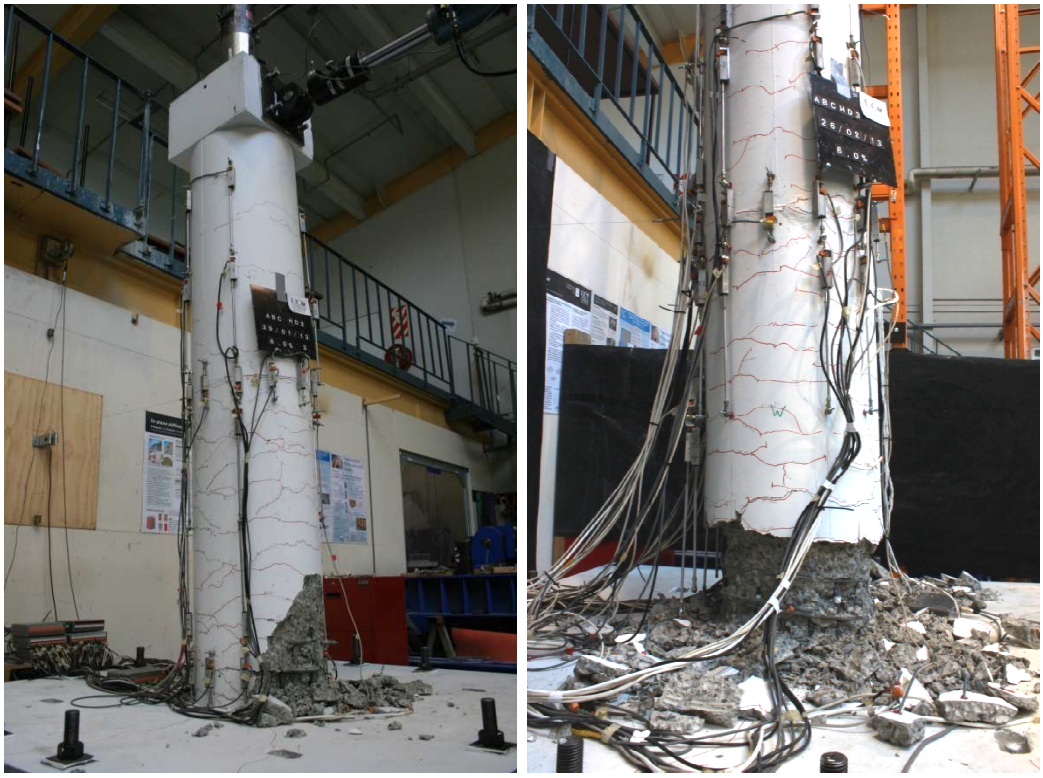

(a) HDC1 at 5% drift ratio **(b) HDC2 at 7% resultant drift ratio**

Figure 3.88. Comparison between the observed damage in HDC1 and HDC2

3.2.8.5 Punching Shear Tests (HDC1 and HDC2)

- Punching shear (pull through) tests were carried out on the footing blocks of HDC1 and HDC2.
- Testing showed that sufficient gravity load carrying capacity of the grouted interface between the footing socket and column stub will remain after uniaxial and biaxial cyclic loading of the column up to the failure point.
- The gravity load carrying capacity of the socket for punching shear failure mode will be at least three times greater than the design gravity load of the column.
- Testing results suggested that the grouted interface around the socket will remain almost intact after cyclic loading of the column.

3.3 ABC High Damage: Multi-Column Pier System (Bent)

In the second phase of testing, a half-scale multi-column precast pier (bent) was developed with High Damage (HD) connections. This solution incorporated emulative Cast-In-Place (CIP) technology which targeted a similar performance as that can be expected of a conventional ductile monolithic bent.

The ABC High Damage Bent "HDB" comprised of two circular columns with a rectangular cap beam on top. The column to footing connection was Member Socket Connection (MSC) while the column to cap beam connection featured Grouted Duct Connection (GDC), as shown in Figure 3.90. The bent concept was similar to that proposed by Marsh et al. (2011), as shown in Figure 3.89. However, the columns were not segmental in HDB.

According to Marsh et al. (2011), plastic hinges are expected to be formed at the top and bottom of the columns during a design level earthquake. In this case, the footings and cap beam are capacity protected elements. This means that there should not be any inelastic action occurring in these elements during an earthquake. The columns are the sacrificial elements in this instance. The column to footing and column to cap beam connections would need to be strong enough to push the damage (plastic hinging) away from the panel zones into the columns. For a bent comprised of two columns, there would be four plastic hinges forming at the top and bottom of the columns during a big earthquake.

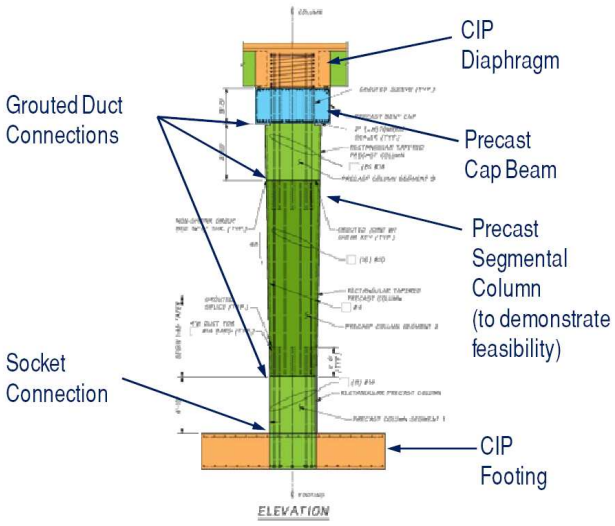

Figure 3.89. Concept for precast bent in seismic regions (Marsh et al., 2011)

HDB was intended to provide insight into seismic performance of a pier system which incorporates combination of GDC and MSC. It was also intended to serve as a benchmark for comparison of seismic performance with a Low Damage Bent (LDB), as will be discussed in Chapter 5. Table 3.12 provides a summarized description of HDB.

Table 3.12. ABC High Damage Bent

Specimen	Connection Type		Section Shape	Quasi-Static Testing Protocol
	Column to Foundation	Column to Cap beam		
HDB	MSC	GDC	Circular	Uniaxial

A general schematic of HDB is shown in Figure 3.90. The prototype structure, testing arrangement, design process, detailing considerations, construction technology, assembly sequence, and experimental testing for HDB are presented in the subsequent sections.

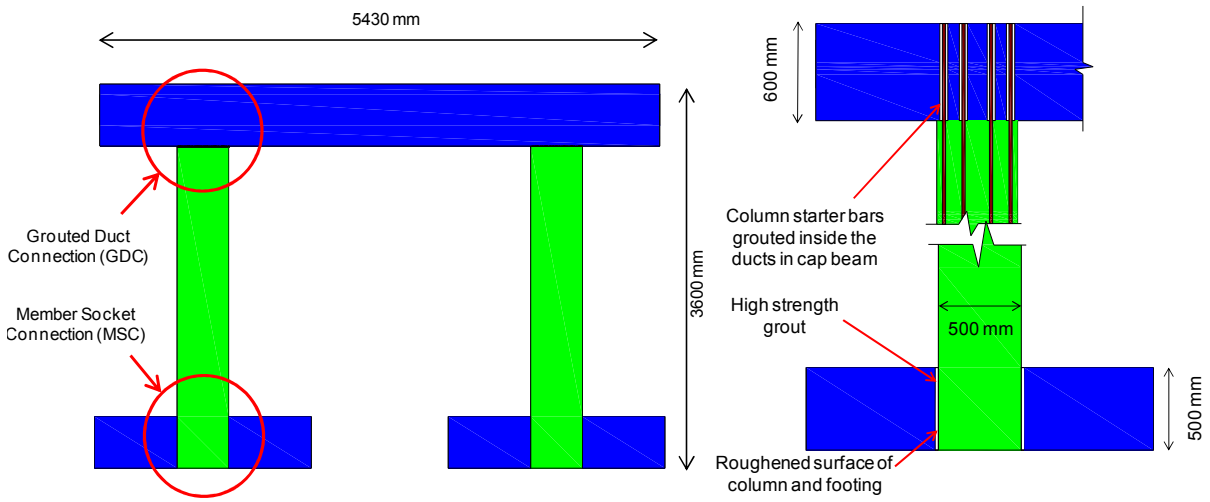

(a) Elevation view **(b) Connection close-up view**

Figure 3.90. Schematic of High Damage Bent (HDB) connections

3.3.1 Prototype Structure

The prototype structure was developed based on a multi-column pier system for a typical highway bridge in New Zealand, as shown in Figure 3.91. The bridge has six spans of equal length. Each span is 16 m which gives a total length of 96 m for the bridge. The height from top of the footing up to the center of mass of the bridge is taken to be 5.8 m. The overall width of the bridge is taken as 10.4 m.

The superstructure is consisted of I-beam 1600 deck system in accordance with NZTA 364 Report (NZTA, 2008). Similar to the prototype developed and discussed for the cantilever segmental pier system in Section 3.2.1, the bridge is assumed to be located on non-liquefiable soils. The base connections are taken to be fully fixed with no soil-structure interaction taken into account. The footing system shown in Figure 3.91 for the prototype structure is only indicative.

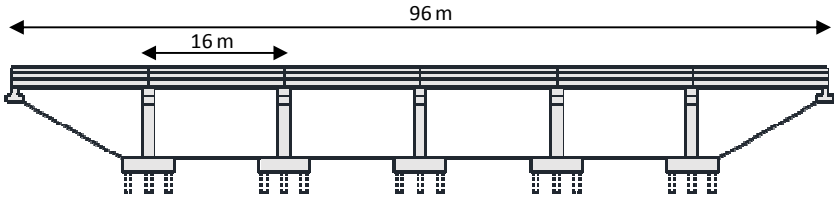

(a) Longitudinal profile

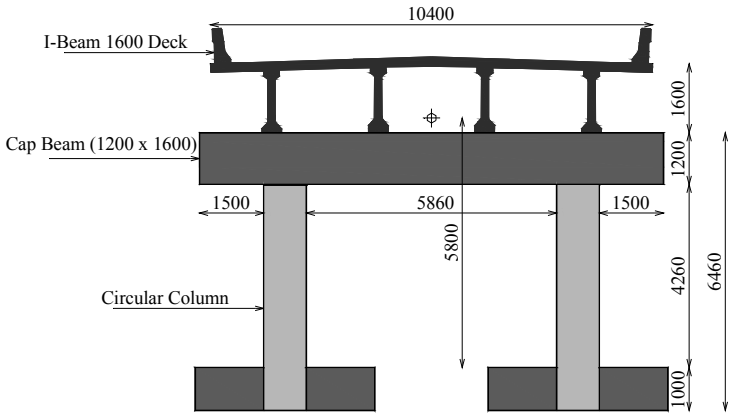

(b) Elevation view (all dimensions are in mm)

Figure 3.91. Prototype Bridge

HDB is a half-scale specimen which was developed based on the prototype shown in Figure 3.91. A force-based design approach was used for the earthquake loading of the prototype structure. This was based on the seismic loading criteria from New Zealand Bridge Manual 3rd Edition (NZTA, 2013) and New Zealand Standards 1170.5 "Structural

Design Actions-Earthquake Actions" (NZS, 2004). There was no consideration given for the service loads on the bridge in combination with earthquake loads, except the gravity loads from the dead load of the superstructure and self-weight of the substructure elements (cap beam and columns).

According to NZTA Bridge Manual (2013) for the earthquake resistant design of the prototype bridge shown in Figure 3.91, the energy dissipation system relies on a ductile or partially ductile substructure system. The plastic hinges are expected to be formed above the ground or normal water level at the top and bottom of the columns during a design level earthquake. According to NZTA Bridge Manual (2013), the maximum allowable design displacement ductility during a maximum considered earthquake level for such a system is limited to 6. Table 3.13 presents a summary of the seismic parameters selected for HDB in accordance with NZS 1170.5 and NZTA Bridge Manual 3rd Edition. More details on the methodology for calculating lateral loads from NZS 1170.5 can be found in Section A.1 of Appendix A. The design drift (2.2%) in Table 3.13 was calculated from a simple nonlinear static (pushover) analysis, refer to Section A.2 of Appendix A.

Table 3.13. Summary of the force-based design parameters for HDB

Seismic Hazard Factor, Z	0.29
Soil Class	E (Soft Soils)
Return Period, T_R	2500 Years
Return Period Factor, R	1.8
Near Fault Factor, N	1
Assumed Ductility, μ (ULS)	3
Structural performance Factor, S_p	0.7
Fundamental Natural Period, T (NZS 1170.5)	0.24 sec
Fundamental Natural Period, T (Modal Analysis)	0.23 sec
Self weight of Bent, W_{sw}	80 kN
Superstructure weight, W_{sp}	390 kN
Design Gravity Load, W (W_{sw}+ W_{sp})	470 kN
Design Lateral Load, V	305 kN
Seismic Coefficient (V/W)	0.65
Design Drift (%)	2.2

3.3.2 Testing Arrangement

The uniaxial testing represents lateral loading of the bent in the transverse direction (East-West). In this case, lateral loads in the longitudinal direction of the bridge are resisted by the abutments. Lateral load for testing of the bent was represented by a horizontally attached ram with 1000 kN capacity which was loading the bent in the East-West direction, as shown in Figure 3.92a. The other end of the ram was attached to a strong reaction frame.

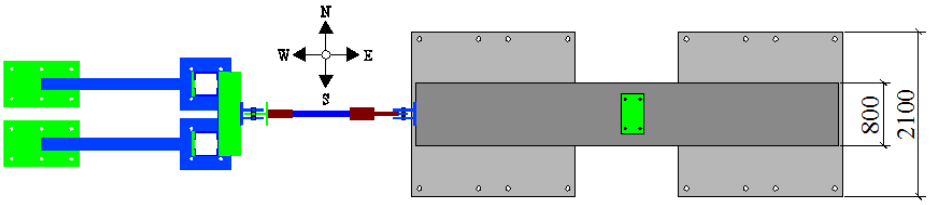

(a) Plan View

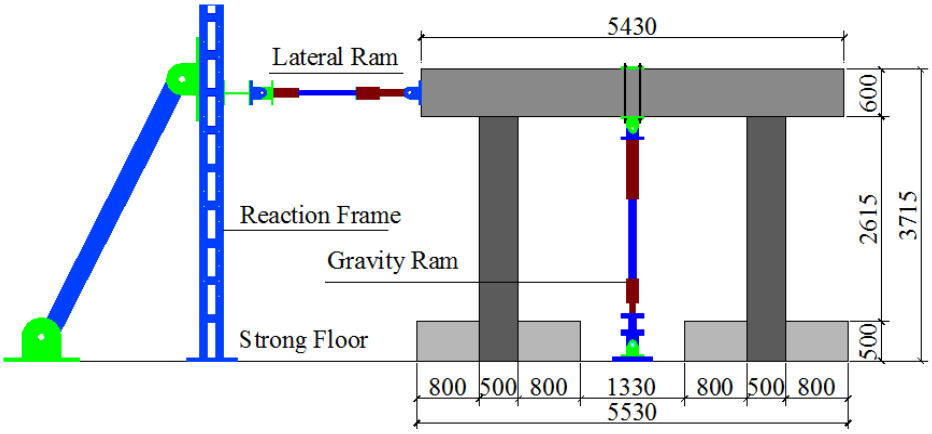

(b) Elevation view

(c) HDB testing arrangement

Figure 3.92. HDB testing setup

The superstructure dead weight on the half-scale bent was simulated by using a vertical ram with a capacity of 1000 kN which was placed between the cap beam and the strong floor, as shown in Figure 3.92b. The ram was pulling the cap beam downwards to a force level of 390 kN (superstructure weight). As the specimen displace, the vertical ram force would increase due to the imposed angularity in the ram. In order to keep the load constant, a manual controller for the ram was used during testing. The gravity load was being held constant (to within approximately ±3%) and monitored throughout testing.

3.3.2.1 Uniaxial Loading Protocol

The uniaxial quasi-static cyclic loading protocol for HDB was identical to that used for the cantilever segmental columns in Section 3.2.2.1 and illustrated in Figure 3.5.

3.3.2.2 Data Acquisition System

The data acquisition system was similar to that discussed in Section 3.2.2.3 for the cantilever segmental columns.

3.3.2.2.1 Lateral Displacement

Lateral displacement in HDB was measured using a rotary string potentiometer (rotary pot) which was mounted on a tower independent of the reaction frame on the East side of the specimen. At the same time, an additional rotary pot was installed to measure the elongation and contraction of the lateral ram at each step of loading. In order to measure any out-of-plane movement of the bent during testing, two rotary pots (one for each column) were installed in the steel towers on the North side of the specimen (Figure 3.93d). This can be seen behind the specimen in Figure 3.92c. These rotary pots were being monitored throughout testing for any excessive out-of-plane movement in the North-South direction as there was no out-of-plane restraint provided for the bent.

3.3.2.2.2 Lateral and Axial Loads

Lateral and gravity loads were measured using load cells which were mounted along the load path in each direction. 1000 kN load cells were used for both lateral and vertical rams.

3.3.2.2.3 Structure Deformation

The instrumentation was similar to that explained for the cantilever segmental columns in Section 3.2.2.3.3. Flexural and shear deformation of the bent under testing were measured using vertical, horizontal, and diagonal array of rod end potentiometers (pots). Figure 3.93 presents external instrumentation of HDB1. Redundant pots were provided at the plastic hinging zones of the bent. Several spring pots were mounted between the footings and strong floor to monitor any sliding of the footings during testing, as shown in Figure 3.93d. In Figure 3.93, the horizontal and vertical arrows represent locations of lateral and gravity rams, respectively.

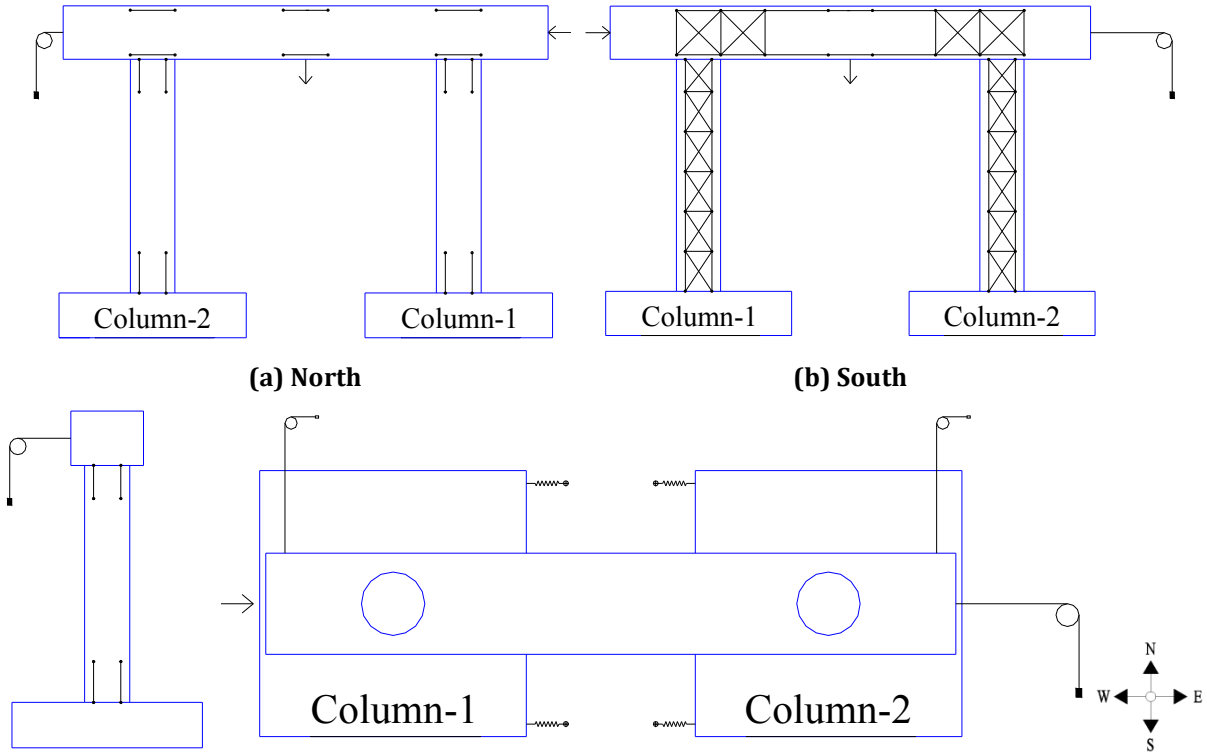

(a) North **(b) South**

(c) West (typical) **(d) Plan view showing spring and rotary pots**

Figure 3.93. Instrumentation of HDB

3.3.2.2.4. Strain Gauges

Strain gauges were installed on the reinforcing bars of the columns at the plastic hinging zones. The procedure was identical to that presented in Section 3.2.2.3.4 for the cantilever columns. Strain gauges were used as a backup source for collecting the data from the column during testing.

3.3.3 Material Characterization and Properties

This part was almost identical to what presented in Section 3.2.3 previously. A summary of the material properties are presented as below.

3.3.3.1. Reinforcing Bars Tension Strength

The reinforcing bars for the columns, footings, and cap beam, were specified as Grade 500E (seismic) Reid bars according to AS/NZS 4671 (NZS, 2001). The Reid bars are different than deformed bars in the sense that they are threaded. This gives the advantage of winding down a coupler or foot insert in the bar when compared against deformed bars. The transverse reinforcing bars in the columns were plain bars. All other rebars were Reid bars. The Reid bar mechanical properties were identical to those presented in Table 3.3 of Section 3.2.3.2 and illustrated in Figure 3.12.

3.3.3.2 Concrete Compressive Strength

The specified minimum concrete compressive strength for all components of HDB (columns, footings, and cap beam) was 40MPa at 28 days. Table 3.14 presents average compressive strength for each component of the specimen on the testing day.

Table 3.14. Summary of the average concrete compressive strength in MPa

Precast Elements	Strength
Footings	54
Columns	50
Cap Beam	47

3.3.3.3 High-Strength Grout Compressive Strength

The specified minimum high strength grout compressive strength for the grouted duct and member socket connections was 40 MPa at 28 days. Similar to Section 3.2.3.4, Sika Grout 215 was used for the grouted duct connections and Sika Grout 212 for the member socket connections in HDB. Table 3.15 presents average compressive strength of grout on the testing day of the bent.

Table 3.15. Summary of the average grout compressive strength in MPa

Connection type	Strength
Grouted Duct Connection	42
Member Socket Connection	48

3.3.4 Detailing Considerations

The columns in HDB were not segmental. Grouted Duct Connection (GDC) was used for the column to cap beam connection. The column to footing connection was Member Socket Connection (MSC).

Given the frame action in HDB, the columns had to be designed for a combination of lateral and vertical forces from Table 3.13, as shown in Figure 3.94a. The design loads (moment and shear) for each components of HDB was obtained from a simple equivalent static analysis of the frame in accordance with NZS 1170.5 (NZS, 2004).

In this instance, the columns were assumed to have cracked sections, in order to neglect the tension capacity of the concrete. This assumption used a cracked moment of inertia (I_{cr}) for the columns which was taken as 35% of the gross moment of inertia (I_g). It should be noted that for HDB, the cap beam was not prestressed. This means that cracking of the cap beam under the concentrated gravity load was expected during testing. For the cap beam, the cracked moment of inertia was taken as $I_{cr} = 0.5I_g$. Figure 3.94b and Figure 3.94c present the resultant moment and shear diagrams under the loading combination shown in Figure 3.94a for HDB, respectively. Table 3.16 presents a summary of the maximum moment and shear demands in each component.

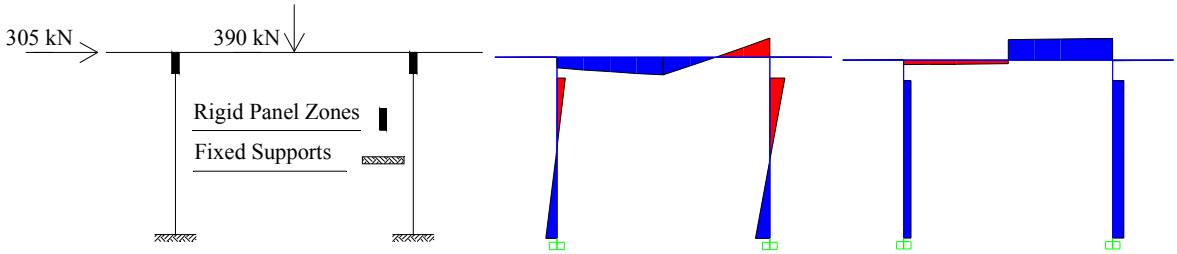

(a) Lateral and gravity loads **(b) Moment diagram** **(c) Shear diagram**

Figure 3.94. Lateral and gravity loads on HDB

Table 3.16. Summary of the maximum moment and shear demands in HDB

Components	Moment (kNm)	Shear (kN)
Footings	236	184
Cap Beam	285	355
Column Base (MSC)	236	184
Column Top (GDC)	241	184

As it can be seen from Table 3.16 and Figure 3.94b, the flexural demand at the column to cap beam GDC is slightly higher than the bottom column to footing MSC. In order to take this into account, the column section capacity had to be designed slightly higher at the top connections as presented in the next section.

The detailing considerations for GDC and MSC were similar to what discussed before in Section 3.2.4 and 3.2.5, respectively. There was 100 mm unbonded length of the starter bars left at the column to cap beam GDC. There was no armoring provided around the column at this location. Foot inserts were provided for the column longitudinal bars inside the socket. To eliminate the observed hairline radial cracking of the footing during testing of HDC1 and HDC2, circular reinforcing bars were provided around the socket at the top and bottom faces of the footing.

3.3.5 Design, Construction, and Assembly

The circular columns were identical and 500 mm in diameter. The columns were solid sections without any central duct. Column design was according to NZS 3101 (NZS, 2006) for the resulting design loads presented in Table 3.16.

Each column consisted of 8-HD16 straight longitudinal rebars with foot inserts in the MSC. Due to a slightly higher moment demand at the top GDC from an equivalent static force procedure, 4-HD10 bars were distributed around the perimeter of the column top cross-section. To provide shear, confinement, and anti-buckling capacity in the plastic hinging zones of the column, transverse reinforcement in terms of HD10 hoops spaced at 75 mm were used. The hoops spacing was 150 mm outside the plastic hinge regions. There was a circular recess at the top of the column to accommodate the cap beam shear key. The recess was 210 mm in diameter and 120 mm deep. This would allow a 20

mm construction tolerance in diameter and depth for the cap beam shear key during assembly. Column reinforcing details are shown in Figure 3.95.

The cap beam was 400 x 800 mm in cross-section with a total length of 5.43 m. The cap beam was designed in a way to be re-used for the third phase of testing for ABC Low Damage bent, as will be discussed in Chapter 5. The cap beam flexural bars consisted of 5-HD20 at the top layer, 2-HD12 at the mid layer (on the sides only), and 8-HD-20 at the bottom layer (Figure 3.96a). HD-12 stirrups and ties were provided at a constant spacing distance of 100 mm throughout the length of the cap beam.

Along the length of the cap beam, two circular shear keys were located at the column to cap beam GDCs. The shear keys were 200 mm in diameter and 100 mm deep. There was a 70 mm duct at the center of each shear key which was running up the height of the cap beam cross-section (Figure 3.96a). These ducts were intended to house the unbonded post-tensioned bars for ABC Low Damage bent (LDB) in the next phase of testing, refer to Chapter 5. The shear keys were designed to transfer the shear loads presented in Table 3.16 across the GDC interfaces. In this instance, the dowel action of the starter bars for shear resistance was neglected. The shear keys were designed using the principals of shear friction according to NZS 3101 (NZS, 2006).

Corrugated galvanized steel ducts were placed inside the cap beam to house the starter bars from the columns. The grouting ducts were 50 mm and 30 mm in internal diameter which were intended for the 16 mm and 10 mm diameter starter bars, respectively. All ducts were extended up the full height of the cap beam cross-section. This gives a development length of 600 mm for the starter bars. According to NZS 3101 (NZS, 2006), a similar development length is required for a conventional monolithic construction.

There were also 4 ducts left at the center of the cap beam. These ducts were 50 mm in diameter and were intended to house the threaded high strength rods which were connecting the vertical ram to the cap beam during testing, refer to Figure 3.92.

The footings were designed to be capacity protected elements. Two 2.1 m identical square footings with 500 mm depth were used. The footings were reinforced with double layers of HD16 bars spaced at 150 mm (Figure 3.96b). The footing sockets were 500 mm deep and 520 mm in diameter. The socket walls and the concrete surface of the

column stub were roughened during the prefabrication process. This was similar to that presented for HDC1 in Section 3.2.6.2.

There were 12 galvanized steel ducts extending up the height and distributed around the perimeter of each footing (Figure 3.96b). The ducts were 50 mm in diameter and were intended to house 38 mm diameter hold-down bolts which were securing the footing block to the strong floor during testing in the lab. A full set of technical drawings for HDB can be found in Appendix C.

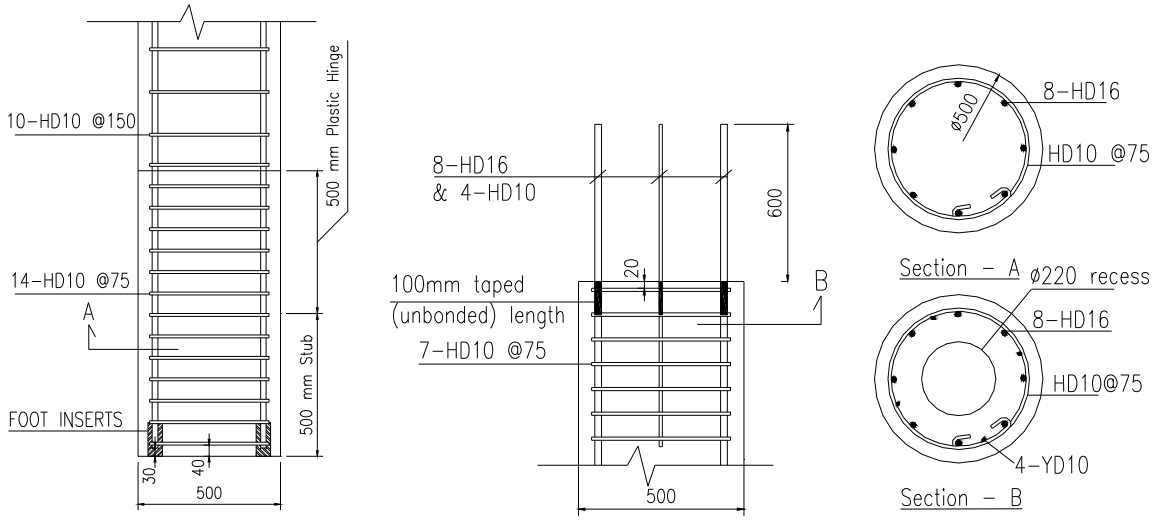

(a) Column base detail (MSC) **(b) Column top detail (GDC)** **(c) Sections**

Figure 3.95. Reinforcing details of the columns for HDB

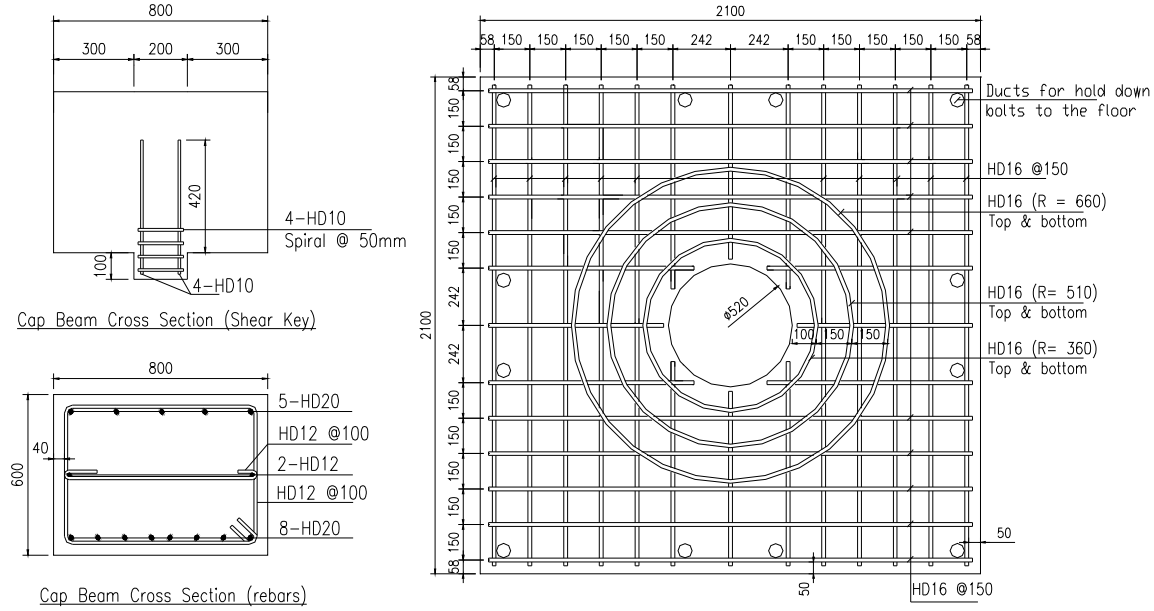

(a) Cap beam cross-sections **(b) Typical footing plan view**

Figure 3.96. Reinforcing details of cap beam and footings for HDB

HDB components were constructed separately at the prefabrication yard. Figure 3.97 presents photos from construction of footings which was similar to HDC1 in Section 3.2.6.2, except the addition of circular bars around the socket (Figure 3.97a).

(a) Footing cage with central socket

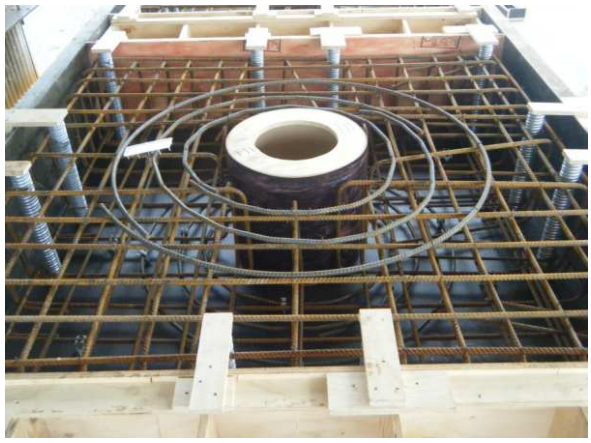

(b) Footing with socket in the formwork

(c) Socket roughened

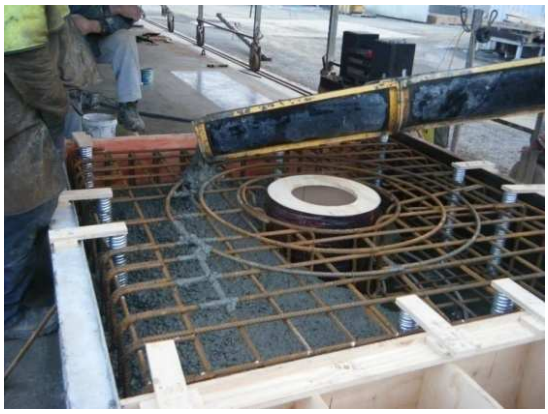

(d) Pouring concrete

(e) Poured footings

Figure 3.97. Construction photos of HDB footings

The cap beam was poured horizontally in a metal formwork. A plastic PVC pipe was used for the formwork of the circular shear key (Figure 3.98d). A plywood template was used for the grouting ducts of the cap beam at each column location (Figure 3.98c). This template was utilized later when aligning the starter bars from the column inside the mould. Plenty of lifters were placed along the length of the cap beam on both top and bottom faces. The lifters will provide flexibility during lifting of the cap beam after removal from the formwork for handling, transportation, and assembly purposes.

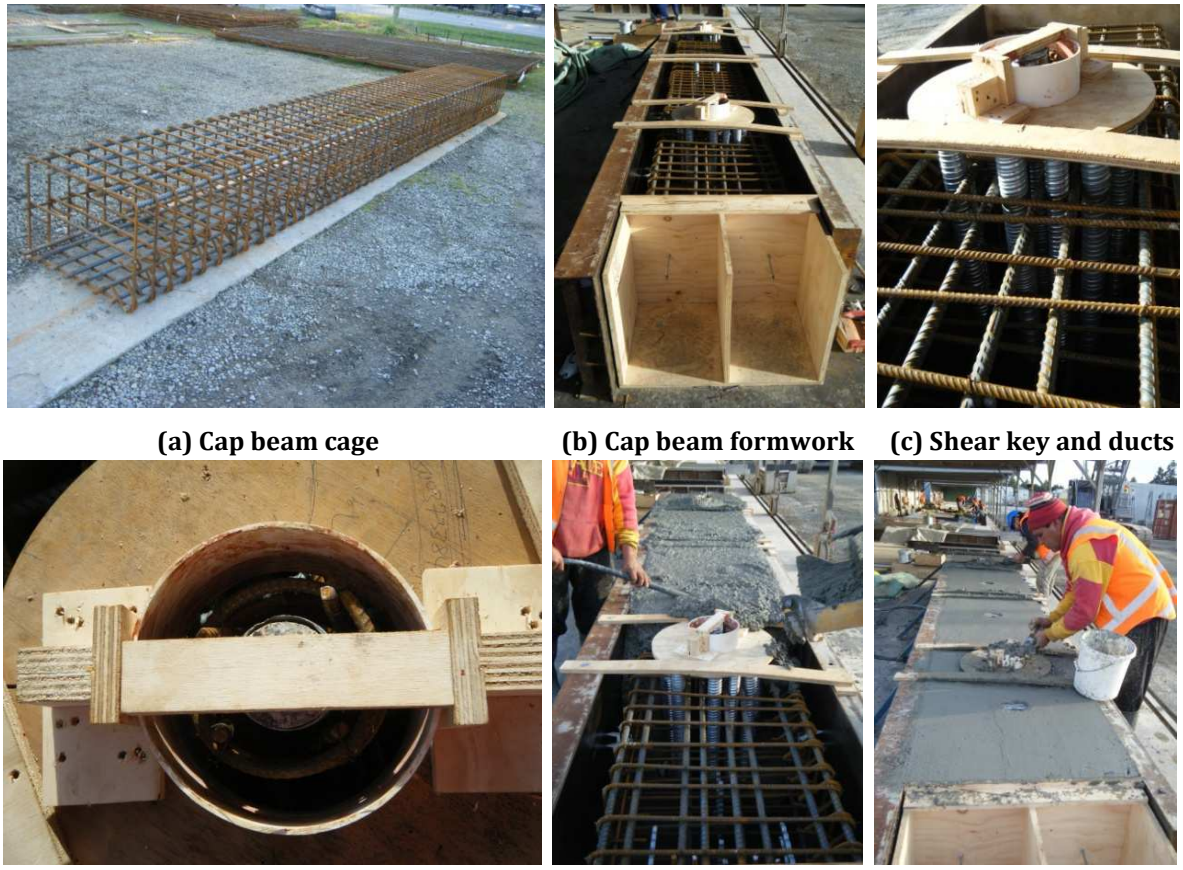

(a) Cap beam cage **(b) Cap beam formwork** **(c) Shear key and ducts**

(d) Shear key formwork looked from top **(e) Pouring concrete** **(f) Pouring shear keys**

Figure 3.98. Construction photos of HDB cap beam

The construction of circular columns was similar to what discussed for HDC1 in Section 3.2.6.2. The foot inserts (Figure 3.99b) at the base of the columns were wound to the Reid bars (Figure 3.99c). In order to prevent from unwinding or loosening of the foot inserts during casting of the column, epoxy was injected inside the foot inserts before they were wound. The plywood templates from the cap beam were used to align the starter bars which were extending out of the column (Figure 3.99d). This was intended to reduce the chances of any misalignment of the starter bars inside the grouting ducts during the assembly of HDB.

A cylindrical recess was left at the top of each column to house the shear keys from the cap beam. The recess was simply made by using a circular foam block, as shown in Figure 3.99g. There was also a lifter placed at the center of the column top section which would be used during lifting and assembly later. Before pouring the columns, a 100 mm length of the starter bars just below the top section of the column was wrapped with duct tape to provide an unbonded length (Figure 3.99g). Construction photos of the

columns are shown in Figure 3.99. The columns were removed out of the formwork and transported to the lab in the next step (Figure 3.100).

(a) Column cages

(b) Foot insert

(c) Foot inserts epoxied and wound up

(d) Column cage inside the steel casing

(e) Plywood template and cylindrical foam visible

(f) Columns ready to be poured

(g) Unbonded (taped) length of the starter bars

Figure 3.99. Construction photos of HDB columns

(a) Cap beam removed from formwork (b & c) Rotating cap beam for transfer purposes

(d) Cap beam rotated and ready for transport (e) Footings cured and ready for removal

(f) Columns cured and ready for removal (g) All components arriving to lab on a trailer

(h) Footings (i) Cap beam (j) Columns

Figure 3.100. Completed components of HDB and delivery to the lab

The assembly process for HDB started with winding the hold-down bolts in the strong floor holes. A ring of foam torus was left at the center of the footing. The outer ring had

slightly bigger diameter than the socket. The foam ring was expected to prevent from the flow of the grout underneath the footing during the grouting stage. This was similar to what discussed for HDC1 in Section 3.2.6.2.

Two persons were needed to assemble the bent. One person was operating the crane while the other one was guiding and positioning each component to its designated location. The footings were lowered on the bolts and were fully secured (Figure 3.101a). The first column was lifted up from its top anchor which was placed at the center of the column top section before casting (Figure 3.101b). The column was then navigated on the footing and inserted inside the socket, as shown in Figure 3.101c.

Temporary wooden wedges were provided at the grouting interface of the socket to keep the column straight and not leaning. Temporary metal props were provided for the column. There were at least two props installed perpendicular to each other (Figure 3.101e). The props were keeping the column stable and were intended to prevent from excessive in-plane and out-of-plane movements until the column is fully grouted. The props length was adjustable by simply removing a pin which was located at their mid length. This would allow for some elongation of the props which was necessary when adjusting the verticality and ensuring the alignment of the whole specimen before grouting. Similar procedure was repeated for the second column (Figure 3.101e).

The 70 mm diameter ducts at the center of the cap beam shear keys were sealed with foam and some beads of silicone caulk (Figure 3.101f). As explained earlier, these ducts were left for the third phase of testing (Chapter 5) as the cap beam was going to be re-used. This was intended to prevent from flow of the grout inside the 70 mm ducts later. In a real life ABC High Damage bent, there would not be any central ducts.

The cap beam was lifted up from its mid-span anchors and was lowered on the starter bars (Figure 3.101g). At this stage, one person would have to reach the column starter bars and align and guide the column starter bars inside the cap beam grouting ducts (Figure 3.101h). The second person would operate the crane which had the cap beam suspended. Based on the observation of the first person, the second person would move the cap beam very carefully in the desired direction. After all starter bars were inside the grouting ducts (Figure 3.101i), the cap beam was lowered on some wooden blocks which were left on top of the columns (Figure 3.101j).

(a) Footings placed and secured

(b & c) Column lifted and positioned in the socket

(d) Column inserted inside the socket

(e) Column propped, second column assembly

(f) Cap beam shear key central duct sealed

(g) Cap beam lifted up

(h & i) Aligning starter bars into the grouting ducts

(j) Cap beam sit on wooden blocks

Figure 3.101. HDB assembly photos

In the next stage of assembly process, it was important to level the cap beam and to ensure its proper alignment. Therefore, the weight of the cap beam was taken by the crane and the wooden blocks were removed. Some steel plates and shims were used at the column to cap beam interfaces to ensure a proper alignment of the cap beam (Figure 3.102a). Once the cap beam was level in both directions (Figure 3.102b and Figure 3.102c), it was necessary to check the verticality of the columns (Figure 3.102d and Figure 3.102e). At this stage, the props were loosened a little bit and by gently moving the crane, the verticality of the columns was ensured. The cap beam alignment was checked once again.

Having the cap beam sitting on the steel shims, a grouting bed around each column at the column to cap beam interface could be placed. The column to cap beam interface was sprayed with fresh water prior to placing the grouting bed (Figure 3.102f). High strength mortar from Sika 212 was mixed in a bucket (Figure 3.102g), and then hand packed at the column to cap beam interface to seal the gaps (Figure 3.102h and Figure 3.102i). A mix of the 5 minute epoxy (Figure 3.102j) was made (Figure 3.102k). A layer of the 5 minute epoxy was applied by a brush around the grouting beds (Figure 3.102l). This was intended to make the grouting beds water tight and to eliminate any chances of grout leaking when the grouting ducts are poured from the top of the cap beam.

In the next stage, the bottom member socket connections were grouted. The procedure was identical to what discussed for HDC1 in Section 3.2.6.2. The grouting sequence for this is presented in Figure 3.103a through Figure 3.103e. In a real life bridge, this step can be done before pouring the grout beds for the top grouted duct connections, as explained in the previous paragraph.

In the last step, the cap beam grouting ducts are filled with high strength mortar using a gravity operated procedure. This was done by reaching the ducts on top of the cap beam and pouring the grout, as shown in Figure 3.103f and Figure 3.103g. The grouting sequence for this was to start pouring the grout in one duct and continue pouring until the grout level in all ducts are rising to an equilibrium point, then filling each duct individually. A thin strip of metal was used to agitate the grout in the ducts throughout the process. This would take the air out of the ducts and would prevent from any voids

in the grout. After grout was cured, the metal props were removed. Figure 3.103h shows the fully assembled bent.

(a) Steel packers at the top interfaces

(b & c) Aligning the cap beam in two directions

(d & e) Ensuring column verticality

(f) Spraying water around the grouting beds

(g) Grouting bed mix

(h) Packing the mortar

(i) Grouting bed placed

(j) 5 minute epoxy

(k) Mixing water tight epoxy

(l) Epoxy applied around interfaces

Figure 3.102. HDB pre-grouting preparations

(a) Water sprayed around MSC

(b) Grouting mix

(c) Grouted MSC

(d) Wooden wedges removed from MSC

(e) MSC fully grouted

(f) Grouting ducts on top of the cap beam

(g) Ducts filled with high strength grout

(h) Fully assembled bent, props removed

(i) Bent painted and instrumented for testing

Figure 3.103. HDB grouting photos

3.3.6 Testing Results and Performance Evaluation

For the bottom Member Socket Connections (MSCs), minor flexural cracks started during the 0.2% drift ratio. Further cracking occurred with the increasing drift ratios. The distribution of the cracks was similar to that observed during testing of HDC1 and HDC2 in Section 3.2.7.3 and Section 3.2.7.4, respectively. For the top Grouted Duct Connections (GDCs), flexural cracks started at similar drifts as those in MSCs. The distribution of the cracks was similar to what observed during testing of HDS1 and HDS2, as discussed in Section 3.2.7.1 and Section 3.2.7.2, respectively.

For MSCs larger cracks were located toward the base of columns which indicated the plastic hinge zone (Figure 3.104). Similar to HDC1 and HDC2, using a measuring tape the observed plastic hinge length was measured to be approximately equal to the diameter of the column section (500 mm). According to NZS 3101 (NZS, 2006), similar plastic hinge length would be expected from a ductile monolithic column with unidirectional plastic hinges.

For GDCs, there were few cracks opening with increasing drift ratios. This means that similar to HDS2, most of the inelastic action was occurring along the unbonded length of the starter bars at the top region of the columns (Figure 3.105). The column plastic hinge length was measured to be approximately half diameter of the column section (250 mm) from the bottom face of the cap beam.

For MSCs, minor spalling of the cover concrete at the base of the Column-1 initiated during the 1.8% drift ratio. More spalling occurred during the 2.2% drift ratio (ULS performance level), as shown in Figure 3.104a. The spalling continued further with increasing drift ratios. There was also some superficial spalling around the sockets (Figure 3.104b). In GDCs, there was less spalling of the cover concrete during the 2.2% drift ratio (Figure 3.5). Some diagonal hairline cracks near MSCs and GDCs were also observed in both columns throughout testing.

During 3.4% drift ratio (MCE performance level), Column-1 which was located adjacent to the lateral actuator had severe concrete spalling in its MSC. There was not any bar rupturing up to this point. Testing was stopped after finishing the cycles for 3.4% drift ratio. At the end of testing, the spalling height at the base of column was measured to be

500 mm from the top of the footing (Figure 3.106). The spalling was more severe on the eastern and western sides of Column-1, as shown in Figure 3.106a and Figure 3.106b, respectively. This was due to close proximity of this column to the loading point (lateral ram). Figure 3.106 presents photos from each column face which shows the extent of damage in MSCs at the end of testing. Some column longitudinal bar buckling was also observed following the testing (Figure 3.108).

In GDCs, minor spalling of cover concrete initiated during 2.8% drift ratio. The grouting bed started flaking at 1.5% drift cycles. Unlike HDS1 and HDS2, the largest crack was located approximately 200 mm down the bottom face of the cap beam during larger drift ratios (Figure 3.107). The reason behind this was the way the unbonded length of the starter bars was left in the column. As shown previously in Figure 3.95b, the 100 mm unbonded length of the bars was left just under the top face of the column, not over the portion of the starter bars which would be grouted inside the grouting ducts of the cap beam. This means the starter bars were fully bonded up the height of the cap beam cross-section. The plastic hinging would occur in the columns and away from the column to cap beam panel zones. Using such a scheme, majority of the inelastic action would be occurring over the portion of the starter bars inside the column, not the part inside the grouting ducts of the cap beam. In a real life bridge, this would offer easier and better inspectability and repairability of the bridge following an earthquake.

In GDCs, the extent of spalling increased during 3.4% drift ratio, reaching a height of approximately 250 mm below the bottom face of the cap beam. The spalling was more severe on the eastern sides of the columns. Figure 3.107 presents photos from each column face which show the extent of damage in GDCs at the end of testing. There was no column starter bar buckling observed during testing. Similarly, it was obvious that the rupturing drift ratio of the starter bars is greater than 3.4%.

Table 3.17 presents a summary of the maximum crack sizes in MSC and GDC at different drift ratios during testing. The crack sizes were measured during the peak drift ratios.

Table 3.17. Summary of the maximum crack widths measured during HDB testing

	Drift Ratios (%)							
	0.35	**0.5**	**1.0**	**1.5**	**1.8**	**2.2**	**2.8**	**3.4**
Column to Footing MSC (mm)	<0.4	0.4	2	3	8	Spall	Spall	Spall
Column to Cap Beam GDC (mm)	<0.4	0.4	0.5	1.5	4	6	7	Spall

(a) Col-1, spalling occurred (b) Col-2, superficial spalling around socket

Figure 3.104. HDB column to footing MSCs at the end of 2.2% drift ratio

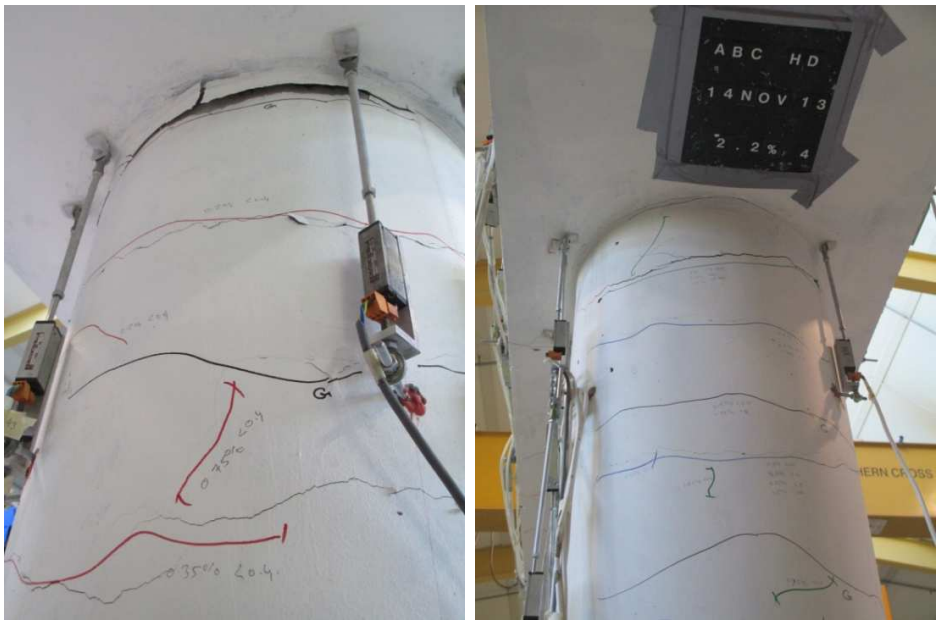

(a) Col-1, superficial epoxy broken (b) Col-2, largest crack in column visible

Figure 3.105. HDB column to cap beam GDCs at the end of 2.2% drift ratio

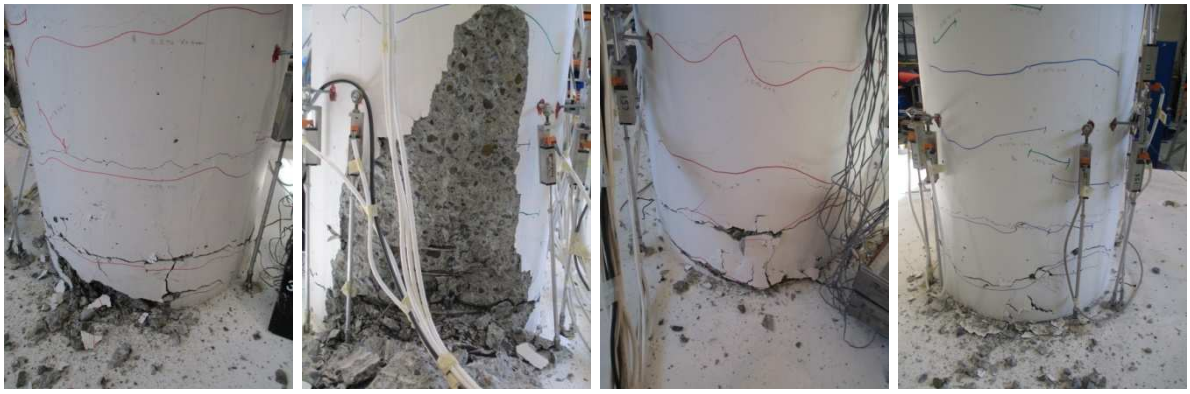

(a) Col-1 East side **(b) Col-1 West side** **(c) Col-2 East side** **(d) Col-2 West side**

Figure 3.106. HDB column to footing MSC at the end of testing (3.4% drift ratio)

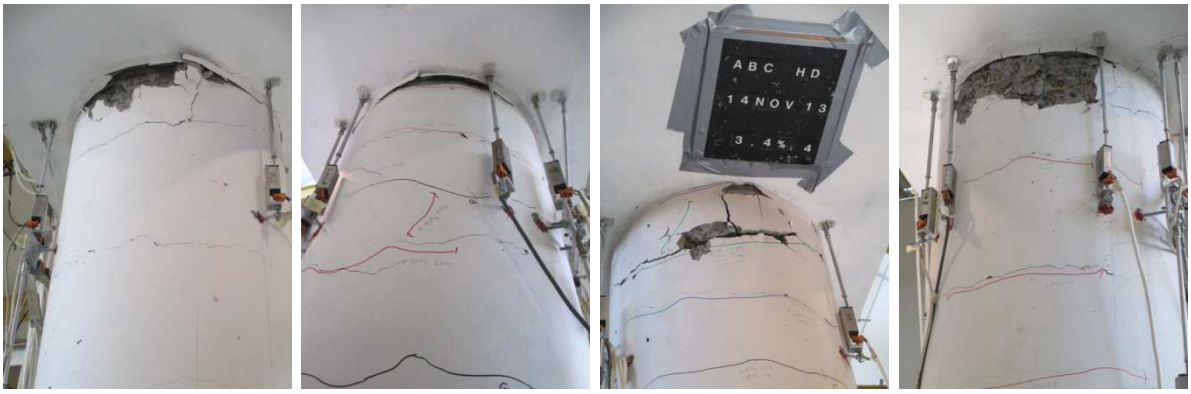

(a) Col-1 East side **(b) Col-1 West side** **(c) Col-2 East side** **(d) Col-2 West side**

Figure 3.107. HDB column to cap beam GDC at the end of testing (3.4% drift ratio)

(a) Bar buckling in Col-1 MSC west side **(b) Close-up view of bar buckling**

Figure 3.108. HDB bar buckling at the end of testing (3.4% drift ratio)

Figure 3.109 and Figure 3.110 present progression of damage in the MSC and GDC at different drift ratios during testing, respectively. The photos were taken at the peak of first cycle at each drift ratio.

(a) Peak of 0.2% drift ratio

(b) Peak of 0.5% drift ratio

(c) Peak of 1.0% drift ratio

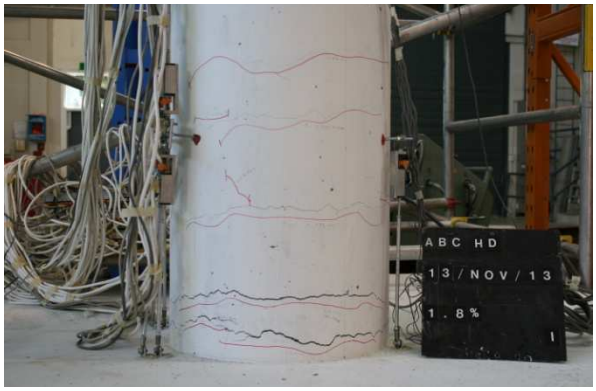

(d) Peak of 1.8% drift ratio

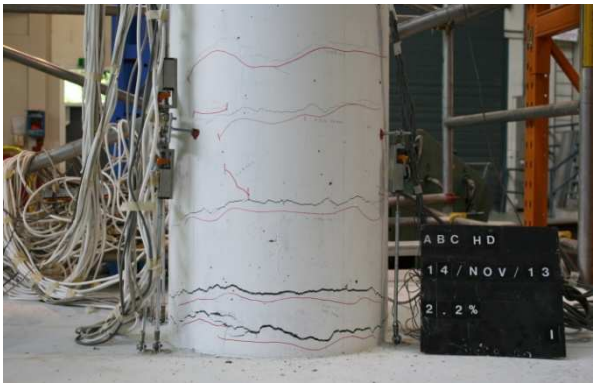

(e) Peak of 2.2% drift ratio

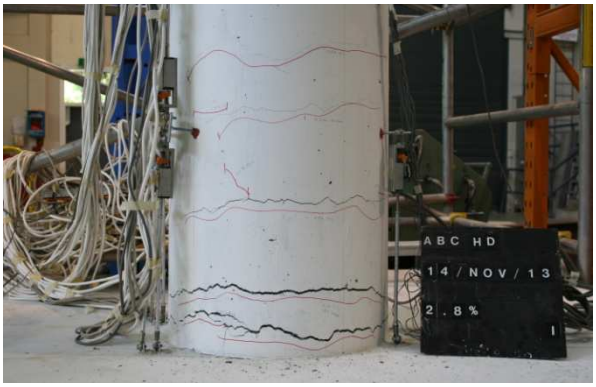

(f) Peak of 2.8% drift ratio

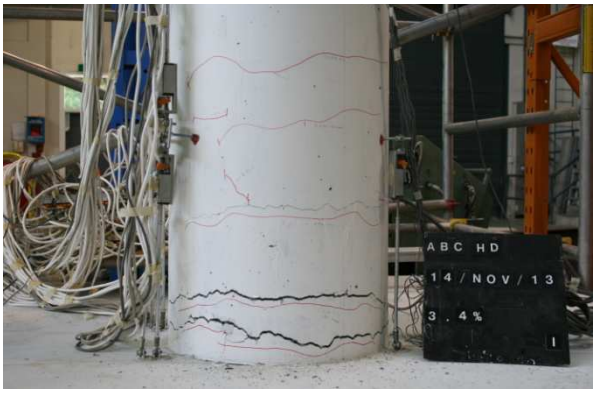

(g) Peak of 3.4% drift ratio

(h) End of 3.4% drift ratio

Figure 3.109. Damage progression in HDB Column-1 MSC (East side) during testing

(a) Peak of 0.2% drift ratio

(b) Peak of 0.5% drift ratio

(c) Peak of 1.0% drift ratio

(d) Peak of 1.8% drift ratio

(e) Peak of 2.2% drift ratio

(f) Peak of 2.8% drift ratio

(g) Peak of 3.4% drift ratio

(h) End of 3.4% drift ratio

Figure 3.110. Damage progress in HDB Column-2 GDC (East side) during testing

There were few diagonal hairline cracks (< 0.4 mm) at the panel zones (Figure 3.111). Some flexural cracking to the cap beam due to gravity loads were also observed (Figure 3.112). This was due to the fact that the cap beam was not a prestressed element. Therefore, flexural cracking due to the concentrated load (vertical ram) was expected during testing. All cracks remained hairline throughout testing.

There was no damage to the footings (Figure 3.113). The addition of circular rebars around the footing socket in HDB was very effective in eliminating the radial cracking to the footings which was previously observed during testing of HDC1 and HDC2.

In summary, as expected the bent formed four plastic hinges at the top and bottom of the columns (Figure 3.114). The extent of damage in MSCs was more than GDCs. Data from the instruments recording the out-of-plane-movement suggested that the out-of-plane movement in HDB was minor (less than 10 mm) when being pushed and pulled in the in-plane direction up to 3.4% drift ratio (100 mm).

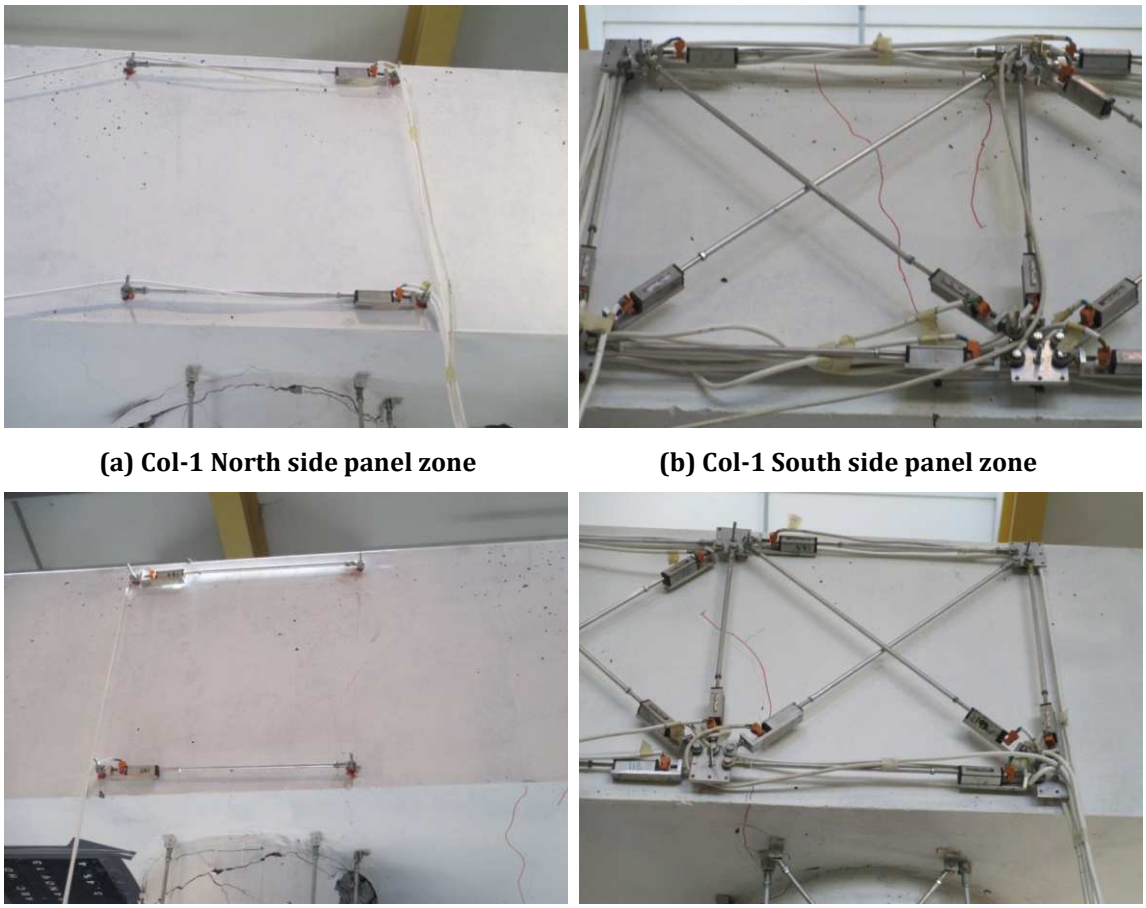

(a) Col-1 North side panel zone **(b) Col-1 South side panel zone**

(c) Col-2 North side panel zone **(d) Col-2 South side panel zone**

Figure 3.111. HDB column to cap beam panel zones at the end of testing (3.4% drift ratio)


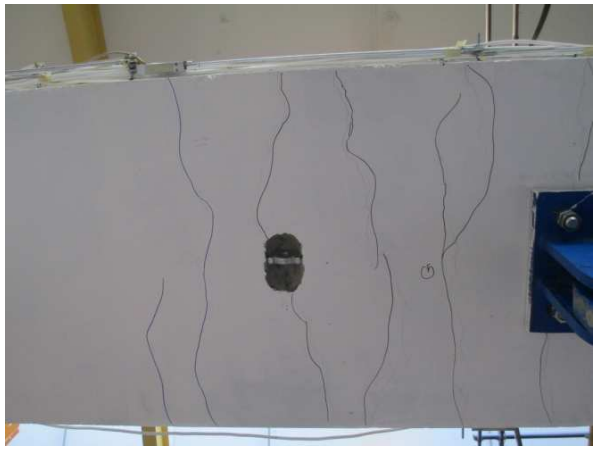

(a) Cap beam flexural cracks under gravity **(b) Cap beam flexural cracks close-up view**

Figure 3.112. HDB cap beam hairline cracking due to concentrated load (gravity ram)

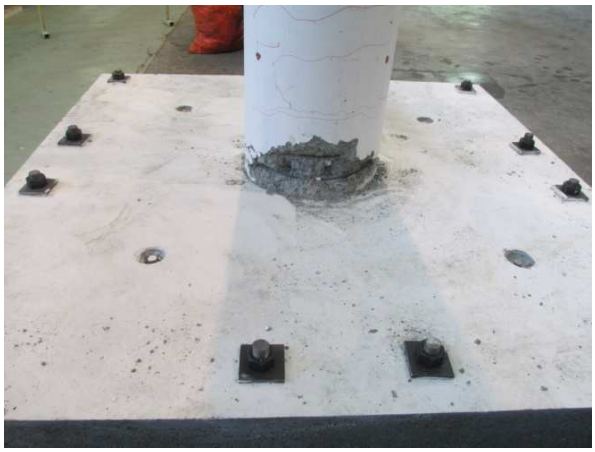


(a) No cracking to Col-1 footing block **(b) No cracking to Col-2 footing block**

Figure 3.113. HDB footings at the end of testing (3.4% drift ratio)




(a) Col-1 East side **(b) Col-1 West side** **(c) Col-2 East side** **(d) Col-2 West side**

Figure 3.114. HDB overall damage at the end of testing (3.4% drift ratio)

The force-drift hysteresis and backbone plots for HDB are shown in Figure 3.115 and Figure 3.116, respectively. The specimen reached its design base shear of 305 kN. The

plots suggest that the bent yielded at 0.85% drift ratio. Given the spalling initiation (ULS performance level) at 2.2%, the displacement ductility at ULS was 2.6. At the end of testing (MCE performance level or 1.5 ULS, 3.4% drift ratio) the displacement ductility was 4. As can be seen from the load-drift hysteresis, there were large residual displacement in the bent after the yielding point. The residual displacement in HDB was approximately 50% of the peak drift during cycles of 2.8% and 3.4% drift ratios.

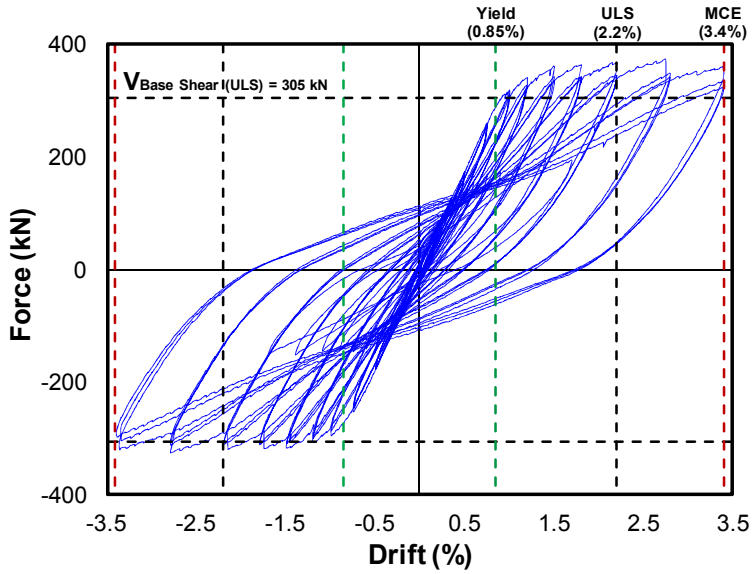

Figure 3.115. HDB force-drift hysteresis

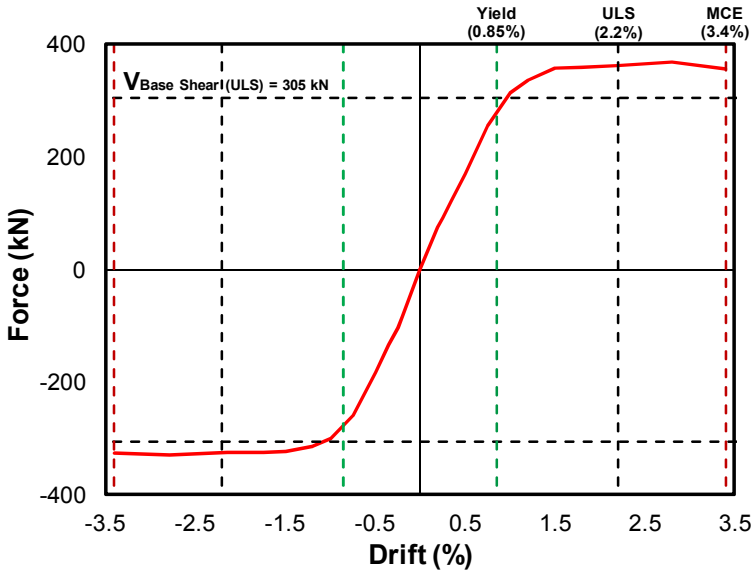

Figure 3.116. HDB backbone curve

It should be noted that in the plots above, the positive vertical axis shows the specimen in pulling. For each cycle of each inputted drift ratio, the specimen was pulled first and

then pushed. The reason behind the specimen being slightly stronger in pulling than pushing in Figure 3.115 was the softening effects following the pulling stage.

The progression of yield at each plastic hinge can be observed from the moment-curvature plots in Figure 3.117. The letters A, B, C, and D, show the sequence of yield progression at the plastic hinges in HDB. From the plots, it may be noticed that the top GDCs had slightly less strength degradation compared to the bottom MSCs. This is compatible with the extent of damage and spalling observed for each connection during testing. It can be seen that once each connection had reached its capacity, with further applied displacement, the strength degradation of the connection had increased.

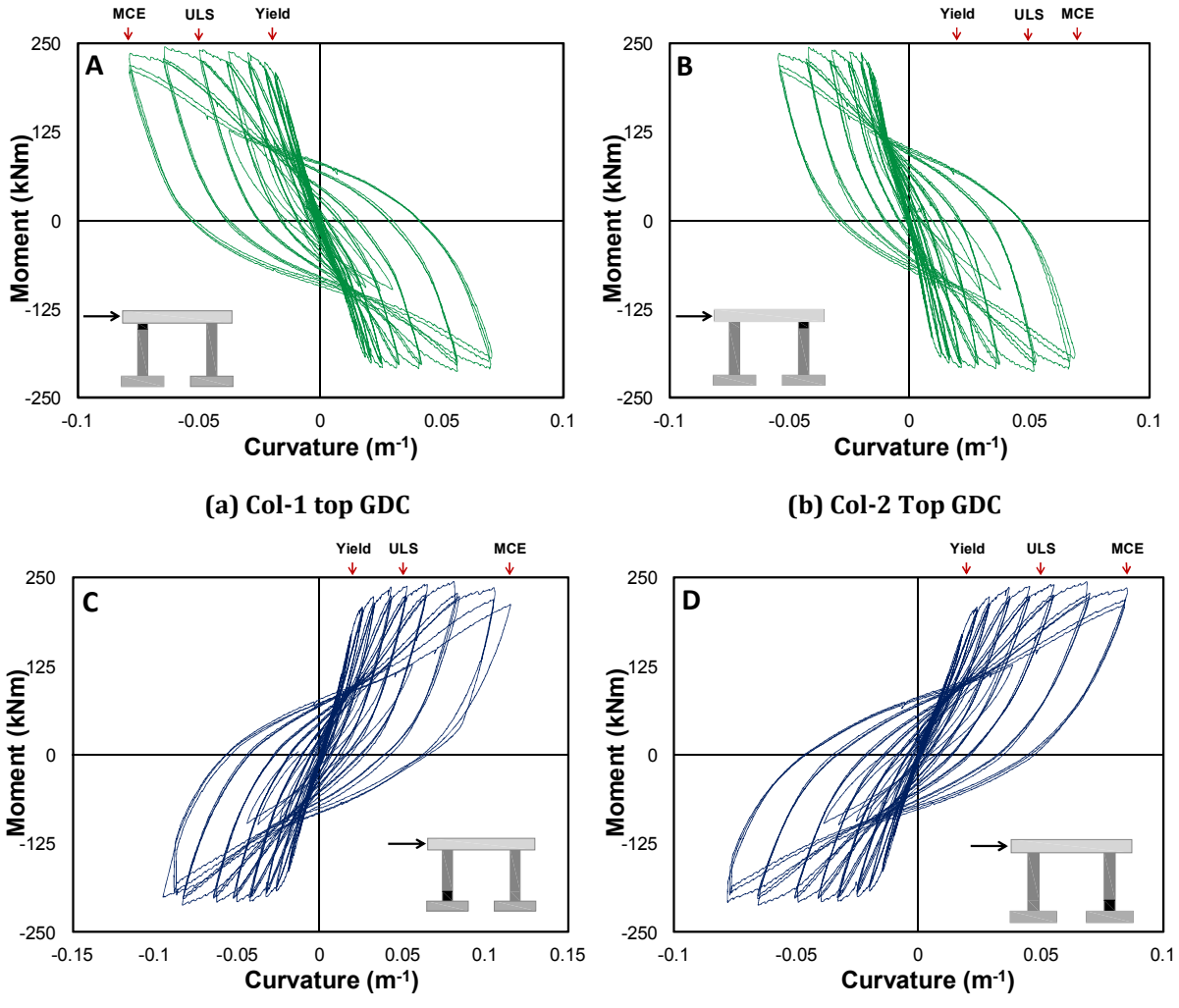

(a) Col-1 top GDC

(b) Col-2 Top GDC

(c) Col-1 bottom MSC

(d) Col-2 bottom MSC

Figure 3.117. HDB moment-curvature hysteresis plots

In Figure 3.117c, it is also obvious that the Column-1 MSC had gone through more deformation (highest curvature value and strength degradation) compared to the other

three connections. As explained previously, this connection had the most spalling compared to the other three during testing. Therefore, the experimental results here show a good correlation with the observation from testing. The higher curvature values for this connection can be due to factors such as variation in construction and proximity of the connection to the loading point (lateral ram).

The corrected area-based damping (hysteretic damping) plot for HDB is presented in Figure 3.118a. Similar to previous tests, there was a relatively linear relationship between the hysteretic damping and the displacement ductility in HDB.

The bent achieved a hysteretic damping of 13.5% at the displacement ductility of 4.3 which corresponded to the 3.4% drift ratio (1.5 times ULS). This was slightly larger than those observed from the experimental results of the cantilever segmental pier systems with MSC and GDC (Section 3.2.7). The experimental hysteretic damping curve for HDB was higher than that of a theoretical Takeda-Thin model up to a ductility of 1.6. The experimental curve was located just under a theoretical Takeda-Thin model up to a ductility of 4.2. Following that, the curve located between the Takeda-Thin and Takeda-Fat curves. It should be noted that the theoretical hysteretic damping curves are plotted for an assumed effective period of $T_{eff} \geq 1\ sec$. The Equivalent Viscous Damping (EVD) at each drift ratio was calculated from Equation 3.19 in Section 3.2.7.1. This is plotted in Figure 3.118b.

A comparison of the hysteretic damping plots between HDB and the cantilever pier system (Section 3.2) are presented in Figure 3.119. It can be observed that the bent had more hysteretic damping compared to four cantilever columns. This was due to presence of more plastic hinges in the bent which enhanced the hysteretic damping in the specimen.

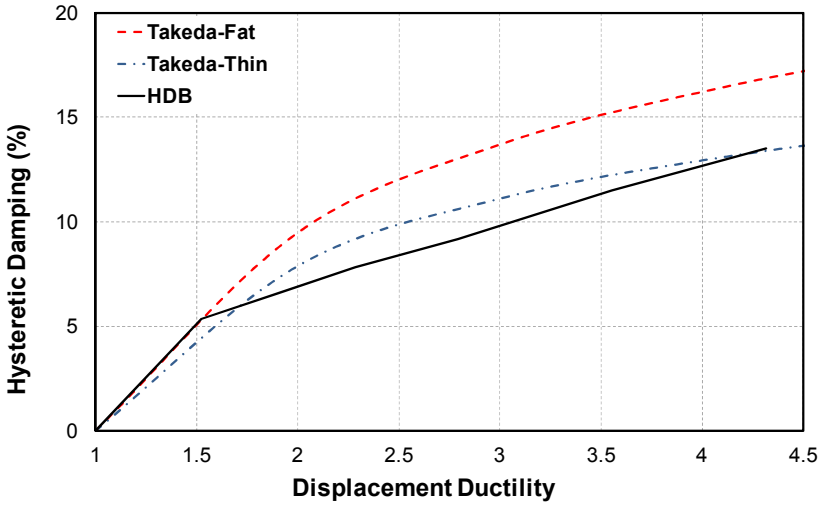

(a) Corrected area-based hysteetic damping (ξ_{hyst})

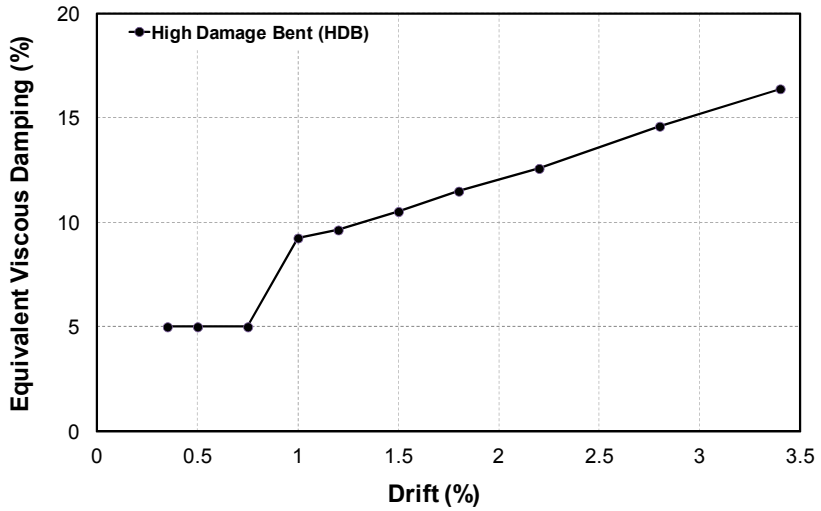

(b) Equivalent viscous damping (ξ_{eq})

Figure 3.118. Hysteretic damping and EVD plots for HDB

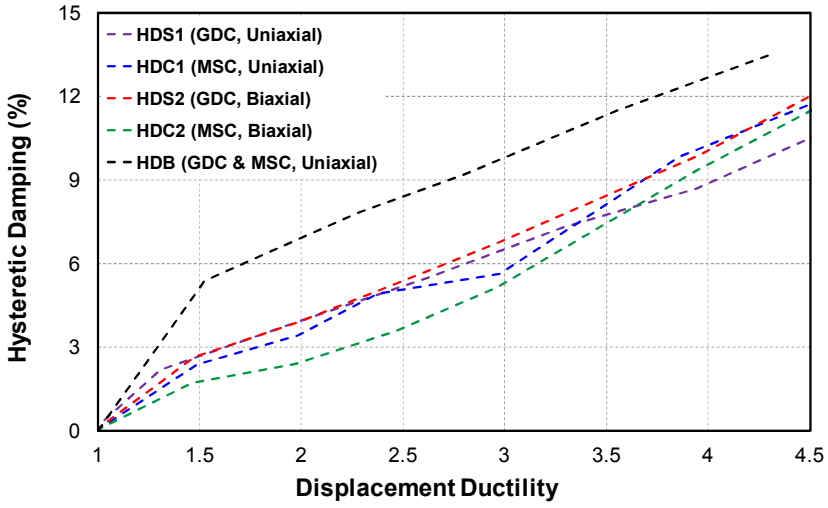

Figure 3.119. Comparison of hysteretic damping (ξ_{hyst}) for HDB and cantilever piers

For a progressive collapse analysis of the bent, the procedure from Austroads Technical Report (Austroads, 2012) was utilized. The report is based on a displacement-based approach and presents strain limits for the reinforcing steel and concrete at the Serviceability and Ultimate Limit States. These limits are defined as follows:

- Strain Limits for Serviceability Limit State:

    a) Reinforcing steel: Tensile strain in reinforcing steel (ε_s) in plastic hinges should not exceed 0.015.

    b) Concrete compressive strain: Compressive strain of concrete (ε_c) in plastic hinges should not exceed 0.004.

- Strain Limits for Ultimate Limit State:

    a) Reinforcing steel: Tensile strain in reinforcing steel (ε_s) in plastic hinges should be calculated in accordance with Equation 3.22 and should not exceed 50% of the cyclic strain at the maximum stress of longitudinal reinforcement (ε_{sul}). In Equation 3.22, ρ_s is the volumetric ratio of lateral reinforcement.

$$\varepsilon_s = 0.015 + 6(\rho_s - 0.005) \leq 0.5\varepsilon_{sul} \tag{3.22}$$

    b) Concrete compressive strain: Compressive strain of concrete (ε_c) in plastic hinges should not exceed the value from Equation 3.23. In Equation 3.23, f'_{cc} is the confined compressive strength of concrete which can be taken as 1.5 time the concrete compressive strength (f'_c), $f_{sy,\,t}$ is the yield strength of lateral reinforcement steel, and ε_{sut} is the strain at maximum stress of lateral reinforcement.

$$\varepsilon_c = 0.004 + 1.4\frac{\rho_s f_{sy,t}\varepsilon_{sut}}{f'_{cc}} \tag{3.23}$$

Using the displacement-based procedure of Austroads Technical Report, a summary of material strain limits with the qualitative performance description (crack widths) for each performance level are presented in Table 3.18.

Table 3.18. Summary of strain limits and associated crack widths for performance levels

Limit States	Reinforcing Steel Strain (ε_s)	Concrete Strain (ε_c)	Crack Width (mm)	Operational Performance Level	Repair Strategy
Yielding (YL)	0.00275	<0.004	<1	Fully Operational	No repair / limited epoxy injection
Serviceability (SL)	0.015	0.004	1-2	Delayed Operational	Epoxy injection / concrete patching
Ultimate Limit State (ULS)	0.0448	0.0176	>2	Delayed Operational	Extensive repair / reconstruction
Maximum Considered Earthquake (MCE)	>0.05	-	Spall	Delayed Operational	Extensive repair / reconstruction

In Accordance with Austroads Technical Report, the yield displacement was calculated to be 24 mm (0.82% drift ratio) for HDB. This is very close to yielding point (0.85%) from the experimental force-drift hysteresis (Figure 3.115). Using the strain limits from Table 3.18, the displacements at the Serviceability and ULS performance limit states were calculated to be 44 mm (1.5% drift ratio) and 79 mm (2.7% drift ratio), respectively.

In accordance with this, at the Serviceability limit state, the ductility (μ) was equal to 1.8. At the design level (ULS), the ductility was 3.3 which satisfied the initially assumed ductility value of 3 adopted during the force-based design process of the bent. At the end of testing (MCE), the ductility was over 4.1. It was clear that the ductility was going to be in excess of 4.1 at the failure point of the bent (rebar rupturing).

Table 3.19 presents a summary of the progressive collapse analysis for HDB in accordance with Austroads Technical Report. Since the bent was tested up to 3.4% drift ratio, the MCE level was taken as this drift ratio which corresponded to 1.25 times ULS drift ratio.

Figure 3.120 presents the deformed shape and progression of force-displacement hysteresis for each of the performance limit states given in Table 3.19. The location of plastic hinges in HDB is shown by circles.

Table 3.19. Summary of progressive collapse analysis for HDB

Limit States	Yielding (YL)		Serviceability (SL)		Ultimate Limit State (ULS)		1.25 ULS (MCE)	
Status	Fully Operational		Delayed Operational		Delayed Operational		Delayed Operational	
Drift (%)	0.82		1.5		2.7		3.4	
Ductility (μ)	1.0		1.8		3.3		4.1	
Moment Capacity	180 kNm		232 kNm		240 kNm		225 kNm	
Strain limits (ε)	ε_c	ε_s	ε_c	ε_s	ε_c	ε_s	ε_c	ε_s
	<0.004	0.00275	0.004	0.015	0.0176	0.0448	-	>0.05
Location	GDC	MSC	GDC	MSC	GDC	MSC	GDC	MSC
Crack size (mm)	0.5	1.5	1.5	3	7	Spall	9	Spall

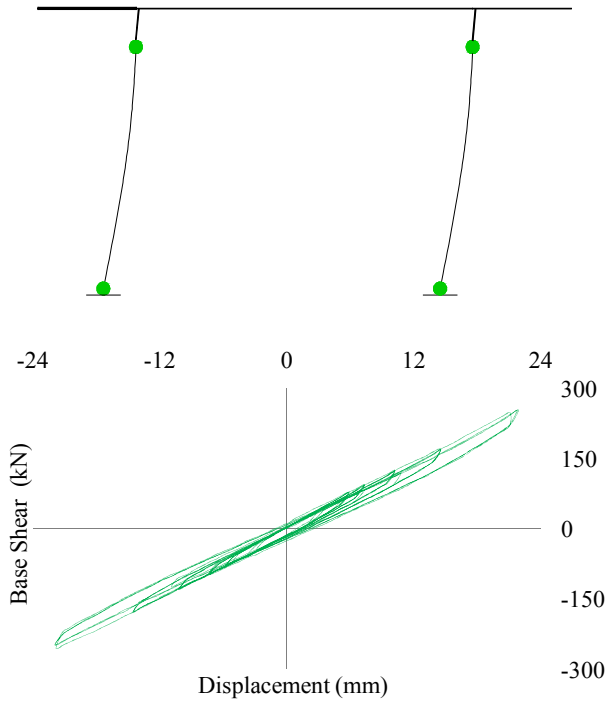

(a) Yielding (0.82%drift ratio)

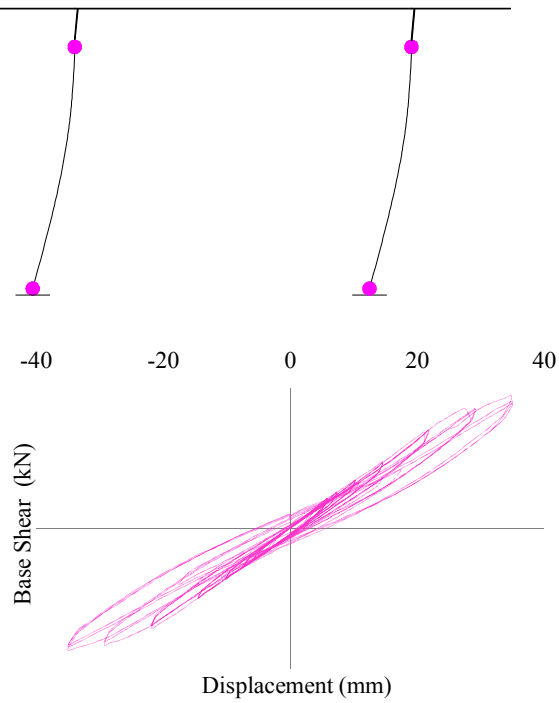

(b) Serviceability (1.5%drift)

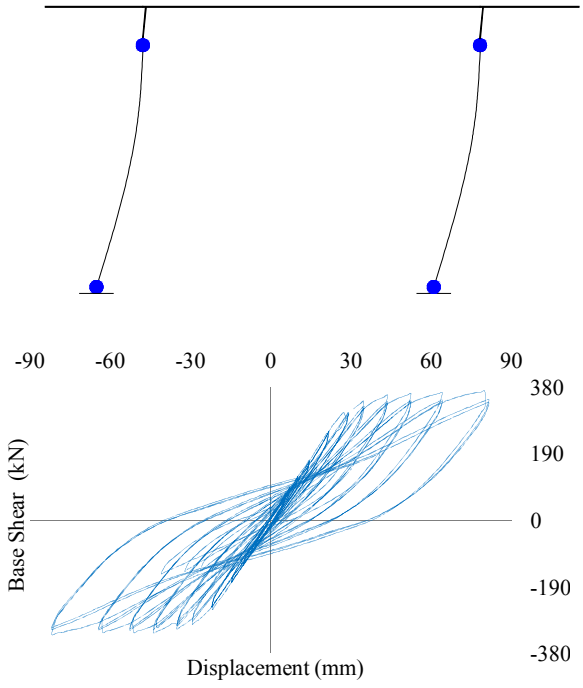

(c) ULS (2.7%drift ratio)

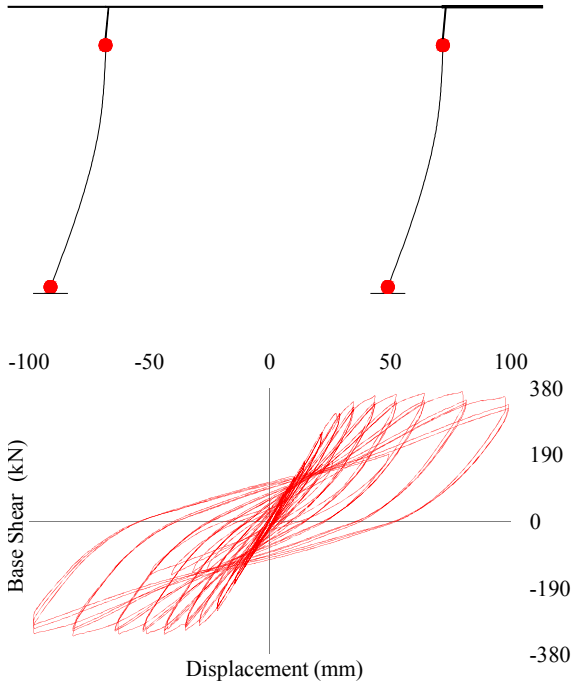

(d) MCE (3.4%drift ratio)

Figure 3.120. HDB deformed shape and Force-drift hysteresis at various limit states

The ADRS plots were constructed using the methodology presented in Section 3.2.71 and shown in Figure 3.48 by taking S_p factor equal to 1.0. The ADRS plots for HDB are

presented in Figure 3.121 for various hazard levels (return periods) from NZS 1170.5 (NZS, 2004).

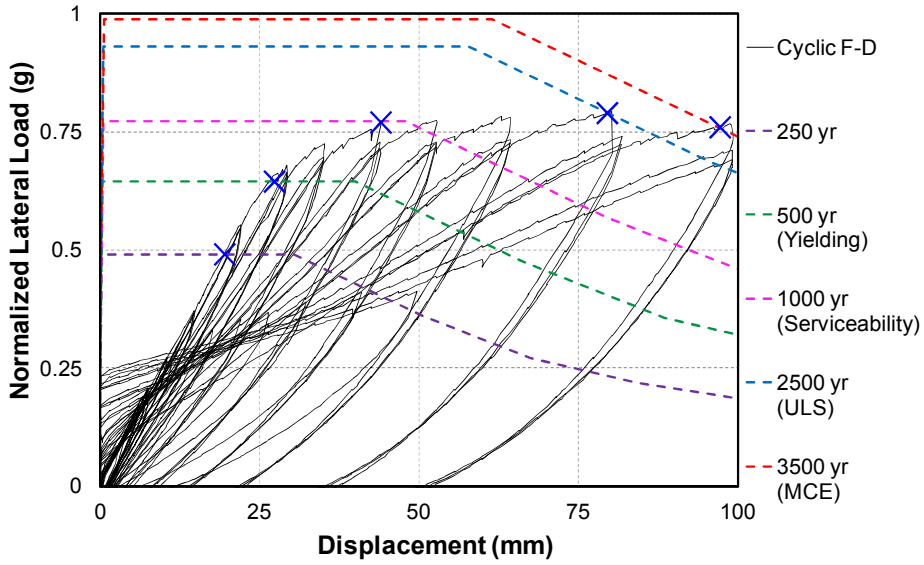

(a) Normalized lateral load - displacement

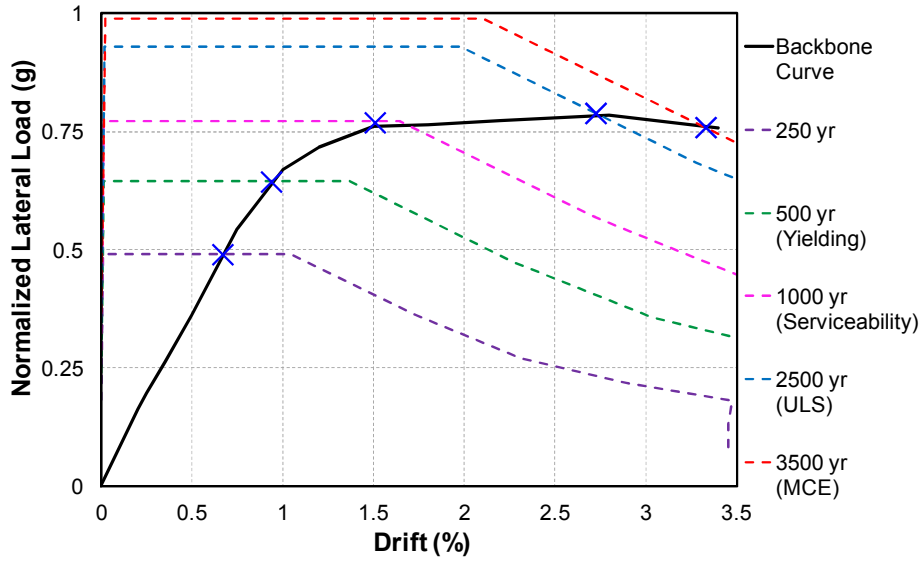

(b) Normalized lateral load - drift

Figure 3.121. ADRS plots for IPT5+GD+AX

According to Figure 3.121, an earthquake with 250 year return period (*R = 0.75*) will generate around 0.67% drift ratio which is well below the yielding point of the bent (0.82%). Similarly, an earthquake with 500 year return period (*R = 1.0*) will result in 0.9% drift ratio in the bent which is just over its yielding point. An event of 1000 year return period (*R = 1.3*) will generate 1.5% drift ratio which corresponds to Serviceability Limit State for the bent.

A ULS earthquake (2500 year return period, *R = 1.8*) will generate 2.7% drift ratio in the bent which corresponds to a ductility of 3.3 at ULS. This is almost equal to ductility that was adopted during the force-based design of the prototype structure ($\mu = 3$). This means that good assumptions were made during the design process of the bent. Finally, a MCE event (3500 year return period, *R = 2.0*) will generate nearly 3.4% drift ratio which is almost 1.2 times greater than ULS drift level. Table 3.20 presents a summary of ADRS results for HDB.

Table 3.20. Summary of ADRS results for HDB

Hazard Levels (Years)	Return Period Factor (R)	Ductility (μ)	Drift (%)	Corrected Equivalent Damping (ξ_{eq}) %
250	0.75	1	0.67	10.37
500	1.0	1.18	0.93	10.75
1000	1.3	1.9	1.5	13
2500	1.8	3.5	2.7	17.85
3500	2.0	4.2	3.33	19.67

The results from ADRS plots in Figure 3.121a and Figure 3.121b are well correlated with the outcome from a progressive collapse analysis of the bent, as presented in Table 3.19 and Figure 3.120 earlier.

The energy dissipated per each cycle of each drift ratio for HDB is presented in Figure 3.122. The dissipated energy was calculated using a numerical integration of the area enclosed inside the hysteresis loop for each four cycles at each drift ratio. It should be noted that the fourth cycle at each drift ratio had half of the amplitude of that drift ratio, as explained in Section 3.2.2.1.

From Figure 3.50 and Figure 3.69, the cumulative dissipated energy for HDS1 (GDC) and HDC1 (MSC) at 3.4% drift ratio can be calculated for each column, respectively. This corresponds to a combined cumulative dissipated energy of approximately 150 kJ. By comparing this value to that of HDB at 3.4% drift ratio in Figure 3.122(120 kJ), the bent had approximately similar cumulative energy dissipation.

However, it should be noted that the longitudinal reinforcing for HDS1 and HDC1 were almost twice of that used in each columns of HDB. At the same time, in HDS1 and HDC1,

there was contribution from a second plastic hinge up at the mid height of the column to a certain level. HDB bent had four plastic hinges (two in GDCs and two in MSCs) and almost half of the longitudinal reinforcing per column as that used in HDS1 and HDC1. The bent had similar cumulative energy dissipation as that of combined HDS1 and HDC1 or that of four cantilever non-segmental columns (2 with GDCs and 2 with MSCs) with the longitudinal reinforcing of each column as half of that shown for HDS1 or HDC1. Figure 123 presents a comparison of the energy dissipation per drift cycle between HDB and the cantilever pier system.

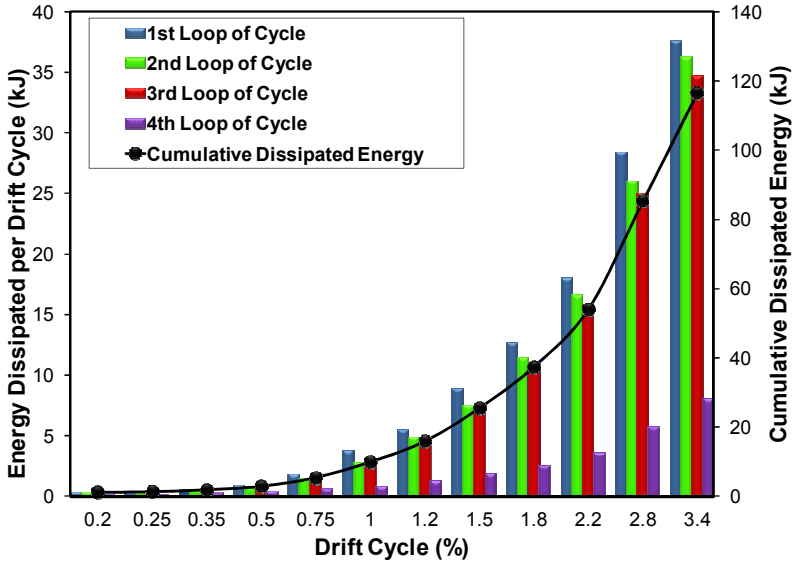

Figure 3.122. HDB dissipated energy (per cycle and cumulative)

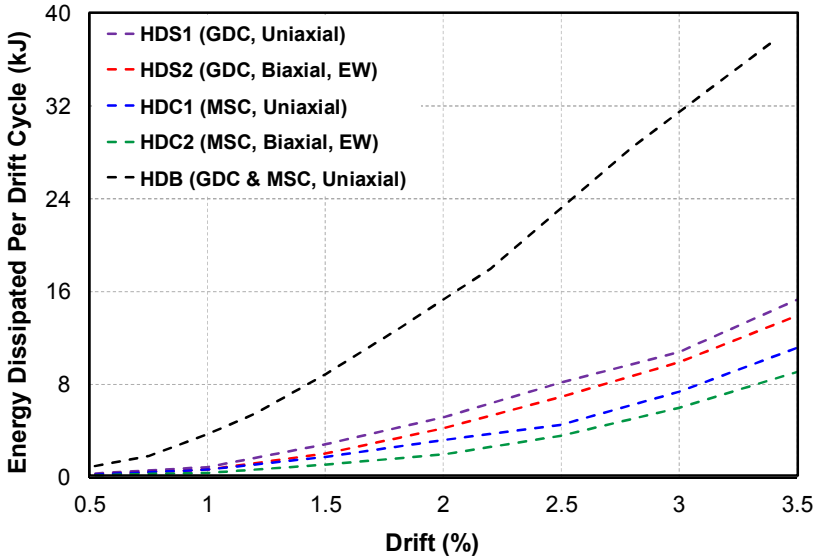

Figure 3.123. Comparison of energy dissipation for HDB and cantilever columns

Figure 3.124 illustrates moment-curvature hysteresis plots for the column to cap beam panel zones. The yield moment and curvature limits of the section have also shown on the plots. The positive vertical axis shows the specimen under pull part of the loading where more cracking was observed. The capacity of the bent was also stronger in pull. From Figure 3.124, it is obvious that both panel zones remained well in their elastic regions. Therefore, it was confirmed that the cap beam remained elastic during testing as it was designed to be a capacity protected element. This shows a good correlation with the observed performance of the cap beam and panel zones during testing.

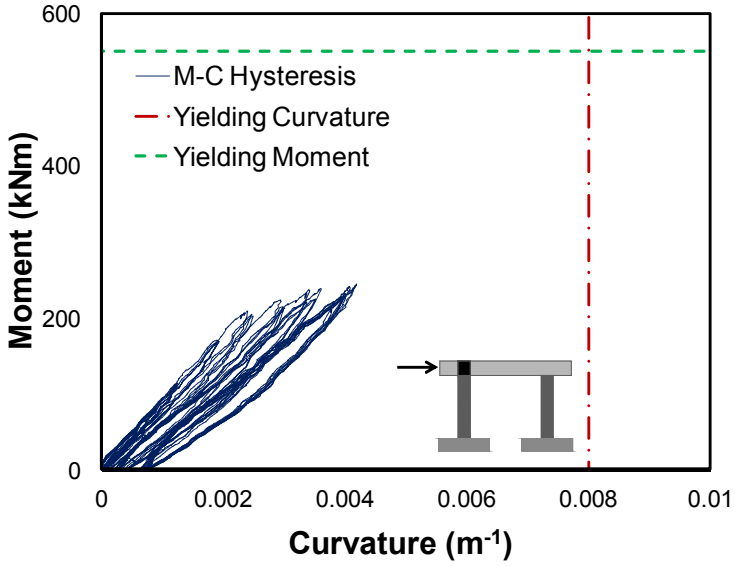

(a) Colum-1 Panel Zone

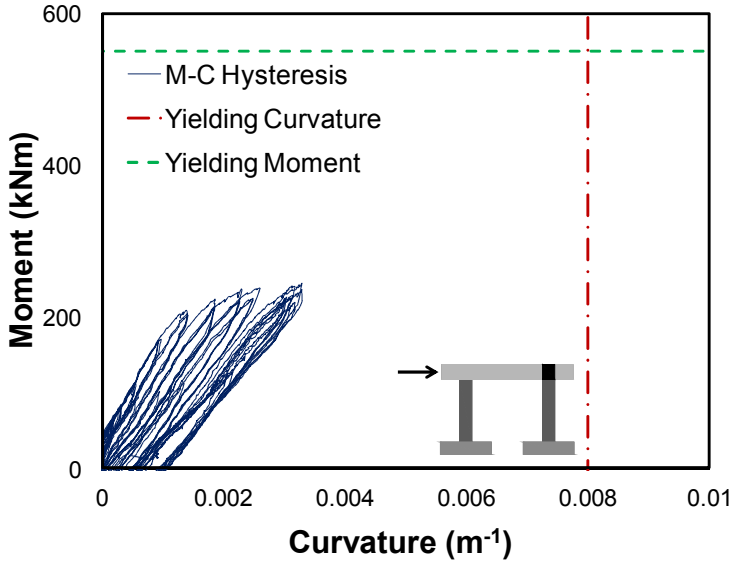

(b) Column-2 Panel Zone

Figure 3.124. HDB column to cap beam panel zone moment-curvature hysteresis plots

3.4 Conclusions

ABC High Damage solution targets a similar seismic performance for the bridge substructure system as that can be expected of a conventional monolithic construction. Therefore, ABC High Damage is sometimes referred as emulative cast-in-place solution.

In the first phase of experimental testing in this research, four half-scale fully precast cantilever segmental piers with High Damage connections were developed and tested. Two columns with square cross-section featured Grouted Duct Connection (GDC) as the primary connection type for the column to footing. The other two columns were circular cross-section and incorporated Member Socket Connection (MSC) as the primary connection type for the column to footing. The segment to segment connection in all cantilever columns was GDC. The columns were tested under uniaxial and biaxial loading. The influence of the axial load was also taken into account during testing of the columns. There were two variations of GDC in the square columns. One type of GDC featured a typical detailing without any extra considerations for limiting the spalling in the column and eliminating the low-cycle fatigue in the starter bars. The other variation of GDC featured armoring of the column base and unbonded length of the starter bars for an enhanced ductility and seismic performance of the column.

In the second phase of testing, a half-scale fully precast bent with two columns was developed and tested. The columns featured MSC for the column to footing connection. The column to cap beam connection was GDC. There was debonding of the starter bars inside the column at the column to cap beam connection. This was intended to limit the damage in the connection and to enhance the overall ductility of the bent.

The prototype development, gravity and lateral loading, design procedure, detailing considerations, construction technology, assembly sequence, experimental testing, observations from testing, and finally experimental results, were thoroughly presented for all four half-scale columns and the half-scale bent. Some of the important detailing considerations for GDC and MSC are summarized here.

For GDC, the length of the grouting ducts were selected to be equal to the development length of that required by NZS 3101 (NZS, 2006) for a conventional monolithic construction. Using steel corrugated grouting ducts provide extra confinement for the

starter bars. This would result in a shorter development length in the starter bars to develop the full capacity of the bar when compared against the monolithic construction. The increase in the confinement of the starter bars can have considerable effects on the strain penetration length which would lead to a strain concentration over shorter length of the starter bars at the column to footing interface. This means, there is a shorter length of the starter bar which has to distribute the total nonlinear deformation in the bar. This would ultimately result into a reduced ultimate drift capacity of the column. The strain concentration at the interface would also make the starter bars susceptible to low-cycle fatigue failure under cyclic loading. Therefore, debonding of the starter bars over certain length at the critical interfaces such as column to footing or column to cap beam would reduce the strain concentration effects which would in return enhances the ultimate drift capacity and ductility of the structure.

Under lateral loading, the opening of a single crack which is also called "gap opening" in GDC was observed in all specimens. This showed a rocking mechanism in GDC which is different than that observed in MSC. The observed plastic hinge length of the columns was approximately equal to the half height/diameter of column cross-section in GDC. According to NZS 3101 (NZS, 2006), this plastic hinge length would correspond to a reversing plastic hinge in a conventional monolithic column.

Another detailing consideration for GDC, in particular for the cantilever pier systems, is the use of armoring to limit the damage and spalling at the base of the column. This would result in an enhanced energy dissipation capacity of the column and would limit any undesirable strength degradation in the connection to great extent.

For MSC, there should be sufficient socket diameter and depth provided during the design stage. Construction tolerances in placing the column inside the socket have to be taken into account. In this research, it was shown that a 20 mm tolerance in the socket diameter was sufficient to allow for the construction tolerances and flow of the grout in between the socket walls and column stub. It is suggested here that further research work is necessary to quantify the maximum gap widths in a MSC for an adequate force transfer between the precast elements. Similarly, the socket depth is of great importance for limiting the stress demands in a MSC. In this research, it was found that a ratio of one to one between the column diameter and the socket depth could be

sufficient enough to push the damage (plastic hinge) away from the footing and socket into the column. However, further investigations are needed to quantify the depth of the footing for various column shapes such as square, octagonal etc.

In terms of construction, MSC offers easier assembly compared to GDC. There is a risk of misalignment of starter bars and grouting ducts in GDC. This carries out a construction risk for GDC as any misalignment would potentially result in significant delay during on-site assembly of the precast elements. Therefore, sufficient tolerances have to be allowed for the grouting ducts during the design process (Marsh et al., 2011). In this research, there was 24 mm tolerance left for the grouting ducts in the cantilever segmental columns. Although, there were some minor misalignment issues during assembly, however, leaving a 34 mm tolerance for the GDCs in the half-scale bent specimen eliminated any misalignment issues during assembly process.

In terms of seismic performance, MSC offers several important advantages over a conventional monolithic construction. In a monolithic construction, it is common to cast the footing first, and then the lower portion of the column which is located just above top face of the footing. This means that there will be a construction joint left at the column to footing interface. It is expected that during a design level earthquake, a full plastic hinge length would occur at the base of the ductile column. However, Canterbury Earthquakes have shown that majority of bridge columns had initiated a single crack opening which was located where the construction joint was left at the column to footing connection (Palermo et al., 2012). Therefore, it had resulted in a shorter plastic hinge length in the column, as well as potential for strain concentrations in the longitudinal bars at the interface. Using a MSC, there will not be any construction joint between the column and footing. This gives the advantage for a longer plastic hinge length in the column during a design level earthquake. The observed plastic hinge length of the columns featuring MSC was approximately equal to the diameter of the column cross-section. According to NZS 3101 (NZS, 2006) this plastic hinge length would correspond to a uni-directional plastic hinge in cast-in-place construction where inelastic rotation can develop on both sides of the critical section.

MSC also offers better durability for the column to footing connection as there would not be any reinforcing interchange between the column and footing (Marsh et al., 2011).

Further research at the University of Canterbury is currently being undertaken on durability of MSC and GDC (Andisheh et al., 2014).

In summary, the precast construction process for the columns and bent was faster and relatively simple compared to a conventional monolithic construction. The construction techniques for precast cantilever segmental column and precast bent provide potential for significant time savings (precast segments, cap beam, columns, and possibly footings) through avoiding the need of pouring concrete on-site. During the assembly process of the precast columns, there was minimal wet work required. This had simplified the construction process to greater extent. At the same time, significantly less equipment and labor would be needed on-site for the assembly of precast elements compared to that required in a monolithic construction.

The experimental testing for GDC and MSC showed promising results for using these type of emulative cast-in-place connections between the precast bridge substructure elements in seismic regions. The connections achieved good strength and ductility levels by formation of plastic hinges in the column which is similar to what can be expected from a monolithic construction. There was no inelastic deformation in the elements which were designed to be capacity protected such as footings and cap beam. The connections had slightly lower energy dissipation when compared against theoretical models for the monolithic construction to a certain level of ductility.

Following the cyclic loading of the columns with MSC up to their failure points, punching shear tests were carried out on the footings to ensure gravity load carrying capacity of MSC. Testing showed sufficient resistance (at least 3 times greater than design gravity load of the column) of the grouting interface between the socket walls and the column stub.

All specimens in this research satisfied the criteria for operational performance levels. This means that by using ABC High Damage solution, the bridge would remain open to traffic with delayed or limited functionality after a design level earthquake. At the same time, the bridge will not collapse during a maximum considered earthquake. This is similar to the current widely practiced philosophy for the seismic design of monolithic bridges around the world. Observations from testing and experimental results showed that ABC High Damage technology would have residual displacement following a big

earthquake. The bridge would need extensive repair or possible replacement for long term resiliency. This means that the cost of repairing, downtime, and residual displacement, will be potential post-earthquake issues for ABC High Damage or High Damage connections. Therefore, in the third phase of testing in Chapter 5, an innovative technology for ABC in high seismicity have been developed and tested. This solution is titled "ABC Low Damage". It is developed as the evolution for ABC High Damage and provides a better seismic performance that minimizes the cost of repairs for the bridge. At the same time, when compared against ABC High Damage or the conventional monolithic construction, it eliminates the residual displacement and downtime in the structure.

3.5 Bibliography

1. American Concrete Institute (ACI) (1991). Standard Practice for Selecting Proportions for Normal, Heavy weight, and Mass Concrete, ACI 211-91. Farmington Hills, Michigan, United States.

2. American Concrete Institute (ACI) (2001). Acceptance Criteria for Moment Frames Based on Structural Testing, Report No. ACI T1.1-01, Farmington Hills, Michigan, United States.

3. American Society for Testing and Materials (ASTM) (2005). Standard Test Method and Definitions for Mechanical Testing of Steel Products, ASTM A370-05. ASTM International, West Conshohocken, Pennsylvania, United States.

4. American Society for Testing and Materials (ASTM) (2005). Standard Test Method for Compressive Strength of Cylindrical Concrete Specimens, ASTM C39/C39M-05. ASTM International, West Conshohocken, Pennsylvania, United States.

5. American Society for Testing and Materials (ASTM) (2005). Standard Test Method for Sampling and Testing Grout, ASTM C1019-05. ASTM International, West Conshohocken, Pennsylvania, United States.

6. American Society for Testing and Materials (ASTM) (2012). Standard Practice for Making and Curing Concrete Test Specimens in the Field, ASTM C31/C31M-12. ASTM International, West Conshohocken, Pennsylvania, United States.

7. American Society for Testing and Materials (ASTM) (2012). Standard Test Method for Slump of Hydraulic-Cement Concrete, ASTM C143/C143M-12. ASTM International, West Conshohocken, Pennsylvania, United States.

8. Andisheh, K., Scott, A., and Palermo, A. (2014). Preliminary Estimation of Reduction Factors in Mechanical Properties of Steel Reinforcement due to Pitting Simulated Corrosion. Proceedings of New Zealand Society for Earthquake Engineering Conference, Auckland, New Zealand.

9. Austroads Technical Report (2012). Bridge Design Guidelines for Earthquakes. Austroads, Sydney, Australia.

10. Boomer, J. J. and Mendis, R. (2004). Scaling of Spectral Displacements Ordinates with Damping Ratios. Earthquake Engineering and Structural Dynamics, 34(2):145–165.

11. Brenes, F., Wood, S., and Kreger, M. (2006). Anchorage Requirements for Grouted Vertical-Duct Connectors in Precast Bent Cap Systems, Report No. 0-4176-S. Center for Transportation Research, the University of Texas at Austin, Texas, United States.

12. California Department of Transportation (Caltrans) (2013). Seismic Design Criteria-Version 1.7. Caltrans, Sacramento, California, United States.

13. Coffin, L. F. J. (1954). A Study of the Effects of Cyclic Thermal Stresses on a Ductile Material. Trans., American Society of Mechanical Engineers (ASME), 76:931-950.

14. Dwairi, H. M., Kowalsky, M. J., and Nau, J. M. (2007). Equivalent Damping in Support of Direct Displacement-Based Design. Journal of Earthquake Engineering, 11(4):512-530.

15. Faccioli, E., Paolucci, R., and Rey, J. (2004). Displacement Spectra for Long Periods. Earthquake Spectra, 20(2):347–376.

16. Haraldsson, O. S., Janes, T. M., Eberhard, M. O., and Stanton, J. F. (2013). Seismic Resistance of Socket Connection between Footing and Precast Column. Journal of Bridge Engineering, 18(9):910-919.

17. Jacobsen, L. S. (1930). Steady Forced Vibrations as Influenced by Damping. American Society of Mechanical Engineers (ASME) Transactions, 52(1):169-181.

18. Kawashima, K., Hosoiri, K., Shoji, G., and Sakai, J. (2001). Effects of Un-Bonding of Main Reinforcements at Plastic Hinge Region on Enhanced Ductility of Reinforced Concrete Bridge Columns. Structural and Earthquake Engineering. Proceedings of Japan Society of Civil Engineering, 689 (I-57):45-64.

19. Macalloy (2011). Bar and Cable Systems: Post-Tensioning System Macalloy 1030/S1030. Sheffield, United Kingdom.

20. Mander, J., Panthaki, F., and Kasalanati, A. (1994). Low-Cycle Fatigue Behavior of Reinforcing Steel. Journal of Materials in Civil Engineering. 6:453-468.

21. Mander, J., Priestley, M. J. N., and Park, R. (1988). Theoretical Stress-Strain Model for Confined Concrete. Journal of Structural Engineering, 114(8):1804-1826.

22. Manson, S. S. (1953). Behavior of Materials under Conditions of Thermal Stress. Heat Transfer Symposium, University of Michigan Engineering Research Institute, Ann Arbor, Michigan, United States, 9-75.

23. Marriott, D. (2009). The Development of High-Performance Post-Tensioned Rocking Systems for the Seismic Design of Structures. PhD Thesis, University of Canterbury, Christchurch, New Zealand.

24. Marsh, M. L., Wenli, M., Garrett, B. E., Stanton, J. F., Eberhard, M. O., and Weinert, M. D. (2011). Application of Accelerated Bridge Construction Connections in Moderate-to-High Seismic Regions, NCHRP Report 698. TRB, National Research Council, Washington, D.C., United States.

25. New Zealand Standards (NZS) (2001). Steel Reinforcing Materials, AS/NZS 4671. Wellington, New Zealand.

26. New Zealand Standards (NZS) (2004). Structural Design Actions: Earthquake Actions, NZS 1170.5. Wellington, New Zealand.

27. New Zealand Standards (NZS) (2006). The Design of Concrete Structures, NZS 3101. Wellington, New Zealand.

28. New Zealand Transport Agency (2003). Bridge Manual, Second Edition. Wellington, New Zealand.

29. New Zealand Transport Agency (2008). Standard Precast Concrete Bridge Beams, Report No. NZTA 364. Wellington.

30. New Zealand Transport Agency (2013). Bridge Manual, Third Edition. Wellington, New Zealand.

31. Osanai, Y., Watanabe, F., and Okamoto, S. (1996). Stress Transfer Mechanism of Socket Base Connections with Precast Concrete Columns. ACI Structural journal, 93(3):266-276.

32. Palermo, A., Wotherspoon, L., Hogan, L. S., Heux, M. L., Camnasio, E., and Brando, M. (2012). Seismic Performance of Concrete Bridge during Canterbury Earthquakes. Proceedings of the American Society of Civil Engineering Structures Congress, Chicago, Illinois, United States.

33. Pampanin, S., Marriot, D., and Palermo, A. (2010). PRESSS Design Handbook. New Zealand Concrete Society (NZCS) Incorporation, Auckland, New Zealand.

34. Pang, J. B. K., Eberhard, M. O., and Stanton, J. F. (2010). Large-Bar Connection for Precast Bridge Bents in Seismic Regions. Journal of Bridge Engineering, 15(3):231-239.

35. Paulay, T., and Priestley, M. J. N. (1992). Seismic Design of Reinforced Concrete and Masonry Buildings. John Wiley & Sons, Incorporation, New Jersey, United States.

36. Priestley, M. J. N., Calvi, G. M., and Kowalsky, M. J. (2007). Displacement-Based Seismic Design of Structures. IUSS Press, Pavia, Italy.

37. Raynor, D.J., Lehman, D.E., and Stanton, J. F. (2002). Bond-Slip Response of Reinforcing Bars Grouted in Ducts. American Concrete Institute Structural Journal, 99(5):568-576.

38. Sika Group (2015). http://www.sika.com/

39. Stanton, J. F., Wacker, J. M., Hieber, D. G., and Eberhard, M. O. (2005). Design of Precast Concrete Piers for Rapid Bridge Construction in Seismic Regions. Washington State Transportation Center (TRAC), University of Washington, Seattle, Washington, United States.

40. White, S. (2014). Controlled Damage Rocking Systems for Accelerated Bridge Construction. Master Thesis, University of Canterbury, Christchurch, New Zealand.

4. DEVELOPMENT AND TESTING OF INNOVATIVE METALLIC DISSIPATERS

4.1 Introduction

This Chapter presents the development and testing of novel metallic energy dissipaters. In the first part of the Chapter, a detailed literature review on the existing technologies for supplemental damping and their past applications in Dissipative Controlled Rocking (DCR) connections is thoroughly discussed.

In the second part of the Chapter, concepts for many variations of innovative metallic dissipaters are presented. The dissipaters are in the shape of bracing and mini plug and play devices which can be used in both building and bridge structures. The energy dissipation mechanism in these metallic dissipaters is through axial deformation in compression and tension. The innovative dissipaters incorporate important features which include, but are not limited to easy replaceability, smart packaging, balanced force in tension and compression, and minimal strength degradation under cyclic loading. Experimental testing was carried out on several prototypes to not only validate the concepts, but also to confirm the dissipater suitability for application in DCR connections for ABC Low Damage. The concepts for the innovative dissipaters contributed into filing of a United States Patent Application (Keats, Palermo, and Mashal) by the University of Canterbury. The objectives of this Chapter are as follows:

- A literature review on the existing supplemental damping systems.
- Development and testing of new bracing type and mini plug and play devices.
- Investigating the suitability of mini plug and play devices for ABC Low Damage.
- Overview of the available dissipation mechanisms for three variations of ABC.

4.2 Literature Review on Dampers

In structural engineering applications, dampers are commonly used for seismic and wind protection of building and bridge structures. There are also other applications of dampers in vibration control of flooring systems, expensive medical and scientific equipment, non-structural components, and electrical transformers.

Over the last five decades, there have been many types of dampers developed and tested around the world. In general, dampers can be classified under three categories that include metallic, friction, and viscous dampers which are discussed as follows.

4.2.1 Metallic Dampers

Metallic dampers or dissipaters are used to absorb the energy generated by earthquakes in a structure. They are part of displacement-activated supplemental damping devices which demonstrate hysteretic behavior under cyclic loading. The energy dissipation mechanism in metallic dampers relies on yielding and inelastic deformation of the metals. The yielding mechanism in a metallic dissipater can be flexural, shear, or axial deformation. A typical hysteretic behavior for metallic dampers is illustrated in Figure 4.1.

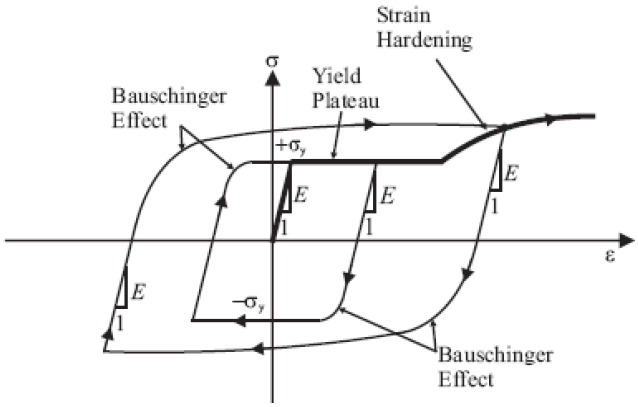

Figure 4.1. Hysteretic response of metallic dampers (Christopoulos and Filiatrault, 2006)

The first application of this type of dampers was in South Rangitikei Viaduct in New Zealand (Kelly et al., 1972), as previously discussed in Section 2.3.3.1 of Chapter 2. More information is presented in Section 4.2.1.4 of this Chapter.

Past research investigations into the use of metallic dampers in Dissipative Controlled Rocking (DCR) connections in buildings include Christopoulos et al. (2002), and Wang

and Filiatrault (2008) (steel buildings), Palermo et al. (2006) and Iqbal et al. (2007) (timber buildings), and Priestley (1991, 1996) Priestley et al., (1999), Stanton et al. (1991, 1997), Stone et al. (1995), and Restrepo et al. (2001) (concrete buildings).

Examples of past research work on metallic dampers in DCR connections for concrete bridges include Palermo (2004), Stanton et al. (2005), Palermo et al. (2005[1], 2007, and 2008), and Marriott (2009).

In the last several decades, there have been many types of metallic dampers developed primarily in New Zealand, Japan, United States, and Canada. A brief summary for some of the popular metallic dampers is presented in the next several sections.

4.2.1.1 Added Damping, Added Stiffness (ADAS)

The early version of Added Damping Added Stiffness (ADAS) systems was known as tapered steel energy dissipaters. This type of dissipaters was originally developed by the Engineering Seismology Section of the Physics and Engineering Laboratory in New Zealand in the late 1970s.

The tapered plate is fixed to a structure in a cantilever plate manner (Figure 4.2a). During an earthquake, the cantilevered plate is loaded along the free end. The deflection of the plate beyond elastic region will cause yielding of the sections along the height of the plate which dissipates energy. This type of dampers was used in seismic protection of King Edward Street Overpass in Dunedin and a rocking chimney at the Christchurch Airport (Figure 4.2d) in New Zealand in 1977, (Tyler, 1978).

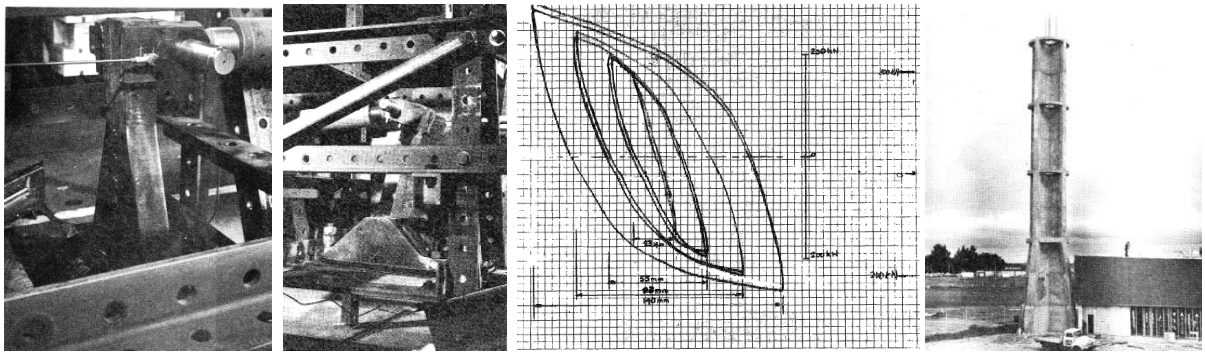

(a) Tapered damper (b) Under testing (c) Hysteretic response (d) Christchurch Airport

Figure 4.2. (a, b, and c) Damper King Edward St. Overpass in Dunedin (250 kN capacity and ±75 mm stroke) (d) Rocking chimney at Christchurch Airport, after Tyler (1978)

ADAS was later developed as an evolution for tapered steel plate dissipaters. In ADAS, several interconnected yielding plates are used in series, as shown in Figure 4.3. Early applications of ADAS devices were intended for piping systems (Stiemer et al., 1981). The first known commercial manufacturer of early versions of ADAS was Bechtel Corporation in the United States.

The device is normally consisted of steel plates. The geometry of the plate can be optimized for enhanced energy dissipation. For this reason, it is preferred that the plastic moment at each section along the height of the plate is reached simultaneously. Past studies have shown that the triangular plate or X-plate geometry (Figure 4.3) can be the desirable configurations for this type of dampers.

Application of ADAS in braced frames was studied and tested by Bergman and Goel (1987), Whittaker et al. (1989), and Whittaker et al. (1991). The damper was used as part of chevron bracing system, as shown in Figure 4.3. During an earthquake, the relative displacement between the apex of chevron and the above floor is causing the device to start yielding, and therefore dissipating seismic energy.

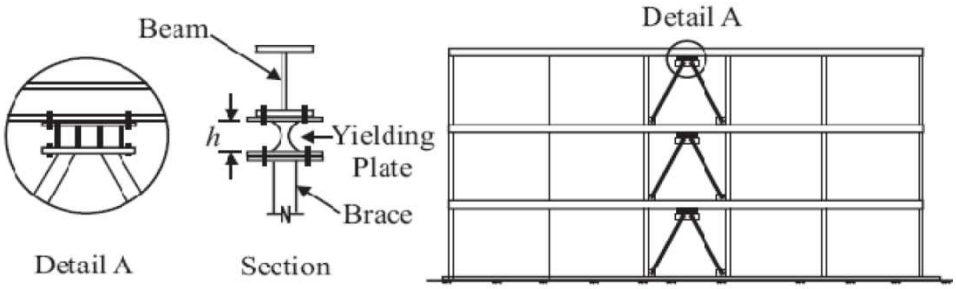

Figure 4.3. ADAS application in chevron bracing systems, after Christopoulos and Filiatrault (2006)

Studies by Whittaker et al. (1991) showed that ADAS elements can sustain 100 loading cycles at a displacement three times greater than their yielding point with no strength degradation, as presented in Figure 4.4. The research concluded that the ADAS elements can achieve a displacement ductility of 10 before failure.

(a) **(b)** **(c)** **(d)**

Figure 4.4. (a) Test frame with ADAS elements (b) A typical X-plate ADAS element detail (c) X-plate after testing (d) Force-displacement hysteresis of ADAS elements, after Whittaker et al. (1991)

Another variation of ADAS called "Triangular Added Damping Added Stiffness" (TADAS) was developed by Tsai et al. (1993) at the National Taiwan University. In TADAS, the elements are triangular plates which are welded to a plate on top, but are free to move in a slotted base plate (Figure 4.5b). The slotted holes at the base plate prevent the plates from being affected by gravity loads. At the same time, there is no need of a rotational restraint at the top of the brace connection. Despite offering additional advantages when compared against ADAS, the construction and welding procedure for a TADAS system can be more complicated and expensive (Christopolous and Filiatrault, 2006). Figure 4.5 presents details of TADAS studied by Tsai et al. (1993).

A variation of TADAS called "Cast Steel Yielding Brace" (YBS) was studied by Gray (2012) at the University of Toronto in Canada. In this type of TADAS, a cast steel connector is used in a concentrically braced frame (Figure 4.6a). The energy dissipation comes from yielding of the steel plates (similar to TADAS) which are cast with the connector. This type of damper eliminates the need for welding and bolting of the plates to the connector. Experimental results have shown stable hysteretic response of the brace (Figure 4.6b). Despite offering advantages such as tension stiffening at large displacements and elimination of welding and bolting, the manufacturing cost of the brace due to casting of the connector can be higher than other versions of TADAS.

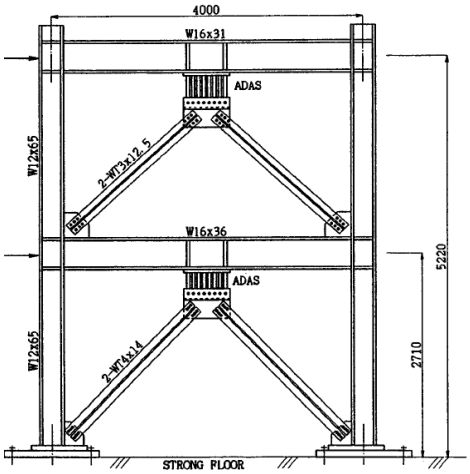

(a) TADAS in a chevron bracing system

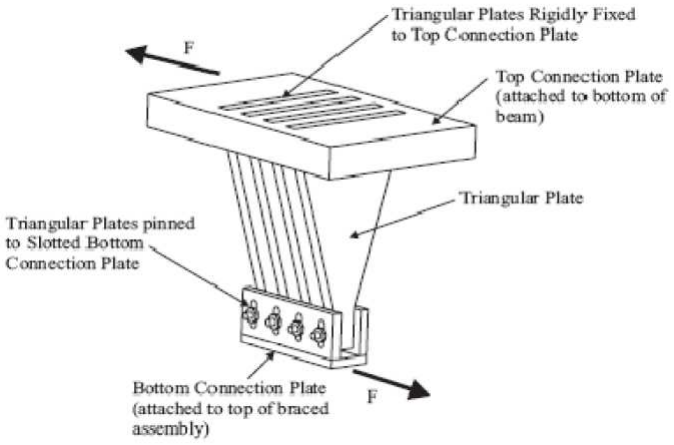

(b) TADAS elements and details

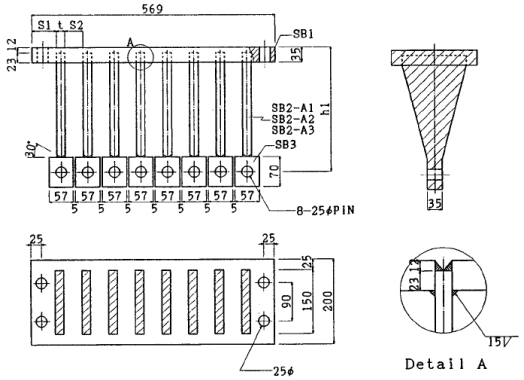

(c) Details of welded TADAS for testing

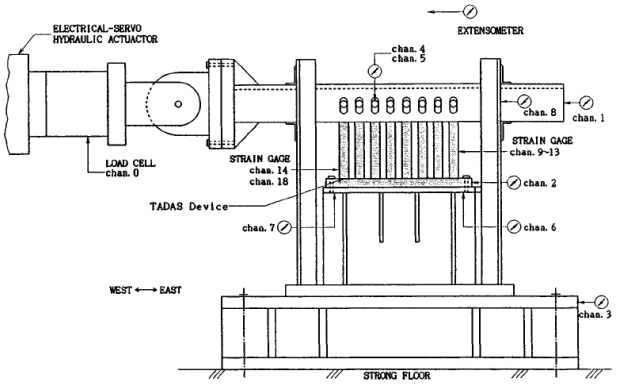

(d) Experimental setup

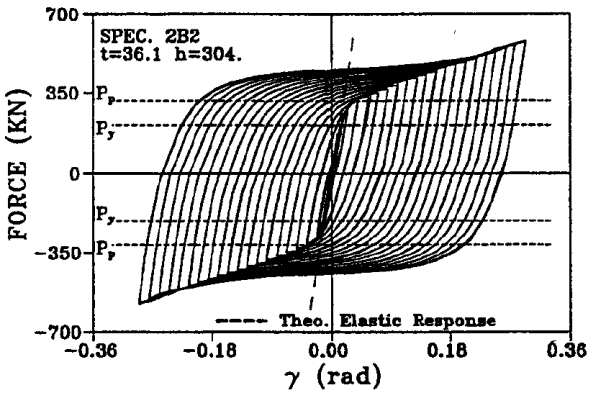

(e) Force-rotation hysteresis loops

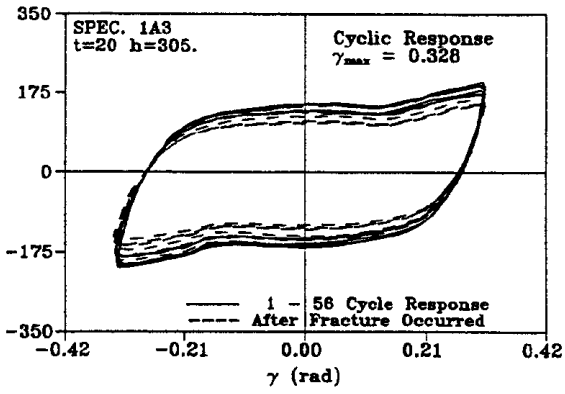

(f) Backbone curve

Figure 4.5. TADAS system, after Tsai et al. (1993)

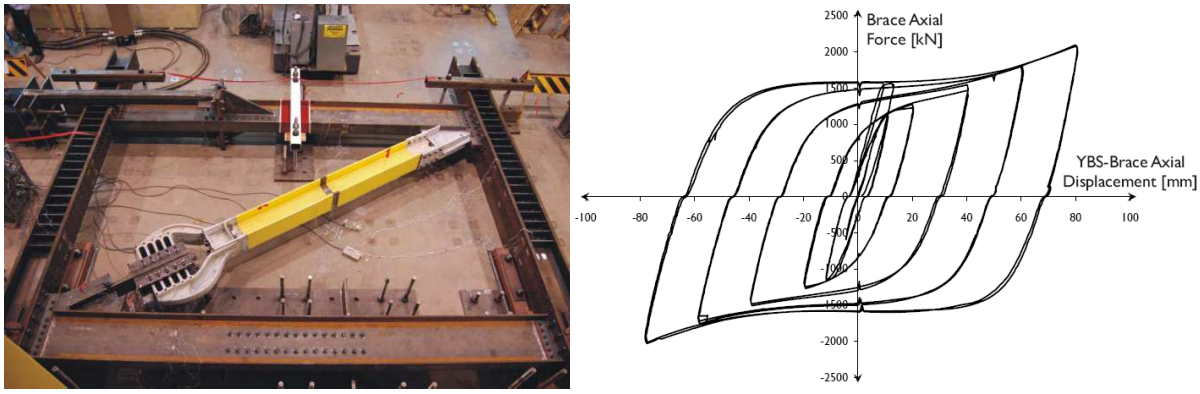

(a) YBS under testing in a steel braced frame **(b) Force-displacement hysteresis of YBS**

Figure 4.6. Cast steel yielding brace, after Gray (2012)

In summary, all variations of ADAS system developed and tested over the last several decades have shown good energy dissipation. ADAS systems have been used in seismic protection of bridges and buildings in New Zealand and the United States. Despite offering many advantages, the low-cycle fatigue failure and the replacement cost of the dampers after a big earthquake are the downsides of this type of metallic dampers.

4.2.1.2 Lead Extrusion Devices

Lead Extrusion Device (LED) was developed in the mid 1970s by Robinson and Greenbank (1976) in New Zealand. In a LED, the lead is extruded through orifices by a steel shaft. There are many advantages associated with LEDs such as the below:

1. Stable hysteretic behavior for a large number of cycles
2. No low-cycle fatigue failure of the device, as lead re-crystallizes in a room temperature
3. Environmental factors do not have a considerable effect on the behavior of LED
4. Strain rate does not affect the hysteretic response
5. Insignificant aging effects of LED

There were two types of LEDs developed by Robinson and Greenbank (1976), the constricted tube (Figure 4.7a, top) and the bulged shaft (Figure 4.7a, bottom). Experimental force-displacement hysteresis plots for the constricted tube and bulged shaft LEDs are presented in Figure 4.7b and Figure 4.7c, respectively.

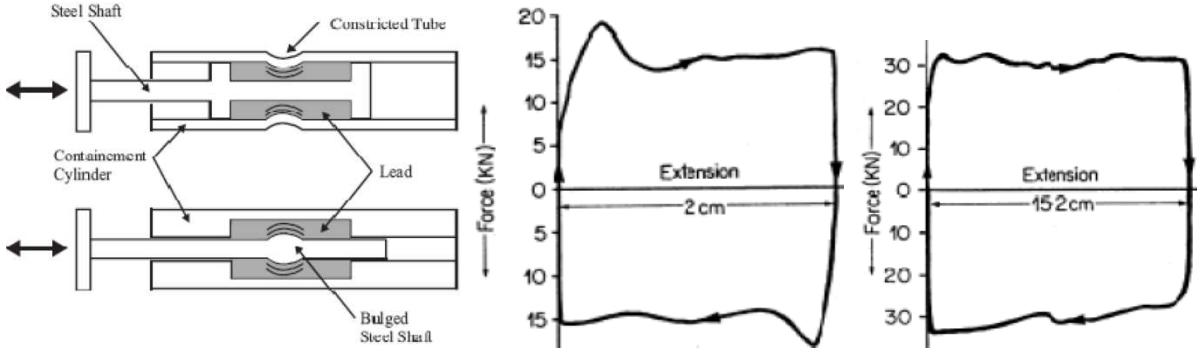

(a) Types of LEDs **(b) Constricted tube hysteresis** **(c) Bulged shaft hysteresis**

Figure 4.7. Lead extrusion devices (Robinson and Greenbank, 1976)

In summary, LEDs have been used in seismic protection of several bridges in New Zealand, as previously presented in Chapter 2 (Robinson, 1995). LEDs have several unique features such as not being susceptible to low-cycle fatigue failure and the behavior is independent of the environmental factors. There have not been many applications of this type of dampers. One of the reasons for this could be the higher cost of manufacturing which would require high precision machining of the parts.

4.2.1.3 Buckling-Restrained Braces (BRBs)

Buckling-Restrained Braces (BRBs) are the most common type of metallic dampers. BRB is used as a bracing element inside a frame. There have been many applications of BRBs in buildings located in seismic and wind prone regions in New Zealand, United States, Europe, and Latin America (Figure 4.8b). Examples of past research investigations on BRBs include Takeda et al. (1976), Murata et al. (1980), Watanabe et al. (1988), and Black et al. (2002). BRBs have been included in the building codes in the United States, "Seismic Provisions for Structural Steel Buildings" (AISC 341, 2010). This makes this type of dampers more attractive for practitioners.

A typical BRB contains an unbonded steel core plate which is encased in a steel tube filled of concrete (Figure 4.8a). A thin layer of lubricant on the inner surface of the tube is normally applied to overcome any friction between the core plate and the concrete surface. During a lateral movement as the brace is stretched, the unbonded steel core carries the axial load and is yielding. When the brace is compressed, the outer tube is confining the steel core, and thus prevents from buckling of the core. This results into a

stable force-displacement hysteresis for the brace in both tension and compression (Figure 4.8c).

In contrast to a BRB, in a conventional Concentrically Braced Frames (CBF) the brace yields in tension, but is not protected against buckling in compression. This means that the hysteresis response of the brace is not balanced in tension and compression. Therefore, it results in a reduced energy dissipation capacity in the brace. At the same time, the brace would be susceptible to premature failure following buckling. Figure 4.8d presents a comparison of hysteresis response between a BRB and CBF.

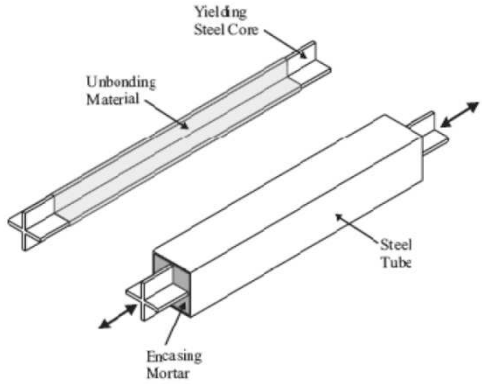

(a) Components of a BRB

(b) BRBs in a building (courtesy of Structure Archives)

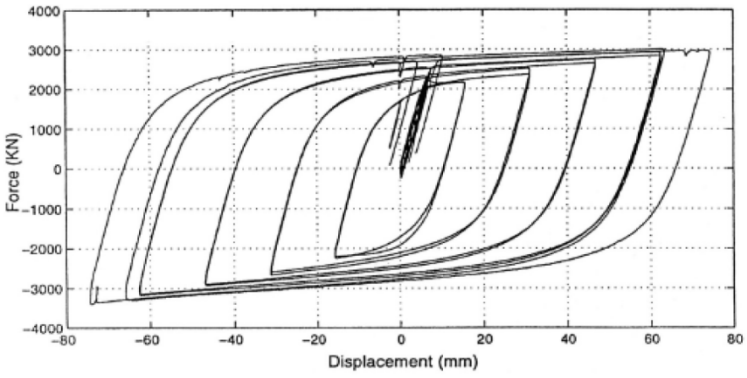

(c) Force-displacement hysteresis of a BRB

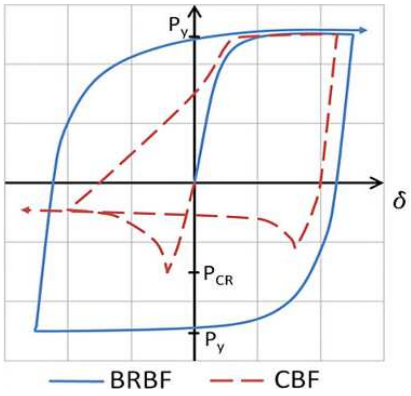

(d) BRB (courtesy of Star Seismic)

Figure 4.8. Buckling Restrained Braces, after Christopoulos and Filiatrault (2006)

In summary, in the last two decades, the technology for BRBs has been significantly evolved. BRBs are adopted into building codes for seismic and wind protection of buildings in several countries. Currently, there are many manufactures of BRBs around the world. BRBs offer many advantages over the other types of metallic dampers. This includes the cost-effectiveness, simple assembly, higher capacity, and lower life-cycle maintenance cost. However, despite offering good advantages, the manufacturing

process, overstrength of the brace after yielding, strength degradation under cyclic loading, low-cycle fatigue fracture, and replacement costs, can be the downsides of BRBs.

4.2.1.4 Torsional Beam Damper

Torsional beam damper was invented by Dr. Ivan Skinner (1923-2014) in the late 1960s in New Zealand. In this type of damper, the energy dissipation comes from torsional yielding of a steel bar which is loaded by a central transverse plate (arm). The bar remains fixed at the two ends, as illustrated in Figure 4.9. Torsional beam damper was studied and tested by Kelly et al. (1972) and Skinner et al. (1980).

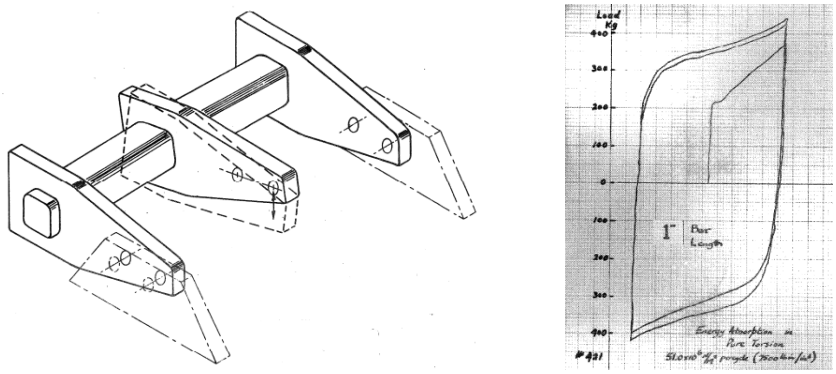

(a) Torsional beam damper working mechanism (b) Hysteresis response

Figure 4.9. Torsional beam damper (Kelly et al., 1972)

This type of damper was used by Beck and Skinner (1974) for the earthquake design of the rocking viaduct over South Rangitikei River in New Zealand (Figure 4.10a). Torsional beam dampers (Figure 4.10b) were used at the column to footing rocking connection. During an earthquake, the dampers absorb the seismic energy while gravity loads provide self-centering capacity for the bridge. The construction of South Rangitikei Viaduct marked the first application of metallic dampers in bridges around the world (Christopolous and Filiatrault, 2006). The Viaduct construction was completed in 1981.

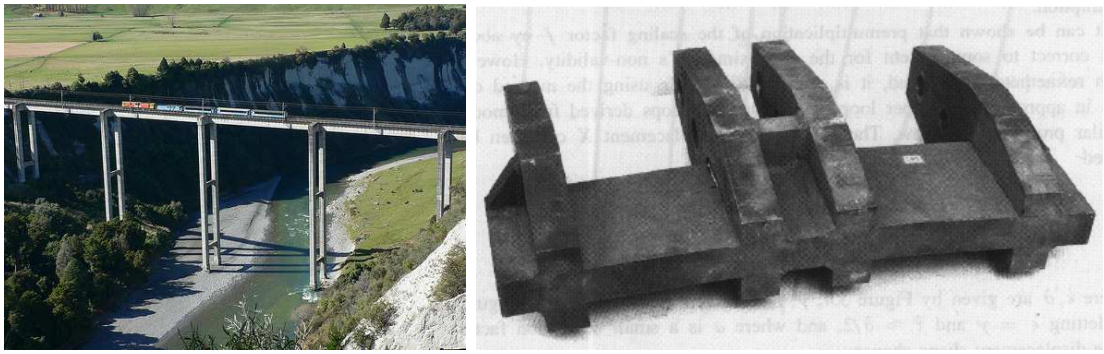

(a) South Rangitikei Viaduct **(b) Torsional damper with transverse loading arms**

Figure 4.10. South Rangitikei Viaduct in New Zealand (Beck and Skinner, 1974)

In summary, torsional beam damper is a cost-effective metallic damper. There have been past applications of this type of damper in seismic protection of bridges. This type of damper can be suitable for the rocking type hollow pier sections. However, given the working mechanism of the damper (loading with transverse arms), it would need to be more compact for a wider application in buildings or in columns with solid sections.

4.2.1.5 U-Shaped Flexural Plates (UFPs)

U-Shaped Flexural Plates (UFPs) were invented by Dr. Ivan Skinner (1923-2014) in the late 1960s in New Zealand (Kelly et al., 1972). UFPs consist of a steel plate which is bent into a U-shape configuration (Figure 4.11a). During an earthquake, the relative sliding of each of the UFP's leg causes yielding of the steel plate along the half-circle length (Figure 4.11b). This is sometimes referred as "rolling deformation" in the steel plate. The rolling deformation of the steel plate absorbs the seismic energy.

UFPs have been demonstrated to have great energy dissipation capacity. They are not easily susceptible to low-cycle fatigue failure or strength degradation for a large number of cycles beyond their yield point, Kelly et al. (1972), Skinner et al. (1980), Iqbal et al. (2010), and Baird et al. (2013). UFPs can be used for absorption of seismic and wind energy in multi-story buildings. They have already been implemented in timber and concrete rocking wall type structures in New Zealand, as presented in Figure 4.12 (Pampanin et al., 2011).

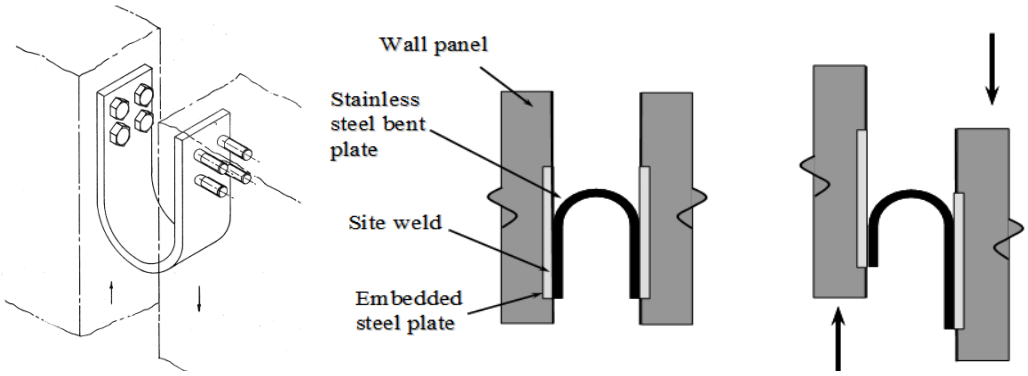

(a) Typical installation of UFPs **(b) UFP working mechanism, after Iqbal et al. (2010)**

Figure 4.11. UFP installation and working mechanism

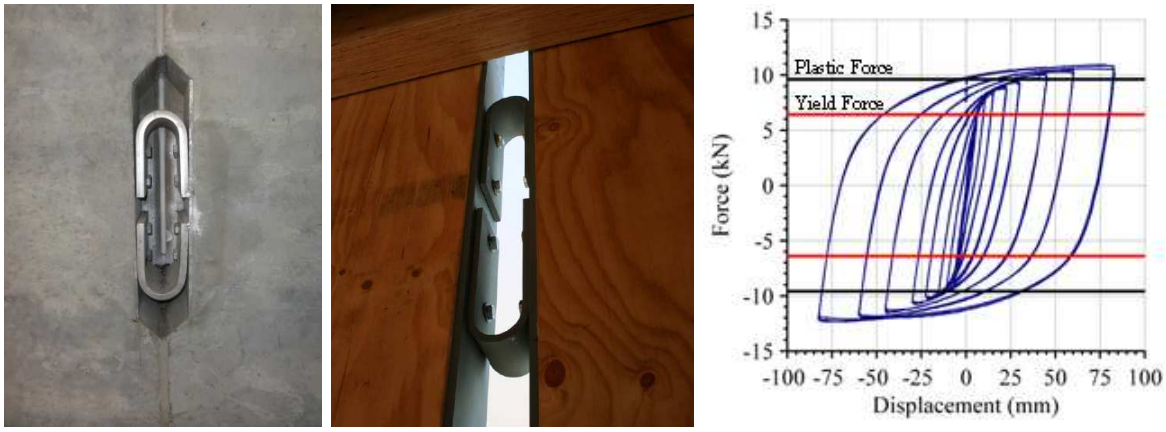

(a) **(b)** **(c)**

Figure 4.12. Application of UFPs (a) Concrete rocking walls of Southern Cross Hospital in Christchurch, after Pampanin et al. (2011) (b) Timber rocking walls of Nelson-Marlborough Institute of Technology Building in Nelson, after Iqbal et al. (2010) (c) Force-displacement hysteresis of UFPs, after Baird et al. (2014)

In summary, past research investigations on UFPs have shown great energy dissipation capacity and response of the dissipater. UFPs are normally made from available mild steel plates. Other advantages include cheaper fabrication cost, stable hysteretic behavior, minimal low-cycle fatigue and strength degradation during cyclic loading, ability to accommodate large displacements, and higher capacity. Application of UFPs in coupled shear walls has been popular in New Zealand, especially in post Christchurch Earthquake rebuild. Despite offering great advantages, application of UFPs has been mostly limited to rocking type walls (PRESSS and PRES-LAM, Priestley et al. 1999, Palermo et al., 2005[2]). Similar to torsional beam damper discussed in the previous

section, the UFPs would need to be more compact for a wider application in bridges and buildings. Refer to Section 4.3 for more details.

4.2.1.6 High Force to Volume Damper

The High Force to Volume (HF2V) damper was developed by Rodgers (2009) at the University of Canterbury (Figure 4.13). The HF2V damper is an evolution of lead extruder damper which was discussed previously in Section 4.2.1.2.

The HF2V damper is able to achieve higher capacity in a compact package. This makes the damper more attractive for implementation between different structural elements. Experimental studies on HF2V dampers have shown very little strength degradation under cyclic loading (Figure 4.13d).

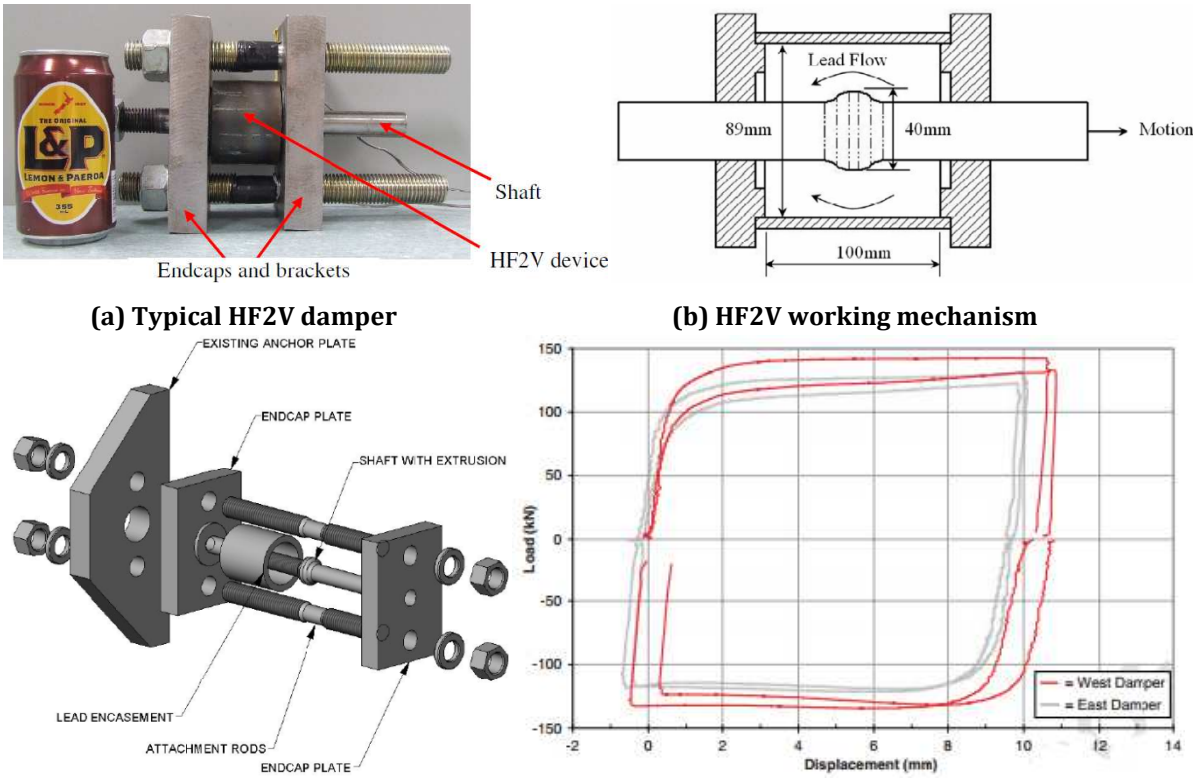

(a) Typical HF2V damper **(b) HF2V working mechanism**

(c) HF2V components **(d) HF2V force-displacement hysteresis**

Figure 4.13. HF2V damper (Rodgers, 2009)

In summary, this type of dampers offer advantages such as smart packaging, higher capacity, and cheaper manufacturing cost when compared to viscous dampers. There has been a few implementation of HF2V in New Zealand following Canterbury Earthquakes (Latham et al., 2013).

4.2.1.7 Buckling-Restrained Fused Type Dissipater

Buckling-Restrained Fused Type (BRF) dissipater is a mini plug and play version of BRB which was explained in Section 4.2.1.3. Due to small and compact nature of BRF, it offers many applications. Past research on the use of BRF in buildings includes Christopoulos et al. (2002), Amaris Mesa (2010), Marriott (2009), and Sarti et al. (2013). Similarly, the use of BRF dissipaters in rocking bridge piers were previously investigated by Marriott (2009) and Guerrini et al. (2012) as discussed in Section 2.3.3.1 of Chapter 2.

A typical BRF dissipater has a stable hysteretic response (Figure 4.14b) and contains a steel core, outer confining tube, and filling material (epoxy or grout), as shown in Figure 4.14a. The steel core is a plain round bar which has been necked down "fused" over a certain length. The inelastic deformation is expected to occur over the fused length when the dissipater is stretched or compressed. It is common to choose a 20% reduction in the sectional area of the bar over the fused length. This prevents from inelastic deformation in the threaded part and the region between the threaded and fused part when the rod starts strain hardening (White, 2014). The fused length can be simply calculated based on the stroke demand by limiting the peak strain in the fused length to 5% (Pampanin et al., 2010).

The round bar is placed inside a sleeve which works as a confining tube for the dissipater. The gap between the outer tube and the plain bar is filled with epoxy or grout. The outer confining tube and filling material (epoxy or grout) prevent from buckling of the plain bar when the dissipater is compressed. According to Sarti et al. (2013), there was little variation observed in the performance of the dissipaters when either epoxy or grout was used.

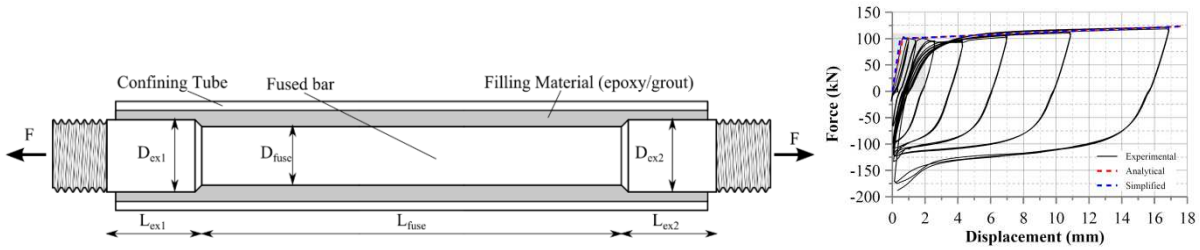

(a) Components of a BRF dissipater **(b) Force-displacement hysteresis**

Figure 4.14. BRF dissipater (Sarti et al., 2013)

There have been many implementations of BRF in concrete, steel, and timber rocking frames and walls in New Zealand and the United States. Examples of BRF in buildings in New Zealand include the Learning and Research Building at Victoria University in Wellington (Figure 4.15a), Merrit building in Christchurch (Figure 4.15b), and Kilmore Street Medical Center in Christchurch (4.15c).

(a) Timber rocking frames **(b) Concrete rocking frames** **(c) Steel rocking frames**

Figure 4.15. Application of BRF dissipaters, (Sarti et al., 2013, Latham et al., 2013)

Research investigation by Amaris Mesa (2010) showed that BRF behaves well when stretched (under net positive deformation), as shown in Figure 4.16a. However, when the dissipater is compressed (under net negative deformation), there is a considerable increase in the stiffness and force of the dissipater, accompanied by buckling at low levels of compression (Figure 4.16c). This is a consequence of the bar bearing against the filling material at the ends (Figure 4.16b). This means that BRF does not have a balanced hysteresis when subjected to full compression strain (similar strain as tension, but on the negative side of the displacement axis in Figure 4.16c). Therefore, a BRF works well in rocking connections where pivoting occurs on the edge of the structural element, and thus the net negative strain in the dissipater is avoided to a considerable extent (Figure 4.14b).

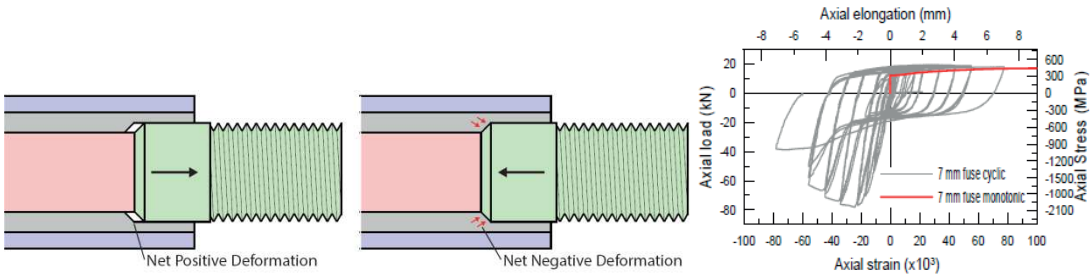

(a) Net positive deformation **(b) Net negative deformation** **(c) Force-displacement hysteresis**

Figure 4.16. Net negative strain effects, after Amaris Mesa (2010) and White (2014)

In summary, BRF is made from ready available steel bars. There have been several implementations of BRF in rocking structures in New Zealand. This type of dissipater offers advantages such as simple fabrication, good hysteretic behavior when compressed or stretched (only under net positive strain), and buckling resistance. The disadvantages of this type of dissipater include use of grout or epoxy as the filling material which complicates the fabrication process and also increases the cost. The other negative aspect of BRF is the remarkable increase in stiffness of the dissipater under net negative strain which makes the dissipater less attractive for applications where both net positive and negative strain is expected. Another drawback is the low-cycle fatigue failure of the dissipater under cyclic loading.

4.2.1.8 Buckling-Restrained Dry Type Dissipaters

White (2014) experimentally investigated the hysteretic response of several types of Buckling-Restrained Dry (BRD) type dissipaters. In a BRD dissipater, the components are similar to a BRF dissipater, except that a BRF dissipater requires filling material (epoxy or gout) for the gap between the plain bar and the outer tube. However, in a BRD dissipater, there is no need of filling materials which makes the fabrication process simpler. Therefore, they are titled “dry” type dissipaters. In a BRD dissipater, the buckling of the bar inside the confining tube is prevented through a direct contact between these elements. A summary for the variations of BRD dissipaters are as follows.

4.2.1.8.1 Split Tube Type Dissipater

This type of BRD dissipater is illustrated in Figure 4.17. The external tube in this type of dissipater needs to be split up after the fabrication. After placing the fused bar inside the split tube, the tube is welded and the dissipater is assembled.

In this type of dissipater, there is a gap between the bar and the confining tube at each end, as shown in Figure 4.17. This allows for the net negative strain to be applied to the dissipater without loading the confining tube which can increase the stiffness. There is a small gap left between the bar and the confining tube to eliminate any contact that generates friction when the dissipater is compressed. The friction increases the stiffness of the dissipater which creates strain concentration in the bar which makes it susceptible to low-cycle fatigue failure.

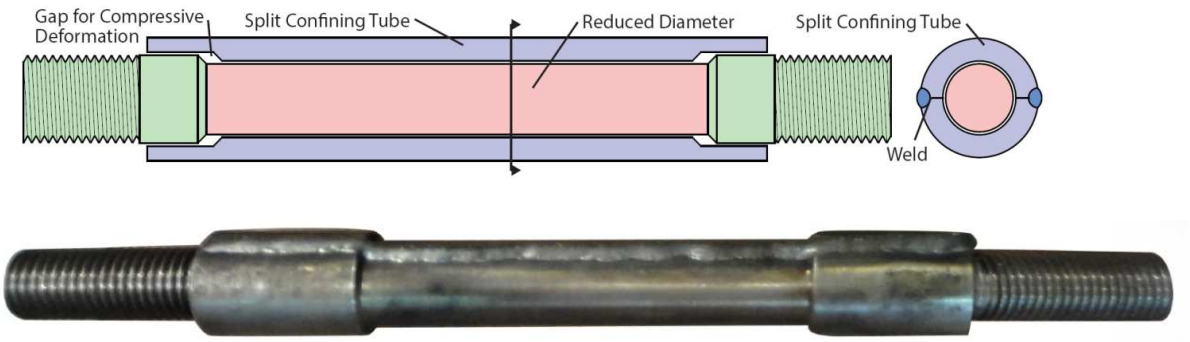

Figure 4.17. Split tube type dissipater, after White (2014)

A prototype dissipater was tested under cyclic displacement loading up to 7.5% strain limit (net positive strain only). Following this, the dissipater was loaded monotonically up to the fracture point. During the cyclic loading portion, three cycles of displacements were applied to the dissipater at each strain limit. The strain limits at ULS and MCE levels were assumed to be 70% and 90% of the maximum completed strain cycle (ε_{max}), respectively. The ductility at (ε_{max}) was calculated by simply dividing it over the yield strain (ε_y). The testing setup and force-strain hysteresis are shown in Figure 4.18a and Figure 4.18b, respectively.

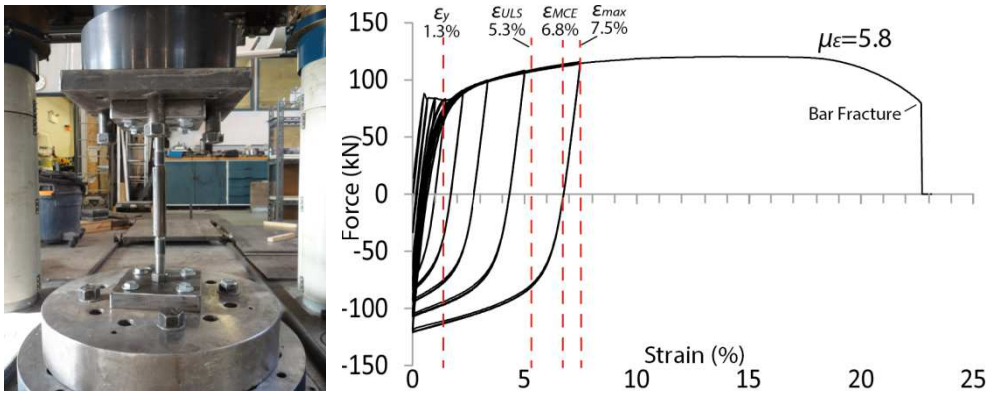

(a) Typical dissipater testing setup **(b) force-axial strain hysteresis**

Figure 4.18. Split tube type dissipater testing, after White (2014)

In summary, the split tube type dissipater provides advantages such as dry connection without any filling material, good hysteretic behavior, expected to accommodate net negative strain (although not tested under that type of loading), and better buckling restraint. The disadvantage of this type of dissipaters is the complexity with the fabrication of the confining tube which requires splitting and welding of the tube. This can increase the fabrication cost of the tube.

4.2.1.8.2 Deformed Tube Type Dissipater

This type of BRD dissipater is illustrated in Figure 4.19. The deformed tube type dissipater is similar to split tube type dissipater, as discussed in the previous section.

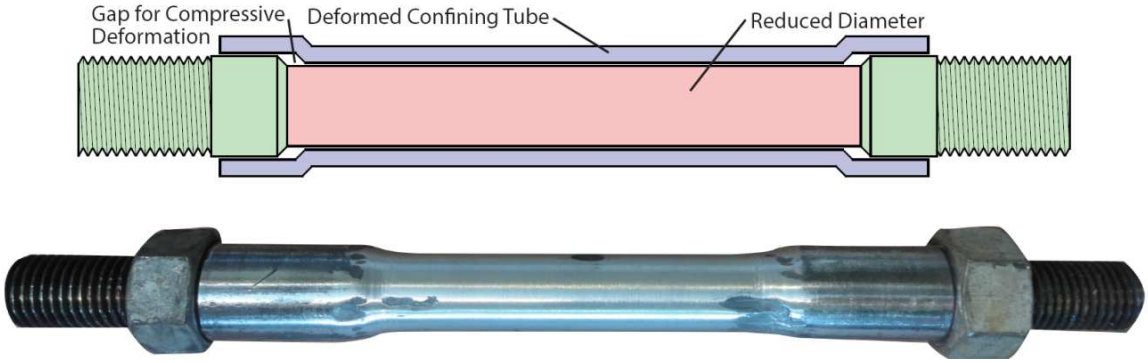

Figure 4.19. Split tube type dissipater, after White (2014)

In this type of dissipater, the fused bar is placed inside a confining tube. The tube is then deformed by reducing its diameter which closes the gap between the bar and the tube. In this type of dissipater, there is no need for welding of the tube. The deformed tube can be made by heating and beating of the tube around the bar or using a rolling machine. It is also possible to avoid the heating of the tube and make it cold formed.

A prototype dissipater was tested under increasing cyclic displacement loading up to the failure point. There were three cycles of displacements applied to the dissipater at each strain limit. The force-strain hysteresis is shown in Figure 4.20. The dissipater failed during cycles of 13% strain which was due to buckling under compression. There was no deformation of the tube throughout testing.

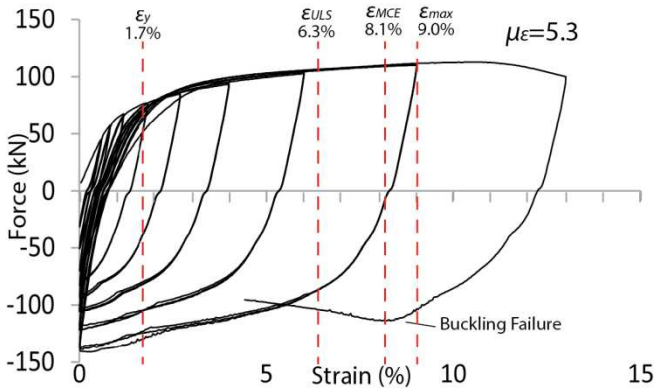

Figure 4.20. Deformed tube type force-strain hysteresis, after White (2014)

In summary, the deformed tube type dissipater offers advantages similar to split tube type dissipater. It also eliminates the need for welding of the tube. The disadvantages include fabrication of the deformed tube which may need specialized machinery.

4.2.1.8.3 Supported Bar Type Dissipater

This type of BRD dissipater is illustrated in Figure 4.21. Several supports are provided along the fused length of the bar to reduce the buckling length of the bar inside the confining tube. However, during compression stage, some buckling of the fused length between the supports can be expected (Figure 4.21b). The fused portions of the bar between the supports are where inelastic action would occur. This means, a longer length of the dissipater would be needed to accommodate the same stroke as for the other types of BRD dissipaters discussed earlier.

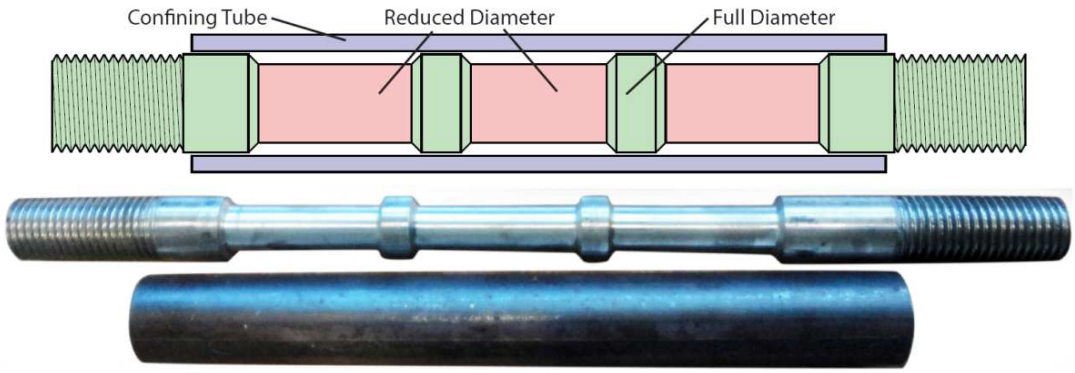

(a) Supported bar type dissipater detail

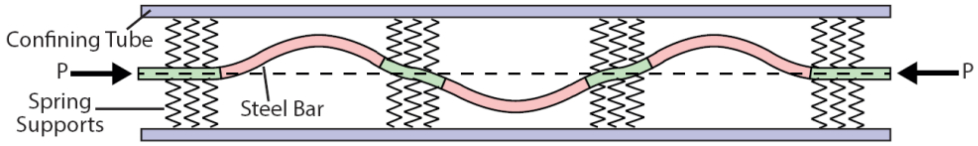

(b) Support mechanism during compression loading

Figure 4.21. Supported bar type dissipater, after White (2014)

The dissipater was tested under the same loading protocol as that for the deformed tube type dissipater. The dissipater failed during the third cycle of 13% strain due to severe buckling under compression as can be seen from the force-strain hysteresis in Figure 4.22. It was concluded that by providing more support points along the fused length of the bar, the buckling of the dissipater could be delayed under larger cycles of deformation, but this would increase the total length of the dissipater.

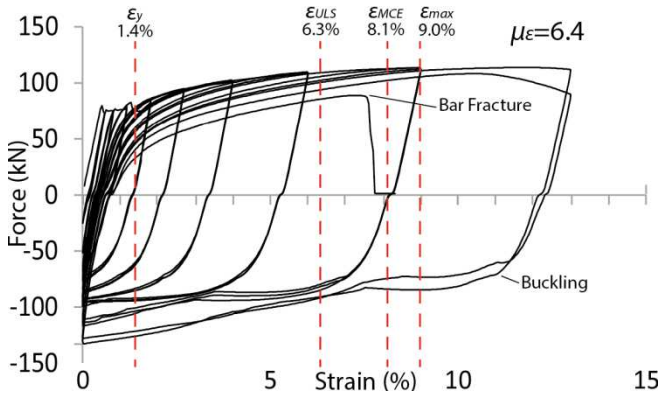

Figure 4.22. Supported bar type dissipater hysteresis, after White (2014)

In summary, the supported bar type dissipater offers more advantages compared to other types of BRD dissipaters. This includes straightforward and cost-effective fabrication process. The disadvantages are the discontinuity in buckling restraints along the fused length of the bar and longer length of the dissipater due to presence of the support points.

4.2.1.8.4 Grooved Type Dissipater

This type of BRD dissipater is illustrated in Figure 4.23. The grooved type dissipater was used for testing of ABC Controlled Damage by White (2014), refer to Section 2.3.3.1 in Chapter 2. In this type of dissipater, a plain bar is used inside an outer confining tube. There are several cuts (grooves) made along the length of the bar where yielding and energy absorption occur. There is a small gap left between the tube and the bar.

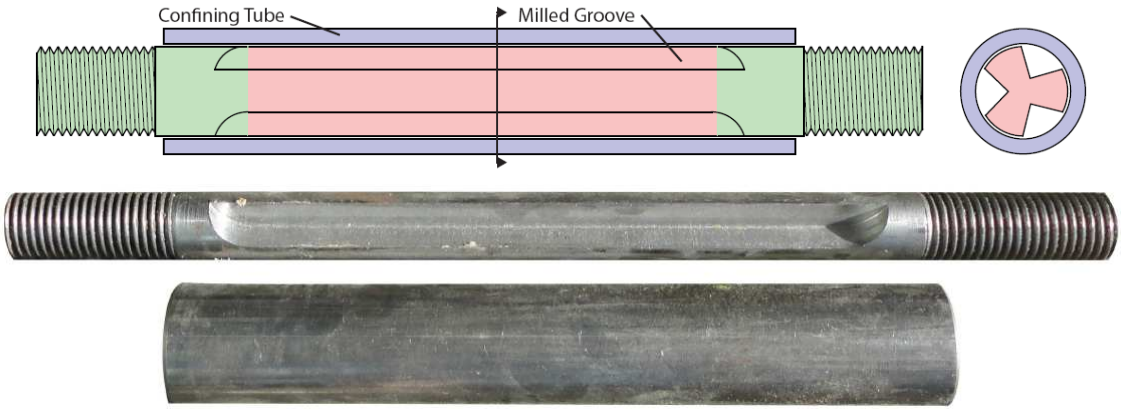

Figure 4.23. Grooved type dissipater, after White (2014)

Grooved dissipaters can be made with two, three, or four cuts in the bar, as shown in Figure 4.24a. Experimental investigation by White (2014) suggested that the best

performance results can be expected from a dissipater with three grooves. It is also necessary to leave a solid portion of the plain bar between the threaded and grooved parts, otherwise premature failure of the dissipater may occur under cyclic loading (Figure 4.24b).

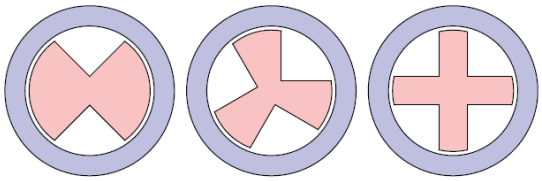

(a) Various number of grooves and their depths

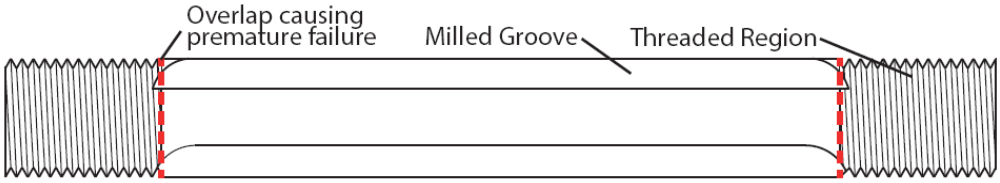

(b) Detailing consideration for ends to avoid premature failure

Figure 4.24. Grooved type dissipater details, after White (2014)

A prototype dissipater was designed in such a way that grooved portion of the dissipater has the same cross-sectional area to match the capacity of the previous types of BRD dissipaters explained earlier. During testing, the dissipater failed during the second cycle of 13% strain due to low-cycle fatigue. Grooved dissipater showed a very stable force-strain hysteresis and achieved a displacement ductility of approximately 7.0, as shown in Figure 4.25. Unlike other BRF and BRD dissipaters, grooved dissipater is expected to have less increase in the stiffness under negative net loading.

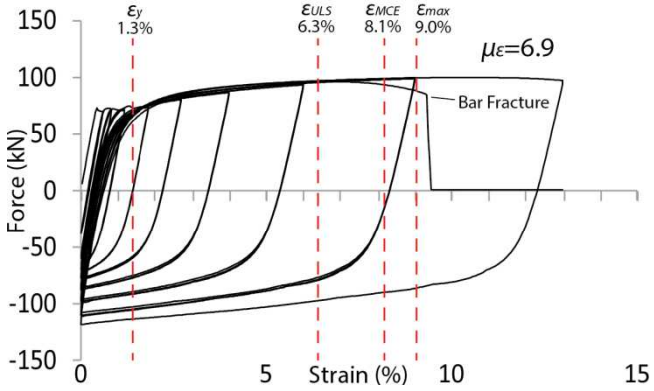

Figure 4.25. Grooved type dissipater hysteresis, after White (2014)

In summary, grooved type dissipater offers advantages of dry connection (no filling material), straightforward and simple fabrication of bar and tube, great hysteretic behavior, good ductility, less increase in stiffness under net negative strain, and better buckling restraint (continuous support of the bar against the inner face of the tube). The disadvantages are the low-cycle fatigue failure, local buckling around the groove cuts, and possible unbalanced force of the dissipater in tension and compression. These issues can be solved through additional research and optimization of the detailing. Further research investigation is currently underway on grooved dissipaters at the University of Canterbury. More details on experimental testing of grooved dissipater under both net positive and negative deformation will be presented in Section 4.3.3.

4.2.1.9 Shape Memory Alloy Dissipaters

Shape Memory Alloys (SMAs) were introduced in Section 2.3.3.2 of Chapter 2. SMA materials are normally made of two or three metals such as Nitinol, Nickel, Titanium, Copper, and Zinc. SMA materials are known to show superelastic and self centering behavior with temperature dependency.

Past research investigations have shown that SMAs can be used as a dissipater in various parts of building and bridge structures. Previous research studies on SMAs and their applications as dissipaters include Aiken et al., 1992, 1993 (steel frames), Witting and Cozzarelli, 1992 (diagonal braces), DesRoches et al., 2004 (SMAs properties), Ocel et al., 2004 (steel beam-column connections), Yossef et al., 2008 (concrete beam-column joints), Roh and Reinhorn, 2010 (precast segmental bridge pier), Saiidi et al., 2006, 2009 (concrete columns), and Varela and Saiidi, 2014 (precast ABC columns).

It is important to note that the hysteretic behavior of self-centering metallic dissipaters such as SMAs is different from that of a non-self-centering metallic dissipater (Figure 4.1). Similar to response of a DCR connection, the hysteretic behavior of self-centering dissipater is commonly referred as “Flag-Shaped”. Figure 4.26b presents a typical hysteresis for SMAs in a precast segmental post-tensioned bridge pier from Roh and Reinhorn (2010).

Past applications of SMA wires and dissipaters in buildings have been primarily limited to seismic retrofitting of historical buildings in Europe. Examples include San Giorgio

Bell Tower in San Martino (Figure 4.26c) and Upper Basilica di San Francesco in Assisi (4.26d) in Italy, (Christopolous and Filiatrault, 2006).

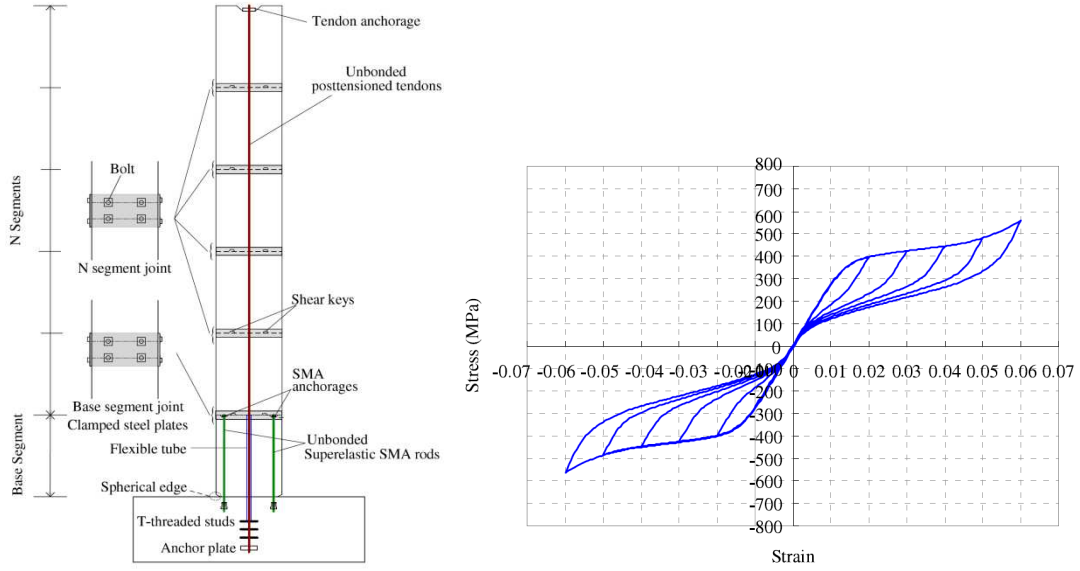

(a) Segmental column elevation view **(b) Hysteretic behavior of SMA bar**

(c) San Giorgio bell tower, San Martino **(d) Upper Basilica di San Francesco, Assisi**

Figure 4.26. Past research on SMAs in precast segmental bridge pier (Roh and Reinhorn, 2010) and applications of SMA wires for seismic retrofit of historical buildings in Italy (Christopolous and Filiatrault, 2006)

In summary, SMA dissipaters have many advantages such as exhibiting high stiffness and strength under small deformations, flexible property under larger deformation, minimal residual deformation, and good energy dissipation capacity. However, strength degradation of SMAs under a larger number of cycles results into residual deformation and fatigue in the dissipater. At the same time, the cost of SMA materials is pretty high compared to other metallic dissipaters. There have been a few applications of SMAs in buildings, but these were mainly limited to seismic retrofitting of historical structures.

4.2.1.10 Self-Centering Buckling-Restrained Brace

The Self-Centering Buckling-Restrained Brace (SC-BRB) was recently developed and studied by Eatherton et al. (2014). The brace components are shown in Figure 4.27a. In SC-BRB, the response of a typical BRB is combined with that of the pre-tensioned SMA rods (Figure 4.27b). The resultant response for the brace is a flag-shaped hysteresis (Figure 4.27c).

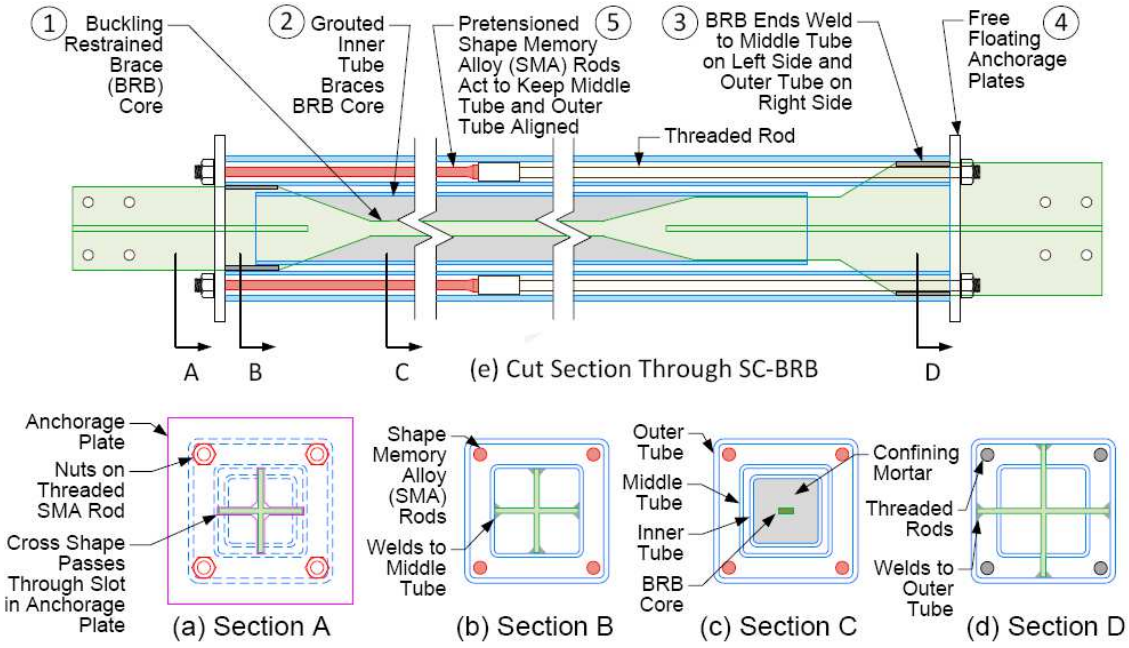

(a) SC-BRB components and details

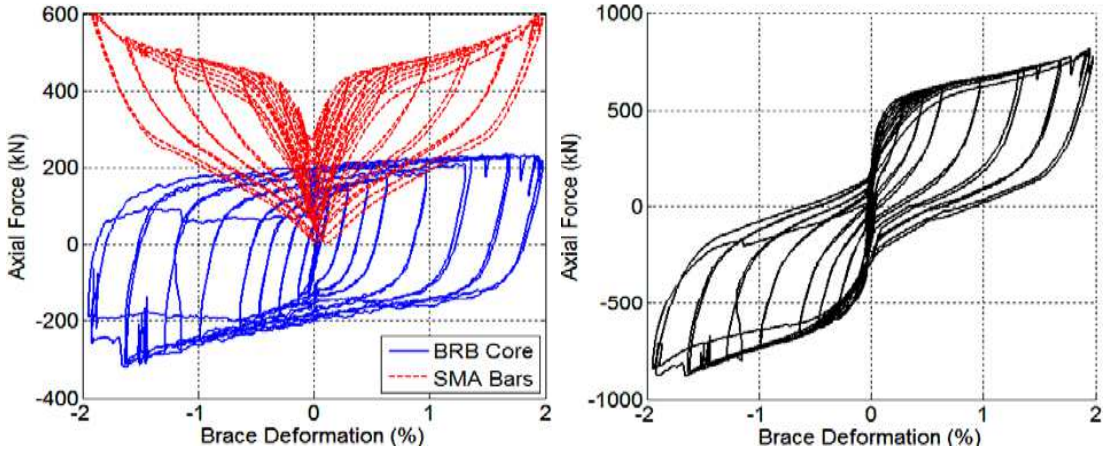

(b) Hysteretic response of parts **(c) Resultant hysteretic response**

Figure 4.27. Self-Centering Buckling-Restrained Braces, after Eatherton et al. (2014)

This type of dissipaters is relatively new and is intended to provide the advantage for energy dissipation and self-centering in a single package. However, past experimental studies have not shown a full re-centering of the brace (Figure 4.27c).

Experimental studies by Eatherton et al. (2014) have shown that following 2% drift ratio in the brace, there was about 1% residual deformation in the brace. This corresponds to 50% of the applied drift ratio. In this sense, the self-centering ratio of the brace would need to be carefully assigned during the design process to limit the residual displacement of the brace. According to Eatherton et al. (2014), self-centering ratios of 0.5 up to 1.5 are recommended to control the residual drifts in SC-BRB.

In summary, although SC-BRB is offering some good advantages compared to a traditional BRB, but the cost of SMA rods can be high for this type of the bracing dissipater. Therefore, the advantage for self-centering would need to be weighed against the material and fabrication costs of the dissipater. So far, there have not been any applications of this type of dissipater in buildings or bridges.

4.2.2 Friction Dampers

Friction dampers show similar hysteretic behavior to that illustrated in Figure 4.1 for metallic dampers. Generally, the slip load in a friction damper is considered as an equivalent yield force of a metallic damper. In a friction damper, the seismic energy is dissipated through friction that builds up at the interface of two sliding solid bodies. Past research investigations into the use of friction dampers in Dissipative Controlled Rocking (DCR) connections in buildings include Ricles et al. (2001), Kim and Christopoulos (2008) (steel), and Morgen and Kurama (concrete) (2004).

There have been several variations of friction damping systems developed over the last three decades. A summary of the popular friction damping systems are presented here.

4.2.2.1 Slotted-Bolted Friction Dampers

The slotted-bolted connection is the simplest form of the friction dampers. It was studied by Tremblay and Stiemer (1993). This type of connection is commonly used at the end of bracing members. It is simply constructed from several plates which are designed to move against each other and are clamped together with a bolt, as shown in Figure 4.28a. It is common to use disc spring washers (Figure 4.28a) to maintain constant slip load in a slotted-bolted connection, (Christopolous and Filiatrault, 2006). A force-drift hysteresis of this type of damper is presented in Figure 4.28b

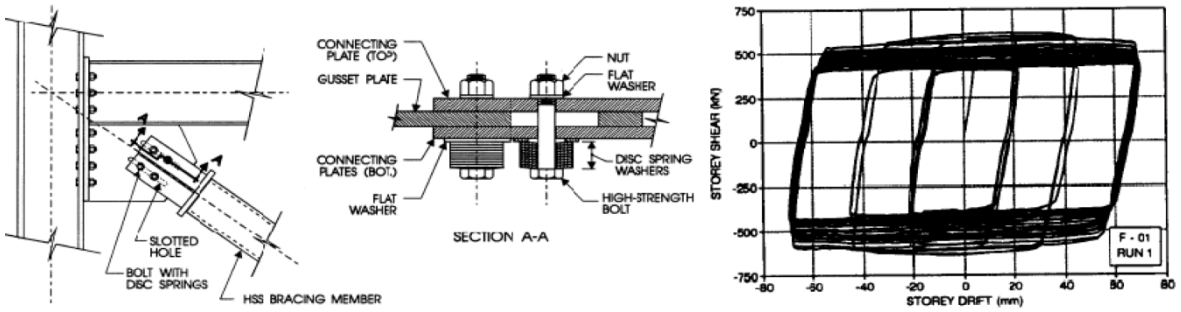

(a) Slotted-bolted connection for steel frames **(b) Force-drift hysteresis of the frame**

Figure 4.28 Slotted-bolted connections, after Tremblay and Stiemer (1993)

Over the years, there have been many variations of slotted-bolted connections developed by researchers around the world. The Asymmetrical Friction Connection (AFC) with brass shims in a sliding hinge joint (Figure 4.29) was developed and studied by Clifton (2005) at the University of Auckland in New Zealand.

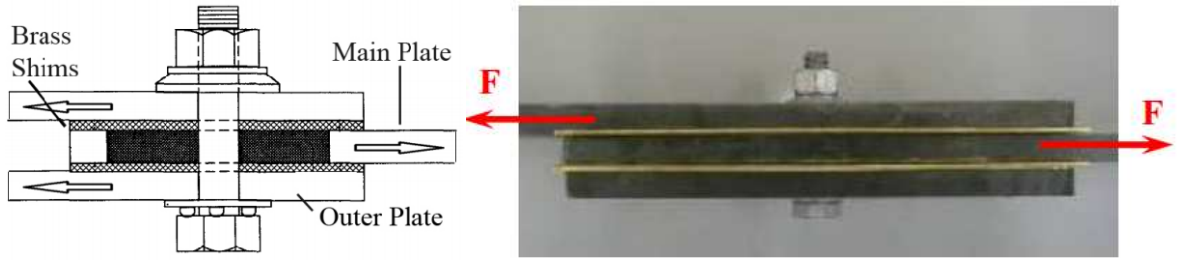

(a) AFC components **(b) A typical AFC**

Figure 4.29 Asymmetrical friction connections, after Clifton (2005)

Morgen and Kurama (2004) investigated a rotational type of slotted-bolted connection which can be used as a dissipater in a beam-column DCR connection (Figure 4.30). Testing results have shown good energy dissipation of the dissipater and re-centering of the connection through unbonded post-tensioning.

As a summary, the slotted-bolted friction dampers have been implemented in buildings in seismic regions. This type of friction dampers offer advantages such as simple fabrication, cost-effectiveness, and good energy dissipation capacity. Over the last two decades, there has been a variety of slotted-bolted connections developed and tested.

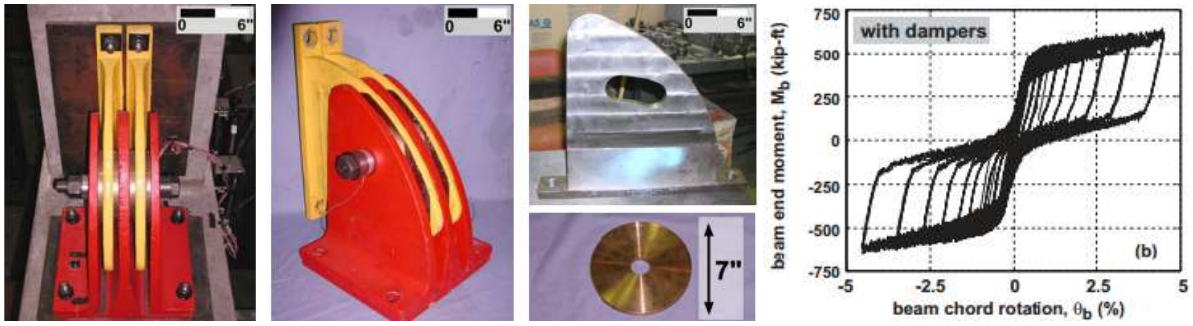

(a) Rotational type friction damper components **(b) Moment-rotation hysteresis**

Figure 4.30 Rotational type friction damper in a dissipative controlled rocking beam-column joint, after Morgen and Kurama (2004)

4.2.2.2 Sumitomo Friction Device

Sumitomo friction device is illustrated Figure 4.31a. This type of friction dissipater is more sophisticated compared to other friction dampers. The dissipater contains a pre-loaded internal spring which is intended to induce a force that will be converted into a normal force through the inner and outer wedges. The normal force will act on the friction pads which are made of copper alloy which also contain graphite plug inserts for lubrication purpose.

This type of friction device was studied by Aiken and Kelly (1993) and was originally manufactured by Sumitomo Metal Industries Ltd. in Japan. The dissipater can be used as bracing elements in a building. A typical force-displacement hysteretic response of the dissipater is shown in Figure 4.31b.

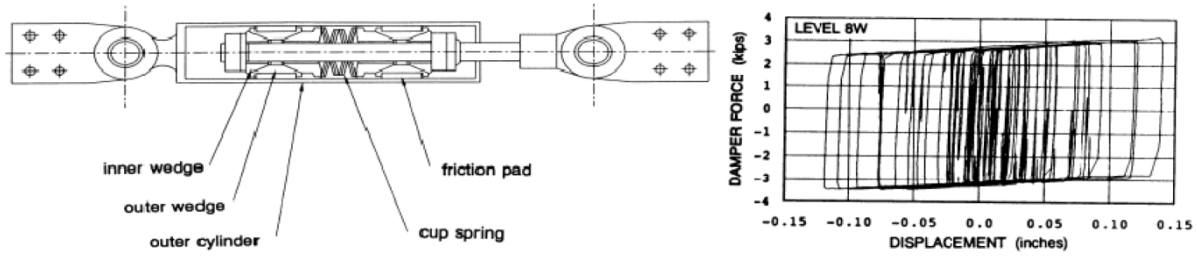

(a) Sumitomo friction device components **(b) Force-displacement hysteresis**

Figure 4.31 Sumitomo friction device, after Aiken and Kelly (1990)

As a summary, there have been a few applications of this type of damper in buildings located in seismic regions in Japan. The Sumitomo friction device is a more complicated when compared against other types of friction dissipaters. Therefore, it makes the fabrication cost of the device higher.

4.2.2.3 Pall Friction Device

This type of friction dissipater is designed for a moment-resisting framed structure. The working mechanism of the dissipater is based on the slotted slip joints which are located at the intersection of the frame cross-braces, as shown in Figure 4.32a. Pall friction device was studied by Filiatrault and Cherry (1987). A force-displacement hysteretic behavior of pall friction device is presented in Figure 4.32b.

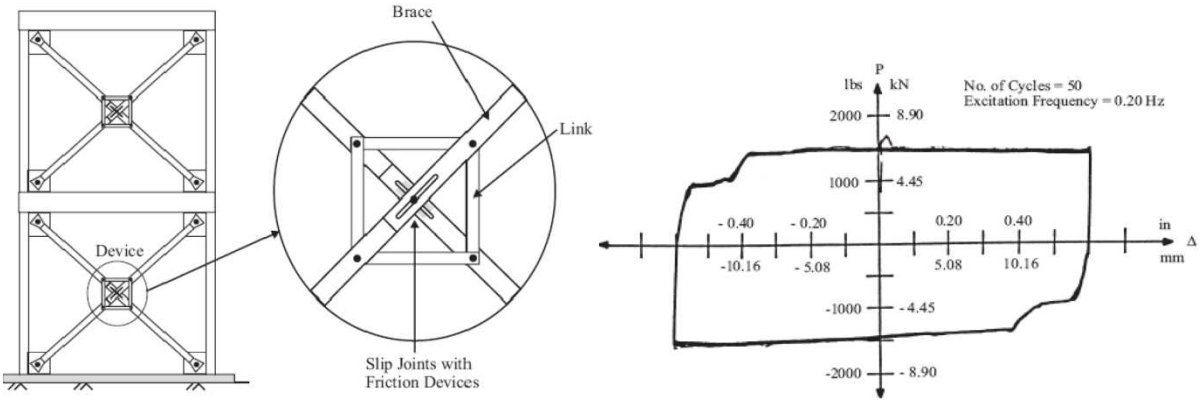

(a) General arraignment of Pall friction device **(b) Force-displacement hysteresis**

Figure 4.32 Pall friction device, after Filiatrault and Cherry (1987)

Pall friction device is the most implemented friction damping system. It has been applied to many buildings located in seismic regions in Canada and the United States. Examples include the Concordia University Library (Figure 4.33a) in Montreal, Canada and the Freeport Water Tower (Figure 4.33b) in Sacramento, California.

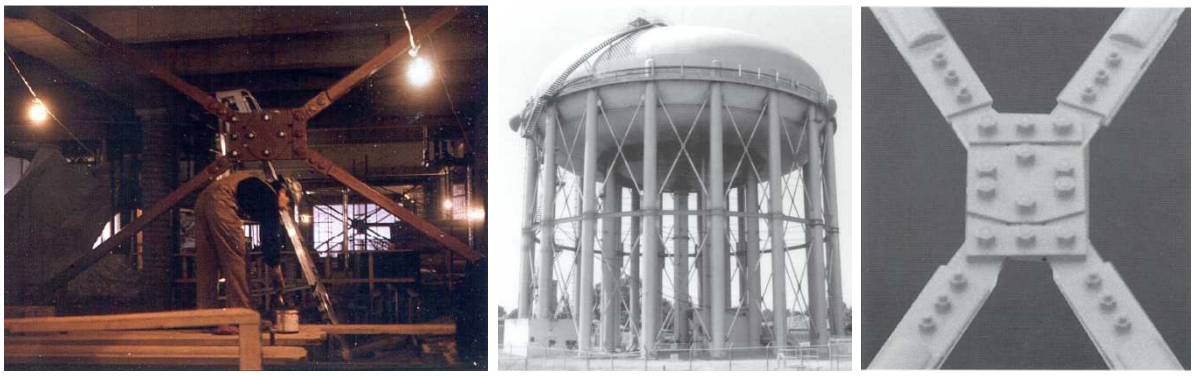

(a) Concordia University Library, Canada **(b & c) Freeport Water Tower in Sacramento, California**

Figure 4.33 Application of Pall friction device, after Christopoulos and Filiatrault (2006)

As a summary, Pall friction device offers advantages such as good energy dissipation, lower cost of fabrication, and simple installation. This type of dissipater has been implemented in many buildings in North America during 1990s.

4.2.2.4 Energy Dissipating Restraint Dampers

The Energy Dissipating Restraint (EDR) damper was originally designed for piping systems. The dissipater consists of an internal spring, steel compression wedges, bronze friction wedges, stops at both ends of the internal spring, and external sleeve as illustrated in Figure 4.34.

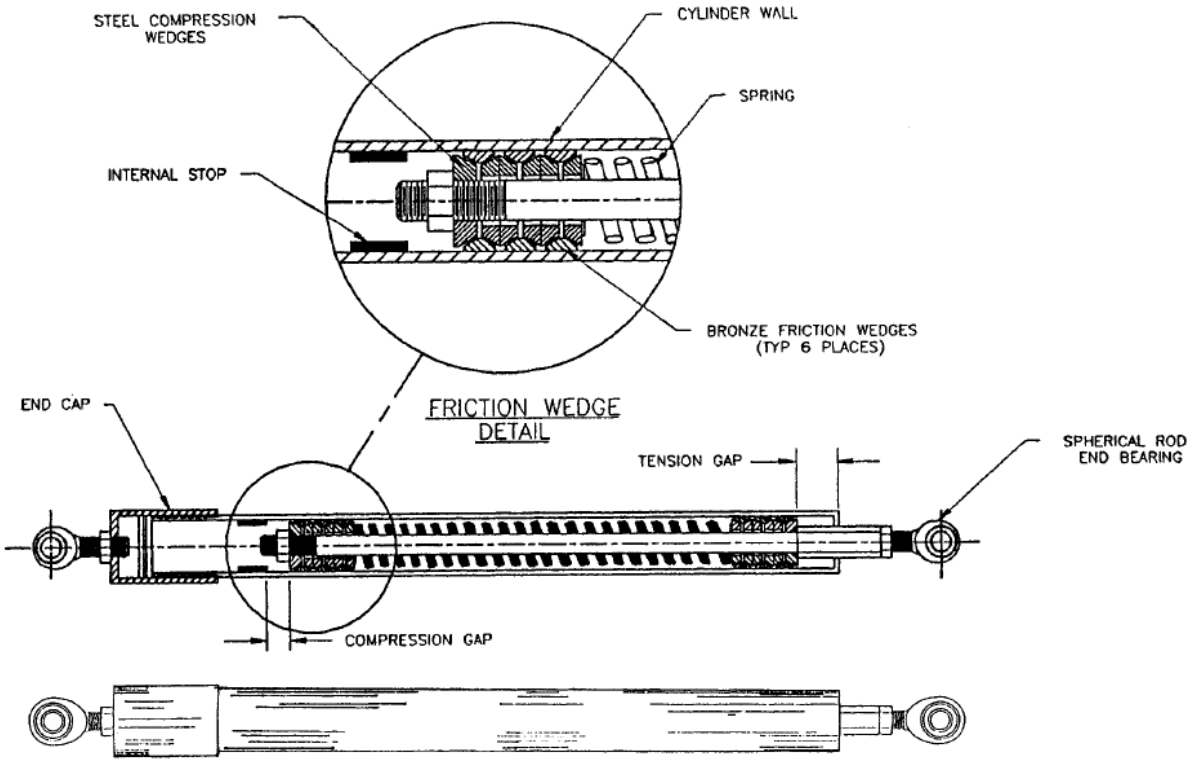

Figure 4.34. Energy dissipating restraint, after Nims et al. (1993)

The hysteretic response of EDR dampers as a bracing element was studied by Richter et al. (1990), Nims et al. (1993), and Aiken et al. (1993). A flag-shaped hysteretic response of the dissipater can be expected if the internal spring is preloaded (Figure 4.35a). For the case where the internal spring in not preloaded, the hysteretic response has shown to become triangular (Figure 4.35b).

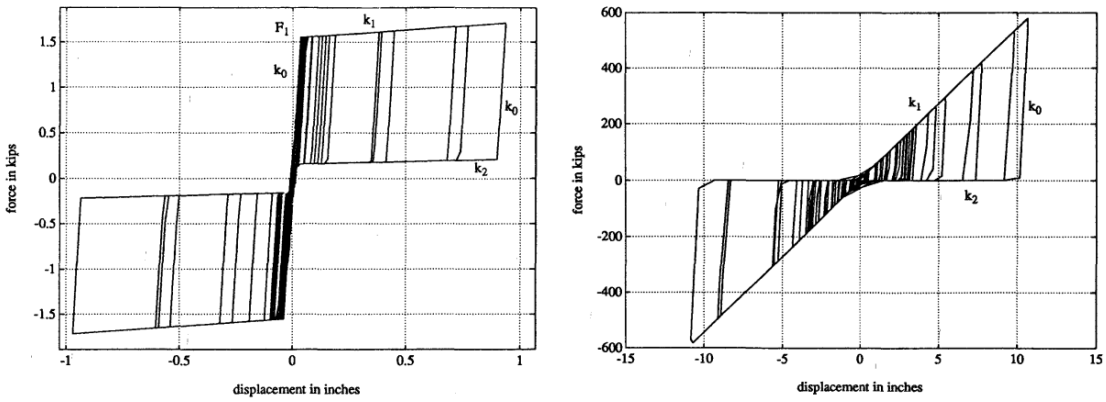

(a) Flag-shaped hysteresis, preloaded spring (b) Triangular hysteresis response, no preloading

Figure 4.35. Effects of internal spring preloading in EDR on force-displacement hysteretic behavior, after Nims et al. (1993)

In summary, EDR damper is a self-centering friction damper. The dissipater is intended as a bracing element inside a frame. Although EDR damper offers good advantages such as self-centering and energy dissipation in the same device, however, there has been very limited application of this type of damper in buildings.

4.2.2.5 Ring Spring Dampers

The dissipater consists of outer and inner stainless steel rings (Figure 4.36a). The rings have tapered mating lubricated surfaces. The rings are stacked on top of each other to make a spring column with a small amount of pre-compression applied on the spring to align the rings. When a ring spring damper is loaded in compression, the rings undergo axial displacement and are sliding on conical friction surfaces (Figure 4.36b). This means that the inner rings are subjected to compression, and thus it would results in a flag-shaped hysteretic (Figure 4.36c) response of the dissipater in compression only.

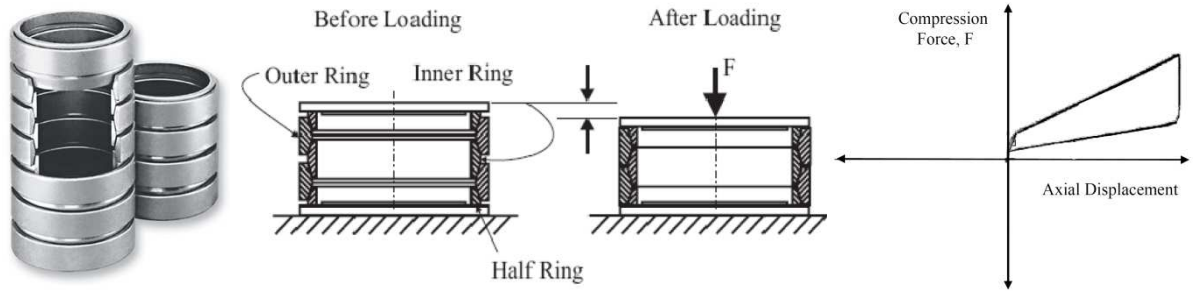

(a) Ring spring damper (b) Working mechanism of damper (c) Flag-shaped response

Figure 4.36. Ring spring dampers, after Filiatrault et al. (2000)

This type of dissipater was studied by Filiatrault et al. (2000). Research by Guerrini et al. (2012) used ring spring damper as a controlling device to prevent yielding of the unbonded post-tensioning tendons in a Dissipative Controlled Rocking (DCR) connection. This was previously discussed in Section 2.3.3.1 of Chapter 2. In this research, the ring spring damper was mounted on top of a cantilever column with DCR column to footing connection. As the column displaced, the unbonded post-tensioning bars inside the column started picking up more forces. The axial stiffness of the ring spring damper was calibrated such that after a certain drift when the post-tensioning bars were close to their yielding point, the ring spring damper was going to be compressed. Thus, it accommodated even larger drift ratios in the column without yielding of the unbonded post-tensioning bars. At the same time, the ring spring damper was helping with the self-centering of the column when the load was removed.

A variation of the ring spring damper is called "Shapia Damper", as shown in Figure 4.37a. This type of friction damper was studied by Filiatrault et al. (2000), and is currently manufactured by Spectrum Engineering in Canada. The damper can be used in bracing element of a moment-resting frame. In this type of damper, the ring spring stack is restrained by cup flanges at the end. This damper gives the advantage of inducing compression in the ring spring stack inside the damper during both tension and compression loading. This results into a symmetrical flag-shaped hysteretic response for Shapia damper, as illustrated in Figure 4.37b, (Christopolous and Filiatrault, 2006).

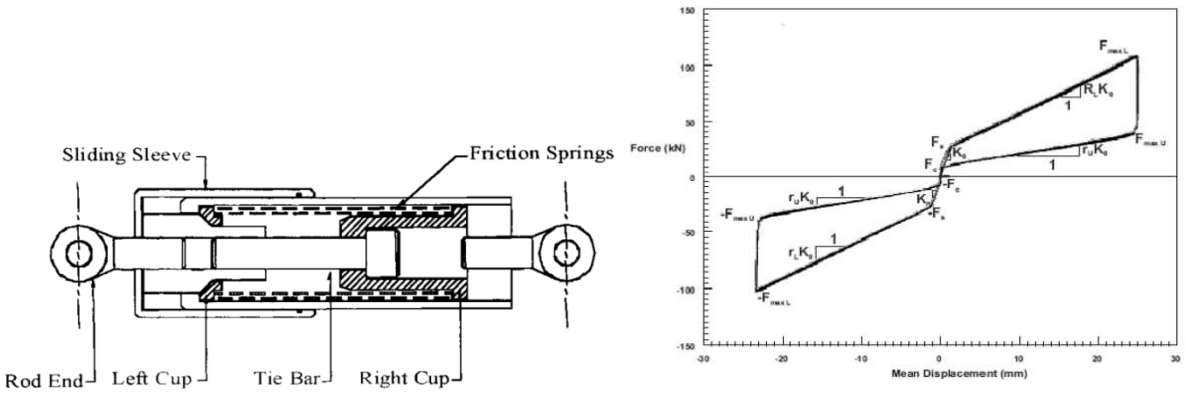

(a) Shapia damper components **(b) Symmetrical flag-shaped hysteresis**

Figure 4.37. Shapia damper, after Filiatrault et al. (2000)

As a summary, ring spring damper offers good advantages such as good energy dissipation and self-centering. There are many potential applications of this type of damper in different parts of a building such as bracings and connections. Past research has shown that ring spring damper can be used in a dissipative controlled rocking connection to protect the unbonded post-tensioning bars from yielding. Shapia damper is a variation of the ring spring damper which offers compact packaging and self-centering under compression and tension loading. Despite offering good advantages, the higher cost of fabrication due to high precision in machining of the parts and the surface preparation of the rings are the disadvantages of this type of damper.

4.2.2.6 Self-Centering Energy Dissipating Bracing

The Self-Centering Energy Dissipating Bracing (SCED) was developed and studied by Christopoulos et al. (2008). SCED can be used as a bracing member in buildings located in regions with high seismicity or wind. SCED can also be used in bridges, provided that the dissipater can accommodate the large displacement of the superstructure system which can be anticipated during a big earthquake.

This type of damper combines energy dissipation capability with self-centering feature in a single bracing element. The concept for SCED is almost identical to that of a Dissipative Controlled Rocking (DCR) where un-bonded post-tensioning bars are used to provide self-centering capacity, and dissipaters are intended to absorb seismic energy. Therefore, this type of bracing system can minimize the residual displacement in a building while providing energy dissipation.

According to Christopoulos et al. (2008), the energy dissipation source in a SCED can be metallic (yielding type), friction, or viscous damper (Figure 4.38a). The self-centering capacity is normally provided through pre-tensioned unbonded tendons which are left inside the damper and are anchored at the ends, as shown in Figure 4.38a. In order to obtain a similar behavior in both tension and compression, a reversing mechanism is provided inside the damper to stretch the pre-tensioned tendons in either case. This would result into a symmetrical behavior for SCED. The resultant hysteresis of the damper from the two springs (energy dissipater and unbonded pre-tensioned tendons) connected in parallel would be similar to that of a DCR connection (flag-shaped hysteresis), as shown in Figure 4.38.

Christopoulos et al. (2008) studied the response of SCED with pre-tensioned tendons and friction energy dissipation (Figure 4.39). Testing results have shown great energy dissipation capacity and re-centering of the brace, as shown previously in Figure 4.38b.

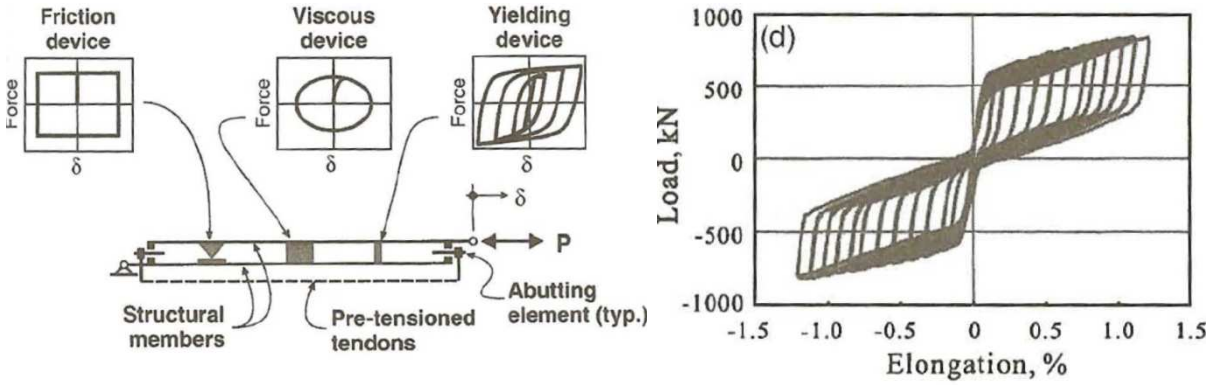

(a) SCED concept **(b) Flag-shaped hysteresis**

Figure 4.38. Self-centering energy dissipating bracing, after Christopoulos et al. (2008)

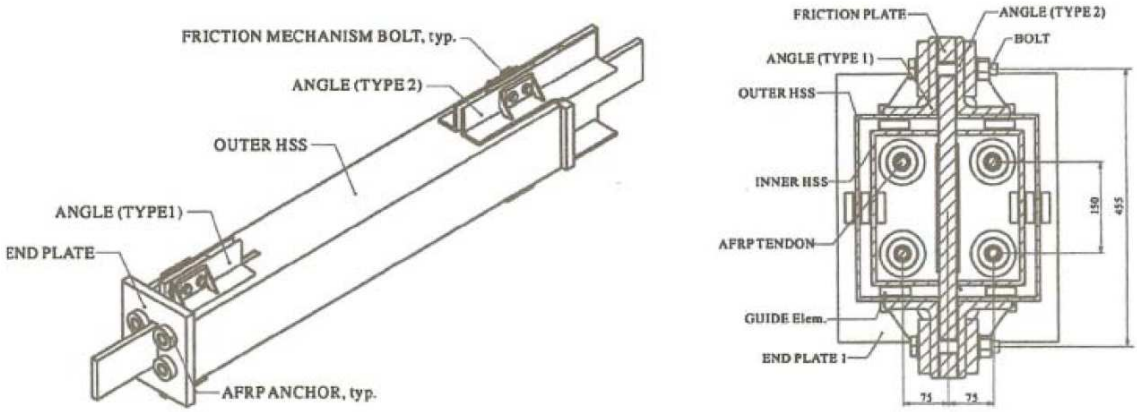

(a) SCED components **(b) Section details for SCED**

Figure 4.39. SCED with friction dissipation source, after Christopoulos et al. (2008)

In summary, the concept for SCED is similar to that of a DCR connection. SCED offers advantage of self-centering which is not integrated inside the conventional metallic bracing systems such as BRBs. SCED can be made of metallic, friction, or viscous energy dissipation source combined with pre-tensioned tendons. Past studies of SCED with friction dissipaters have shown good energy absorption and self-centering of the brace. Despite offering good advantages, the cost of fabrication could be high due to high precision machining of the parts which greatly influences the overall behavior for this type of damper, especially with friction source of dissipation.

4.2.3 Viscous Dampers

Viscous dampers are primarily velocity dependent system which dissipate energy through viscous friction. Past research investigations on viscous dampers for a variety of structures include Constantinou and Symans (1992, 1993), Filiatrault et al. (2001), and Lee (2001).

Viscous dampers are used in regions with high winds and seismicity. Given the velocity dependency, viscous dampers are particularly effective for the near-fault earthquakes where high velocity content of the ground motions can be expected.

The first known use of viscoelastic dampers (a variation of viscous dampers) in civil engineering structures was in the twin towers of late World Trade Center in New York in 1969. The dampers were intended to reduce wind vibration in the buildings (Christopoulos and Filiatrault, 2006).

Application of viscous dampers in DCR connections was previously studied by Kurama (2000), Kam et al. (2008), and Marriott (2009). Over the last two decades, there have been a variety of viscous dampers developed. This includes viscous dampers, viscoelastic dampers, and lock-up devices (shock absorbers). A summary for the most common types of viscous dampers are presented as follows.

4.2.3.1 Fluid Viscous Dampers

Fluid dampers are the most common variation of viscous dampers which are currently produced by several companies in the United States, Europe, Japan, and China. This type of damper was investigated by Constantinou and Symans (1992) and Makris and Constantinou (1992).

A typical fluid damper consists of a stainless steel piston with bronze orifice head inside a cylinder. The damper is filled with silicone oil. When loaded, the piston head orifices modify the flow attributes with the fluid relative velocity. The force in the damper is generated by the differential pressure across the piston head. The details of a typical fluid damper are illustrated in Figure 4.40.

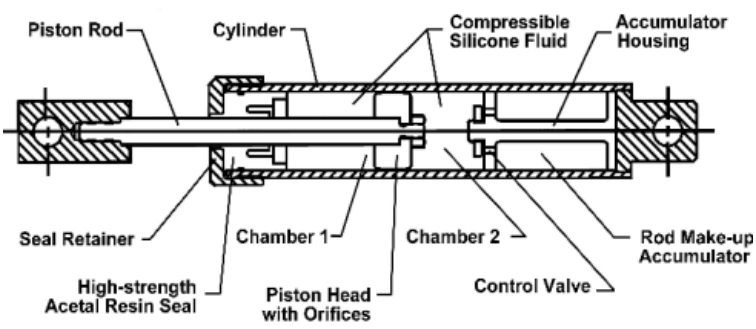

(a) Fluid viscous damper components

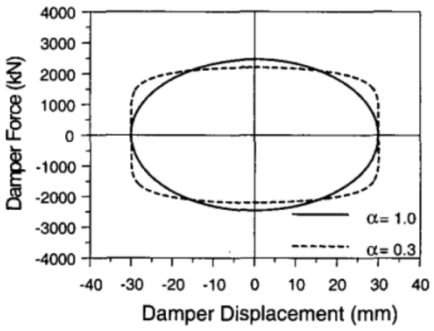

(b) Force-displacement hysteresis

(c) Typical fluid viscous damper (courtesy of M. Constantinou)

Figure 4.40. Fluid viscous dampers, after Lee (2003) and Filiatrault et al. (2013)

There have been many applications of fluid dampers in a variety of configurations in structures located in seismic regions (Figure 4.41).

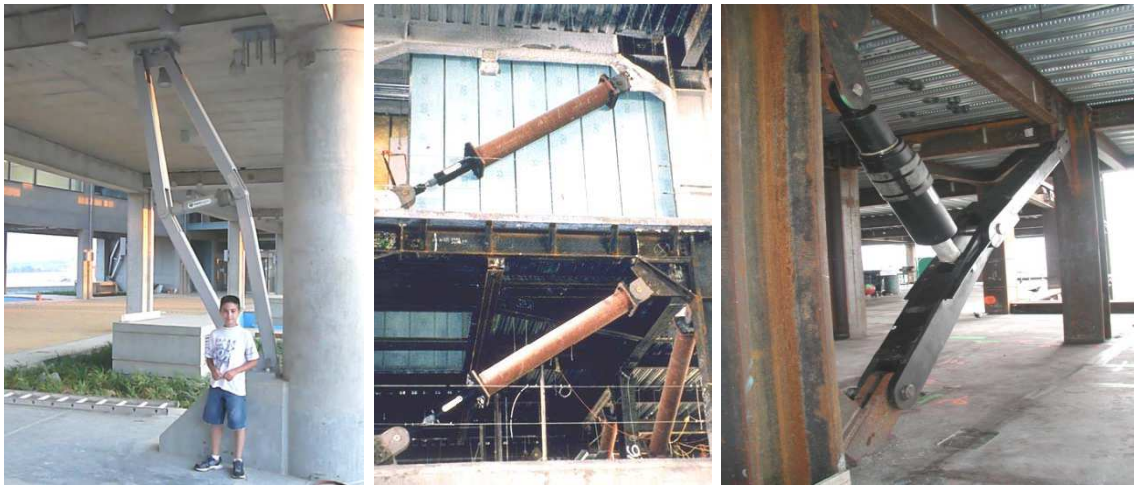

(a) Olympic building, Cyprus (b) San Francisco Civil Center (c) Yerba-Buena tower, San Francisco

Figure 4.41. Applications of fluid viscous dampers (courtesy of M. Constantinou)

In summary, fluid viscous damper offers advantages such as high capacity, stroke, and good energy dissipation without strength degradation or low-cycle fatigue failure. For seismic applications, this type of damper is more effective for the near-fault ground motions. There have been past applications of fluid viscous damper in a large number of buildings and bridges around the world. The damper can be used as a bracing element

in buildings in different configurations. Despite offering good advantages, the fabrication process for a fluid damper is not as simple as for friction or metallic dampers. The fabrication and the life-cycle maintenance costs are the common disadvantages for this type of damper.

4.2.3.2 Viscous Wall Damper

The viscous wall damper (Figure 4.42c) consists of a steel box filled with viscous fluid (Figure 4.42a). There is a vane dipped inside the wall (Figure 4.42b). The inside fluid is normally under atmospheric pressure which makes the damper a low-pressure device with large area. A typical hysteretic behavior is shown in Figure 4.42d.

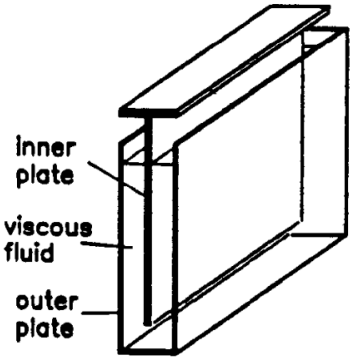

(a) Viscous Wall Damper (VWD)

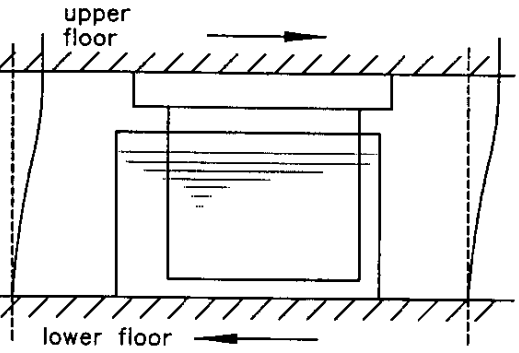

(b) VWD working mechanism

(c) Application of VWD

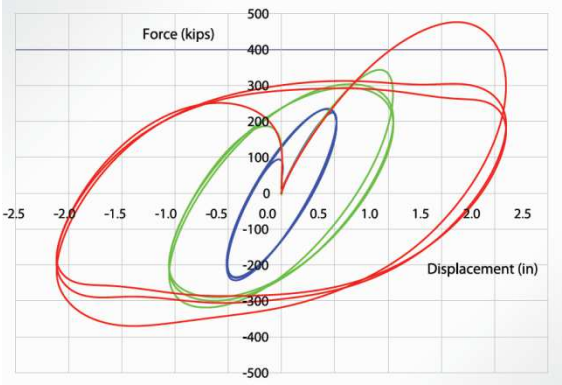

(d) VWD hysteretic behavior (Courtesy of DIS)

Figure 4.42. Viscous wall damper, after Christopoulos and Filiatrault (2006)

In summary, viscous wall damper provides advantages such as good energy dissipation, less architectural constraints (can be placed instead of a partition wall), and minimal strength degradation and low-cycle fatigue failure under cyclic loading. This type of damper has been used in over 100 buildings in Japan. Past research investigations have shown that the damper is more effective for taller flexible buildings. The main

disadvantage of this type of damper is the fabrication cost which can be higher than friction or metallic dampers. At the same time, viscous dampers are generally more effective for near- field ground motions compared to far-field excitations, (Filiatrault et al., 2001, Tan et al. 2005).

4.3 Development and Testing of New Metallic Dissipaters

In this research, several types of metallic dissipaters were invented by Gavin Keats, Alessandro Palermo, and Mustafa Mashal at the University of Canterbury. The dissipaters can be used in DCR connections for ABC Low Damage. The concepts were validated through experimental testing at the University of Canterbury. This invention resulted into filing of a United State Patent Application by the University of Canterbury (Keats, Palermo, and Mashal).

The innovative metallic dissipaters combine UFP plates (as explained in Section 4.2.15) in a smart package. Several pairs of UFPs are positioned parallel to each other to work together as a single strong spring which yields under axial displacement. The dissipaters have the following advantages:

1. Cost-effectiveness
2. Made from available mild steel material
3. Higher capacity and stroke with compact dimensions
4. Higher seismic and wind performance
5. Minimal strength degradation under cyclic loading
6. No low-cycle fatigue failure under a large number of cyclic deformation
7. Easy replaceability of the components
8. Option for multi-performance feature which would allow parts to activate during variable levels of earthquake intensity

Two types of innovative dissipaters, the bracing type and mini plug and play devices, are proposed. Each type is discussed in detail in the following sections.

4.3.1 Bracing Type Damping System

This type of damping system can be used as a bracing element in buildings and bridges in various configurations, as illustrated in Figure 4.43.

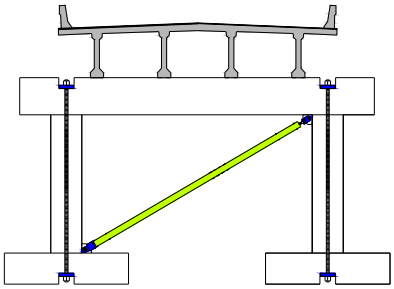

(a) Single bracing in a rocking bent

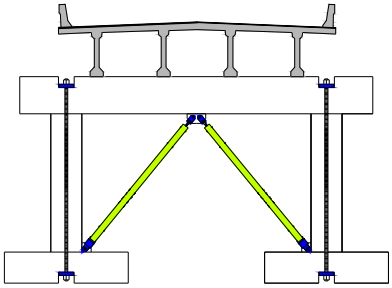

(b) Chevron bracing in a rocking bent

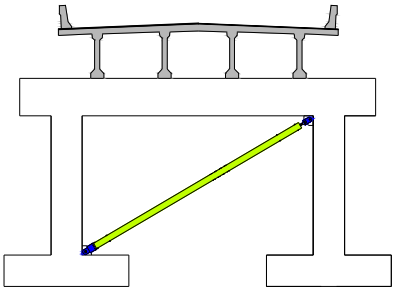

(c) Single bracing in a monolithic/precast bent

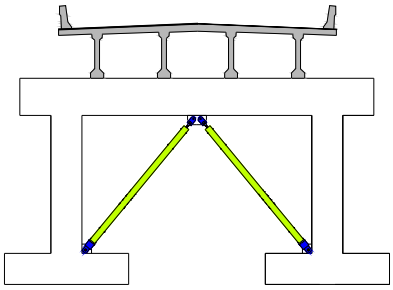

(d) Chevron bracing in a monolithic/precast bent

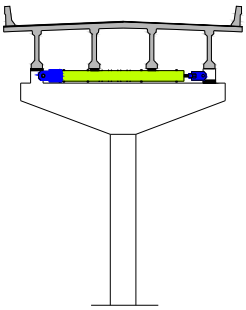

(e) Hammerhead pier (DCR or monolithic)

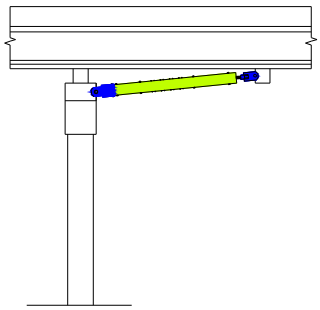

(f) Hammerhead pier (longitudinal)

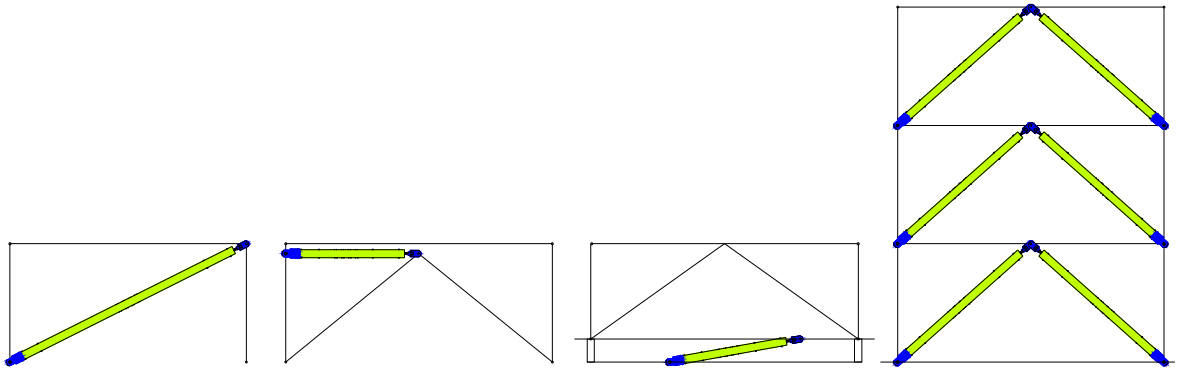

(g) Bracing for single and multi-storey buildings in various configurations

Figure 4.43. Application of bracing type dissipaters in structures

In Figure 4.43a and Figure 4.43b, the bracing dissipater is shown for implementation in ABC Low Damage. In this case, the plastic hinging zones near the column to footing and column to cap beam interfaces are replaced by rocking connections. There is no supplementary energy dissipation provided at the rocking connections. The unbonded post-tensioning inside the columns is intended to provide self-centering of the bent with the bracing dissipater absorbing the seismic energy. The resultant hysteretic behavior of the bent is expected to be similar to that of a typical DCR connection (flag-shaped). The system shown here can be a variation of ABC Low Damage bent that will be discussed in Chapter 5.

In Figure 4.43c and Figure 4.43d, the bracing damper is shown as a dissipative link in monolithic (cast-in-place) or emulative cast-in-place (ABC High Damage) bent. The bracing dissipater can be designed as a weak element to start yielding first, and thus undergo inelastic deformation with all other components (cap beam, columns, and footings) remaining in their elastic range. In this scheme, there will be minimal damage occurring to the elements and the formation of plastic hinges at the column to footing and column to cap beam interfaces can be avoided. The system may end up with residual displacement after a design level earthquake, unless the dissipater features self-centering aspect to minimize the post-earthquake displacement. The self-centering dissipater is a variation of the innovative dissipaters, refer to Section 4.3.1.2.

Figure 4.43e and Figure 4.43f show implementation of the dissipater in a hammered pier. The pier may incorporate monolithic, ABC High Damage, or rocking solutions. In this case, the dissipater is mounted just under the superstructure to absorb the seismic energy of the structure. This minimizes the inputted energy and demand on the substructure system. Therefore, the substructure system can be designed to remain elastic which in return minimizes the post-earthquake functionality and repairs of the whole bridge.

It should be noted that all innovative dissipaters proposed here can also be used for retrofitting of existing structures. Therefore, Figure 4.43c through Figure 4.43f also present cases where the substructure is retrofitted with a bracing dissipater. Figure 4.43g presents different configurations for application of the bracing dissipater in new/existing single or multi-storey buildings.

4.3.1.1 UFP Brace Dissipater

This type of damper is illustrated in Figure 4.44. The damper consists of bolted UFPs to an internal loading rod encased by a hollow square or rectangle section sleeve. The internal rod has an I-shaped section at its midspan to ease bolting of the UFPs. The ends of the loading rod can be circular or any other appropriate section. The opposite leg of the UFPs is bolted to the external sleeve. The dissipater can be stretched or compressed from one of the ends, as shown in Figure 4.44. When the dissipater is loaded in tension or compression, the UFPs are flexing with the loading rod which creates a relative sliding between the internal rod and the external sleeve. This relative movement causes yielding of the UFPs in a rolling deformation (as explained in Section 4.2.1.5) and provides energy dissipation.

In order to prevent from buckling of the internal rod, guides which provide constrains for the unsupported length of the internal rod are positioned along the length of the brace dissipater. Redundant (unbolted) UFPs can also be left in the dissipater to reinstate or increase the capacity of the brace following a big earthquake. The working mechanism of the dissipater is illustrated in Figure 4.44.

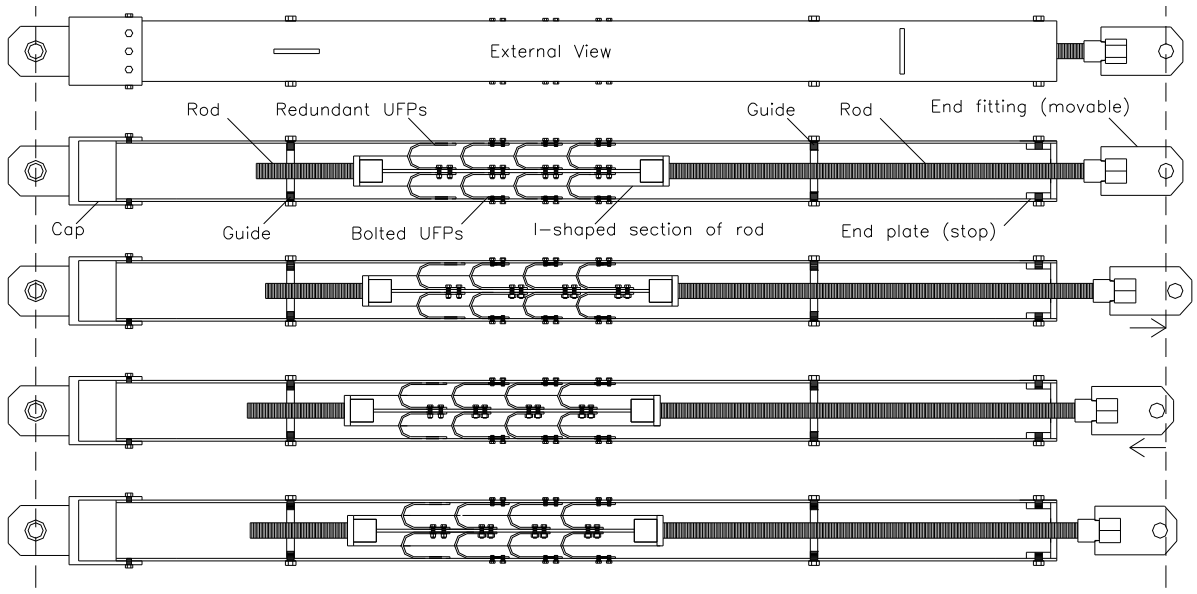

Figure 4.44. Concept for UFP brace dissipater (Keats, Palermo, and Mashal)

As it can be seen from the last sketch in Figure 4.44, the UFP bracing dissipater may be left with residual displacement following an earthquake. Therefore, it does not provide any supplemental self-centering of the brace following the earthquake.

4.3.1.2 Self-Centering UFP Brace Dissipater

The Self-Centering UFP Brace Dissipater (SCUD) is illustrated in Figure 4.45. The dissipater details are similar to that of UFP bracing dissipater, discussed in the previous section and shown in Figure 4.44. The only difference is that in SCUD, unbonded pre-tensioned high strength steel tendons are placed as a parallel spring with the UFPs. The pre-tensioned tendons are anchored at both ends. Pushing nuts are wound to the ends of the internal rod facing the movable plates.

When the dissipater is stretched or compressed, the pushing nuts and movable plates will always stretch the tendons. The tendons are intended to eliminate any residual displacement in the brace that could result from the inelastic deformation of the UFPs. Therefore, SCUD offers the advantage for self-centering of the dissipater. This concept is similar to the concept for DCR where unbonded post-tensioning provides self-centering and the dissipaters yield to absorb energy.

In SCUD, the self-centering ratio and pre-tensioning force in the tendons should be selected and designed such that during a design level loading, the tendons force should be greater than the capacity of the combined UFPs to eliminate any residual displacement in the brace. Generally, a self-centering ratio of 1.5 can be adopted for the brace at the design level loading. This is similar to the value recommended by NZS 3101 (2006) for the design of a typical DCR connection.

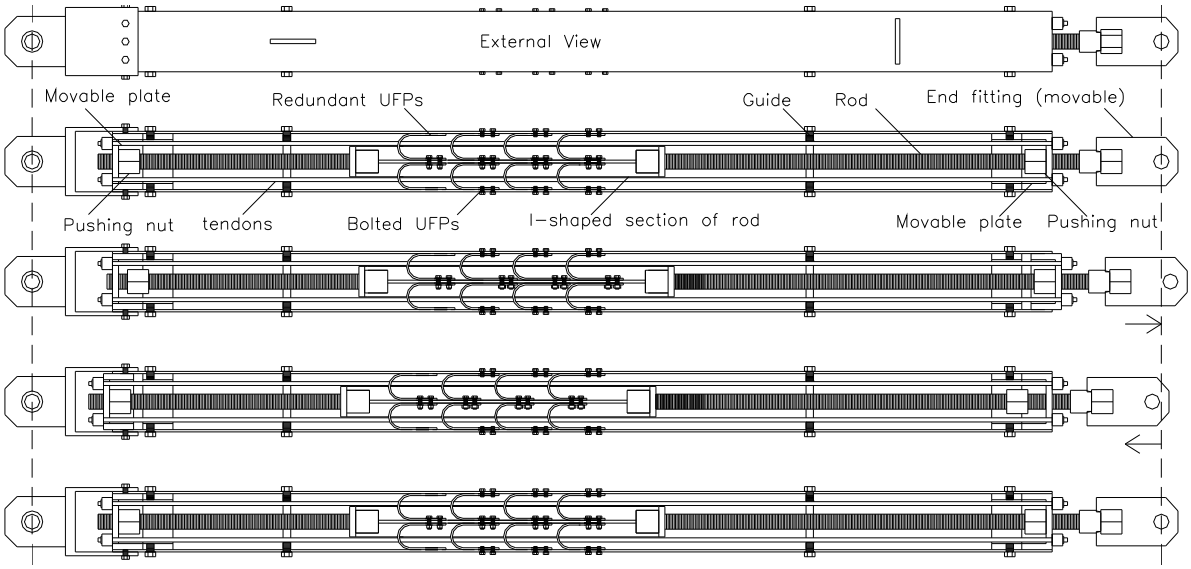

Figure 4.45. Concept for SCUD (Keats, Palermo, and Mashal)

4.3.1.3 Multi-Performance UPF Brace Dissipater

This type of dissipater is similar to the other two discussed earlier. The dissipater offers additional advantages such as enhanced stroke and activation of different parts during various earthquake levels. The end cap of the dissipater does not have to be fixed to the external sleeve. Instead, the cap can be connected to the sleeve by another type of dissipaters such as Grooved Dissipater (GD).

The capacity of grooved dissipaters can be designed such that when the brace is stretched or compressed, they activate before or after the internal UFPs yield. In the latter case, when the UFPs are near their stroke limits, grooved dissipaters will activate, and thus provide further stroke for the dissipater. This adds the multi-performance feature in the brace which means that even during a larger earthquake, the brace will be functional, and hence preventing damage to the structure. This concept can be thought similar to opening of a telescope where parts open at different stages one after another.

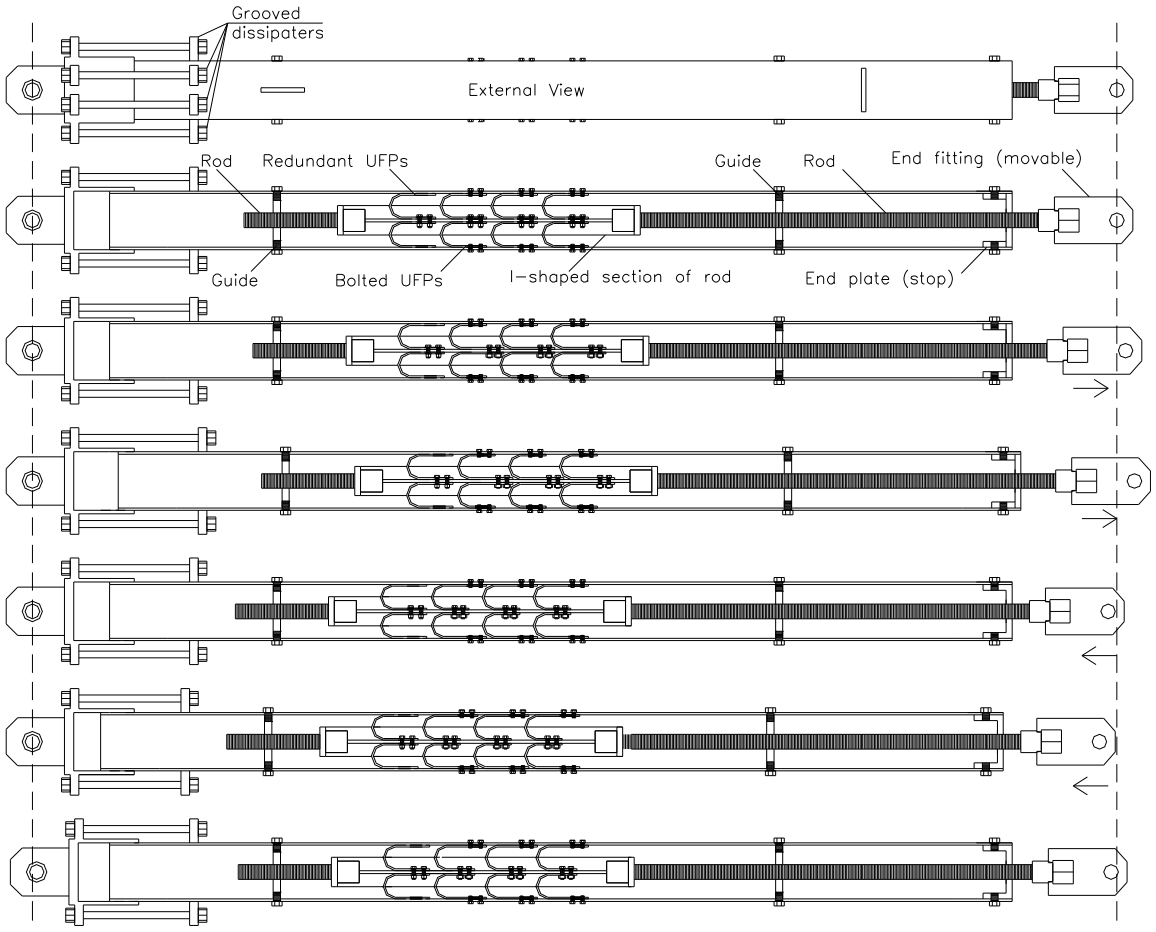

Figure 4.46. Concept for Multi-performance UFP brace dissipater (Keats, Palermo, and Mashal)

A close-up view of the concepts for a dissipative cap is presented in Figure 4.47. One variation can be using some additional UFPs between the cap and the external sleeve instead of grooved dissipaters (Figure 4.47d). Other dissipation mechanisms such as using a slotted-bolted friction connection at the cap to external sleeve connection (Figure 4.47a) may also be feasible. It is also possible to have internal grooved dissipaters instead of a dissipative cap (Figure 4.47c). In this case, grooved dissipaters are mounted parallel with the UFPs. When the brace dissipater hits the stroke limit (Δ), the grooved dissipaters will activate.

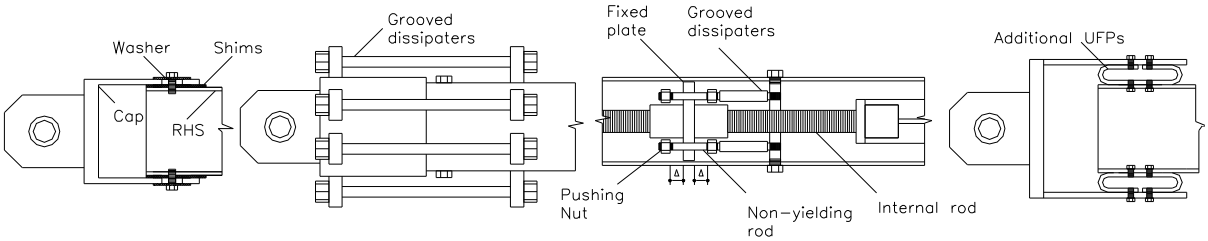

(a) Slotted-bolted cap **(b) External GD cap** **(c) Internal GD** **(d) Additional UFPs cap**

Figure 4.47. Options for multi-performance feature (Keats, Palermo, and Mashal)

Similar to SCUD, self-centering can be introduced in this type of dissipater through unbonded pre-tensioned tendons.

4.3.1.4 Prototype Brace Dissipater

The prototype brace dissipater is based on a simple portal frame which can be a multi-column pier support for a bridge (bent). The portal frame incorporates dissipaters in a chevron bracing configuration, as shown in Figure 4.48.

For the portal frame, the drift ratio at ULS level was assumed to be 0.83%. The MCE level drift ratio has been assumed to be two times greater than ULS drift ratio which equals 1.67%. Based on these drift ratios, the dissipater stroke for each of the chevron bracings was calculated to be 0.4% and 0.8% at the ULS and MCE levels, respectively. It should be noted that these drift ratios were used in testing of UFP bracing damper only. For testing of SCUD, the drifts had to be lowered down to avoid yielding of the unbonded pre-tensioned tendons, refer to Section 4.3.1.4.3.

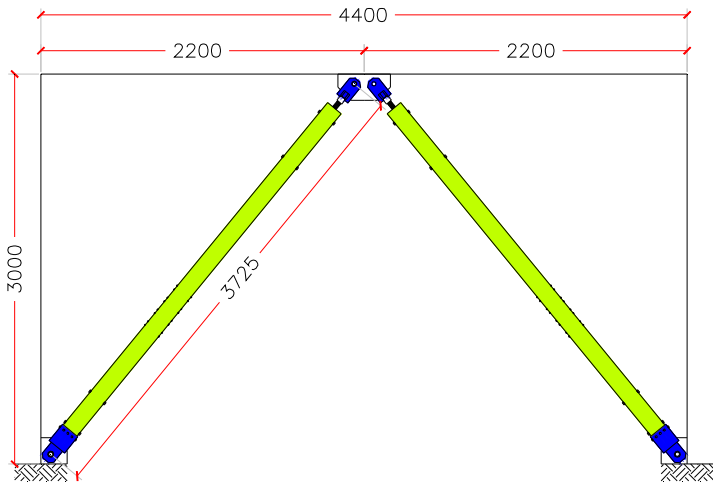

Figure 4.48. Prototype structure with chevron bracing dissipaters (dimensions in mm)

4.3.1.4.1 Brace Dissipater Specimen

To validate the concepts for some of the innovative brace dissipaters, a specimen (UFP-BD) was fabricated using some recycled steel materials in the lab. The specimen was a full-scale dissipater of that shown in Figure 4.48 with a total length of 3725 mm, weight of 330 kg, and external sleeve dimensions of 200x200x8 mm.

UFP-BD was intended for testing of the first two variations (UFP Bracing Dissipater and SCUD) of the innovative dissipaters discussed earlier. The third variation (multi-performance UFP bracing dissipater) was not tested. Given the similarity of the concept and individual testing of UFP bracing and grooved dissipaters (Section 4.3.3), the concept is expected to pass experimental validation.

For UFP-BD, the tendons were not pre-tensioned and were left loose. This transforms the brace to a UFP bracing dissipater (Figure 4.44). After testing the UFP bracing dissipater, the tendons were pre-tensioned and anchored at both ends to modify the brace dissipater into SCUD (Figure 4.45).

Using this scheme, it allowed testing of two variations of the innovative bracing type dissipaters on same specimen (UFP-BD) with slight modifications. There were three tests carried out on the bracing specimen. A description of each test is presented in Table 4.1.

Table 4.1. Description of testing on the bracing specimen (UFP-BD)

Test Name	Test No 1	Test No 2	Test No 3
Description of Specimen	**UFP Bracing Dissipater**	**SCUD: Low Pre-tensioning**	**SCUD: High Pre-tensioning**
Pre-Tensioning Per Tendon (kN)	-	13	33.5
Pre-Tensioning (f_{pt}) as Percentage of Tendon Yielding Strength (f_{py})	-	6.5	16.8
Brace ULS Drift / Displacement	±0.4% (15 mm)	±0.27% (10 mm)	±0.3% (11.25 mm)
Brace MCE Drift /Displacement	±0.8% (30 mm)	±0.6% (22.5 mm)	±0.4% (22.5 mm)
Self-Centering ratio at ULS (f_{pt} /f_{py})	-	6.1	7.5

4.3.1.4.2 Testing Arrangement and Data Acquisition System

UFP-BD was tested under the 10,000 kN DARTEC machine at the University of Canterbury Structures Lab, as shown in Figure 4.49a. The dissipater was connected under the machine using pinned connections (Figure 4.49b and Figure 4.49c).

For testing of SCUD, 250 kN load cells were installed along the load path of the tendons (Figure 4.49b). The load cells were recording tendon forces at each step of testing. The DARTEC machine was recording the overall force and displacement in the bracing specimen. During testing, the DARTEC machine was pulling and pushing the brace specimen from the bottom connection where the movable end of the dissipater was located. The top connection remained fixed throughout testing.

(a) UFP-BD under DARTEC (b) Bottom connection, movable (c) Top connection, fixed

Figure 4.49. Testing arrangement for the bracing type dissipaters

4.3.1.4.3 Loading Protocol

The specimen was tested under quasi-static cyclic loading. The loading protocol was according to the American Institute of Steel Construction (AISC) 341-05 "Seismic Provisions for Structural Steel Buildings: Qualifying Cyclic Tests of Buckling-Restrained Braces" (AISC, 2005). The AISC 341-05 presents amplitude of displacements to be applied on the specimen to produce the following axial deformations.

I. 2 cycles of loading at the deformation corresponding to $\Delta_b = \Delta_{by}$

II. 2 cycles of loading at the deformation corresponding to $\Delta_b = 0.5\Delta_{bm}$

III. 2 cycles of loading at the deformation corresponding to $\Delta_b = 1\Delta_{bm}$

IV. 2 cycles of loading at the deformation corresponding to $\Delta_b = 1.5\Delta_{bm}$

V. 2 cycles of loading at the deformation corresponding to $\Delta_b = 2.0\Delta_{bm}$

VI. Additional complete cycles of loading at the deformation corresponding to $\Delta_b = 1.5\Delta_{bm}$ as required for the brace test specimen to achieve a cumulative inelastic axial deformation of at least 200 times the yield deformation.

Where,

Δ_b = Deformation quantity used to control loading of the test specimen

Δ_{by} = Value of deformation quantity at first significant yield of specimen (Equation 4.1)

Δ_{bm} = Value of deformation quantity corresponding to design storey drift

The loading sequence for each of the three tests carried out (Table 4.1) was as follows:

A. Test No 1 Loading Sequence (UFP Bracing Dissipater, UFP-BD)

I. 2 cycles of loading at the deformation corresponding to $\Delta_b = 3.2$ *mm* (Yield)

II. 2 cycles of loading at the deformation corresponding to $\Delta_b = 7.5$ *mm*

III. 2 cycles of loading at the deformation corresponding to $\Delta_b = 15$ *mm* (ULS)

IV. 2 cycles of loading at the deformation corresponding to $\Delta_b = 22.5$ *mm*

V. 2 cycles of loading at the deformation corresponding to $\Delta_b = 30$ *mm* (MCE)

VI. 8 cycles of loading at the deformation corresponding to $\Delta_b = 22.5$ *mm*

A plot of the loading sequence is presented in Figure 4.50.

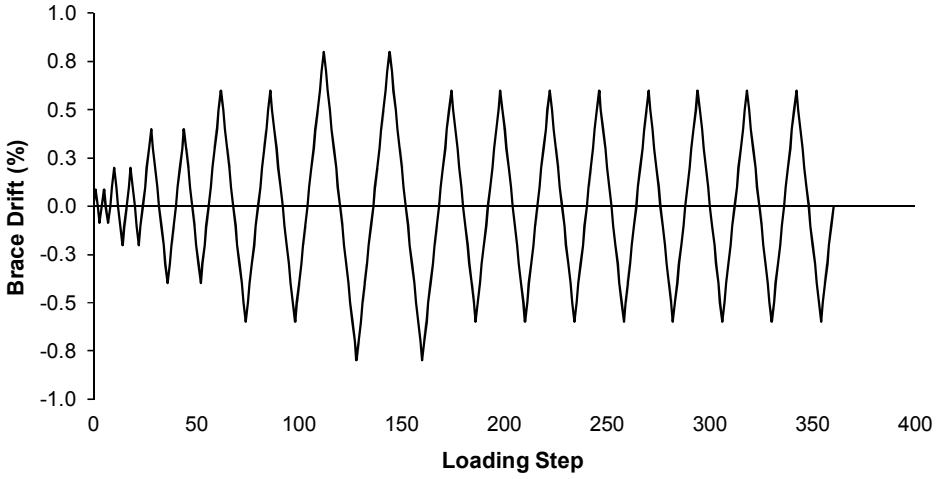

Figure 4.50. Loading sequence for Test No 1: UFP Bracing Dissipater

B. Test No 2 Loading Sequence: SCUD - Low Pre-tensioning (PT = 6.5%f_{py})

I. 2 cycles of loading at the deformation corresponding to $\Delta_b = 3.2$ *mm* (Yield)

II. 2 cycles of loading at the deformation corresponding to $\Delta_b = 2.5$ *mm*

III. 2 cycles of loading at the deformation corresponding to $\Delta_b = 5$ *mm*

IV. 2 cycles of loading at the deformation corresponding to $\Delta_b = 7.5$ *mm*

V. 2 cycles of loading at the deformation corresponding to $\Delta_b = 10$ *mm* (ULS)

VI. 8 cycles of loading at the deformation corresponding to $\Delta_b = 22.5$ *mm* (MCE)

A plot of the loading sequence is presented in Figure 4.51.

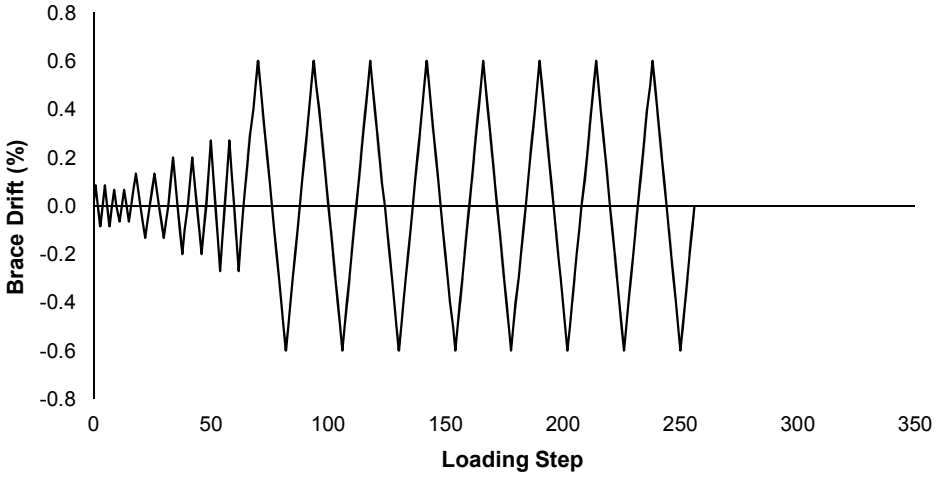

Figure 4.51. Loading sequence for Test No 2: SCUD, PT = 6.5%f_{py} or 13 kN per tendon

C. Test No 3 Loading Sequence: SCUD - High Pre-tensioning (PT = 16.8%f_{py})

I. 2 cycles of loading at the deformation corresponding to $\Delta_b = 3.2$ *mm* (Yield)

II. 2 cycles of loading at the deformation corresponding to $\Delta_b = 3.75$ *mm*

III. 2 cycles of loading at the deformation corresponding to $\Delta_b = 7.5$ *mm*

IV. 2 cycles of loading at the deformation corresponding to $\Delta_b = 11.25$ *mm* (ULS)

V. 4 cycles of loading at the deformation corresponding to $\Delta_b = 15$ *mm* (MCE)

VI. 15 cycles of loading at the deformation corresponding to $\Delta_b = 11.25$ *mm*

A plot of the loading sequence is presented in Figure 4.52.

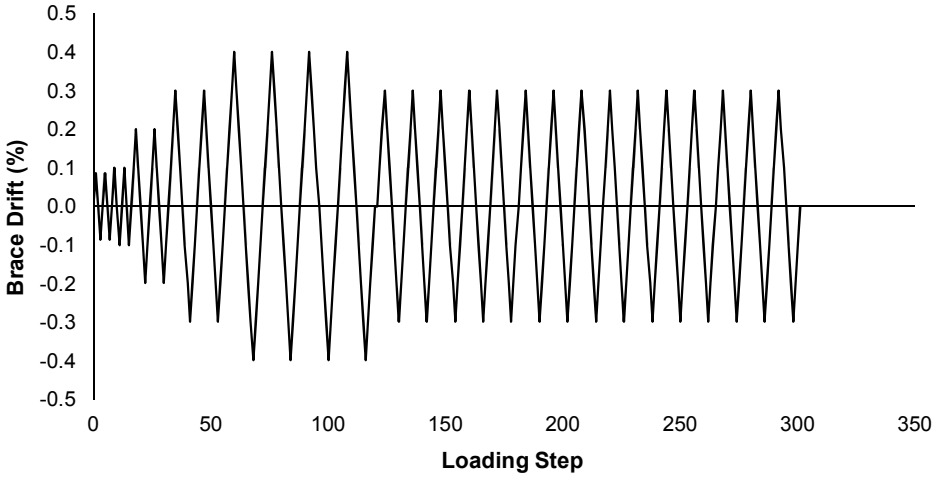

Figure 4.52. Loading sequence for Test No 3: SCUD, PT = 16.8%fpy or 33.5 kN per tendon

4.3.1.4.4 Design of UFP-BD

The yielding force (F_y) of a single UFP can be calculated using Equation 4.1 in accordance with Kelly et al. (1972).

$$F_y = \frac{\sigma_y \, b_u t_u^2}{2D_u} \tag{4.1}$$

In Equation 4.1, σ_y is the yielding strength of the mild steel UFP plates (assumed as 300 MPa for UFP-BD), b_u, t_u, and D_u parameters are the width, thickness, and diameter of the UFPs, respectively. It should be noted that D_u is measured from center to center of the UFP legs, as shown in Figure 4.53.

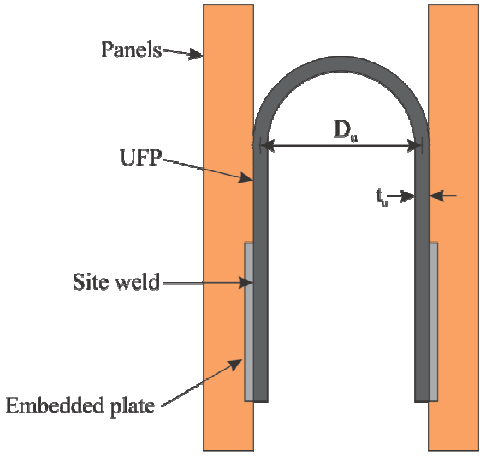

Figure 4.53. Parameters for a UFP mounted between two panels, after Baird et al. (2014)

Equation 4.2 presents the yield displacement of a UFP from Baird et al. (2014).

$$\Delta_y = \frac{27\pi F_y D_u^3}{16E \, b_u t_u^3} \tag{4.2}$$

In Equation 4.2, E is the modulus of elasticity for UFP steel plates. The maximum strain (ε_{max}) of UFP is given by Equation 4.3.

$$\varepsilon_{max} = \frac{t_u}{D_u} \tag{4.3}$$

Kelly et al. (1972) found an overstrength factor of 1.45 to 2.15 greater than the yield force for the UFPs by conducting direct tension tests. However, the tests carried out by

Kelly et al. (1972) had the UFPs subjected to high displacements relative to their radius. This produced higher strains and larger overstrength factors for the UFPs which in return reduced the number of cycles to UFP failure point. Testing on the UFPs under reversed cyclic loading by Iqbal et al. (2007) observed the failure mechanism of the UFPs. The failure started with localized kinking of the plate and followed by rapid plate transverse fracture.

Baird et al. (2014) observed an overstrength factor of 1.3 of the UFP's yield force. According to Baird et al. (2014), there was no degradation of strength in the UFPs after twenty cycles at the maximum stroke, and therefore no failure occurred. At the same time, the study suggested that there was no existing data that showed failure of the UFPs under cyclic loading, if the maximum strain in the UFP (Equation 4.3) was in the range of 6.5%.

UFP-BD was initially designed to represent a UFP bracing dissipater which incorporated 8 UFPs each with 6 mm thickness, 90 mm width, and 75 mm rolled diameter. Using Equation 4.1 and $f_y = 300\ MPa$, the yield capacity of single UFP was calculated to be 6.5 kN. This means that the yield capacity for the combined 8 UFPs was expected to be 52 kN. The yield displacement of the UFP was calculated to be in order of less than 3.7 mm in accordance with Equation 4.2. This was taken as 3.2 mm for the bracing specimen. Using Equation 4.3, the maximum strain (ε_{max}) in the UFP was 8%.

Test No 1 was intended to validate the concept for a UFP bracing dissipater. The UFPs were designed to accommodate a maximum stroke of ±30 mm (0.8% drift ratio in the brace). Assuming an overstrength factor of 1.5 for the mild steel plates, the brace specimen was expected to achieve a maximum capacity of approximately 78 kN at the maximum stroke (30 mm).

For the subsequent testing and validation of the concept for SCUD, the UFP-BD was modified to represent a SCUD through anchoring and pre-tensioning of the tendons. Given the limitation on the length of the tendons and height of the DARTEC machine, the brace stroke had to be reduced in order to avoid yielding and rupturing of the tendons, refer to Table 4.1. In SCUD, as the brace is stretched or compressed, the brace force level can significantly increase due to presence and stretching of the tendons. The brace force

was designed to be under 450 kN due to strength of the recycled parts such as welding, bolts, fittings etc.

Test No 2 and Test No 3 were carried out to just validate the concept for SCUD for two levels of pre-tensioning of the four tendons in the brace. It should be noted that the full development, design, optimization, experimental testing, and analytical modeling of prototypes for SCUD are out of the scope of this research.

In Test No 2, the combined pre-tensioning force in the tendons was selected such to be approximately equal to the yield capacity of the brace (52 kN). This means that each tendon was pre-tensioned to a force level of 13 kN (6.5% of tendon yield capacity) which gives a combined pre-tensioning force of 52 kN for four tendons in the brace. Thus, the self-centering ratio (λ) was expected to be 1.0 and 6.1 at the yield and ULS levels, respectively. It was expected that such level of pre-tensioning in the tendons may not be able to overcome the combined capacity of the UFPs to re-center the brace, and hence the brace may be left with some residual displacement.

In Test No 3, the combined pre-tensioning force in the tendons was increased to a higher level of 134 kN or 33.5 kN per tendon (16.8% of tendon yield capacity). This gives self-centering ratios of 2.6 and 7.5 at the yield and ULS levels, respectively. It was expected that the increased level of pre-tensioning in the tendons should be sufficient to fully overcome the combined capacity of the UFPs, and thus re-center the brace with no residual displacement.

For UFP-BD, the UFPs were the only part in the dissipater where inelastic deformation would be concentrated. This means that all other parts had to be designed to remain in their elastic range throughout testing. The buckling load of the internal rod was calculated using simple approach as that from an Euler's column formula. Sufficient number of guides was provided to reduce the unsupported length of the Macalloy bar to prevent any buckling of the rod under 500 kN axial force.

4.3.1.4.5 Fabrication and Assembly of Brace Specimen

The UFPs were made of available steel plates in the lab. The plates were rolled into UFPs using a hand-operated roller which is commonly used for bending rebars to stirrups, as shown in Figure 4.54a and Figure 4.54b. The internal rod consisted of a 50 mm

diameter Macalloy bar. The midspan section of the internal rod was made of an I-shaped beam to ease bolting of the UFPs. The I-beam was simply made by welding three steel plates in the form of I-shaped section (Figure 4.54d). Each UFP was connected to the I-beam using four 12 mm diameter high strength bolts. The assembled internal rod with the bolted UFPs was inserted into an external tube (Figure 4.54f). The free legs of the UFPs were then bolted to the tube from outside (Figure 4.54g).

Four 12.7 mm diameter high strength steel tendons (f_y *=1560 MPa)* were placed inside the dissipater and anchored at the cap end (Figure 4.54h). The tendons were left loose at the movable end (Figure 4.54k) during Test No 1 (UFP Bracing Dissipater), but were subsequently pre-tensioned and anchored for Test No 2 and Test No 3 (SCUD).

(a) UFP Roller

(b) Close-up view of the UFP roller

(c) UFP-BD components

(d) UFPs bolted to the I-beam part of internal rod

(e) Guides and the Macalloy bar at the ends

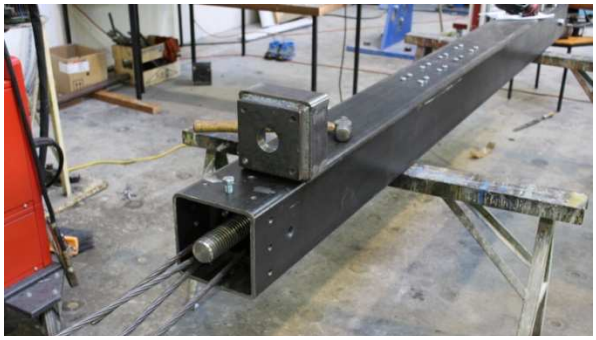

(f) Assembled internal rod inside the tube

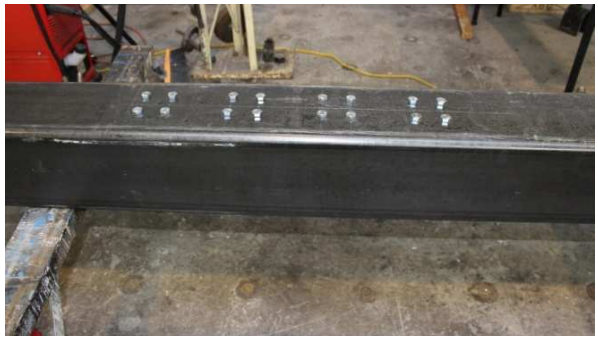

(g) UFPs bolted from outside into the tube

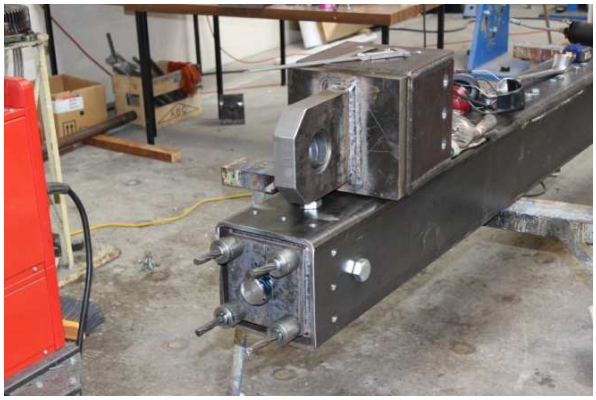

(h) Tendons anchored on the cap end

(i) Cap inserted and bolted

(j) Movable end, pushing nut visible

(k) Movable end and plate, tendons left loose

Figure 4.54. Fabrication and assembly of bracing specimen (UFP-BD)

For testing of SCUD, the tendons were pre-tensioned using a hand-operated hydraulic pump, as shown in Figure 4.55. The load cell along the load path of each tendon was measuring the pre-tensioning force. Once the desirable force level was achieved in the tendon, steel washers and spacers were placed between the anchor and the load cell to lock the pre-tensioning force in the tendon (Figure 4.55c). The pressure in the pump was then released and the jack was removed.

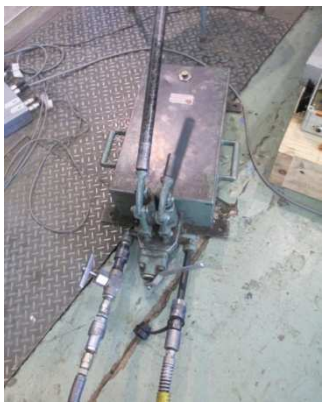

(a) Hydraulic hand pump (b) Pre-tensioning tendons (c) Close-up view

Figure 4.55. Pre-tensioning of tendons using hydraulic hand pump for SCUD

4.3.1.4.6 Testing Results and Performance Evaluation

A. Test No 1 (UFP Bracing Dissipater): The dissipater completed all loading cycles without any failure. The axial force-displacement hysteresis is plotted in Figure 4.56 where the positive vertical and horizontal axes show the bracing dissipater during the pull stage of the loading. The bracing dissipater showed a very stable hysteresis with no signs of strength degradation or low-cycle fatigue failure.

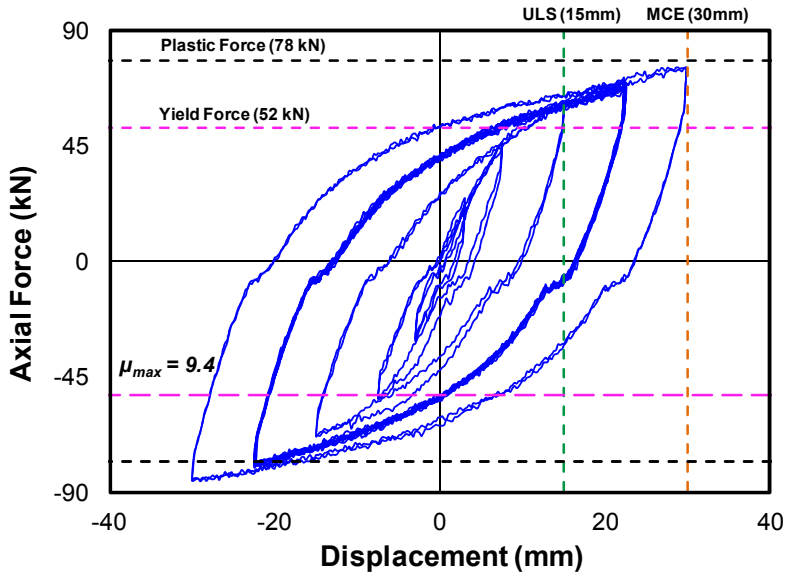

Figure 4.56. Force-displacement hysteresis for UFP bracing dissipater

In Figure 4.56, the dissipater achieved its predicted maximum capacity of 78 kN during the cycles of 30 mm displacement which corresponds to MCE level displacement (0.8% drift ratio). The residual displacement in the dissipater following testing was in order to 23.5 mm (0.63% drift ratio). This corresponds to almost 80% of MCE level drift.

In Figure 4.56, there is a slight slacking in the hysteresis loops as the dissipater is unloading. This was thought to be due to tolerances in the drilled holes and some movement of the bolts which were connecting the UFPs to the internal rod and the external tube. As mentioned previously, the dissipater was fabricated using available materials and recycled steel plates in the lab. If the parts are machined by fabricator, the slacking effects can be eliminated and, thus the hysteretic response will be improved. An alternative to bolting the UFPs could be welding. This would eliminate any undesirable movement in the bolt holes and could enhance the efficiency of the UFPs.

The backbone curve for the bracing dissipater is plotted in Figure 4.57. The dissipater showed a very smooth envelope curve with negligible difference in force level (less than 10 kN) during tension and compression stages of loading.

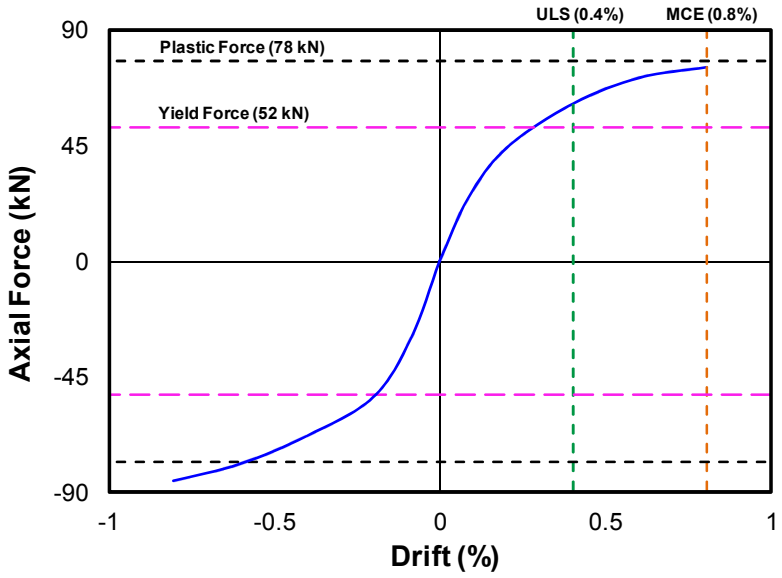

Figure 4.57. Backbone curve for UFP bracing dissipater

The energy dissipated per each cycle of each drift ratio is presented in Figure 4.58.

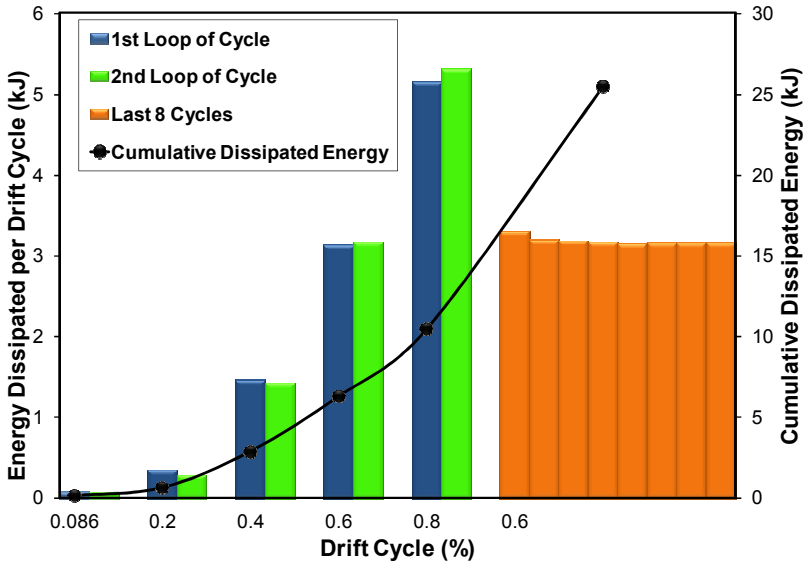

Figure 4.58. Dissipated energy (per cycle and cumulative) for UFP bracing dissipater

In Figure 4.58, during MCE level loading (0.8% drift ratio), unlike other drift ratios, the dissipater had slightly more energy dissipation in the second cycle compared to first one. This was thought to be due to presence of friction and contact between the internal parts of the dissipater as the UFPs are rolled to their maximum displacement. However,

this is not a significant issue and could be overcome by lubricating the parts to maximize the efficiency of the UFPs. It is also obvious that there was no noticeable reduction in energy dissipation capacity of the brace during the last 8 consecutive cycles of 0.6% drift ratio (1.5 ULS). This represents a good performance of the UFPs under cyclic loading as the brace strength does not degrade under a large number of cycles beyond yield point.

In accordance with Priestley et al. (2007), the corrected experimental area-based damping curve for the UFP bracing dissipater is plotted against the displacement ductility in Figure 4.59. Using Dwairi-Kowalsky damping rule (Dwairi et al., 2007), the theoretical hysteretic damping curves for steel structures such as Ramberg-Osgood, Elastic-Perfectly Plastic, and Bilinear (with a ratio of post-yield to initial stiffness (r) equal 0.2) were also plotted alongside the experimental hysteretic damping curve for UFP-BD. For the theoretical damping curves, it was assumed that the system had an effective period ($T_{eff} \geq 1\ sec$).

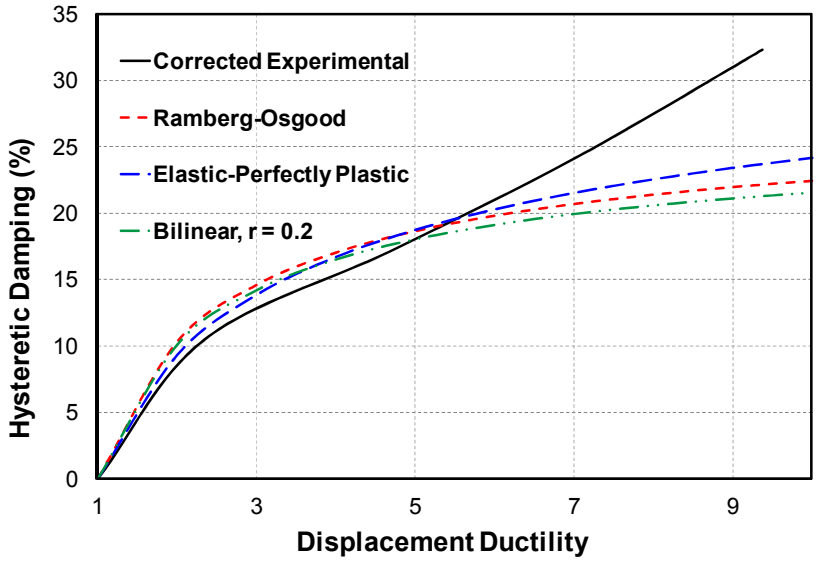

4.59. Corrected area-based hysteretic damping for UFP bracing dissipater

According to Figure 4.59, values of hysteretic damping for the UFP dissipater were slightly lower than the other three hysteretic models shown up to a ductility of 5. For ductilities just over 5, the experimental hysteretic damping curve is located above the Ramberg-Osgood, Elastic-Perfectly Plastic, and Bilinear models.

The experimental hysteretic damping curve attained a peak value of 32.3% at a displacement ductility of 9.3 during MCE level drift ratio (0.8%). Unlike other metallic dampers, there was no strength degradation in the UFPs, and hence no failure was imminent. This means that the dissipater was able to achieve higher levels of hysteretic damping with increasing displacement ductility.

B. Test No 2 (SCUD - Low Pre-Tensioning): The axial force-displacement hysteresis plot is presented in Figure 4.60. The self-centering brace dissipater showed a stable hysteresis. Since the brace was subjected to a test prior to modifying it to SCUD, the UFPs had previous yield from Test No 1.

The strength degradation noticeable in Figure 4.60 after the first cycle of 22.5 mm displacement was thought to be due to pre-tensioning relaxation and losses in the tendons, not the strength degradation in the UFPs. This can also be observed in the hysteresis plot for the combined tendon forces against brace drift ratio in Figure 4.60. The reason behind this was the lower level of pre-tensioning in the tendons ($6.5\%f_{py}$). The UFPs inside the brace did not show any noticeable signs of strength degradation. This is clear following the first cycle in the subsequent cycles at each drift ratio. The backbone curve for the brace is shown in Figure 4.61.

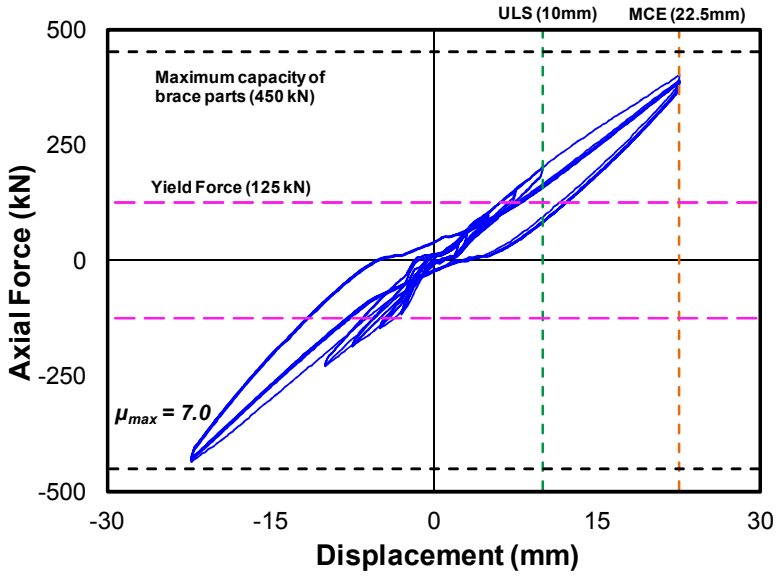

Figure 4.60. Force-displacement hysteresis for SCUD-Low Pre-Tensioning

In Figure 4.61, it can be seen that as the drift increases, the brace capacity also increases rapidly. This is due to presence of the steel tendons which attract more force with

further displacement. Therefore, as expected, the addition of pre-tensioned tendons had significantly increased the capacity of the brace. The brace achieved a maximum capacity of nearly 450 kN during MCE level loading (0.6%). The residual displacement in the dissipater following MCE level loading was in order of 5 mm (0.134% drift ratio). This corresponds to almost 22% of MCE level drift ratio. The residual displacement was due to the lower pre-tensioning force in the tendons and also some pre-tensioning losses during cyclic loading.

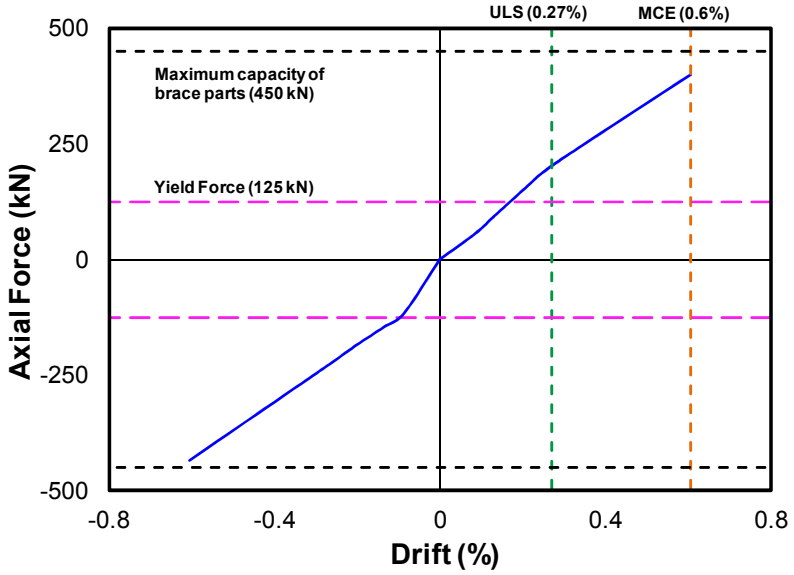

Figure 4.61. Backbone Curve for SCUD-Low Pre-Tensioning

Figure 4.62 presents hysteresis plot for the combined tendon forces against the brace drift ratio. The steel tendons remained elastic throughout testing. However, the combined pre-tensioning force of 52 kN in the tendons had dropped significantly during the larger cycles of loading. By the end of testing, there was nearly an average of 67% loss in pre-tensioning force of the tendons. Therefore, the tendon force was not able to overcome the capacity of the combined UFPs. This contributed into some residual displacement in the brace following testing. The drop in pre-tensioning force was a result of pre-tensioning losses in the tendons due to the lower pre-tensioning force ($6.5\%f_{py}$).

The pre-tensioning losses may have resulted from anchorage loss, friction, elastic deformation of steel parts, and tendon relaxation during larger drifts. It is expected that a higher level of pre-tensioning which takes into account the above losses could eliminate the drop in the pre-tensioning force of the tendons as discussed in Test No 3.

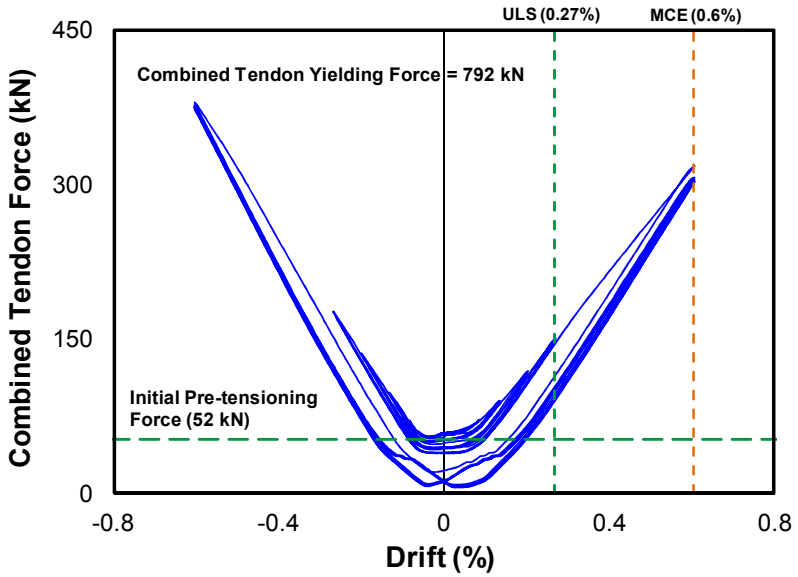

Figure 4.62. Tendon force-drift hysteresis for SCUD-Low Pre-Tensioning

The energy dissipated per each cycle of each drift ratio is presented in Figure 4.63. During 0.6% MCE drift ratio, the energy dissipation capacity was comparable to that of the UFP bracing dissipater (Figure 4.58). The increase in the first cycle of the 0.6% drift ratio is thought to be caused by the friction between the parts. This effect was reduced during the subsequent cycles, as shown Figure 4.63. It is also obvious that there is no significant reduction in energy dissipation capacity during the last 7 consecutive cycles of 0.6% drift ratio (2.0 ULS).

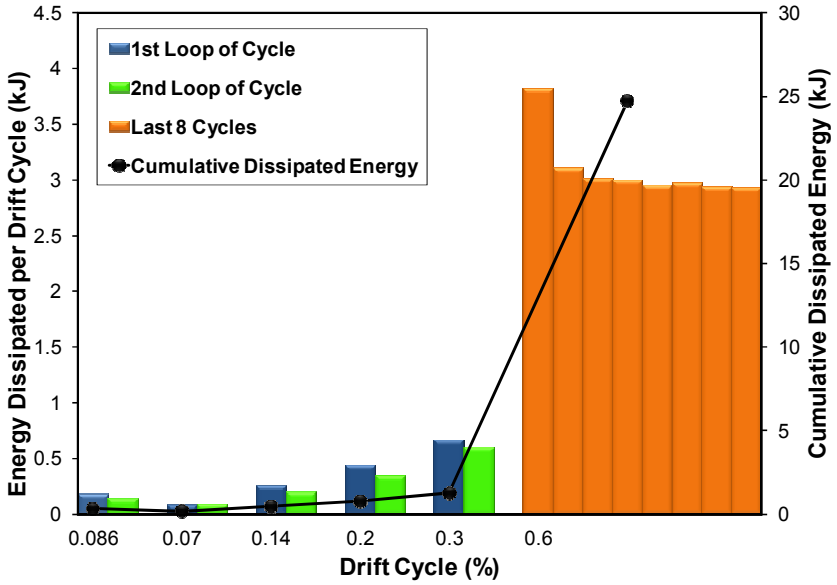

Figure 4.63. Dissipated energy (per cycle and cumulative) for SCUD-Low Pre-Tensioning

The corrected experimental area-based damping curve for the self-centering brace is plotted in Figure 4.64a. For a comparison, the theoretical hysteretic damping curve for a Flag-Shaped model with force ratio (β) of 0.35 and effective period of $T_{eff} \geq 1\ sec$ in accordance with Priestley et al. (2007) is also plotted. The theoretical Flag-Shaped hysteretic rule is shown in Figure 4.64b.

In Figure 4.64a, the hysteretic damping values for the self-centering brace were slightly lower than those for a theoretical flag-shaped model between ductilities of 1 to 7. The experimental hysteretic damping curve attained a peak value of 8.2% at the displacement ductility of 7 during MCE level drift ratio (0.6%).

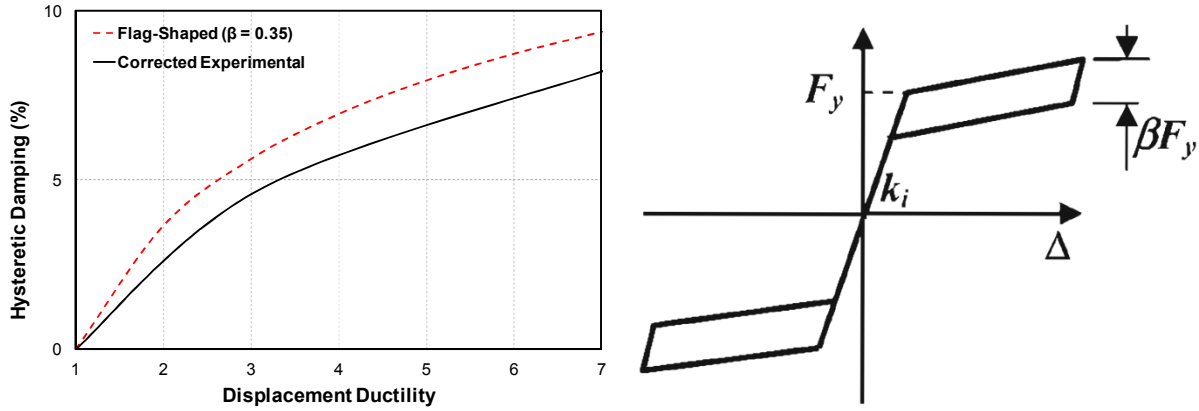

(a) Hysteretic damping for SCUD **(b) Flag-Shaped hysteresis (Priestley et al., 2007)**

Figure 4.64. Corrected area-based hysteretic damping for SCUD-Low Pre-tensioning

C. Test No 3 (SCUD - High Pre-Tensioning): The axial force-displacement hysteresis plot is presented in Figure 4.65. The flag-shaped response of the brace dissipater can be observed. The brace showed a high level of self-centering with small energy dissipation, but no signs of strength degradation and almost zero residual displacement following testing. The brace achieved a maximum capacity of about 450 kN during MCE level loading (0.4%). The backbone curve is plotted in Figure 4.66.

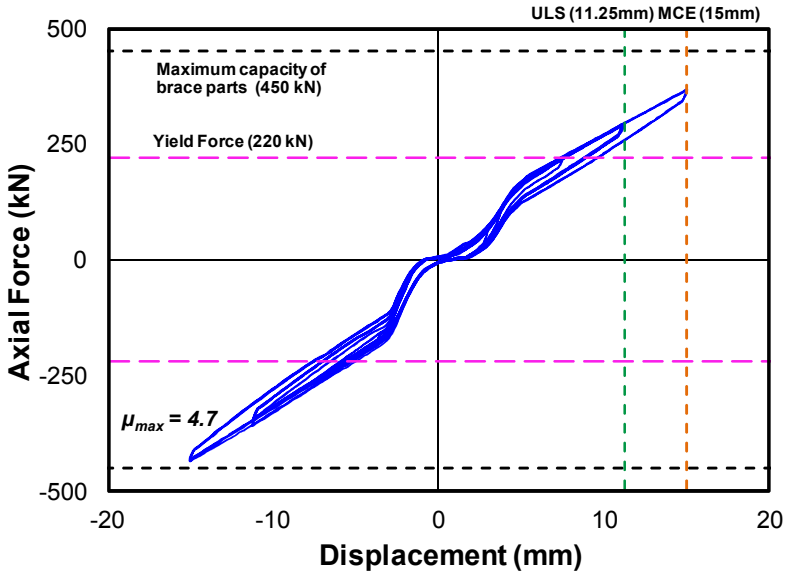

Figure 4.65. Force-displacement hysteresis for SCUD-High Pre-Tensioning

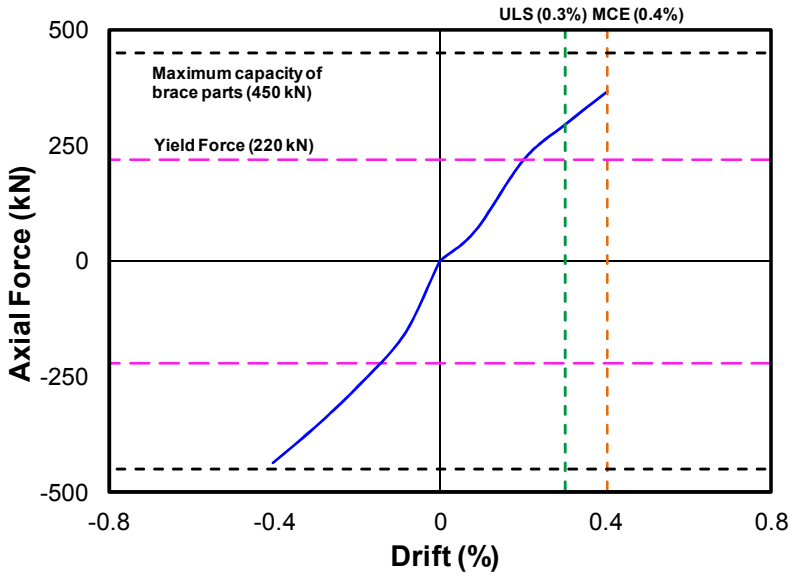

Figure 4.66. Backbone Curve for SCUD-High Pre-Tensioning

The combined tendon force-brace drift hysteresis is plotted in Figure 4.67. The tendons did not show a symmetrical behavior during tension and compression stages of loading. This was thought to be due to poor fabrication (recycled materials and parts) of the brace. This can be improved by accurate machining and fabrication of the parts. The higher pre-tensioning force in the tendons was able to overcome the capacity of the combined UFPs, and hence re-centered the brace. By the end of testing, there was only 6 kN drop in the combined pre-tensioning force of the tendons which corresponds to less than 4.5% of the initial pre-tensioning force (134 kN).

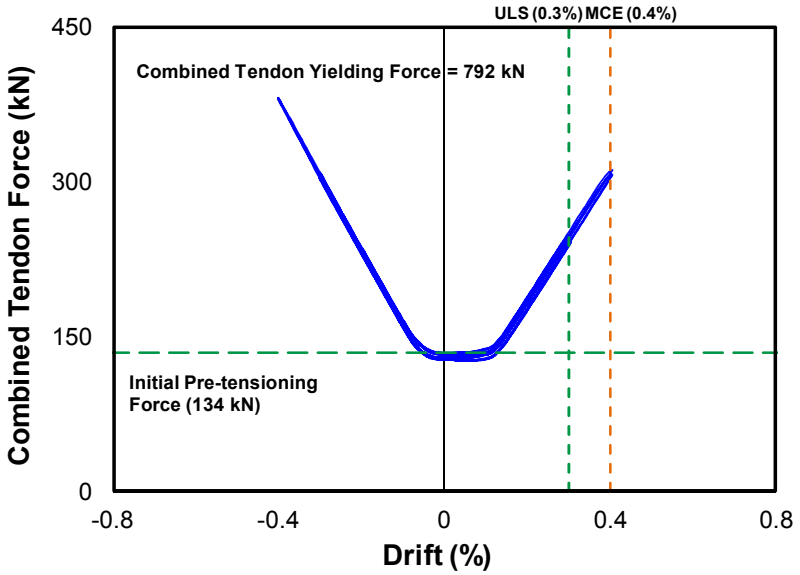

Figure 4.67. Tendon force-drift hysteresis for SCUD-High Pre-Tensioning

The energy dissipated per each cycle of each drift ratio is shown in Figure 4.68. During 0.4% MCE drift ratio, the energy dissipation capacity was slightly lower compared to UFP bracing dissipater (Figure 4.58). In Figure 4.68, there was almost zero reduction in energy dissipation capacity during the last 15 cycles of 0.3% drift ratio (ULS).

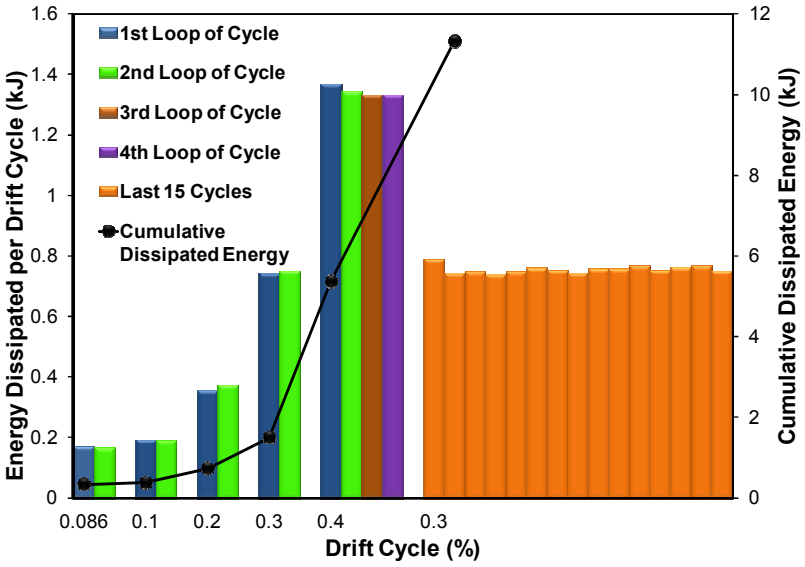

Figure 4.68. Dissipated energy (per cycle and cumulative) for SCUD-High Pre-Tensioning

The corrected experimental area-based damping curve is plotted in Figure 4.69. The hysteretic damping values were considerably lower than those for the theoretical flag-shaped model with $\beta = 0.35$ and SCUD with Low Pre-tensioning. This was due to a very

high re-centering ratio in the brace. The experimental hysteretic damping curve attained a peak value of 4.2% at a ductility of 4.7during MCE drift ratio (0.4%).

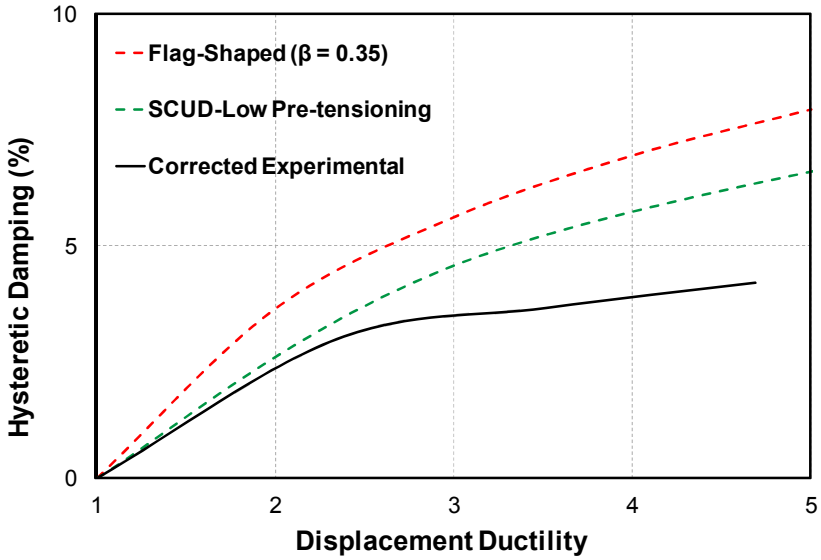

Figure 4.69. Corrected area-based hysteretic damping for SCUD-High Pre-Tensioning

4.3.1.5 Summary of Testing Results for Bracing Type Damping System

The concept for two variations of bracing type damping system, the UFP Bracing Dissipater and Self-Centering UFP Bracing Dissipater (SCUD), were experimentally validated. Based on the testing results, it is expected that the proposed concept for the third variation (Multi-Performance UFP Bracing Dissipater) could also pass the experimental validation.

Test No 1 which represented the UFP bracing dissipater showed a very stable hysteresis with higher levels of hysteretic damping (bigger than 32%). The displacement ductility reached a value of almost 10 with no obvious signs of strength degradation or fatigue failure in the specimen. Based on Dwairi-Kowalsky damping rule, following displacement ductility of 5, the brace had higher values of hysteretic damping compared to those from theoretical models of Ramberg-Osgood, Elastic-Perfectly Plastic, and Bilinear models.

The UFP bracing dissipater specimen was later modified to a SCUD, and was tested under two levels of pre-tensioning force (low and very high) in the tendons. Both tests showed good performance of the dissipate. As expected, the flag-shaped hysteretic

behavior of the UFPs combined with the pre-tensioned tendons was obvious. Similar to the UFP bracing dissipater, there was no strength degradation or signs of low-cycle fatigue failure in the dissipater under cyclic loading. However, there were some stiffness degradation in the UFPs after the first cycle at each drift ratio.

Testing of SCUD with lower pre-tensioning force in the tendons (6.5% of tendon yield strength) showed slightly lower hysteretic damping values compared to the theoretical model for a flag-shaped system with $\beta = 0.35$. The level of pre-tensioning was set equal to the capacity of the UFPs at the yield point. This resulted into self-centering ratio of approximately 1.0 for the brace. Following testing, there was 5 mm residual displacement in the brace which corresponded to 22% of MCE level deformation (0.6% drift ratio or 22.5 mm displacement). There was also considerable loss of pre-tensioning in the tendons which was thought to be mainly due to pre-tensioning losses.

Testing of SCUD with higher pre-tensioning force in the tendons (16.8% of tendon yield strength) demonstrated a very high level of self-centering with smaller energy dissipation in the brace. The hysteretic damping values were smaller than those observed in testing of SCUD with the lower pre-tensioning. The level of pre-tensioning corresponded to almost 2.6 times capacity of the combined UFPs at the yield point. Following testing, there was zero residual displacement of the brace and negligible loss in pre-tensioning force of the tendons (less than 4.5%).

In summary, Test No 2 and Test No 3 represented SCUD with lower and higher pre-tensioning force in the tendons, respectively. These tests were carried out to validate the concept for SCUD. The energy dissipation capacity and hysteretic damping for SCUD, can be increased and optimized by inserting more UFPs and adopting appropriate design parameters, respectively. The behavior of the brace can be enhanced through better design considerations, detailing, and precise fabrication of the parts. It is important to take into account the pre-tensioning losses in the tendons, especially for lower levels of pre-tensioning in the tendons. Therefore, further theoretical and experimental investigations are required to improve the behavior of SCUD by providing good levels of energy dissipation and self-centering during a design level earthquake. This is out of the scope of this research.

The UFPs did not show any signs of distress or strength degradation after being subjected to dozens of cycles of almost ten times greater than their yield point during a series of testing. This confirmed that despite a higher maximum strain (8%), the UFPs were able to perform and dissipate energy without signs for any imminent failure. The maximum strain level in the UFPs tested here was higher than the UFPs tested by other researchers such as Baird et al. (2014) (maximum strain of 6.3%).

4.3.2 Mini Plug and Play Dissipating System

Figure 4.70 presents application of this type of damping system in a variety of structural and non-structural elements.

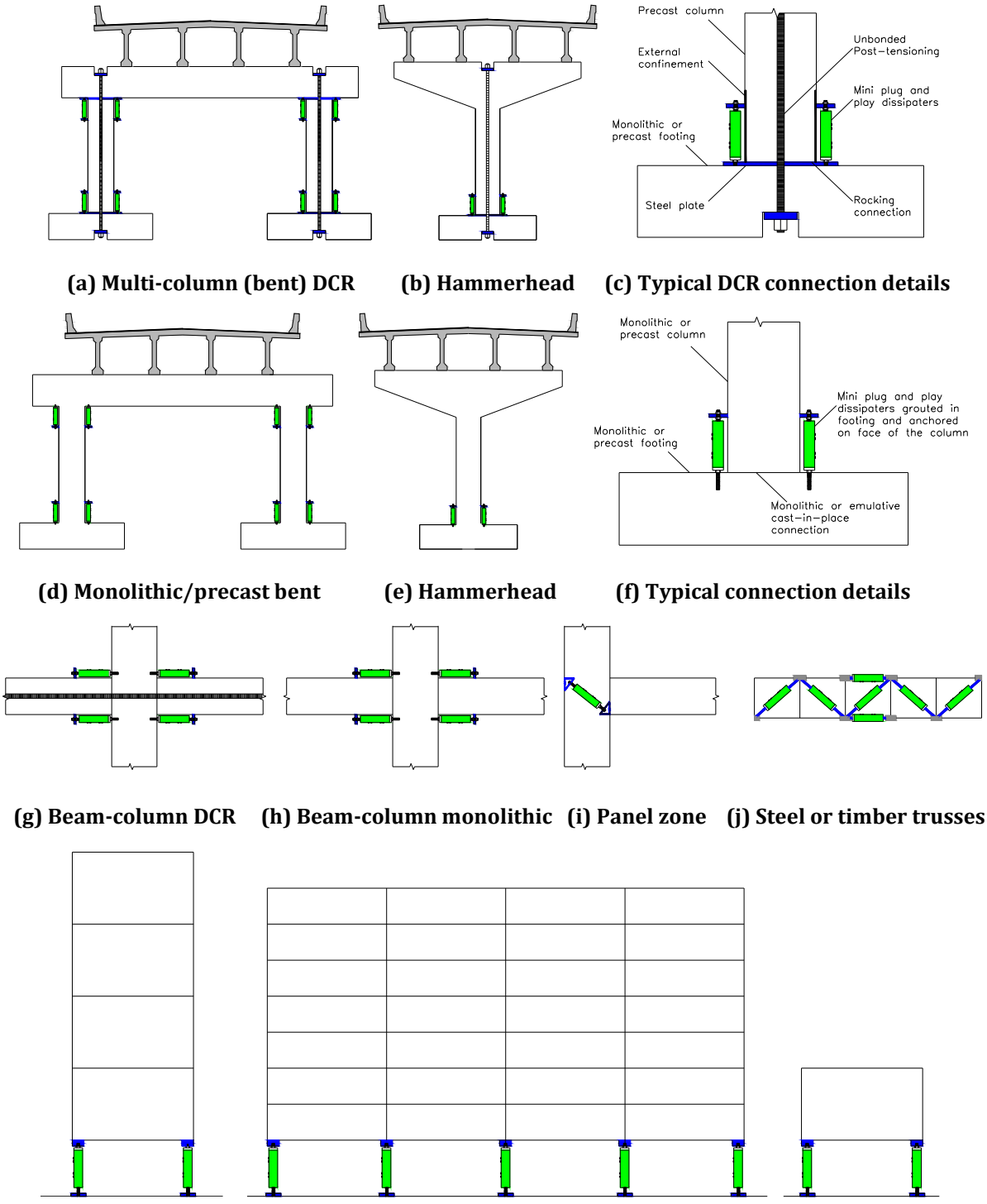

(a) Multi-column (bent) DCR **(b) Hammerhead** **(c) Typical DCR connection details**

(d) Monolithic/precast bent **(e) Hammerhead** **(f) Typical connection details**

(g) Beam-column DCR **(h) Beam-column monolithic** **(i) Panel zone** **(j) Steel or timber trusses**

(k) Computer servers **(l) Merchandize pallet racks** **(m) Transformers**

Figure 4.70. Applications of mini plug and play type dissipaters in a variety of structures

As shown in Figure 4.70, the mini plug and play dissipating system offers a wider range of applications. This includes application of the devices as external dissipaters in DCR connections (Figure 4.70a through Figure 4.70c), beam-column assemblies (Figure 4.70g through Figure 4.70i), trusses (Figure 4.70j), and seismic protection of non-structural components (expensive equipment, computer servers, electrical transformers, and merchandize pallet racks etc) (Figure 4.70k through Figure 4.70m). Given the simple installation of the device in a variety of structures, they are commonly referred as "plug and play" devices.

The smart packaging of the device enables the dissipater to be used in steel, timber, monolithic concrete, and emulative cast-in-place building and bridge structures. As an example this is illustrated in Figure 4.70d through Figure 4.70f. In this case, the dissipaters are designed to yield first, and hence prevent or delay yielding of the column longitudinal rebars. The system may be left with residual displacement following an earthquake, unless the mini plug and play device features a self-centering aspect. In this system, the components such as beam, columns, and footings, are designed to remain elastic during an earthquake. Several variations of this type of dampers were developed at the University of Canterbury (Keats, Palermo, and Mashal, 2015) which are discussed in the next sections.

4.3.2.1 Mini UFP Dissipater

Mini UFP Dissipater (MUD) is illustrated in Figure 4.71. The damper consisted of bolted double UFPs to the internal loading cassette (c-shaped section) which is placed inside a hollow square or rectangle section tube. The opposite legs of the double UFPs are bolted to the external sleeve. One end of the cassette is connected to the movable (loading) end of the dissipater through a welded washer which has a threaded hole at its center. A piece of high strength threaded rod is then wound to the washer and is secured with a nut. The other end of the dissipater is not movable and is designed to remain fixed. It has similar detail with a washer welded to the sleeve and another piece of the threaded rod wound to the center of the washer, as shown in Figure 4.71.

The dissipater can be stretched or compressed from the movable end. Similar to UFP bracing dissipater, when it is loaded in tension or compression, the UFPs are flexing with the loading cassette which creates a relative sliding between the cassette and the

external sleeve. This relative movement causes yielding of the UFPs in a rolling deformation and hence, provides energy dissipation. All other parts are designed to remain essentially elastic during loading of the device.

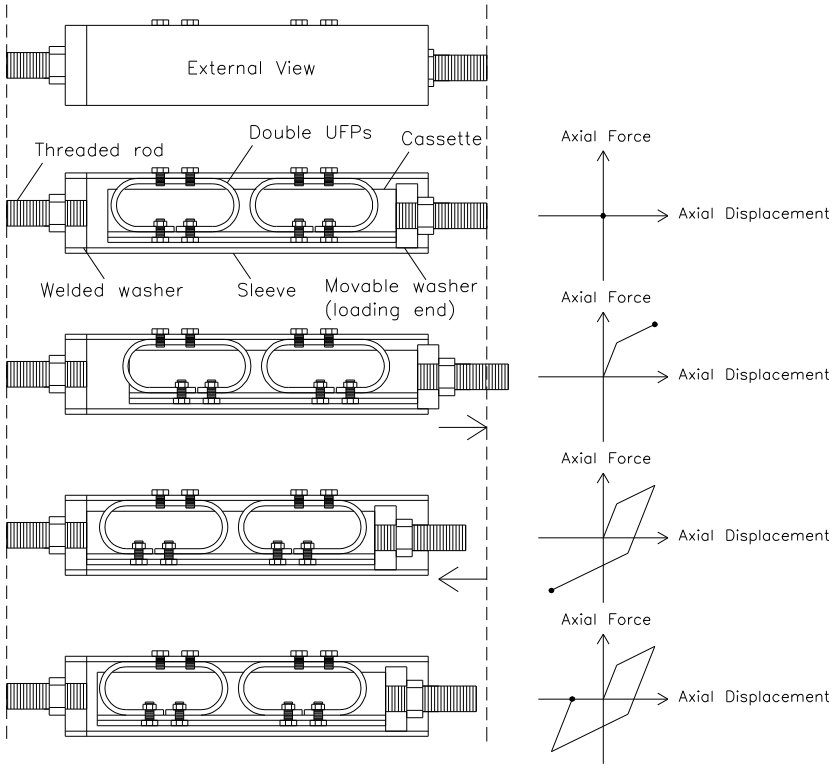

Figure 4.71. MUD details and working mechanism (Keats, Palermo, and Mashal)

From the last sketch in Figure 4.71, it is obvious that MUD does not provide any supplemental self-centering, and thus the device may be left with some residual displacement following an earthquake. The concept for MUD was experimentally tested and validated on three prototypes, as will be explained later in this Chapter.

4.3.2.2 Self-Centering Mini UFP Dissipater

Self-Centering Mini UFP Dissipater (SMUD) is similar to MUD which was discussed in the previous section. The only difference is that the double UFPs in a SMUD are made of Shape-Memory Alloy (SMA) plates instead of mild steel plates. As explained earlier in Section 4.2.1.9, SMAs are a class of alloys that have unique characteristics such as shape memory effects, high damping, and the temperature-induced phase change characteristics. For superelastic SMAs, the nonlinear deformation is reversible, unlike other plastically deforming metals such as mild steel. SMUD offers additional advantages such as self-centering and excellent corrosion resistance of the device.

It is important to note that SMAs plates (either superelastic or Nitinol) can also be used for SCUD which was discussed in Section 4.3.1.2. In SCUD, the mild steel UFPs can be replaced by SMA UFPs which would enhance the seismic performance of the brace by introducing self-centering capability. This would eliminate the need for pre-tensioned tendons to achieve self-centering of the dissipater following an earthquake. However, large SMA UFPs may not be cost-effective due to higher price of the SMAs.

For SMUD, given the small size of the device, application of SMA UFPs may be feasible for specific applications. However, the advantage for self-centering would have to be weighed against the cost of materials and fabrication for the device.

The concept for SMUD was not experimentally tested, as it is out of the scope of this research. However, given the existing data on SMA plates (Heresi et al., 2014) and UFPs, it was expected to pass experimental validation. Further investigations into SMUD would be necessary to validate the concept, optimize the capacity and shape, and provide guidelines on appropriate detailing , fabrication, and analytical modeling of the device.

4.3.2.3 Multi-Performance Mini UFP Dissipater

The concept for Multi-Performance Mini UFP Dissipater (Multi-Performance MUD) is another type of the innovative mini plug and play devices proposed by Keats, Palermo, and Mashal (2015). There are three variations of this type of device which are described as follows:

A. Dissipative End Plate Type: This is similar to what presented in Figure 4.47a for Multi-Performance UFP bracing dissipater. The concept for this device is illustrated in Figure 4.72. In this type of device, the slotted-bolted friction connection at the movable end of the device works as a supplementary source of energy dissipation. The friction connection can be designed such that it activates after or before the UFPs are yielded. It can also be adjusted to activate at a certain earthquake level. For example, if the connection was designed to activate after the UFPs are close to their maximum stroke, the friction connection starts sliding and provides further stroke and energy dissipation capacity for the device.

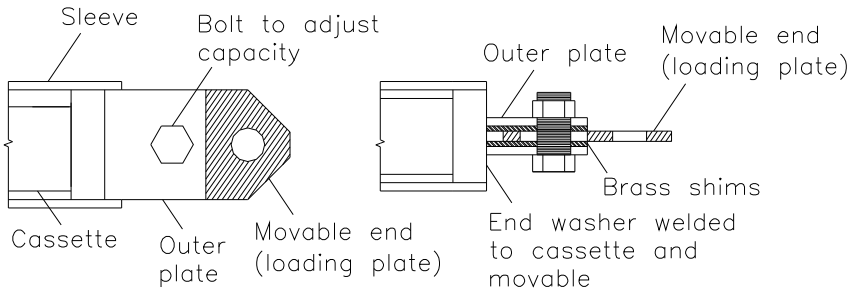

(a) Dissipative end plate side view (b) Top section view

Figure 4.72. Dissipative End Plate Type (Keats, Palermo, and Mashal)

B. Nested UFPs - Type I: In this type of device, two or more double UFPs are nested inside each other in a configuration shown in Figure 4.73 with no gap between the double UFPs. This device offers the advantage for an enhanced capacity and redundancy against low-cycle fatigue failure of the UFPs under a larger number of cycles.

As explained earlier, the maximum strain in a UFP is related to thickness of the plate and diameter of the rolled shape. Generally, the smaller the rolled diameter in the UFP, the higher strain in the plate which could make it susceptible to strength degradation and low-cycle fatigue failure under cyclic loading. The nested UFPs embodiment provides the advantage that if the inner UFPs are fractured after a number of loading cycles, the outer UFPs will still provide energy dissipation. The capacity of the device would be reduced, but it would still dissipate energy and keep its integrity.

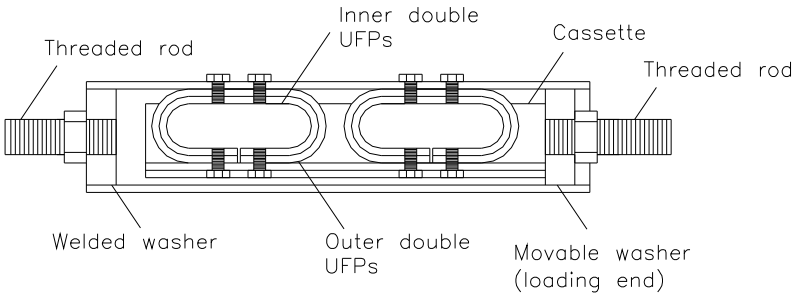

Figure 4.73. Nested UFPs Type - I (Keats, Palermo, and Mashal)

B. Nested UFPs - Type II: The concept for this device is presented in Figure 4.74. In this embodiment, there is a steel packer plate placed between the nested double UFPs. The packer plate works as a continuous support surface for the legs of the UFPs when the device is loaded and the UFPs start flexing. This embodiment provides the advantage for using thicker inner UFPs with smaller diameter. This is expected to increase the maximum strain in the inner UFPs quite significantly. To prevent from a total loss of the

device capacity due to low-cycle fatigue failure in the inner UFPs, the outer UFPs are designed such to maintain a reduced capacity for the device with lower maximum strain. At the same time, this type of device eliminates the need for keeping a tight fabrication tolerance for the UFPs nested inside each other with no gap as previously shown in Figure 4.73.

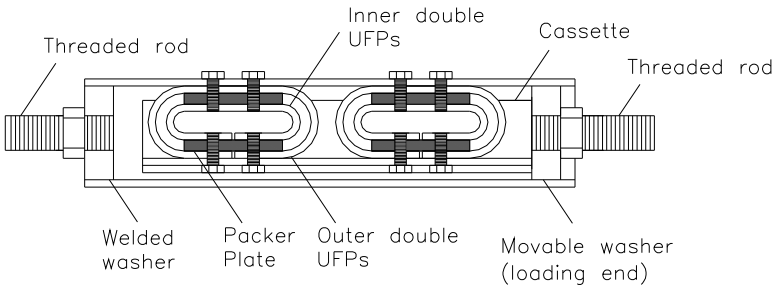

Figure 4.74. Nested UFPs Type - II (Keats, Palermo, and Mashal)

It is important to mention that other concepts for variations of Multi-Performance MUD can also be developed through a combination of the variation types discussed here. An example is shown in Figure 4.75 where the concept of Nested UFP Type II has been combined with the concept for that of Dissipative End Plate Type device. The multi-performance concepts discussed here (or a combination of them) could be utilized for SMUD and for all variations of the bracing type dissipaters discussed in Section 4.3.1. Testing of Multi-Performance MUD is out of the scope of this research.

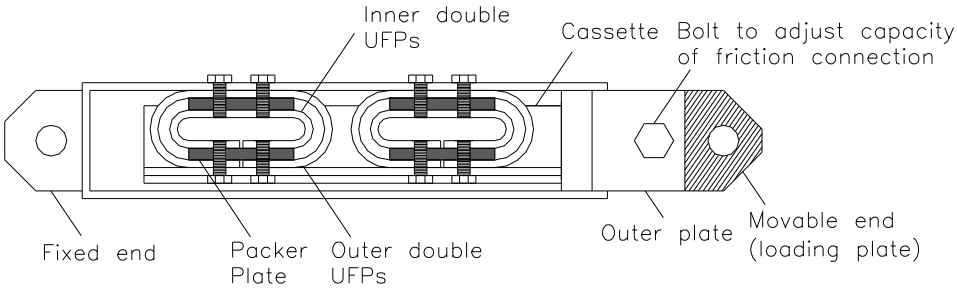

Figure 4.75. Multi-Performance MUD: Combination of two concepts (Keats, Palermo, and Mashal)

4.3.2.4 Prototype Mini UFP Dissipater

The prototype device was based on the column to footing DCR connection of the hammerhead pier shown in Figure 4.76a. The gap opening in the DCR connection was assumed to be 10 mm and 20 mm during the ULS and MCE level drifts, respectively. These gap opening values correspond to 2.2% and 4.4% drift ratios in the device and the structure at the ULS and MCE levels, respectively. The prototype dimensions are shown in Figure 4.76b. The external sleeve had dimensions of 75x75x5 mm.

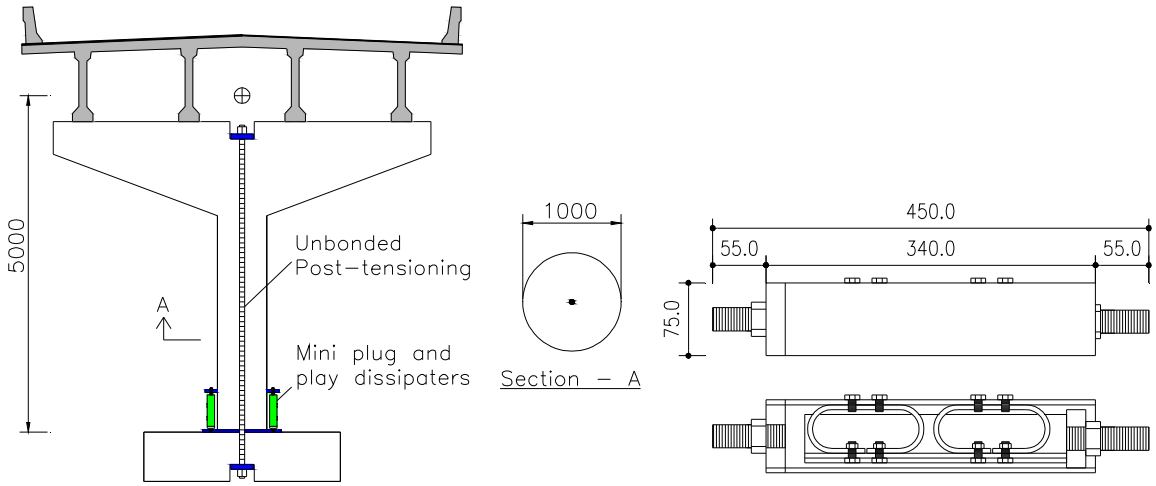

(a) Prototype bridge with DCR connection **(b) MUD prototype dimensions**

Figure 4.76. Prototype hammerhead pier and dissipater dimensions in (mm)

Three identical full-scale MUD prototypes were constructed to validate the concept. There were four tests carried out on the three prototypes. A summary of testing description is provided in Table 4.2.

Table 4.2. Description of testing on MUD prototypes

Prototype Number	**MUD-1**	**MUD-2**	**MUD-3**	
Test Name	**Test No 1**	**Test No 2**	**Test No 3**	**Test No 4**
Maximum Capacity (kN)	25	25	25	25
Loading Strain	Net Positive	Net Positive	Net Positive	Net Positive and Negative
Maximum Displacement (mm)	20	20	20	±20
ULS Drift Ratio (%)	2.2	2.2	2.2	2.2
MCE Drift Ratio (%)	4.4	4.4	4.4	4.4

4.3.2.5 Testing Arrangement and Data Acquisition System

The testing arrangement for MUD prototypes is illustrated in Figure 4.77. The dissipaters were tested under the same DARTEC machine as that used for testing of the brace dissipater specimen. This was done by adjusting the height of DARTEC based on the length of the MUD prototype. The data acquisition system was similar to what discussed for the brace dissipater specimen (UFP-BD) in Section 4.3.1.4.2 earlier.

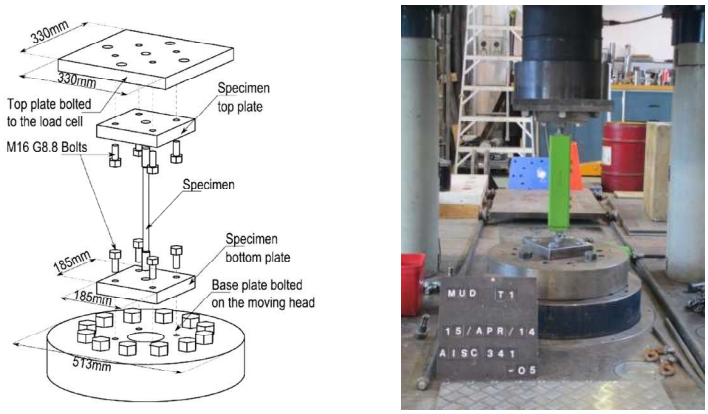

(a) Testing arrangement (Sarti et al., 2013) (b) MUD prototype under DARTEC

Figure 4.77. Testing setup for MUD prototypes

4.3.2.6 Loading Protocol

The loading protocol for all four tests was quasi-static cyclic loading similar to AISC 341-05 as described in Section 4.3.1.4.3 for the brace dissipater specimen. The loading sequence for the first three tests was identical as follows:

A. Test No 1, Test No 2, and Test No 3 Loading Sequence (MUD, Net Positive Strain)

I. 4 cycles of loading at the deformation corresponding to $\Delta_b = 2$ *mm* (Yield)

II. 4 cycles of loading at the deformation corresponding to $\Delta_b = 5$ *mm*

III. 4 cycles of loading at the deformation corresponding to $\Delta_b = 10$ *mm* (ULS)

IV. 4 cycles of loading at the deformation corresponding to $\Delta_b = 15$ *mm*

V. 4 cycles of loading at the deformation corresponding to $\Delta_b = 20$ *mm* (MCE)

VI. 14 cycles of loading at the deformation corresponding to $\Delta_b = 15$ *mm*

In this type of loading, the specimen is subjected to only net positive deformation which can represent the case where the dissipater is used in a DCR connection. A plot of the loading sequence is presented in Figure 4.78.

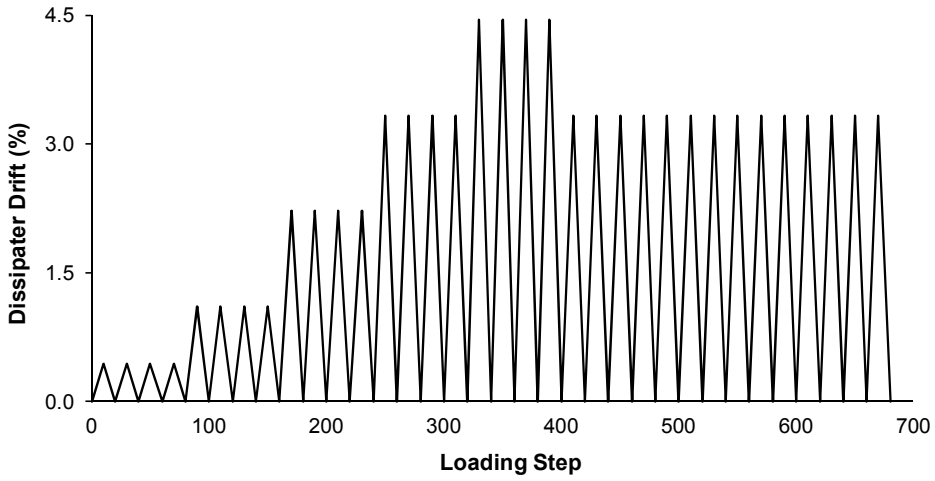

Figure 4.78. Loading sequence for MUD (Net Positive Strain)

B. Test No 4 Loading Sequence (MUD, Net Positive and Negative Strain)

I. 2 cycles of loading at the deformation corresponding to $\Delta_b = 2\ mm$ (Yield)

II. 2 cycles of loading at the deformation corresponding to $\Delta_b = 5\ mm$

III. 2 cycles of loading at the deformation corresponding to $\Delta_b = 10\ mm$ (ULS)

IV. 2 cycles of loading at the deformation corresponding to $\Delta_b = 15\ mm$

V. 2 cycles of loading at the deformation corresponding to $\Delta_b = 20\ mm$ (MCE)

VI. 7 cycles of loading at the deformation corresponding to $\Delta_b = 15\ mm$

This loading sequence illustrates a case where the dissipater is subjected to both net positive and negative. Test No 4 was intended to show that MUD can be used in applications where the dissipater is expected to undergo both net positive and negative displacements such as that in a truss bracing. A plot of the loading sequence is presented in Figure 4.79.

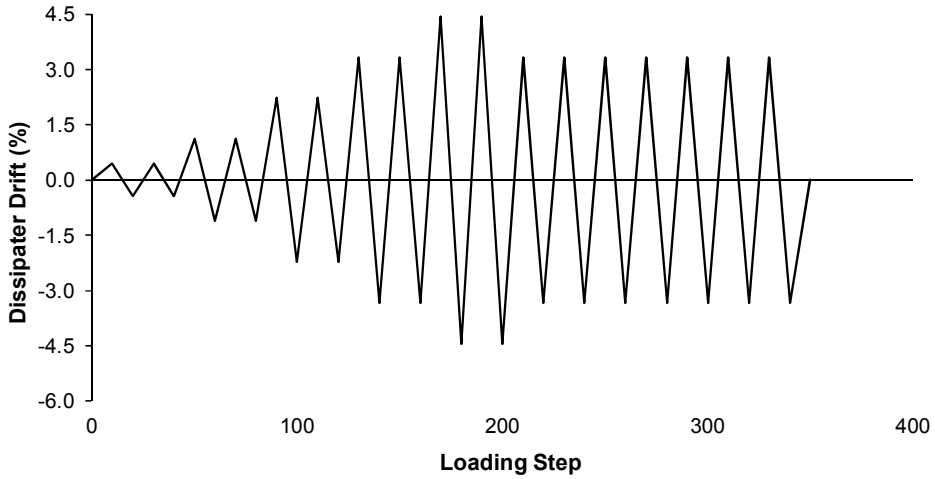

Figure 4.79. Loading sequence for MUD (Net Positive and Negative Strain)

4.3.2.7 Design, Fabrication, and Assembly of MUD Prototypes

All three MUD prototypes incorporated identical design and were similar to the specimen shown in Figure 4.76b. Each prototype consisted of two double UFPs bolted to an internal cassette (Figure 4.80b) with a 20 mm thick washer welded in the end. The cassette was inserted inside a 75x75x5 mm tube (Figure 4.80d). Extension rods were wound and tightened into the washers on the ends to provide anchoring points for the dissipater, as shown in Figure 4.80f.

Each leg of the double UFPs was secured to the cassette and the external tube using two 8 mm diameter high strength bolts (Figure 4.80c). The cassette was simply made of three pieces of flat steel bars (270x50x5 mm) welded to each other in a c-shaped section (Figure 4.80b). The washers at the loading and fixed ends of the device were identical. The washer dimensions were 60x60x20 mm with threaded holes at the center (24 mm in diameter). Two pieces of high strength threaded rod, each 75 mm long and 24 mm in diameter, were wound to the end washer plates and secured with nuts (Figure 4.80f).

The double UFPs were made of 5 mm thick, 50 mm wide, and 45 mm in rolled diameter mild steel plates ($f_y = 300\ MPa$). Using Equation 4.1 and Equation 4.2, the yield capacity and yield displacement for each of the double UFPs were calculated to be 8.3 kN and 1.6 mm, respectively. For the whole device incorporating two double UFPs, the yield capacity was 16.6 kN. Using an overstrength factor of 1.5 for the steel hardening (similar to that assumed for the brace dissipater specimen) in accordance with Baird et

al. (2014), the maximum capacity of the device was expected to be 25 kN at the maximum stroke of 20 mm (4.4% drift ratio, MCE level).

The maximum strain from Equation 4.3 was calculated to be 11.1%. This is higher than that of the brace dissipater specimen in Section 4.3.1.4.4.

All parts of the device were made of available and recycled materials in the lab. The double UFPs were rolled using the same hand-operated roller, as previously shown in Figure 4.54a. The assembly process for MUD prototypes is presented in Figure 4.80.

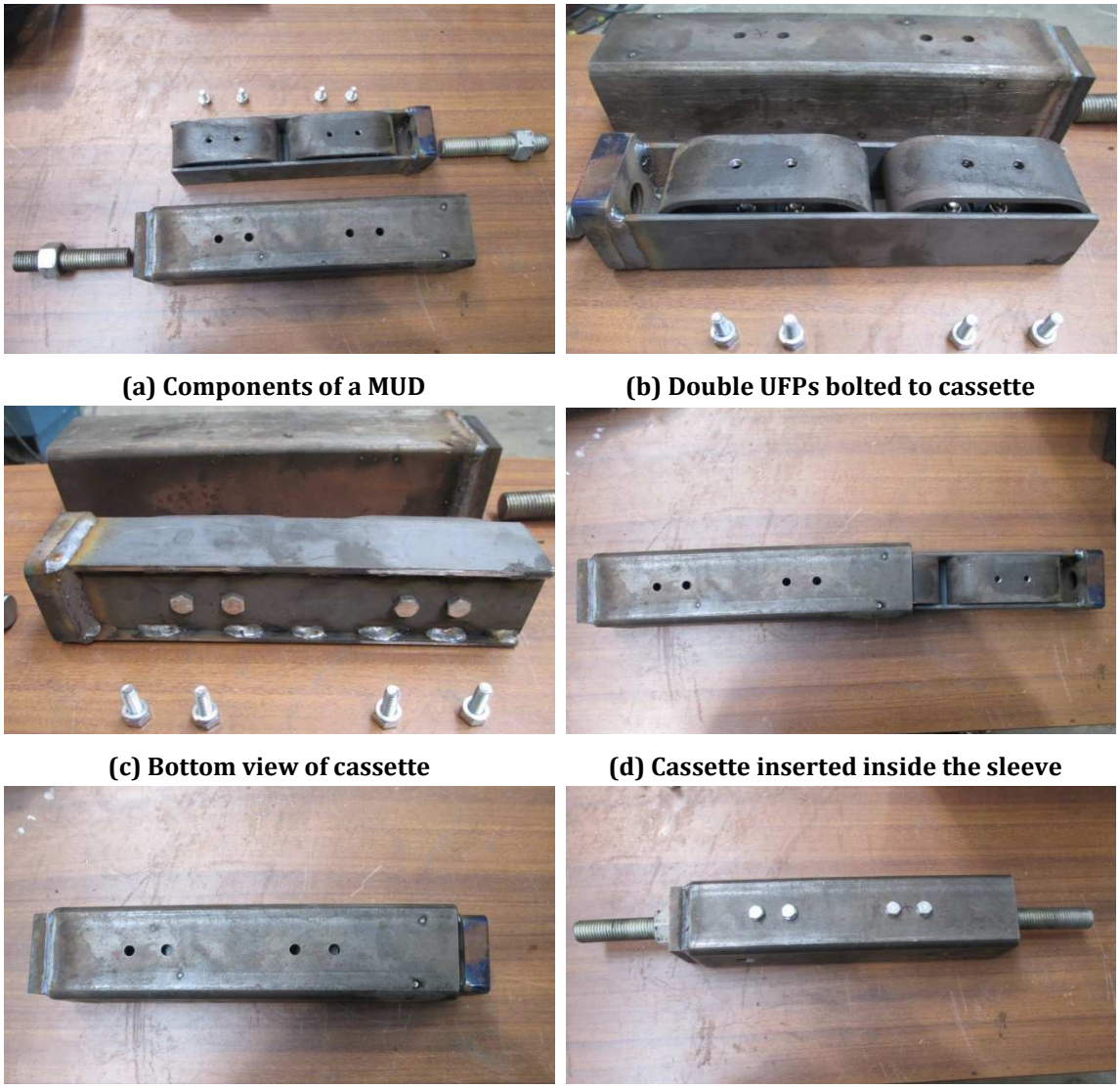

(a) Components of a MUD **(b) Double UFPs bolted to cassette**

(c) Bottom view of cassette **(d) Cassette inserted inside the sleeve**

(e) Holes are aligned **(f) Bolts and end rods are wound and tightened**

Figure 4.80. Components and assembly of a typical MUD prototype

Figure 4.81 presents completed MUD prototypes. It should be noted that in Figure 4.81a, the holes in the external sleeves are not a design or fabrication feature for MUD.

The external tube was recycled steel, the holes were from a previous usage. A qualitative comparison between size of MUD and SCUD is provided in Figure 4.81d.

(a) MUD prototypes

(b) Movable end view

(c) Fixed end view

(d) MUD versus SCUD

Figure 4.81. Completed MUD prototypes for experimental testing

4.3.2.8 Testing Results and Performance Evaluation

A. Test No 1, Test No 2, and Test No 3: The three identical MUD prototypes were subjected to the same loading sequence and completed all cycles without any failure. Following testing, the prototypes were disassembled and all parts were inspected for any damage. Except residual deformation of the UFPs, there were no other obvious signs of inelastic deformation or failure in the components of the device. All other parts behaved well and remained intact throughout testing.

The axial force-displacement hysteresis for each prototype is plotted in Figure 4.82a through Figure 4.82c, where positive vertical and horizontal axes show MUD during the pull stage of the loading. The prototypes showed similar behavior with a very stable

hysteresis. There were no signs of strength degradation or low-cycle fatigue failure from the hysteresis. There were some stiffness degradation in all prototypes following the first cycle at each drift ratio. However, there was no noticeable difference in the stiffness of the dissipaters for the subsequent cycles at each drift ratio. This was similar to what observed in testing of UFP bracing type dissipaters in Section 4.3.1.4.6. The backbone curve of the prototypes is plotted in Figure 4.82d. It is can be observed that out of the three prototypes, MUD-1 had slightly higher capacity.

All three prototypes achieved their predicted maximum capacity of 25 kN during the cycles of 20 mm displacement (4.4% drift ratio, MCE level). The displacement ductility at the maximum stroke of the prototypes was 12.5. The residual displacement following cycles of 4.4% drift ratio was in order to 17 mm (3.7% drift ratio) which corresponds to 85% of MCE level drift.

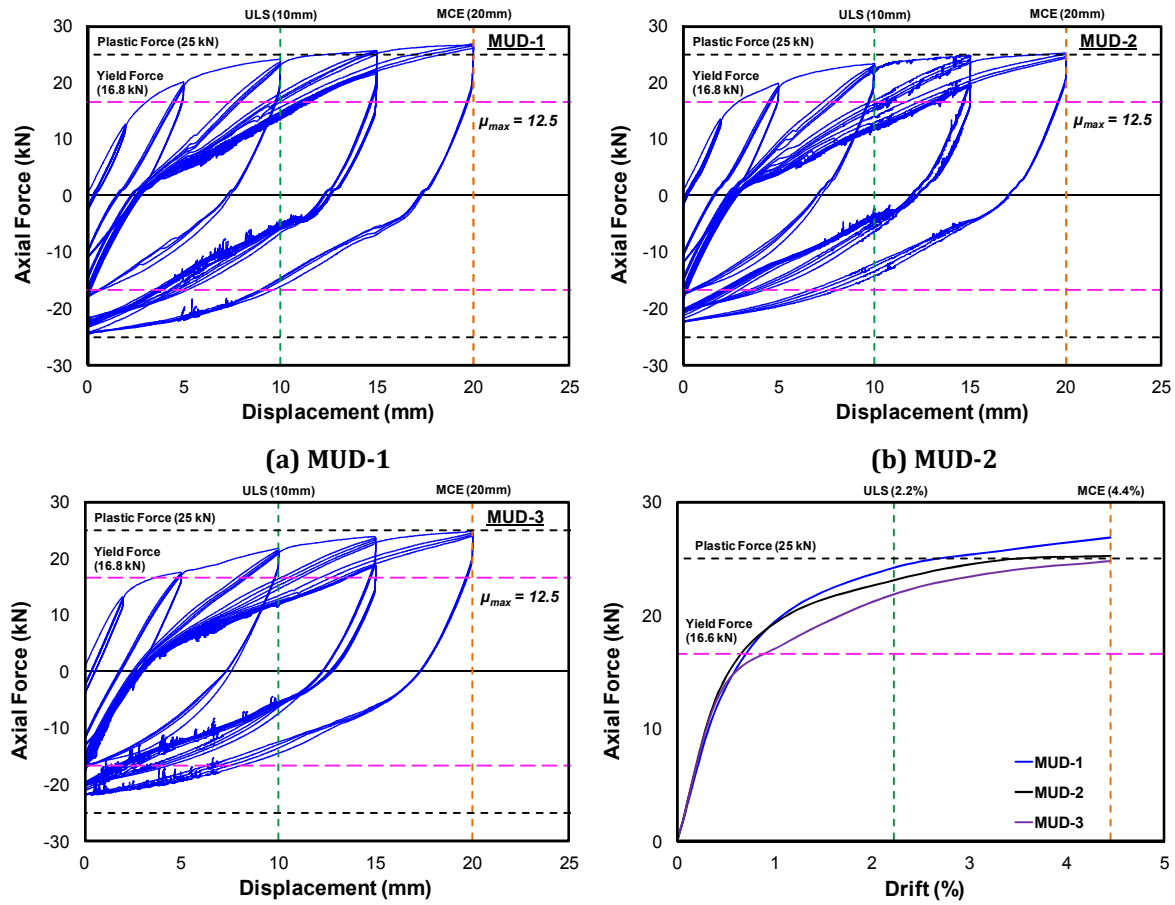

Figure 4.82. Force-displacement hysteresis and backbone curves for MUD prototypes

The energy dissipated per each cycle of each drift ratio for MUD prototypes is presented in Figure 4.83a through 4.83c. As shown, the first prototype (MUD-1) had slightly higher cumulative dissipated energy compared to the other two. It is also obvious that the there is no significant reduction in the energy dissipation during the last 14 consecutive cycles of 3.3% drift ratio which corresponds to 1.5 times ULS level. This suggests that the prototype tested were not susceptible to low-cycle fatigue failure for a great number of cycles beyond the yield point.

The experimental hysteretic damping curve of the prototypes is plotted in Figure 4.83d in accordance with Priestley et al. (2007). Following displacement ductility of around 8, MUD-1 had slightly higher hysteretic damping values compared to other theoretical models shown. All prototypes achieved similar hysteretic damping level to that of a theoretical Ramberg-Osgood model following ductility of just over 11. The prototypes attained hysteretic damping of around 24% at ductility of 12.5 during the MCE level drift ratio (4.4%).

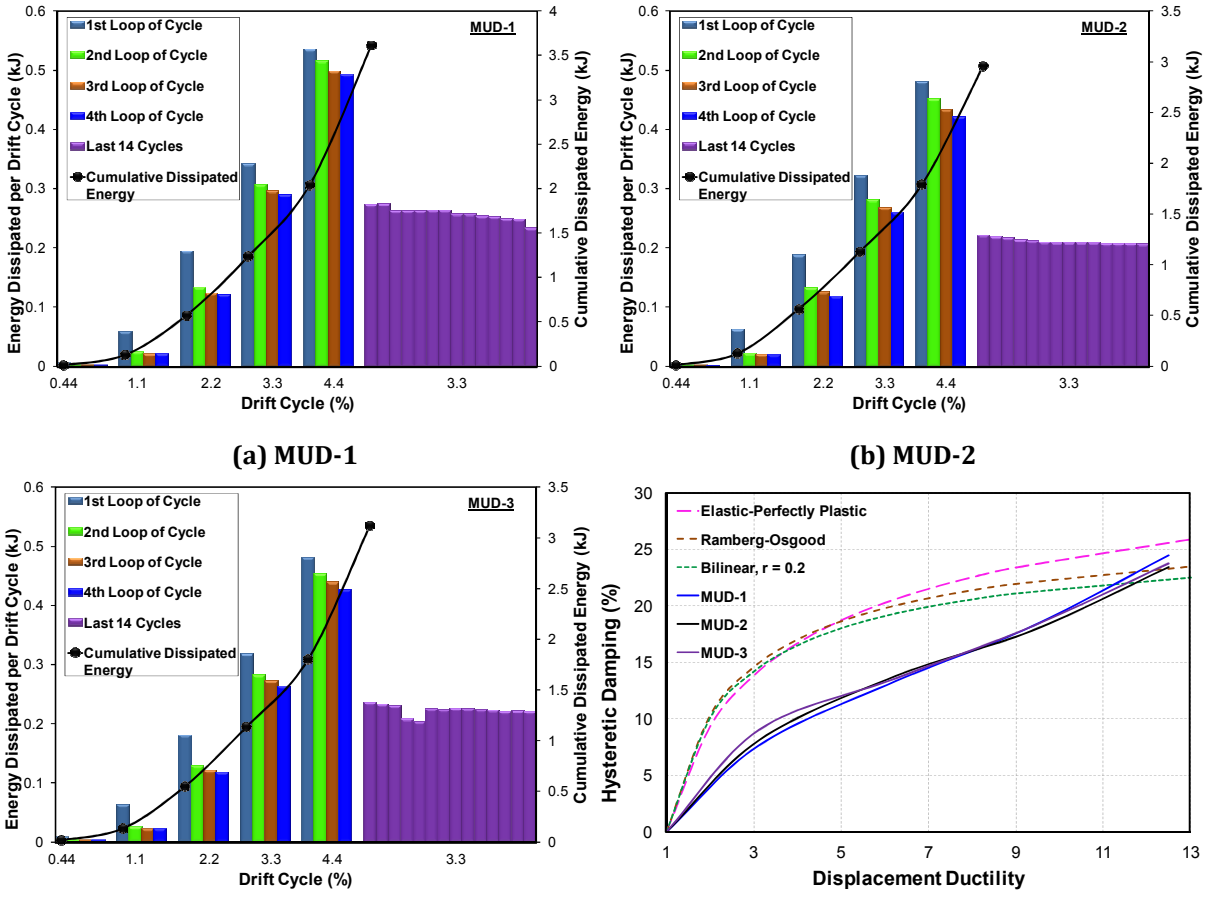

(a) MUD-1 **(b) MUD-2**

(c) MUD-3 **(d) Corrected area-based hysteretic damping**

Figure 4.83. Dissipated energy and hysteretic damping plots for MUD prototypes

B. Test No 4: This test was performed on MUD-3 after testing of the device under net positive deformation. During Test No 4, the device was subjected to both net positive and negative deformation. The device completed all loading cycles without any strength reduction or fatigue failure.

Following testing, MUD-3 was disassembled and all parts were inspected for any damage. Residual deformation of UFPs was apparent from the misalignment of the bolt holes in the UFPs' legs (Figure 4.83a). There was no visible damage to the internal cassette (Figure 4.83c). There was some distortion of the bolts which were used to connect the double UFPs to the internal cassette (Figure 4.83b). This was thought to be due to a more demanding loading protocol on MUD-3. The dissipater was subjected to two different loading protocols (over 51 cycles of net positive and negative deformation beyond the yield point). Using bigger bolts is thought to eliminate the excessive deformation under cyclic loading.

(a) Residual deformation in UFPs (b) Deformation in the UFP bolts (c) No damage to cassette

Figure 4.84. Inspection of MUD-3 parts following testing under cyclic loading

The axial force-displacement hysteresis for MUD-3 under net positive and negative deformation is plotted in Figure 4.85a. The positive vertical and horizontal axes show MUD-3 during the pull stage of the loading (net positive deformation). The prototype showed a stable hysteresis. Despite a more demanding loading protocol, there was no signs of strength degradation or immanent low-cycle fatigue failure. In Figure 4.85a, the slacking in the hysteresis is due to movement and deformation in the bolts as explained earlier. The backbone curve is plotted in Figure 4.85b. The reduction in the initial stiffness of the dissipater is due to previous yield from testing of the device under net positive deformation.

The slight kinking under compression in Figure 4.85b is thought to be due to deformation of the bolts (Huang et al., 1973). As explained before, this can be improved by using bigger bolts for the double UFPs to the cassette and external tube fixings.

The prototype achieved its predicted maximum capacity of 25 kN during the cycles of 20 mm displacement (4.4% drift ratio, MCE level) which corresponds to displacement ductility of 12.5. The residual displacement in the device was similar to those observed for MUD prototypes under net positive deformation loading.

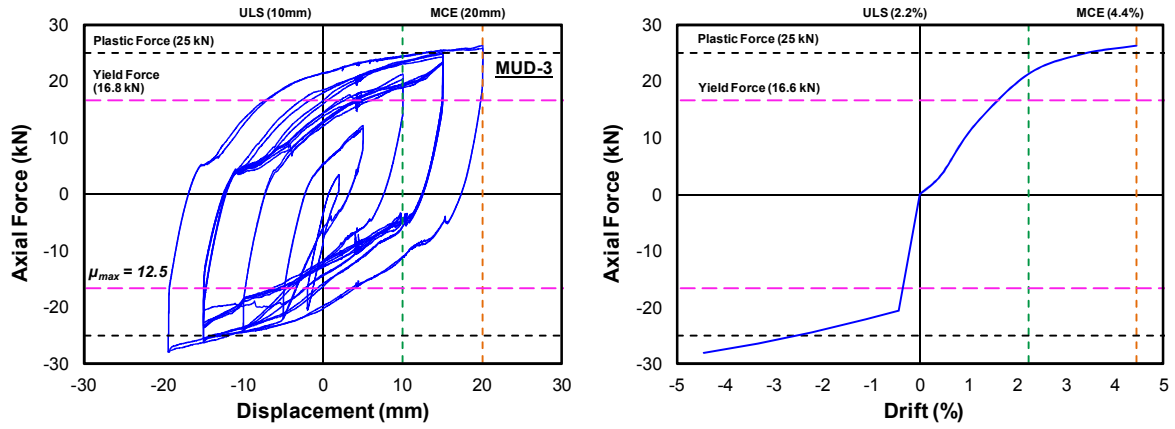

(a) Force-displacement hysteresis **(b) Backbone curve**

Figure 4.85. Hysteresis plots for MUD-3 under net positive and negative deformation

The energy dissipated per each cycle of each drift ratio under net positive and negative deformation is presented in Figure 4.86a. By the end of testing, the cumulative dissipated energy was slightly lower than twice times of that presented for MUD prototypes under only net positive deformation (Figure 4.83). The decrease in energy dissipation following the first two cycles of the last 7 consecutive cycles of 3.3% drift ratio was thought to be due to deformation of bolts which caused some slacking effects. This had the efficiency of the UFPs reduced to some level. Apart from this, the energy dissipation plot does not suggest any considerable strength degradation of the device under cyclic loading.

The experimental hysteretic damping curve is plotted in Figure 4.86b. The hysteretic damping values were bigger compared to those in testing of MUD prototypes under net positive strain (Figure 4.83d). This was due to bigger energy dissipation in testing of MUD under net positive and negative strain (larger enclosed area in the hysteresis). The corrected experimental damping values were similar to those observed in testing of the

UFP Bracing Dissipater under a similar testing protocol and loading sequence (Figure 4.59).

In Figure 4.86b, following a displacement ductility of 5, the device had hysteretic damping values higher than those for theoretical models shown on the plot. The prototype achieved a hysteretic damping value of 44% at displacement ductility of 12.5 during MCE level drift ratio (4.4%).

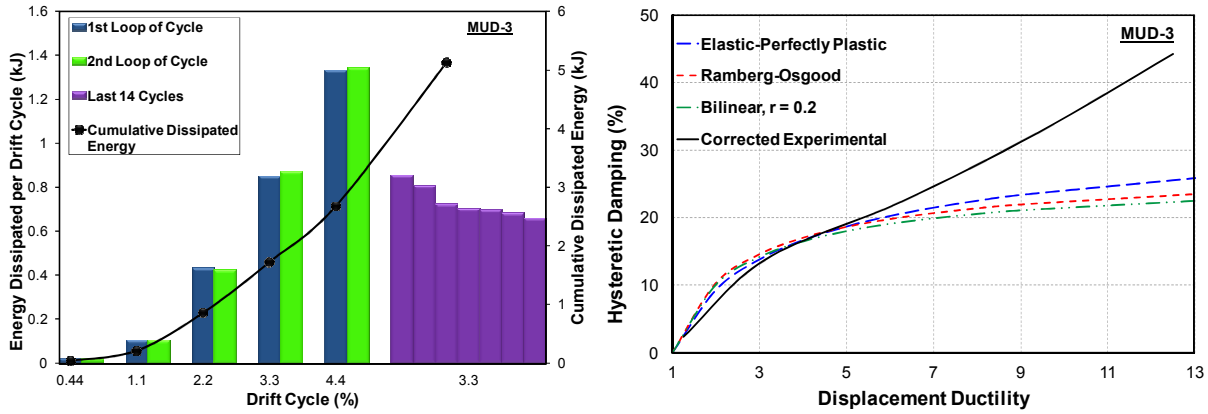

(a) Dissipated energy (per cycle and cumulative) **(b) Corrected area-based hysteretic damping**

Figure 4.86. Dissipated energy and hysteretic damping plots for MUD-3 (Test No 4)

4.3.2.9 Summary of Testing Results for Mini Plug and Play Type Damping System

The concept for Mini UFP Dissipater (MUD) was validated through experimental testing. Based on the testing results from three prototypes, it has been assumed that the concept for other variations of mini plug and play devices may also pass experimental validation.

Test No 1, Test No 2, and Test No 3 were carried out to show the response of MUD under cyclic net positive deformation. This type of loading represented a case similar to what can be expected of external dissipaters in a DCR connection. All three MUD prototypes achieved their predicted maximum capacity without any strength degradation or low-cycle fatigue failure. The prototypes attained maximum displacement ductility of 12.5 at the MCE drift ratio (4.4%). Following ductility of 11, the corrected experimental damping values for all prototypes reached those obtained from theoretical models such as Ramberg-Osgood, Elastic-Perfectly Plastic, and Bilinear. By the end of testing, MUD prototypes attained an average hysteretic damping of 24%.

In Test No 4, one of the prototypes (MUD-3) was subjected to a more demanding loading protocol. MUD-3 was tested under cyclic net positive and negative deformation. This type of loading can be expected for that of bracing element in a truss.

MUD-3 showed a stable hysteresis similar to that observed in testing of UFP Bracing Dissipater (UFP-BD). The device achieved its predicted capacity during tension and compression stages of loading. The corrected experimental damping values were similar to those observed in testing of UFP-BD. The prototype achieved a maximum hysteretic damping of 44% at the displacement ductility of 12.5 during MCE level drift ratio (4.4%).

Although the maximum strain in all three MUD prototypes (11%) was considerably higher than that for UFP-BD (8%), however, MUD did not show any signs of distress or strength degradation. This was despite being subjected to dozens of cycles (up to 10 times greater than the yield point). This confirmed efficiency and good performance of the UFPs inside the device under cyclic loading despite keeping a higher level of strain in the UFPs. The strain level here (11%) was almost twice of that used in the previous tests on the UFPs by Baird et al. (2014) which was in order of 6.3%. There was no signs of immanent failure in the double UFPs at this strain level (11%).

4.3.3 Further Testing on Grooved Type Dissipater

This section presents further experimental testing on Grooved Dissipater (GD) which was developed by White (2014) and explained in Section 4.2.1.8.4. GD offers the advantage for higher capacity in a smaller package compared to MUD. The higher capacity and compactness of the device makes the device more attractive in a DCR connection for ABC Low Damage.

Further testing on GD in this research aims to investigate the response of the dissipater under cyclic loading to explore suitability of the device for ABC Low Damage which will be discussed in Chapter 5.

4.3.3.1 Prototype Grooved Dissipater

The prototype dissipater (Figure 4.87) was based on the DCR connection of the hammerhead pier shown in Figure 4.76a. Three prototypes were constructed. Table 4.3 summarizes the design and testing parameters.

Table 4.3. Description of testing on GD prototypes

Prototype Number	**GD-1**	**GD-2**
Test Name	**Test No 1**	**Test No 2**
Maximum Capacity (kN)	100	100
Loading Strain	Net Positive	Net Positive and Negative
Maximum Displacement (mm)	25	15
ULS Drift Ratio (%)	2.3	1.4
MCE Drift Ratio (%)	4.6	2.3

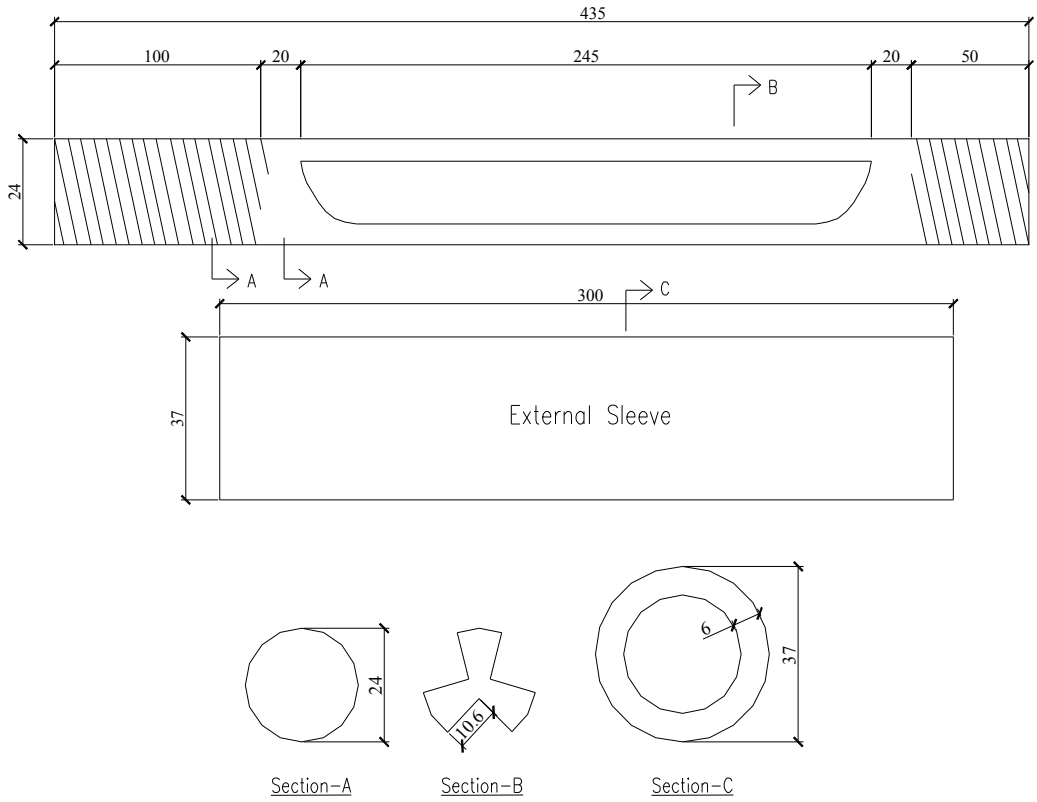

Figure 4.87. Prototype grooved dissipater parts dimensions in (mm)

4.3.3.2 Testing Arrangement and Data Acquisition System

The testing arrangement for GD prototypes was similar to that discussed previously for MUD prototypes. It should be noted that when carrying out a cyclic testing of GD under net positive and negative deformation (Test No 2 of Table 4.3), sufficient gap would have to be left between the external tube and end fixing. This would accommodate the net negative deformation of the dissipater during testing without loading the external tube when the dissipater is compressed.

Figure 4.88. Grooved dissipater under DARTEC testing machine

4.3.3.2 Loading Protocol

The loading protocol for all tests was quasi-static cyclic loading according to ACI Innovation Task Group 1 (2001). The loading sequence for each test is presented as follows:

A. Test No 1 (GD-1, Net Positive Strain)

I. 3 cycles of loading at the deformation corresponding to $\Delta_1 = 2$ *mm*

II. 3 cycles of loading at the deformation corresponding to $\Delta_2 = 3.5$ *mm*

III. 3 cycles of loading at the deformation corresponding to $\Delta_3 = 6$ *mm*

IV. 3 cycles of loading at the deformation corresponding to $\Delta_4 = 10$ *mm* (ULS)

V. 3 cycles of loading at the deformation corresponding to $\Delta_5 = 15$ *mm*

VI. 3 cycles of loading at the deformation corresponding to $\Delta_6 = 20$ *mm* (MCE)

VII. 3 cycles of loading at the deformation corresponding to $\Delta_7 = 25$ *mm*

A plot of the loading sequence is presented in Figure 4.89. This represents the case where the dissipater is used in a DCR connection.

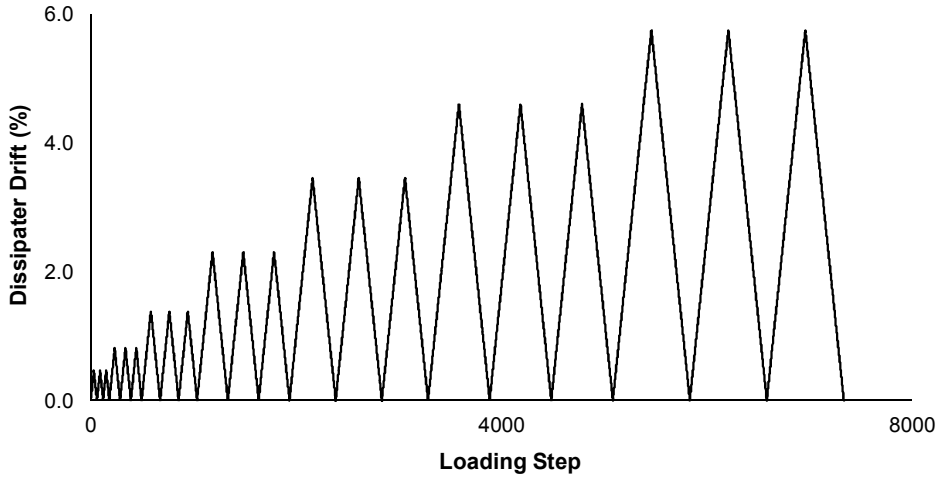

Figure 4.89. Loading sequence for GD-1 (Net Positive Strain)

B. Test No 2 Loading Sequence (GD-2, Net Positive and Negative Strain)

The number of loading cycles at each drift ratio was similar to what explained for GD-1. However, for GD-2, the ULS and MCE drift levels were reduced to 6 mm (1.4% drift ratio) and 10 mm (2.3% drift ratio), respectively. This was due to a more demanding loading protocol. In this type of loading, the dissipater was subjected to net positive and negative strain. This may represent a scenario where GD is used as bracing element in a truss. A plot of the loading sequence is presented in Figure 4.90.

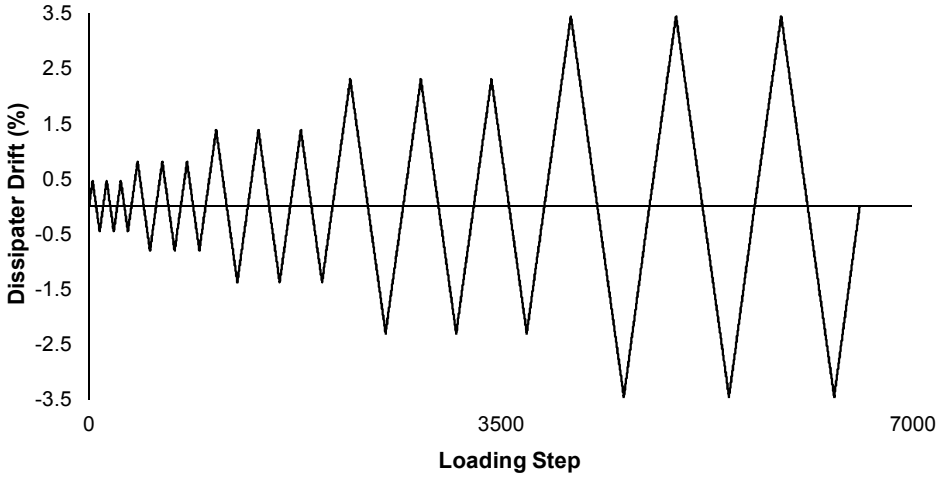

Figure 4.90. Loading sequence for GD-2 (Net Positive and Negative Strain)

4.3.3.3 Design and Fabrication of Grooved Dissipater Prototypes

Two identical specimens were fabricated. The dimensions of the dissipater are shown in Figure 4.87. Each dissipater consisted of a grooved bar with threaded ends, external tube, and two end nuts (Figure 4.91a).

The mild steel bar ($f_y = 350\ MPa$) had a solid diameter of 24 mm with a total length of 435 mm. Three grooves each with a depth of 10.6 mm were cut into the solid bar (Figure 4.91b). This would give a reduced sectional area of 203.129 mm^2 over the 245 mm grooved length of the dissipater. The reduced sectional area can be thought of that of an equivalent 16 mm diameter solid bar. A 20 mm portion of the solid bar was left between the grooved and threaded parts near each end. This was intended to prevent from a premature failure in the dissipater during testing as suggested by White (2014). The threaded ends were fabricated to be 100 mm and 50 mm.

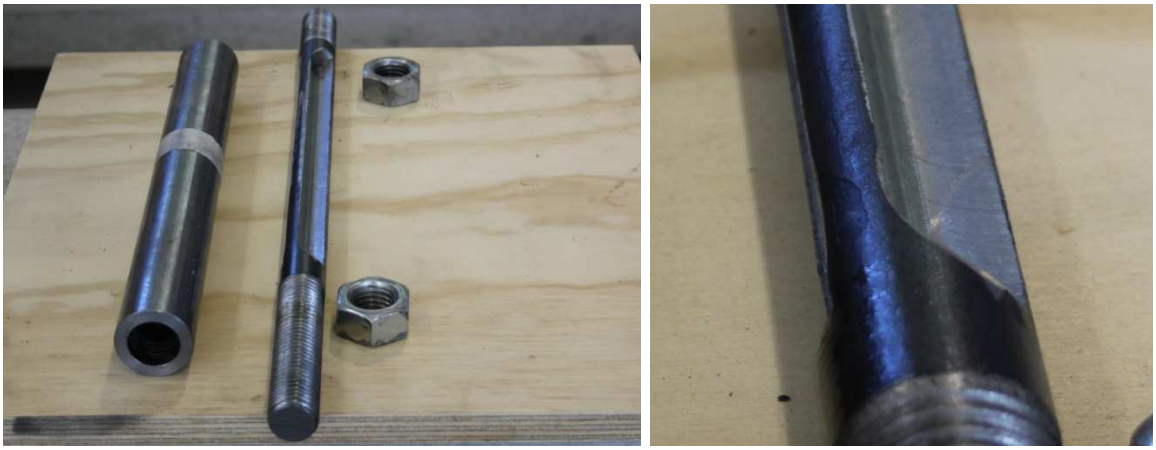

(a) Components of a grooved dissipater **(b) Grooves close-up view**

Figure 4.91. Components and assembly of GD prototypes

The external tube was made of a solid mild steel bar (37 mm in diameter) by simply hollowing the bar using a drill machine and leaving 6 mm wall thickness for the tube. There was 1 mm gap between the grooved bar and the inner diameter of the tube. This was sufficient to slide the grooved bar inside the tube without any issue.

One of the most important parameters in the design of grooved dissipater is the fused length of the dissipater which controls the maximum allowable strain in the grooved bar. According to PRESS Design Handbook (Pampanin et al., 2010), for a DCR connection with internal source of dissipation such as mild steel reinforcing, the unbonded length of the bar has to be chosen such to limit the peak strain in the bar to 5%. This peak strain threshold already accounts for the reduction in the deformation capacity under reversed cyclic loading, bar buckling, and low-cycle fatigue failure. The effects of leaving an unbonded length of the bars were explained in detail in Section 3.2.4 of Chapter 3.

Using a similar threshold of 5% maximum strain for the fused length of the dissipater, the required fused length can be simply calculated for the design level (ULS) displacement of 10 mm (2.3% drift ratio in the dissipater) in GD-1. This would give a minimum required fused length of 200 mm. Using a similar procedure, the minimum fused length for GD-2 can be calculated to be 120 mm. In this study, a fused length of 245 mm was chosen for both specimens. This would give peak strain of 4% and 3% at ULS level for GD-1 and GD-2, respectively.

Using basic principles of engineering mechanics, the yield force for the fused length of the dissipater was calculated to be 71 kN. Assuming an overstrength factor of 1.3, the

capacity of the dissipater was estimated to be 92 kN at the maximum displacement under net positive deformation. Given the similarity of this type of dissipater to those studied by Amaris Mesa, 2010 (Figure 4.16) and Sarti et al., 2013 (Figure 4.14), the capacity of the dissipater was expected to increase by a factor of 2 in compression. This means, the capacity of the dissipater under maximum net negative strain could be as high as approximately 150 kN.

4.3.3.4 Testing Results and Performance Evaluation

A. Test No 1 (GD-1): The dissipater behaved well with no premature failure during testing. The dissipater fractured during the second cycle of 25 mm displacement. Following testing, the fractured dissipater was disassembled and all parts were inspected for any damage. As expected all inelastic deformation appeared to be concentrated over the fused length of the dissipater. Evidence of buckling in a snake-shaped local buckling pattern along the grooves was obvious (Figure 4.92a). The solid and threaded parts of the grooved bar appeared to be intact.

(a) Fracture in GD-1 along the fused length **(b) Snake-shaped buckling, close-up view**

Figure 4.92. Fracture and deformation of GD-1 following cyclic loading

The axial force-displacement hysteresis for GD-1 under net positive strain is plotted in Figure 4.93a. The stress-strain hysteresis is shown in Figure 4.93b. The dissipater showed a very stable hysteresis and behaved similar to what previously tested by White (2014). Considering the lower yield point on the backbone curve of Figure 4.93c, the dissipater yielded at 0.8% drift ratio.

The dissipater completed all cycles of 20 mm MCE level displacement (4.6% drift ratio). The dissipater fractured under tensile loading during the second cycle of 25 mm displacement (5.7% drift ratio or 2.5 times ULS). The fracturing cause was due to

strength degradation during higher drift ratio which triggered the low-cycle fatigue failure in the dissipater. In Figure 4.94a, GD-1 achieved a maximum capacity of just less than 100 kN in tension and approximately 150 kN in compression during the first cycle of 25 mm displacement (5.7% drift ratio). The ductility at the maximum displacement was 7.1. This was close to the value observed (6.9) by White (2014) in a similar test on GD. The residual displacement in the dissipater following the first cycle of 5.7% drift ratio was in order of 23.7 mm (5.45% drift ratio) which corresponds to almost 95% of the maximum drift ratio (5.7%).

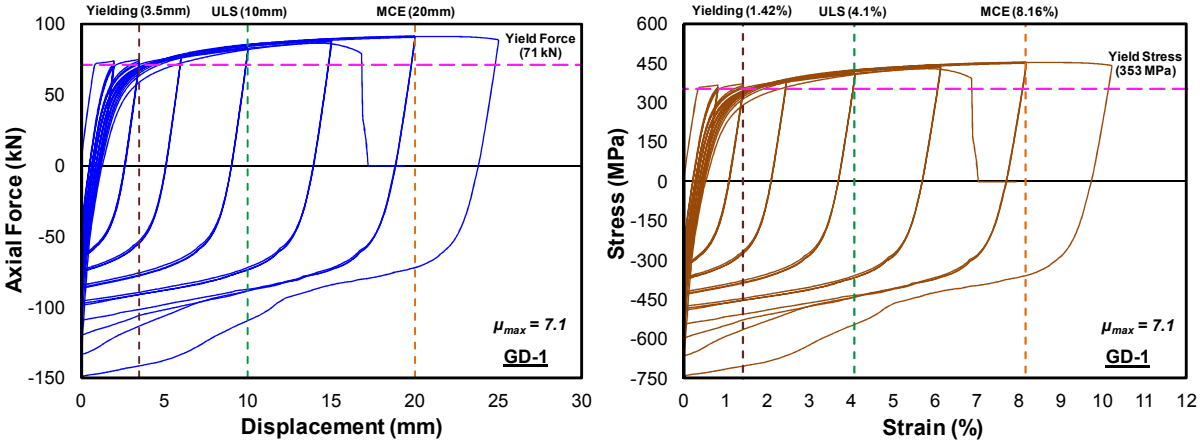

(a) Force-displacement hysteresis **(b) Stress-strain hysteresis**

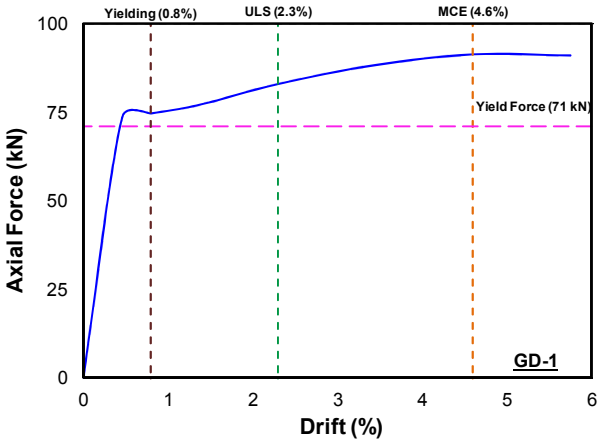

(c) Backbone curve

Figure 4.93. Hysteresis and backbone plots for GD-1

The energy dissipated per each cycle of each drift ratio for GD-1 is presented in Figure 4.94a. The dissipater maintained good energy dissipation capacity under cyclic loading up to the end of first cycle at 5.7% drift ratio. As shown, the dissipater had fractured during the second cycle of 5.7% drift ratio. This reduced the amount of cumulative

energy dissipated during this drift ratio significantly. This suggests that GD would be susceptible to strength degradation and low-cycle fatigue failure during cycles of large deformation. Therefore, unlike MUD, the dissipater cannot maintain steady energy dissipation capacity and strength for a high number of cycles beyond the yield point.

The experimental hysteretic damping curve for GD-1 is plotted in Figure 4.94b in accordance with Priestley et al. (2007). From ductility of 1 up to 2.5, the hysteretic damping values for the dissipater located above those from the theoretical models for Elastic-Perfectly Plastic, Ramberg-Osgood, and Bilinear (*r = 0.2*). From ductility of 2.5 up to 5.5, the values for hysteretic damping are just under the theoretical models. Following this, the hysteretic damping values are above the theoretical models up to the fracturing point. GD-1 attained a maximum hysteretic damping value of 24% at ductility of 7.1 during first cycle at maximum drift ratio of 5.7%.

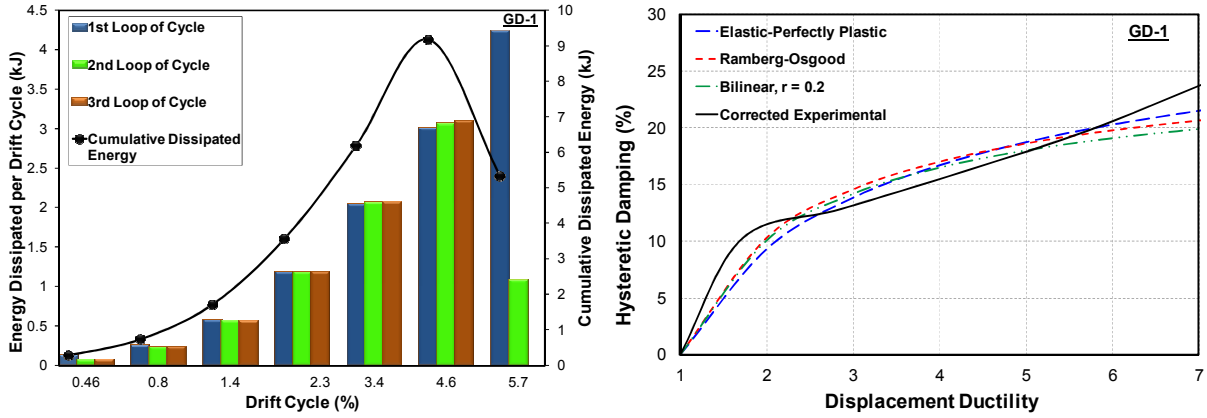

(a) Dissipated energy (per cycle and cumulative) **(b) Corrected area-based hysteretic damping**

Figure 4.94. Dissipated energy and hysteretic damping plots for GD-1

B. Test No 2 (GD-2): The dissipater completed all cycles of 10 mm MCE level displacement (2.3% drift ratio) without failure. GD-2 reaced maximum displacement of 15 mm (3.4% drift ratio) under net negative strain (μ = *4.3*), but fractured as the dissipater was loaded to a similar displacement under net positive strain. Therefore, it did not complete a full cycle of 3.4% drift ratio. The fracture was thought to be due to low-cycle fatigue and local buckling along the grooves. An inspection of the parts for the fractured dissipater showed significant snake-shaped local buckling along the grooves near the loading end (Figure 4.95b). The local buckling in GD-2 was more obvious than what observed in GD-1 (Figure 4.95a).

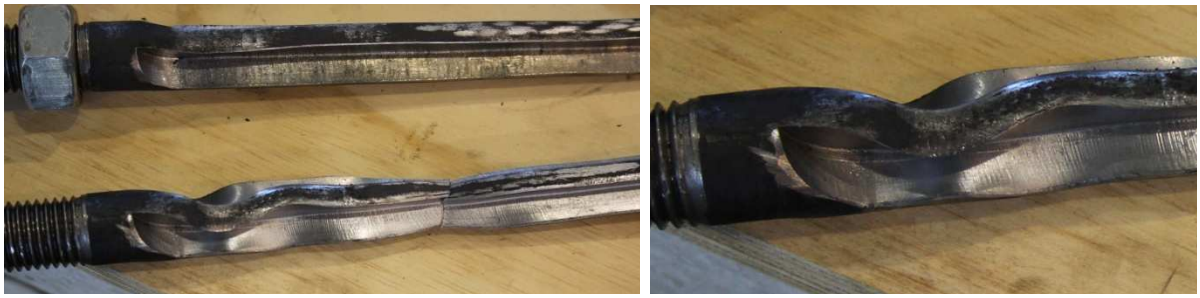

(a) Local buckling, Top (GD-1), Bottom (GD-2) **(b) Snake-shaped buckling in GD-2, close-up**

Figure 4.95. Fracture and deformation of GD-2 following cyclic loading

The axial force-displacement and stress-strain hysteresis plots are presented in Figure 4.96a and Figure 4.96b, respectively. The yield point was similar to that of GD-1 (0.8% drift ratio). The dissipater showed a stable response with slight increase in strength under compression. The backbone plot is shown in Figure 4.96c.

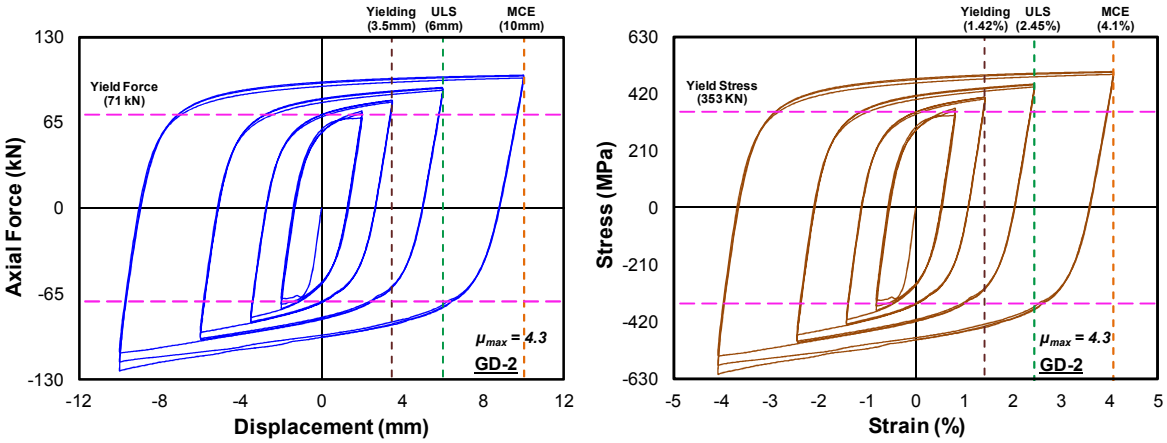

(a) Force-displacement hysteresis **(b) Stress-strain hysteresis**

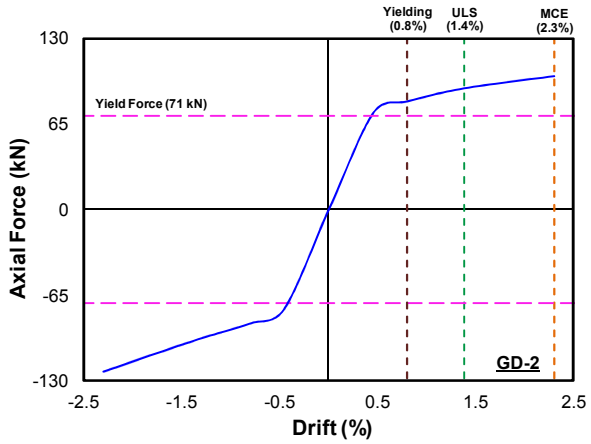

(c) Backbone curve

Figure 4.96. Hysteresis and backbone plots for GD-2

From Figure 4.96a, the ductility at MCE level drift ratio (2.3%) was 2.9. The dissipater completed half-cycle of 3.4% drift ratio Therefore, if this drift ratio (3.4%) is taken as the final deformation level, the maximum displacement ductility was 4.3 at the failure point. This corresponds to 60% of the final ductility observed during testing of GD-1 under net positive strain. The reduction in ductility was thought to be due to a more demanding loading protocol which had contributed in more strength degradation and deformation in GD-2. The residual displacement in the dissipater was similar to that observed in testing of GD-1.

The energy dissipated per each cycle of each drift ratio for GD-2 is plotted in Figure 4.97a. The slight increase in energy dissipation capacity during 2nd and 3rd cycles of 2.3% drift ratio was thought to be due to some induced friction between the grooved bar and the tube inner surface as the dissipater Poisson's ratio is affected under axial loading.

From a comparison of the cumulative dissipated energy in GD-2 during 2.3% drift ratio (10 kJ) to that of GD-1 (3.5 kJ), the dissipater had almost 3 times greater energy dissipation. Similar to GD-1, the dissipater could not maintain its energy dissipation capacity under a large number of cycles beyond the yield point, and hence it failed under low-cycle fatigue.

The experimental hysteretic damping curve for GD-2 is plotted in Figure 4.97b. According to this Figure, between ductility of 1 up to almost 2, the dissipater had higher values of hysteretic damping compared to those from the theoretical models. From ductility of 2 up to 4.3 (failure point), the hysteretic damping values for GD-2 located under those from the theoretical models shown in Figure 4.97b. GD-2 attained a maximum hysteretic damping value of 14% at ductility of 4.3 during the first cycle of maximum drift ratio (3.7%, 2.6 times ULS).

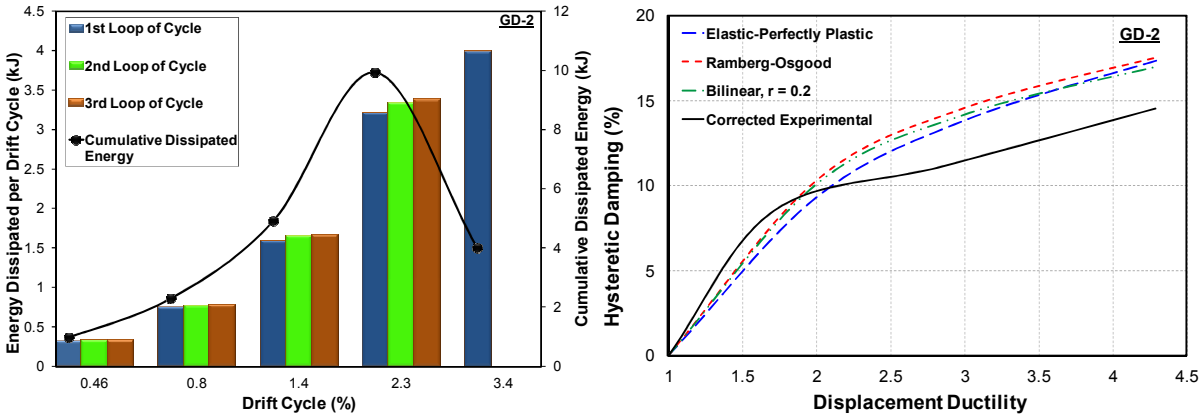

(a) Dissipated energy (per cycle and cumulative) **(b) Corrected area-based hysteretic damping**

Figure 4.97. Dissipated energy and hysteretic damping plots for GD-2

4.3.3.5 Summary of Testing Results for Grooved Type Dissipater

Grooved Dissipater (GD) was originally developed and tested by White (2014). Past research has shown suitability of this type of dissipater in DCR connections for ABC Controlled Damage. GD offers good advantages such as higher capacity in a smaller package, easy fabrication, and good energy dissipation. Findings from White (2014) have suggested possible application of GD in DCR connections for ABC Low Damage.

Experimental testing in this research aimed to further investigate the response of GD under two types of quasi-static loading. Two identical specimens were developed and tested. Test No 1 aimed to study the response of GD under net positive strain while Test No 2 included testing of GD under both net positive and negative strain.

The loading protocol for Test No 1 represented a case similar to what can be expected of external dissipaters in a DCR connection. GD-1 achieved its predicted capacity and maximum displacement ductility of 7.1 before fracturing in low-cycle fatigue during the second cycle of 5.7% drift ratio. The maximum drift ratio for which the dissipater could complete all three cycles was at MCE level loading (4.6%). The corrected experimental damping curve suggested that the dissipater reached maximum hysteretic damping of 24% before the failure. This was slightly higher than those from theoretical models such as Ramberg-Osgood, Elastic-Perfectly Plastic, and Bilinear ($r = 0.2$).

In Test No 2, GD-2 was subjected to positive and negative strain which is a more demanding loading protocol. This type of loading can represent a scenario where the

dissipater is used as bracing element in a truss. GD-2 showed a stable hysteresis with similar response to that for GD-1 under net positive strain. There was a slight increase (22%) in the strength of the dissipater under compression during cycles of MCE level drift ratio.

GD-2 achieved a maximum ductility of 4.3 before fracturing in low-cycle fatigue during the first cycle of 3.4% drift ratio. The corrected experimental damping values were slightly lower than those observed in testing of GD-1. This could have been a consequence of more deformation in GD-2 such as snake-shaped local buckling along the grooves which had induced higher strains in the dissipater. Before fracturing in low-cycle fatigue, the dissipater attained a maximum hysteretic damping of 14%.

As a summary for this Chapter, the innovative dissipaters discussed here offer many advantages compared to existing damping technologies in the market such as Buckling-Restrained Braces (BRBs) and fluid viscous dampers, refer to Table 4.4. Experimental results in this Chapter showed that MUD offers great performance under larger cyclic deformation without any strength degradation or being susceptible to low-cycle fatigue failure. There were some stiffness degradation of the dissipater following the first cycle at each drift ratio. However, there was not any noticeable difference in the stiffness of the dissipater during the subsequent cycles at the same drift ratio. Grooved Dissipater (GD) was shown to have higher capacity in a compact package, better performance compared to previous BRFs, and simple fabrication process. However, GD was still susceptible to strength degradation and low-cycle fatigue failure under larger drifts. Experimental testing from MUD and GD in this Chapter suggested that these devices can be used to absorb seismic energy in DCR connections for ABC Low Damage.

In the next Chapter (Chapter 5), the concept for using MUD and GD or a combination of them in DCR connections for ABC Low Damage system will be experimentally tested and validated. In general, it is recommended that MUD should be used in locations where the largest gap opening occurs in the rocking connection. MUD has a robust performance against low-cycle fatigue failure under larger drifts. Similarly, GD can be used in locations where a smaller gap opening (deformation) is expected in the rocking connection. This means that the dissipater could go through more cycles of loading before a low-cycle fatigue failure occurs. This would elongate the service life of the

dissipater as it will not be undergoing larger deformation under cyclic loading. Using improved detailing and better arrangement of the dissipaters in DCR connections for ABC Low Damage, the repairs and replacement cost of the dissipaters following an earthquake can be minimized. The improved detailing and application of the innovative dissipaters in DCR connections for ABC Low Damage aim to fulfill the following objectives:

1. To minimize the fabrication cost of the dissipaters.
2. To facilitate the fabrication, construction, and assembly process of the dissipaters and precast elements.
3. To make the installment work of the dissipaters simple such as by unwinding and winding down of a nut inside the dissipater bracket.
4. To provide an enhanced self-centering of the bridge with flag-shaped response.
5. To increase the final ductility of the connection during a large earthquake.
6. To solve the issues observed in the previous studies and experimental testing of DCR connections such as low-cycle fatigue failure and excessive deformation of the dissipaters.
7. To prevent any type of earthquake damage such as cracking, spalling etc in the columns.
8. To eliminate the need for replacement of the external dissipaters following an earthquake.
9. To further reduce the maintenance and life-cycle cost of the bridge.
10. To make DCR connections architecturally attractive by considering bridge aesthetic in the design of dissipaters and detailing.

Table 4.4. Comparison of advantages between existing and innovative dissipaters

Important Features	Buckling-Restrained Braces (BRBs)	Fluid Viscous Dampers	Innovative Dissipaters
Cost-effectiveness	Yes	No	Yes
Made from available materials in the market (e.g. mild steel)	Yes	No	Yes
Easy to manufacture	No	No	Yes
Easy to assemble	Yes	No	Yes
Easy to install in a structure	Yes	Yes	Yes
Can be made in the shape of mini plug and play devices	Yes	Yes	Yes
Can be made to function as a Lock-Up Device	No	Yes	Yes
Lightweight	No	No	Yes
Higher capacity and stroke	Yes	Yes	Yes
Compactness	No	Yes	Yes
Can be used in short spans as a bracing	No	No	Yes
Reliable to accommodate large cyclic displacement after a major earthquake	No	Yes	Yes
Overstrength of the brace	Yes	No	No
Strength degradation under cyclic loading	Yes	No	No
Low-cycle fatigue fracture	Yes	No	No
Option for self-centering capability	No	No	Yes
Rapid reinstatement with higher capacity	No	No	Yes
Have to be taken out of the structure for inspection or repair after an earthquake	Yes	No	No
Easy repleacibility of the damper and its parts	No	No	Yes
Easy to repair	No	No	Yes
Low life cycle maintenance	Yes	No	Yes
Recycling of the components	No	No	Yes

4.4 Overview of Energy Dissipation Mechanisms for ABC

In this part of the Chapter, the current energy dissipation mechanisms for ABC High Damage, ABC Controlled Damage, and ABC Low Damage, are discussed. As an overview, Figure 4.98 presents a general schematic for energy dissipation mechanisms for the three variations of ABC which are discussed in the following sections.

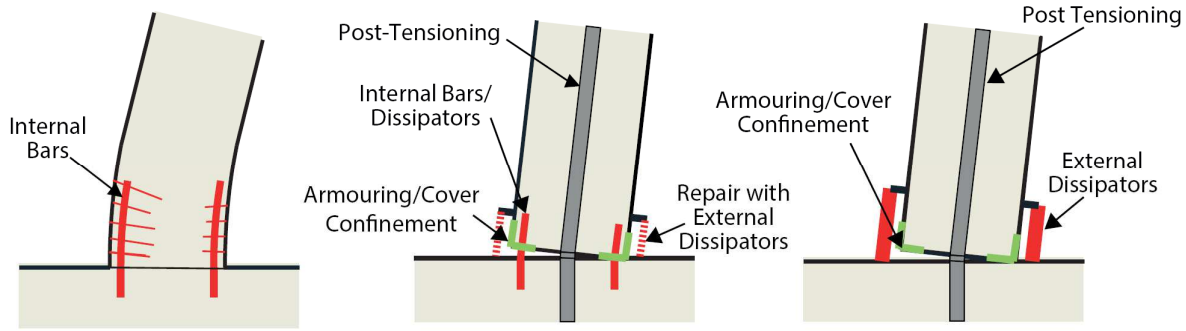

(a) ABC High Damage **(b) ABC Controlled Damage** **(c) ABC Low Damage**

Figure 4.98. Energy dissipation mechanisms in ABC in seismic regions

4.4.1 ABC High Damage

In ABC High Damage (Figure 4.98a), yielding of the internal reinforcing rebars provide energy dissipation. This has been the most common and widely practiced solution. This concept is similar to that of monolithic construction where reinforcing rebars at the plastic hinges are designed and detailed to yield, and thus absorb seismic energy during an earthquake. This option was explained and tested in detail in Chapter 3. The advantages of using reinforcing rebars as dissipative elements are as follows:

1. Use of the same rebars for both strength and energy dissipation capacity inside the precast element
2. No need for introducing additional sources of dissipation at the plastic hinges
3. Rebars are readily available
4. Rebars are generally cheaper
5. Ease of construction
6. No fabrication required apart from that for cutting and bending of rebars

7. Rebars have ductile behavior with higher strain capacity
8. Rebars exhibit good hysteretic behavior under tension and compression
9. Good durability of rebars which are protected by the surrounding concrete

Although this option offers good advantages, however, following a big earthquake, the inspection, repair, and replacement of the yielded, buckled, and fractured reinforcing rebars inside the precast element are the most undesirable aspects of this solution. Research by Priestley et al. (1996) suggested that in post-earthquake scenarios where there is buckling and fracturing of the reinforcing rebars in reinforced concrete column, a whole replacement of the column should be adopted than repair. This means that there is a chance that following a design level earthquake, a bridge incorporating this type of energy dissipation mechanism (e.g. formation of plastic hinges) may have to be completely replaced.

Another issue for this type of solution is the uncertainty around the extent of deformation and the residual low-cycle fatigue life in the rebars following an earthquake. Past research investigations have demonstrated the complexity of determining the levels of strain and residual strength and ductility in post-earthquake assessment of reinforced concrete columns, (Manson, 1953, Coffin, 1954, Mander et al., 1994, and Momtahan et al., 2009).

In order to overcome the issue for low-cycle fatigue failure in ABC High Damage, debonding of the reinforcing bars can be viable at the potential plastic hinge locations where a single gap opening is expected (such as that in a grouted duct connection). This was discussed in detail in Section 3.2.4.1 in Chapter 3. A schematic effect of debonding on bar strain is presented in Figure 4.99. An alternative method to that presented in Chapter 3 is to consider the single gap opening connection as a rocking interface and to limit the strain demand (ε_s) in the reinforcing bars to a threshold of 5%, as presented in the PRESSS Design Handbook (Pampanin et al., 2010). According to Pampanin et al. (2010), the strain demand in a rocking connection can be calculated using Equation 4.4.

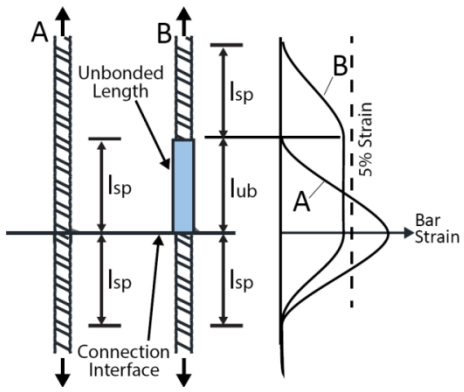

Figure 4.99. Effect of unbonded length on bar strain, after White (2014)

$$\varepsilon_s = \frac{\Delta_s + (2/3)L_{sp}\varepsilon_y}{l_{ub} + 2L_{sp}} \tag{4.4}$$

Where,

ε_y is the yield strain of the steel

Δ_s is the elongation of the mild steel bar in (mm)

L_{sp} is the strain penetration length, equals $0.022 f_y\, d_{bl}$ in (mm)

f_y is the yield strength of the reinforcement in (MPa)

d_{bl} is the diameter of the reinforcing bar in (mm)

l_{ub} is the unbonded length of the mild steel reinforcement in (mm)

Replacing ε_s by 0.05 in Equation 4.4 and solving for l_{ub} would give the required unbonded length of the rebars in (mm) as presented in Equation 5.5. In this Equation, Δ_{sd} is elongation of the mild steel bar at the design level drift in the structure.

$$l_{ub} = 20\left[\Delta_{sd} + \left(\frac{2}{3}\right)L_{sp}\varepsilon_y\right] - 2L_{sp} \tag{4.5}$$

In summary, using reinforcing bars as energy dissipaters in ABC High Damage includes the following disadvantages:

1. Transverse reinforcing (stirrups) with closer distance to each other is required at the plastic hinges to provide buckling restraints and confinement

2. Limited post-earthquake inspectability with intrusive work to assess the rebars condition

3. Limited option for repairability and retrofitting of the columns

4. Low-cycle fatigue failure which could be delayed through debonding of the rebars

4.4.2 ABC Controlled Damage

ABC Controlled Damage (Figure 4.98b) was developed and tested by White (2014). This solution was previously explained in Section 2.3.3.1 in Chapter 2. Initially, the energy dissipation for ABC Controlled Damage relies on internally placed dissipative rebar links which can be replaceable. Following an earthquake, the links have to be replaced with new ones or an external source of dissipation with or without the use of internal dissipaters. This offers the following advantages:

1. Use of the same rebars for both strength and energy dissipation capacity inside the precast element prior to an earthquake

2. Dissipative links are made of rebars which are readily available and cheap

3. No fabrication required apart from cutting and bending of the rebars

4. Replacing dissipative rebar links after an earthquake will remove all uncertainty about the residual ductility, capacity, and low-cycle fatigue life of the connection

5. Option for using externally attached dissipaters for energy absorption

The post-earthquake disadvantages are:

1. Limited post-earthquake inspectability of the dissipative rebar links, intrusive work would be needed to replace them which is a time consuming process

2. Construction risks with the replacement of rebar links due to any misalignment

3. Fabrication cost of the external dissipaters

4.4.3 ABC Low Damage

ABC Low Damage (Figure 4.98c) provides a better seismic performance compared to the other two variations of ABC (High Damage and Controlled Damage). One of the options for energy dissipation mechanism in ABC Low Damage is application of externally attached plug and play dissipaters (Figure 4.70f). Following an earthquake, the dissipaters can be simply inspected for any damage and if needed, can be replaced with new ones almost immediately.

Past research on DCR connections for precast bridge piers incorporated mini Buckling-Restrained Fused type dissipaters (BRF) as the energy dissipation source (Marriott, 2009, and Guerrini et al., 2012). Previous research showed good performance of the system with mini BRFs, however, there was some minor damage to the columns after testing. The dissipaters also suffered excessive damage during larger drift ratios and were susceptible to low-cycle fatigue failure. In a real life precast bridge, this would mean that minor to moderate repair work would be needed for the bridge pier following a big earthquake. At the same time, as part of the post-earthquake efforts to reinstate the ductility and capacity of the bridge, the external dissipaters would have to be replaced with new ones.

Given the extent of damage observed in the aforementioned research studies, the tested solutions can be classified under ABC Low Damage. However, the solutions accept minor to moderate damage to the piers and replacement of the dissipaters as part of post-earthquake repairs. The concept for ABC Low Damage system in this thesis is based on eliminating any type of damage to both columns and dissipaters while ensuring full re-centering of the bridge. This will be discussed in Chapter 5 where improved connection detailing and application of Mini UFP Dissipater (MUD) and Grooved Dissipater (GD) in DCR connections for ABC Low Damage are proposed, and validated through experimental testing. This resulted into an enhanced performance of the bridge piers which would require cosmetic to no repairs following an earthquake.

4.5 Conclusions

In the first part of this Chapter, a comprehensive literature review on three categories of existing damping systems was presented. The systems discussed in this Chapter included metallic, friction, and viscous damping systems. Many popular variations of each damping system with their advantages and disadvantages were thoroughly discussed. Past research and applications of some of these dampers in DCR connections were also presented.

The second part of the Chapter discussed concepts for the development of innovative metallic dampers. The innovative dampers offer advantages which are not integrated in the existing dampers in the market. This includes, but not limited to cost-effectiveness, higher capacity and stroke, multi-performance feature, minimum strength degradation under cyclic loading, and almost zero low-cycle fatigue failure.

Two types of innovative dampers, the Bracing Type and Mini Plug and Play Type, were proposed and discussed. Concepts for several variation of each type of dissipater were also presented. The variations provide better and enhanced performance.

For the brace dissipater, concepts for application of the device in building and bridge structures were discussed. Two variation of the dissipater was experimentally tested and validated. A prototype for UFP Brace Dissipater was fabricated using recycled materials in the lab. The prototype was later modified to a UFP Self-Centering Brace Dissipater (SCUD). Experimental results from quasi-static loading showed promising performance of the brace dissipaters under cyclic loading. The UFPs were very effective to dissipate energy and maintain their capacity for a large number of cycles beyond the yield point. There was no signs of strength degradation or low-cycle fatigue failure in the UFPs.

The UFP Brace Dissipater achieved a maximum hysteretic damping of 32.3% at its stroke limit which corresponded to displacement ductility of 9. Similarly, testing of SCUD showed re-centering of the brace using pre-tensioned tendons inside the dissipater. However, the dissipater exhibited lower energy dissipation capacity due to a flag-shaped response.

For Mini Plug and Play Devices, several concepts for application of the devices in DCR connections, retrofitting of buildings and bridges, and seismic protection of non-structural components were presented. The concept for Mini UFP Damper (MUD) was experimentally tested and validated. Three identical MUD prototypes were fabricated. The prototypes were tested under quasi-static cyclic loading. Experimental observations and results from testing showed great performance of MUD. The dissipater was able to achieve maximum displacement ductility of 12.5 which corresponded to a strain level of 11% in the UFPs. The UFPs did not show any signs of distress or low-cycle fatigue failure at 11% strain. The maximum hysteretic damping at the stroke limit of the dissipater was 44%.

In the third part of the Chapter, further experimental testing on Grooved Dissipater (GD) was carried out. Two identical GD prototypes were fabricated and tested under different loading protocols. Testing of GD under net positive strain showed similar results to that obtained by White (2014). The dissipater achieved final displacement ductility of 7.1 and maximum hysteretic damping of 24% before fracturing under low-cycle fatigue. Testing of GD under net positive and negative deformation showed similar behavior of the dissipater. However, there was a significant reduction in the displacement capacity of the dissipater. The dissipater achieved maximum hysteretic damping of 14% at ductility of 4.3. Evidence of snake-shaped local buckling pattern was more obvious in testing of GD under positive and negative deformation. At the same time, there was a slight increase in the axial strength of the dissipater under compression. The behavior of the dissipater could be improved with further refinement of the detailing.

4.6 Bibliography

1. Aiken, I. D., and Kelly, J. M. (1990). Earthquake Simulator Testing and Analytical Studies of Two Energy Absorbing Systems for Multistory Structures, Report No. UCB/EERC-90/03. University of California, Berkeley, California, United States.

2. Aiken, I. D., Nims D. K., Whittaker, A. S., and Kelly, J. M. (1993). Testing of Passive Energy Dissipation Systems. Earthquake Spectra, 9(3).

3. Aiken, I. D., Nims, D. K., and Kelly, J. M. (1992). Comparative Study of Four Passive Energy Dissipation Systems. Bulletin of New Zealand Society for Earthquake Engineering, 25(3).

4. Amaris Mesa, A. D. (2010). Developments of Advanced Solutions for Seismic Resisting Precast Concrete Frames. PhD thesis, University of Canterbury, Christchurch, New Zealand.

5. American Concrete Institute (ACI) (2001). Acceptance Criteria for Moment Frames Based on Structural Testing, Report No. ACI T1.1-01, Farmington Hills, Michigan, United States.

6. American Institute of Steel Construction (AISC) (2005). Seismic Provisions for Structural Steel Buildings, ANSI/AISC 341-05. AISC, Chicago, Illinois, United States.

7. American Institute of Steel Construction (AISC) (2010). Seismic Provisions for Structural Steel Buildings, ANSI/AISC 341-10. AISC, Chicago, Illinois, United States.

8. Baird A., Smith, T., Palermo, A., and Pampanin, S. (2014). Experimental and Numerical Study of U-Shaped Flexural Plate (UFP) Dissipaters. Proceedings of New Zealand Society for Earthquake Engineering, Auckland, New Zealand.

9. Beck, J. L. and Skinner, R. I. (1974). The Seismic Response of a Reinforced Concrete Bridge Pier Designed to Step. International Journal of Earthquake Engineering and Structural Dynamics, 2(4):343-358.

10. Bergman, D. M., and Goel, S. C. (1987). Evaluation of Cyclic Testing of Steel-Plate Devices for Added Damping and Stiffness, Report UMCE 87-10. University of Michigan, Ann Arbor, Michigan, United States.

11. Black, C., Makris, N., and Aiken, I. (2002). Component Testing, Stability Analysis, and Characterization of Buckling-Restrained Unbonded Braces, PEER Report No. 2002/08. University of California, Berkeley, California, United States.

12. Christopoulos, C., and Filiatrault, A. (2006). Principles of Passive Supplemental Damping and Seismic Isolation. IUSS Press, Pavia, Italy.

13. Christopoulos, C., Filiatrault, A., Uang, C., and Folz, B. (2002). Post-Tensioned Energy Dissipating Connections for Moment-Resisting Steel Frames. Journal of Structural Engineering, 128(9):1111-1120.

14. Christopoulos, C., Filiatrault, A., Uang, C.-M., and Folz, B. (2002). Post-Tensioned Energy Dissipating Connections for Moment Resisting Steel Frames. ASCE Journal of Structural Engineering, 128(9):1111-1120.

15. Christopoulos, C., Tremblay, R., Kim, H., and Lacerte, M. (2008). Self-Centering Energy Dissipative Bracing System for the Seismic Resistance of Structures: Development and Validation. ASCE Journal of Structural Engineering, Special Issue: Design and Analysis of Structures with Seismic Damping Systems, 134:96–107.

16. Clifton, G. (2005). Semi-Rigid Joints for Moments Resisting Steel Framed Seismic Resisting Systems. PhD thesis, University of Auckland, Auckland, New Zealand.

17. Coffin, L. F. J. (1954). A Study of the Effects of Cyclic Thermal Stresses on a Ductile Material. Trans., American Society of Mechanical Engineers (ASME), 76:931-950.

18. Constantinou, M. C., and Symans M. D. (1992). Experimental and Analytical Investigation of Seismic Response of Structures with Supplemental Fluid Viscous Dampers, Technical Report NCEER-92-0032. University at Buffalo (SUNY), New York, United States.

19. Constantinou, M. C., and Symans, M. D. (1993). Experimental Study of Seismic Response of Buildings with Supplemental Fluid Dampers. Structural Design of Tall Buildings, 2(2):93-132.

20. DesRoches, R., McCormick, J., and Delemont, M. (2004). Cyclic Properties of Superelastic Shape Memory Alloy Wires and Bars. Journal of Structural Engineering, 130(1):38-46.

21. Dwairi, H. M., Kowalsky, M. J., and Nau, J. M. (2007). Equivalent Damping in Support of Direct Displacement-Based Design. Journal of Earthquake Engineering, 11(4):512-530.

22. Eatherton, M. R., Fahnestock, L. A., and Miller, D. J. (2014). Self-Centering Buckling Restrained Brace Development and Application for Seismic Response Mitigation. Proceedings of 10th United States National Conference on Earthquake Engineering, Anchorage, Alaska.

23. Filiatrault, A., and Cherry, S. (1987). Performance Evaluation of Friction Damped Braced Steel Frames Under Simulated Earthquake Loads. Earthquake Spectra, 3(1): 57-78.

24. Filiatrault, A., Tremblay, R., and Kar, R. (2000). Performance Evaluation of Friction Spring Seismic Damper. ASCE Journal of Structural Engineering, 126(4): 491–499.

25. Filiatrault, A., Tremblay, R., and Wanitkorkul, A. (2001). Performance Evaluation of Passive Damping Systems for the Seismic Retrofit of Steel Moment Resisting Frames Subjected to Near Field Ground Motions. Earthquake Spectra, 17(3):427-456.

26. Gray, M. G. (2012). Cast Steel yielding Brace System for Concentrically Braced Frames. PhD Thesis, University of Toronto, Toronto, Canada.

27. Guerrini, G., Restrepo, J. I., Massari, M., and Vervelidis, A. (2012). Self-Centering Precast Concrete Dual-Shell Steel Columns. Proceedings of 15th World Conference on Earthquake Engineering, Lisbon, Portugal.

28. Heresi, P., Herrera, R. A., and Moroni, M. O. (2014). Testing and Modeling of Shape Memory Alloy Plates for Energy Dissipators. Journal of Smart Structures and Systems, 14(5):883-900.

29. Huang, J. S., Chen, W. F., and Beedle, L. S. (1973). Behavior and Design of Steel Beam-to-Column Moment Connections, Fritz Engineering Laboratory Report No. 333.20. Lehigh University, Bethlehem, Pennsylvania, United States.

30. Iqbal, A., Pampanin, S., Buchanan, A. H., and Palermo, A. (2007). Improved Seismic Performance of LVL Post-tensioned Walls Coupled with UFP devices. Proceedings of 8th Pacific Conference on Earthquake Engineering, Singapore.

31. Iqbal, A., Pampanin, S., Palermo, A., Buchanan, A. (2010). Seismic Response of Post-Tensioned Timber Walls. Proceedings of 14th European Conference on Earthquake Engineering. Skopie-Ohrid, Republic of Macedonia.

32. Kam, W. Y., Pampanin, S. Palermo, A., and Carr, A. (2008). Implementation of Advanced Flag-Shaped (AFS) Systems for Moment-Resisting Frame Structure. Proceedings of 14th World Conference on Earthquake Engineering, Beijing, China.

33. Keats, G., Palermo, A., and Mashal, M. Energy Dissipation Device. United States Provisional Patent Application: 61/149,199. Filing Date April 17 2015.

34. Kelly, J. M., Skinner, R. I., and Heine, A. J. (1972). Mechanisms of Energy Absorption in Special Devices for use in Earthquake Resistant Structures. Bulletin of the New Zealand Society for Earthquake Engineering, 5(3).

35. Kim, H. J., and Christopoulos, C. (2008). Friction Damped Post-Tensioned Self-Centering Steel Moment Resisting Frames. ASCE Journal of Structural Engineering, 134(11): 1768-1779.

36. Kurama, Y. (2000). Seismic Design of Unbonded Post-Tensioned Precast Walls with Supplemental Viscous Damping. ACI Structural Journal, 97(4):648-658.

37. Latham D.A., Reay, A. M., and Pampanin, S. (2013). Kilmore Street Medical Center: Application of an Advanced Flag-Shape Steel Rocking System. Proceedings of New Zealand Society for Earthquake Engineering, Wellington, New Zealand.

38. Lee, D., and Taylor, D. P. (2001). Viscous Damper Development and Future Trends. The Structural Design of Tall Buildings, 10(5):311-320.

39. Makris, N., and Constantinou, M. C. (1992). Spring-Viscous Damper Systems for Combined Seismic and Vibration Isolation. Earthquake Engineering and Structural Dynamics, 21(8):649-664.

40. Mander, J., Panthaki, F., and Kasalanati, A. (1994). Low-Cycle Fatigue Behavior of Reinforcing Steel. Journal of Materials in Civil Engineering. 6:453-468.

41. Manson, S. S. (1953). Behavior of Materials under Conditions of Thermal Stress. Heat Transfer Symposium, University of Michigan Engineering Research Institute, Ann Arbor, Michigan, United States, 9-75.

42. Marriott, D. (2009). The Development of High-Performance Post-Tensioned Rocking Systems for the Seismic Design of Structures. PhD Thesis, University of Canterbury, Christchurch, New Zealand.

43. Momtahan, A., Dhakal, R., and Rieder, A. (2009). Effects of Strain-Ageing on New Zealand Reinforcing Steel Bars. Bulletin of the New Zealand Society for Earthquake Engineering, 42(2):179-186.

44. Morgen, B., and Kurama, Y. (2004). A Friction Damper for Post-tensioned Precast Concrete Beam-to-Column Joints. Proceedings of 13th World Conference on Earthquake Engineering, Vancouver, Canada.

45. Murata, Y., Mochizuki, S., Andou, N., Takahashi, S. (1980). An Experimental Study on Buckling of Unbonded Braces Under Centrally Applied Loads. Proceedings of Annual Meeting Architectural Institute of Japan, 1913-1914 (in Japanese).

46. New Zealand Standards (NZS) (2006). The Design of Concrete Structures, NZS 3101. Wellington, New Zealand.

47. Nims, D. K., Richter, P. J., and Bachman, R. E. (1993). The Use of the Energy Dissipating Restraint for Seismic Hazard Mitigation. Earthquake Spectra, 9(3):467-489.

48. Ocel, J., DesRoches, R., Leon, R. T., Hess, W. G., Krumme, R., and Hayes, J. R. (2004). Steel Beam-Column Connections Using Shape Memory Alloys. ASCE Journal of Structural Engineering, 130(5):732-740.

49. Palermo, A. (2004). The Use of Controlled Rocking In the Seismic Design of Bridges. PhD Thesis, Politecnico Di Milano (Technical University of Milan), Milan, Italy.

50. Palermo, A. and Pampanin, S. (2008). Enhanced Seismic Performance of Hybrid Bridge Systems: Comparison with Traditional Monolithic Solutions. Journal of Earthquake Engineering, 12(8):1267-1295.

51. Palermo, A., Pampanin, S., and Calvi, G. M. (2005[1]). Concept and Development of Hybrid Solutions for Seismic Resistant Bridge Systems. Journal of Earthquake Engineering, 9(6):899-921.

52. Palermo, A., Pampanin, S., Buchanan, A. and Newcombe, M. (2005[2]). Seismic Design of Multi-Storey Buildings using Laminated Veneer Lumber (LVL). Proceeding of New Zealand Society Earthquake Engineering Conference, Wairakei, New Zealand.

53. Palermo, A., Pampanin, S., and Marriott, D. (2007). Design, Modeling, and Experimental Response of Seismic Resistant Bridge Piers with Post-tensioned Dissipating Connections. Journal of Structural Engineering, 133(11):1648-1661.

54. Palermo, A., Pampanin, S., Fragiacomo, M., Buchanan, A.H., and Deam, B.L. (2006) Innovative Seismic Solutions for Multi-Storey LVL Timber Buildings. Proceedings of 9th World Conference on Timber Engineering, Portland, Oregon, United States, 3(16):1-8.

55. Pampanin, S., Kam W., Haverland, G., and Gardiner, S. (2011). Expectation Meets Reality: Seismic Performance of Post-Tensioned Precast Concrete Southern Cross Endoscopy Building during the 22nd February 2011 Christchurch Earthquake. Proceedings of New Zealand Concrete Industry Conference, Rotorua, New Zealand.

56. Pampanin, S., Marriot, D., and Palermo, A. (2010). PRESSS Design Handbook. New Zealand Concrete Society (NZCS) Incorporation, Auckland, New Zealand.

57. Priestley, M. J. N. (1991). Overview of PRESSS Research Program. Precast/Prestressed Concrete Institute Journal, 36(4):50-57.

58. Priestley, M. J. N. (1996). PRESSS Program - Current Status and Proposed Plans for Phase III. Precast/Prestressed Concrete Institute Journal, 41(2):22-40.

59. Priestley, M. J. N., Calvi, G. M., and Kowalsky, M. J. (2007). Displacement-Based Seismic Design of Structures. IUSS Press, Pavia, Italy.

60. Priestley, M. J. N., Seible, F., and Calvi, G. (1996). Seismic Design and Retrofit of Bridges. John Wiley & Sons, New York, United States.

61. Priestley, M. J. N., Sritharan, S., Conley, J. R., and Pampanin, S. (1999). Preliminary Results and Conclusions from the PRESSS Five-Story Precast Concrete Test Building. Precast/Prestressed Concrete Institute Journal, 44(6):42-67.

62. Restrepo, J. I., Mander, J., and Holden, T. J. (2001). New Generation of Structural Systems for Earthquake Resistance. Proceedings of New Zealand Society for Earthquake Engineering (NZSEE) Conference, Wairakei, New Zealand.

63. Richter, P. J., Nims, D. K., Kelly, J. M., and Kallenback, R. M. (1990). The EDR-Energy Dissipating Restraint, A New Device for Mitigating Seismic Effects. Proceedings of Structural Engineers Association of California (SEAOC) Annual Convention, Lake Tahoe, California, United States.

64. Ricles, J. M., Sause, R., Garlock, M. M., and Zhao, C. (2001). Post-Tensioned Seismic-Resistant Connections for Steel Frames. ASCE Journal of Structural Engineering, 127(2):113-121.

65. Robinson, W. H. (1995). Seismic Isolation, the New Zealand Experience. American Society of Mechanical Engineering, New York, United States.

66. Robinson, W. H., and Greenbank, L. R. (1976). An Extrusion Energy Absorber Suitable for the Protection of Structures during an Earthquake. Earthquake Engineering and Structural Dynamics, 4:251-259.

67. Rodgers, G. (2009). Next Generation Structural Technologies: Implementing High Force-To-Volume Energy Absorbers. PhD Thesis, University of Canterbury, Christchurch, New Zealand.

68. Roh, H., and Reinhorn, A. M. (2010). Hysteretic Behavior of Precast Segmental Bridge Piers with Superelastic Shape Memory Alloy Bars. Engineering Structures, 32(10): 3394–3403.

69. Saiidi, M. S., and Wang, H. (2006). Exploratory Study of Seismic Response of Concrete Columns with Shape Memory Alloys Reinforcements. ACI Structural Journal, 103(3):435-442.

70. Saiidi, M. S., O'Brien, M., and Mahmoud, S. (2009). Cyclic Response of Concrete Bridge Columns using Superelastic Nitinol and Bendable Concrete. ACI Structural Journal, 106(1):69–77.

71. Sarti, F., Smith, T., Palermo, A., Bonardi, D., and Carradine, D. M. (2013). Experimental And Analytical Study of Replaceable Buckling-Restrained Fuse-Type (BRF) Mild Steel Dissipaters. Proceedings of New Zealand Society for Earthquake Engineering Conference, Wellington, New Zealand.

72. Skinner, R. I, Tyler, R. G, Heine, A. J., and Robinson, W. H. (1980). Hysteretic Dampers for the Protection of Structures from Earthquakes. Bulletin of the New Zealand Society for Earthquake Engineering, 13 (1), 22-36.

73. Stanton, J. F., Wacker, J. M., Hieber, D. G., and Eberhard, M. O. (2005). Design of Precast Concrete Piers for Rapid Bridge Construction in Seismic Regions. Washington State Transportation Center (TRAC), University of Washington, Seattle, Washington, United States.

74. Stanton, J., Hicks, T., and Hawkins, N. (1991). PRESSS Project 1.3 - Connection Classification and Evaluation. PCI Journal, 36(5):62-71.

75. Stanton, J., Stone, W. C., and Cheok, G. S. (1997). Hybrid Reinforced Precast Frame for Seismic Regions. PCI Journal, 42(2):20-32.

76. Steimer, S. F., Godden, W. G., and Kelly, J. M. (1981). Experimental Behavior of a Spatial Piping System with Steel Energy Absorbers Subjected to a Simulated Differential Seismic Input, Report No. UCB/EERC-81/09. University of California, Berkeley, California, United States.

77. Stone, W. C., Cheok, G. S., and Stanton, J. F. (1995). Performance of Hybrid Moment Resisting Precast Beam-Column Concrete Connections Subjected to Cyclic Loading. ACI Structural Journal, 91(2):229-249.

78. Takeda, Y., Kimura, Y., Yoshioka, K., Furuya, N., and Takemoto, Y. (1976). An Experimental Study on Braces Encased in Steel Tube and Mortal. Proceedings of Annual Meeting Architectural Institute of Japan, 1041-1042 (in Japanese).

79. Tan, P., Agarwal, A. K., and Pan, Y. (2005). Near-Field Effects on Seismically Excited Highway Bridge Equipped with Nonlinear Viscous Dampers. Bridge Structures: Assessment, Design, and Construction, 1(3):307-318.

80. Tremblay, R., Stiemer, S. F. (1993). Energy Dissipation through Friction Bolted Connections in Concentrically Braced Steel Frames. Proceedings of Applied Technology Council (ATC 17-1) Seminar on Seismic Isolation, Passive Energy Dissipation, and Active Control, Redwood City, California, United States, 2:557-568.

81. Tsai, K. C., Chen, H. W., Hong, C. P., and Su, Y. F. (1993). Design of Steel Triangular Plate Energy Absorbers for Seismic Resistant Construction. Earthquake Spectra, 9(3).

82. Tyler, R. G. (1978). Tapered Steel Energy Dissipators for Earthquake Resistant Structures. Bulletin of New Zealand Society for Earthquake Engineering, 11(4).

83. Varela, S., and Saiidi, M. S. (2014). Damage-Free Earthquake-Resistant Deconstructible Columns for ABC. Proceedings of National Accelerated Bridge Conference, 620-629, Miami, United States.

84. Wang, D., and Filiatrault, A. (2008). Numerical and Experimental Studies of Self-Centering Post-Tensioned Steel Frames, Technical Report MCEER-08-0017. Multidisciplinary Center for Earthquake Engineering Research, University at Buffalo, State University of New York, Buffalo, New York, United States.

85. Watanabe, A., Hitomi, Y., Saeki, E., Wada, A., and Fujimoto, M. (1988). Proceedings of 9th World Conference on Earthquake Engineering, 6(7):719-724.

86. White, S. (2014). Controlled Damage Rocking Systems for Accelerated Bridge Construction. Master Thesis, University of Canterbury, Christchurch, New Zealand.

87. Whittaker, A. S., Bertero, V. V., Alonso, J. L., and Thompson, C. L. (1989). Earthquake Simulator Testing of Steel Plate Added Damping and Stiffness Elements, Report No. UCB/EERC- 89/02. University of California, Berkeley, California, United States.

88. Whittaker, A. S., Bertero, V. V., Thompson, C. L., and Alonso, L. J. (1991). Seismic Testing of Steel Plate Energy Dissipation Devices. Earthquake Spectra, 7(4):563-604.

89. Witting, P. R., and Cozzarelli, F. A. (1992). Shape Memory Structural Dampers: Material Properties, Design, and Seismic Testing, Technical Report NCEER-92-0013. University at Buffalo (SUNY), New York, United States.

90. Youssef, M. A., Alam, M. S., and Nehdi, M. (2008). Experimental Investigation on the Seismic Behavior of Beam-Column Joints Reinforced with Superelastic Shape Memory Alloys. Journal of Earthquake Engineering, 12(7):1205–1222.

5. DEVELOPMENT AND TESTING OF ABC LOW DAMAGE PIER SYSTEM

5.1 Introduction

This Chapter presents the development and testing of low damage technologies for Accelerated Bridge Construction (ABC Low Damage). ABC Low Damage was previously introduced in Chapter 2 and 4.

The concept for ABC Low Damage is different than ABC High Damage. As a brief review, ABC Low Damage aims to minimize and eliminate damage in the bridge during a big earthquake. This means that following the earthquake, the bridge will remain immediately functional and the repair cost and down time of the bridge can be eliminated.

ABC Low Damage incorporates Dissipative Controlled Rocking (DCR) connection between the precast elements in a bridge substructure system. The DCR connections are intended to replace plastic hinging in the bridge during an earthquake, thus it eliminates damage to the structure as previously proposed and studied by Palermo (2004), Stanton et al. (2005), Palermo et al. (2005, 2007, and 2008), Marriott (2009, 2011), Solberg et al. (2009), and Guerrini et al. (2012).

The concept for a DCR connection is illustrated in Figure 5.1a. In this type of connection, the unbonded post-tensioning tendons which are running inside the precast element are expected to provide self-centering capacity. At the same time, the external dissipaters are intended to absorb seismic energy generated during a ground motion in the structure. Steel armoring is generally provided at the rocking interface to limit damage to the precast element (Figure 5.1b).

The history for the development of DCR connection go back to a jointed United States-Japan research program titled “PREcast Seismic Structural Systems” (PRESSS) which

was coordinated by the University of California, San Diego (Priestley, 1991, 1996, Priestley et al., 1999, Stanton et al., 1991, 1997, Stone et al., 1995). There were many connections tested in the PRESSS Program. One of the connections was called "Hybrid Jointed Ductile" which is referred as DCR connection in the research here.

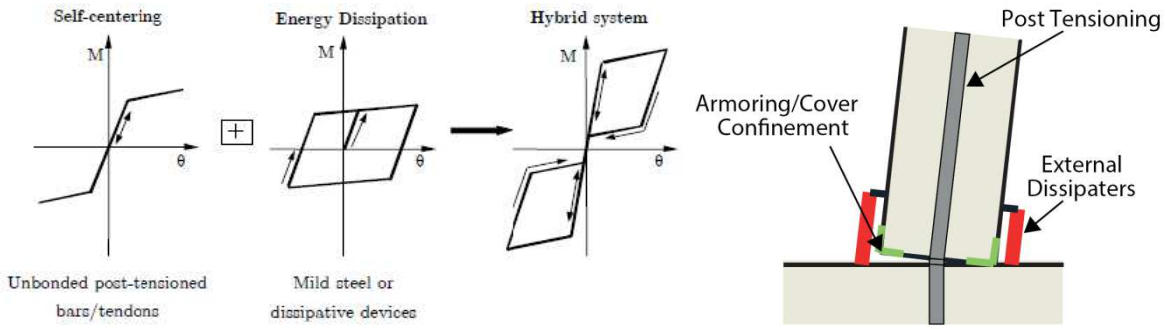

(a) Concept for DCR (Priestley et al., 1999) **(b) ABC Low Damage with DCR**

Figure 5.1. Concept for ABC Low Damage Systems with DCR

The results from Chapter 4 on Grooved Dissipater (GD) and Mini UFP Dissipater (MUD) are utilized in this Chapter to experimentally investigate the behavior of ABC Low Damage with these dissipaters. A half-scale multi-column bridge pier (bent) specimen, similar to High Damage Bent (HD) in Chapter 3, was developed and subsequently tested under several variations of DCR connection in the context of ABC Low Damage.

In the first part of the Chapter, the seismic performance of DCR connection with internal shear key and incorporating GD is experimentally investigated. Using the results from this part, in the second part of the Chapter, the detailing of the DCR connection is optimized using external shear key and incorporating several arrangements of GD and MUD. The three arrangements of the dissipater investigated are:

1. ABC Low Damage with Grooved Dissipater
2. ABC Low Damage with Mini UFP Dissipater
3. ABC Low Damage with a combination of Grooved and Mini UFP Dissipaters

In the last part of the Chapter, based on the experimental observations and results, qualitative and quantitative comparisons between seismic performance of ABC High Damage and ABC Low Damage are presented accordingly.

In summary, the objectives of this Chapter are as follows:

1. Presenting design procedure and detailing considerations for DCR connection in ABC Low Damage.

2. Discussing construction technologies and assembly procedure for ABC Low Damage.

3. Investigating the seismic performance of ABC Low Damage bent with internal and external shear keys under uni-directional quasi-static cyclic loading.

4. Investigating the seismic response of ABC Low Damage bent through an experimental parametric study under several levels of self-centering ratio and presence of:

    A. Unbonded post-tensioning only.

    B. Post-tensioning and external dissipaters.

    C. Post-tensioning, external dissipaters, and gravity.

5. Investigating the performance of optimized solutions for ABC Low Damage bent with energy dissipation coming from:

    A. Mini UFP Dissipater (MUD) which was developed in Chapter 4.

    B. Grooved Dissipater (GD) which was tested in Chapter 4.

    C. Combination of MUD and GD.

6. Using the observations and results from the experimental testing in Chapter 3 and Chapter 5, presenting qualitative and quantitative comparisons between ABC High Damage and ABC Low Damage.

5.2. Development and Construction of ABC Low Damage Bent

A half-scale multi-column Low Damage Bent (LDB) with almost identical dimensions to High Damage Bent (HDB) specimen was developed for the experimental testing. A general schematic of LDB is illustrated in Figure 5.2.

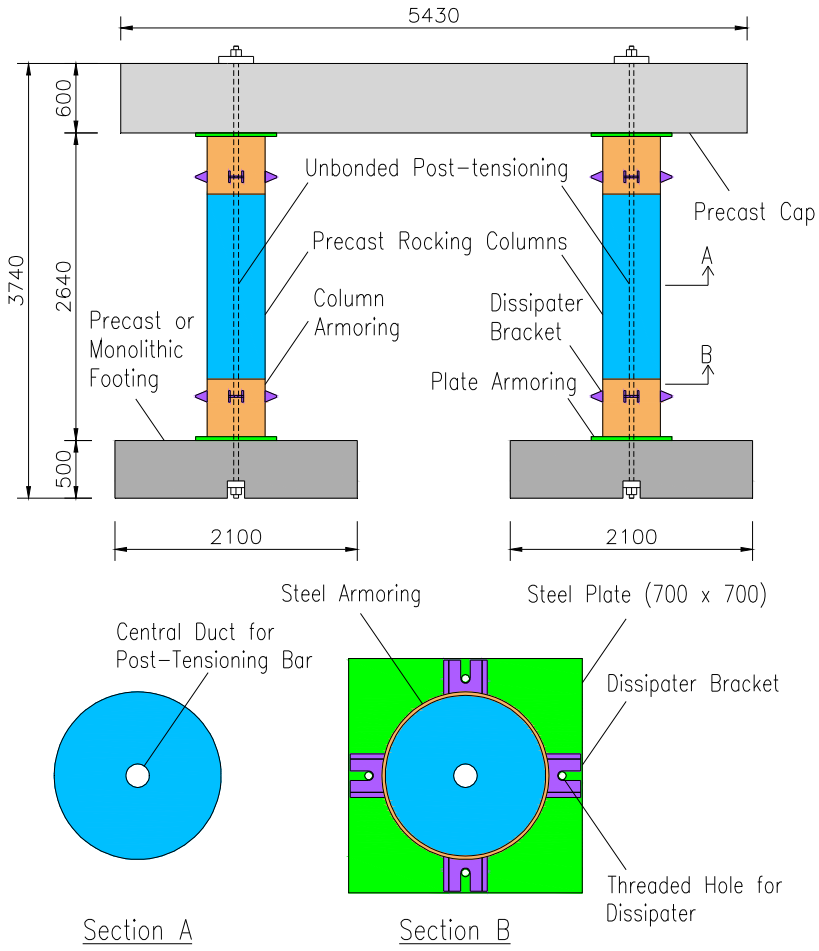

Figure 5.2. Schematic of Low Damage Bent (LDB)

As shown in Figure 5.2, the four plastic hinges in HDB have been replaced with DCR connections. In LDB, armoring of the columns and rocking interfaces are also incorporated. A central duct is provided for each column which accommodates the unbonded post-tensioning (Macalloy) bar. Dissipater brackets are welded around the face of the column armoring to provide anchoring points for the mini plug and play dissipaters. Threaded holes are left at the base armoring plate where the other end of the dissipaters will be wound and secured.

HDB was developed and tested as a benchmark for comparison of the performance against LDB. Therefore, the prototype structure, dimensions, seismic design parameters,

and loading protocol for LDB were completely identical to what discussed for HDB in Section 3.3 of Chapter 3. There was some slight difference in testing arrangement details, instrumentation and data acquisition, and material characterization in testing of LDB which are discussed in the following sections.

5.2.1 Testing Arrangement

Test setup for LDB is illustrated in Figure 5.3a. The testing arrangement was similar to that used for HDB. However, in LDB there was addition of post-tensioning anchor, load cell, and hydraulic jack on top of each column (Figure 5.3b).

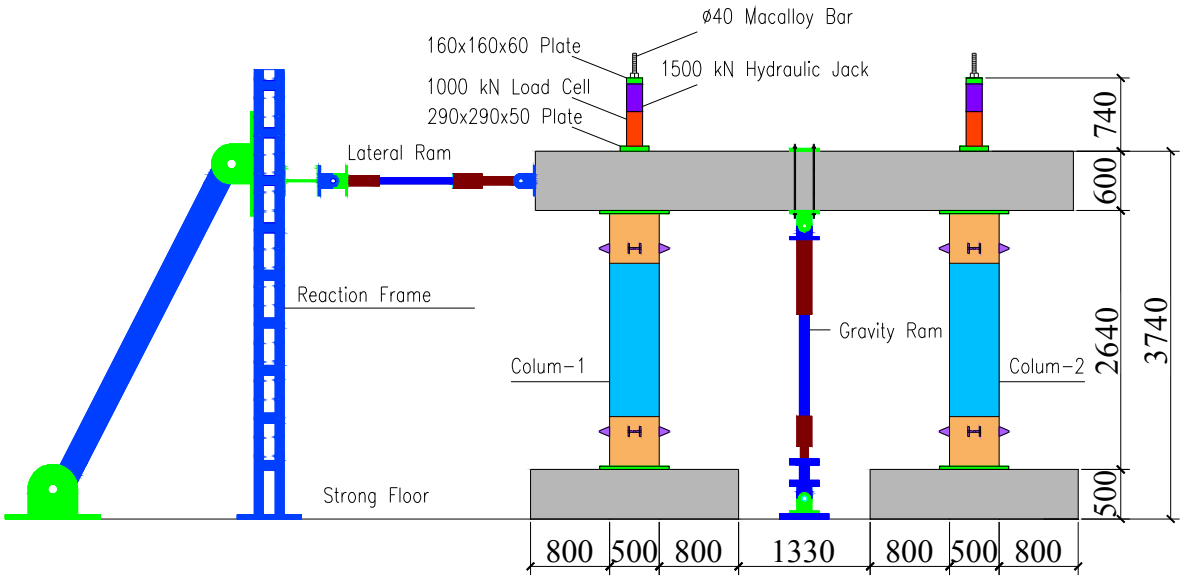

(a) Elevation view of testing arrangement

(b) Macalloy bar anchor

(c) LDB testing arrangement

Figure 5.3. LDB testing setup

5.2.1.1 Data Acquisition System

The data acquisition system was similar to that used for HDB and explained in Section 3.3 of Chapter 3. For a typical column in LDB, the post-tensioning force of the Macalloy bar was measured using a 1000 kN load cell which was mounted on top of the column and along the post-tensioning load path. The load cell was recording the post-tensioning force at each increment of lateral displacement throughout testing. For initial post-tensioning of the Macalloy bar, a hydraulic jack with a capacity of 1500 kN was placed on top of the load cell. The hydraulic jack was connected to the pump where the pressure was regulated to desirable initial post-tensioning force.

The instrumentation of the bent was similar to HDB. However, for LDB the arrangement and number of potentiometers (pots) were slightly modified. For a typical DCR connection in the bent, two pots were positioned at each dissipater location (Figure 5.4c). The pots measured displacement (gap opening) of the rocking connection throughout testing. The results from these pots were used to calculate the neutral axis depth of the section at the rocking connection.

Sufficient quantity of pots around the column and at the critical locations such as where the column armoring discontinues were also installed. This was expected to measure any slipping of the armoring shoe during rocking of the column. Spring pots were installed around the base plate armoring. This aimed to measure any inelastic deformation (buckling) in the plate when the dissipaters are stretched. This was important as one end of the dissipaters was wound to the base plate at each DCR connection.

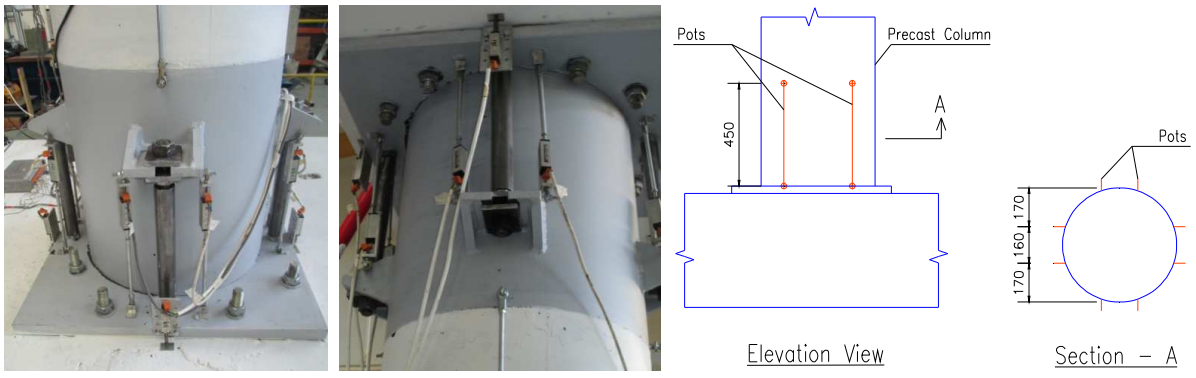

(a) Column to footing DCR (b) Column to cap beam DCR (c) Typical instrumentation

Figure 5.4. Typical arrangement of pots at the DCR connections in LDB

5.2.2 Material Properties

The footings from HDS1 and HDS2 and precast cap beam from HDB were modified and re-used in testing of LDB. Therefore, refer to material properties reported in Section 3.2 and Section 3.3 of Chapter 3 for these elements. For LDB, two rocking columns had to be constructed. There was also fabrication of armoring and external dissipaters. A summary of the material properties for each component is presented as follows.

5.2.2.1 Reinforcing Bar Tension Strength

The reinforcement grade for the rocking columns was specified as Grade 500E (seismic) Reid bars in accordance with AS/NZS 4671 (NZS, 2001). The Reid bar mechanical properties were identical to those presented in Table 3.3 of Section 3.2.3.2 in Chapter 3. The transverse reinforcement (stirrups) included plain bars with similar yield strength as Reid bars ($f_y = 516\ MPa$).

5.2.2.2 Concrete Compressive Strength

The specified minimum concrete compressive strength for the rocking columns of LDB was 40 MPa at 28 days. The average compressive strength of the concrete during testing day was 42.5 MPa.

5.2.2.3 High-Strength Mortar Compressive Strength

High-strength Mortar was used only for casting of new internal shear keys in the existing footings and cap beam. The mortar type used was Sika Mono Top with specified minimum compressive strength of 40 MPa at 28 days. The average compressive strength of the mortar on the testing day was 45 MPa.

5.2.2.4 Armoring Components

The armoring included steel shoe at each end of the rocking column, steel plate at the rocking interface, four brackets for the dissipaters around the steel shoe, and external shear keys. All armoring work was Grade 300 Mild Steel ($f_y = 300\ MPa$).

5.2.2.5 External Dissipaters

Material properties for GD and MUD were similar to those explained in Chapter 4. The components for MUD (UFPs, internal cassette, end washers, and external sleeve) were

made of mild steel with a minimum yield strength of 300 MPa. For GD, the grooved bar and tube had a yield strength of 350 MPa. All other components of the dissipater such as end nuts, bolts, and threaded ends, were made of high-strength steel with a minimum yield strength of 600 MPa.

5.2.2.6 Unbonded Post-Tensioned Bar

The unbonded post-tensioned Macalloy bar inside each rocking column had identical mechanical properties to that explained in Table 3.6 of Section 3.2.3.5 in Chapter 3. The bar was 40 mm in nominal diameter with minimum yield and tensile strength of 835 MPa and 1030 MPa, respectively.

5.2.3 Detailing Considerations and Design

The rocking column had circular section (500 mm in diameter). The reinforcing details of the column were similar to that for HDB, as discussed in Section of 3.3.4 of Chapter 3. Each column consisted of 8-YD16 straight longitudinal rebars. The transverse reinforcement included YD10 hoops, spaced at 75 mm near the ends and spaced at 150 mm away from the ends. Each end of the column had a circular recess to accommodate the circular shear key from the other precast element. The recess was 210 mm in diameter and 120 mm deep. This allowed for a 20 mm tolerance in diameter and depth of the recess during assembly of the bent. A central duct (70 mm in diameter) was left in each column to house the Macalloy post-tensioned bar. The duct was made of corrugated galvanized steel. Figure 5.5a shows reinforcing detailing of the column.

The armoring detail is also shown in Figure 5.5a. The armoring was designed as a steel shoe which could be placed inside the formwork before pouring the column. There were 6 high-strength studs, each 70 mm long with 50 kN tension capacity, welded around the inside face of the shell. The studs were connecting the armoring shoes to the concrete column core. The dissipater brackets (Figure 5.5b) can be welded around the steel shell upon the removal of the column from the formwork or during the on-site assembly.

When designing the number of studs, there would be some cohesion and friction between the surface of the confined concrete and the inner face of the steel shell. However, for a conservative estimate this bond was neglected in this study. The studs

were designed to be the only elements which would transfer the tensile force of the dissipater from the steel shoe to the longitudinal rebars of the column.

The armoring shoe consisted of a steel shell with welded ring-shaped base plate (12 mm thick). The initial thickness of the shell was calculated based on the procedure presented in Section 3.2.4.1 of Chapter 3 in accordance with Mander et al. (1988). Another alternative can be using Finite Element Methodology or an elastic stress analysis of the concentrated forces on the shell. The minimum confinement ratio was targeted to be 1.3 in accordance with Priestley et al. (2007) which gives $f'_l = 2\ MP$. The confinement effectiveness coefficient (k_e) can be calculated from Equation 5.1.

$$k_e = \frac{(1 - \frac{s'}{2d_s})^2}{1 - \rho_{cc}} \tag{5.1}$$

Where,

s' = Height of the shell (500 mm)

d_s = Diameter of confined concrete (approximately 500 mm)

ρ_{cc} = Ratio of the area of longitudinal reinforcement to the area of core section (0.016384)

From Equation 5.1, k_e was calculated to be 0.254 which gives $f_l = 7.87\ MPa$. Using Equation 5.2, the ratio of the volume of armoring confining steel to the volume of confined concrete core (ρ_s) was calculated to be 0.0524.

$$f_l = \frac{1}{2}\,\rho_s\, f_{yh} \tag{5.2}$$

Where in Equation 5.2, f_{yh} is the yield strength of the armoring (300 MPa).

The volume of confined concrete (ρ_{con}) was simply calculated considering a cylindrical end of the column which was 500 mm in both height and diameter. Given the height of the armoring confining steel as 500 mm, the required confining steel (shell) sectional area can be calculated to be 10288.7 mm^2. Since the shell section is in the shape of a ring with outer diameter of 500 mm, the thickness of the shell was computed to be 6.7 mm.

Since the dissipater brackets will be welded to the face of the shell later on, and hence the shell would have to be thick enough to not deform under the maximum capacity of the dissipater (100 kN), the computed thickness was increased to 10 mm. Considering a 100 mm wide and 10 mm thick longitudinal strip of the shell resisting against the tensile force of 100 kN, the safety factor in this case was 3 at the yield point of the shell strip, and hence the thickness was sufficient to transfer the dissipater load without any inelastic deformation occurring in the shell.

Another reason behind using thicker steel shell was the fact that when the dissipater brackets are welded around the shell, a very high level of heat could be expected on the face of the confined concrete. For a thin shell, this might have very detrimental effects in the concrete such as cracking and fracturing that would affect the performance and efficiency of the inside studs which eventually may contribute to a loosening effects in the steel shoe under tensile forces. A thicker steel shell is thought to reduce the amount of heat transferred to the face of the encased concrete which in return would prevent from any undesirable damage. Another reason for using thicker steel shell could be durability of armoring, especially if the bridge is located in a corrosive environment, (Albrecht and Hall, 2003).

The height of the shell was selected to be equal to the plastic hinge length of a ductile monolithic column (equal to column diameter) in accordance with NZS 3101 (NZS, 2006). A similar plastic hinge length (500 mm) was also observed in testing of member socket connection for the emulative cast-in-place solution (ABC High Damage) as explained in Chapter 3. Therefore, the height of the shell was chosen to be 500 mm.

Each dissipater bracket was made of two triangular shaped arm plates with a washer plate in between (10 mm thick), as shown in Figure 5.5b. The side of the washer plate which was facing the shell was cut in a curved shape to provide simple welding of the bracket against the round surface of the shell.

The armoring base plate at each rocking interface was 700x700x32 mm in dimensions, as shown in Figure 5.5a. Four threaded holes, one on each principle axis direction of the plate, were made in the plate to provide anchoring points for the dissipaters.

The plate was designed to remain elastic during testing. This was done by considering a simple four point bending model where there are 8 hold-down bolts around the plate (two on each side) which provide supports against the tensile concentrated load of the dissipaters. The hold-down bolts for the plate were all high-strength threaded rods (24 mm in diameter) which were grouted using Hilti HIT-RE 500 epoxy to a depth of at least 200 mm inside the precast element (cap beam or footing) in accordance with the epoxy instruction for use manual. A full set of technical drawings for LDB can be found in Section C.1 of Appendix C.

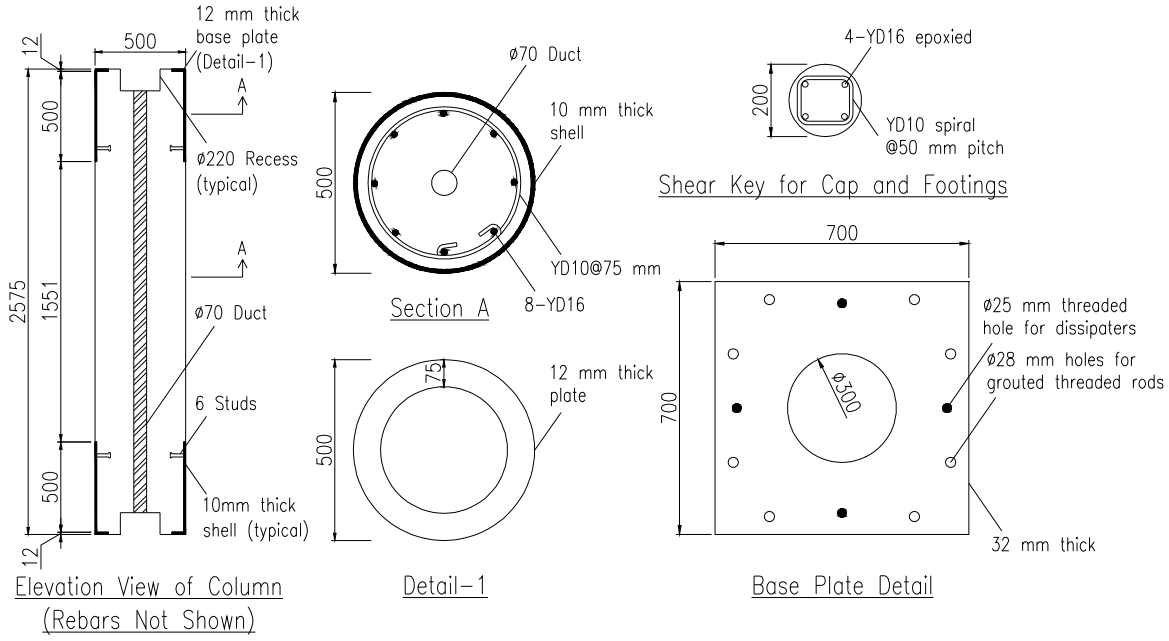

(a) Rocking column and armoring details

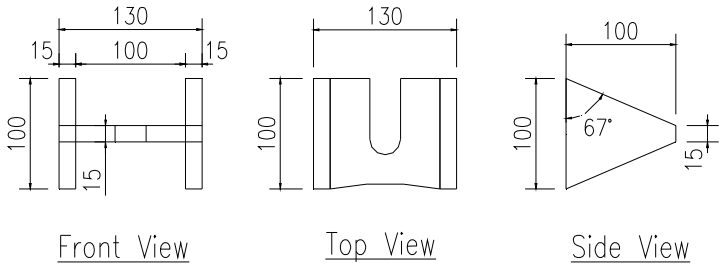

(b) Dissipater bracket details

Figure 5.5. Reinforcing and armoring details for LDB

The internal circular shear key at each DCR connection was designed to transfer the shear force across the rocking interface. The shear key was designed using the principals of shear friction according to NZS 3101 (NZS, 2006). The shear key was 200 mm in diameter and 100 mm in height (Figure 5.5a). 4-YD16 rebars was grouted inside

the precast element (cap beam or footing) using high-strength epoxy to a depth of 200 mm. YD10 spiral stirrup with 50 mm pitch was provided around the grouted rebars. Sika Mono Top high strength mortar was used to pour the shear key.

It is important to note that if external steel shear key is used (such as that discussed in Section 5.4 of this Chapter), then it would eliminate the need for any concrete internal shear key in the cap beam or footing, as well as any recess at the end of the rocking column to house it.

A total of 24 Grooved Dissipaters (GDs) and 8 Mini UFP Dissipaters (MUD) were designed with similar capacity and dimensions as presented for the tested prototypes of GD and MUD in Chapter 4. The only difference was that the stroke limit of MUDs was slightly increased from 20 mm to 25 mm, in order to accommodate larger displacement at the rocking connections. The overall UFPs capacity and dimensions remained the same (Figure 5.6).

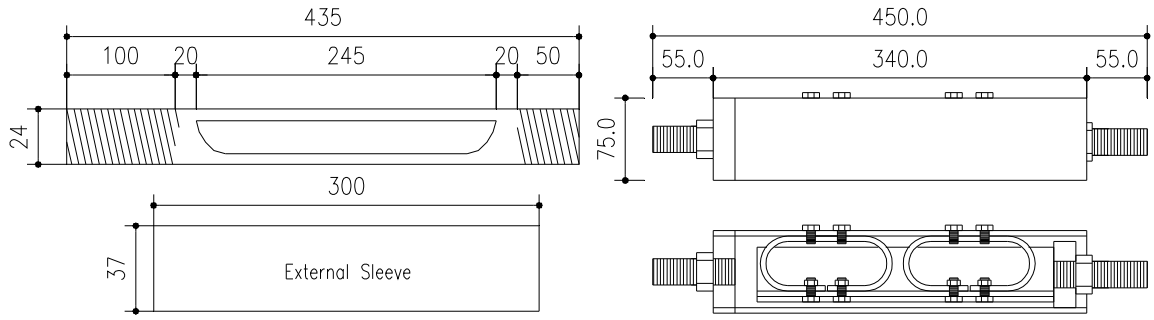

(a) Grooved Dissipater **(b) Mini UFP Dissipater**

Figure 5.6. Dissipater dimensions for LDB

The reinforcing details of the footings and cap beam were previously discussed and shown in Chapter 3. A full set of technical drawings for each components can be found in Section B.1 of Appendix B and Section C.1 of Appendix C, respectively.

5.2.4 Construction and Assembly

For assembling a typical column armoring shoe, the steel shell and its base plate (Figure 5.7a) had to be aligned first, and then fully welded at a workshop (Figure 5.7c). The studs (Figure 5.7b) were also welded to the inner face of the shell to complete the shoe assembly (Figure 5.7d).

(a) Shells and base plates prior to assembly

(b) 50 kN capacity studs with round bases

(c) Assembled and fully welded shoe (armoring)

(d) Welded studs around the steel shoe

Figure 5.7. Assembly and welding of shell armoring for a typical column in LDB

The columns were constructed at a prefabrication facility. After cleaning the mould, in the first step, a plywood template and a cylindrical recess which was cut from a block of foam, were bolted to the mould. In the second step, the first armoring shoe was placed in the mould (Figure 5.8a). The column cage was then inserted inside the shoe. This would require some adjustment of the end stirrups due to presence of studs which may create obstacle for the cage to go easily inside the shoe. Therefore, it would be necessary to leave the end stirrups loose and tie them after the cage is inside the shoe (Figure 5.8b). For a real life ABC Low Damage column, the addition of stirrups in the plastic

hinge zone may not be necessary, as the outer steel shoe with sufficient thickness would provide both shear resistance and confinement for the section.

In the third step, the second shoe is positioned on the other end of the cage using similar technique to that of step two (Figure 5.8c). In the fourth step, identical foam block for a recess similar to step one is placed and bolted in the mould. In the final step, the mould is closed (Figure 5.8d) and the column is transported to the pouring platform where it is poured vertically.

(a) First armoring shoe placed inside mould

(b) Column cage is placed inside the shoe

(c) Second end shoe is placed and cage is aligned

(d) Top recess is made and mould is closed

Figure 5.8. Construction photos for rocking columns in LDB

The concrete pouring process for the columns was similar to what explained for construction of ABC High Damage columns in Chapter 3. After pouring the columns, it would be advantageous to insert a couple of lifters on top of each column (Figure 5.9b) before the concrete start curing. The lifters would be very useful during assembly of the columns as they would facilitate the vertical lifting of the elements while they are being

positioned and aligned. The column lifter would be cut off following the assembly to provide a smooth rocking interface between the column top and the cap beam. Figure 5.9a shows completed rocking columns for LDB.

(a) Rocking columns with armoring at the ends (b) Typical end section of column, lifters visible

Figure 5.9. Completed rocking columns in LDB

The footings from HDS1 and HDS2 were re-used for LDB with some modifications. For a typical modified footing, the starter bars from the previous test were cut off and the surface of the footing was cleared from loose concrete. New circular shear key was cast at the center of the footing. The longitudinal rebars for the shear key were grouted using epoxy. After placement of the spiral transverse reinforcement for the shear key, a piece of plastic pipe was used to provide formwork before the mortar is poured.

Using a plywood template of the base plate shown in Figure 5.4, 8 holes (28 mm in diameter) were drilled in the footing to house the hold-down threaded rods. Ferro scanner (Hilti Group, 2015) was used to detect the location of the rebars inside the footing, and thus avoid potential risk of drilling over the rebars. The drilled holes were at least 200 mm in depth and were cleaned out of debris and dust in accordance with Hilti HIT-RE 500 (Hilti Group, 2015) instruction manual before pouring epoxy. Eight 24 mm diameter threaded rods with sufficient length were grouted inside the holes using Hilti HIT-RE 500 epoxy.

Once the epoxy cured, the plywood was removed and a layer of high strength Sika Mono Top mortar (Sika Group, 2015) was poured to fill any voids and provide a smooth surface at the bottom of the plate. While the mortar was still fresh, the 32 mm plate was lowered on the footing and guided on top of the grouted rods. Once the plate is lowered

on the mortar bed, it would squeeze out any extra mortar. The plate is then aligned using a hand level while the mortar is still fresh (Figure 5.10a). In order to prevent from the flow of fresh mortar into the threaded holes of the plate, temporary bolts were wound in the holes to avoid this issue, as shown in Figure 5.10b. This was very important as the threaded holes were intended for fixing of the dissipaters later, and hence removing cured mortar from the threaded holes would carry the risk of damaging the threads in the dissipater holes. Once the mortar was cured, a nut was wound and fastened on top of each of the grouted rod to fully secure the plate.

(a) Placing the plate on top of the footing **(b) Mortar under footing armoring set to cure**

Figure 5.10. Photos from armoring of footings in LDB

The cap beam from HDB was re-used for LDB after some modifications. Armoring and new shear keys were provided at the location of DCR connections in the cap beam. The cap beam was flipped upside down and the shear keys from the previous test (HDB) were cleared. The procedure for casting new shear keys and grouting of the threaded rods were similar to what discussed for the armoring of footing in the previous paragraph. However, the only difference was that epoxy grouted bed was used for the steel base plate instead of mortar (Figure 5.11a).

Figure 5.12 presents completed armored footings and cap beam for LDB. It is important to mention that in a real life ABC Low Damage substructure system, the armoring plates can be left inside the precast element before pouring the concrete. This can be simply done before the cap beam is cast at the prefabrication yard or the footing is poured on-site. A typical base plate in this case would have to incorporate welded or bolted hairpins to provide an appropriate load path to transfer tensile forces from the plate to

the inside cage of the precast element. One of the advantages for leaving the armoring plate inside the precast element is the extra protection of the 5 faces of the plate for a better durability. At the same time, leaving the base plates inside the precast element can provide a more architecturally attractive DCR connection with base plate not being visible at all.

(a) Epoxy grout bed for the cap beam armoring **(b) Epoxy under cap beam armoring set to cure**

Figure 5.11. Photos from armoring of cap beam in LDB

(a) Armored footings **(b) Armored cap beam**

Figure 5.12. Armored footings and cap beam with new shear keys for LDB

The dissipaters (GD and MUD) were fabricated using solid steel bar, plate, and recycled square section tube. Given the simple fabrication process, all dissipaters were made in the lab using some basic tools and machineries. Figure 5.13 and Figure 5.14 show photos of the fabricated GDs and MUDs, respectively.

(a) Grooved bars **(b) Assembled dissipaters**

Figure 5.13. Photos from fabrication of Grooved Dissipaters (GDs)

(a) Rolled double UFPs **(b) UFPs bolted to the cassettes**

(c) Cassettes and external sleeves **(d) Assembled MUDs**

Figure 5.14. Photos from fabrication of Mini UFP Dissipaters (MUDs)

The assembly process for LDB was similar to that of HDB which was discussed in Section 3.3.4 of Chapter 3. However, for LDB the connection between the precast elements were dry type (DCR). Therefore, no grouting work was needed. In the first

step, one of the precast footing was lifted up to insert the Macalloy bar mechanical anchor (Figure 5.15a) inside the recess under the footing (Figure 5.15b). The mechanical anchor consisted of a thick washer plate and a high strength Macalloy nut. Originally, the washer plate and nut were not welded together. The elements were tack welded to make sure they remain vertically aligned during the assembly process. Four bolts were welded to the corners of the plate to prevent from tilting of the anchoring assembly while the footing was being lowered down (Figure 5.15c).

In a real life bridge, it would be possible to leave the mechanical anchor inside the footing before pouring the concrete. A plastic or steel central duct would have to be used to maintain the alignment of the anchor, as well as to house the portion of the post-tensioned bar at the center of the footing.

In the second step, four dissipaters were wound to the threaded holes of the footing armoring plate. Using the lifters provided at the top of the column, the precast element was lifted up and lowered on the footing (Figure 5.15d and Figure 5.15e). The Macalloy bar can be left inside the column, and thus when lowered on the footing, it can be guided into the central duct of the footing and wound to the anchoring assembly underneath the footing. When lowering the column, it was important to align the column recess on to the footing shear key. Once the column is all aligned, the dissipater brackets were fully welded around the armoring shell of the column (Figure 5.15f and Figure 5.15g). Similar procedure was used for assembly of the second column (Figure 5.15h).

In the third step, the lifters on top of the column were cut off (Figure 5.16a) and the cap beam was rotated (Figure 5.16b). Given the slightly higher weight of the cap beam due to armoring and filled grouted ducts from the previous testing (HDB), the lab crane was not able to lift it up. A mobile crane with higher capacity had to be used to lower the cap beam on the columns (Figure 5.16c). Each Macalloy bar was guided into its corresponding duct in the cap beam (Figure 5.16d). It was also important to align each cap beam shear key into the column recess (Figure 5.16e). Once the cap beam rested on the columns, temporary dissipaters and threaded rods were wound to each base plate. The dissipater brackets were then installed and welded for each column (Figure 5.16f).

The methodology used here for welding of the dissipater brackets would eliminate any chances of misalignment of the dissipater inside its bracket. However, in a real life

bridge, this means that on-site welding may be required. An alternative to this methodology can be welding of the brackets to the armoring shell at the prefabrication yard. This means that on-site welding can be avoided in this case. This would require using bigger bracket washer that could accommodate construction tolerances during installation of the dissipaters. Additional washers on the top and bottom of the bracket can be provided to restrain any slacking of the dissipater, as shown in Figure 5.15g.

(a) Macalloy bar anchor **(b) Lifting up the footing** **(c) Sliding anchor under footing**

(d) Column lifted **(e) Aligning the column** **(f) Installing and welding the brackets**

(g) Dissipater brackets fully welded **(h) Assembled columns**

Figure 5.15. Photos from assembly of the columns in LDB

(a) Column lifters were cut-off **(b) Rotating the cap beam** **(c) Lowering cap beam**

(d) Macalloy bar guided through (e) Aligning cap beam shear key (f) Dissipater brackets welded

Figure 5.16. Photos from assembly of the cap beam in LDB

In the last step, for each column, the Macalloy bar accessories on top of the cap beam were positioned (Figure 5.17a). The completed and painted LDB is shown in Figure 5.17b. Close-up view of the DCR connections is shown in Figure 5.17c and Figure 5.17d.

The external plug and play dissipater's fixings are shown in Figure 5.17d. A small gap (6 mm) is left between the tube and the dissipater to allow for compression deformation (Figure 5.17e), and hence to prevent from vertical loading of the tube during rocking. This is applicable for DCR connection with GDs only. There is no need of placing this gap for DCR connection with MUDs.

The arrangement of dissipaters shown in Figure 5.17 was used during the first part of testing on ABC Low Damage with internal shear keys as will be discussed in Section 5.3 of this Chapter. In the first part of testing, the low damage bent was tested with internal concrete shear keys. The internal shear key detailing is shown in Figure 5.17i. The reinforcing details of the shear key were previously shown in Figure 5.5.a.

(a) Macalloy bar anchors, load cells, and jacks

(b) Assembled Low Damage Bent (LDB)

(d) Column to footing DCR connection

(e) Column to cap beam DCR connection

(f) Typical dissipater fixing

(g) Top fixing to the bracket

(h) Bottom fixing to armoring plate

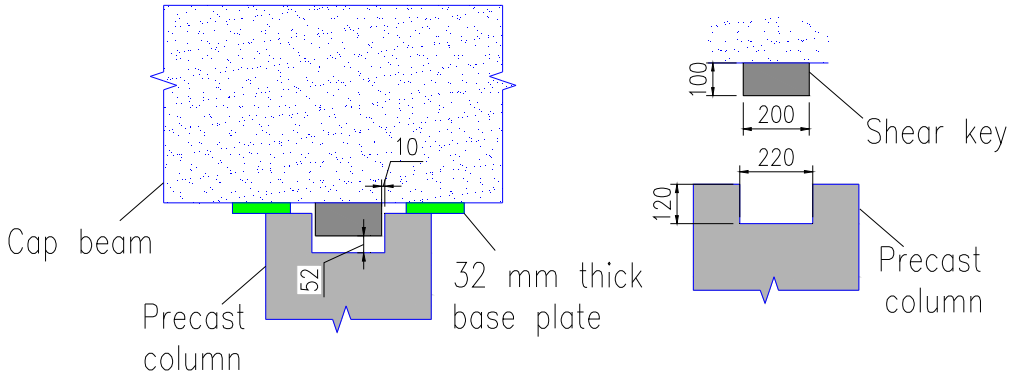

(i) Typical details of an internal shear key

Figure 5.17. Assembled LDB ready for testing

5.3 Testing of ABC Low Damage Bent with Internal Shear Keys

In the first part of testing, ABC Low Damage Bent (LDB) was tested with internal shear keys (Figure 5.17). The first three tests were carried out with unbonded post-tensioning only without any contribution from the dissipaters or gravity (apart from the self weight of the bent). Three levels of Initial Post-Tensioning (IPT) were considered. Each level of IPT was corresponding to 15%, 30%, and 45% of the yield strength of the Macalloy bar, respectively. The bent was pushed and pulled under the quasi-static cyclic loading with increasing drifts up to 2.2% drift ratio(ULS drift ratio for HDB, refer to Section 3.3 in Chapter 3).

In the second part of testing, LDB was tested with a combination of post-tensioning, grooved dissipaters, and gravity. The bent was designed to match the capacity of HDB at ULS drift ratio (base shear of 305 kN). The design of the Dissipative Controlled Rocking (DCR) connections for LDB was based on the procedure outlined in the PRESSS Design Handbook (Pampanin et al., 2010). Each DCR connection incorporated four grooved dissipaters which were identical to the dissipaters tested in Section 4.3.3 of Chapter 4. The IPT was calculated to be 5% to match the base shear force of HDB (305 kN) at 2.2% drift ratio. Similarly, the gravity (superstructure weight) was simulated through a vertical ram. The gravity was kept at 390 kN with approximately ±3% tolerance throughout testing. The resultant re-centering ratio at the yield and ULS levels was calculated to be 1.4 and 1.7, respectively.

Table 5.1 presents a summary of tests on LDB with internal shear keys. Observations from testing and experimental results for each test are presented in the next sections.

Table 5.1. Description of tests on LDB with internal shear keys

Test No	Part	Testing Type	Test Name	IPT per Column (%)	Axial Load (kN)
1	**Part - I**	Post-Tensioning Only	IPT15	15	-
2			IPT30	30	-
3			IPT45	45	-
4	**Part - II**	Post-Tensioning with Grooved Dissipaters and Axial Loads	IPT5+GD+AX	5	390

5.3.1 Part-I: LDB with Post-Tensioning Only

For testing of LDB with post-tensioning only, the vertical ram was released and the nuts on top of the dissipaters were removed to allow free sliding of the dissipaters inside their brackets during rocking. Each Macalloy bar was pre-loaded to a given level of initial post-tensioning force.

From a theoretical aspect, since there is not any contribution from the dissipaters at a connection, the self-centering ratio is equal to infinity for the connection and the overall bent. In this part of testing, three levels of increasing initial post-tensioning were tested. A higher initial post-tensioning force for a DCR connection would mean an increase in the elastic stiffness, delay in gap opening, and higher base shear force at the ULS performance level.

Using the methodology from the PRESSS Design Handbook, the capacity of the bent was calculated under each level of initial post-tensioning at the ULS performance level. It is important to note that when designing the rocking section, the contra flexure point at each column was assumed to be at the mid height of the column. This means that for each DCR connection, the column could be considered as a short cantilever column with half of the actual column height. Section D.1 through D.3 in Appendix D provide summary of the design spreadsheets for LDB with post-tensioning only.

Observations from testing and experimental results for each test at a specified level of post-tensioning are discussed as follows.

5.3.1.1LDB with Initial Post-Tensioning = 15% (IPT15)

Each Macalloy bar was post-tensioned to 165 kN which corresponded to 15% of the Macalloy bar yield strength (1100 kN).

Gap opening started during the 0.35% drift ratio. At the same time, there was evidence of sliding at all four DCR connections during cycles of this drift ratio. Gap opening and sliding continued to increase during cycles of larger drifts. During 2.2% drift ratio (ULS), the largest gap opening was measured to be 15 mm (Figure 5.18).

The residual displacement in the bent was a consequence of the sliding at the DCR connections. It was clear that the post-tensioning force of 165 kN on each column was

not sufficient to produce enough friction in the DCR interfaces to prevent sliding. The sliding occurred at all four rocking joints (Figure 5.19). There was also evidence of some twisting in the columns. It was clear that the internal shear keys did not perform as they were intended during the design process.

As explained earlier, there was approximately 10 mm tolerance gap between the internal shear key and its socket (recess) inside the column. This means that the only restraint against sliding at the DCR connection was the friction force up to 10 mm. In this case, the internal shear key would prevent from excessive sliding (more than 10 mm) as soon as the shear key hits the socket wall. In general, testing observations showed inadequacy of relying on the friction force to prevent sliding under lower level of post-tensioning in DCR connections. Similarly, the shear keys did not restraint the twist in the columns.

For a real life ABC Low Damage bent, if internal shear keys are used, the gap between the shear key and the recess could be filled with a filling material such as synthetic rubber. The filling material would engage the shear key as soon as there is a slide at the DCR connection. However, proper attention has to be paid that use of filling material should not restrain the rocking mechanism of the DCR connection which could damage the shear key. This solution may prevent from the sliding, however, it is not expected to restrain the column from twisting when it starts rocking.

Apart from what discussed above, there was no other damage observed to the precast columns and armoring. Some existing cracks in the cap beam and footings from the previous tests opened up. However, all cracks remained hairline (smaller than 0.4 mm) throughout testing.

(a) 15 mm gap opening at the base connection **(b) 15 mm gap opening at the top connection**

Figure 5.18. Maximum gap opening during 2.2% drift ratio for IPT15

(a) 12 mm sliding at the base connection **(b) 12 mm sliding at the top connection**

Figure 5.19. Sliding at DCR connections at the end of testing (2.2% drift ratio) for IPT15

The force-drift hysteresis for LDB with 15% initial post-tensioning force is plotted in Figure 5.20. In this Figure, the positive horizontal and vertical axes represent the response of the bent during the pull stage of the loading. The bent showed an asymmetrical behavior during testing. The ULS base shear force was higher than the predicted 207 kN during the pull stage of the loading, but lower than that in during the push. The reason behind this was thought to be the residual drift (0.7% drift ratio) during the push stage of the loading which was caused by sliding of the columns. Figure 5.20 suggests that the bent could have reached the predicted 207 kN base shear if it was pushed further than 2.2% drift ratio to drift level of 2.9%. There was also some twisting of the columns which may have contributed to residual drift.

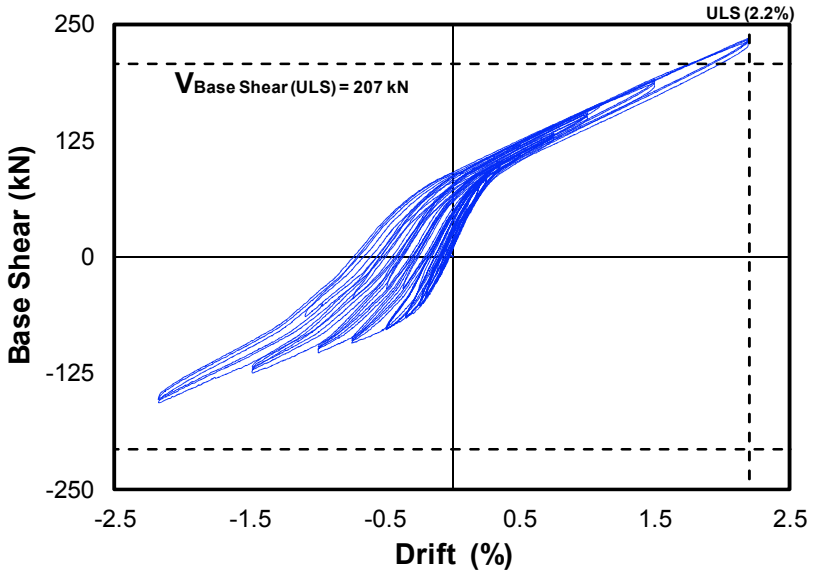

Figure 5.20. LDB force-drift hysteresis for IPT15

From Figure 5.20, it is obvious that the bent had more sliding during the push stage of the loading which lowered down the base shear capacity. By the end of testing, there was a residual drift ratio of 0.75% (22 mm) in the bent. This showed the inadequacy of internal shear keys in preventing sliding at the DCR connections which is well correlated with the observed performance during testing.

The post-tensioning force in each Macalloy bar is plotted against the lateral drift in Figure 5.21. The asymmetrical behavior of the post-tensioning bar is obvious. The bar achieved a higher force level during the pull stage of the loading compared to that in the push. Apart from the fact that there were more sliding during the push stage of the loading, another factor which is thought to have mainly caused this asymmetrical behavior is the Macalloy bar shifting inside the central duct during rocking of the bent. The diameter of the central duct (70 mm) was almost twice as big as the diameter of the Macalloy bar (40 mm). As the specimen is pushed and pulled, the lever arm in one of the Macalloy bars increases while it decreases in the other one. This will cause drop of post-tensioning in one column, but results into an increase in the post-tensioning of the second column. Addition of gravity load is expected to improve this behavior and minimize the asymmetrical response of the post-tensioning bars.

By comparing the response of Macalloy bars (Figure 5.21) to force-drift hysteresis plot in Figure 5.20, it is obvious that the bent had more re-centering during the pull stage of the loading. Similarly, the slacking effects in the post-tensioned bars is more noticeable

during the push stage of the loading where the initial post-tensioning force had dropped significantly due to sliding and twisting of the columns.

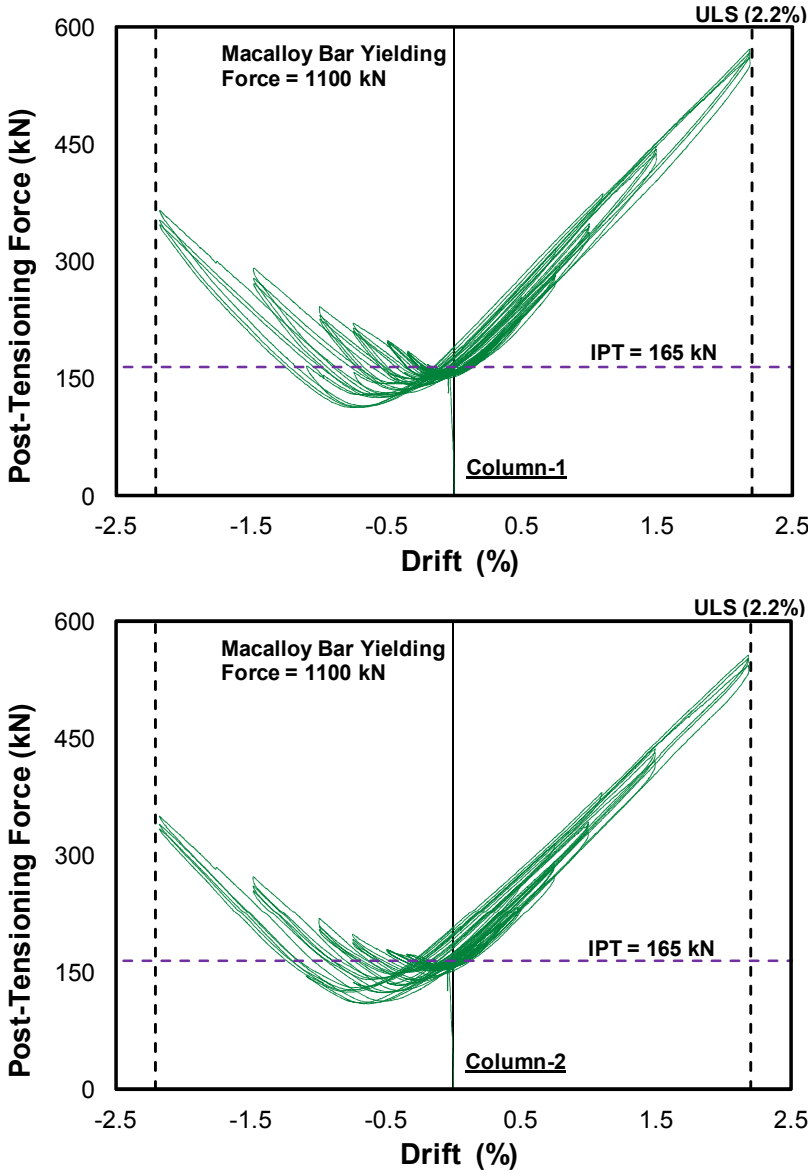

Figure 5.21. Post-tensioning force-drift hysteresis for IPT15

The post-tensioning drop in both columns was comparable. During testing, the maximum drop in the post-tensioning was in the vicinity of 53 kN which corresponded to 32% of the initial post-tensioning force of 165 kN.

5.3.1.2 LDB with Initial Post-Tensioning = 30% (IPT30)

The specimen performed similar to IPT15 which was discussed in the previous section. However, a higher level of post-tensioning force in the Macalloy bars had improved the overall performance of LDB. There was smaller sliding and twisting at the DCR

connections compared to that observed in IPT15. It appeared that a higher post-tensioning force had generated more friction at the DCR connections which in return decreased sliding and twisting of the columns.

During 0.5% drift ratio, gap opening started. During the ULS drift ratio (2.2% drift ratio), the gap opening had increased to 12 mm.

The force-drift hysteresis is plotted in Figure 5.22. The bent still showed an asymmetrical behavior, but not to the extent that was observed in Figure 5.20 for IPT15. There was still some sliding at the DCR connections during the push stage of the loading. There was 0.35% residual drift ratio (10 mm) in the bent following testing.

A higher level of post-tensioning resulted into less sliding of the columns. This is in agreement with conclusions from Cheok et al. (1998) where shear resistance through friction can be increased by using a higher level of post-tensioning in the tendons.

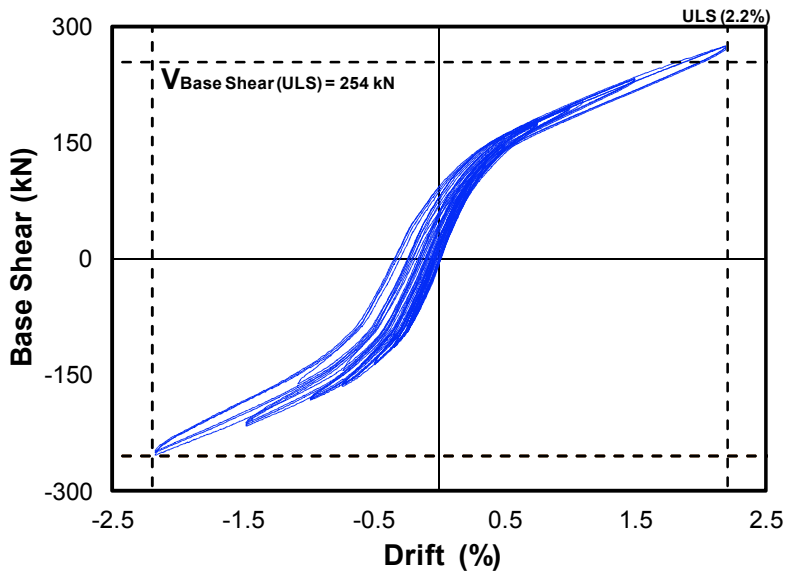

Figure 5.22. LDB force-drift hysteresis for IPT30

Figure 5.23 shows the post-tensioning response for LDB. The asymmetrical behavior of the post-tensioning was considerably improved with higher level of initial post-tensioning force. However, the bars still had some slacking and drop of post-tensioning, specifically during the push stage of the loading. The maximum drop in post-tensioning was approximately 32 kN during testing. This corresponded to just less than 10% of the initial post-tensioning force of 330 kN in each Macalloy bar.

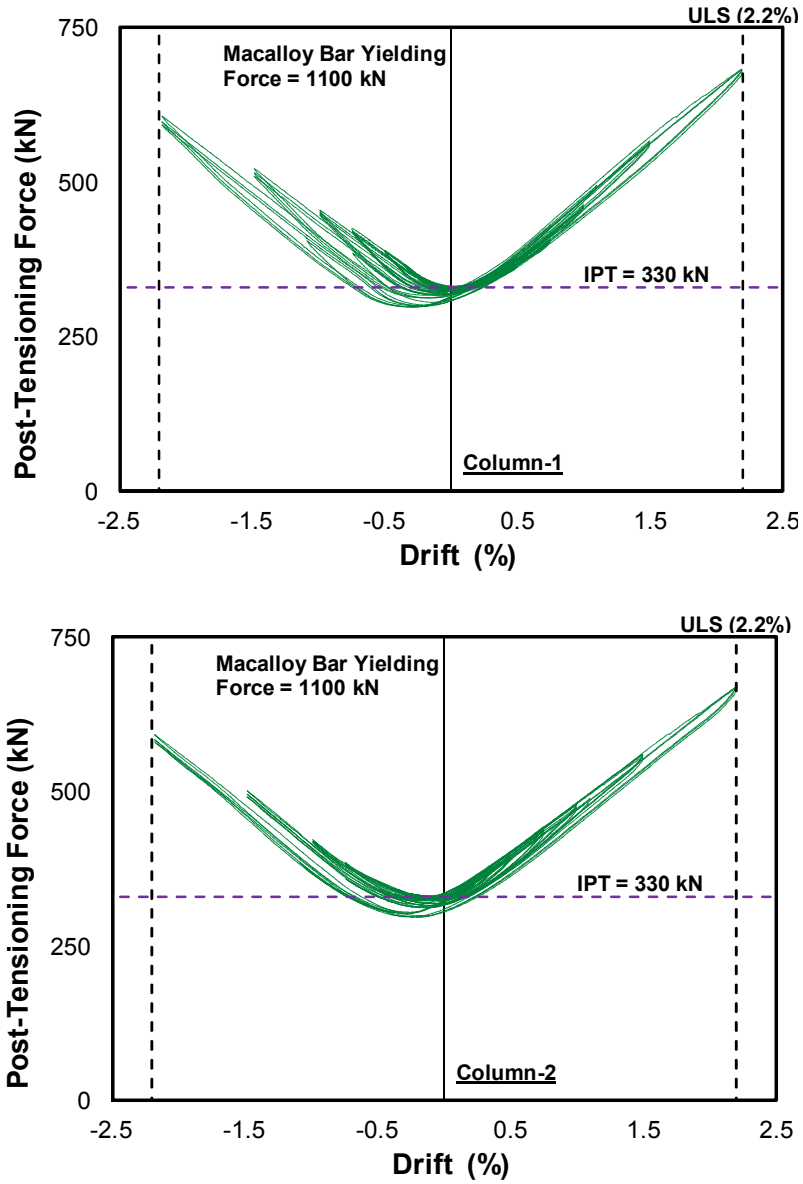

Figure 5.23. Post-tensioning force-drift hysteresis for IPT30

Overall, the force-drift hysteresis for LDB with 30% initial post-tensioning force showed an improved behavior of the bent. However, there was still some sliding at the DCR connections, as well as some asymmetrical behavior in the post-tensioning bars.

5.3.1.3 LDB with Initial Post-Tensioning = 45% (IPT45)

Experimental results from testing of LDB with 45%f_{py} initial post-tensioning showed improved behavior and self-centering of the bent. Gap opening started during the 0.75% drift ratio. At ULS level (2.2% drift ratio), there was 10 mm gap opening.

The force-drift hysteresis is presented in Figure 5.24. The bent had slightly higher capacity compared to its predicted ULS capacity during the 2.2% drift ratio. Following testing, there was less than 5 mm (0.15% drift ratio) residual displacement in the bent.

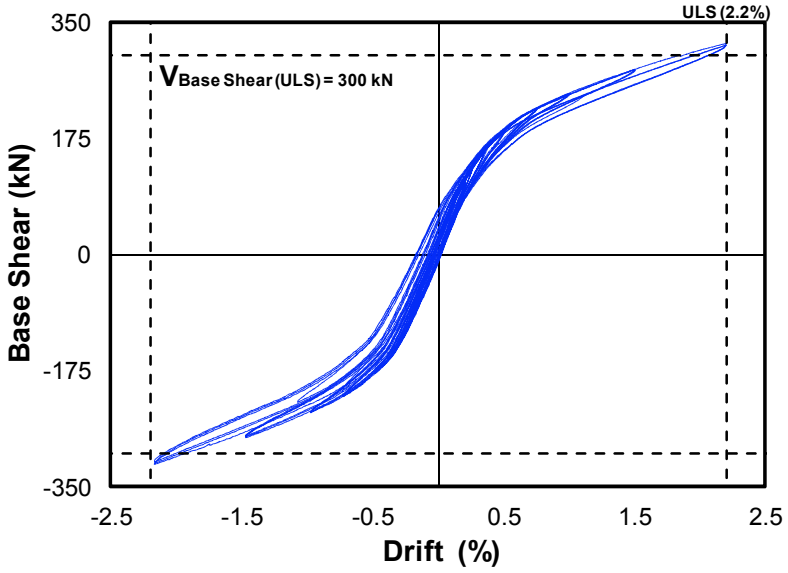

Figure 5.24. LDB force-drift hysteresis for IPT45

The post-tensioning hysteresis plots are presented in Figure 5.25. The asymmetrical behavior of the post-tensioning bars was almost eliminated. The bent showed a fairly symmetrical behavior. The maximum drop in post-tensioning was approximately 47 kN which corresponded to 9.5% of the initial post-tensioning force of 495 kN in each Macalloy bar.

In summary, testing of LDB with post-tensioning showed no damage to the rocking columns. A lower level of initial post-tensioning resulted in significant sliding at the DCR connections. The performance of the bent was improved with a higher level of post-tensioning. The 45%f_{py} for initial post-tensioning in the tendons is normally a typical value used in the design of DCR connections, (Pampanin et al., 2010).

Despite an improved performance, the residual twist in the columns was obvious following the testing (Figure 5.26). It was concluded that using the internal shear key detail developed here, the sliding and twisting of the columns could not be prevented.

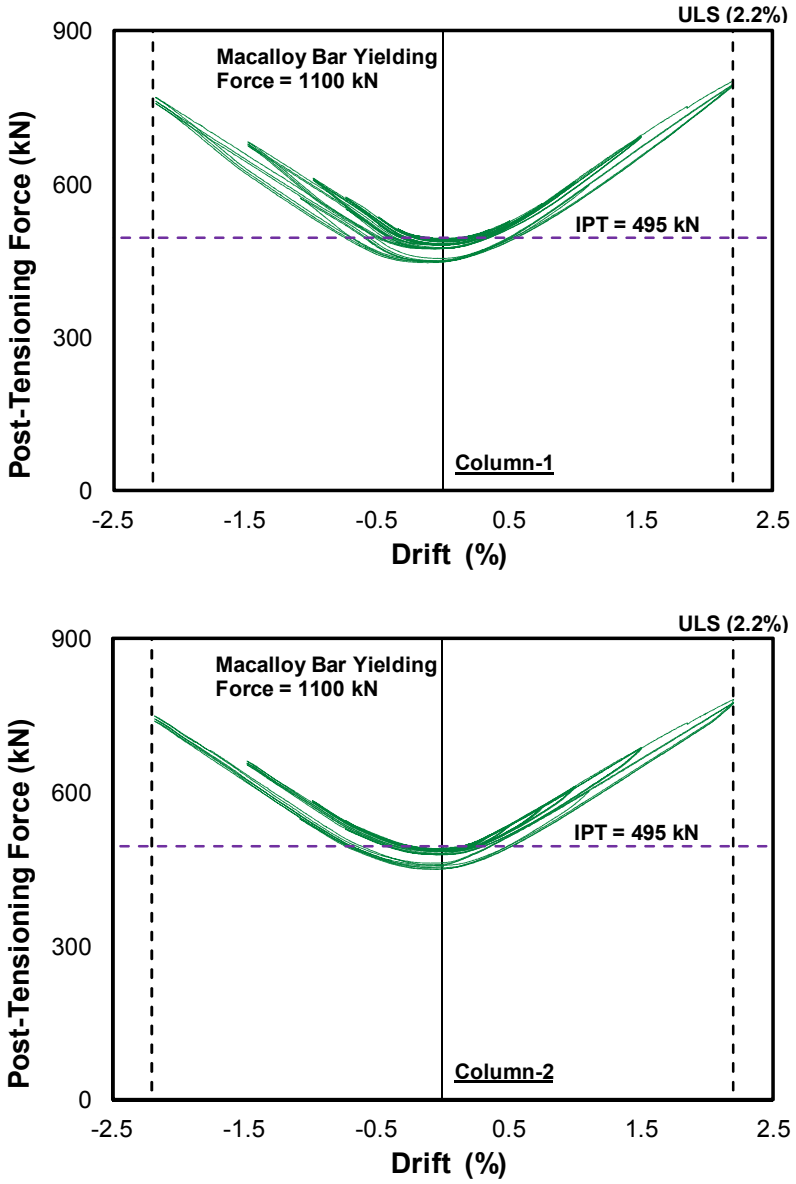

Figure 5.25. Post-tensioning force-drift hysteresis for IPT45

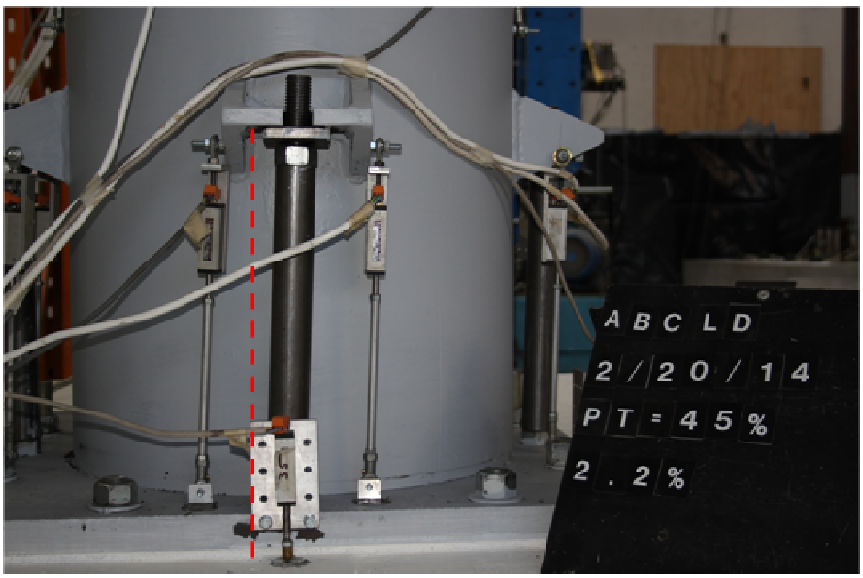

Figure 5.26. Evidence of residual twist in LDB following testing with post-tensioning only

5.3.2 Part-II: LDB with Post-Tensioning, GDs, and Gravity

In this part of testing, grooved dissipaters were connected again by winding a nut down on top of each of them in the dissipater bracket. The vertical ram was also connected which was exerting a concentrated load of 390 kN (superstructure weight) on the bent. The force in the vertical ram was controlled using a manual jogger box which was similar to that in testing of HDB in Chapter 3. The force was kept constant within approximately ±3% tolerance throughout testing.

5.3.2.1 LDB with 5%IPT, Grooved Dissipaters, and Axial Load (IPT5+GD+AX)

The capacity of the bent was calculated to match that of HDB at the ULS level. Using the methodology presented in the PRESSS Design Handbook for designing of DCR connection, the self-centering ratio, and base shear at each performance level were calculated and are summarized in Table 5.2.

There were four grooved dissipaters at each DCR connection which were located on the four principal axes of the column section. The initial post-tensioning force in each Macalloy bar was set to 55 kN which corresponded to 5% of the yield strength in the bar. The lower level of post-tensioning was due to presence of gravity (axial load) on the bent. A higher level of post-tensioning in the tendons was expected to increase the capacity of the bent slightly higher than that of HDB at the ULS level.

Table 5.2. Summary of design parameters for LDB with IPT5+GD+AX

Performance Level	Self-Centering ratio (λ)	Drift (δ)	Base Shear (V_b)
Yielding	1.4	0.53%	182 kN
ULS	1.7	2.2%	350 kN

Observation from testing showed first gap opening at the DCR connection to start during the 0.35% drift ratio. Gap opening continued to increase with further drift ratios. During 2.2% drift ratio (ULS), the gap opening was measured to be 15 mm. The size of gap opening was almost similar in all DCR connections throughout testing. A summary of the measured gap opening at different drift ratios is presented in Table 5.3.

Table 5.3. Summary of the maximum gap opening for IPT5+GD+AX

	Drift Ratios (%)						
	0.35	**0.5**	**1.0**	**1.5**	**1.8**	**2.2**	**2.5**
Column 1 to Footing DCR (mm)	0.5	2	5	8	10	15	15
Column 2 to Footing DCR (mm)	0.5	2	5	9	10	11	15

During cycles of the 1.5% drift ratio, two hairline flexural cracks appeared in Column-1 near the column to shell region at the base (Figure 5.27a). Similarly, during the 1.8% drift ratio, another flexural crack appeared in the similar region in Column-2 (Figure 5.27b). During the 2% drift ratio, two more flexural cracks appeared in similar location in Column-1 and Column-2, but near the top connections, as shown in Figure 5.27a and Figure 5.27b, respectively. All cracks remained of hairline thickness (smaller than 0.4 mm) throughout testing. The cracking was thought to be a consequence of strain hardening in the grooved dissipaters during larger drift ratios which caused tension stresses on the face of the column that were higher than the concrete modulus of rupture.

(a) Column-1 **(b) Column-2**

Figure 5.27. Hairline flexural cracks near the armoring shell

Similar to previous tests on LDB with post-tensioning, there was sliding and twisting of the column at the DCR connections. The extent of sliding increased during the larger drift ratios. By the end of testing, there were 20 mm and 15 mm displacement in Column-1 and Column-2, respectively, as shown in Figure 5.28. This once again confirmed insufficiency of the internal circular shear keys to restrain undesirable movement at the DCR connections despite presence of axial load on the bent.

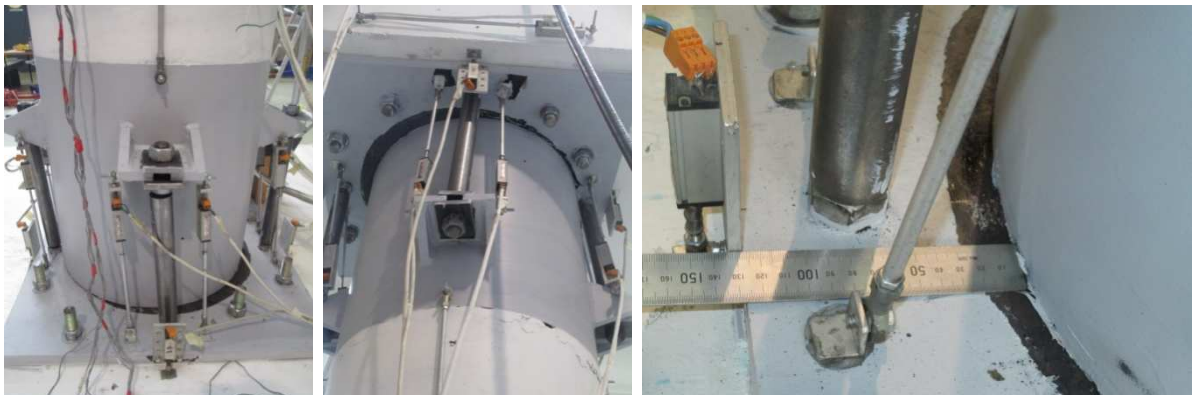

(a) Column-1 base DCR (b) Column-2 top DCR (c) 20 mm movement in Colum-1, close up

Figure 5.28. Sliding and twisting movements in DCR connections

The first grooved dissipater fractured during the third cycle of the 2.5% drift ratio which corresponded to 1.13 times ULS. This dissipater was located on the East side in Column-1 at the column to footing DCR connection. The test was stopped following completion of cycles of the 2.5% drift ratio.

Based on testing of the grooved dissipaters in Chapter 4, a fracture in the dissipater should have not occurred up to 3% drift ratio. However, the excessive sliding and twisting in the bent had distorted the dissipaters and destroyed their axial alignment. The distortion of the dissipaters resulted in more strain concentration in addition to low-cycle fatigue during larger drift ratios. This eventually caused the fracture of the dissipater.

Observation from the test showed no damage to the armoring plates and shells. There was no obvious slip between the armoring shoe (shell) and the column. This showed a good performance of the welded studs detail inside the shell. By the end of testing, there was some superficial surface spalling in concrete close to the region where the shell was discontinued (Figure 5.29). This was thought to be due to concentration of the higher compressive stresses at this location of the column during rocking motion. There was

no other damage to the precast elements (cap beam and footings) apart from opening of the existing cracks from the previous tests.

(a) Column-1 top DCR **(b) Column-2 top DCR**

Figure 5.29. Superficial spalling at the column to shell regions

Figure 5.29 and Figure 5.30 present progression of sliding and twisting at the bottom DCR connection during testing in Column-1 and Column-2, respectively. The photos are taken at the end of the each drift ratio.

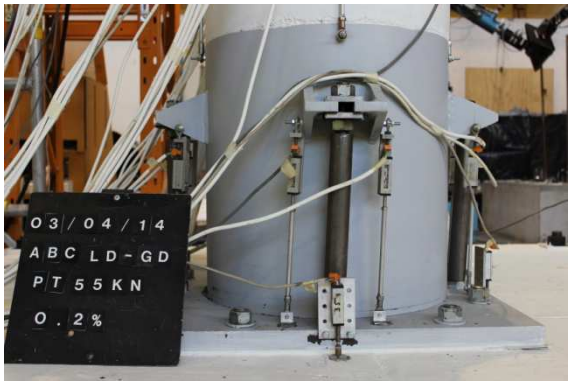

(a) Testing start

(b) End of 0.35% drift ratio

(c) End of 0.5% drift ratio

(d) End of 1.0% drift ratio

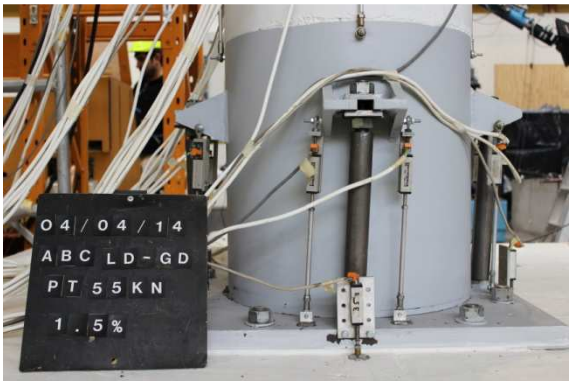

(e) End of 1.5% drift ratio

(f) End of 1.8% drift ratio

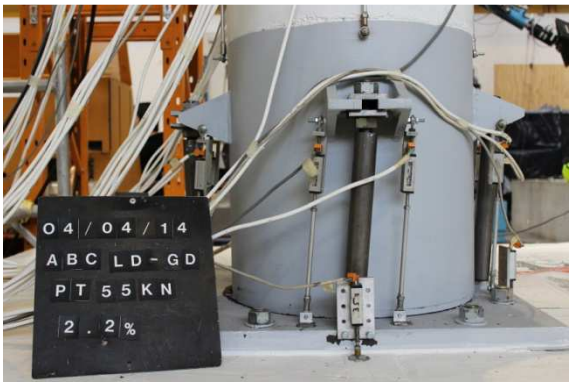

(g) End of 2.2% drift ratio

(h) End of 2.5% drift ratio

Figure 5.30. Progression of sliding and twisting in Column-1 base DCR connection

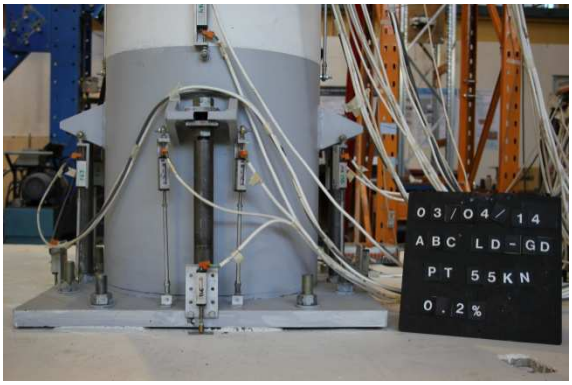

(a) Testing start

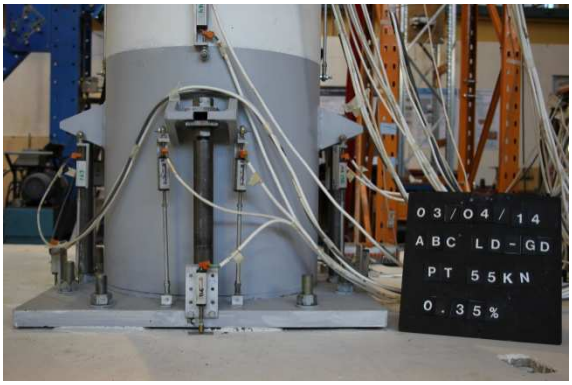

(b) End of 0.35% drift ratio

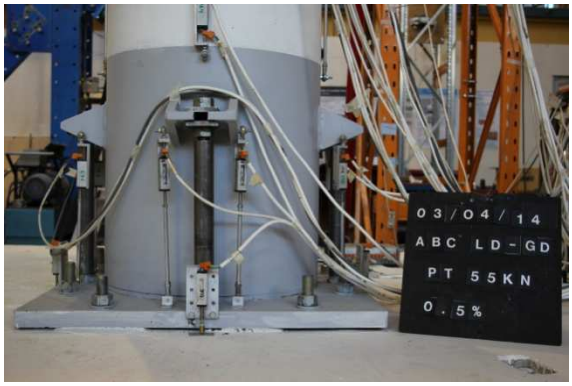

(c) End of 0.5% drift ratio

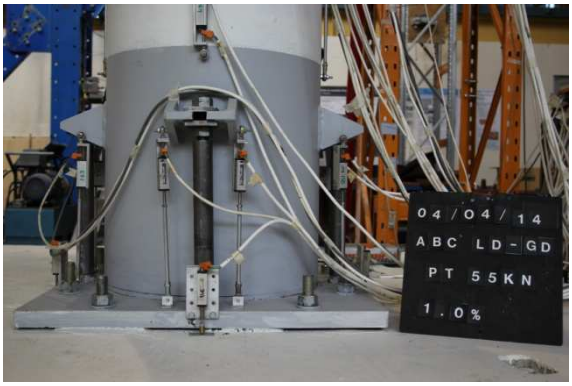

(d) End of 1.0% drift ratio

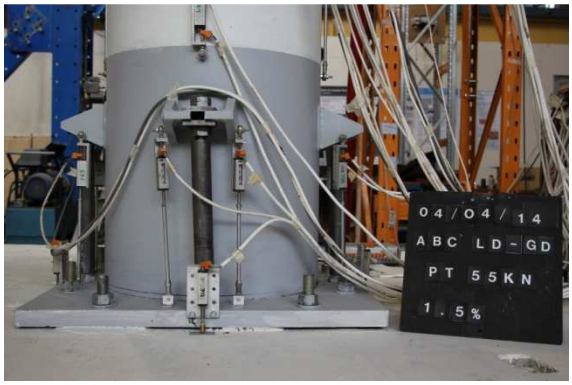

(e) End of 1.5% drift ratio

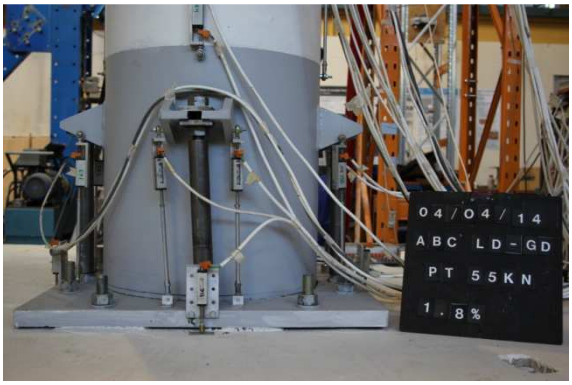

(f) End of 1.8% drift ratio

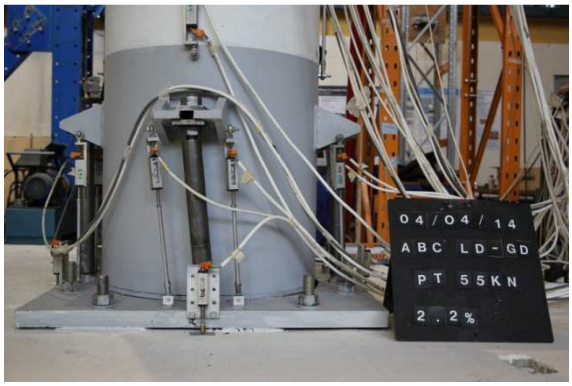

(g) End of 2.2% drift ratio

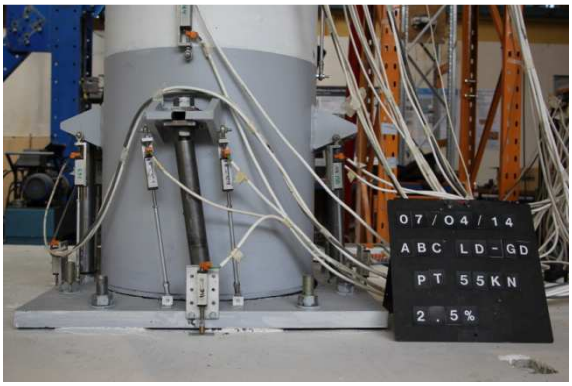

(h) End of 2.5% drift ratio

Figure 5.31. Progression of sliding and twisting in Column-2 base DCR connection

The force-drift hysteresis for LDB is shown in Figure 5.32. The bent did not show a visible flag-shaped hysteresis due to excessive sliding and twisting of the columns. This showed inadequacy of the internal shear key to restrain undesirable movement at the DCR connections.

The bent yielded at the 0.53% drift ratio. The base shear at the yield point was almost equal to the predicted force of 182 kN. The bent achieved its design base shear of 350 kN during the 2.2% drift ratio. At the ULS performance level (2.2% drift ratio), the displacement ductility was 4.1. This value is considerably higher to that of HDB (2.6) and assumed value of ductility (3) at ULS. The fracture of the dissipater in tension during the third cycle of the 2.5% drift ratio can be noticed from the backbone curve where the bent capacity had reduced. The displacement ductility by the end of testing (2.5% drift ratio or 1.13 times ULS) was 4.7.

The residual displacement in the bent was 23 mm and 28 mm following cycles of the 2.2% and 2.5% drift ratio, respectively. This corresponded to 35% and 38% of the peak drift ratio, respectively. This also shows 15% and 12% less residual displacement compared to that observed in testing of HDB for each performance level, respectively.

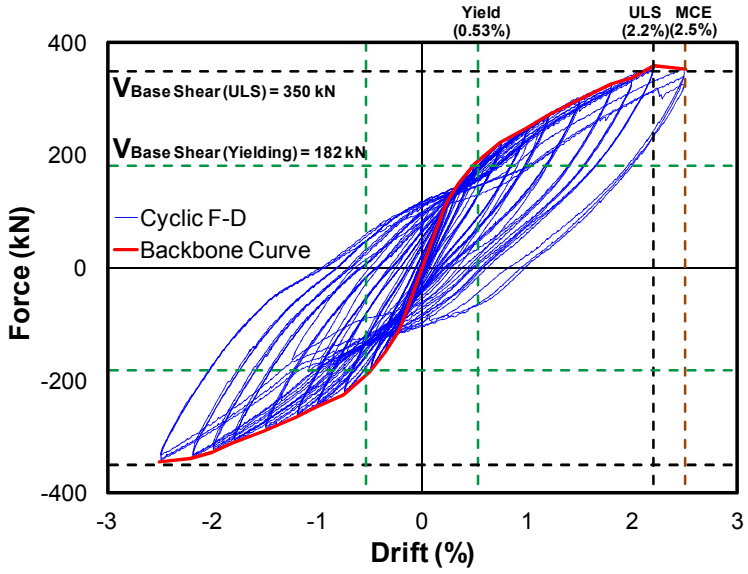

Figure 5.32. Force-drift hysteresis for IPT5+GD+AX

The post-tensioning force-drift hysteresis plot for each rocking column is presented in Figure 5.33. There was not any considerable drop in the post-tensioning force throughout testing. However, there was some asymmetrical response of the post-

tensioning bars. This was thought to be due to sliding and twisting at the DCR connections which resulted into the asymmetrical behavior in the post-tensioned Macalloy bars during the pull and push stages of the loading.

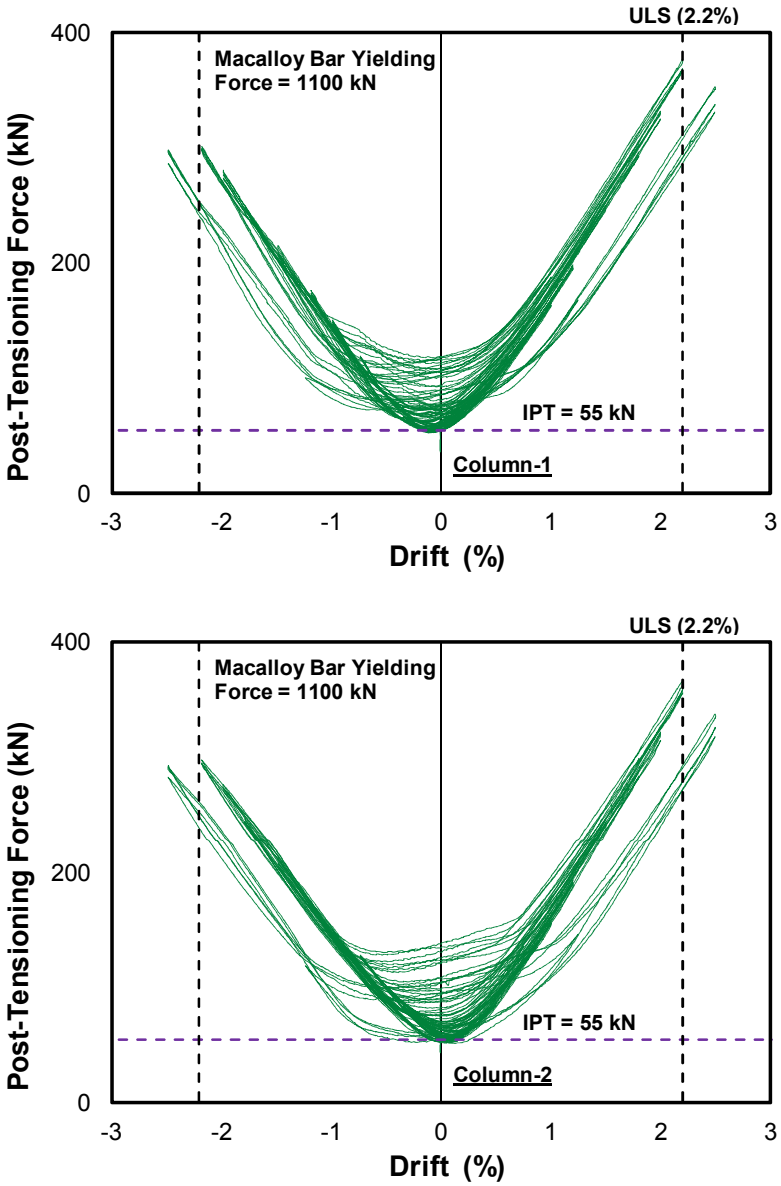

Figure 5.33. Post-tensioning force-drift hysteresis for IPT5+GD+AX

The corrected area-based damping (hysteretic damping) is plotted in Figure 5.34a. There was a relatively linear relationship between the hysteretic damping and the displacement ductility in LDB. The bent achieved hysteretic damping of 12.5% at the displacement ductility of 4.7 which corresponded to the 2.5% drift ratio. Up to a ductility value of close to 2.2, LDB had similar values of hysteretic damping to those of the theoretical Takeda-Thin model. Following that, the curve located below the

theoretical Takeda-Thin model. Compared to HDB, the bent had lower hysteretic damping values for almost all values of displacement ductility. It should be noted that in Figure 5.34a, the hysteretic damping curve for theoretical models is plotted for an assumed effective period of $T_{eff} \geq 1\ sec$ for the structure in accordance with Priestley et al. (2007). The Flag-Shaped model is plotted for a force ratio of $\beta = 0.35$ in Figure 4.64b. The EVD plot is presented in Figure 5.34b.

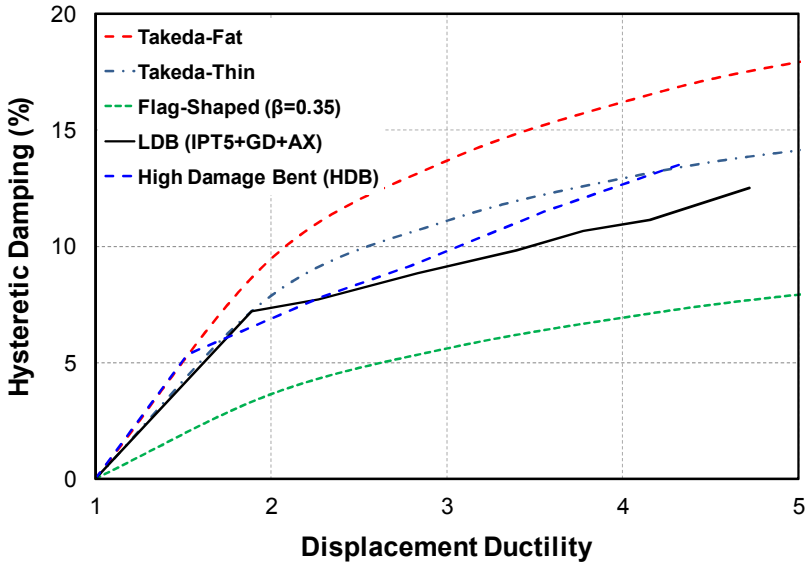

(a) Corrected area-based hysteetic damping (ξ_{hyst})

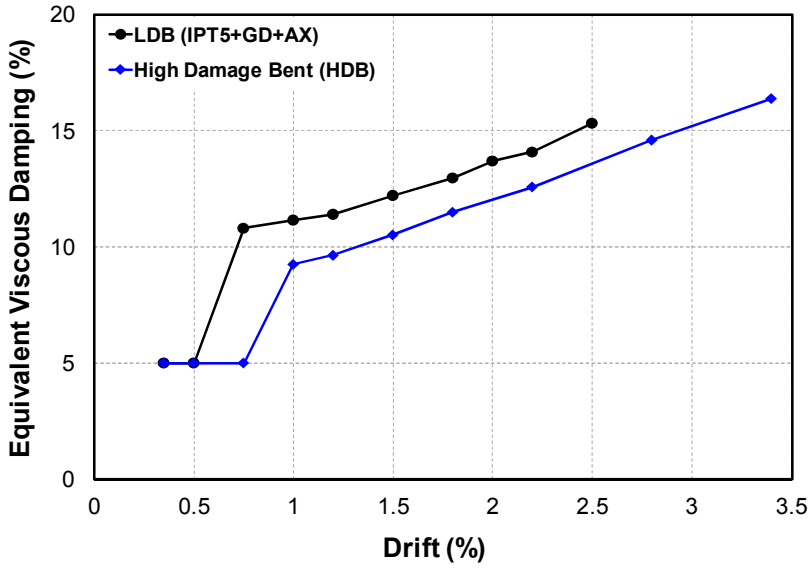

(b) Equivalent viscous damping (ξ_{eq})

Figure 5.34. Hysteretic damping and EVD plots for IPT5+GD+AX

The ADRS plot for LDB is presented in Figure 5.35 for various hazard levels (return periods) from NZS 1170.5 (NZS, 2004). In Figure 5.35, the increasing stiffness of LDB with further drift ratios is due to presence of post-tensioning bars and lack of strength degradation due to good confinement of the concrete column (armoring shoe). This means that the backbone curve of the bent would intersect the hazard curves for higher return period earthquakes such as 3500 year and 6000 year in smaller drift ratios compared to those in HDB.

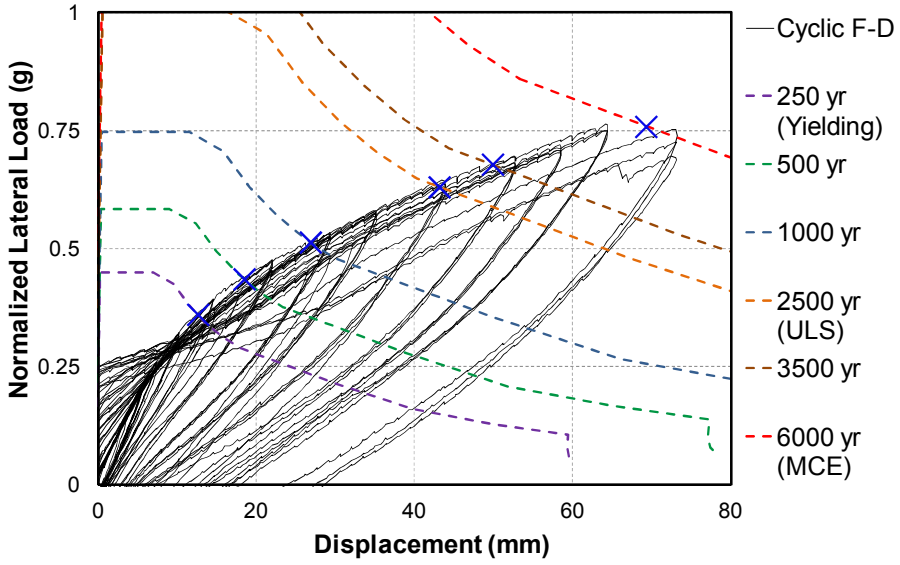

(a) Normalized lateral load - displacement

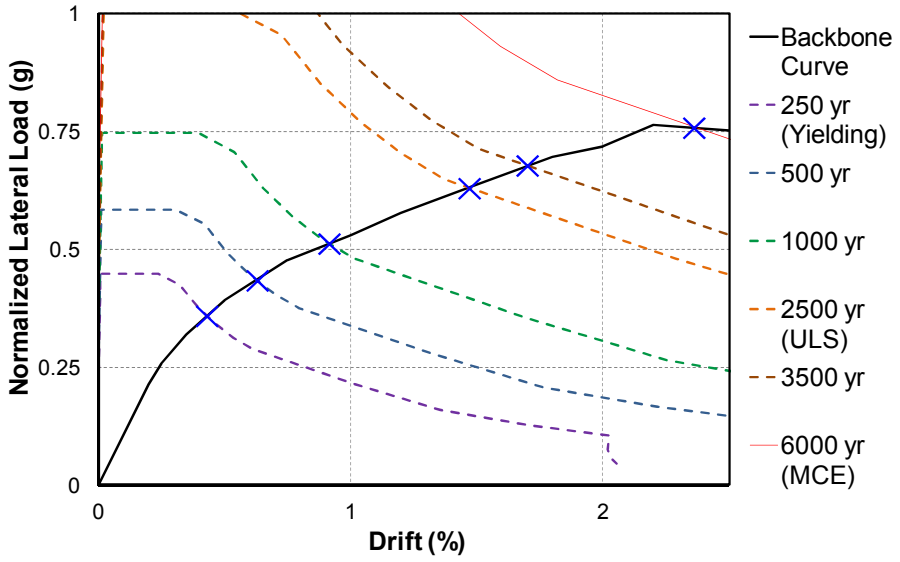

(b) Normalized lateral load - drift

Figure 5.35. ADRS plots for IPT5+GD+AX

Table 5.4 presents a summary of ADRS results for LDB. Based on Table 5.4, a ULS earthquake (2500 year return period, *R = 1.8*) will generate 1.47% drift ratio in the bent

which corresponds to ductility of 2.8 at ULS. This is almost equal to the ductility that was adopted during the force-based design of the prototype structure ($\mu = 3$) in Section 3.3.1 of Chapter 3.

Table 5.4. Summary of ADRS results for LDB under IPT5+GD+AX

Hazard Levels (Years)	Return Period Factor (R)	Ductility (μ)	Drift (%)	Corrected Equivalent Damping (ξ_{eq}) %
250	0.75	1	0.43	12.75
500	1.0	1.2	0.63	13.51
1000	1.3	1.7	0.92	14.06
2500	1.8	2.8	1.47	14.89
3500	2.0	3.2	1.7	15.27
6000	2.5	4.5	2.36	16.57

It is important to mention that the 2.2% drift ratio was the ULS performance level for HDB based on the testing observation (spalling of concrete) and the predicted pushover analysis (Section A.2 in Appendix A). However, as discussed in Chapter 3, the ADRS plot and results from the collapse analysis (refer to Table 3.19 in Chapter 3) of HDB showed that the ULS performance level had indeed occurred at 2.7% drift ratio for the bent. Similarly, the ADRS plot for LDB under IPT5+GD+AX testing showed that the ULS performance level occurs at the 1.47% drift ratio. This means the MCE performance level was 1.7 times ULS for LDB (2.5% drift ratio).

The energy dissipated per each cycle of each drift ratio for LDB is presented in Figure 5.36. It should be noted that the fourth cycle at each drift ratio was the unloading cycle and had half of the amplitude of that drift ratio, as presented in Section 3.2.2.1 of Chapter 3. Therefore, for comparison of strength degradation during cyclic loading, this cycle should not be considered.

According to Figure 5.36, the bent had the maximum energy dissipation capacity during the first cycle of loading at each drift ratio. A noticeable reduction in energy dissipation can be observed during the third cycle of the 2.5% drift ratio. This was due to fracture of one of the grooved dissipaters during this cycle.

By comparing the cumulative dissipated energy at 2.2% drift ratio for HDB and LDB, it can be concluded that LDB had almost 18% extra energy dissipation capacity than HDB. This was thought to be a consequence of less strength degradation in LDB which had resulted in more energy dissipation. At the same time, some energy dissipation in LDB could have been a result of sliding and twisting in the columns.

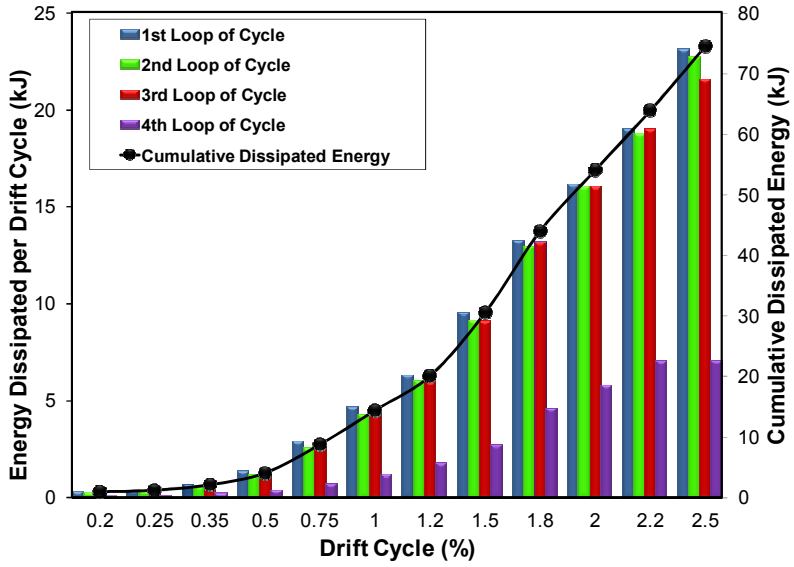

Figure 5.36. Dissipated energy (per cycle and cumulative) for IPT5+GD+AX

In summary, testing of LDB showed a better performance compared to that of HDB. The rocking columns suffered minimal damage. There was no spalling of concrete in testing of LDB. The only sacrificial elements were the externally mounted grooved dissipaters. The bent achieved a higher design base shear force compared to HDB. LDB had lower residual displacement and hysteretic damping, higher ductility, and more energy dissipation capacity compared to what observed in the testing of HDB.

Despite a good performance, there was some sliding and twisting at the DCR connections. There was insufficiency of the internal shear keys to restrain undesirable movement in the bent. This had reduced the efficiency of dissipaters to absorb energy, as well as the post-tensioning bars to provide self-centering for the bent. Based on the observations from testing of the bent with post-tensioning only, a higher level of initial post-tensioning would have increased self-centering of the bent, and thus reduced the sliding in the columns.

The testing also confirmed that relying solely on friction between the precast elements in the DCR connection would not prevent from excessive twisting and sliding of the elements relative to each other. This was even noticed with higher levels of post-tensioning to a some level. Based on the observations from performance of the bent with the internal shear key, Figure 5.37 presents concepts for improved detailing of the shear key for the DCR connections in the bent. In this concept, the shear key can be made of steel or high-strength concrete. The gap between the shear key and the recess in the column can be filled with synthetic rubber or any other suitable filling material. The geometry of the shear key (inclined edges) is expected to prevent from twisting of the column without locking the rocking motion.

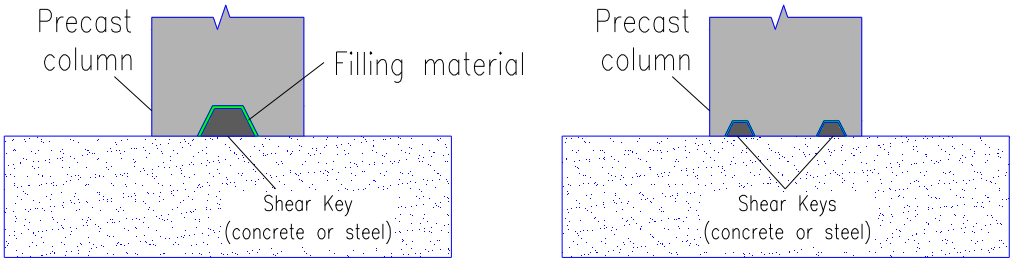

(a) Single shear key **(b) Double shear key**

Figure 5.37. Concepts for improved detailing for internal shear key

Another alternative for the internal shear key is to use short steel dowels which can provide the restraint needed in the columns. Rahman and Restrepo (2005) used short dowels for the rocking precast walls successfully.

In the next stage of testing, the contribution of the internal concrete shear keys and friction to restrain undesirable movement in LDB were totally neglected. Instead, it was preferred to introduce new external steel shear keys to restrain the twisting and sliding of the columns.

5.4 Testing of ABC Low Damage Bent with External Shear Keys

Following testing of LDB with internal shear keys, the grooved dissipaters were removed. The post-tensioning and axial load (gravity) were released to remove the residual twist and slide at the DCR connections. All elements and connections were re-centered using crane and a hand operated jack. The hairline flexural cracks in the column from the previous test were painted to see if the cracks were going to open again in this phase of testing. New external shear keys were welded at each DCR connection in LDB to perform primarily two functions:

1. To prevent from sliding of the columns
2. To restrain twisting of the columns

The shear keys were made of mild steel solid bars with square section, as shown in Figure 5.38a. The bar had a 5^0 cut on the end that would face the round column. This was intended to accommodate the angularity generated during rocking of the column, and hence the shear key would not intercept the gap opening. The arrangement of the shear keys in a typical DCR connection is shown in Figure 5.38c and Figure 5.38d.

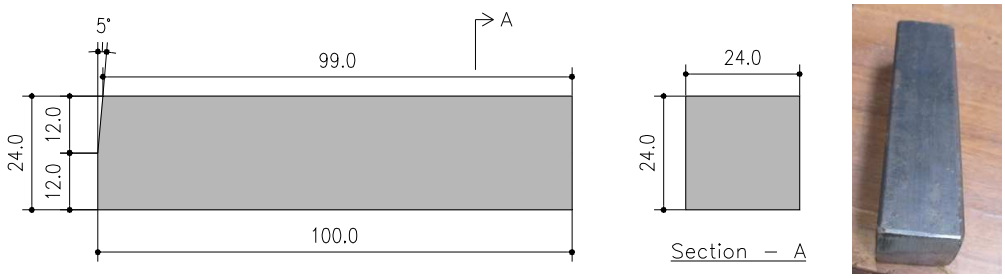

(a) Steel bar dimensions for shear key **(b) Steel bar**

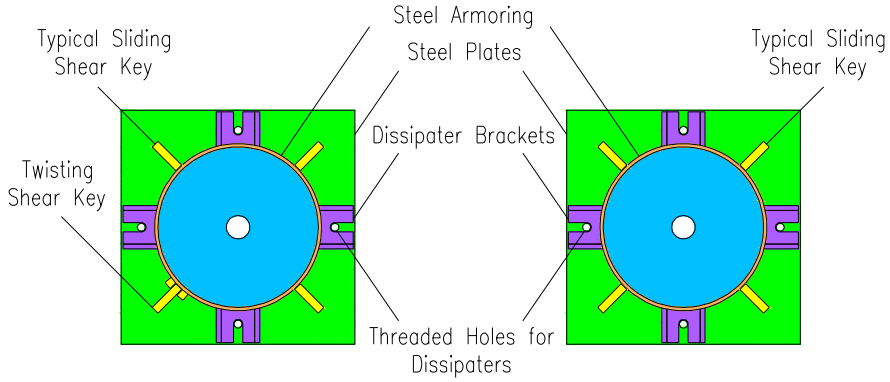

(c) Base DCR connection **(d) Top DCR connection**

Figure 5.38. Details and arrangement of external steel shear keys in LDB

In Figure 5.38c and Figure 5.38d, the shear keys were arranged such to restrain both sliding and twisting in the column. There were four sliding shear keys at each DCR connection. The shear keys were welded to the base armoring plate (Figure 5.39f). One of the sliding shear keys (Figure 5.39d) was also performing the task for restraining the twist in the column. This shear key was accommodated between the two bars which were welded vertically on the face of the column (Figure 5.39e). There was one shear key for restraining the twist per column which was located at the base DCR connection. Figure 5.39 shows photos from a re-centered LDB with new external shear keys.

(a) Re-centered bent **(b) Base DCR connection** **(c) Top DCR connection**

(d) Twisting shear key at base **(e) Twisting shear key close-up** **(f) Typical sliding shear key**

Figure 5.39. Re-centered LDB with new external shear keys

In the first part of this phase of testing, three tests on LDB with external shear keys and post-tensioning only were performed. This was similar to that for LDB with internal shear keys (Section 5.3.1). This was intended to see how effective the external shear keys were to restrain the undesirable movement in the bent. The external shear keys were thought to enhance the response of the bent. The level of initial post-tensioning for each test was identical to that discussed in Section 5.3.1.

In the second part of testing, the response of LDB with post-tensioning, gravity, and Grooved Dissipaters (GDs) was tested. This was similar to the test presented in Section 5.3.2 earlier (IPT5+GD+AX) with internal shear keys. However, the only difference was that the initial post-tensioning force in each Macalloy bar was increased to 11.8% instead of 5%.

In the third part of testing, the response of LDB with post-tensioning and Mini UFP Dissipaters (MUDs) was tested. Three tests with different level of initial post-tensioning were performed without gravity. This part of testing was intended to show how the response of the bent is changing by applying different level of self-centering ratio. Therefore, it presented a type of experimental parametric study for a variety of self-centering ratios.

In the fourth part of testing, the response of LDB with post-tensioning, MUD, and gravity was experimentally tested.

In the fifth part of testing, the response of LDB with a combination of post-tensioning, MUD, and GD, was tested under three levels of post-tensioning. This part of the experimental testing aimed to present a similar parametric study as discussed above for the third part. At the same time, the concept for combination of MUD and GD in DCR connection was validated through experimental testing.

In the sixth part of testing, the response of LDB with combination of post-tensioning, MUD, GD, and gravity, was investigated. The bent was designed to match the capacity and ductility of HDB at the ULS performance level. This part of testing showed the performance of MUD and GD in a DCR connection in presence of post-tensioning and gravity.

Table 5.5 presents a summary of tests on LDB with external shear keys. Observations from testing and experimental results for each test are presented in the next sections.

Table 5.5 Description of tests on LDB with external shear keys

Test No	Part	Testing Type	Test Name	IPT per Column (%)	Axial Load (kN)	λ (ULS)
1	**Part - I**	Post-Tensioning Only	IPT15-EX	15	-	∞
2			IPT30-EX	30	-	∞
3			IPT45-EX	45	-	∞
4	**Part - II**	Post-Tensioning with Grooved Dissipaters and Gravity (Axial Load)	IPT11.8+GD+AX	11.8	390	1.9
5	**Part - III**	Post-Tensioning with Mini UFP Dissipaters	IPT1.8+MUD	1.8	-	6.9
6			IPT3.6+MUD	3.6	-	7.8
7			IPT9+MUD	9	-	9.1
8	**Part - IV**	Post-Tensioning with Mini UFP Dissipaters and Gravity	IPT9+MUD+AX	9	390	13
9	**Part - V**	Post-Tensioning with Mini UFP and Grooved Dissipaters	IPT9+MUD+GD	9	-	2.4
10			IPT11.4+MUD+GD	11.4	-	2.5
11			IPT13.6+MUD+GD	13.6	-	2.6
12	**Part - VI**	Post-Tensioning with Mini UFP Dissipaters, Grooved Dissipaters, and Gravity	IPT11.4+MUD+GD+AX	11.4	390	3.5

5.4.1 Part-I: LDB with Post-Tensioning Only

This part of testing was identical to what discussed in Section 5.3.1. The testing arrangement for LDB was similar to that shown in Figure 5.39 with no dissipaters and gravity.

5.4.1.1 Initial Post-Tensioning = 15% (IPT15-EX)

Gap opening started during the 0.2% drift ratio in contrast with the 0.35% drift ratio during identical testing of the bent, but with internal shear keys (Section 5.3.1.1). The size of gap opening in all DCR connections was almost similar. During 2.2% drift ratio (ULS), the maximum gap opening was measured to be 13 mm (Figure 5.40).

There was no sliding or twisting of the columns throughout testing which showed great performance of the external shear keys. The 5^0 angle on the face of the shear key was very effective to accommodate the rocking movement of the column (Figure 5.40c). Similarly, the twisting shear key allowed gap opening to occur freely, but restrained twisting of the column (Figure 5.40d).

By the end of testing, there was no damage to the shear keys, rocking columns, and DCR connections. Some existing cracks in the cap beam and footings from the previous tests opened up, but remained of hairline thickness (smaller than 0.4 mm) throughout testing.

The force-drift hysteresis is plotted in Figure 5.41. The bent showed a very symmetrical hysteresis. The response of LDB with a lower post-tensioning level (15%) was indeed much improved compared to similar testing with internal shear keys. The capacity of the bent during the 2.2% drift ratio was slightly lower than its predicted base shear capacity. This was because of some flexibility at the connections due to such a lower level of post-tensioning with no other contribution from the dissipaters or gravity.

Following testing, there was residual displacement of less than 3 mm (0.1% drift ratio) in the bent. This is substantially smaller than the 22 mm residual displacement (0.75% drift ratio) in an identical test with internal shear keys as presented earlier in Section 5.3.1.1. The 3 mm residual displacement was due to a smaller gap that had to be left between each sliding shear key and the face of the column. The gap corresponded to

less than 0.1% drift ratio. Thus, in reality the net residual displacement in the bent was zero. By the end of testing, all connections had re-centered despite a lower level of initial post-tensioning.

(a) 13 mm gap opening at the base connections

(b) 13 mm gap opening at the top connections

(c) Typical sliding shear key during rocking

(d) Typical twisting shear key during rocking

Figure 5.40. Maximum gap opening during 2.2% drift ratio and efficiency of external shear keys during gap opening (rocking of the columns) in LDB

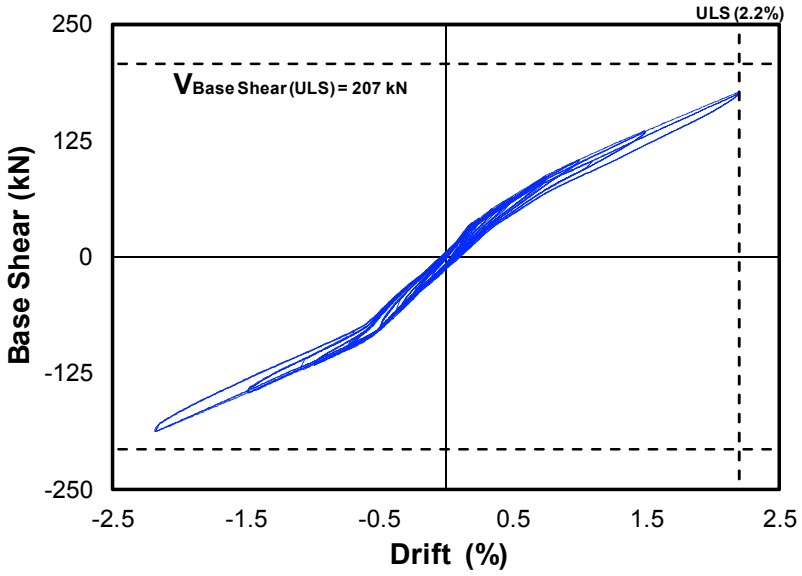

Figure 5.41. LDB force-drift hysteresis for IPT15-EX

The axial force-drift hysteresis for each Macalloy bar is plotted in Figure 5.42. The Macalloy bar in Column-1 showed some asymmetrical response of the post-tensioning. There was some slacking in the bar during the pull stage of the loading. This was thought to be due to close proximity of the Column-1 to the loading point (horizontal ram). Another factor could have been the presence of a swivel at the tip of the ram which was able to rotate in order to accommodate the angularity generated due to horizontal displacement in the specimen. The size of the post-tensioning duct may have also been a contributing factor. As a result, there was a lower increase of force in the Macalloy bar compared to that in Column-2 during the pull stage of the loading.

In contrast to Column-1, the Macalloy bar in Column-2 showed a fairly symmetrical response. During testing, the maximum drop in the post-tensioning force was in the vicinity of 24 kN. This corresponded to 24% of the initial post-tensioning force of 165 kN. This was significantly lower than that of an identical test presented in Section 5.3.1.1 with internal shear keys.

As explained in Section 5.3.1.1, the slight asymmetrical response of the columns could have been due to the diameter of the central duct (70 mm) which was almost twice as big as the diameter of the Macalloy bar (40 mm). This would have caused shifting of the tendons (Macalloy bars) inside the central duct during testing. In this instance, given the generated lever arm in the tendon, the post-tensioning would have increased in one

column, but decreased in the second column. This behavior is expected to be improved and almost eliminated if gravity is acting on the bent.

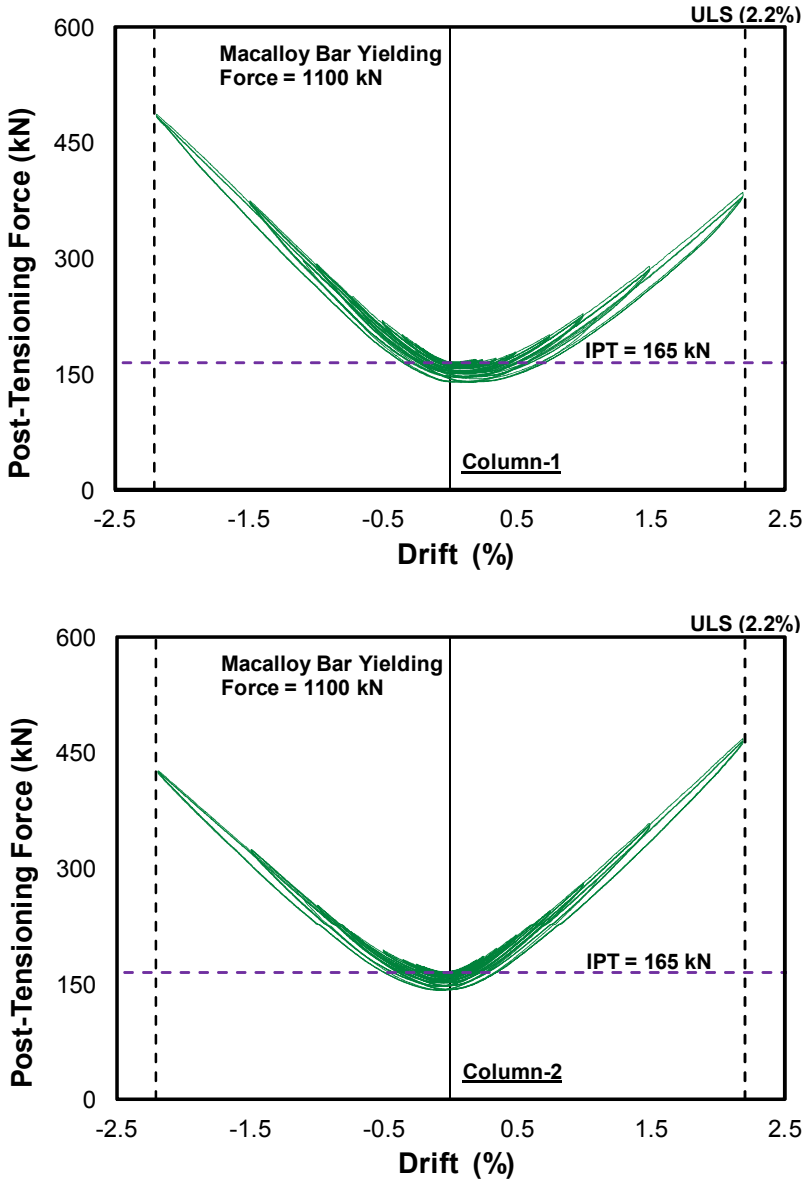

Figure 5.42. Post-tensioning force-drift hysteresis for IPT15-EX

5.4.1.2 Initial Post-Tensioning = 30% (IPT30-EX)

The bent response was similar to that under IPT15-EX testing. First gap opening started during the 0.35% drift ratio. Gap opening increased with further drift ratios. During the 2.2% drift ratio, the maximum gap opening was measured to be 12 mm.

The force-drift hysteresis of the bent is plotted in Figure 5.43. The bent showed a good symmetrical behavior and achieved its predicted base shear capacity of 254 kN during the push stage of the loading. The residual displacement was similar to the previous test (3 mm or 0.1% drift ratio). This confirmed the conclusion from the previous test that the 3 mm was actually the construction gap between the sliding shear key and the face of the column. Thus, the net residual displacement was indeed zero.

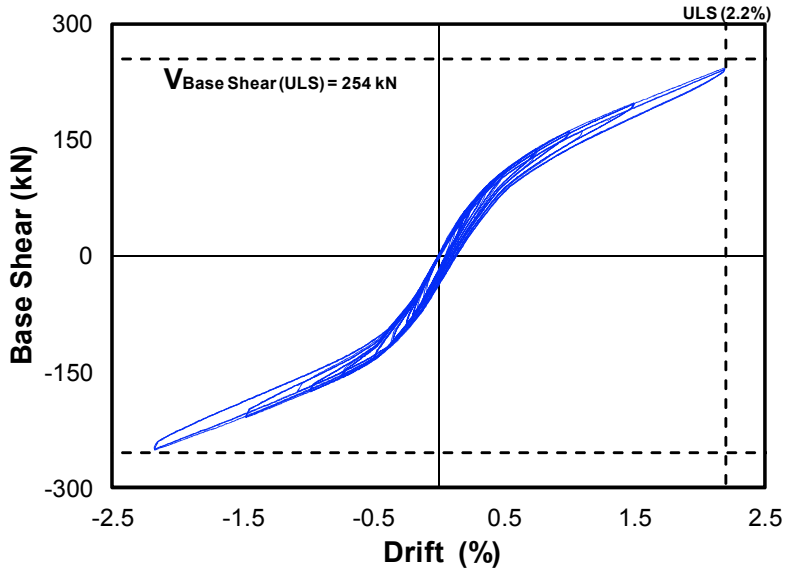

Figure 5.43. LDB force-drift hysteresis for IPT30-EX

Figure 5.44 presents hysteresis plot of the post-tensioning in each column. The maximum drop in post-tensioning was approximately 35 kN. This corresponded to 10% of the initial post-tensioning force of 330 kN in each Macalloy bar.

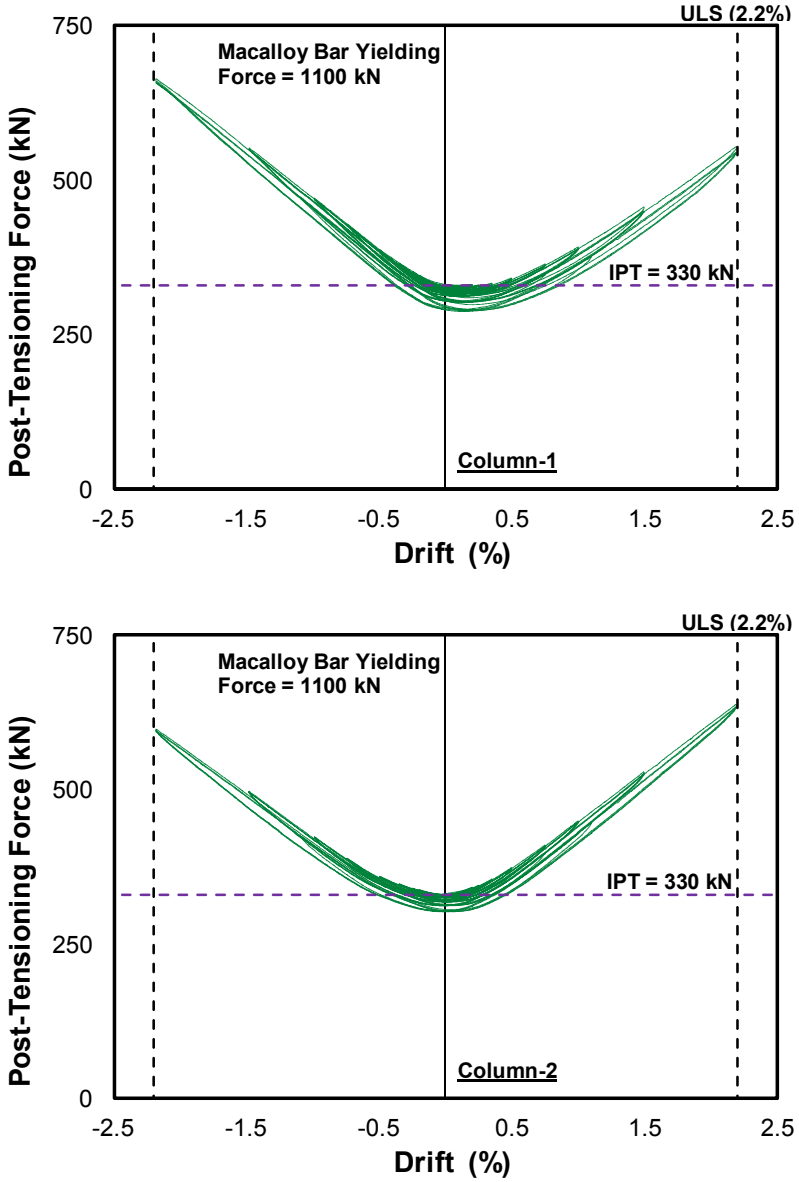

Figure 5.44. Post-tensioning force-drift hysteresis for IPT30-EX

5.4.1.3 Initial Post-Tensioning = 45% (IPT45-EX)

Gap opening initiated during the 0.5% drift ratio. During 2.2% drift ratio, the gap opening had increased to 11 mm. The force-drift hysteresis is plotted in Figure 5.45. The bent achieved its ULS base shear capacity (300 kN) during the 2.2% drift ratio in a symmetrical response. Similar to the other two previous tests, at the end of testing, the net residual drift was zero in the bent.

The post-tensioning force-drift hysteresis is presented in Figure 5.46. The maximum drop in the post-tensioning was approximately 38 kN which corresponded to 7.5% of the initial post-tensioning force of 495 kN in each Macalloy bar.

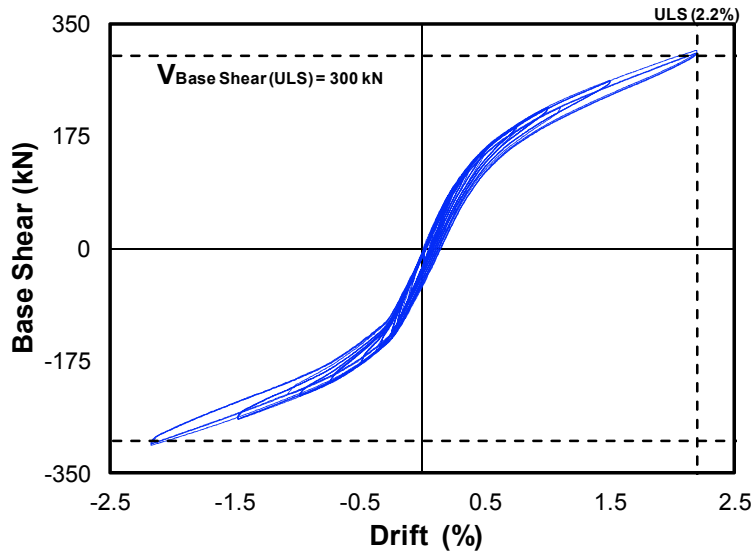

Figure 5.45. LDB force-drift hysteresis for IPT45-EX

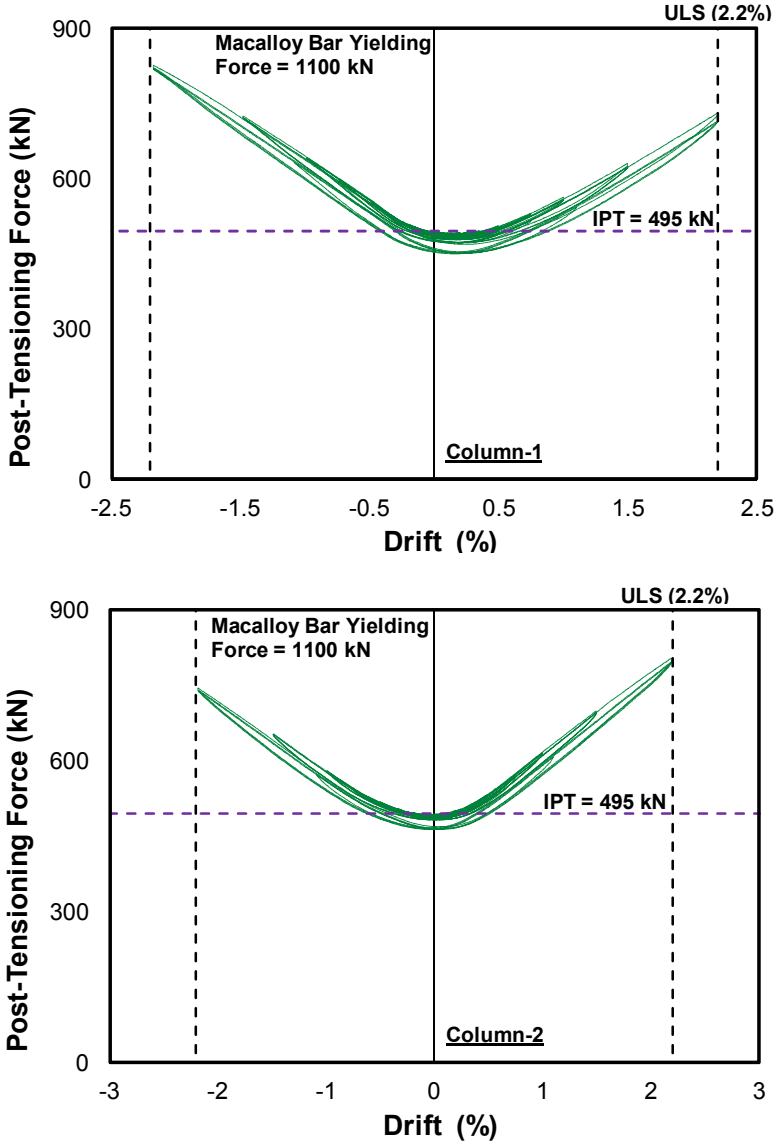

Figure 5.46. Post-tensioning force-drift hysteresis for IPT45-EX

In summary, testing of LDB with post-tensioning and external shear keys showed very improved response of the bent. The bent remained fully intact. The residual displacement in three tests with different level of initial post-tensioning was limited to the construction gap between the sliding shear key and the face of the column (3 mm or 0.1% drift ratio). The sliding and twisting shear keys were very effective in restraining any undesirable movement of the columns. As a comparison of the performance, Table 5.6 presents a summary of the testing of LDB with post-tensioning and internal and external shear keys up to the drift ratio of 2.2% (ULS).

Table 5.6. Comparison of LDB performance with internal and external shear keys

Shear Key	**IPT (%)**	**Predicted Force (kN)**	**$V_{base\ shear}$ (Pull) (kN)**	**$V_{base\ shear}$ (Push) (kN)**	**Gap Opening Drift (%)**	**Max Gap (mm)**	**Δ_{Res}** (%)	**Max PT Drop (%)**
Internal	15	207	234	157	0.35	15	0.75	32
	30	254	275	254	0.5	12	0.35	10
	45	300	318	316	0.75	10	0.15	9.5
External	15	207	176	188	0.2	13	0.1	24
	30	254	243	251	0.35	12	0.1	10
	45	300	309	306	0.5	11	0.1	7.5

5.4.2 Part-II: LDB with Post-Tensioning, GDs, and Gravity

This part of testing was identical to what discussed in Section 5.3.2, but with external shear keys. Gravity was applied on the bent to simulate the superstructure weight. New grooved dissipaters were connected at each DCR connection. The initial post-tensioning force was increased for an enhanced self-centering of the bent.

Since sliding and twisting of the rocking column were restrained by the shear keys, it was expected that there should not be any excessive non-axial deformation in the grooved dissipaters. This means that a dissipater fracture should not occur up until the last cycle of the 2.5% drift ratio.

5.4.2.1 LDB with 11.8%IPT, Grooved Dissipaters, and Gravity (IPT11.8+GD+AX)

The design of DCR connections was according to PRESSS Design Handbook (Pampanin et al., 2010). A summary of the design spreadsheet for a typical DCR connection can be found in Section D.4 of Appendix D.

There were four grooved dissipaters at each DCR connection. The initial post-tensioning force in each Macalloy bar was increased from 55 kN in IPT5+GD+AX to 130 kN in IPT11.8+GD+AX. Given the increase in the initial post-tensioning force, the capacity of the bent was calculated to be higher than HDB and LDB under IPT5+GD+AX during the ULS drift ratio (2.2%). Table 5.7 presents a summary of the design parameters.

Table 5.7. Summary of design parameters for LDB with IPT11.8+GD+AX

Performance Level	Self-Centering ratio (λ)	Drift (δ)	Base Shear (V_b)
Yielding	1.7	0.53%	205
ULS	1.9	2.2%	369

The behavior was similar to that explained in Section 5.3.2.1 previously. However, there was no sliding or twisting of the columns which enhanced the response of LDB. Some existing cracks in the columns started opening, but remained of hairline thickness (less than 0.4 mm) throughout testing. There was no fracture of the grooved dissipaters up to the end of testing (2.5% drift ratio).

The force-drift hysteresis is plotted in Figure 5.47. The flag-shaped response of the bent with post-tensioning, gravity, and grooved dissipaters, is clearly visible. The bent showed a very symmetrical behavior in both push and pull stages of the loading. It also achieved its predicted capacity at the yielding and ULS performance levels. There was some stiffness degradation of the bent under the cycles at each drift ratio. This was not only observed in the second cycle, but also in the third cycle. As explained in Chapter 4, grooved dissipaters are susceptible to degradation under cyclic loading. Therefore, this may have contributed to the degradation visible in Figure 5.47.

The residual displacement in the bent was 6 mm (0.2% drift ratio) and 9 mm (0.3% drift ratio) following the cycles of the 2.2% and 2.5% drift ratio, respectively. Given the 0.1% drift ratio for the gap between the sliding shear keys and face of the column, in reality the residual displacement was 0.1% (3 mm) and 0.2% (6 mm) at the ULS and MCE performance level, respectively. This was significantly lower (an average of 85% reduction) than what observed during the testing of LDB with internal shear keys.

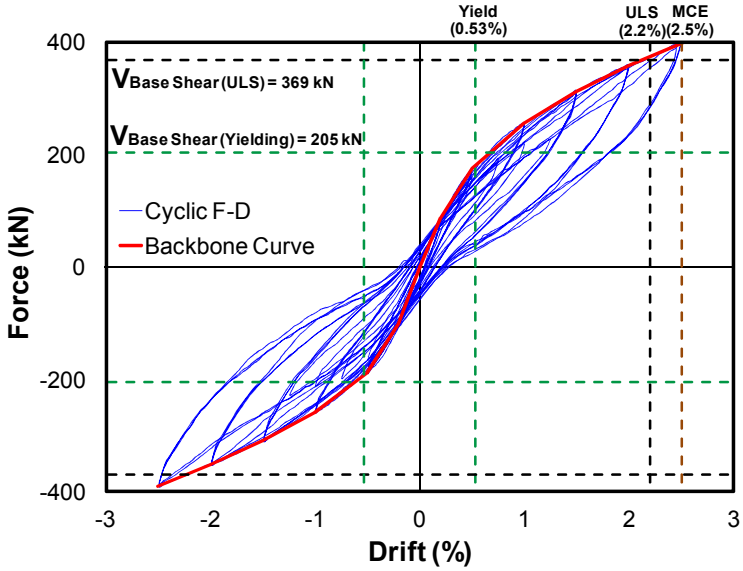

Figure 5.47. Force-drift hysteresis for IPT11.8+GD+AX

Figure 5.48 presents the post-tensioning response in the bent. The tendons did not show any significant asymmetrical behavior as was observed in the testing of the bent without gravity. The drop in the post-tensioning during the testing was also negligible. The improved behavior here is thought to have been influenced by the presence of gravity on the bent. The neutral axis depth response (Figure 5.48c) shows a fairly symmetrical behavior in one of the typical DCR connections in the bent.

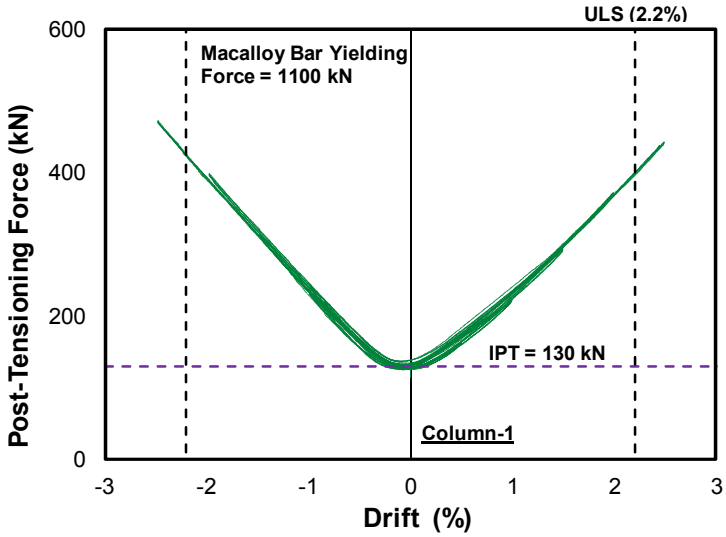

(a) Column - 1 post-tensioning-drift hysteresis

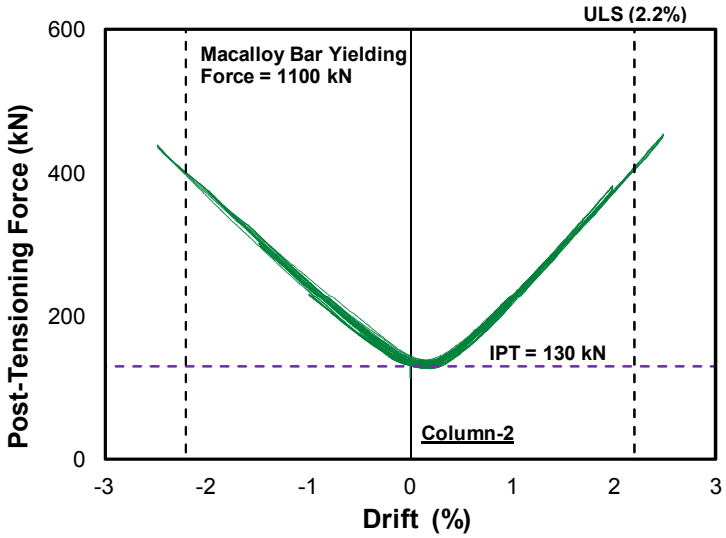

(b) Column - 2 post-tensioning-drift hysteresis

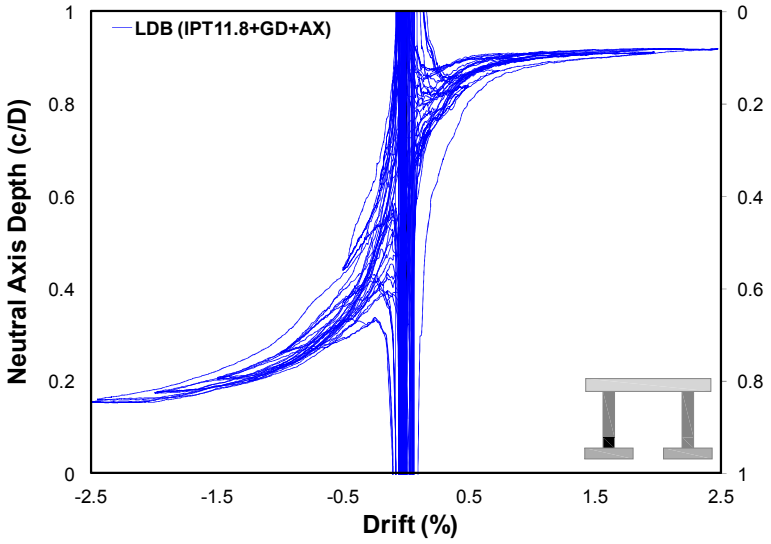

(c) Neutral axis depth-drift hysteresis

Figure 5.48. Post-tensioning and neutral axis plots for IPT11.8+GD+AX

The hysteretic damping and EVD plots are shown in Figure 5.49a and Figure 5.49b, respectively. The bent achieved hysteretic damping of 9.85% at the displacement ductility of 4.7 which corresponded to the 2.5% drift ratio. The bent had higher hysteretic damping values compared to theoretical flag-shaped ($\beta = 0.35$) model. It is also obvious that the hysteretic damping was lower than that of LDB with internal shear keys. The reason behind this was that in testing of LDB with internal shear keys, there was also contribution from the friction dissipation due to sliding which resulted in larger residual displacement. At the same time, LDB with internal shear keys (IPT5+GD+AX) incorporated a lower level of initial post-tensioning which means larger energy dissipation capacity and lower self-centering ratio.

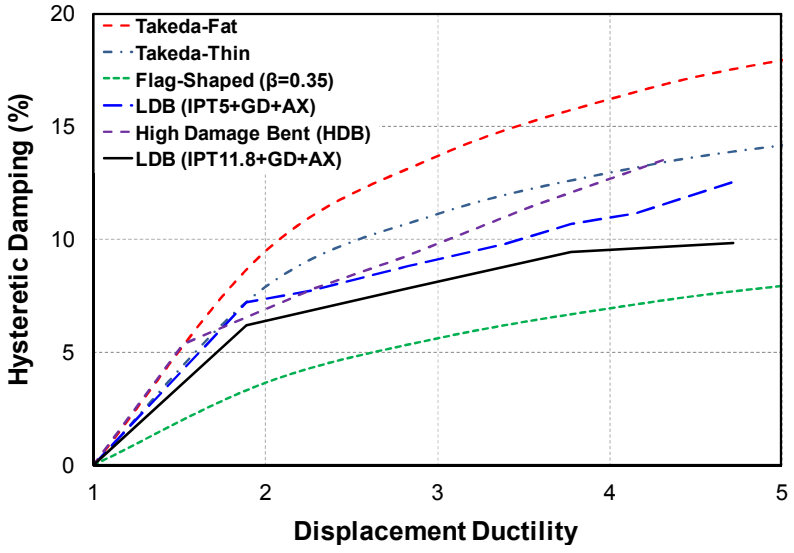

(a) Corrected area-based hysteetic damping (ξ_{hyst})

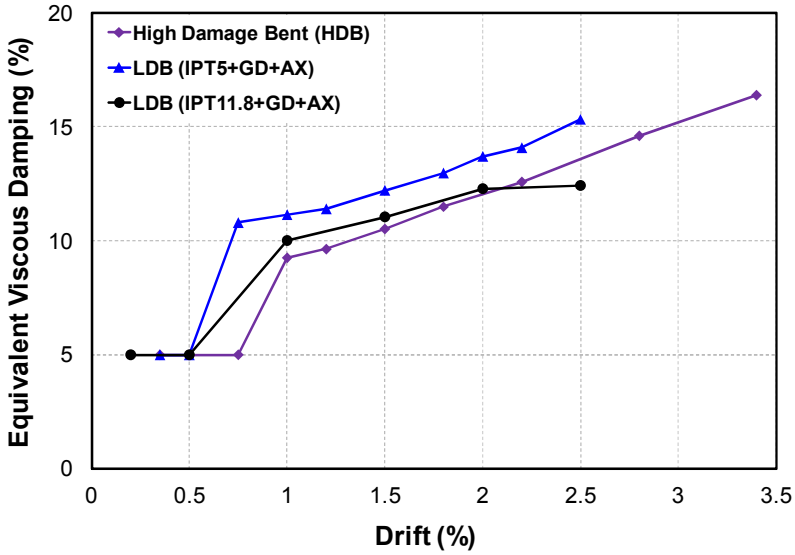

(b) Equivalent viscous damping (ξ_{eq})

Figure 5.49. Hysteretic damping and EVD plots for HDB for IPT11.8+GD+AX

The ADRS plot for LDB is presented in Figure 5.50 for various hazard levels. The performance points were similar to those presented in testing of LDB with IPT5+GD+AX in Section 5.3.2.1. However, there was no signs of strength degradation in the backbone curve up to the end of testing (2.5% drift ratio). Table 5.8 presents a summary of ADRS results for IPT11.8+GD+AX.

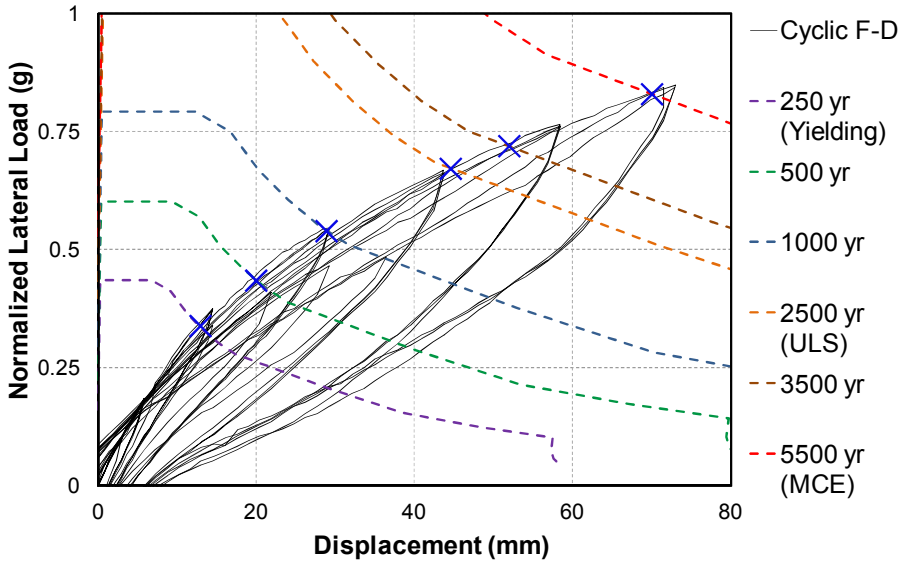

(a) Normalized lateral load - displacement

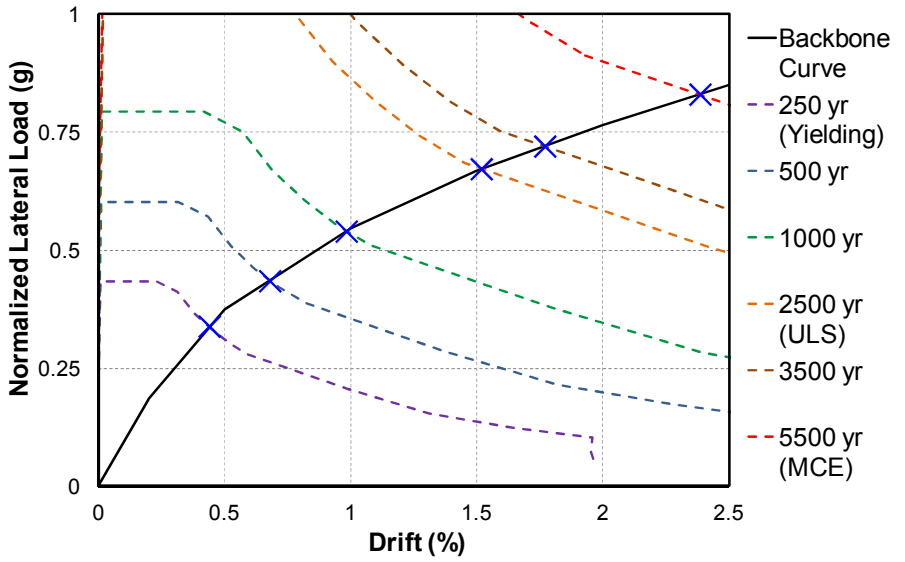

(b) Normalized lateral load - drift

Figure 5.50. ADRS plots for IPT11.8+GD+AX

Table 5.8. Summary of ADRS results for LDB under IPT11.8+GD+AX

Hazard Levels (Years)	Return Period Factor (R)	Ductility (μ)	Drift (%)	Corrected Equivalent Damping (ξ_{eq}) %
250	0.75	1	0.43	13.77
500	1.0	1.3	0.68	12.59
1000	1.3	1.9	0.98	12.24
2500	1.8	2.9	1.52	13.13
3500	2.0	3.3	1.77	13.52
5500	2.4	4.5	2.39	13.16

The energy dissipation plot is presented in Figure 5.51. The noticeable drop in energy dissipation after the first cycle of the loading, especially during the larger drift ratios, was due to strength degradation in the grooved dissipaters under cyclic loading.

By comparing the cumulative dissipated energy at 1.5% and 2.5% drift ratio for LDB with internal shear keys (IPT5+GD+AX) and LDB with external shear keys (IPT11.8+GD+AX), the latter had 13% and 32% less energy dissipation capacity, respectively. This was due to the fact that friction dissipation was eliminated in the testing of LDB under IPT11.8+GD+AX. At the same time, a higher level of post-tensioning (self-centering ratio) was adopted in the design of DCR connections.

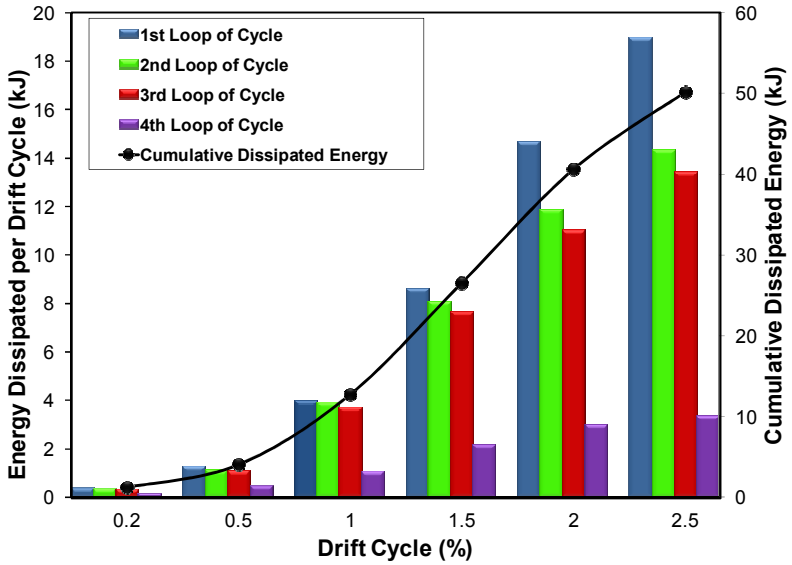

Figure 5.51. Dissipated energy (per cycle and cumulative) for IPT11.8+GD+AX

A comparison of performance factors from the experimental testing of HDB and LDB with grooved dissipaters and internal/external shear keys is summarized in Table 5.9. The drift ratio at each performance level (e.g. yielding, ULS, and MCE) was adopted from the progressive collapse analysis and ADRS plot for HDB and LDB, respectively.

In Table 5.9,

Δ = drift ratio in (%)

V_b = Base shear force for the bent in (kN)

Δ_{Res} = Residual drift (%)

μ = Displacement ductility

ξ_{hyst} = Corrected area-based hysteretic damping in (%)

HDB = High Damage Bent (refer to Section 3.3 in Chapter 3)

LDB-INT = Low Damage Bent with internal shear keys (Section 5.3.2.1)

LDB-EXT = Low Damage Bent with external shear keys (Section 5.4.2.1)

Table 5.9. Comparison of performance factors from testing of HDB and LDB with grooved dissipaters and internal/external shear keys

Specimen	Performance Levels												
	Yielding			ULS					MCE				
	Δ (%)	V_b (kN)	Δ_{Res} (%)	Δ (%)	V_b (kN)	μ	ξ_{hyst} (%)	Δ_{Res} (%)	Δ (%)	V_b (kN)	μ	ξ_{hyst} (%)	Δ_{Res} (%)
HDB	0.82	280	0.14	2.7	370	3.3	11	1.3	3.4	360	4.1	13.5	1.8
LDB - INT	0.53	190	0.23	1.47	290	2.8	8.84	0.4	2.5	357	4.7	12.54	0.95
LDB - EXT	0.53	195	0	1.52	316	2.9	7.85	0.1	2.5	400	4.7	9.85	0.2

In summary, testing of LDB with external shear keys and grooved dissipaters showed a very improved performance of the bent. The bent showed a clear flag-shaped hysteresis with negligible residual displacement during the larger drift ratios. There was no premature failure of the grooved dissipaters throughout testing. In comparison to HDB,

the bent did not suffer any significant structural damage except some cosmetic damage (e.g. a opening of a few existing hairline cracks and superficial spalling). The bent achieved good levels of hysteretic damping and displacement ductility. There were no signs of strength degradation under cyclic loading up to the 2.5% drift ratio from the force-drift hysteresis plot.

Given the strength degradation of the grooved dissipater under cyclic loading, the dissipater can be susceptible to low-cycle fatigue failure after several cycles of large drift ratio. For a real life ABC Low Damage bridge, the external dissipaters would have to be replaced with new ones following a big earthquake. The replacement of the dissipaters and repairs of hairline cracking would be the only post-earthquake renovation works required for the bridge.

In the next section, LDB is tested with Mini UFP Dissipater (MUD) for an enhanced performance. A combination of MUD and GD is also developed and tested. This aims to eliminate the aforementioned cosmetic damage in the columns, as well as any low-cycle fatigue failure of the dissipaters during a big earthquake. For a real life ABC Low Damage bridge, this solution will ideally eliminate any damage, and hence there will be no post-earthquake repairs needed for the bridge.

5.4.3 Part-III: LDB with Post-Tensioning and MUDs

In this part of testing, LDB was tested with Mini UFP Dissipaters (MUDs) instead of Grooved Dissipaters (GDs). The grooved dissipaters from the previous test (IPT11.8+GD+AX) were removed. Two MUDs were plugged in at each DCR connection (Figure 5.52). In a typical DCR connection, MUDs were located at the East and West sides of the connection where the maximum gap opening occur during rocking of the column. This was due to the fact that MUD can undergo many cycles of large drift ratio without any noticeable strength degradation or low-cycle fatigue failure. This feature makes the application of MUDs in DCR connection more attractive.

MUDs used in this part of testing had similar height compared to grooved dissipaters in the previous test. This had simplified the installation process of the damper between the bracket and armoring plate in the DCR connection. Each MUD had a capacity of 25 kN with a stroke of ± 25 mm as previously discussed in Section 5.2.3. The lower capacity of MUD was due to the limited facilities in the lab to roll thicker steel plate into double UFPs. However, using thicker steel plate, the capacity of MUD can be increased to an equivalent grooved dissipater used in this research (71 kN).

Three tests were carried out without applying gravity to validate the concept of MUD in the DCR connection. The tests incorporated increasing level of initial post-tensioning to provide a general insight into the performance of the bent. The higher level of post-tensioning was expected to provide higher self-centering ratio in the bent which in return would decrease energy dissipation capacity. The tests also aimed to provide an insight into the response of MUD with post-tensioning for a variety of self-centering ratios. Three levels of the initial post-tensioning were selected to be 20 kN, 40 kN, and 100 kN for each Macalloy bar which corresponded to 1.8%, 3.6%, and 9% of the yield strength of the bar, respectively.

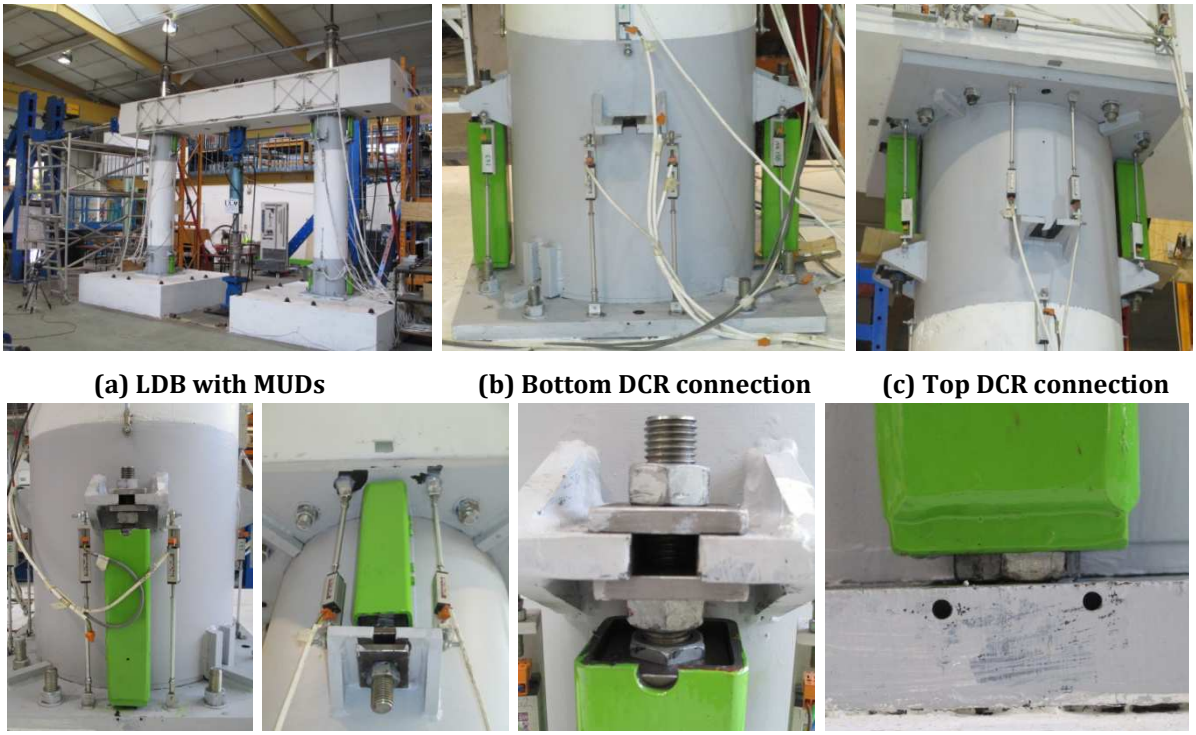

(a) LDB with MUDs **(b) Bottom DCR connection** **(c) Top DCR connection**

(d) Bottom MUD **(e) Top MUD** **(f) Typical bracket fixing** **(g) Typical base plate fixing**

Figure 5.52. Application of MUD at the DCR connections of LDB

5.4.3.1 LDB with 1.8%IPT and Mini UFP Dissipaters (IPT1.8+MUD)

The design of DCR connection was similar to what described previously for the other tests. In this regards, experimental results on MUDs from Chapter 4 were utilized for the design of the DCR connection. Table 5.10 presents a summary of the design parameters for the bent.

Table 5.10. Summary of design parameters for LDB with IPT1.8+MUD

Performance Level	Self-Centering ratio (λ)	Drift (δ)	Base Shear (V_b)
Yielding	12.5	0.43	35
ULS	6.9	2.2	152

Gap opening started during the 0.25% drift ratio. The maximum gap opening was 11 mm during the 2.2% drift ration (ULS). The activation of MUDs at the DCR connection was visible during rocking of the column throughout testing (Figure 5.53).

(a) Start of the test **(b) Maximum gap opening at 2.2% drift ratio**

Figure 5.53. Activation of MUD in a typical DCR connection

The force-drift hysteresis is shown in Figure 5.54. The bent showed a very symmetrical hysteresis. The smaller enclosed area in the hysteresis suggests small energy dissipation capacity of the bent. The capacity of LDB at ULS was less than 305 kN (HDB design base shear). This was due to smaller capacity of MUDs, lower initial post-tensioning force, and absence of gravity.

Figure 5.54 shows residual drift of 0.2% in the bent. It is important to note that there was a small gap that had to be left between the face of the external shear key and outer face of the column (approximately 3 mm or 0.1% drift ratio), see Figure 5.39f. This means that the actual residual drift in the bent was in fact 0.1% drift ratio.

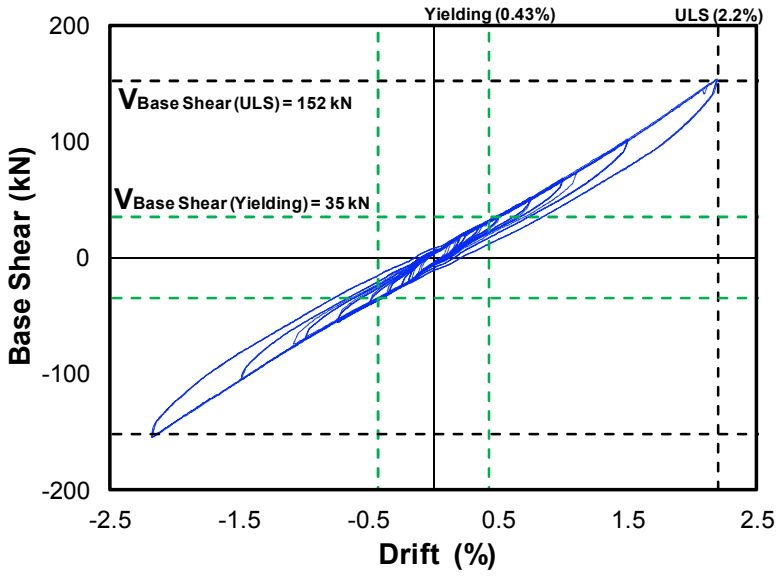

Figure 5.54. LDB force-drift hysteresis for IPT1.8+MUD

The axial force-drift hysteresis for each Macalloy bar is plotted in Figure 5.55. The response was similar to what discussed previously for the tests explained in Section 5.4.1. There was some drop in the post-tensioning. However, this was thought to be due to low level of initial post-tensioning (1.8% of the yield strength of the bar).

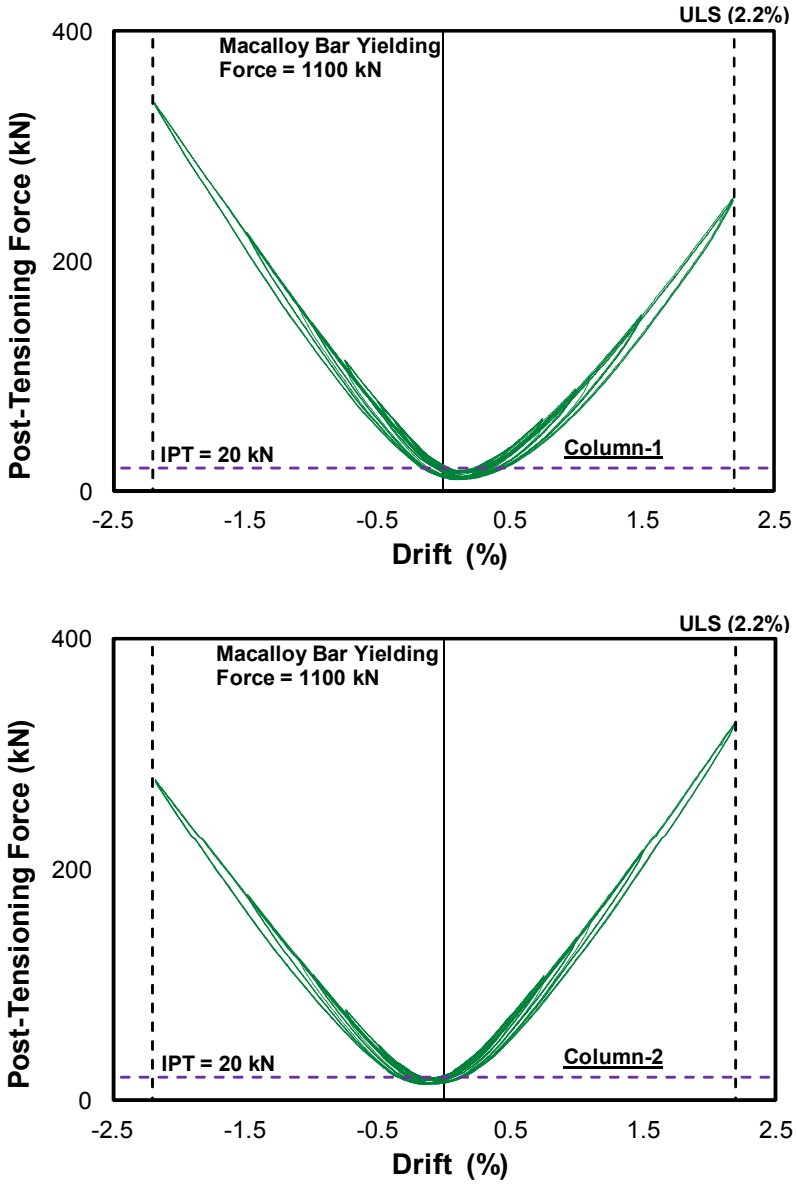

Figure 5.55. Post-tensioning force-drift hysteresis for IPT1.8+MUD

5.4.3.2 LDB with 3.6%IPT and Mini UFP Dissipaters (IPT3.6+MUD)

In this test the level of initial post-tensioning was increased to 3.6%. This means that the capacity of the bent and the self-centering ratio would be slightly higher at the ULS drift ratio. Table 5.11 presents a summary of the design parameters for the bent.

Table 5.11. Summary of design parameters for LDB with IPT3.6+MUD

Performance Level	Self-Centering ratio (λ)	Drift (δ)	Base Shear (V_b)
Yielding	15.2	0.43	41
ULS	7.8	2.2	170

The first gap opening started during the 0.5% drift ratio. At the ULS drift ratio (2.2%), the gap opening was measured to be 10 mm.

The overall behavior was similar to that of IPT1.8+MUD. The force-displacement hysteresis is plotted in Figure 5.56. The bent behaved symmetrically with almost zero actual residual displacement.

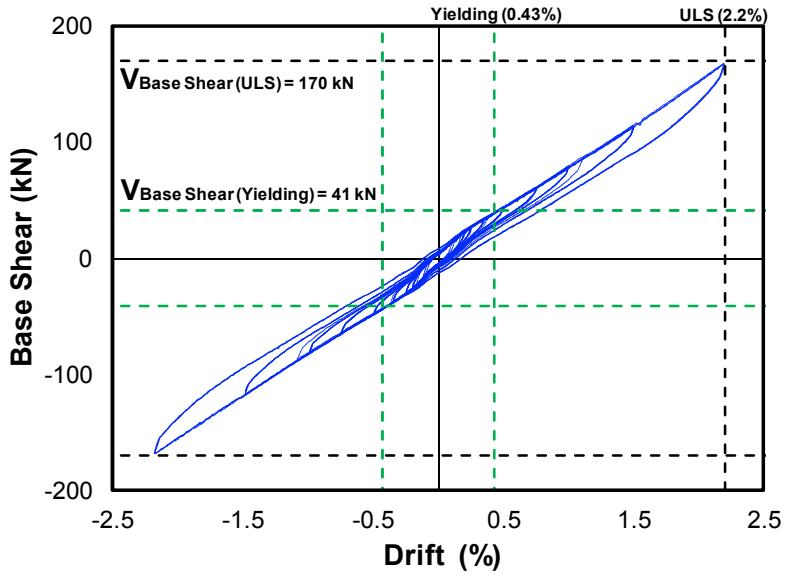

Figure 5.56. LDB force-drift hysteresis for IPT3.6+MUD

Figure 5.57 present hysteresis for the Macalloy bars. The behavior was improved due to higher level of initial post-tensioning. There was negligible drop in the post-tensioning force throughout testing.

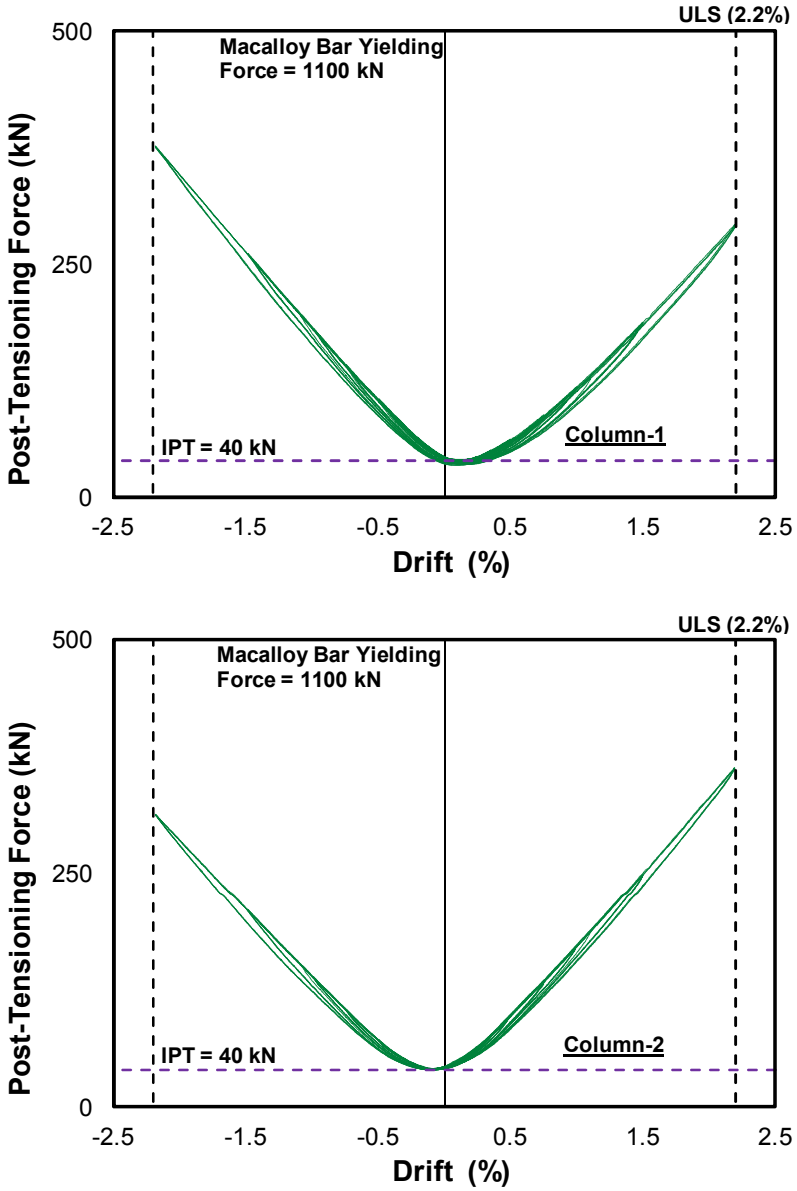

Figure 5.57. Post-tensioning force-drift hysteresis for IPT3.6+MUD

5.4.3.3 LDB with 9%IPT and Mini UFP Dissipaters (IPT9+MUD)

In this test, the level of initial post-tensioning was increased to 9%. This was expected to result into very high self-centering ratio for the bent at the ULS performance level. Similarly, the capacity of the bent was predicted to be higher compared to the other two previous tests. Table 5.12 presents a summary of the design parameters for the bent.

Table 5.12. Summary of design parameters for LDB with IPT9+MUD

Performance Level	Self-Centering ratio (λ)	Drift (δ)	Base Shear (V_b)
Yielding	23.2	0.43	61
ULS	9.1	2.2	195

The first gap opening was observed during the cycles of the 0.75% drift ratio. There was approximately 10 mm gap opening during the 2.2% drift ratio. The bent behaved similar to the other two previous tests. However, the force-drift hysteresis showed a more visible flag-shaped response and higher self-centering of the bent with almost zero actual residual displacement, as shown in Figure 5.58.

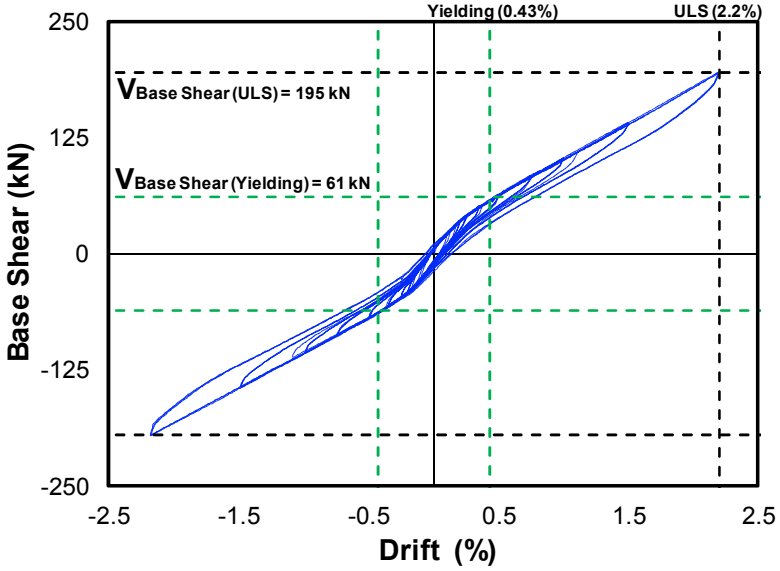

Figure 5.58. LDB force-drift hysteresis for IPT9+MUD

The axial force-drift hysteresis plot for the post-tensioning is presented in Figure 5.59. The bars did not show any noticeable drop in the initial post-tensioning during testing.

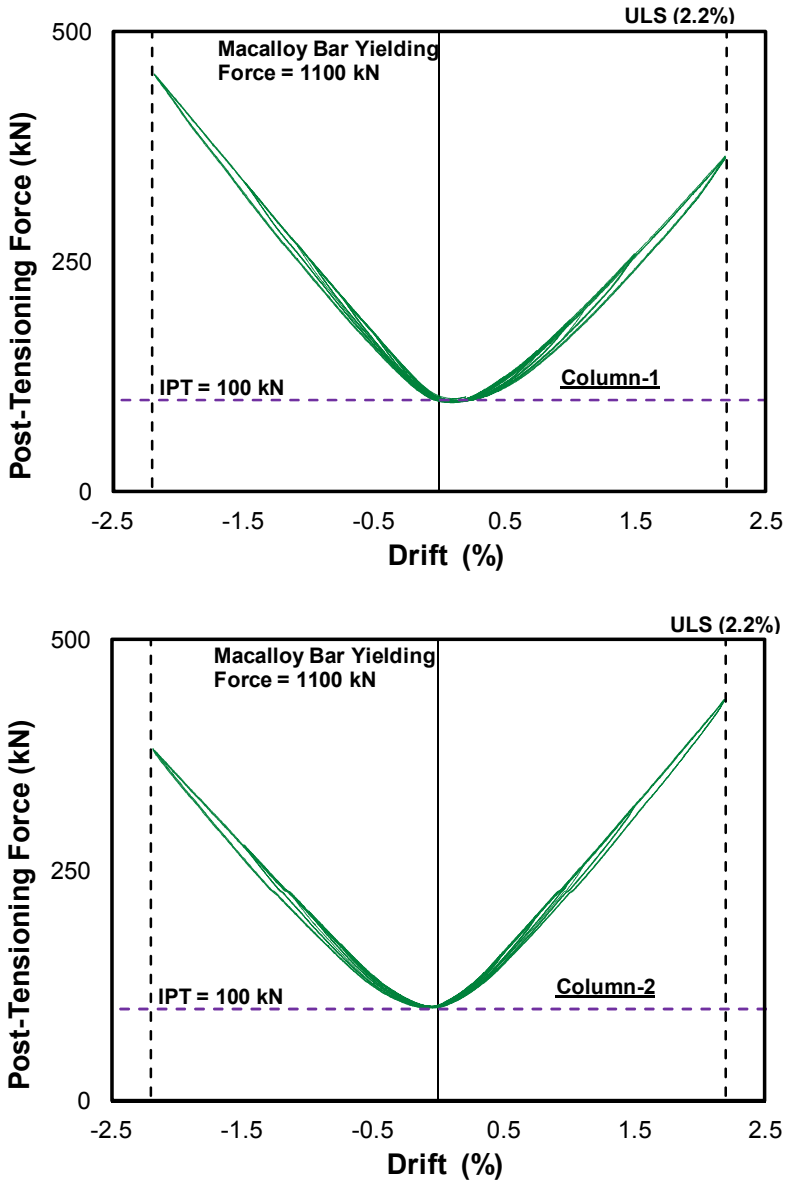

Figure 5.59. Post-tensioning force-drift hysteresis for IPT9+MUD

In summary, testing of LDB with MUD and post-tensioning showed a good performance of the bent. Following testing, there was almost zero residual displacement in the bent. The small residual drift noticeable in the force-drift hysteresis plot was mainly caused by the 3 mm construction gap that had to be left between the face of the external shear key and outer face of the column. Because of lower capacity of MUDs used in this part of testing, the base shear and the energy dissipation capacity were considerably lower than those in the testing of IPT5+GD+AX and IPT11.8+GD+AX. It was expected that the presence of gravity would increase the capacity of the bent to a considerable extent. Therefore, in the next part of the testing, gravity applied to investigate the performance of MUD with post-tensioning in the presence of gravity.

5.4.4 Part-IV: LDB with Post-Tensioning, MUDs, and Gravity

This part of testing investigated the response of LDB with post-tensioning, Mini UFP Dissipater (MUD), and gravity. The only difference between this test and that discussed in the previous section (IPT9+MUD) was the presence of superstructure weight (gravity) on the bent. This test was intended to show how much the presence of gravity would change the hysteretic response of the bent.

The capacity of the bent was predicted to reach the design base shear force (305 kN) at a higher drift ratio (2.5%) than the ULS drift ratio (2.2%). This was due to lower capacity of the fabricated MUDs as explained earlier.

5.4.4.1 LDB with 9%IPT, MUD, and Gravity (IPT9+MUD+AX)

Table 5.13 presents a summary of the design parameters for the bent.

Table 5.13. Summary of design parameters for LDB with IPT9+MUD+AX

Performance Level	Self-Centering ratio (λ)	Drift (δ)	Base Shear (V_b)
Yielding	48	0.43	122
ULS	13	2.2	269

The behavior was similar to that observed in testing of LDB under IPT9+MUD. Gap opening started during the 0.35% drift ratio and continued to increase to 12 mm during the 2.5% drift ratio. A summary of the gap opening is presented in Table 5.14 at different drift ratios during testing.

Table 5.14. Summary of the maximum gap opening for IPT9+MUD+AX

	Drift Ratios (%)						
	0.35	**0.5**	**1.0**	**1.5**	**1.8**	**2.2**	**2.5**
Column 1 to Footing DCR (mm)	0.5	2	6	8	10	11	12
Column 2 to Footing DCR (mm)	0.5	1.5	5	8	9	10	12

During testing, some existing cracks from the previous tests were opening in the cap beam and footings. However, they well remained of hairline thickness throughout testing. The existing hairline cracks in the column from the testing of LDB under IPT5+GD+AX did not seem to open up. This was due to lower capacity of MUDs, as well

as lower strain hardening stiffness of the dissipaters compared to that of the grooved dissipaters.

The force-drift hysteresis is presented in Figure 5.60. It is important to note that in all testing carried out in this study, the MCE level was taken as the drift ratio at the end of the test. From Figure 5.60, the bent showed a very symmetrical flag-shaped hysteresis with very high self-centering. The capacity of the bent was lower than 305 kN during the 2.2% drift ratio. The bent achieved the capacity of nearly 305 kN during the cycles of the 2.5% drift ratio. There was no signs of strength degradation or fatigue failure in MUDs even after taking dozens of loading cycles beyond the yield point from the previous tests and during IPT9+MUD+AX.

Following the cycles of the 2.5% drift ratio, the residual displacement in the bent was nearly zero. This was lower than that of LDB with the grooved dissipaters (IPT11.8+GD+AX) which showed 0.2% residual drift ratio, refer to Section 5.4.2.1.

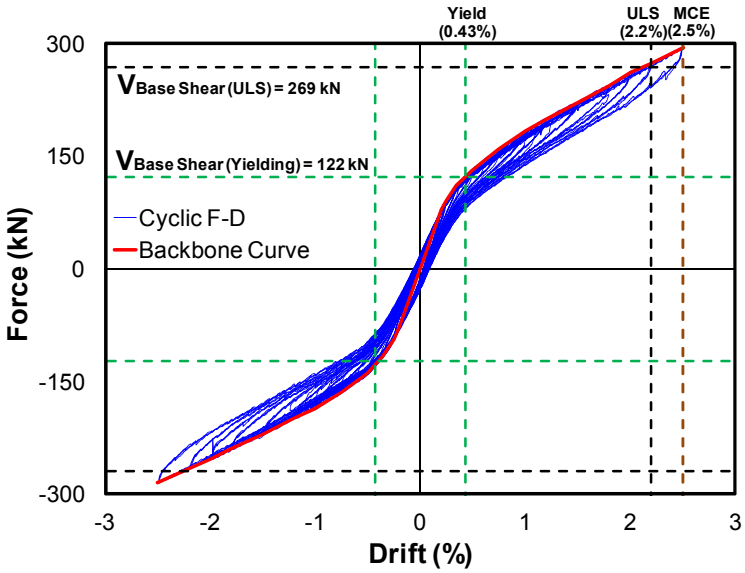

Figure 5.60. Force-drift hysteresis for IPT9+MUD+AX

Figure 5.61 presents response of the post-tensioning. By comparing the behavior to that of IPT9+MUD (Figure 5.59), the post-tensioning showed a very symmetrical behavior. This was thought to had been influenced by the presence of gravity which had prevented from any slacking and post-tensioning losses in the bars. The depth of the rocking contact (Neutral Axis) is plotted against drift in Figure 5.61c for the bottom DCR connection in Column-1. The plot suggests good performance of the connection.

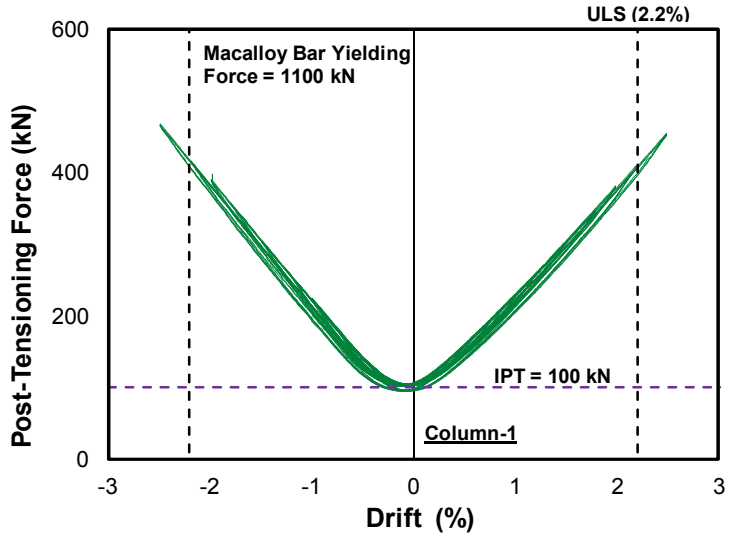

(a) Column - 1 post-tensioning-drift hysteresis

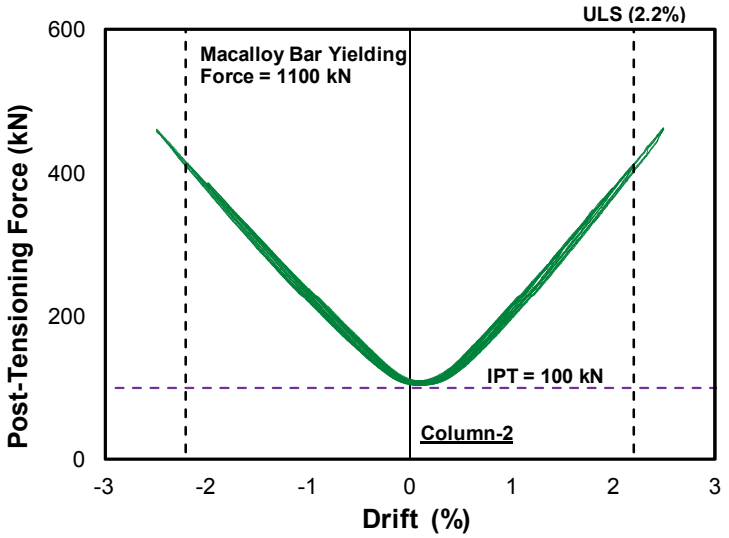

(b) Column - 2 post-tensioning-drift hysteresis

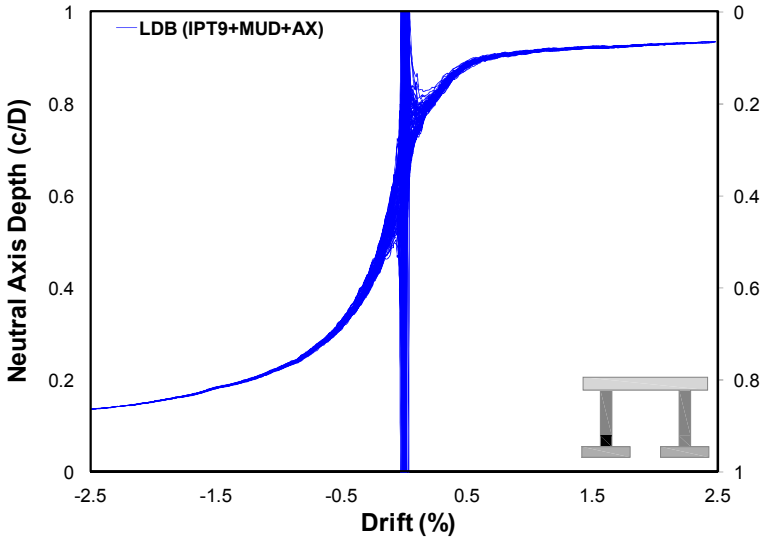

(c) Neutral axis depth-drift hysteresis

Figure 5.61. Post-tensioning and neutral axis plots for IPT9+MUD+AX

The corrected area-based damping (hysteretic damping) is plotted in Figure 5.62a. The plot shows a relatively bi-linear relationship between the hysteretic damping and the displacement ductility.

The maximum hysteretic damping was 4.8% at the displacement ductility of 6.8 which corresponded to the 2.5% drift ratio. The bent had values of hysteretic damping lower than those from theoretical flag-shaped ($\beta = 0.35$) model for the values of ductility beyond 2. This was thought to be due to higher re-centering ratio which means less energy dissipation capacity in the bent. The EVD plot is presented in Figure 5.62b.

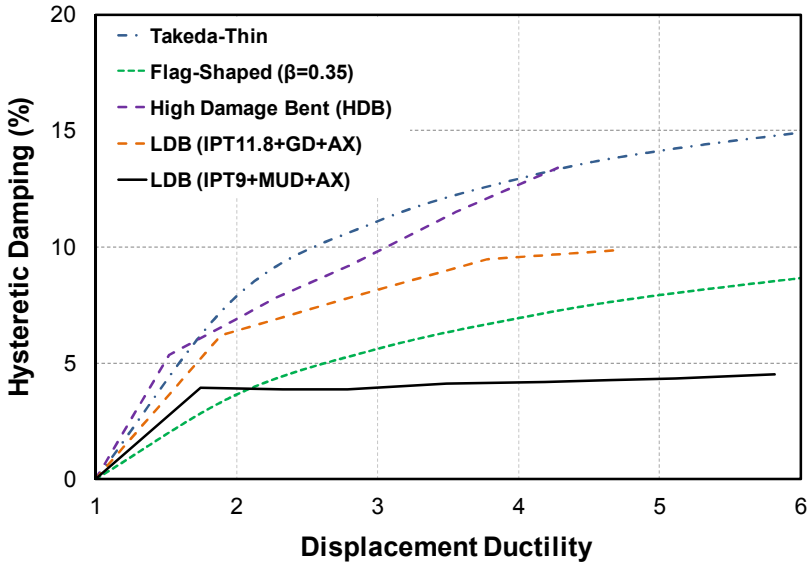

(a) Corrected area-based hysteetic damping (ξ_{hyst})

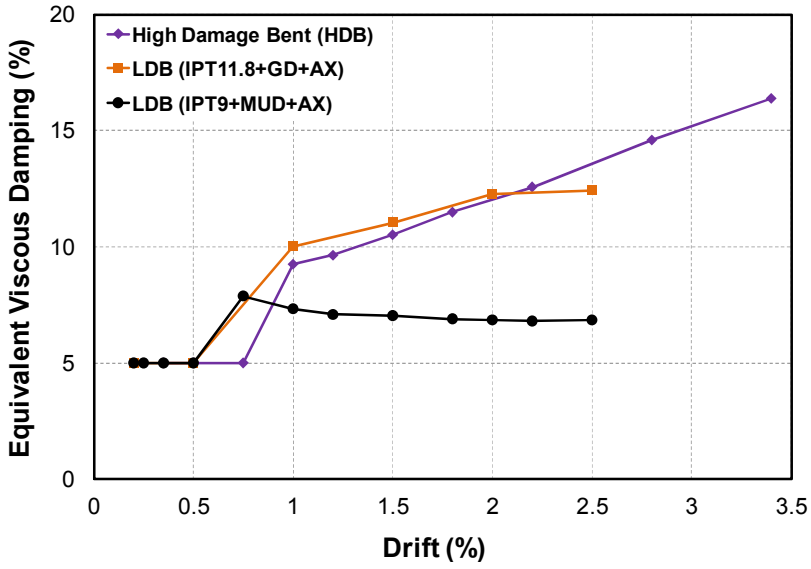

(b) Equivalent viscous damping (ξ_{eq})

Figure 5.62. Hysteretic damping and EVD plots for IPT9+MUD+AX

The ADRS plot is presented in Figure 5.63 for various hazard levels (return periods) from NZS 1170.5 (NZS, 2004). It is obvious that the bent did not achieve its design level performance point (2500 years return period). This was because of smaller energy dissipation due to lower capacity of the dissipaters. Compared to the previous tests of LDB with the presence of gravity, the post-yield stiffness of the bent was lower in Figure 5.63. This is because MUD has lower strain hardening stiffness (similar behavior to an elasto-plastic model) compared to that of the grooved dissipater or reinforcing bar (bi-linear).

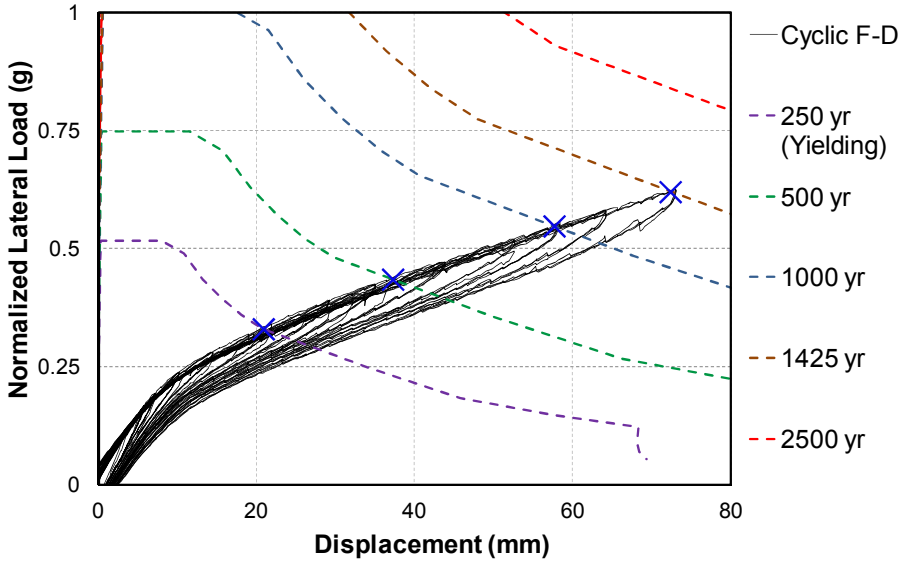

(a) Normalized lateral load - displacement

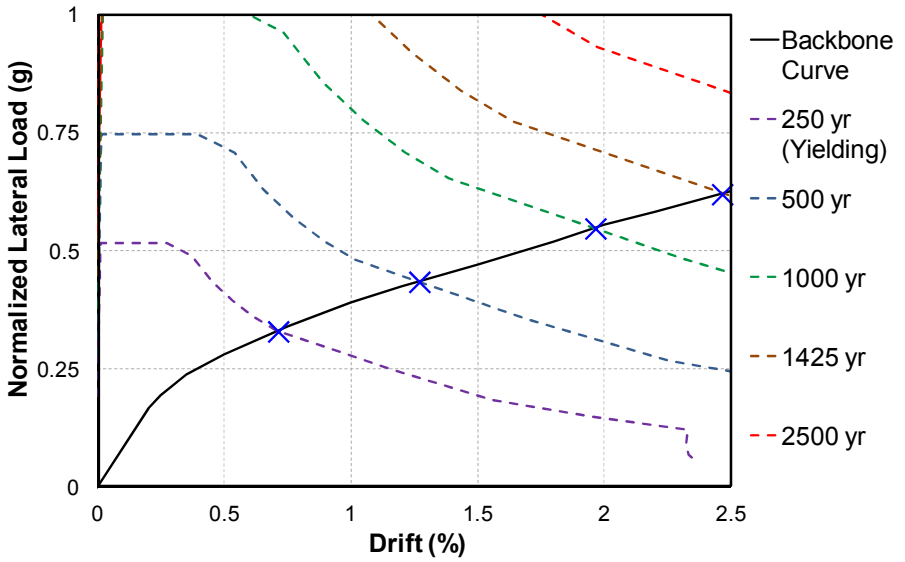

(b) Normalized lateral load - drift

Figure 5.63. ADRS plots for IPT9+MUD+AX

Table 5.15 presents a summary of the ADRS results for IPT9+MUD+AX. The decreasing values of ξ_{eq} with increasing drift ratio is due to the elastic tangent damping ($\xi_{el,\ tangent}$) which decreases with ductility increases, refer to Equation 3.18 in Chapter 3. Since the capacity of MUD was low, it resulted into smaller values for the hysteretic damping and therefore, ξ_{eq} was more influenced by $\xi_{el,\ tangent}$ at each level of ductility. The hysteretic damping plot in Figure 5.62a does not show a decreasing curve for the hysteretic damping with increasing values of ductility.

Table 5.15. Summary of ADRS results for LDB under IPT9+MUD+AX

Hazard Levels (Years)	Return Period Factor (R)	Ductility (μ)	Drift (%)	Corrected Equivalent Damping (ξ_{eq}) %
250	0.75	1.7	0.73	9.16
500	1.0	3	1.3	7.48
1000	1.3	4.6	2	6.66
1425	1.5	6.2	2.5	6.24

The energy dissipated per each cycle of each drift ratio is presented in Figure 5.64. The bent had less reduction in energy dissipation capacity between the first and the other two consecutive cycles at each drift ratio. As an example, this reduction was in order of 24.5% between the first and second cycles at the 2.5% drift ratio for testing of LDB with the grooved dissipaters (IPT11.8+GD+AX, Figure 5.51). However, this reduction was only 2% between the same cycles at the same drift ratio for LDB with MUD, as shown in Figure 5.64. This once again confirms the insignificant strength degradation in MUD compared to that in GD or reinforcing bar under cyclic loading.

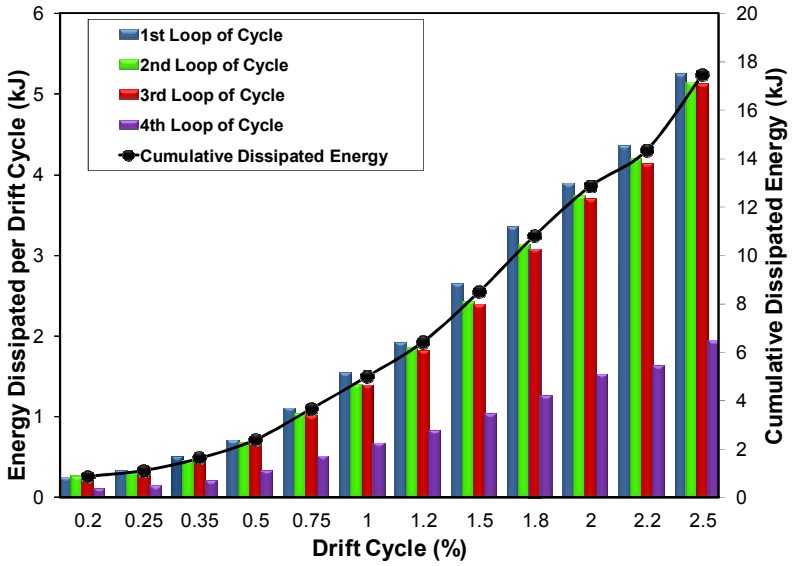

Figure 5.64. Dissipated energy (per cycle and cumulative) for IPT9+MUD+AX

In summary, testing of LDB with MUD, post-tensioning, and gravity showed a good performance of the bent with zero residual displacement. The testing confirmed the concept of using MUD in the locations of higher gap opening. The dissipater was not susceptible to low-cycle fatigue failure. There was not any noticeable reduction in energy dissipation capacity of MUD throughout testing. After almost dozens of testing, all MUDs stayed intact. For a real life ABC Low Damage bridge this means that the dissipaters will not have to be replaced following a big earthquake.

Despite a good performance, the bent had less base shear capacity, energy dissipation, and hysteretic damping compared to LDB with the grooved dissipaters. However, this was due to smaller capacity of MUDs used in this testing. The reason behind this was the limitations on rolling thicker steel plate to make double UFPs in the lab. As mentioned in Chapter 4, the rolling machine to fabricate double UFPs was a recycled hand-operated equipment that was originally designed for bending rebars to stirrups. Using thicker steel plate and proper rolling equipment, MUD can be made with any desirable capacity in a fabricator shop. Thus, it can be made to match the capacity of that of grooved dissipater which would enhance the aforementioned performance parameters. Another alternative is using a combination of MUD and GD in DCR connection. This is investigated in the next section.

5.4.5 Part-V: LDB with Post-Tensioning, MUDs, and GDs

In this part of testing, a combination of MUD and GD in DCR connection was investigated. The dissipaters from the previous part of testing (MUD) were left at their locations (East and West sides of the column) where maximum gap opening occur during lateral loading. New GDs were installed on the North and South faces of the column where smaller gap opening was expected. GDs were intended to provide extra capacity and energy dissipation for the DCR connection while being less susceptible to any low-cycle fatigue failure due to the novel arrangement, as shown in Figure 5.65.

As explained earlier, GD has a higher post-yield stiffness compared to that of MUD. This means that the more the dissipater is stretched, the more force in the dissipater due to strain hardening effect. In contrast, MUD has a more elastic-perfectly plastic hysteresis response which would minimize the chance for formation of flexural cracks even during a big gap opening in the connection.

The increase due to strain hardening effect in GD may cause tension stresses bigger than the concrete modulus of rupture. This may cause formation of hairline cracks at the portion of the column near the armoring shoe (Figure 5.27). The cracks in the column would require minor repair work following the earthquake. In this part of testing, this problem was solved by arranging GDs such that the possibility for cracking is kept at its minimum.

In order to validate the concept for a combination of MUD and GD in LDB, initially three tests with post-tensioning without gravity were carried out. The tests incorporated increasing level of initial post-tensioning to provide an insight into the performance of the bent in terms of base shear, self-centering ratio, and energy dissipation capacity.

Three levels of the initial post-tensioning were selected to be 100 kN, 125 kN, and 150 kN for each Macalloy bar which corresponded to 9%, 11.4%, and 13.6% of the yieldistrength of the bar, respectively.

(a) New plug and play GD

(b) LDB with a combination of MUD and GD in DCR connections

(c) Typical bottom DCR connection

(d) Typical top DCR connection

Figure 5.65. Application of MUD and GD at the DCR connections of LDB

In summary, the arrangement of dissipaters (MUD and GD) used here was intended for an improved ABC Low Damage system with below objectives:

1. Integration of simple plug and play dissipaters.
2. Assurance on full self-centering of the bridge following a big earthquake.
3. Avoidance of spalling and formation of hairline flexural cracks in the columns.
4. Elimination of the need for replacement of the dissipaters following dozens of earthquakes or aftershocks.
5. Arrangement of the dissipaters not only for structural purpose, but also for aesthetic.

5.4.5.1 LDB with 9%IPT, Mini UFP, and Grooved Dissipaters (IPT9+MUD+GD)

The design of the DCR connection was based on the PRESSS Design Handbook. Table 5.16 presents a summary of the design parameters for the bent.

Table 5.16. Summary of design parameters for LDB with IPT9+MUD+GD

Performance Level	Self-Centering ratio (λ)	Drift (δ)	Base Shear (V_b)
Yielding	2.7	0.53	81
ULS	2.4	2.2	236

Gap opening initiated during the 0.5% drift ratio and kept increasing to 11 mm during the 2.2% drift ratio. The activation of MUD and GD in a typical DCR connection in LDB was visible during the rocking of the columns (Figure 5.66).

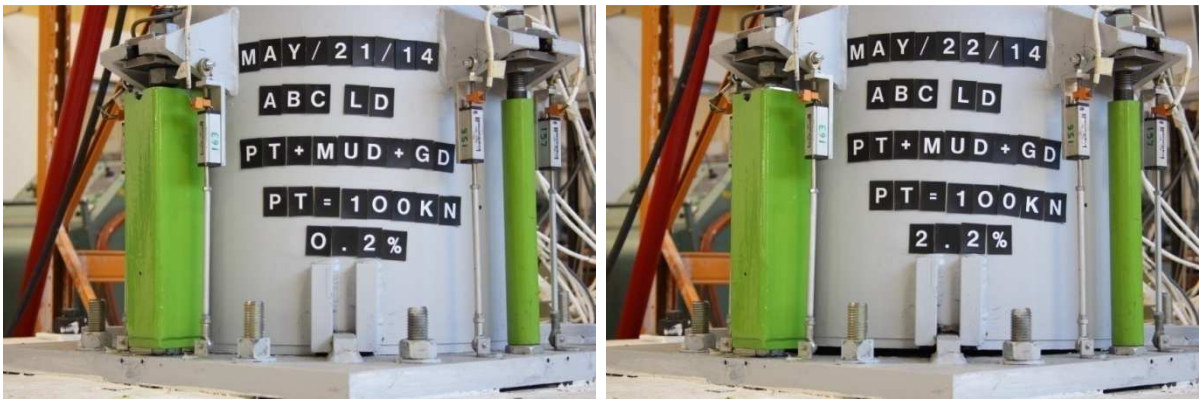

(a) Start of the test **(b) Maximum gap opening at 2.2% drift ratio**

Figure 5.66. Activation of MUD and GD in a typical DCR connection in LDB

Figure 5.67 presents the force-drift hysteresis for LDB. The bent showed a symmetrical response. In comparison to IPT9+MUD (Figure 5.58), the addition of GDs had increased the capacity and energy dissipation of the bent.

Following the cycles of the 2.2% drift ratio, the net residual displacement in the bent was less than 4.5 mm (0.15% drift ratio) which is insignificant.

Figure 5.68 presents hysteresis response of the post-tensioning. The response was very similar to what observed during testing of IPT9+MUD (Figure 5.59).

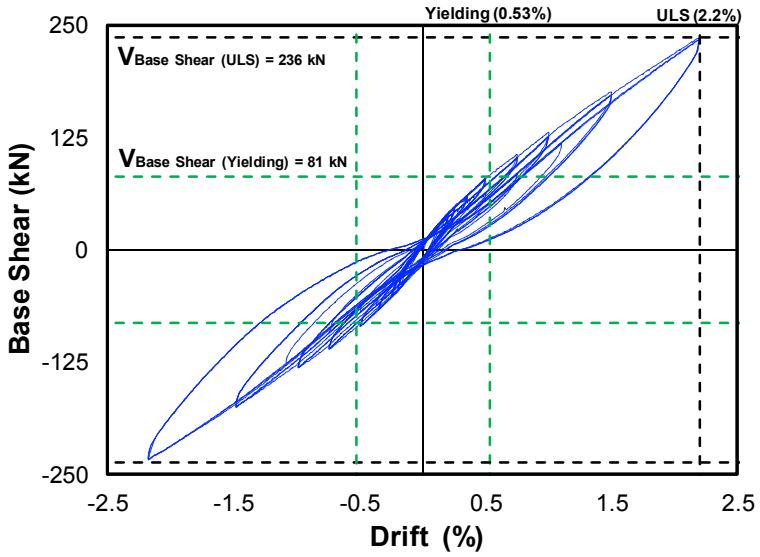

Figure 5.67. LDB force-drift hysteresis for IPT9+MUD+GD

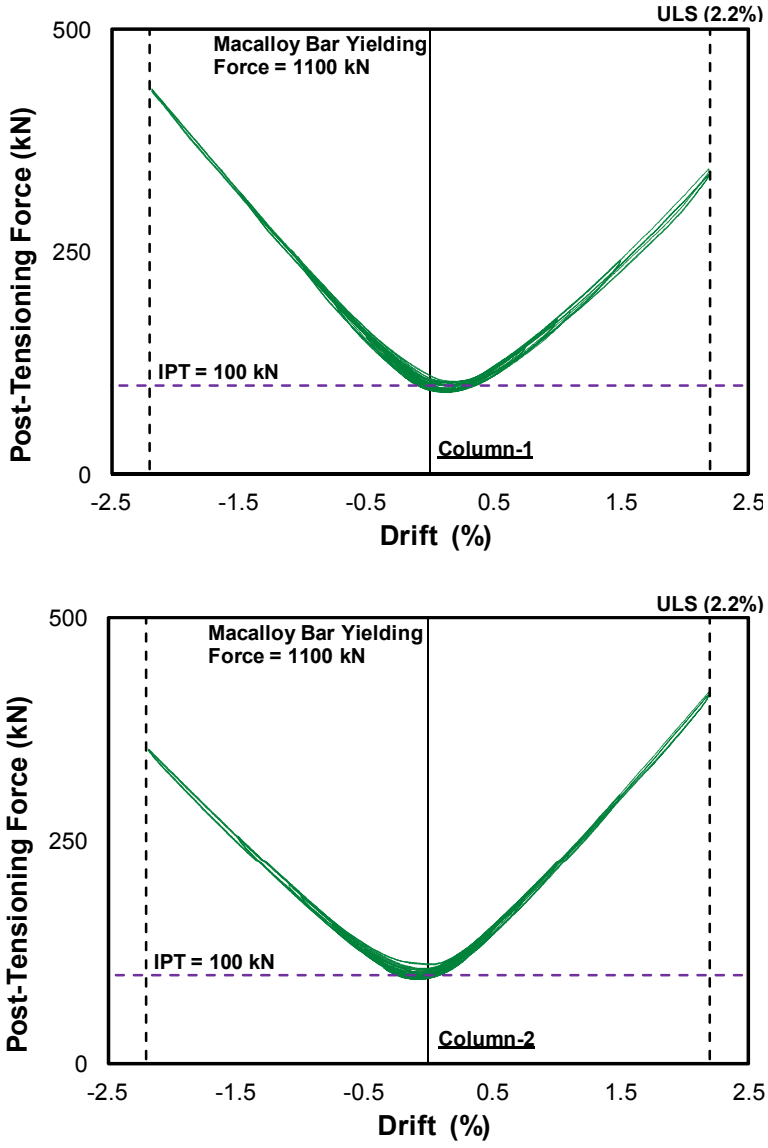

Figure 5.68. Post-tensioning force-drift hysteresis for IPT9+MUD+GD

5.4.5.2 LDB with 11.4%IPT, Mini UFP, and Grooved Dissipaters (IPT11.4+MUD+GD)

In this test, the initial post-tensioning force was slightly increased by 25 kN. This resulted into small increase in the self-centering ratio at the ULS level.

Table 5.17 presents a summary of the design parameters for the bent.

Table 5.17. Summary of design parameters for LDB with IPT11.4+MUD+GD

Performance Level	Self-Centering ratio (λ)	Drift (δ)	Base Shear (V_b)
Yielding	3.1	0.53	88
ULS	2.5	2.2	244

The gap opening was measured to be similar to what observed in testing of LDB under IPT9+MUD+GD as presented in the previous section.

The force-drift hysteresis is plotted in Figure 5.69. Given the small increase in the initial post-tensioning, the capacity of the bent and the self-centering ratio were slightly higher. This had resulted into less energy dissipation in the bent compared to that of IPT9+MUD+GD (Figure 5.67). The initial stiffness of the bent was also lower than that for IPT9+MUD+GD which was due to previous yield of the GDs. Following testing, there was less than 3 mm net residual displacement (0.1% drift ratio) in the bent.

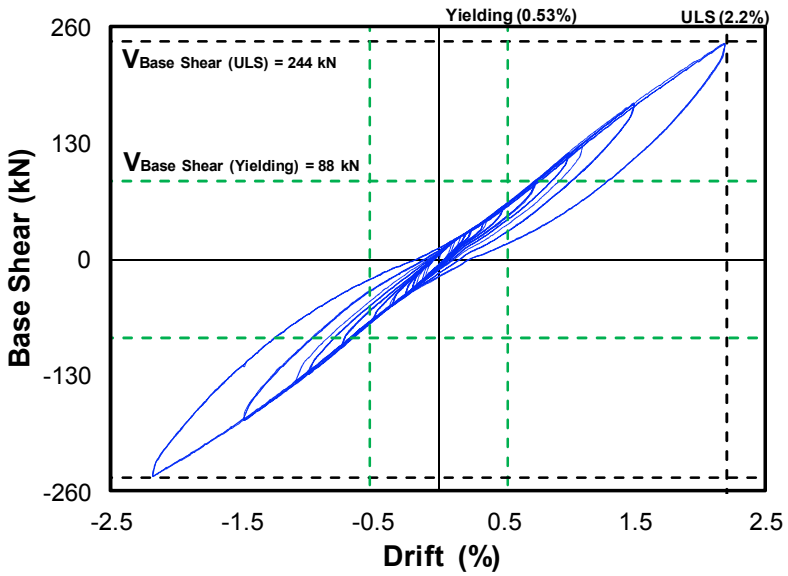

Figure 5.69. LDB force-drift hysteresis for IPT11.4+MUD+GD

The axial force-drift hysteresis plot for the post-tensioning (Figure 5.70) showed an improved behavior compared to that of IPT9+MUD+GD (Figure 5.68). This was due to higher initial post-tensioning which resulted into less slacking and drop in the post-tensioning.

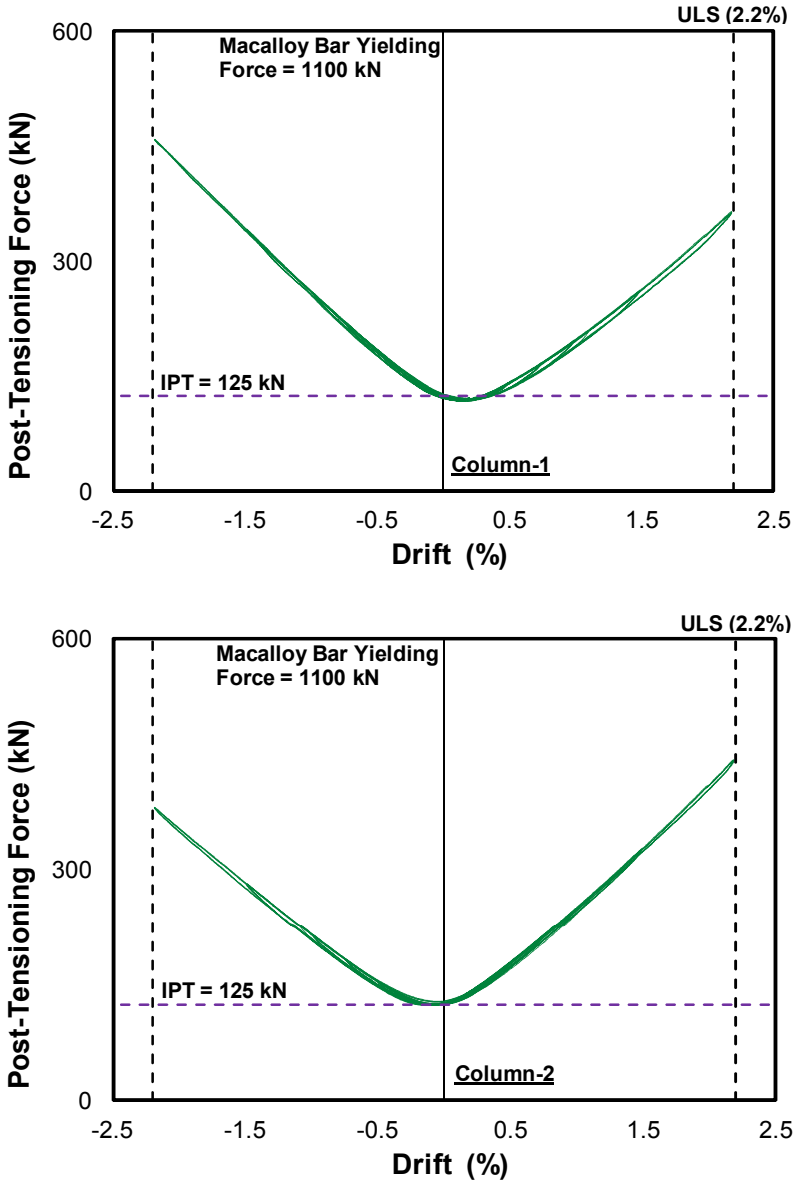

Figure 5.70. Post-tensioning force-drift hysteresis for IPT11.4+MUD+GD

5.4.5.3 LDB with 13.6%IPT, Mini UFP, and Grooved Dissipaters (IPT13.6+MUD+GD)

In this testing, a bigger self-centering ratio was targeted at the ULS performance level. This was done by increasing the level of initial post-tensioning in the column. Table 5.18 presents a summary of the design parameters for the bent.

Table 5.18. Summary of design parameters for LDB with IPT13.6+MUD+GD

Performance Level	Self-Centering ratio (λ)	Drift (δ)	Base Shear (V_b)
Yielding	3.6	0.53	96
ULS	2.6	2.2	252

The first gap opening was observed during the cycles of the 0.5% drift ratio. The largest gap opening was measured to be 10 mm during the cycles of the 2.2% drift ratio.

The force-drift hysteresis (Figure 5.71) suggests a symmetrical response of LDB with increased capacity at the ULS drift ratio. Following testing, there was little net residual displacement (less than 0.1% drift ratio) in the bent. Similarly, the axial force-drift hysteresis plot for the post-tensioning (Figure 5.72) was improved due to higher initial post-tensioning which had resulted into higher self-centering ratio.

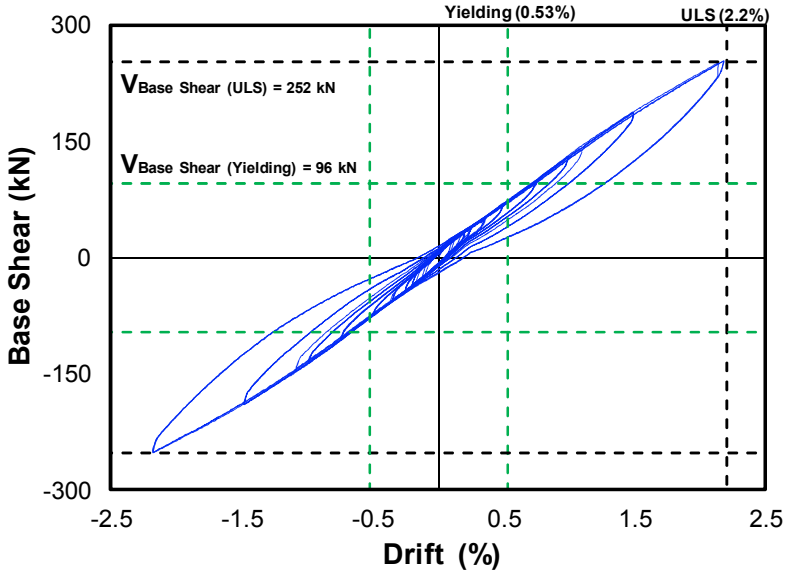

Figure 5.71. LDB force-drift hysteresis for IPT13.6+MUD+GD

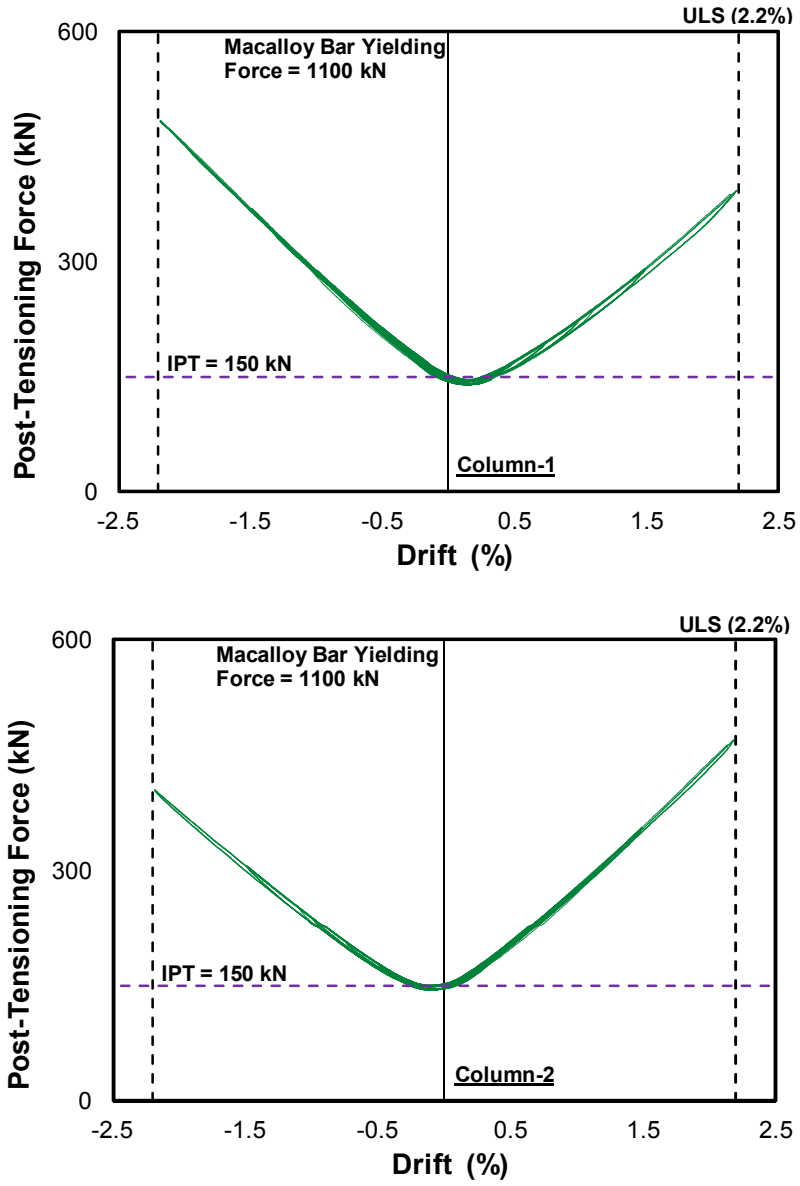

Figure 5.72. Post-tensioning force-drift hysteresis for IPT13.6+MUD+GD

In summary, testing of MUD and GD in Low Damage Bent (LDB) showed a very good performance. The dissipaters showed a very stable response of the bent. Despite being subjected to dozens of cycle beyond the yield point, there was no apparent strength degradation or low-cycle fatigue failure in the dissipaters. Testing of LDB with higher level of initial post-tensioning showed increased self-centering of the bent with lower energy dissipation. The residual displacement in the bent following the three tests with post-tensioning without gravity was almost zero. Similarly, there was no apparent damage including any hairline cracking to the columns throughout testing. In the next part of the testing, gravity was applied on the bent. The capacity of the bent was designed to match the base shear force in HDB (305 kN) at the ULS drift ratio (2.2%).

5.4.6 Part-VI: LDB with Post-Tensioning, MUDs, GDs, and Gravity

In this part of testing, the response of LDB with unbonded post-tensioning, Mini UFP Dissipaters (MUDs), Grooved Dissipaters (GDs), and gravity was investigated.

The arrangement of the dissipaters from the previous test (IPT13.6+MUD+GD) was unchanged. The vertical ram was connected to exert the superstructure weight (390 kN) on the bent. The level of initial post-tensioning in each Macalloy bar was set to 125 kN which corresponded to 11.4% of the yield strength of the bar.

5.4.6.1 LDB with 11.4%IPT, MUD, GD, and Gravity (IPT11.4+MUD+GD+AX)

The capacity of the bent was designed to match the base shear force of HDB (305 kN) at the ULS drift ratio (2.2%). Table 5.19 presents a summary of the design parameters for the bent.

Table 5.19. Summary of design parameters for LDB with IPT11.4+MUD+GD+AX

Performance Level	Self-Centering ratio (λ)	Drift (δ)	Base Shear (V_b)
Yielding	6.5	0.53	149
ULS	3.5	2.2	315

The first gap opening was observed during the cycles of the 0.5% drift ratio. There was 10 mm gap opening during the cycles of the 2.2% drift ratio. During the cycles of the 3% drift ratio, the maximum gap opening was measured to be 15 mm. Table 5.20 presents a summary of the observed gap opening at different drift ratios throughout testing.

Table 5.20. Summary of the maximum gap opening for IPT11.4+MUD+GD+AX

	Drift Ratios (%)							
	0.35	**0.5**	**1.0**	**1.5**	**1.8**	**2.2**	**2.5**	**3.0**
Column 1 to Footing DCR (mm)	0	1	5	7	9	10	11	15
Column 2 to Footing DCR (mm)	0	1	5	7	9	10	11	15

Figure 5.73 presents progression of gap opening and activation of MUD and GD at the bottom DCR connection in Column-2. The photos are taken at the peak of each drift ratio.

(a) Peak of 0.25% drift ratio

(b) Peak of 0.35% drift ratio

(c) Peak of 0.5% drift ratio

(d) Peak of 1.0% drift ratio

(e) Peak of 1.5% drift ratio

(f) Peak of 1.8% drift ratio

(g) Peak of 2.2% drift ratio

(h) Peak of 3.0% drift ratio

Figure 5.73. Progression of gap opening in Column-2 bottom DCR connection

There was no fracture of any dissipaters during testing up to 3% drift ratio. This showed a great performance of MUD and GD in the connection which would minimize the chance of fracturing a dissipater during the cycles of larger drift ratios.

Following testing, there was no apparent resdiual drift in the bent. Figure 5.74 shows photos from the bottom DCR connection in Column-2 at the start and the end of testing.

(a) Start of testing **(b) End of testing**

Figure 5.74. Photos from the start and end of testing at the Col-2 base DCR connection

There was no opening of any flexural cracks in the rocking columns. As mentioned earlier, there were a few hairline flexural cracks near the column to shell regions from the testing of LDB under IPT5+GD+AX, refer to Section 5.3.2.1. Similarly, no damage was observed to the armoring plates, steel shoes, and other precast elements (cap beam and footings). There were some existing cracks in the cap beam and footings from the previous tests which opened up during testing. However, these cracks remained of hairline thickness (less than 0.4 mm).

The force-drift hysteresis is plotted in Figure 5.75. The bent showed a very stable, symmetrical, and enhanced flag-shaped hysteresis. The capacity of the bent was almost equal to that of HDB (305 kN) during the 2.2% drift ratio. The bent achieved maximum base shear capacity of just under 400 kN during the 3% drift ratio. There was no signs of strength degradation or fatigue failure up to the 3% drift ratio. It was clear that with further drift ratio, the capacity of the bent would increase due to growing level post-tensioning in the Macalloy bars. Following the cycles of the 3.0% drift ratio, the net residual displacement in the bent was 1.6 mm (0.05% drift ratio). This was lower than

that of LDB with the grooved dissipaters (IPT11.8+GD+AX) which showed 0.2% residual drift ratio, refer to Section 5.4.2.1.

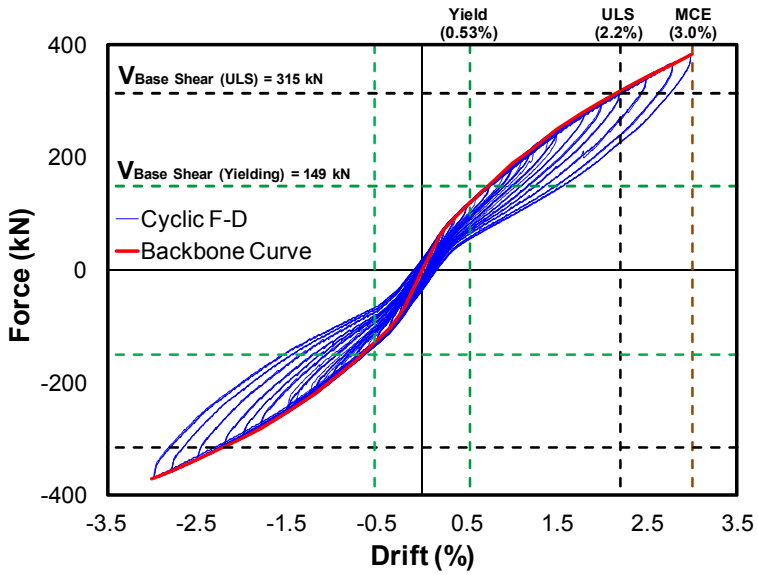

Figure 5.75. Force-drift hysteresis for IPT11.4+MUD+GD+AX

The post-tensioning force-drift hysteresis plots is presented in Figure 5.76a. The plots show a very improved performance of the bars compared to any other test discussed previously. There was no slacking and almost zero drop in the post-tensioning.

The neutral axis depth is plotted against the drift in Figure 5.76c for one of the DCR connections in the bent. The plot shows an improved response of the connection with a combination of MUD and GD in the presence of post-tensioning and gravity.

Figure 5.77a shows the corrected area-based damping (hysteretic damping) plot for the bent. The plot suggests a bi-linear relationship between the hysteretic damping and the displacement ductility. The bent achieved a maximum hysteretic damping of 7.21% at the displacement ductility of 5.7.

Compared to a theoretical flag-shaped ($\beta = 0.35$) model, LDB had higher values of hysteretic damping up to ductility of just over 2. Following that, the experimental curve located slightly lower than the theoretical flag-shaped model. In comparison with LDB under IPT11.8+GD+AX and IPT9+MUD+AX, the experimental curve located between the two. The EVD plot is presented in Figure 5.77b.

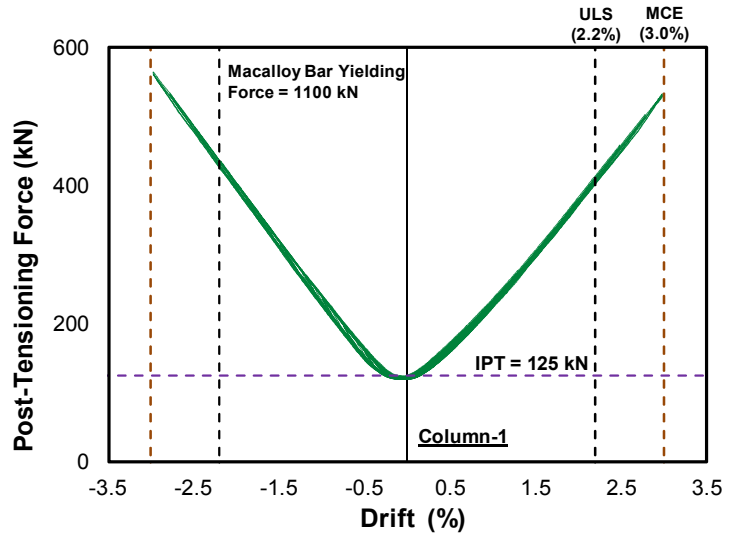

(a) Column - 1 post-tensioning-drift hysteresis

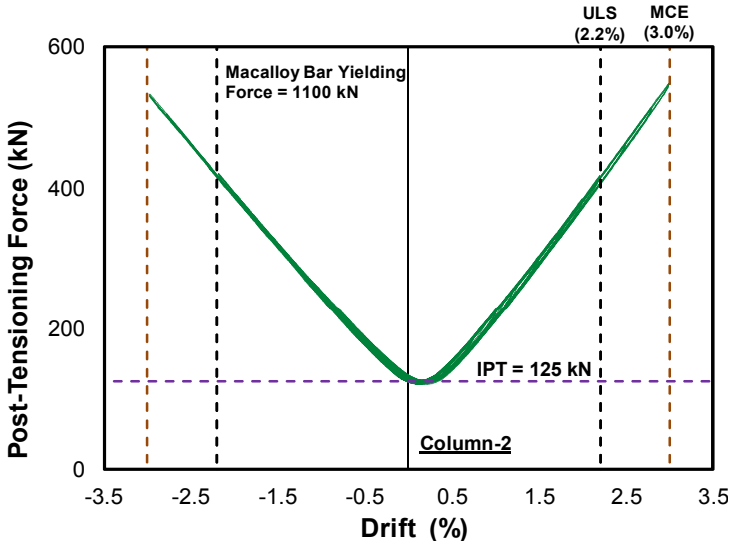

(b) Column - 2 post-tensioning-drift hysteresis

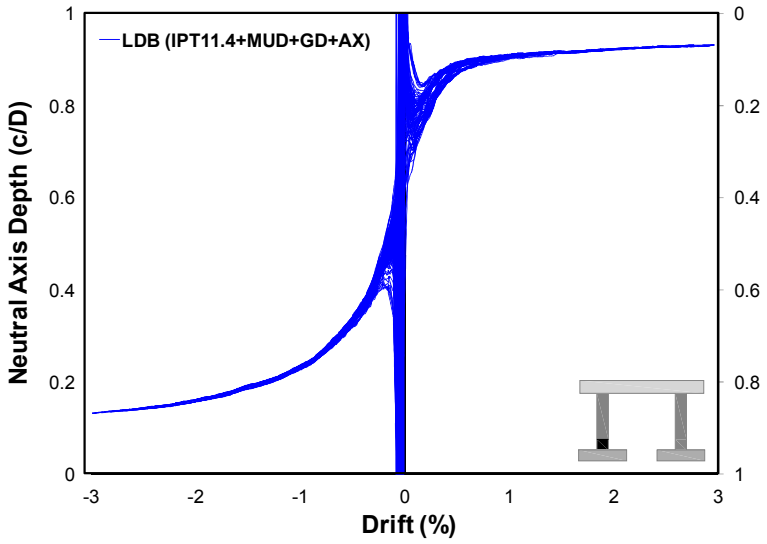

(c) Neutral axis depth-drift hysteresis

Figure 5.76. Post-tensioning and neutral axis plots for IPT11.4+MUD+GD+AX

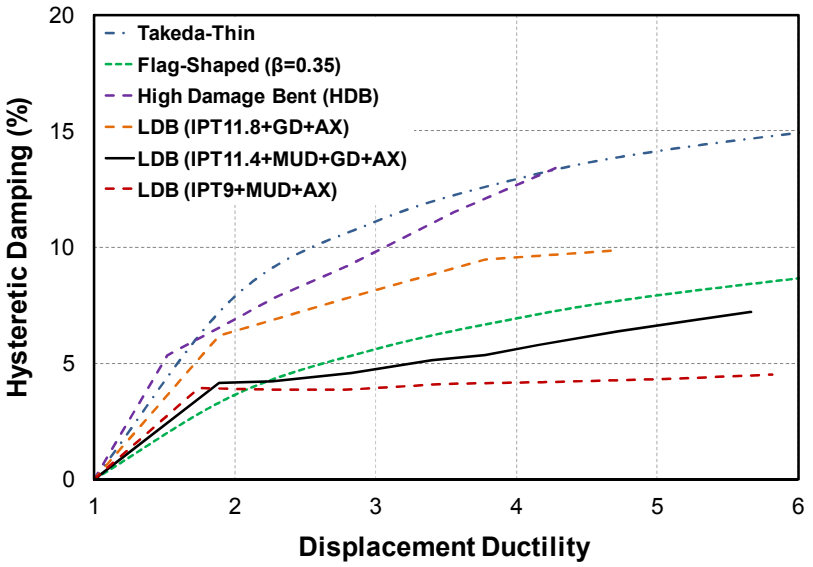

(a) Corrected area-based hysteetic damping (ξ_{hyst})

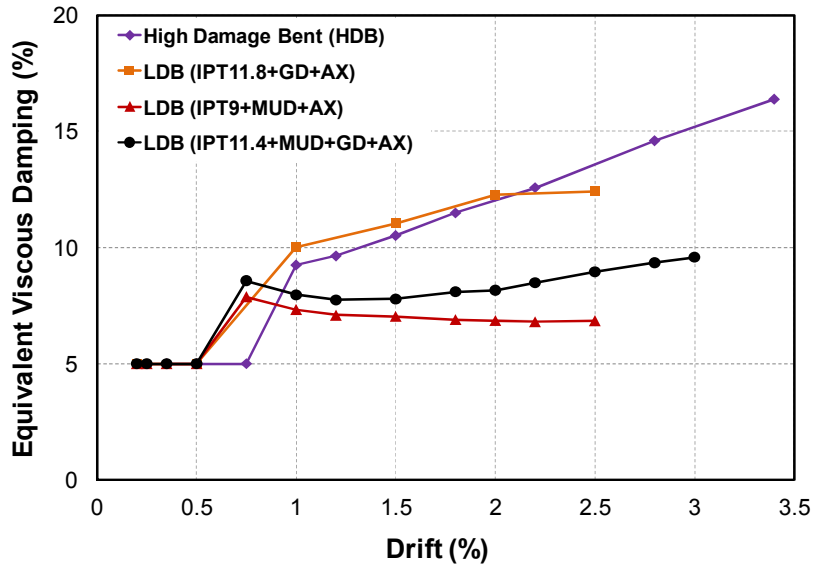

(b) Equivalent viscous damping (ξ_{eq})

Figure 5.77. Hysteretic damping and EVD plots for IPT11.4+MUD+GD+AX

Figure 5.78 presents the ADRS plot for various hazard levels (return periods) from NZS 1170.5 (NZS, 2004). The ADRS results are summarized in Table 5.21. The reason behind the higher value of ξ_{eq} at the 0.7% drift ratio in Table 5.21 is similar to what explained previously for Table 5.15 in Section 5.4.4.1 (influence of elastic tangent damping due to lower capacity of MUDs, $\xi_{el,\,tangent}$). The bent achieved its performance goal of having ductility of 3 or higher (force-based design of HDB, refer to Chapter 3) at the design hazard level of 2500 years (ULS). The bent achieved displacement ductility of 5.7 at the MCE performance level (4500 years return period). This corresponded to 1.7 times ULS drift ratio in accordance with ADRS results.

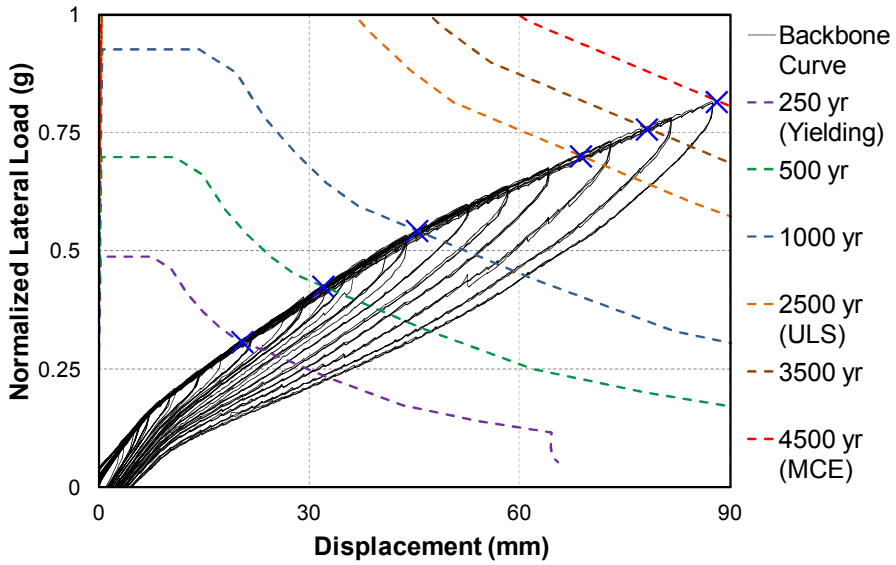

(a) Normalized lateral load - displacement

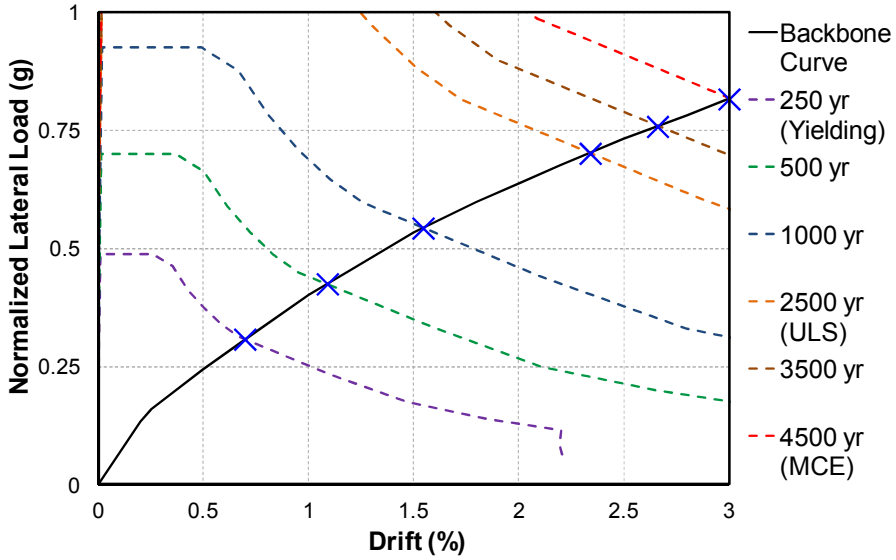

(b) Normalized lateral load - drift

Figure 5.78. ADRS plots for IPT11.4+MUD+GD+AX

Table 5.21. Summary of ADRS results for LDB under IPT11.4+MUD+GD+AX

Hazard Levels (Years)	Return Period Factor (R)	Ductility (μ)	Drift (%)	Corrected Equivalent Damping (ξ_{eq}) %
250	0.75	1.3	0.7	10.5
500	1.0	2.1	1.1	8.83
1000	1.3	2.9	1.55	8.44
2500	1.8	4.4	2.34	8.69
3500	2	5	2.66	8.85
4500	2.2	5.7	3	8.92

Figure 5.79 presents energy dissipation plot of LDB. The bent had the highest energy dissipation during the first cycle at each drift ratio. For the second and third cycles at each drift ratio, there was very less reduction in energy dissipation. For example, there was almost zero reduction in the bent energy dissipation between the second and third cycles of the 2.5% drift ratio. However, for the same cycles and the drift ratio, the reduction was 24.5% and 2% for testing of LDB with the grooved dissipaters (IPT11.8+GD+AX) and LDB with MUD (IPT9+MUD+AX), respectively. This confirms the better performance of LDB with a combination of MUD and GD compared to the other solutions.

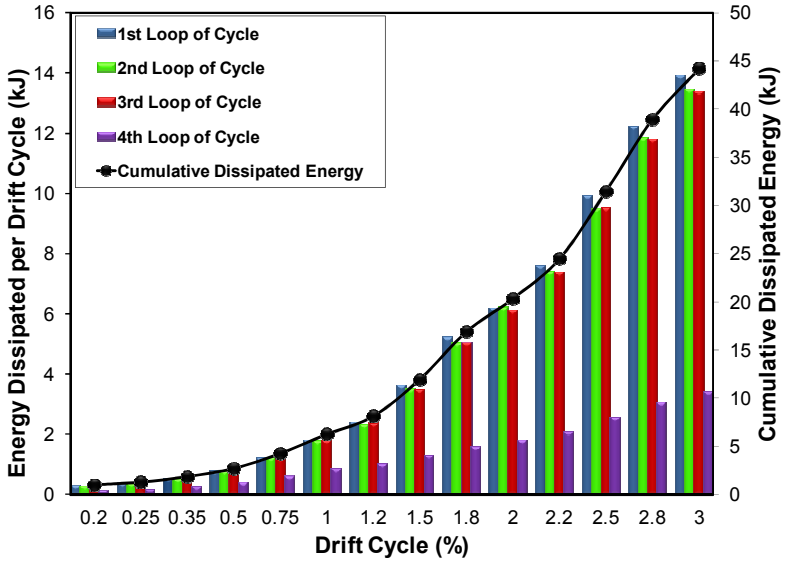

Figure 5.79. Dissipated energy (per cycle and cumulative) for IPT11.4+MUD+GD+AX

In summary, testing of LDB with unbonded post-tensioning, MUD, GD, and gravity showed the best performance among the solutions tested in this Chapter. The bent achieved good levels of ductility and strength with almost zero residual displacement. The dissipaters were very effective in absorbing the energy without any strength degradation or low-cycle fatigue failure for a large number of cycles beyond the yield point. The force-displacement hysteresis suggested a very stable and balanced flag-shaped hysteresis of the bent. The bent had hysteretic damping values similar to those of theoretical flag-shaped model ($\beta = 0.35$). Following testing, there was no damage to the rocking columns, dissipaters, armoring, and other precast elements.

5.5 Comparison: ABC High Damage and ABC Low Damage

In this part of the Chapter, two types of comparison (qualitative and quantitative) between ABC High Damage and Low Damage are presented. For ABC High Damage, the HDB specimen tested in Section 3.3 of Chapter 3 is used as a benchmark structure. For ABC Low Damage, the LDB specimen under three variation of dissipation source is considered. The three variations are as follows:

1. LDB with Grooved Dissipaters (LDB-1): IPT11.8+GD+AX (Section 5.4.2.1)
2. LDB with Mini UFP Dissipaters (LDB-2): IPT9+MUD+AX (Section 5.4.4.1)
3. LDB with GDs and MUDs (LDB-3): IPT11.4+MUD+GD+AX (Section 5.4.6.1)

5.5.1 Qualitative Comparison

Observations from the extent of damage during the testing of HDB and LDB are used to present a qualitative comparison between the two fully precast bents.

In HDB, there were four plastic hinges in the columns which located above and below the column to footing and column to cap beam connections. There were crushing and spalling of concrete at the plastic hinges followed by buckling of the longitudinal rebars. There were extensive flexural cracks up the height of the columns.

In LDB, there were four Dissipative Controlled Rocking (DCR) connections which had replaced the plastic hinges. For LDB with external shear keys which restrained the undesirable sliding and twisting of the column at the DCR connection, there was no apparent damage to the armored parts of the column. Similarly, there was no spalling or flexural cracks in both columns. The column and the DCR connection remained totally intact throughout testing. Figure 5.80 and Figure 5.81 present qualitative comparison between the extent of damage observed in the testing of ABC High Damage Bent (HDB) and ABC Low Damage Bent (LDB).

(a) High Damage Bent (HDB)

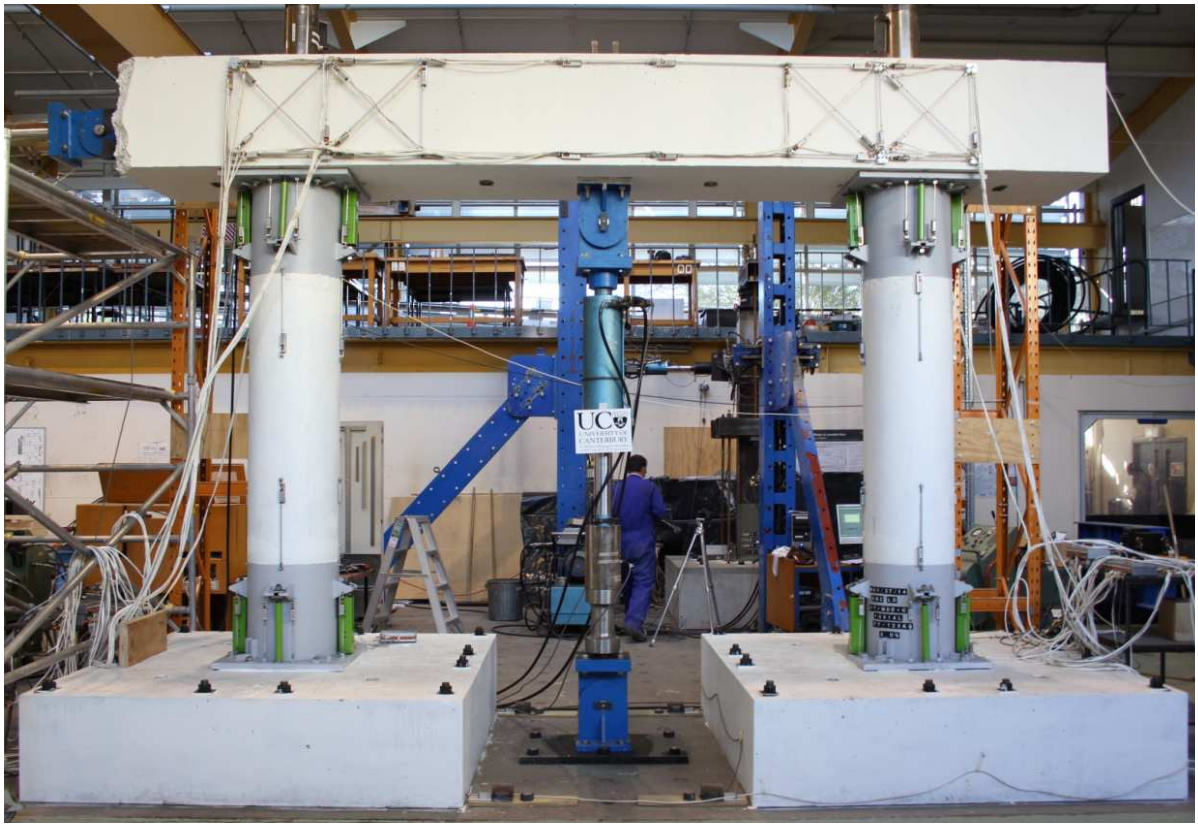

(b) Low Damage Bent (LDB)

Figure 5.80. Extent of damage in HDB and LDB following testing

(a) Column-1 in HDB

(b) Column-1 in LDB

(c) Column-2 in HDB

(d) Column-2 in LDB

Figure 5.81. Extent of damage in HDB and LDB columns following testing

In HDB, the extent of spalling was more severe at the bottom column to footing Member Socket Connection (MSC), as shown in Figure 5.82a and Figure 5.82c. Although there was an unbonded length of the starter bars left at the column to cap beam Grouted Duct Connection (GDC) to limit damage to the concrete, however, there was still moderate spalling and crushing of the grouted bed (Figure 5.83a and Figure 5.83c).

In LDB, there was no apparent damage to the DCR connections. Despite the fact that LDB was subjected to more than a dozen of testing, the top and bottom DCR connections remained fully intact.

(a) Column-1 bottom MSC in HDB

(b) Column-1 bottom DCR connection in LDB

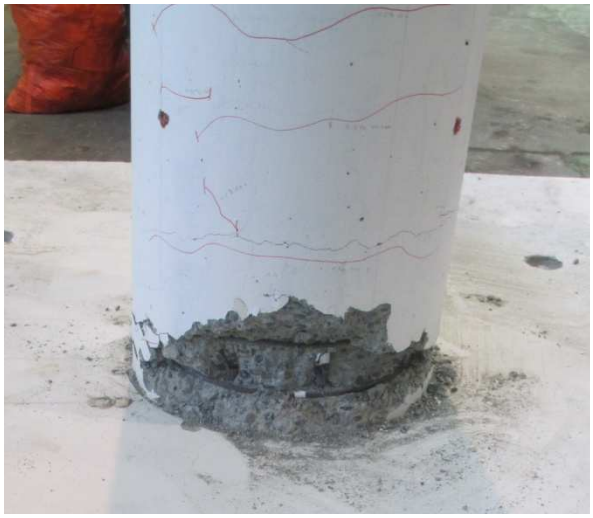

(c) Column-2 bottom MSC in HDB

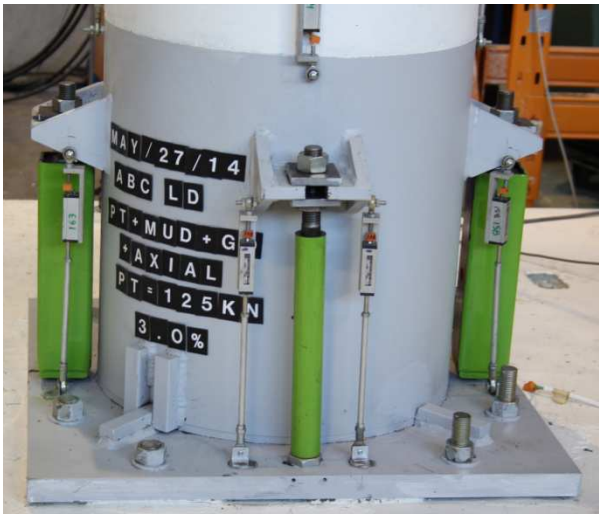

(d) Column-2 bottom DCR connection in LDB

Figure 5.82. Extent of damage in HDB and LDB base connections following testing

(a) Column-1 top GDC in HDB

(b) Column-1 top DCR connection in LDB

(c) Column-2 top GDC in HDB

(d) Column-2 top DCR connection in LDB

Figure 5.83. Extent of damage in HDB and LDB top connections following testing

5.5.2 Quantitative Comparison

Testing results are used to provide quantitative comparison between the seismic performance of ABC high Damage and ABC Low Damage.

Figure 5.84 presents the force-drift hysteresis and backbone curve for HDB and the three variations of LDB. From the plots presented in Figure 5.84, LDB-2 (IPT9+MUD+AX) and HDB had the least and the most energy dissipation capacity, respectively. The least energy dissipation capacity of LDB-2 was due to lower capacity of the fabricated MUDs as explained earlier in Section 5.4.4.1.

By comparing all four hysteresis plots, evidence of significant strength degradation and asymmetrical performance can be noticed in the hysteretic response of HDB only. There is some noticeable stiffness degradation in the testing of LDB with the grooved dissipaters (LDB-1, Figure 5.84b), but this is smaller than that visible in testing of HDB.

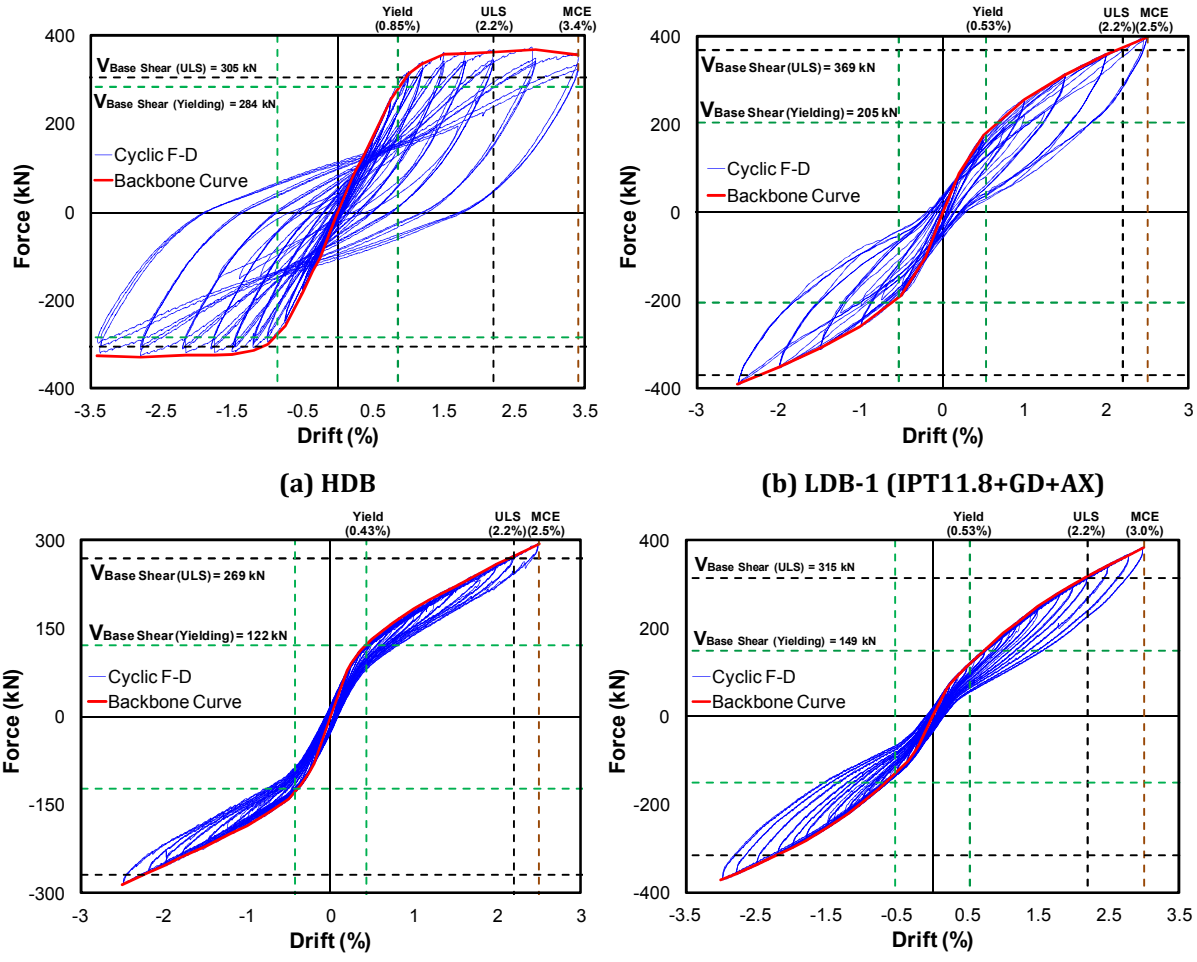

(a) HDB **(b) LDB-1 (IPT11.8+GD+AX)**

(c) LDB-2 (IPT9+MUD+AX) **(d) LDB-3 (IPT11.4+MUD+GD+AX)**

Figure 5.84. Force-drift hysteresis for HDB and the three variations of LDB

Table 5.22 summarizes the most important parameters from the force-drift hysteresis plots of Figure 5.84 for each performance level. It should be noted that in Table 5.22, results from the progressive collapse and ADRS analysis are used for HDB and the three variations of LDB, respectively.

Table 5.22. Comparison of parameters for HDB and the three variations of LDB

Specimen	Performance Levels												
	Yielding			ULS					MCE				
	Δ (%)	V_b (kN)	Δ_{Res} (%)	Δ (%)	V_b (kN)	μ	ξ_{hyst} (%)	Δ_{Res} (%)	Δ (%)	V_b (kN)	μ	ξ_{hyst} (%)	Δ_{Res} (%)
HDB	0.82	280	0.14	2.7	370	3.3	11	1.3	3.4	360	4.1	13.5	1.8
LDB-1	0.53	185	0	1.52	316	2.9	7.85	0.1	2.5	400	4.7	9.85	0.2
LDB-2	0.43	123	0	-	-	-	-	-	-	-	-	-	-
LDB-3	0.53	136	0	2.34	330	4.4	6.06	0.03	3.0	384	5.7	7.21	0.05

Figure 5.85 presents comparison of hysteretic damping against displacement ductility for HDB and the three variations of LDB. It is obvious that HDB had the highest hysteretic damping compared to the others. However, in terms of displacement ductility, HDB did not achieve similar values of ductility to those of the three variations of LDB. A comparison of the EVD curve is shown through the plots in Figure 5.86.

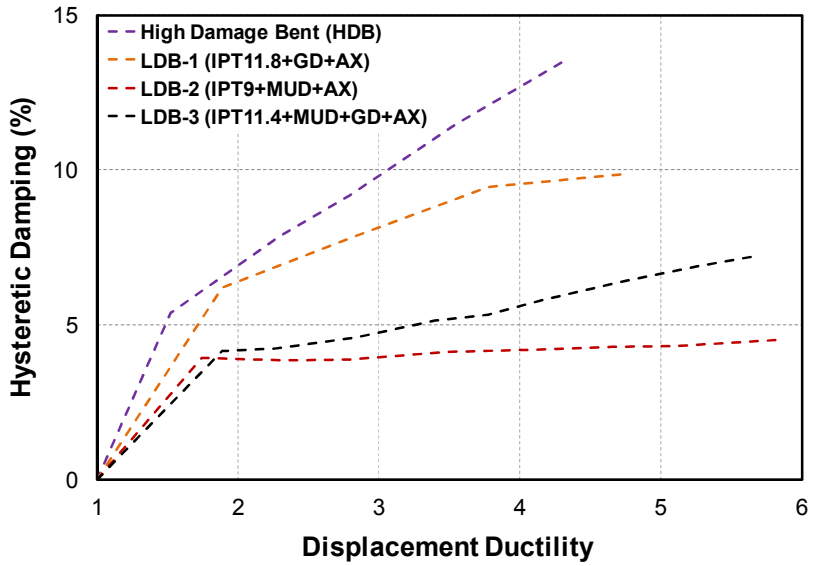

Figure 5.85. Hysteretic damping curve for HDB and the three variations of LDB

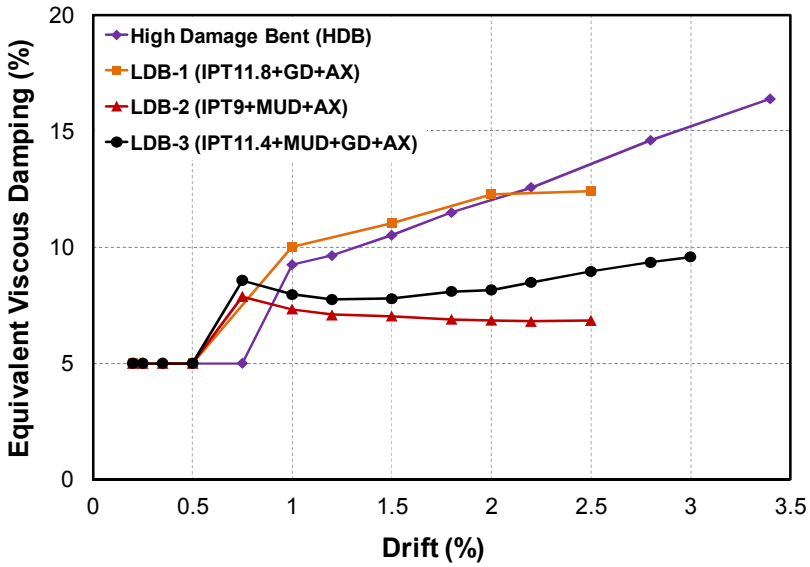

Figure 5.86. EVD curve for HDB and the three variations of LDB

Figure 5.87 presents comparison of the cumulative energy dissipated per each drift ratio. It can be observed that HDB had the highest energy dissipation.

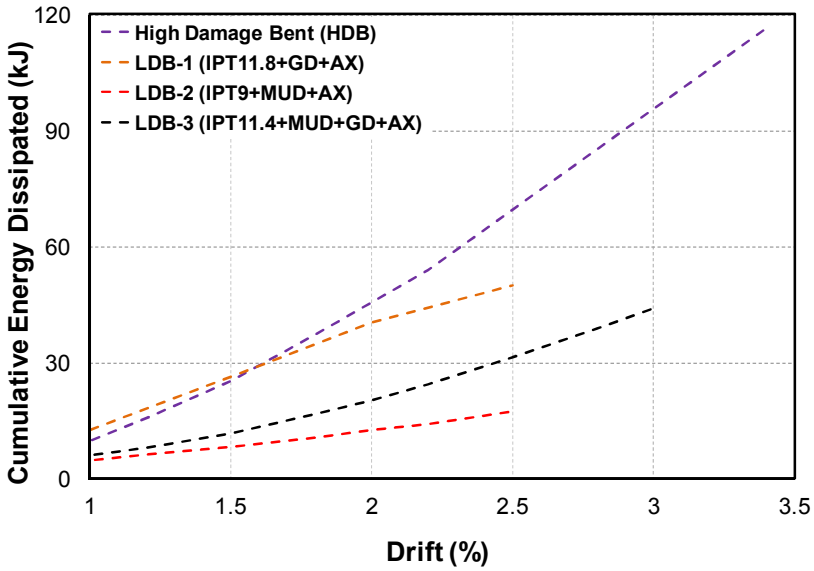

Figure 5.87. Energy dissipation plot for HDB and the three variations of LDB

A summary of the ADRS results for each solution is summarized in Table 5.23.

Table 5.23. Summary of ADRS results for HDB and LDB under different hazard levels

Testing	Hazard Levels (Years)	Return Period Factor (R)	Ductility (μ)	Drift (%)	Corrected Equivalent Damping (ξ_{eq}) %
HDB	250	0.75	1	0.67	10.37
	500	1.0	1.18	0.93	10.75
	1000	1.3	1.9	1.5	13
	2500	1.8	3.5	2.7	17.85
	3500	2.0	4.2	3.33	19.67
LDB-1	250	0.75	1	0.43	13.77
	500	1.0	1.3	0.68	12.59
	1000	1.3	1.9	0.98	12.24
	2500	1.8	2.9	1.52	13.13
	3500	2.0	3.3	1.77	13.52
	5500	2.4	4.5	2.39	13.16
LDB-2	250	0.75	1.7	0.73	9.16
	500	1.0	3	1.3	7.48
	1000	1.3	4.6	2	6.66
	1425	1.5	6.2	2.5	6.24
LDB-3	250	0.75	1.3	0.7	10.5
	500	1.0	2.1	1.1	8.83
	1000	1.3	2.9	1.55	8.44
	2500	1.8	4.4	2.34	8.69
	3500	2	5	2.66	8.85
	4500	2.2	5.7	3	8.92

5.6 Conclusions

This Chapter covered the development of ABC Low Damage system. In the first part of the Chapter, a Low Damage Bent (LDB) was developed. The bent incorporated Dissipative Controlled Rocking (DCR) connection at the plastic hinging locations. A typical DCR connection consisted of unbonded post-tensioning tendons inside the column with externally attached dissipaters. The post-tensioning is intended to provide self-centering of the bent with the external dissipaters absorbing the seismic energy. The resultant hysteresis from this concept is commonly referred as "flag-shaped".

In the first phase of the testing, LDB was developed and tested with internal concrete shear key at the DCR connections. The internal shear keys were expected to restrain sliding in the bent during lateral loading.

In this first part of this phase of testing, three variation of initial post-tensioning with no external dissipaters and gravity was tested. Although higher level of initial post-tensioning showed a fair performance of the bent, however, testing observations showed inadequacy of internal shear key to restrain sliding at the DCR connections. This had contributed into residual displacement in LDB. There was also some twisting of the columns in the bent.

In the second part of the testing, the bent was tested under post-tensioning, grooved dissipaters, and gravity. The capacity of the bent was designed to match the design base shear of High Damage Bent (HDB) in Chapter 3. Observations from testing showed excessive sliding and twisting of the columns. This had distorted the axial alignment of the grooved dissipaters and ultimately contributed into dissipater fracture at a drift ratio which was just beyond the ULS point. Experimental results did not show a clear flag-shaped hysteresis of the bent. There was significant residual displacement in the bent following testing. This was due to undesirable movement at the DCR connections. Overall this phase of testing showed inadequacy of internal shear keys in LDB, and hence the detailing of shear key had to be improved for a better and enhanced performance.

In the second phase of testing, new external shear keys were provide at each rocking joint. The external shear keys were detailed to restrain both sliding and twisting of the columns.

In the first part of the second phase of testing, testing of LDB under three variation of post-tensioning with no dissipaters and gravity was repeated. Observations from testing showed better performance of the bent with external shear keys. The shear keys were able to prevent from sliding and twisting of the columns while allowing the rocking of motion to occur. Testing results showed enhanced self-centering of the bent with no residual displacement.

In the second part of the testing, LDB was re-tested with the grooved dissipaters, post-tensioning, and gravity. The bent performed adequate and testing results suggested a clear flag-shaped response of the bent. There was no dissipater fracture up to the drift ratio where there was fracture of dissipater in a similar test but with internal shear keys. This presented an improved performance of the bent. The external shear keys were able to prevent from any undesirable distortion in the dissipaters. The bent achieved a capacity higher than HDB at the ULS performance level. However, this was due to higher level of initial post-tensioning in the columns which increased the self-centering and capacity of the bent. Overall, testing of LDB with the grooved dissipaters showed great promise for ABC Low Damage. However, given the susceptibility of the grooved dissipaters to low-cycle fatigue failure, for a real life ABC Low Damage bridge this would mean that the dissipaters would have to be replaced following an earthquake.

In the third part of the testing, LDB was tested with Mini UFP Dissipaters (MUDs) and under three levels of post-tensioning without gravity. The bent performed well, even under very low level of post-tensioning. There was no signs of strength degradation in MUD under dozens of cycles beyond the yield point. Despite a good performance, the energy dissipation capacity of the bent was low. This was due to lower capacity of the fabricated MUD. Given the limitations on rolling thicker steel plate into double UFPs in the lab, the thickness of the plate had to be limited to 5 mm. This means that the overall capacity of the dissipater would be lower. However, for a real life ABC Low Damage bridge with MUD, the dissipater can be manufactured in a fabricator shop where there

would be proper machineries which could roll thicker steel plate, and thus produce MUD with any desirable capacity.

In the fourth part of the testing, the bent was tested with post-tensioning, MUD, and gravity. There was no damage observed to LDB. Experimental results suggested high self-centering flag-shaped hysteresis of the bent with small energy dissipation. This was due to lower capacity of MUD, as discussed in the previous paragraph. The bent did not reach the design base shear of HDB at the ULS drift ratio. Instead, the bent had to be pushed further beyond the ULS level to reach the capacity of HDB. This suggested that more energy dissipation capacity had to be introduced in the system to enhance the flag-shaped response and capacity of the bent.

In the fifth part of the testing, LDB was tested with a combination of GDs, MUDs, and post-tensioning without gravity. The arrangement of the dissipaters aimed an enhanced performance of the system which would not be susceptible to low-cycle fatigue failure for a great number of cycles beyond the yield point. In a typical DCR connection for this solution, MUDs were positioned in locations where large gap opening is expected under lateral loading. As explained in Chapter 4, MUD is not susceptible to strength degradation and low-cycle fatigue failure for a large number of cycles. Therefore, this type of dissipater is particularly suitable for the aforementioned locations in a DCR connection. GDs were positioned where there would be smaller gap opening expected in the DCR connection. This would enhance the life of GD under repeated cycles of loading, and hence makes the dissipater less susceptible to low-cycle fatigue failure. Observations from testing showed great performance of the bent with a combination of GD and MUD in the DCR connections. The bent reached good levels of self-centering and energy dissipation. The force-drift hysteresis also suggested a clear flag-shaped response of the system. The bent did not reach the capacity of HDB at the ULS level due to absence of gravity.

In the sixth part of the testing, the response of LDB with GDs, MUDs, post-tensioning, and gravity, was investigated. The capacity of the bent was designed to match the design base shear of HDB at the ULS performance level. Observation from testing showed the best performance of the bent in comparison to all other solutions tested previously. Experimental results showed an enhanced flag-shaped response of the bent with good

energy dissipation. There was almost zero residual displacement in the bent following the cycles of the 3% drift ratio (1.4 times ULS). A comparison of the experimental hysteretic damping plot of the system against theoretical flag-shaped model with $\beta = 0.35$ showed almost similar values of hysteretic damping. For a real life ABC Low Damage bent incorporating such solution this would mean that the bridge would be immediately functional after a design level earthquake with no residual displacement. Given the great performance of the dissipaters, there would be no post-earthquake repairs needed for the replacement of the dissipaters. Similarly, the possibility for any damage or hairline cracking to the columns during the earthquake would be minimal.

In the last part of the Chapter, qualitative and quantitative comparison between seismic performance of ABC High Damage and ABC Low Damage was presented.

For the qualitative comparison, observations from the extent of damage in testing of ABC High Damage Bent, especially at the plastic hinges, suggested extensive structural damage in the columns. For a real life ABC High Damage bridge this would mean delayed functionality, extensive repair work, and downtime of the bridge after a big earthquake. A full replacement of the bridge may also be required if the extent of damage was beyond the limits of repairability. In contrast, ABC Low Damage Bent performed very good. Observations from testing showed no signs of damage to the rocking columns and the connections. For a real life ABC Low Damage bridge this would eliminate any post-earthquake repairs and downtime.

For the quantitative comparison, experimental results from testing of ABC High Damage bent suggested significant strength degradation, residual displacement, and decreasing energy dissipation, under cyclic loading. However, all these issues were eliminated in the testing of ABC Low Damage. Results from the ADRS analysis suggested that ABC Low Damage had higher ductility than that of ABC High Damage at the ULS performance level. Similarly, for a Maximum Considered Earthquake (MCE), ABC Low Damage had higher values of displacement ductility than that of ABC High Damage. In terms of capacity, both solutions had almost identical design base shear at the ULS performance level. However, there was no strength degradation in ABC Low Damage, and hence the capacity of the bent was increasing with further displacement. In terms of energy dissipation, ABC High Damage had higher energy dissipation capacity compared to ABC

Low Damage. However, this was expected to be reduced significantly once the longitudinal rebars start rupturing under low-cycle fatigue or excessive deformation in ABC High Damage. In contrast, in ABC Low Damage, the dissipaters would continue dissipating more energy with further displacement without any fracture or low-cycle fatigue failure for a large number of cycles beyond the yield point.

5.7 Bibliography

1. Albrecht, P., and Hall, T. T. (2003). Atmospheric Corrosion Resistance of Structural Steels. Journal of Materials in Civil Engineering, 15(1):2-24.

2. Cheok, G. S., Stone, W. C., and Kunnath, S. K. (1998). Seismic of Precast Concrete Frames with Hybrid Connections. ACI Structural Journal, 95(5):527-539.

3. Guerrini, G., Restrepo, J. I., Massari, M., and Vervelidis, A. (2012). Self-Centering Precast Concrete Dual-Shell Steel Columns. Proceedings of 15th World Conference on Earthquake Engineering, Lisbon, Portugal.

4. Hilti Group (2015). https://www.hilti.com/

5. Mander, J., Priestley, M. J. N., and Park, R. (1988). Theoretical Stress-Strain Model for Confined Concrete. Journal of Structural Engineering, 114(8):1804-1826.

6. Marriott, D., Pampanin, S., and Palermo, A. (2009). Quasi-Static and Pseudo-Dynamic Testing of Unbonded Post-Tensioned Rocking Bridge Piers with External Replaceable Dissipaters. Earthquake Engineering and Structural Dynamics, 38(3):331-354.

7. Marriott, D., Pampanin, S., and Palermo, A. (2011). Biaxial Testing of Unbonded Post-Tensioned Rocking Bridge Piers with External Replaceable Dissipaters. Earthquake Engineering and Structural Dynamics, 40(15):1723-1741.

8. New Zealand Standards (NZS) (2004). Structural Design Actions: Earthquake Actions, NZS 1170.5. Wellington, New Zealand.

9. New Zealand Standards (NZS) (2006). The Design of Concrete Structures, NZS 3101. Wellington, New Zealand.

10. New Zealand Standards (NZS) (2001). Steel Reinforcing Materials, AS/NZS 4671. Wellington, New Zealand.

11. Palermo, A. (2004). The Use of Controlled Rocking In the Seismic Design of Bridges. PhD Thesis, Politecnico Di Milano (Technical University of Milan), Milan, Italy.

12. Palermo, A. and Pampanin, S. (2008). Enhanced Seismic Performance of Hybrid Bridge Systems: Comparison with Traditional Monolithic Solutions. Journal of Earthquake Engineering, 12(8):1267-1295.

13. Palermo, A., Pampanin, S., and Calvi, G. M. (2005). Concept and Development of Hybrid Solutions for Seismic Resistant Bridge Systems. Journal of Earthquake Engineering, 9(6):899-921.

14. Palermo, A., Pampanin, S., and Marriott, D. (2007). Design, Modeling, and Experimental Response of Seismic Resistant Bridge Piers with Post-tensioned Dissipating Connections. Journal of Structural Engineering, 133(11):1648-1661.

15. Pampanin, S., Marriot, D., and Palermo, A. (2010). PRESSS Design Handbook. New Zealand Concrete Society (NZCS) Incorporation, Auckland, New Zealand.

16. Priestley, M. J. N. (1991). Overview of PRESSS Research Program. Precast/Prestressed Concrete Institute Journal, 36(4):50-57.

17. Priestley, M. J. N. (1996). PRESSS Program - Current Status and Proposed Plans for Phase III. Precast/Prestressed Concrete Institute Journal, 41(2):22-40.

18. Priestley, M. J. N., Sritharan, S., Conley, J. R., and Pampanin, S. (1999). Preliminary Results and Conclusions from the PRESSS Five-Story Precast Concrete Test Building. Precast/Prestressed Concrete Institute Journal, 44(6):42-67.

19. Priestley, M. J. N., Calvi, G. M., and Kowalsky, M. J. (2007). Displacement-Based Seismic Design of Structures. IUSS Press, Pavia, Italy.

20. Rahman, A. and Restrepo, J. I. (2000). Earthquake Resistant Precast Concrete Buildings: Seismic Performance of Cantilever Walls Prestressed using Unbonded Tendons. Research Report 2000-5, Department of Civil Engineering, University of Canterbury, Christchurch, New Zealand.

21. Sika Group (2015). http://www.sika.com/

22. Solberg, K., Mashiko, N., Mander, J. B., and Dhakal, R. P. (2009). Performance of a Damage-Protected Highway Bridge Pier Subjected to Bi-directional Earthquake Attack. Journal of Structural Engineering, 135(5), 469-478.

23. Stanton, J., Hicks, T., and Hawkins, N. (1991). PRESSS Project 1.3 - Connection Classification and Evaluation. PCI Journal, 36(5):62-71.

24. Stanton, J., Stone, W. C., and Cheok, G. S. (1997). Hybrid Reinforced Precast Frame for Seismic Regions. PCI Journal, 42(2):20-32.

25. Stanton, J. F., Wacker, J. M., Hieber, D. G., and Eberhard, M. O. (2005). Design of Precast Concrete Piers for Rapid Bridge Construction in Seismic Regions. Washington State Transportation Center (TRAC), University of Washington, Seattle, Washington, United States.

26. Stone, W. C., Cheok, G. S., and Stanton, J. F. (1995). Performance of Hybrid Moment Resisting Precast Beam-Column Concrete Connections Subjected to Cyclic Loading. ACI Structural Journal, 91(2):229-249.

6. MODELING THE RESPONSE OF ABC HIGH DAMAGE AND ABC LOW DAMAGE

6.1 Introduction

This Chapter presents simplified analytical modeling tools for predicting the response and validating the experimental results for ABC High Damage and ABC Low Damage which discussed in Chapter 3 and Chapter 5, respectively. The Chapter also discusses analytical modeling procedure for the innovative dissipaters discussed in Chapter 4.

The simplified analytical procedures described in this Chapter aim to provide macro-modeling of the tested columns under quasi-static cyclic loading. The most important elements of the analytical modeling in this Chapter are to capture the force-drift hysteresis and backbone plot of the tested specimens to a high level of accuracy. For this reason, existing theoretical models for the simplified modeling of reinforced concrete and steel are utilized. The necessary parameters in the theoretical model are calibrated with the experimental data to provide a simplified and accurate analytical model for the each specimen.

It should be noted that the modeling procedure in this Chapter are solely developed for the specimens where there was no construction error or undesirable behavior during the testing. For example, in testing of HDS1 (Section 3.2.7.1 in Chapter 3), the central Macalloy bar was fully bonded and acting as a reinforcing bar at the center of the column section. This was a construction error which resulted into an increase in the post-yield stiffness of the column. Another example is in testing of LDB with internal shear keys (Section 5.3 in Chapter 5). During the testing, there was undesirable sliding and twisting of the columns in the bent. Therefore, in this Chapter, there is no modeling procedure proposed to match the experimental results for HDS1 and LDB with internal shear keys.

Modeling the response of Self-Centering UFP Bracing Dissipater (SCUD) and Grooved Dissipater under net positive and negative deformation are also out of the scope of this thesis.

In summary, the objective of this Chapter is to use some existing modeling techniques and hysteresis rules to predict the monotonic and cyclic response of the systems tested in the previous chapters. Analytical models are calibrated with the experimental data. Recommended modeling parameters are presented for each of the below systems.

1. ABC High Damage (Chapter 3): Modeling the response of cantilever and multi-column pier system with grouted duct and member socket connections. Displacement-based formulas and Takeda-Thin hysteretic rule are used to capture the response of the columns.

2. Innovative Dissipaters (Chapter 4): Modeling the response of UFP Bracing Dissipater (UFP-BD), Mini UFP Dissipater (MUD), and Grooved Dissipater (GD). The Bilinear and Ramberg-Osgood hysteretic rules, in addition to some previous research on the UFPs and Buckling-Restrained Fused Type Dissipater (BRF), are utilized to capture the response of the aforementioned dissipaters.

3. ABC Low Damage (Chapter 5): Modeling the response of the bent with Dissipative Controlled Rocking (DCR) connections. The Monolithic Beam Analogy (MBA) procedure and existing lumped plasticity models are used to model the monotonic and cyclic response of the rocking connection under:

    A. Post-tensioning only

    B. Post-tensioning, GDs, and gravity

    C. Post-tensioning, MUDs, and gravity

    D. Post-tensioning, GDs, MUDs, and gravity

6.2.1 Cantilever Pier System

Using a Moment-Curvature (M-ϕ) analysis for the column section, the yield curvature (ϕ_y) and plastic moment capacity (M_p) were calculated for each column. The M-ϕ analysis also derives a set of values for the curvature and moment capacity for the column cross-section. This type of analysis is based on strain compatibility and equilibrium of forces on the column section.

For a simplified section analysis, an elastic-perfectly plastic moment-curvature relationship in accordance with Caltrans Idealized Model (Caltrans, 2013) was considered. In this model, the elastic portion of the curve should always pass through the point where the first reinforcing bar yields (M_y). The plastic moment capacity of the section can be calculated by balancing the areas between the exact (actual) and the idealized elastic-perfectly plastic M-ϕ curve, as shown in Figure 6.1. The M-ϕ curve can be simply calculated using software packages such as SAP 2000 (Computers and Structures Inc., 2015) by considering the Mander confinement model for the core concrete (Mander et al.,1988).

Results from M-ϕ analysis is used to calculate the yield curvature, drift, and yield moment (M_y) to construct the backbone curve of the column. Experimental observations from testing of the segmental cantilever column system showed little deformation occurring at the column segment to segment connection under the lateral loading. Thus, excluding the contribution from the second plastic hinge at the segment to segment connection, the backbone curve can be constructed for each cantilever column using Equation 6.1 through Equation 6.7 in accordance with Priestley et al. (2007).

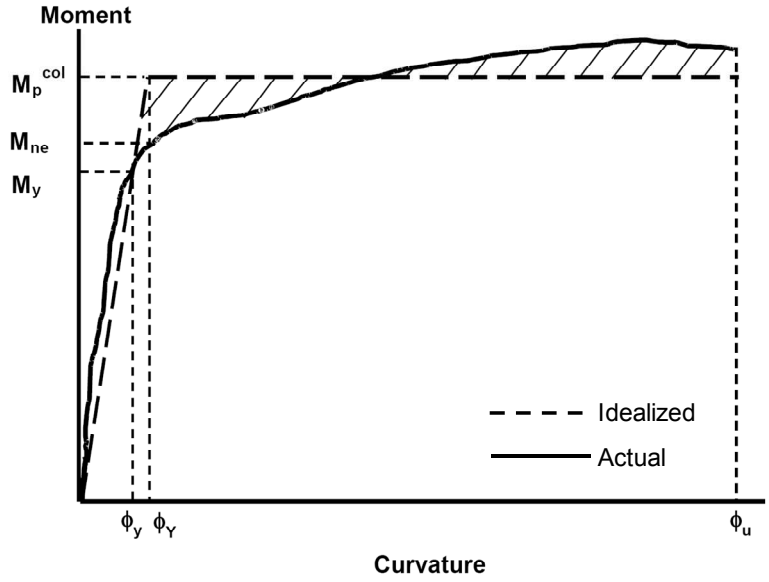

Figure 6.1. Moment-curvature curve, after Caltrans (2013)

$$\Delta_y = \phi_y \frac{(L + L_{sp})^2}{3} \tag{6.1}$$

$$\Delta_Y = \phi_Y \frac{(L + L_{sp})^2}{3} \tag{6.2}$$

$$L_{sp} = 0.022\, f_{ye} d_b \tag{6.3}$$

$$\phi_Y = \phi_y \frac{M_p}{M_y} \tag{6.4}$$

$$F_y = \frac{M_y}{L} \tag{6.5}$$

$$F_p = \frac{M_p}{L} \tag{6.6}$$

$$\Delta_u = \Delta_Y + \left[(\phi_u - \phi_Y) L_p \left(L - \frac{L_p}{2}\right)\right] \tag{6.7}$$

Where,

Δ_y = Lateral displacement at the first bar yield point (mm or % in terms of drift ratio)

Δ_Y = Lateral displacement at the global yield point (mm or % in terms of drift ratio)

Δ_p = Plastic displacement, see Figure 6.2 (mm or % in terms of drift ratio)

Δ_u = Maximum displacement at the failure point (mm or % in terms of drift ratio)

Δ_c = Total column displacement see Figure 6.2 (mm or % in terms of drift ratio)

ϕ_y = Curvature at the first bar yield point (mm^{-1})

ϕ_Y = Curvature at the global yield point (mm^{-1})

ϕ_u = Ultimate curvature at the failure point (mm^{-1})

θ_p = Plastic rotation (rad), see Figure 6.2

L = Height of the column (mm)

L_{sp} = Strain penetration length (mm)

L_p = Plastic hinge length of the column (mm)

f_{ye} = Effective yield stress of the rebar (MPa)

d_b = Diameter of the longitudinal rebar (mm)

M_y = Moment capacity at the first bar yield point (kNm)

M_P = Plastic moment capacity (kNm)

F_y = Lateral force at the first bar yield point (kN)

F_P = Plastic lateral force (kN)

Figure 6.2 presents important parameters for evaluating the displacement capacity of cantilever column system with fixed base support from Caltrans Seismic Design Criteria (Caltrans, 2013).

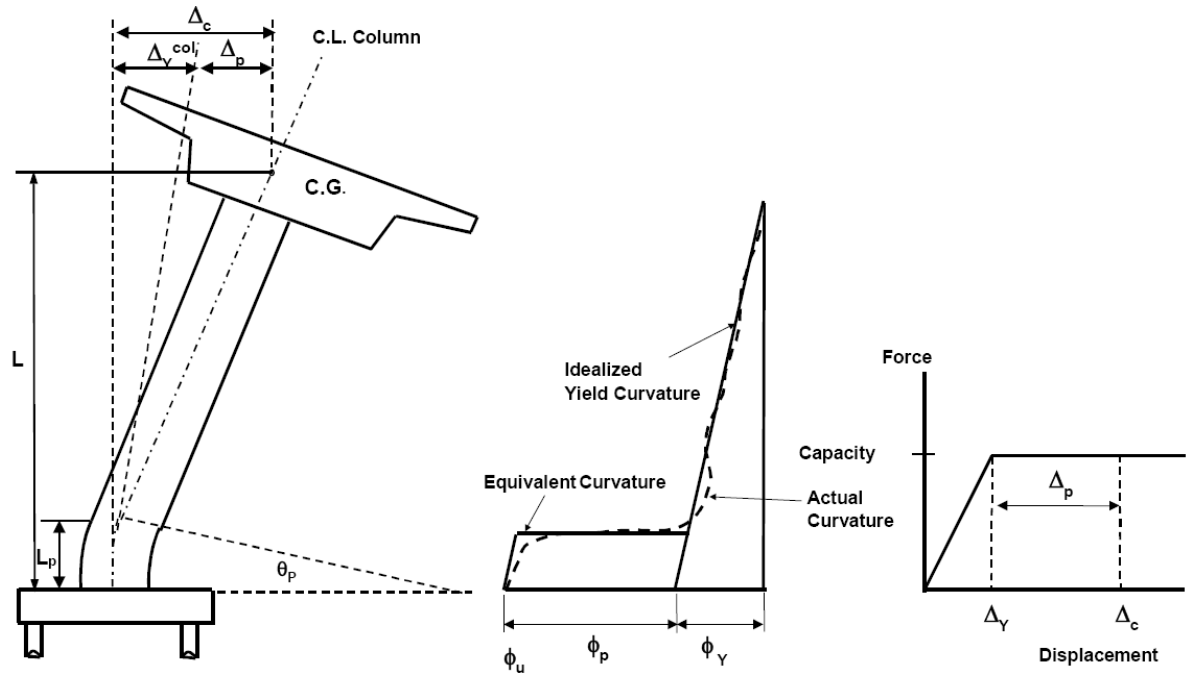

Figure 6.2. Displacement capacity of a cantilever column with fixed base (Caltrans, 2013)

Using the backbone curve, the cyclic response of the column under the uni-directional loading can be simulated using a Takeda-Thin model (Takeda et al., 1970). Figure 6.3 presents parameters of Takeda-Thin model. In this Figure, K_0 is the elastic stiffness, r is the post-yield stiffness factor (taken to be zero here for an elastic-perfectly plastic model), and α is an unloading coefficient which can be taken as 0.4 for the cantilever column with grouted duct or member socket connection.

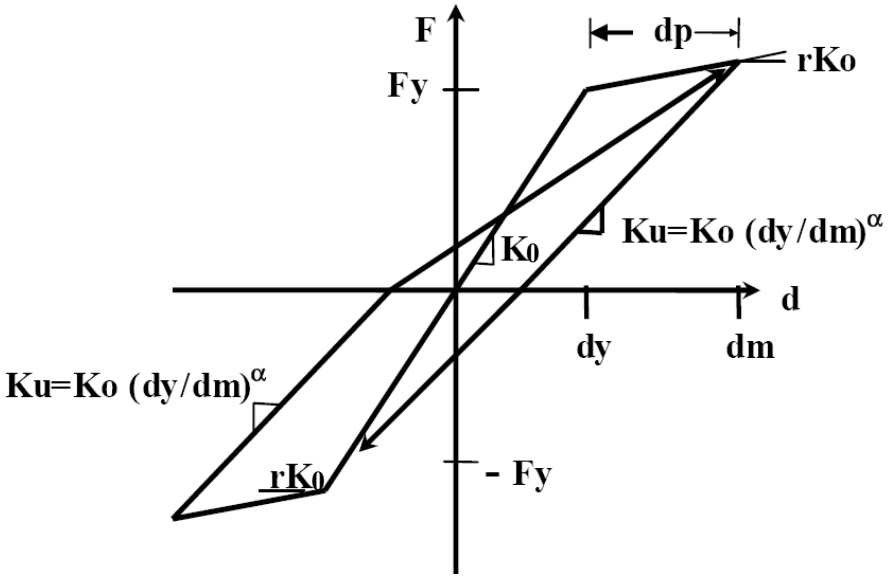

Figure 6.3. Takeda-Thin Model from Kowalsky and Ayers (2002)

Using the simplified modeling procedure presented above, the response of HDS2, HDC1, and HDC2 under the uni-directional loading was generated using simplified spreadsheets. The Moment-Curvature plot for each section was obtained from the section analysis using SAP 2000 (Computers and Structures Inc., 2015) software package. It is also possible to model the response of the column in SAP 2000 instead of using spreadsheet calculations. In this instance, a lumped plasticity model can be used. The assumption is that elastic deformation occurs over the member length, however, deformation beyond the yield point occurs only in the plastic hinge which is positioned in discrete user-defined location in the column. To capture the response of the structure, the software integrates the plastic strain and curvature over the user-defined hinge length. Modeling the strength degradation in the software is normally avoided, (Computers and Structures Inc., 2015). As mentioned earlier, analytical modeling for HDS1 is not carried out due to a construction error in testing of the column.

6.2.1.1 HDS2: Grouted Duct Connection

HDS2 incorporated a 120 mm unbonded length of the starter bars at the column to footing connection. In addition, external confinement (angle shoe) was provided at the base of the column to limit damage to the cover concrete (Figure 6.4). This means that when modeling the response of the column under uni-directional loading, there would not be any significant strength degradation due to loss of cover concrete until the failure point. A similar conclusion can be made during bi-directional loading of the column.

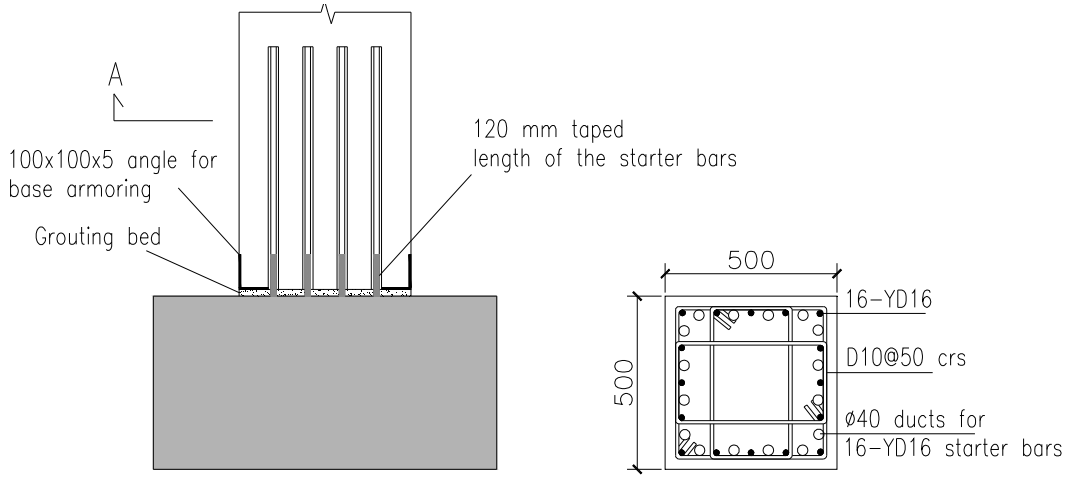

(a) Column to footing GDC connection (b) Column reinforcing details (Section - A)

Figure 6.4. Connection and section details for HDS2

In this section, the uni-directional response of HDS2 in the North-South direction is analytically modeled. The modeling parameters for HDS2 are presented in Table 6.1. It should be noted that in this Table, the plastic hinge length (L_p) was taken based on the observations from testing of the column with grouted duct connection. The observed plastic hinge length in testing of the columns with square section (HDS1 and HDS2) and grouted duct column to footing connection, was half height of the column section (b). This length would be equal to half diameter of the column for the circular sections. In accordance with NZS 3101 (NZS, 2006), this plastic hinge length would correspond to length of reversing plastic hinge in a conventional monolithic column. Thus, in this case using the formula proposed by Priestley et al. (2007) for computing the plastic hinge length of a ductile monolithic column would over predict the ultimate drift capacity of the column, refer to Equation 6.7.

Table 6.1. Summary of modeling parameters for HDS2

mm^{-1}	**%**	**kNm**	**mm**	**Takeda-Thin Parameters**	
$\phi_y = 8.17x10^{-6}$	$\Delta_y = 0.78$	$M_y = 310.4$	L = 2500	$f_{ye} = 516$ MPa	$K_0 = 6.34$ kN/mm
$\phi_Y = 1.16x10^{-5}$	$\Delta_Y = 1.11$	$M_Y = 439$	b = 500	$d_b = 16$ mm	r = 0
$\phi_u = 1.77x10^{-4}$	$\Delta_u = 5$	$M_P = 439$	$L_p = 250$	$L_{sp} = 181.6$ mm	$\alpha = 0.4$

Figure 6.5 presents plots for the moment-curvature and backbone curve of HDS2 in the North-South direction. In Figure 6.5a, both actual and idealized curve are plotted for a comparison. The analytical backbone curve in Figure 6.5b is in good agreement with the experimental results.

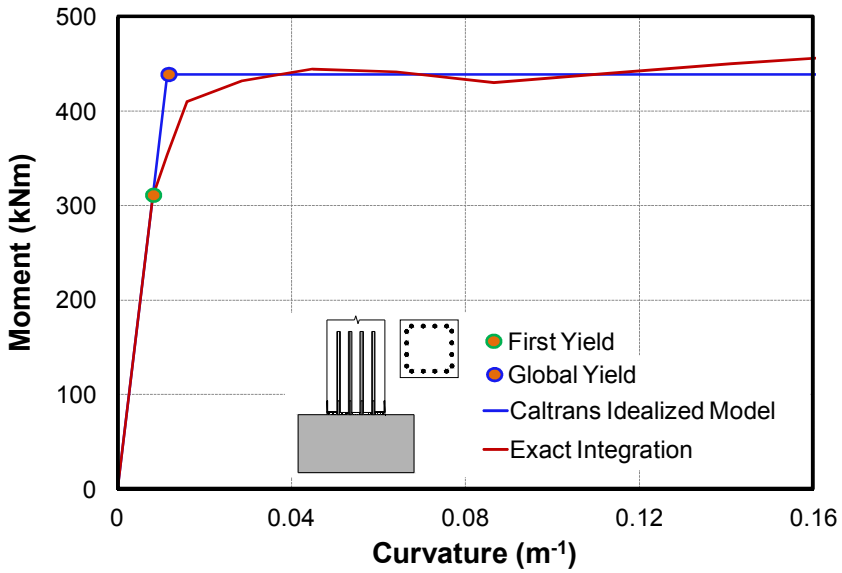

(a) Moment-curvature plot

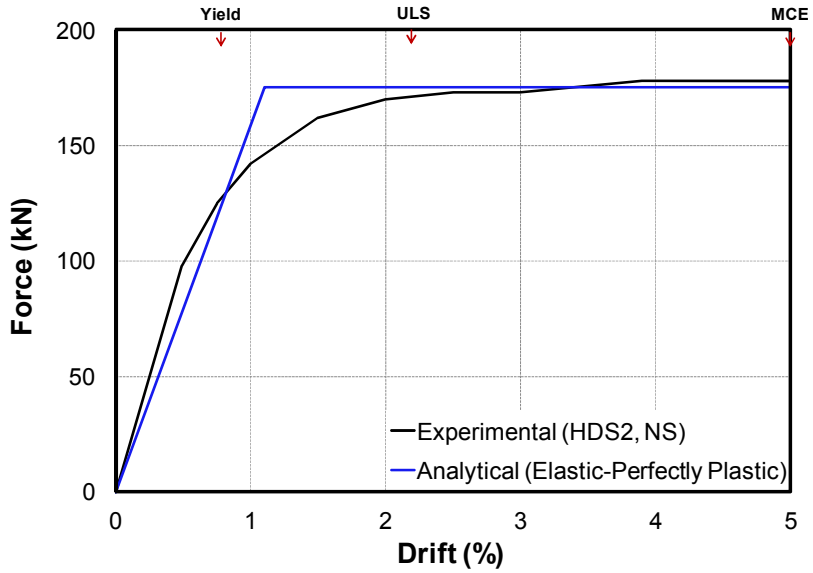

(b) Backbone curve plot

Figure 6.5. Moment-curvature and backbone curve plots for HDS2

Figure 6.6a shows the force-drift hysteresis plot of the column. The unloading coefficient for Takeda-Thin model (α) was taken as 0.4 after calibration of the analytical cyclic response with the experimental results. The simplified analytical model in Figure 6.6a well correlates with the overall behavior of the column up to 5% drift ratio. For a comparison, Figure 6.6b presents hysteretic response of the column using an unloading coefficient $\alpha = 0.5$ which is typically adopted when modeling the response of cast-in-place piers, (Blandon, 2004). It is shown that this model under predicts the residual drift of the column, especially during larger drift ratios.

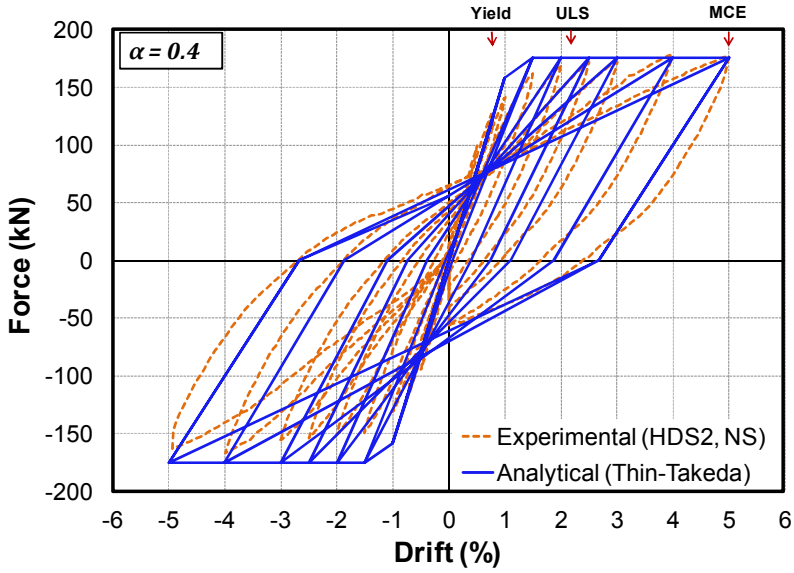

(a) Force-drift hysteresis for α = 0.4 (calibrated with experimental results)

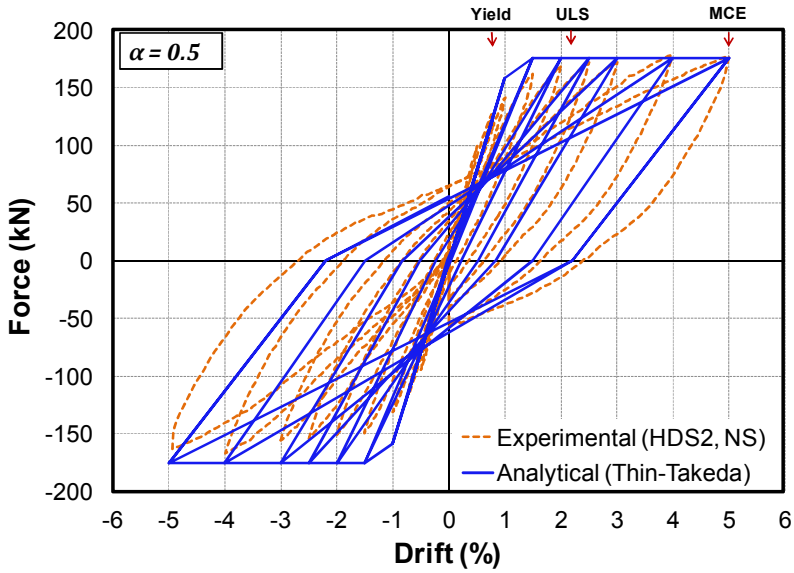

(b) Force-drift hysteresis for α = 0.5 (cast-in-place piers)

Figure 6.6. Force-drift hysteresis for HDS2

6.2.1.2 HDC1: Member Socket Connection

The reinforcing and connection details for HDC1 is shown in Figure 6.7. Generally, circular section provides a better confinement compared to other types of section such as rectangular, square etc (Mander et al., 1988). Therefore, a substantial strength degradation despite the loss of the unconfined concrete cover may not occur before failure of the first longitudinal rebar. This means that an elastic-perfectly plastic response, similar to that explained for HDS2 in the previous section, can still be used for HDC1. However, the observed plastic hinge length for the columns with member socket connection (HDC1 and HDC2) was equal to the diameter of the column (*d*).

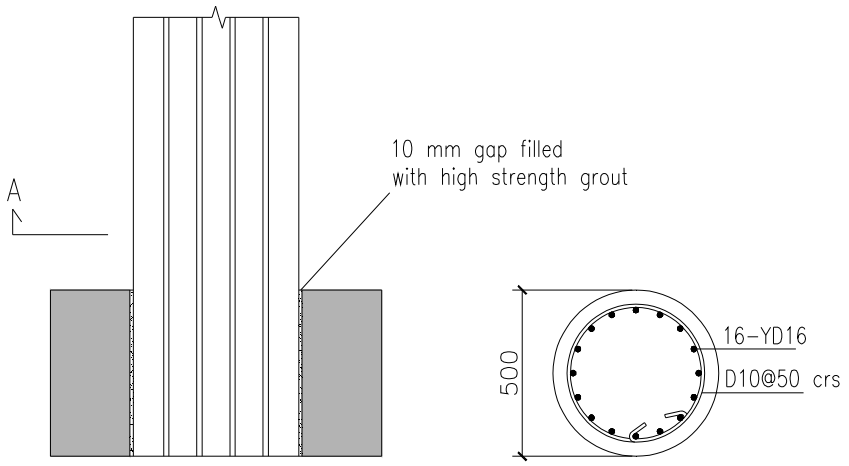

(a) Column to footing MSC connection (b) Column reinforcing details (Section - A)

Figure 6.7. Connection and section details for HDC1

In accordance with NZS 3101 (NZS, 2006), this plastic hinge length would be expected from a ductile monolithic column with unidirectional plastic hinges where inelastic rotation can develop on both sides of the critical section.

Table 6.2 presents a summary of the modeling parameters for HDC1.

Table 6.2. Summary of modeling parameters for HDC1

mm^{-1}	%	kNm	mm	Takeda-Thin Parameters	
$\phi_y = 9.03x10^{-6}$	$\Delta_y = 0.87$	$M_y = 272$	L = 2500	$f_{ye} = 516$ MPa	$K_0 = 5.03$ kN/mm
$\phi_Y = 1.24x10^{-5}$	$\Delta_Y = 1.19$	$M_Y = 375$	d = 500	$d_b = 16$ mm	r = 0
$\phi_u = 1.24x10^{-4}$	$\Delta_u = 6.2$	$M_P = 375$	$L_p = 500$	$L_{sp} = 181.6$ mm	$\alpha = 0.4$

The moment-curvature and backbone plots are shown in Figure 6.8a and Figure 6.8b, respectively. In Figure 6.8a, it can be observed that the Caltrans Idealized Model results

into a very similar curve to the actual one for HDC1. Similarly, the analytical backbone curve in Figure 6.8b is in good agreement with the experimental results.

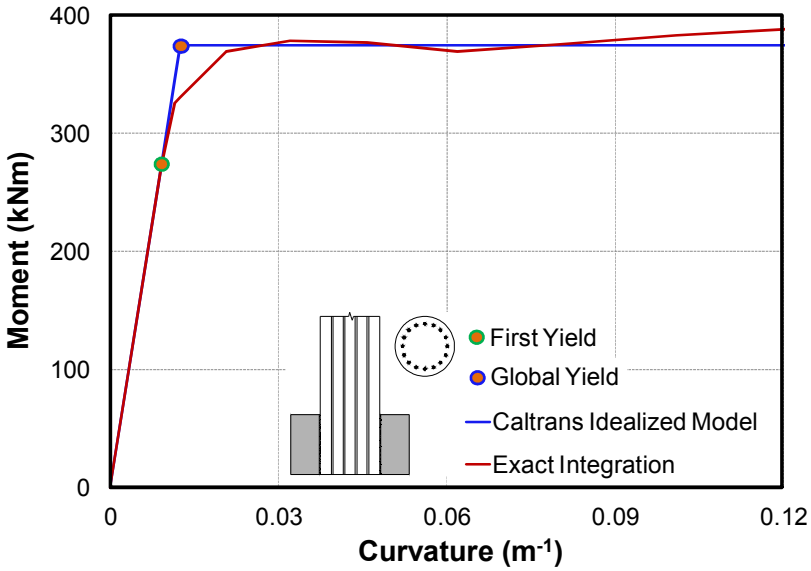

(a) Moment-curvature plot

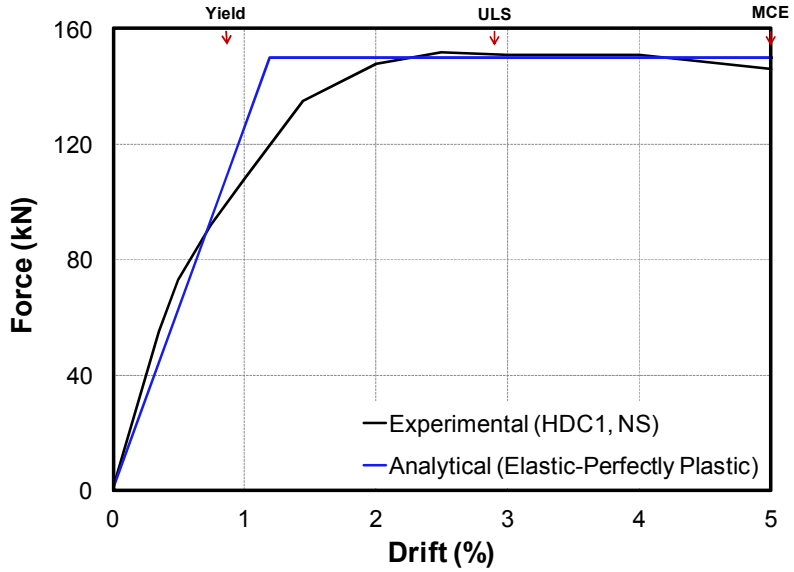

(b) Backbone curve plot

Figure 6.8. Moment-curvature and backbone curve plots for HDC1

The force-drift hysteresis plot for HDC1 is shown in Figure 6.9a. Similar to HDS2 with grouted duct connection, the unloading coefficient (α) for HDC1 with member socket connection can be taken as 0.4. Figure 6.9b shows the cyclic response of the column if the unloading coefficient (α) is taken to be 0.5. This is shown to under predict the residual drift in the column.

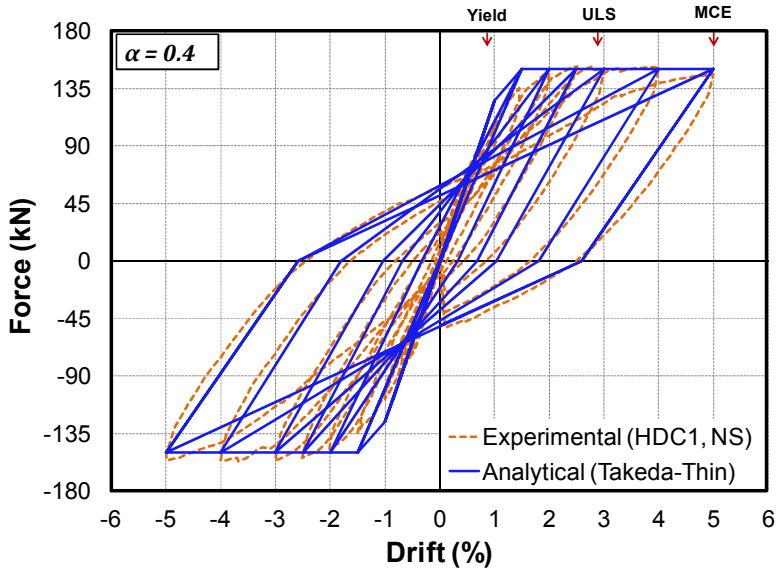

(a) Force-drift hysteresis for α = 0.4 (calibrated with experimental results)

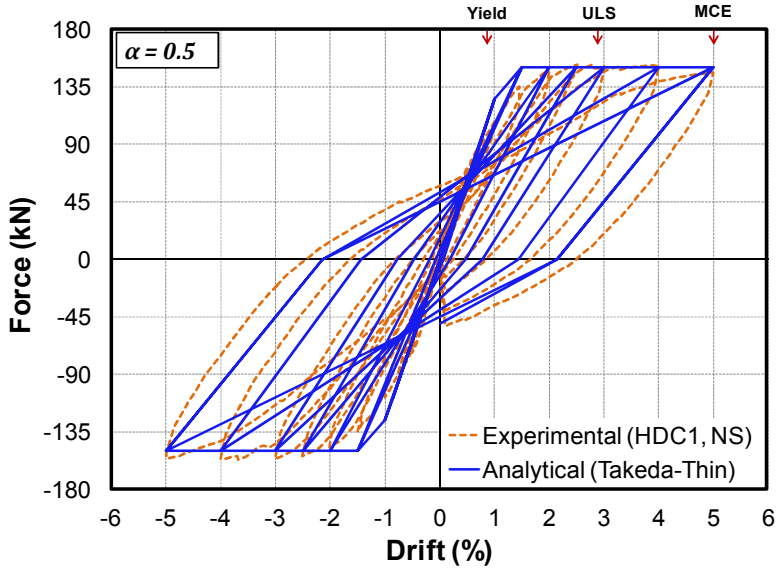

(b) Force-drift hysteresis for α = 0.5 (cast-in-place piers)

Figure 6.9. Force-drift hysteresis for HDC1

6.2.1.3 HDC2: Member Socket Connection

HDC1 and HDC2 had identical reinforcing details (see Figure 6.7). Therefore, analytical model from HDC1 (uni-directional) can also be used for HDC2 (bi-directional), but with some slight modifications. Under a bi-directional loading, there would be a reduction in the capacity of the column in the same principal direction compared to the uni-directional loading. This reduction is due to a more demanding loading type which would result into excessive deformation in the rebars and earlier loss of the unconfined cover concrete.

For a simplified approach and considering a particular principal direction such as North-South (NS), the reduction in capacity of the column can be taken into account by applying a factor of less than 1.0 to the moment capacity of the section at different performance points. The values of the curvature remain unchanged.

NZS 3101 provides a reduction factor of 0.85 when calculating the nominal capacity of the members under flexural action. Using an approximation by applying a reduction factor equal to this value (0.85), the bi-directional effects on decreasing the flexural capacity of the circular column can be considered to a certain level. Table 6.3 presents a summary of the modeling parameters for HDC2.

Table 6.3. Summary of modeling parameters for HDC2

mm^{-1}	**%**	**kNm**	**mm**	**Takeda-Thin Parameters**	
$\phi_y = 9.03x10^{-6}$	$\Delta_y = 0.87$	$M_y = 231$	L = 2500	f_{ye} = 516 MPa	K_0 = 4.28 kN/mm
$\phi_Y = 1.24x10^{-5}$	$\Delta_Y = 1.19$	$M_Y = 319$	H = 500	d_b = 16 mm	r = 0
$\phi_u = 1.24x10^{-4}$	$\Delta_u = 6.2$	$M_P = 319$	L_p = 500	L_{sp} = 181.6 mm	α = 0.4

Figure 6.10 presents the moment-curvature and backbone curve plots for HDC2 in the North-South direction. The analytical plots appear to be in good agreement with the experimental results up to 5% drift ratio.

The force-drift hysteresis plot is shown in Figure 6.11. It can be observed that if $\alpha = 0.5$, it results into a slightly better prediction of the response of the column, compared to taking the unloading coefficient similar to that used for HDC1 ($\alpha = 0.4$) in the previous section.

Another methodology to model the response of the column is to develop a three dimensional interaction diagram for the column section, considering axial load (gravity) and flexural action from the two perpendicular axes. However, this can be more complicated than a simplified model. Marriott (2009) presents modeling tools for biaxial loading of columns with emulative and dissipative controlled rocking connection.

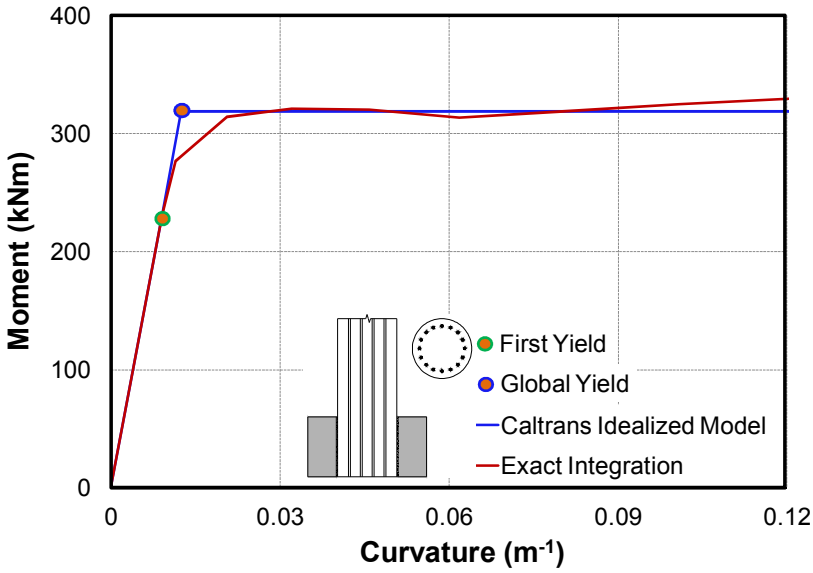

(a) Moment-curvature plot

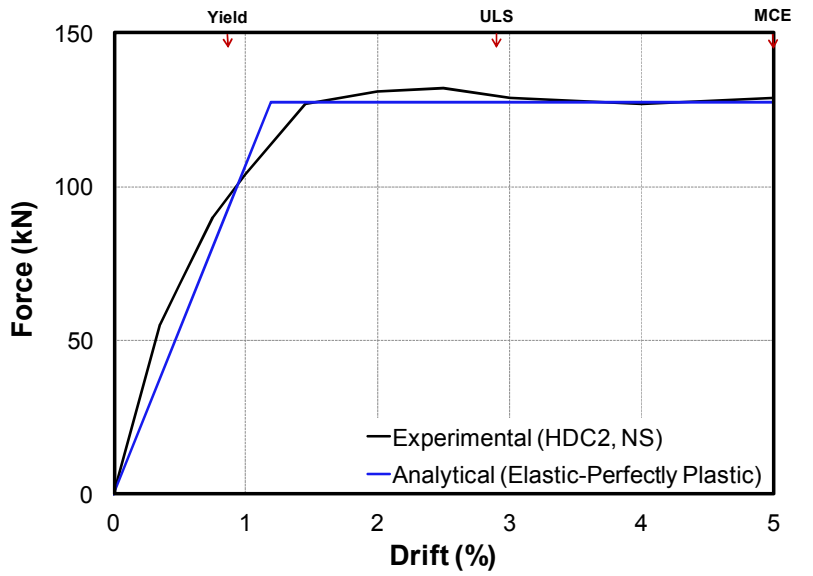

(b) Backbone curve plot

Figure 6.10. Moment-curvature plots for HDC2

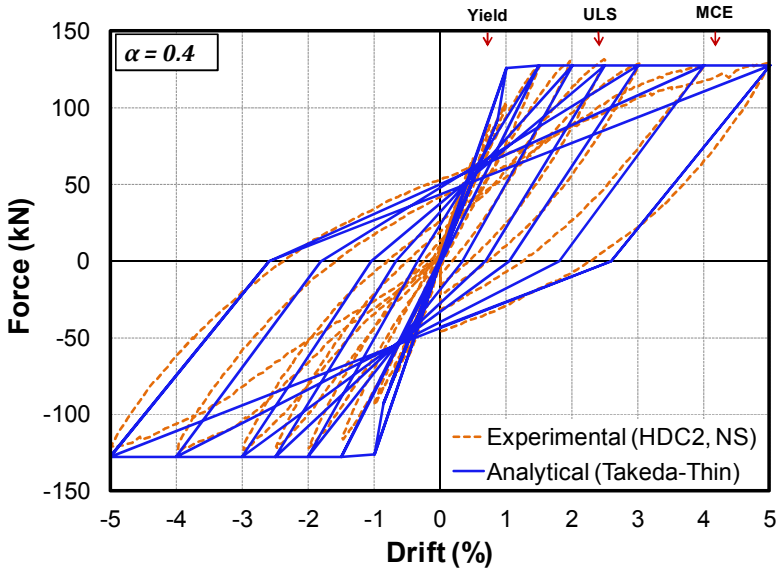

(a) Force-drift hysteresis for α = 0.4 (calibrated with experimental results)

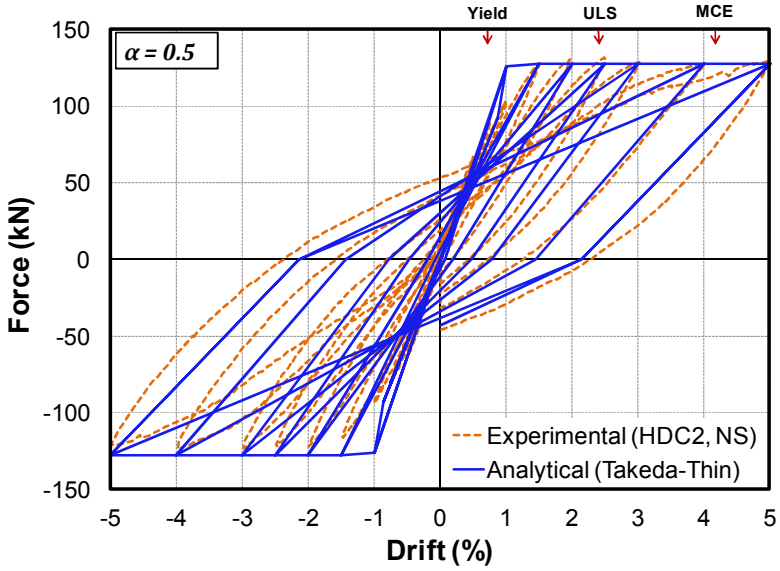

(b) Force-drift hysteresis for α = 0.5 (cast-in-place piers)

Figure 6.11. Force-drift hysteresis for HDC2

6.2.2 Multi-Column Pier System

The simplified analytical modeling procedure for multi-column pier system (bent) is similar to that described previously for the cantilever system, but with slight modifications as will be discussed in the next section.

6.2.2.1 HDB: Combination of Grouted Duct and Member Socket Connections

A typical column in a bent will undergo double curvature bending under combined action of gravity and lateral load. The point of contra flexure in the column is of high importance as the column can be considered as two short cantilever columns with fixed end supports (Figure 6.12).

For the bent incorporating member socket connection for the column to footing and grouted duct connection for the column to cap beam connection, each of the four short columns should be evaluated separately. For this purpose, a generic procedure from Priestley et al. (2007) and Caltrans Seismic Design Criteria (Caltrans, 2013) can be adopted. This is shown in Figure 6.13.

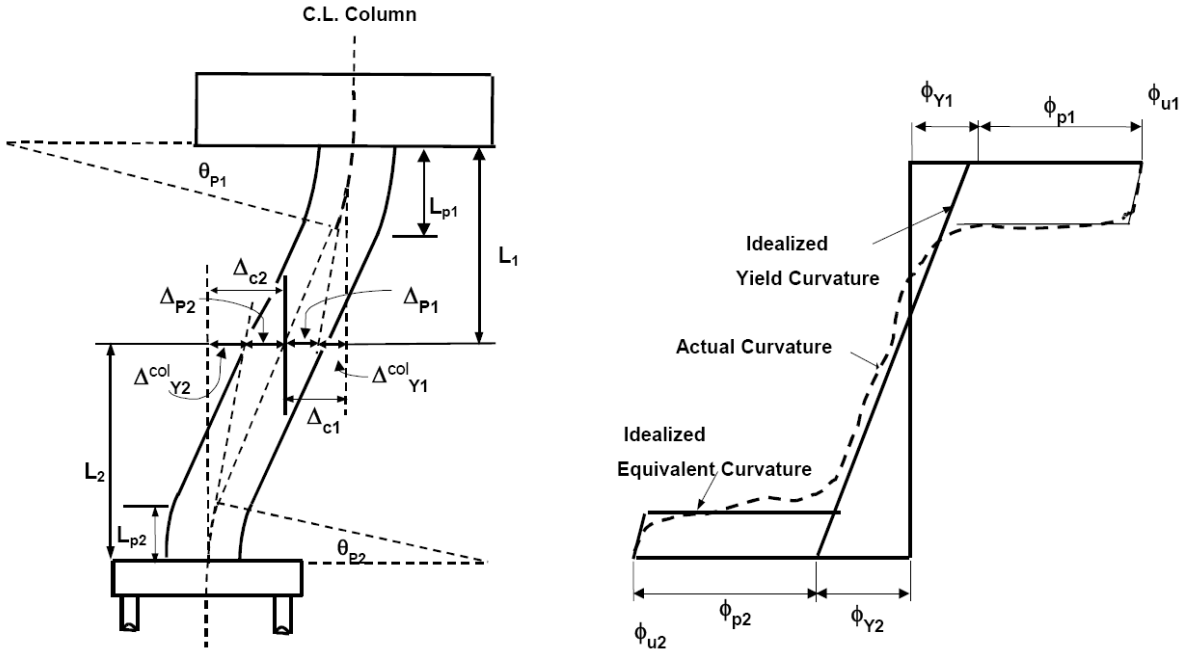

Figure 6.12. Displacement capacity of column in a bent with fixed-fixed supports (Caltrans, 2013)

The elastic-perfectly plastic moment-curvature (M-ϕ) analysis procedure described in Section 6.2.1 can also be adopted for the bent. The yield capacity (M_y) should be taken

from the M-ϕ analysis of the section. If the column features slightly different reinforcing details at the column to footing and column to cap beam connection (such as that in HDB), then M_y can be taken for the column section with the lower yield moment.

In HDB, there were 16-YD16 rebars for the member socket connection (Figure 6.13) and 16-YD16 plus 4-YD10 rebars at the grouted duct connection (Figure 6.14). The increase in reinforcing details of the column section at the grouted duct connection was due to a slight increase in the demand under the loading condition used (equivalent static forced-based analysis), refer to Section 3.3.4 in Chapter 3. Therefore, using M-ϕ analysis, M_y can be taken as the yield capacity of the column section at the column to footing member socket connection which has lower yield moment capacity. The yield force of the bent (F_y) equals M_y divided by the height of the short column with member socket connection, then multiplying the result by two to account for the presence of the two columns in HDB.

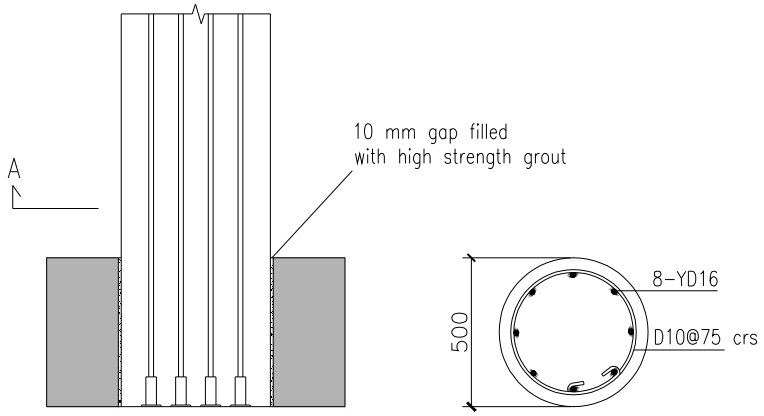

(a) Column to footing connection (b) Column reinforcing (Section - A)

Figure 6.13. Member socket connection details for HDB

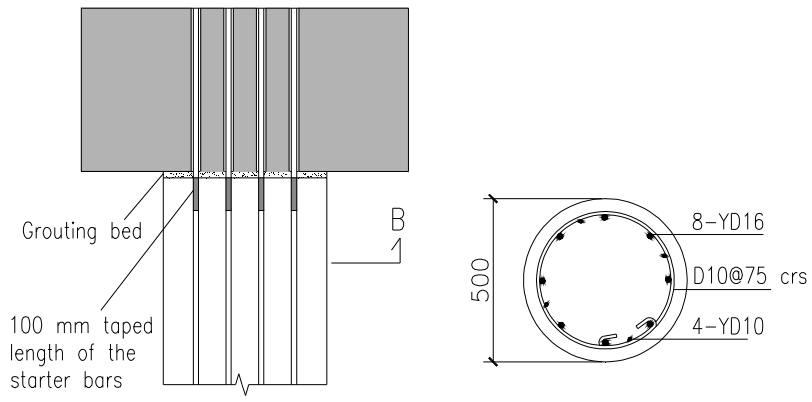

(c) Column to footing cap beam connection (d) Column reinforcing (Section - B)

Figure 6.14. Grouted duct connection details for HDB

For computing ϕ_y, a displacement-based procedure can be adopted. Using ϕ_y for a particular section as substitute for the global curvature may produce unrealistic results. In this instance, given the fact that two different types of connection are implemented in the bent, a generic procedure similar to that proposed by Priestley et al. (2007) can be appropriate. Equation 6.8 presents an expression to calculate ϕ_y for circular sections from Priestley et al. (2007). This value can be adopted for both connections as the column top and bottom diameter is identical.

$$\phi_y = 2.25 \frac{f_{ye}}{E\ d} \tag{6.8}$$

Where,

E = Modulus of elasticity of steel (normally taken as 200,000 MPa)

d = Diameter of the section

For calculation of the first yield displacement (Δ_y), Equation 6.1 can be used for each short column as follows:

$$\Delta_{y1} = \phi_y \frac{(L_1 + L_{sp})^2}{3} \tag{6.9}$$

$$\Delta_{y2} = \phi_y \frac{(L_2 + L_{sp})^2}{3} \tag{6.10}$$

$$\Delta_y = \Delta_{y1} + \Delta_{y2} \tag{6.11}$$

After computing Δ_y in accordance with Equation 6.8 through Equation 6.11, it can be linearly scaled up to obtain the displacement at the centerline of the cap beam. In this instance, Equation 6.12 can be used to calculate the Scaling Factor (SF) as follows:

$$SF = \frac{L_{cb}}{L} = 1.1145 \text{ for HDB} \tag{6.12}$$

Where,

L_{cb} = Height from top of the footing up to centerline of the cap beam (2920 mm for HDB)

L = Height from top of the footing up to bottom face of the cap beam (2620 mm for HDB)

When computing L_1 and L_2 for HDB, the contraflexure point under the loading condition presented in Section 3.3.4 of Chapter 3 is located at height of 1289 mm from top of the footing in HDB. This gives L_1 and L_2 to be equal to 1331 mm and 1289 mm, respectively.

The plastic moment capacity (M_p) can be taken from the column section with higher capacity. This would show the maximum capacity of the bent. For HDB, the plastic moment capacity of the top grouted duct connection from M-ϕ analysis times 2 (two columns in HDB) would be the maximum capacity of the bent. The plastic force (F_p) can be calculated by dividing M_p over the length of the short column with grouted duct connection, then multiplying the result by two to account for the presence of two columns in the bent.

The global yield curvature (ϕ_Y) and displacement (Δ_Y) can be computed using Equation 6.4 and Equation 6.9 through Equation 6.12, respectively. ϕ_{u1} and ϕ_{u2} can be taken from the M-ϕ analysis for each section, respectively. Δ_u should be taken as the lesser of Δ_{u1} and Δ_{u2}. Table 6.4 presents a summary of the parameters for each short column in HDB. It should be noted that in Table 6.4, the plastic hinge length for each connection is taken from the experimental observations.

Table 6.4. Summary of parameters for each short cantilever column in HDB

Top Cantilever Column (Grouted Duct Connection)	**Bottom Cantilever Column (Member Socket Connection)**
L_1 = 1331 mm	L_2 = 1289 mm
d_b = 16 mm	d_b = 16 mm
f_{ye} = 516 MPa	f_{ye} = 516 MPa
L_{sp} = 181.6 mm	L_{sp} = 181.6 mm
$\phi_y = 1.161 \times 10^{-5}$ mm^{-1}	$\phi_y = 1.161 \times 10^{-5}$ mm^{-1}
$\phi_Y = 1.783 \times 10^{-5}$ mm^{-1}	$\phi_Y = 1.783 \times 10^{-5}$ mm^{-1}
$\phi_{u1} = 1.51 \times 10^{-4}$ mm^{-1}	$\phi_{u2} = 1.55 \times 10^{-4}$ mm^{-1}
L_{p1} = 250 mm	L_{p2} = 500 mm
Δ_{y1} = 8.9 mm	Δ_{y2} = 8.4 mm
Δ_{Y1} = 13.6 mm	Δ_{Y2} = 12.9 mm
Δ_{u1} = 53.8 mm	Δ_{u2} = 79.7 mm
M_{y1} = 171 kNm	M_{y2} = 153 kNm
M_{p1} = 235 kNm	M_{p2} = 208 kNm
F_{y1} = 128.5 kNm	F_{y2} = 118.7 kNm
F_{p1} = 176.6 kNm	F_{p2} = 161.4 kNm

The *M-ϕ* of the section for each short cantilever column with grouted duct and member socket connection is plotted in Figure 6.15a and Figure 6.15b, respectively.

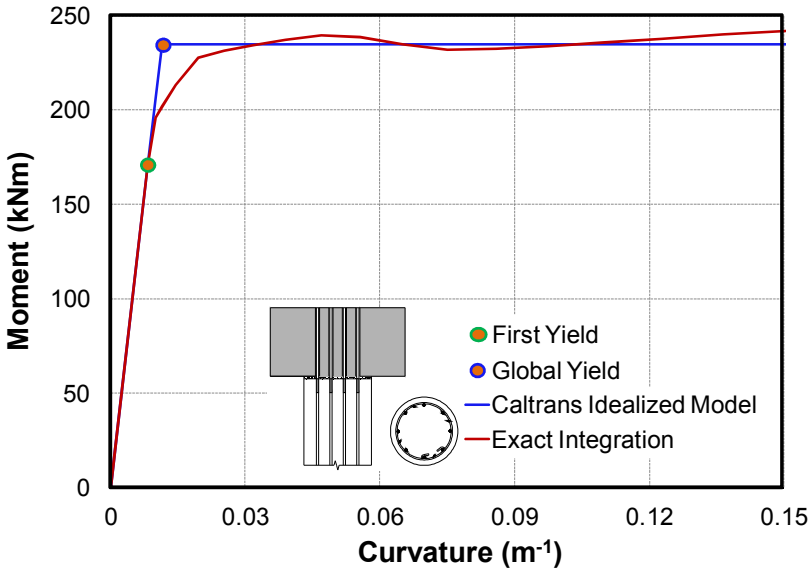

(a) column section at the top grouted duct connection

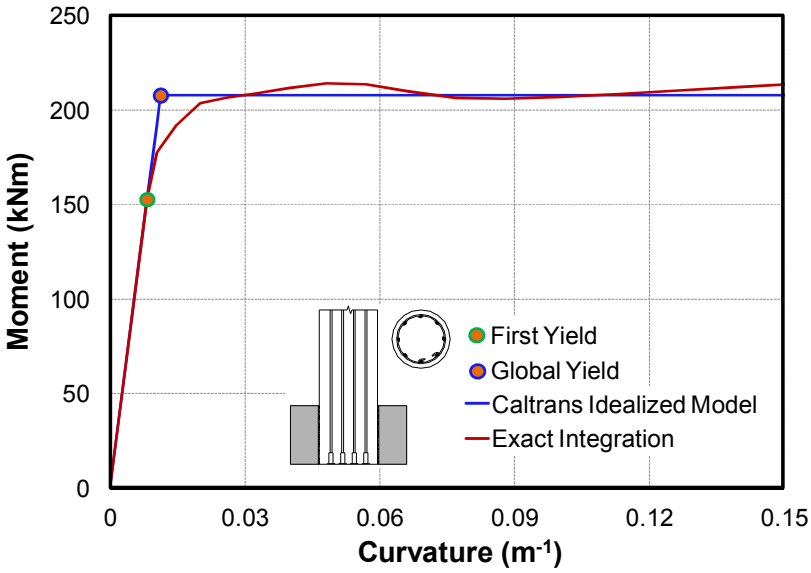

(b) Column section at the bottom member socket connection

Figure 6.15. Moment-curvature plots for column sections in HDB

Table 6.5 presents a summary of the final modeling parameters for HDB. In this Table, values of F_Y and F_P are already multiplied by two, in order to account for contribution of the two columns in the bent. Using parameters from Table 6.5, the backbone curve is plotted in Figure 6.16.

Table 6.5. Summary of final modeling parameters for HDB

mm^{-1}	%	kNm	kN	Takeda-Thin Parameters
$\phi_y = 1.161x10^{-5}$	$\Delta_y = 0.66$	$M_y = 153$	$F_y = 237.4$	$K_0 = 12.3$ kN/mm
$\phi_Y = 1.783x10^{-5}$	$\Delta_Y = 1$	$M_Y = 235$	$F_Y = 353.2$	r = 0
$\phi_u = 1.51x10^{-4}$	$\Delta_u = 5.7$	$M_P = 235$	$F_p = 353.2$	$\alpha = 0.3$

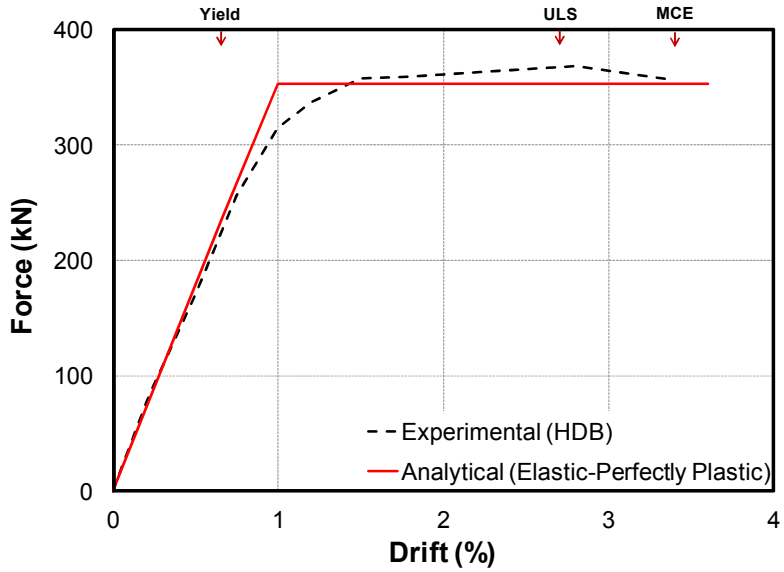

Figure 6.16. Backbone plots for HDB

Using data from the backbone curve, the cyclic response of the bent under the uni-directional loading can be simulated using Takeda-Thin model (Figure 6.17).

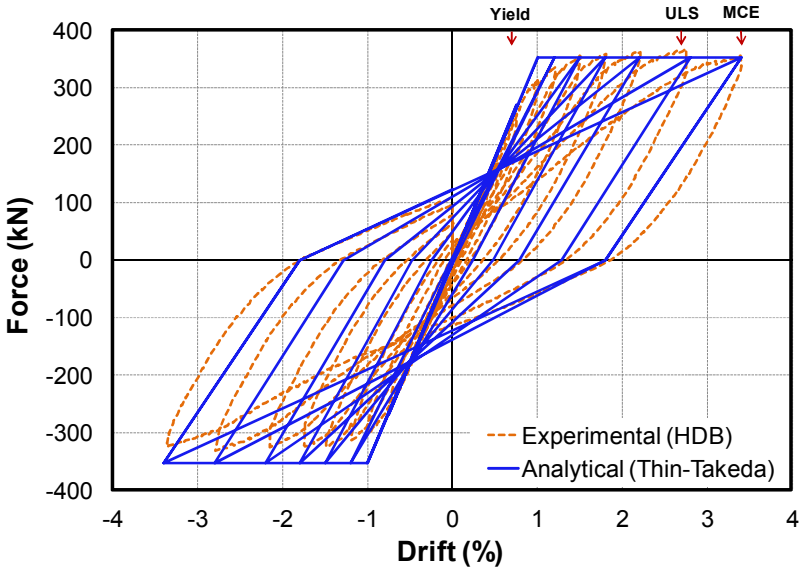

Figure 6.17. Force-drift hysteresis for HDB

The analytical plots in Figure 6.16 and Figure 6.17 well correlate with the experimental results. It should be noted that for HDB, the post-yield stiffness factor (r) can be taken to be zero for elastic-perfectly plastic response. The unloading coefficient (α) can be taken to be 0.3 for a combination of grouted duct and member socket connection in the bent. The reason behind using lower value of α for the bent in comparison to cantilever columns ($\alpha = 0.4$), is that given higher number of connections (4) in the bent, the residual drift can be expected to be higher than a simple cantilever column.

As a summary, the simplified analytical models presented in this part of the Chapter are predicting the response of ABC High Damage system uni-directional quasi-static cyclic loading to a good level of accuracy under. The analytical models are based on the results from moment-curvature analysis and displacement-based design by Priestley et al. (2007).

When modeling the response of ABC High Damage with grouted duct or member socket connection, the plastic hinge length would have to be taken as half diameter/height of the section for the grouted duct, and full diameter/height of the section for the member socket connection. For modeling the response of cantilever columns, the backbone curve can be constructed using the results from a moment-curvature analysis of the column section at the plastic hinge zone. For the bent with combination of grouted duct and member socket connection, a more generic procedure in accordance with Priestley et al. (2007) would have to be adopted. The yield curvature would have to calculated using the expression proposed by Priestley et al. (2007), not from the moment-curvature analysis of the column section. Each column in the bent can be considered as two short cantilever columns. The yield displacement for each short column can be calculated separately. The summation of the yield displacement of the short columns would be the total yield displacement of the bent.

Existing theoretical models such as Takeda-Thin can be used to simulate the cyclic response of ABC High Damage system. The unloading coefficient can be taken to be 0.4 and 0.3 for the cantilever and multi-column pier system, respectively. The post-yield stiffness factor can be taken as zero for an elastic-perfectly plastic response.

6.3 Modeling the Response of Innovative Dissipaters

This section presents simplified analytical models for the innovative dissipaters discussed in Chapter 4. The analytical models are developed to match the overall backbone and hysteretic response of the dissipaters.

Two theoretical models, the Ramberg-Osgood (Ramberg and Osgood, 1943) and Bilinear (Naeim and Kelly, 1999), are used to simulate the backbone curve and cyclic response of the dissipaters. The Ramberg-Osgood and Bilinear hysteresis rules are illustrated in Figure 6.18. The models incorporate balanced hysteresis in tension and compression stages of the loading.

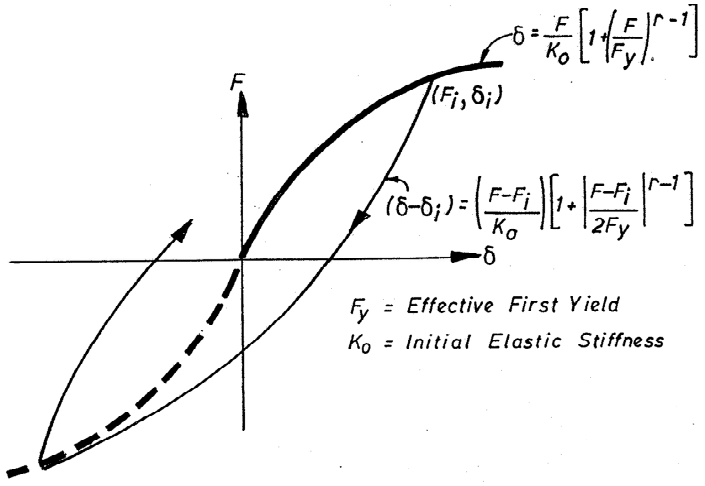

(a) Ramberg-Osgood hysteresis rule

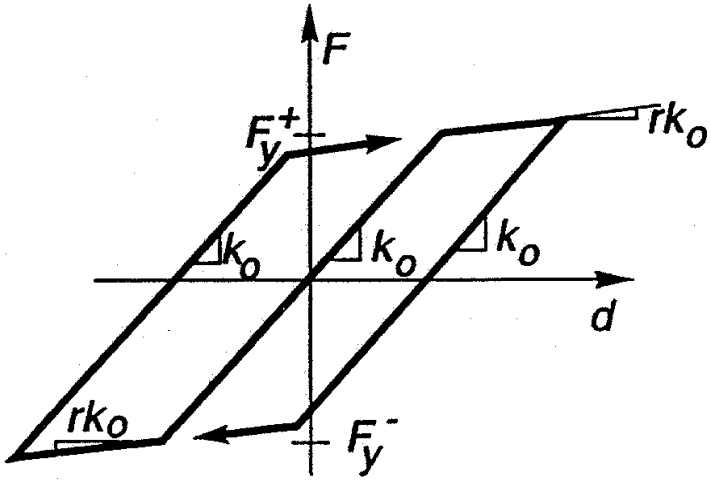

(b) Bilinear hysteresis rule

Figure 6.18. Hysteresis rules to model cyclic response of steel, after Carr (2005)

Traditionally, the Ramberg-Osgood model has been used to model the cyclic response of steel members in a frame structure. In this model, one of the most important

parameters is the (r) coefficient. For a linear elastic system $r = 1.0$. With increasing values of (r), the post-yield stiffness of the system is decreasing. This means that with $r = \infty$, the response of the system would be that of elastic-perfectly plastic model.

The Bilinear hysteretic model was originally developed to capture the dynamic behavior of a system that incorporates isolation devices, in particular the friction pendulum. However, this model can also be utilized as a simplified tool for modeling the response of mini dissipaters.

In general, past research studies have shown that the response of axial dissipaters made of steel material can be simulated better using a Ramberg-Osgood model compared to a more simplified Bilinear model (Sarti et al., 2013 and Baird et al., 2014).

6.3.1 UFP Bracing Type Dissipater (UFP-BD)

Kelly et al. (1972) formulated the force resistance of UFP by providing an expression between the coupling shear and the plastic moment (Figure 6.19).

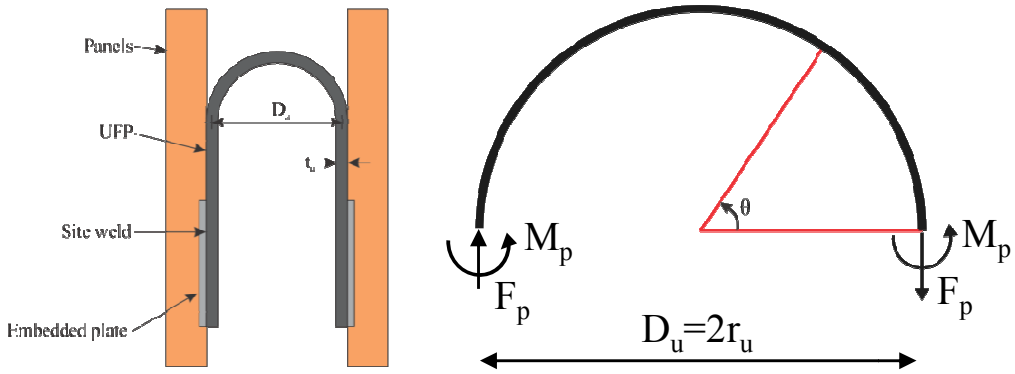

(a) UFP arrangement **(b) Coupling shear of UFP**

Figure 6.19. UFP arrangement and formulation parameters, after Baird et al. (2014)

The plastic force (F_P) can be obtained from Equation 6.13. The plastic force is generally taken as 1.5 times the yield force (F_Y) in accordance with Kelly et al. (1972) and Baird et al. (2014). The yield force (F_Y) and initial stiffness (K_0) are calculated using Equation 6.15 and Equation 6.16 in accordance with Baird et al. (2014), respectively. The yield displacement (Δ_Y) of the UFP can be calculated using Equation 6.17. The maximum displacement capacity of the UFP (Δ_u) depends on the stroke limit of the UFP. The

maximum stroke of a UFP is the distance between the location of the leg fixing to the start point of the half circle.

$$F_P = \frac{2M_P}{D_u} \tag{6.13}$$

$$F_P = 1.514\, F_Y \tag{6.14}$$

$$F_Y = \frac{\sigma_y\, b_u\, t_u^2}{2D_u} \tag{6.15}$$

$$K_0 = \frac{16\, E\, b_u}{27\pi} \left(\frac{t_u}{D_u}\right)^3 \tag{6.16}$$

$$\Delta_Y = \frac{F_Y}{k_0} \tag{6.17}$$

Where,

M_P = Plastic Moment capacity of the UFP (kNm)

F_P = Maximum Capacity of the UFP (kN)

F_Y = Yield capacity of the UFP (kN)

K_0 = Initial Stiffness of the UFP (kN/mm)

Δ_Y = Yield displacement of the UFP (mm)

Δ_P = Maximum displacement of the UFP (mm)

σ_y = Yield stress of the UFP plate (MPa)

b_u = Width of the UFP plate (mm)

t_u = Thickness of the UFP plate (mm)

D_u = Diameter of the UFP bend (mm)

E = Elastic modulus of the plate material (MPa)

For calculating the yield and plastic capacity of several UFPs which are connected in parallel (such as that inside the UFP Bracing Damper), the yield and plastic capacity from Equation 6.14 and Equation 6.15 should be multiplied by the number of the UFPs (n_u) inside the dissipater.

To model the backbone and cyclic response of the UFP Bracing Dissipater (UFP-BD), two models (Bilinear and Ramberg-Osgood) were considered. The Bilinear model can be constructed using the parameters F_Y, k_0, Δ_Y, F_P, n_u, and Δ_P. For the Ramberg-Osgood model, a coefficient of $r = 5$ could be used to capture the response of the UFP Bracing Damper. Table 6.6 presents a summary of the modeling parameters for UFP-BD.

Table 6.6. Summary of modeling parameters for UFP-BD

%	kN	mm	mm	MPa	Ramberg - Osgood Parameters
$\Delta_Y = 0.1$	$F_Y = 51.8$	$b_u = 90$	$D_u = 75$	$\sigma_y = 300$	$K_0 = 13.91$ kN/mm
$\Delta_P = 0.805$	$F_P = 78.5$	$t_u = 6$	L = 3725	E = 200,000	r = 5 and $n_u = 8$

The backbone plot for UFP-BD is shown in Figure 6.20. Both models provide good estimate of the brace post-yield strength, but over predict the initial stiffness of the dissipater. As explained in Chapter 4, UFP-BD was constructed using recycled parts with some slackness in the brace due to construction tolerance in the bolt holes. This had resulted into a reduction in the initial stiffness of the brace.

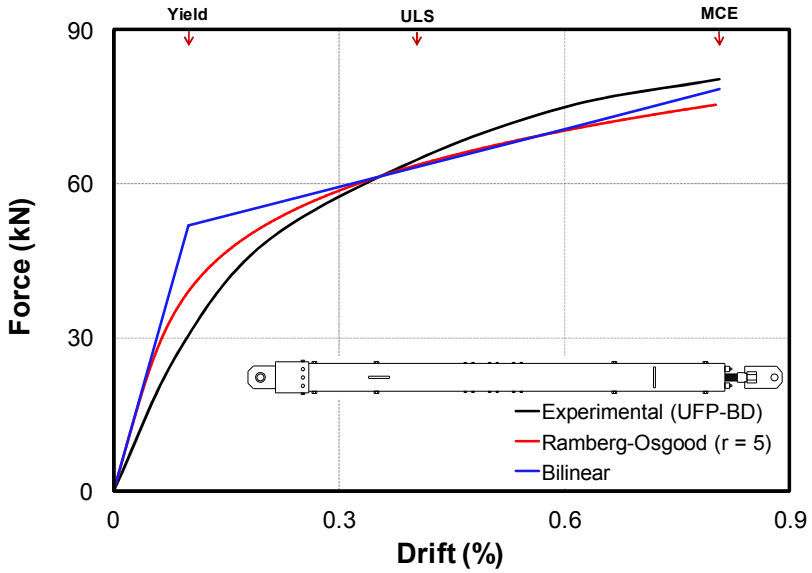

Figure 6.20. Backbone plots for UFP-BD

The analytical cyclic force-drift response for the Bilinear and Ramberg-Osgood models is plotted in Figure 6.21. The Bilinear model (Figure 6.21a) captures an overall behavior of the brace. The Ramberg-Osgood model appears to be more accurate and compatible with the experimental results. Experimental results suggested slight increase in the capacity of the brace during compression stage of the loading. This was due to poor fabrication of the brace and its internal parts. For a properly manufactured UFP Bracing Damper, this effect can be eliminated with proper fabrication of the parts and lubrication of the contact surfaces to minimize friction.

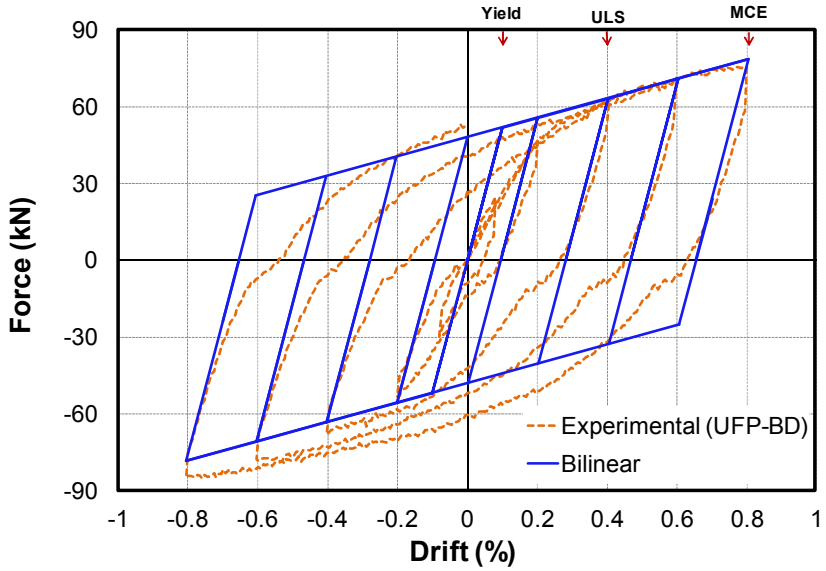

(a) Bilinear model

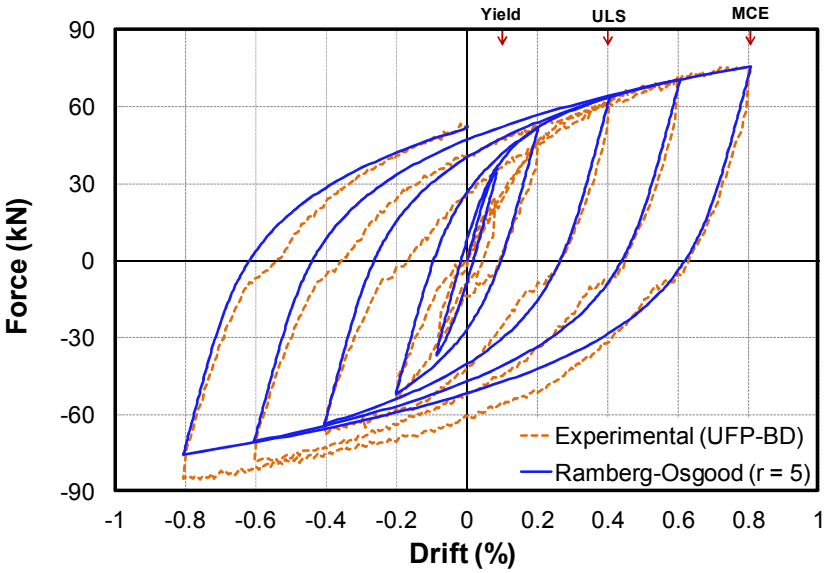

(b) Ramberg-Osgood model

Figure 6.21. Force-drift hysteresis for UFP-BD

6.3.2 UFP Mini Plug and Play Dissipater (MUD)

The analytical modeling procedure for Mini UFP Damper (MUD) was similar to what explained for the UFP Bracing Dissipater in the previous section. The Bilinear response can be plotted after calculating the parameters F_Y, k_0, Δ_Y, F_P, n_u, and Δ_P. The Ramberg-Osgood coefficient can be taken similar to what proposed for the UFP Bracing Dissipater ($r = 5$).

There were four tests carried out on three MUD prototypes, as presented in Table 4.3 of Chapter 4. The first three tests consisted of cyclic loading of MUD under net positive deformation. The fourth test included cyclic loading of MUD-3 under both positive and negative deformation. Modeling the response of MUD under both positive and negative deformation is outside the scope of this thesis. However, a Bilinear analytical model is presented for the test carried out on MUD-3.

6.3.2.1 Modeling Response of MUD under Net Positive Deformation

Table 6.7 presents a summary of the modeling parameters for MUD prototypes.

Table 6.7. Summary of modeling parameters for MUD

%	kN	mm	mm	MPa	Ramberg - Osgood Parameters
$\Delta_Y = 0.36$	$F_Y = 16.7$	$b_u = 50$	$D_u = 45$	$\sigma_y = 300$	$K_0 = 10.35$ kN/mm
$\Delta_P = 4.44$	$F_P = 25.2$	$t_u = 5$	L = 450	E = 200,000	r = 5 and $n_u = 4$

The backbone plot for MUD under net positive strain is presented in Figure 6.22. An average of the three tests is used to compare the experimental response against the analytical model. It is obvious that the Ramberg-Osgood model better captures the behavior of the dissipater. The Bilinear model presents fair estimate of the dissipater strength at the yield point, but provides better result for the strength at the maximum displacement.

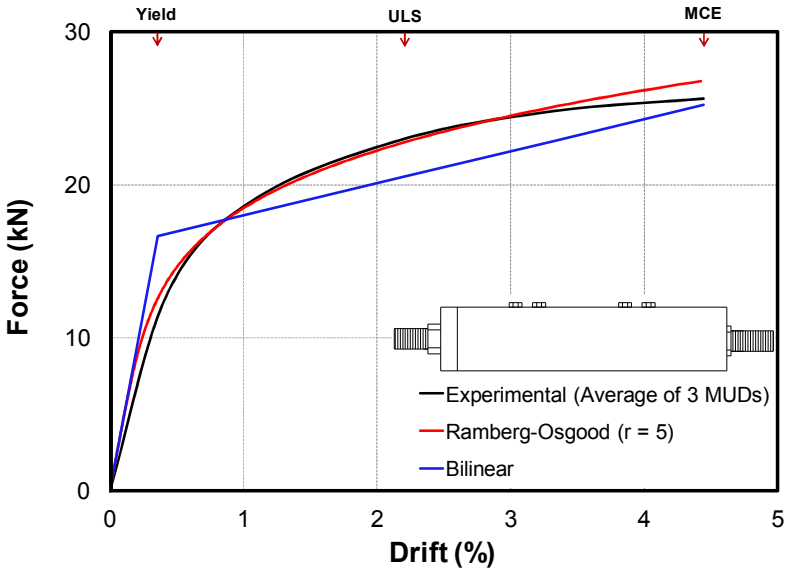

Figure 6.22. Backbone plots for MUD under net positive deformation

Using the results from the backbone plot in Figure 6.22, the cyclic force-drift response of the dissipater is plotted in Figure 6.23. The Bilinear model (Figure 6.23) does not show a good prediction of the stiffness and strength degradation. It also cannot predict the Bauschinger effects in the hysteresis.

The Ramberg-Osgood model captures the behavior better than Bilinear model. However, it does not represent a very accurate stiffness degradation of the dissipater during the cyclic loading.

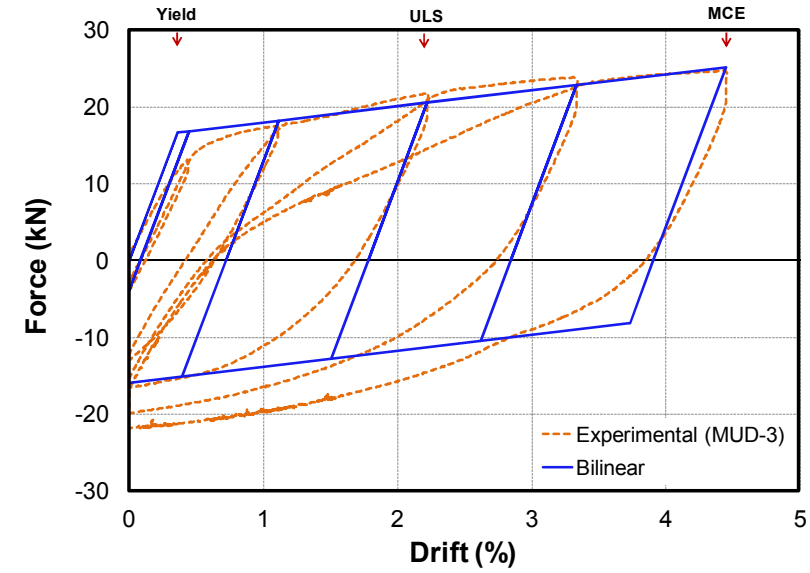

(a) Bilinear model

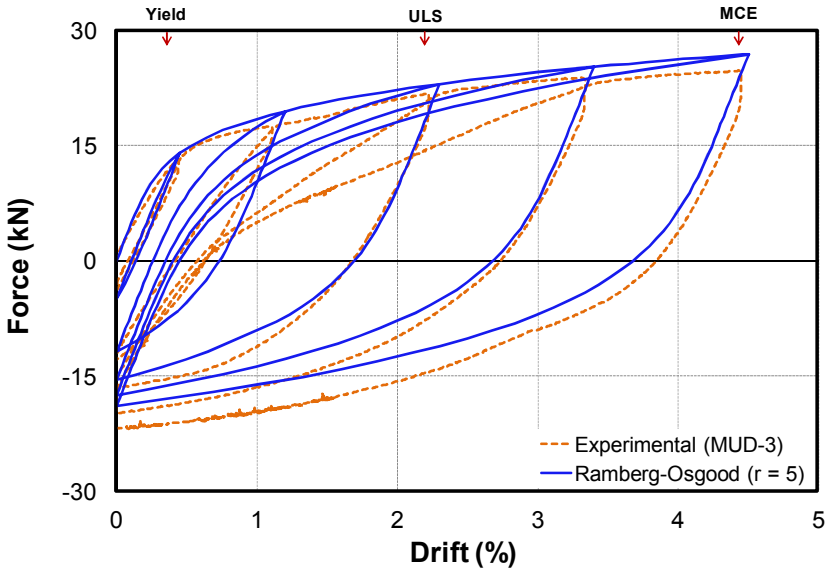

(b) Ramberg-Osgood model

Figure 6.23. Force-drift hysteresis for MUD under net positive deformation

6.3.2.2 Modeling Response of MUD under Net Positive and Negative Deformation

The modeling parameters were identical to those presented in Table 6.7 for MUD under net positive deformation. It is important to note that MUD-3 had previous yield from the testing under net positive deformation (Figure 6.23). Therefore, the initial stiffness of the dissipater under the net positive portion of the loading was significantly lower as can been noticed in the experimental backbone plot of Figure 6.24. The experimental backbone plot of the dissipater under the net negative portion of the loading had a slight increase in the capacity which was thought to be due to Bauschinger effects.

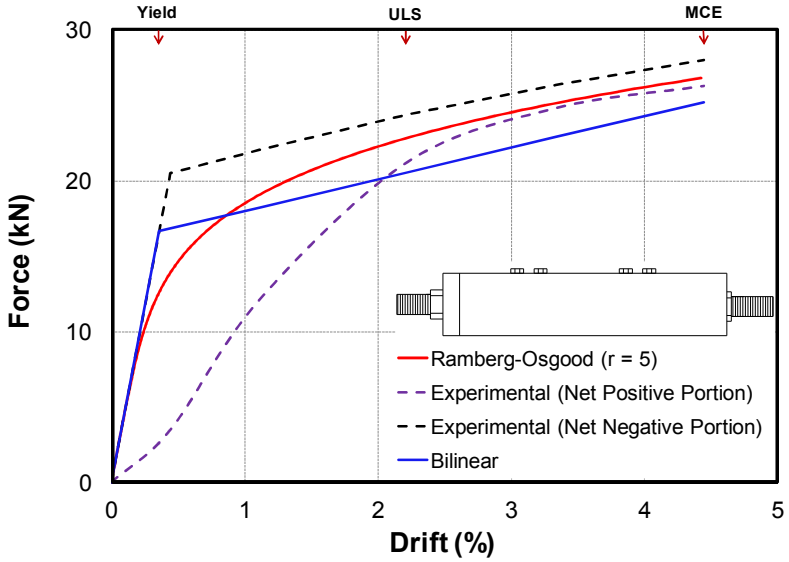

Figure 6.24. Backbone plots for MUD under net negative and positive deformations

The analytical cyclic response of the yielded dissipater under net positive and negative deformation is plotted in Figure 6.25. It is obvious that similar to what described for the testing of MUD under net positive deformation, the Bilinear model does not capture the Bauschinger effects in the hysteresis. It under predicts the capacity of the dissipater. However, this was thought to have been due to previous yield in the dissipater. The Bilinear model for MUD under net positive deformation represented a good estimate of the capacity, refer to Figure 6.23a.

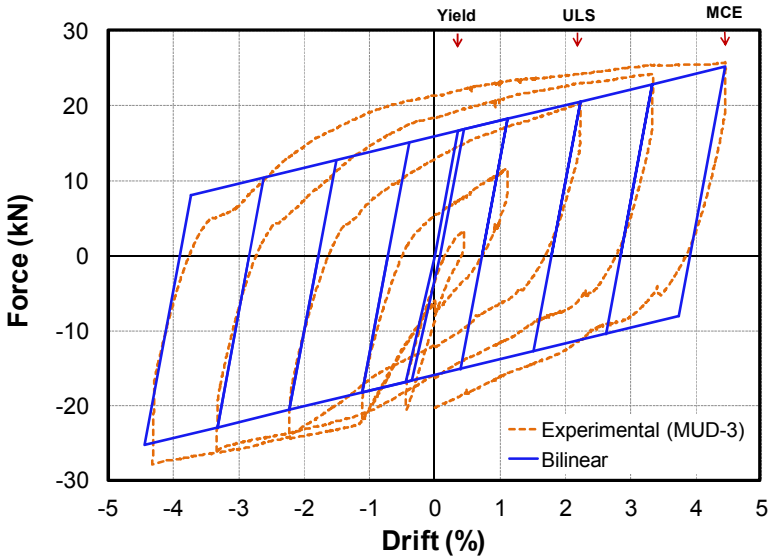

Figure 6.25. Force-drift hysteresis for MUD under net positive and negative deformation

6.3.3 Grooved Dissipater (GD)

The Ramberg-Osgood and Bilinear models can be used to predict the response of the Grooved Dissipater (GD). In this regards, the initial stiffness of the dissipater is one of the most important parameters. This can be calculated by using similar procedure to that presented in Sarti et al. (2013) for modeling the response of Buckling-Restrained Fused Type (BRF) dissipater. In this approach when calculating the initial stiffness of the dissipater, the influence of the elastic deformation over the non-yielding portions of the dissipater are taken into account. The details of a typical GD is shown in Figure 6.26.

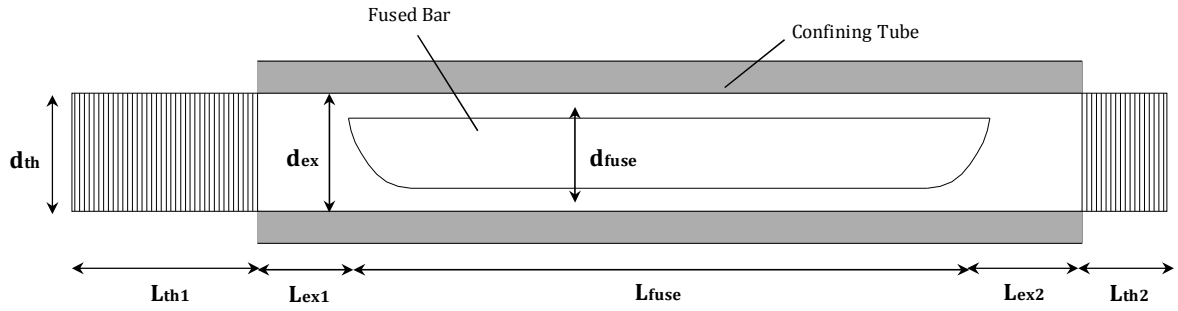

Figure 6.26. General schematic of a grooved dissipater

Using the procedure from Sarti el al. (2013), the yield displacement (Δ_Y) can be calculated from Equation 6.18.

$$\Delta_Y = \frac{\sigma_y A_{fuse} L_{ex1}}{E A_{ex1}} + \frac{\sigma_y A_{fuse} L_{fuse}}{E A_{fuse}} + \frac{\sigma_y A_{fuse} L_{ex2}}{E A_{ex2}} + \frac{\sigma_y A_{fuse} L_{th1}}{E A_{th1}} + \frac{\sigma_y A_{fuse} L_{th2}}{E A_{th2}} \quad (6.18)$$

In most cases, $A_{ex1} = A_{ex2}$ and $A_{th1} = A_{th2}$. Therefore, an identical value of A_{ex} and A_{th} can be used and Equation 6.17 is written as follows:

$$\Delta_Y = \frac{\sigma_y A_{fuse} (L_{ex1} + L_{ex2})}{E A_{ex}} + \frac{\sigma_y L_{fuse}}{E} + \frac{\sigma_y A_{fuse} (L_{th1} + L_{th2})}{E A_{th}} \quad (6.19)$$

Using $L_{ex} = L_{ex1} + L_{ex2}$, $L_{th} = L_{th1} + L_{th2}$, $A_{fuse} = (\pi/4)\, d^2_{fuse}$, $A_{ex} = (\pi/4)\, d^2_{ex}$ and $A_{th} = (\pi/4)\, d^2_{th}$, Equation 6.19 can be written as:

$$\Delta_Y = \frac{\sigma_y L_{fuse}}{E} \left[\left(\frac{d_{fuse}}{d_{ex}} \right)^2 \frac{L_{ex}}{L_{fuse}} + 1 + \left(\frac{d_{fuse}}{d_{th}} \right)^2 \frac{L_{th}}{L_{fuse}} \right] \quad (6.20)$$

Generally $A_{th} \approx 0.75\ A_{ex}$ which gives $d_{th} \approx 0.866\ d_{ex}$. The maximum stress ($\sigma_u$) in the dissipater under cyclic loading can be taken as 1.3 times σ_y. This means that the ultimate force (F_U) in the dissipater under net positive deformation would be approximately 1.3 times the yield force (F_Y).

To calculate the Ramberg-Osgood coefficient (r), a rupturing strain (ε_r) of 10% can be assumed for the dissipater under the cyclic loading. Using Equation 6.21 and Equation 6.22, the Ramberg-Osgood coefficient (r) can be calculated in accordance with MMPDS-01"Metallic Materials Properties Development and Standardization" (2003). The value of *r* was calculated to be approximately 15 for the grooved dissipater (GD-1) under net positive deformation.

$$r = \frac{l_n\left(\frac{\varepsilon_{us}}{0.2}\right)}{l_n\left(\frac{\sigma_u}{\sigma_y}\right)} \tag{6.21}$$

$$\varepsilon_{us} = 100\left(\varepsilon_r - \frac{\sigma_u}{E}\right) \tag{6.22}$$

In Equation 6.21 and 6.22, ε_{us} is the uniform strain which can be defined as the plastic strain at the end of uniform elongation at the maximum tensile load.

Utilizing Equation 6.20 through Equation 6.22, Table 6.8 presents a summary of the modeling parameters for GD-1.

Table 6.8. Summary of modeling parameters for GD-1

Δ_Y = 0.14%	d_{bar} = 24 mm	L_{bar} = 435 mm	σ_y = 350 MPa	ε_y = 0.175%
Δ_U = 5.75%	d_{fuse} = 16 mm	L_{fuse} = 245 mm	σ_u = 455 MPa	ε_r = 10%
F_Y = 70.4 kN	d_{ex} = 24 mm	L_{ex} = 40 mm	E = 200,000 MPa	ε_{us} = 9.77%
F_U = 91.5 kN	d_{th} = 20.8 mm	L_{th} = 150 mm	K_0 = 114.35 kN/mm	r = 15

Figure 6.27 presents the analytical backbone plot for GD-1. It can be observed that the Bilinear model predicts the initial stiffness of the dissipater better than the Ramberg-Osgood model (Figure 6.27b). However, for an overall behavior, the Ramberg-Osgood model provides better results (Figure 6.27a).

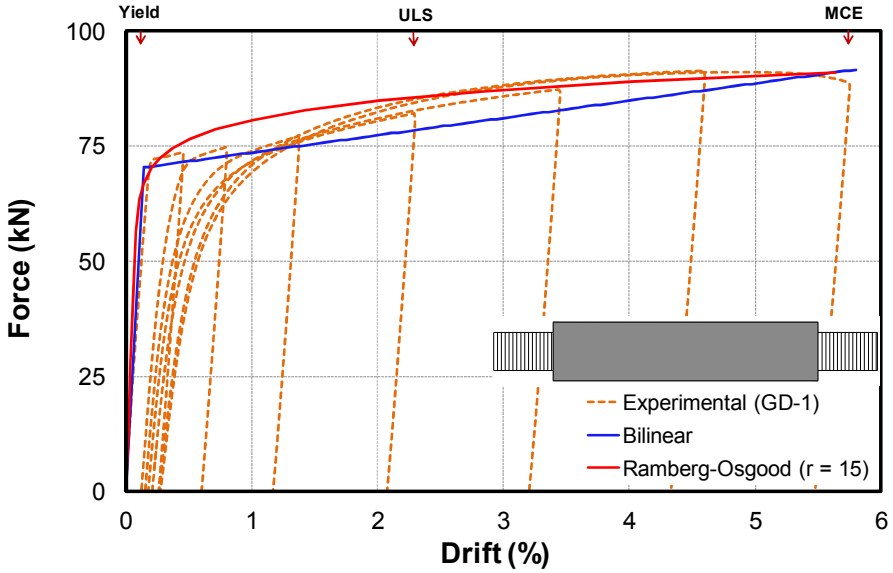

(a) Backbone plot

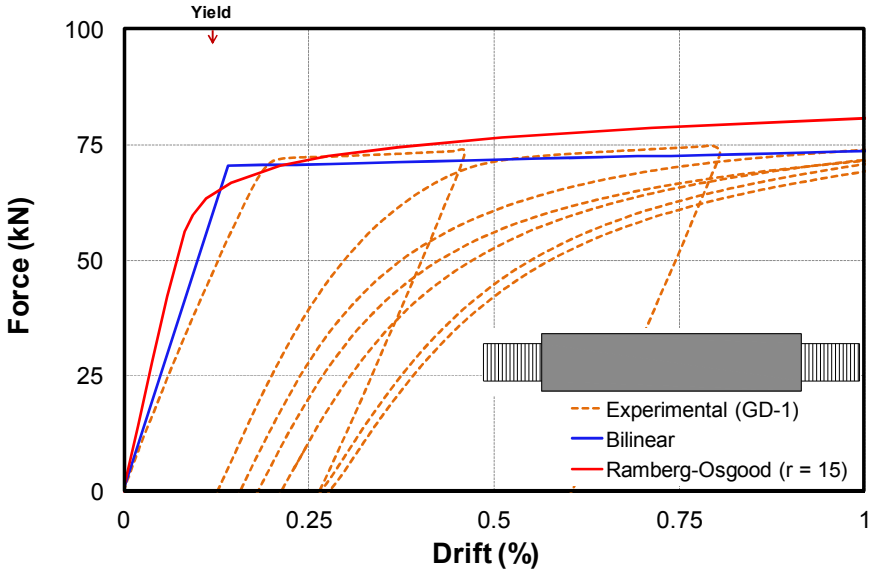

(b) Backbone plot (close-up view of initial stiffness)

Figure 6.27. Backbone plots for Blinear and Ramberg-Osgood models for GD-1 under net positive deformation

The force-drift hysteresis plots for the Blinear and Ramberg-Osgood models are shown in Figure 6.28. It can be noticed that the Ramberg-Osgood model provides a better analytical model for the dissipater. The Bilinear model also captures the cyclic response of the dissipater to a good level of accuracy.

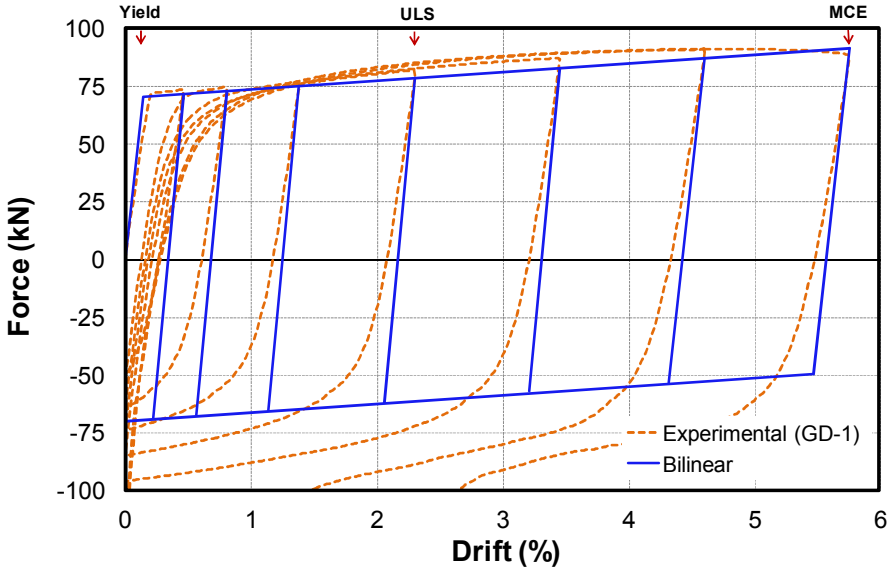

(a) Bilinear model

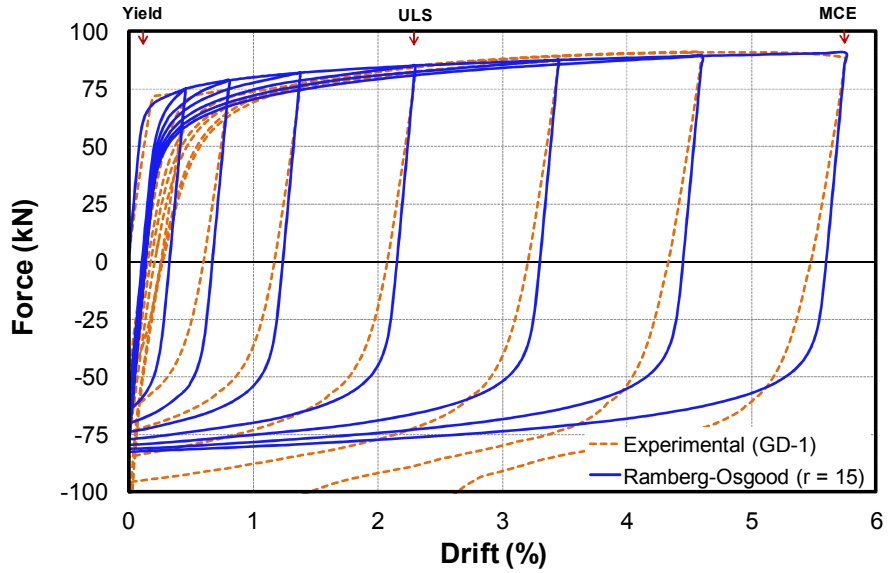

(b) Ramberg-Osgood model

Figure 6.28. Force-drift hysteresis for GD-1 under net positive deformation

In summary, simplified analytical models such as Ramberg-Osgood and Bilinear can be used to predict the monotonic and cyclic response of GD. When calculating the initial stiffness of the dissipater, the influence of elastic deformation over the non-yielding parts of the bar would need to be considered for better results. The maximum force in GD under net positive deformation can be approximated to be 1.3 times the yield force. For the Ramberg-Osgood model, the coefficient *r* can be taken to be 15 for the dissipater under net positive deformation. This is valid only if the grooved bar is made of mild steel material.

6.4 Modeling the Response of ABC Low Damage Pier System

6.4.1 Literature Review on Modeling Rocking Connections

Over the last 15 years, there have been many procedures proposed for modeling the response of Dissipative Controlled Rocking (DCR) connections. These are briefly discussed in the next sections.

6.4.1.1 Lumped Plasticity Model

This type of model use rotational springs to model the moment-rotation response of elements in a post-tensioned rocking system. Past references on this type of modeling for DCR connections include El Sheikh et al. (1999), Pampanin et al. (2001), fib (2003), and Palermo et al. (2005[1]).

In this type of modeling procedure, two rotational springs are placed in parallel with zero length to model the response of the unbonded post-tensioning and dissipaters at the rocking interface. The precast elements is modeled as an elastic member. This means that the inelastic behavior is assumed to be concentrated at the connection region only.

Section analysis of the rocking interface would be required to construct the monotonic response of the unbonded post-tensioning and dissipaters. The effect of gravity (axial load) can be combined with the post-tensioning spring. It is common to use bilinear or trilinear models to construct the hysteresis model of each rotational spring (post-tensioning or dissipaters).

Figure 6.29 presents a typical lumped plasticity model for a cantilever structure with DCR connection at the base. The summation of the response from the springs would be the total response of the system.

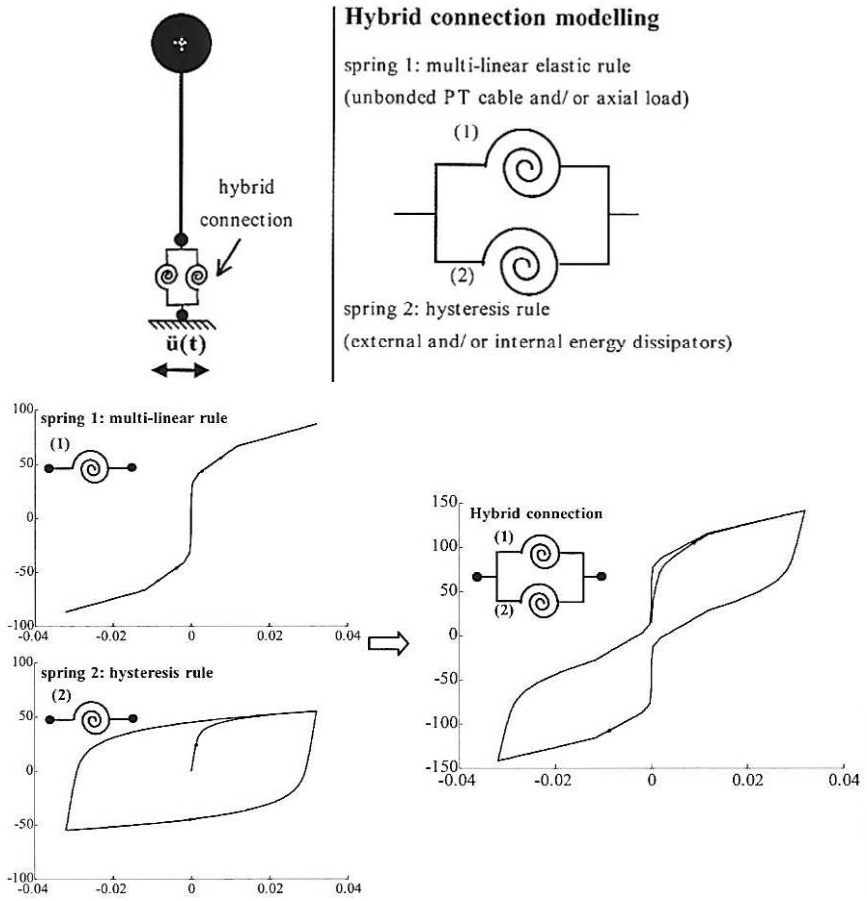

Figure 6.29. Lumped plasticity model for DCR connection, after Palermo et al. (2005)

6.4.1.2 Multi-Spring Model

This type of model initially used two axial springs (Figure 6.30) which were located at the rocking interface to model the response of rocking wall, Conley et al. (1999). The axial springs are elastic compression-only which are intended to capture the actual rocking response of the wall as the wall uplifts on one end. The response of post-tensioning and dissipaters are modeled using additional springs with hysteretic response. This model was concluded to overestimate the tendon elongation and internal moment non-conservatively. Therefore, it was subsequently refined by Marriott (2009).

Latest research investigations on multi-spring model by Kim (2002), Spieth et al. (2004), and Palermo et al. (2005[2]), incorporate multiple axial springs which are distributed along the rocking interface. The multi-spring element was recently added in the finite element program called "Ruaumoko", refer to Figure 6.31a, (Carr, 2005). Figure 6.31c presents implementation of multi-spring element to capture the response of cantilever pier with DCR connection from Marriott (2009).

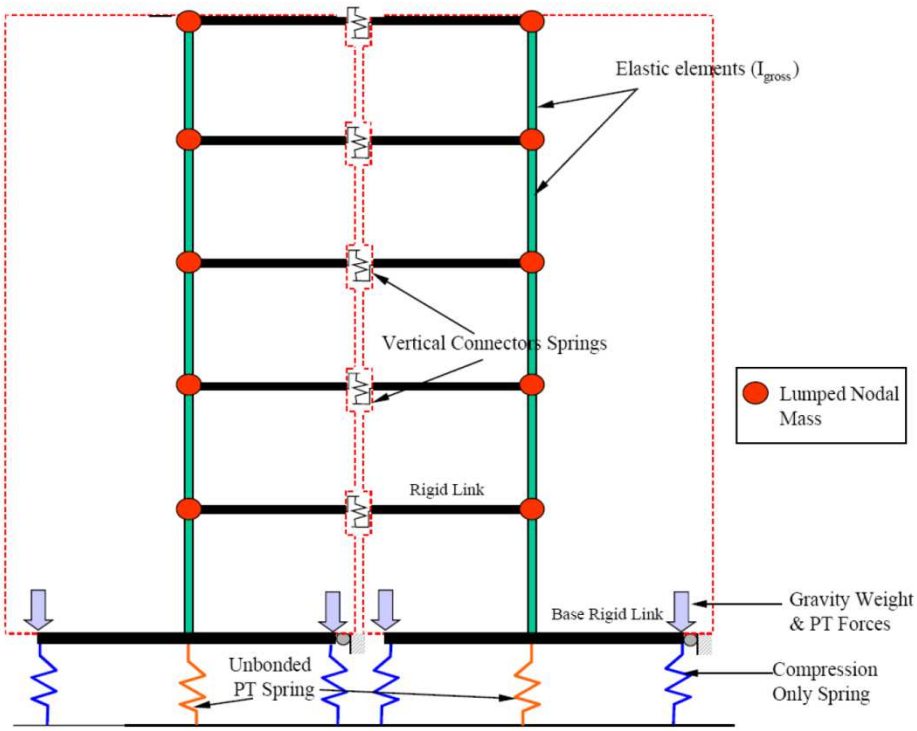

Figure 6.30. Two spring model for post-tensioned coupled wall, Conley et al. (1999)

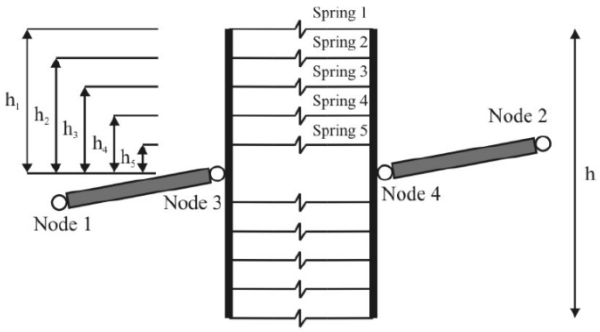

(a) Multi-spring element in Ruaumoko, Carr (2005)

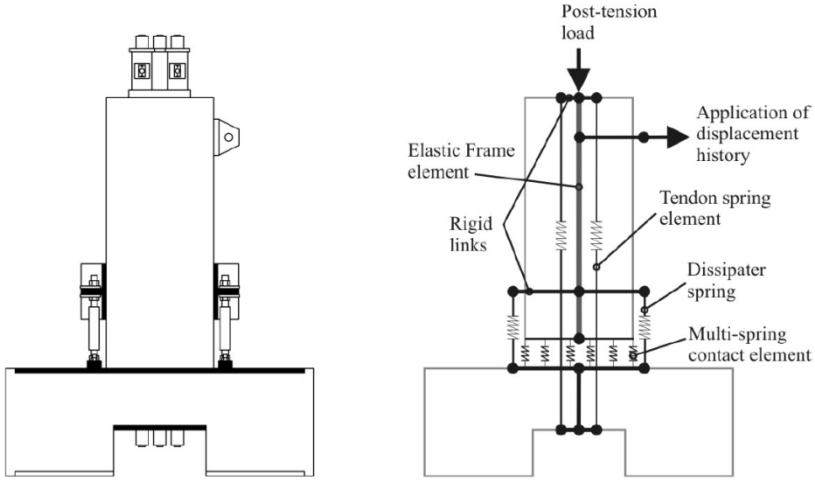

(b) Cantilever pier with DCR connection (c) Multi-spring model, Marriott (2009)

Figure 6.31. Multi-spring model for analytical modeling of DCR connection

6.4.1.3 Fiber Element Model

Fiber model was developed to predict the response of rocking beam-column joints. Past research investigations on this type of model include El-Sheikh et al. (1998) and Kurama et al. (1998). In fiber modeling, an element is divided into several segments which are consisted of discrete fiber layers. The fibers represent specific material (concrete or dissipaters) and its uniaxial stress-strain relationship. When the element starts rocking, the uplift (gap opening) is calculated by integrating the tension strain along the length of each segment, Marriott (2009). Figure 6.32 presents fiber element model for a post-tensioned beam-column joint.

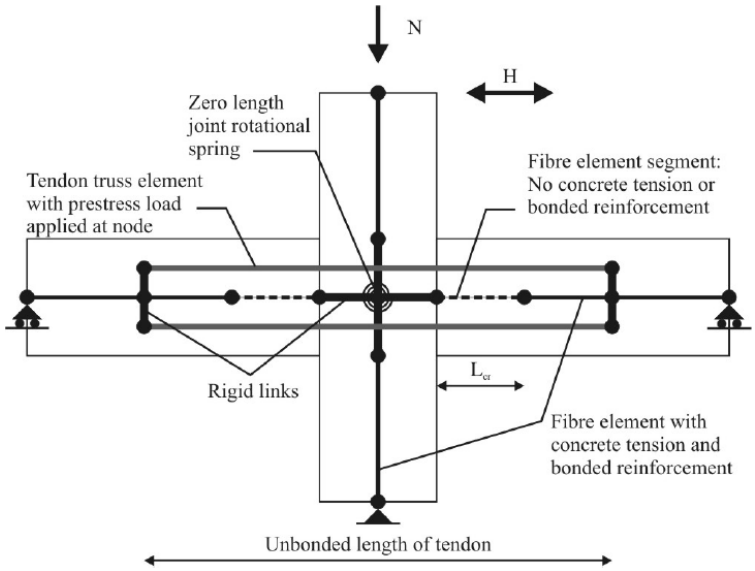

Figure 6.32. Fiber element model for rocking beam-column joint, (modified from El-Sheikh et al.,1998 by Marriott, 2009)

6.4.1.4 Finite Element Model

This type of model has been used by Kurama (2000) and Allen and Kurama (2002) to model the response of post-tensioned rocking walls. The finite element model requires modeling of the elements and joints in a Finite Element (FE) software package such as ABAQUS (Dassault Systemes, 2015). The rocking interface is modeled using gap/contact element which would allow the uplift. Past research investigations have shown that the finite element model is well correlated to its equivalent fiber element model, Marriott (2009).

6.4.2 Modeling the Response of Low Damage Bent

In order to model the response of DCR connections tested in this research, the procedure outlined in the PRESSS Design Handbook (Pampanin et al., 2010) was utilized.

Similar to Section 6.2.2.1, the bent can be assumed as four short cantilever columns, each with a Dissipative Controlled Rocking (DCR) connection at the column base. The total capacity and response of the bent would be that of the short cantilever column times two, given the fact that all DCR connections incorporate identical detailing.

The monotonic behavior of DCR connection was modeled using a section analysis procedure tilted "Monolithic Beam Analogy" (Pampanin et al., 2001, Palermo, 2004). In this procedure, member compatibility condition is used to provide a compatibility equation for the controlled rocking connection. This analogy is presented in Figure 6.33 where the two beams have identical section and reinforcement details, and hence the elastic deformation in both beams would be the same. This means that when imposing an identical total displacement to each beam, the plastic deformation is also similar with difference in the mechanism only. For the precast beam with rocking connection, the nonlinear deformation is concentrated at the connection, while for the monolithic beam the inelastic deformation is distributed along the plastic hinge length of the beam.

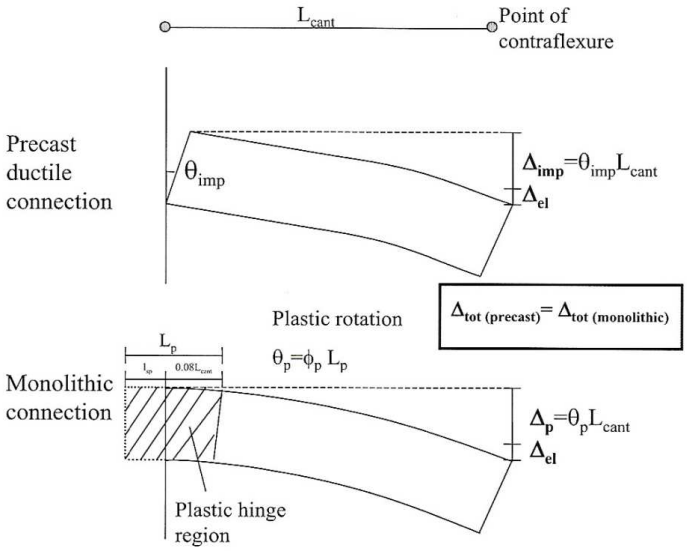

Figure 6.33. Monolithic Beam Analogy (MBA) concept, after Pampanin et al., (2001)

By equating the total displacement in the precast beam ($\Delta_{tot\ (precast)}$) to that of the monolithic beam $\Delta_{tot\ (monolithic)}$, the final outcome of the analysis would be Equation 6.23 for the member compatibility relationship. Using this expression, a trial and error procedure can be used to obtain the concrete strain for each guessed value of the neutral axis position until the local equilibrium is satisfied.

$$\varepsilon_c = \left[\frac{\theta_{imp}\, L_{cant}}{\left(L_{cant} - \frac{L_p}{2}\right) L_p} + \phi_y\right] c \tag{6.23}$$

Where,

θ_{imp} = Imposed rigid rotation (rad)

L_{cant} = Distance from column face to point of beam contraflexure (mm)

L_p = Plastic hinge length, taken as $0.08L_{cant} + L_{sp}$ (mm)

c = Neutral axis depth (mm)

Using Equation 6.24 through Equation 6.38, all necessary parameters to model the monotonic response of Dissipative Controlled Rocking (DCR) connection with circular section can be calculated in accordance with PRESSS Design Handbook.

A. Unbonded Post-tensioned Tendons:

$$\Delta_{pt} = (0.5d - c) \tag{6.24}$$

$$\varepsilon_{pt}(\theta) = \frac{n\Delta_{pt}}{l_{ub}} \tag{6.25}$$

$$\Delta T_{pt} = E_{pt}\, \varepsilon_{pt}(\theta) n_{pt} A_{pt} \tag{6.26}$$

$$T_{pt} = T_{pt,initial} + \Delta T_{pt} \tag{6.27}$$

B. Tension Mild Steel (Dissipater):

$$\Delta_s = \theta(d_i - c) \tag{6.28}$$

$$\varepsilon_s = \frac{\Delta_s + \frac{2}{3} l_{sp} \varepsilon_y}{l'_{ub} + 2l_{sp}} \tag{6.29}$$

$$T_s = f_s A_s \tag{6.30}$$

C. Compression Mild Steel (Dissipater):

$$\Delta'_s = \theta(d_i - c) \tag{6.31}$$

$$\varepsilon'_s = \frac{\Delta'_s + \frac{2}{3} l_{sp} \varepsilon_y}{l'_{ub} + 2l_{sp}} \tag{6.32}$$

$$C_s = f'_s A'_s \tag{6.33}$$

D. Concrete Compression:

$$C_c = \alpha f'_c \beta A_c \tag{6.34}$$

E. Equilibrium of the Section:

$$C_c = C_s + T_s + T_{pt} + N \tag{6.35}$$

F. Moment Capacity of the Section:

$$M_n = \left[T_{pt} \left(d_{pt,i} - \frac{a}{2} \right) + T_s \left(d_i - \frac{a}{2} \right) + C_s \left(\frac{a}{2} - d' \right) + N \left(\frac{d-a}{2} \right) \right] \tag{6.36}$$

G. Decompression Point (Gap opening):

$$\frac{M_{dec}}{Z} - \frac{T_{pt,initial} e}{Z} - \frac{T_{pt,initial} + N}{A} = 0 \tag{6.37}$$

H. Self-Centering Ratio:

$$\lambda = \frac{M_{pt} + M_N}{M_s} \tag{6.38}$$

Where,

Δ_{pt} = Elongation of the unbonded post-tensioned tendon (mm)

d = Diameter of column (mm)

$\varepsilon_{pt}\ (\theta)$ = Increment of tendon strain at θ rotation (mm)

n = Total number of gap openings along the unbonded tendon

l_{ub} = Unbonded length of the post-tensioned tendon (mm)

ΔT_{pt} = Increment of tendon load (kN)

E_{pt} = Modulus of elasticity of tendons (MPa)

n_{pt} = Number of post-tensioned tendons

A_{pt} = Cross-sectional area of post-tensioned tendon (mm^2)

T_{pt} = Tendon force (kN)

$T_{pt,\ initial}$ = Initial post-tensioning load in the tendons (kN)

Δ_s = Elongation of the mild steel reinforcement (dissipater) in tension (mm)

d_i = Depth to centroid of tension steel reinforcement (dissipater) (mm)

ε_s = Mild steel (dissipater) strain in tension

l_{sp} = Strain penetration length (mm)

ε_y = Yield strain

l'_{ub} = Unbonded length (fused) of the mild reinforcement (dissipater) (mm)

T_s = Tension steel force (kN)

f_s = Steel reinforcement (dissipater) tension stress (MPa)

A_s = Area of tension reinforcement (dissipater) (mm^2)

Δ'_s = Elongation of the mild steel reinforcement (dissipater) in compression (mm)

C_s = Compression steel force (kN)

ε'_s = Mild steel (dissipater) strain in compression

f'_s = Steel reinforcement (dissipater) compression stress (MPa)

A'_s = Area of compression reinforcement (dissipater) (mm^2)

C_c = Resultant concrete compression force (kN)

α = Concrete stress block factor for strength

β = Concrete stress block factor for depth

f'_c = Unconfined concrete compression strength (MPa)

A_c = Area of circle segment in compression (mm^2)

N = Axial load (kN)

M_n = Nominal moment capacity (kNm)

a = Equivalent concrete stress block depth (mm)

$d_{pt,i}$ = Depth to post-tensioned steel (mm)

d' = Depth to centroid of compression reinforcement (dissipater)

M_{dec} = Decompression moment (kNm)

e = Distance between the centroid of the section and post-tensioned tendons (mm)

Z = Section modulus of the section (mm^3)

A = Cross-sectional area of the section

λ = Self-centering ratio

M_{pt} = Moment contribution from post-tensioned tendons (kNm)

M_s = Moment contribution from mild steel reinforcement (dissipaters) (kNm)

M_N = Moment contribution from gravity (axial load) (kNm)

It should be noted that due to smaller decompression moment in all tests presented in Chapter 5, the decompression point was taken to be at the origin (zero drift, zero force). This is applicable to all tests modeled in this part of the Chapter.

As a summary, three points (origin, yield level, and design level) are needed to plot Bilinear moment-rotation curve (monotonic behavior) for each of the four DCR connections in LDB. Using above section analysis method, these points can be simply calculated by setting up above formulas into a spreadsheet. Appendix D includes spreadsheets used for calculation of the necessary parameters to model the monotonic response of a typical DCR connection in LDB for the tests discussed here. The cyclic response can be modeled using the data from the backbone, post-tensioning, and dissipater hysteresis plots. It should be noted that the MCE level drift in all tests was taken as the final drift that the bent was tested under.

6.4.2.1 ABC Low Damage with Post-Tensioning Only

As explained in Section 5.4.1 of Chapter 5, three tests with initial post-tensioning levels of 15%, 30%, and 45%, were carried out. In this instance, there was no contribution from the external dissipaters and gravity in the DCR connection. Using the procedure explained in the previous section, the backbone curve and cyclic response of ABC Low Damage Bent (LDB) with external shear keys and post-tensioning are modeled here.

Table 6.9 presents a summary of the calculated performance points for LDB with post-tensioning only.

Table 6.9. Summary of the calculated points for LDB with post-tensioning only

Test Name	Drift (%)		Force (kN)	
	Yielding	ULS	Yielding	ULS
IPT15-EX	0.53	2.2	81	207
IPT30-EX			133	254
IPT45-EX			183	300

Figure 6.34a presents the moment-rotation plot for a typical DCR connection in LDB. The force-drift response of LDB under IPT15-EX is shown in Figure 6.34b. It can be noticed that the analytical model slightly over predicts the capacity of the bent at the

ULS drift ratio. This was due to a very low level of post-tensioning which had caused some flexibility in the bent.

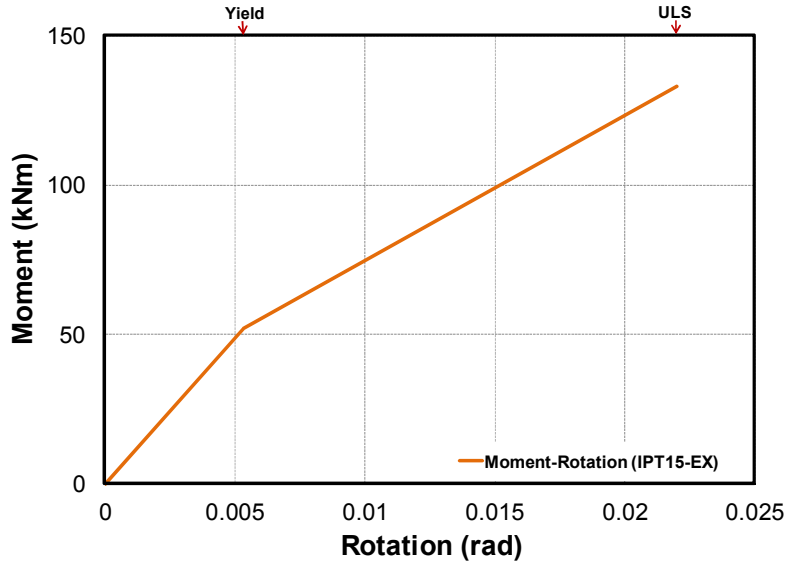

(a) Moment-rotation plot for a typical DCR connection

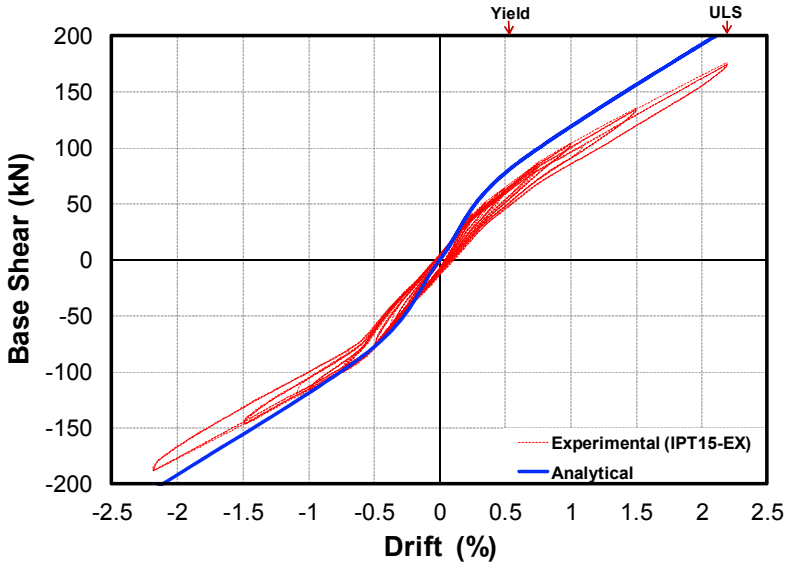

(b) Force-drift hysteresis for the bent

Figure 6.34. Analytical response of LDB under IPT15-EX

Analytical plots for LDB under IPT30-EX are presented in Figure 6.35. An increased level of post-tensioning in the bent had eliminated any flexibility in the bent. Therefore, it is obvious that the analytical model in Figure 6.35b captures the response of the bent to a good level of accuracy, especially during the push stage of the loading.

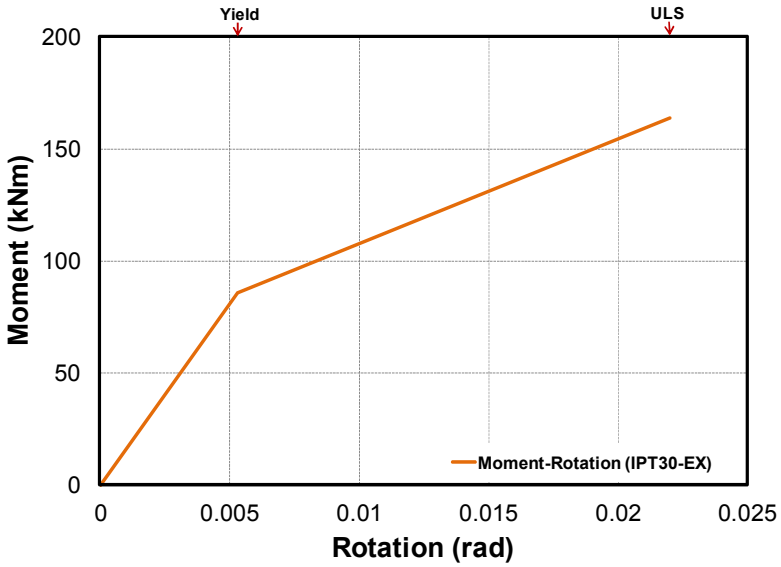

(a) Moment-rotation plot for a typical DCR connection

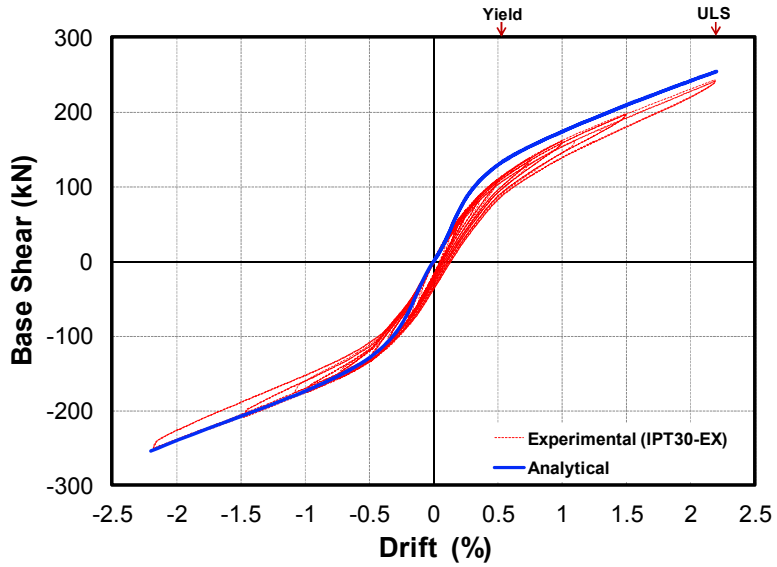

(b) Force-drift hysteresis for the bent

Figure 6.35. Analytical response of LDB under IPT30-EX

Figure 6.36 presents analytical plots for LDB under IPT45-EX. The analytical model in Figure 6.36b well correlates with the experimental results.

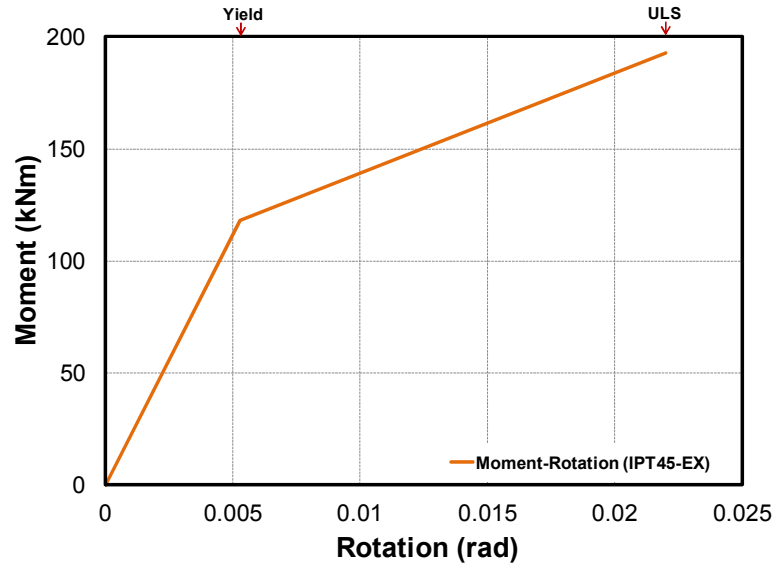

(a) Moment-rotation plot for a typical DCR connection

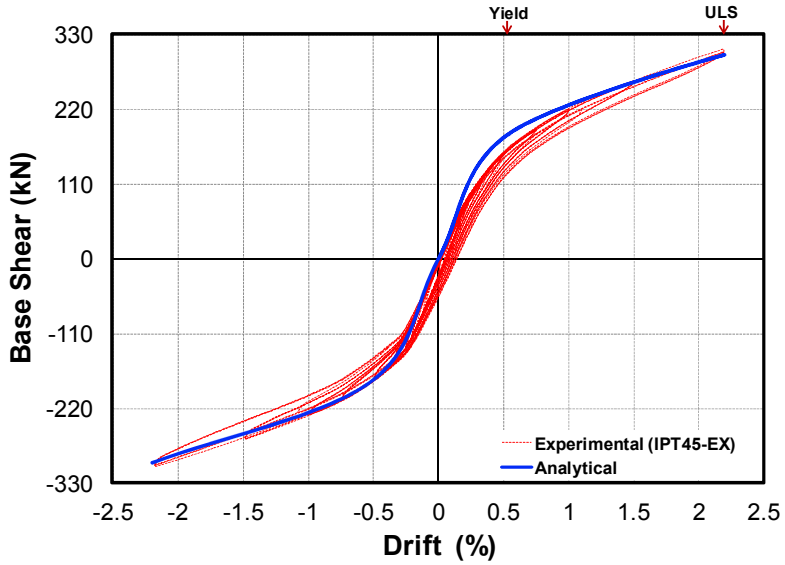

(b) Force-drift hysteresis for the bent

Figure 6.36. Analytical response of LDB under IPT45-EX

6.4.2.2 ABC Low Damage with Grooved Dissipaters (GDs)

In this part, the response of LDB under IPT11.8+GD+AX (Section 5.4.2 in Chapter 5) is analytically modeled up to the 2.5% drift ratio (drift at the end of testing). The moment contribution from GDs and gravity were taken into account in the total moment capacity of the DCR connection. The dissipaters were modeled using a Bilinear hysteretic rule (Figure 6.37) as discussed in Section 6.3.3 previously. The hysteretic response of the unbonded post-tensioning was combined with gravity and is plotted in Figure 6.38.

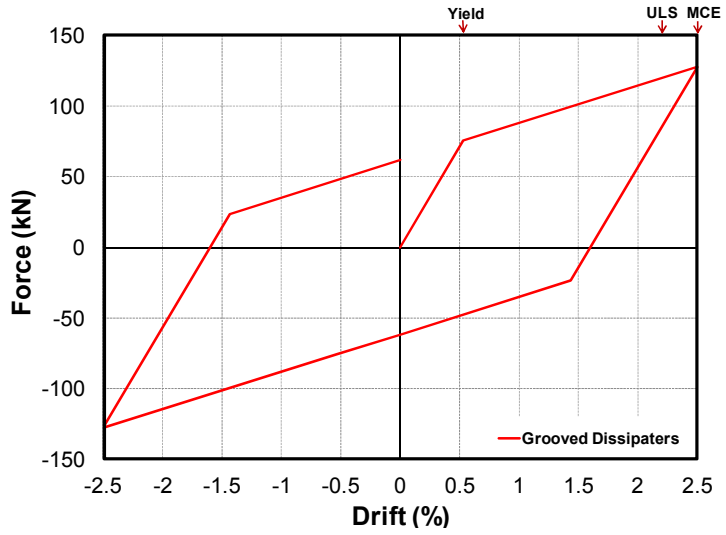

Figure 6.37. Force-drift hysteresis for GDs in LDB under IPT11.8+GD+AX

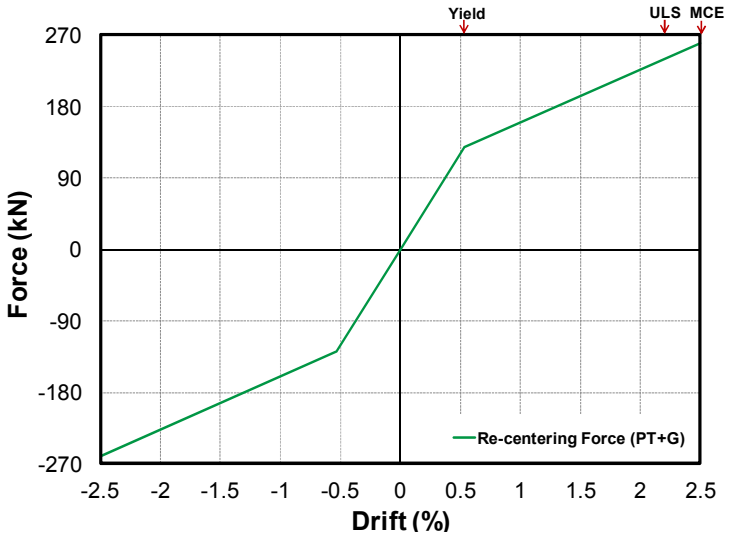

Figure 6.38. Force-drift hysteresis for the post-tensioning and gravity in LDB under IPT11.8+GD+AX

Table 6.10 provides a summary of the calculated performance points for the combined flag-shaped response of LDB under IPT11.8+GD+AX.

Table 6.10. Summary of the calculated points for LDB under IPT11.8+GD+AX

Test Name	Drift (%)			Force (kN)		
	Yielding	ULS	MCE	Yielding	ULS	MCE
IPT11.8+GD+AX	0.53	2.2	2.5	205	369	388

Figure 6.39a presents the analytical moment-rotation plot for one of the four identical DCR connections in LDB. The analytical backbone curve is shown in Figure 6.39b which shows good correlation with the experimental results.

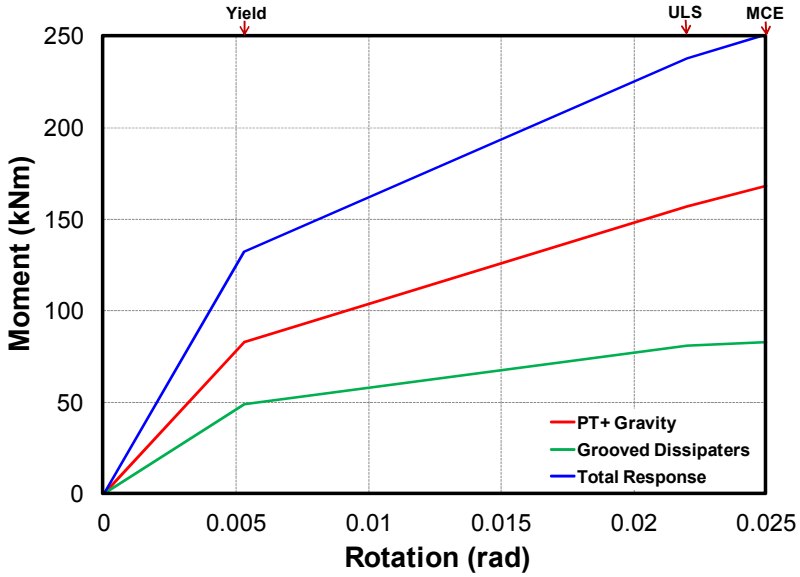

(a) Moment-rotation plot for a typical DCR connection

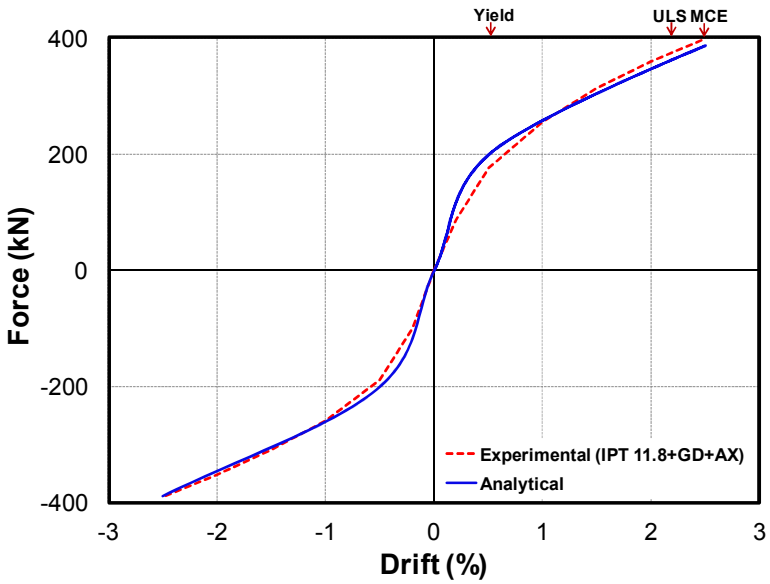

(b) backbone curves for the bent

Figure 6.39. Analytical response of LDB under IPT11.8+GD+AX

The analytical force-drift hysteresis is plotted in Figure 6.40. The plot conservatively represents a good overall behavior of the bent. As explained in Chapter 4, there was approximately 3 mm construction gap (0.1% drift ratio) between the face of the shear key and outer face of the column. The analytical model in Figure 6.40 does not take into account this gap. Therefore, it appears that following testing, the bent had slightly higher residual drift (0.25% drift ratio) compared to the analytical model. By subtracting 0.1% (gap size) from 0.25% drift, the actual residual drift in the bent was in the order of 0.15% or 4 mm. This residual drift is almost equal to that shown in the analytical model in Figure 6.40. In general, the simplified analytical model shows good correlation with the experimental results up to the 2.5% drift ratio.

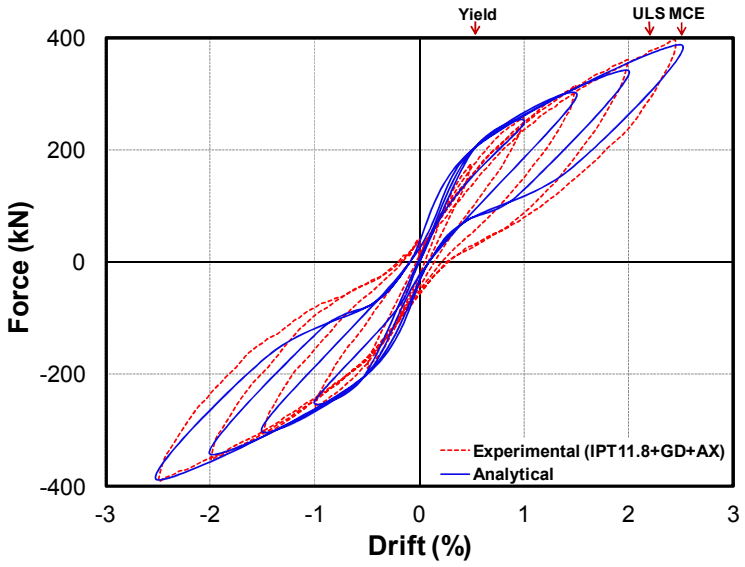

Figure 6.40. Force-drift hysteresis for LDB under IPT11.8+GD+AX

6.4.2.3 ABC Low Damage with Mini UFP Dissipaters (MUDs)

In this part, analytical model to predict the response of LDB under IPT9+MUD+AX is presented. The contribution of Mini UFP Dissipaters (MUDs) was computed using a Bilinear model as presented in Section 6.3.2 previously. The hysteretic response of MUDs and re-centering force (post-tensioning and gravity) are plotted in Figure 6.41 and Figure 6.42, respectively.

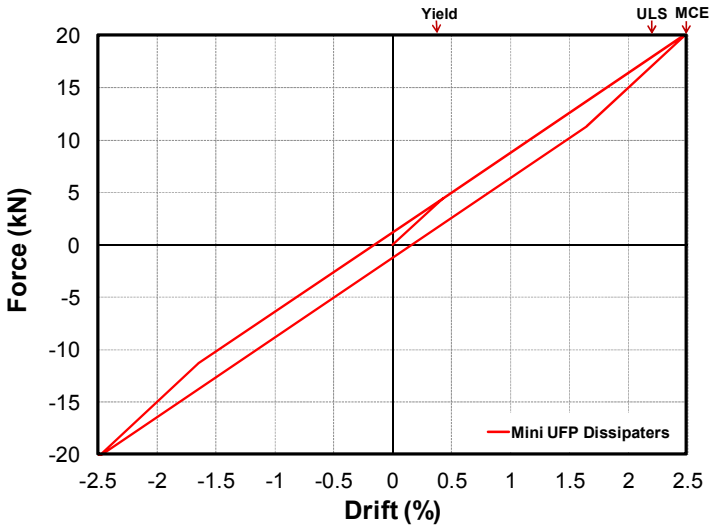

Figure 6.41. Force-drift hysteresis for MUDs in LDB under IPT9+MUD+AX

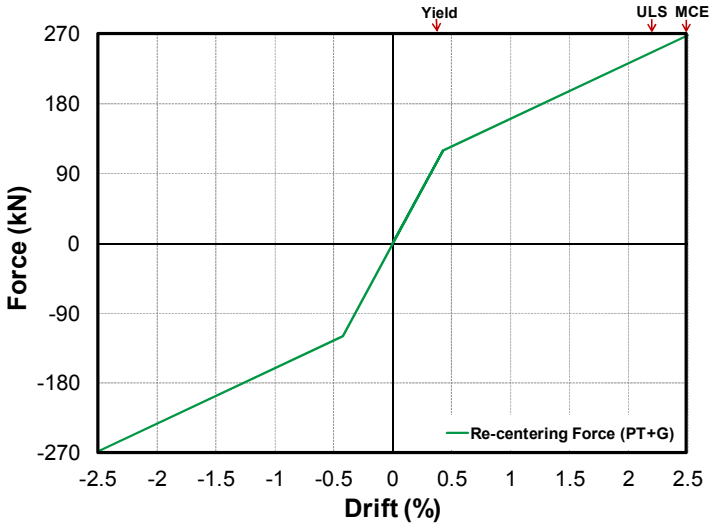

Figure 6.42. Force-drift hysteresis for post-tensioning and gravity in LDB under IPT9+MUD+AX

A summary of the calculated performance points for the combined flag-shaped response of LDB under IPT9+MUD+AX is presented in Table 6.11.

Table 6.11. Summary of the calculated point for LDB under IPT9+MUD+AX

Test Name	Drift (%)			Force (kN)		
	Yielding	ULS	MCE	Yielding	ULS	MCE
IPT9+MUD+AX	0.43	2.2	2.5	122	264	288

Figure 6.44a shows the analytical moment-rotation plot for one of the DCR connections in LDB. The low dissipation of MUD was due to fabrication constraints in the lab, as explained in Chapter 5. Figure 6.44b presents the analytical backbone plot. The model is well correlated with the experimental results.

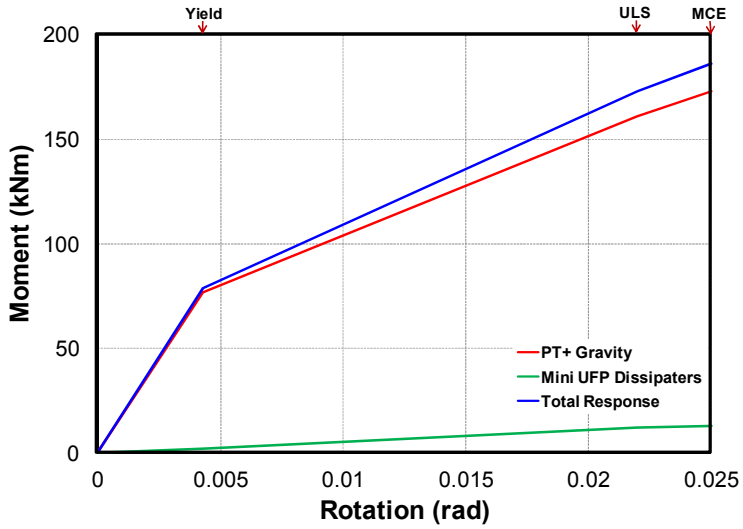

(a) Moment-rotation plot for a typical DCR connection

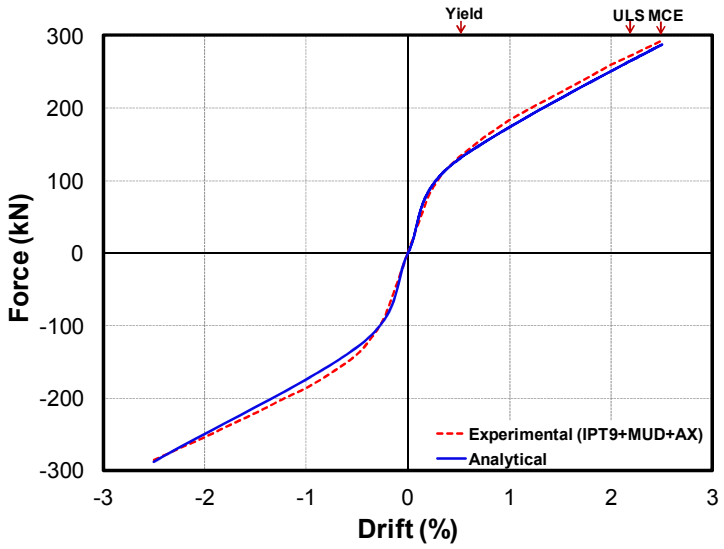

(b) backbone curves for the bent

Figure 6.43. Analytical response of LDB under IPT9+MUD+AX

The cyclic response of the bent is shown in Figure 6.44. The analytical plot is in good agreement with the experimental results.

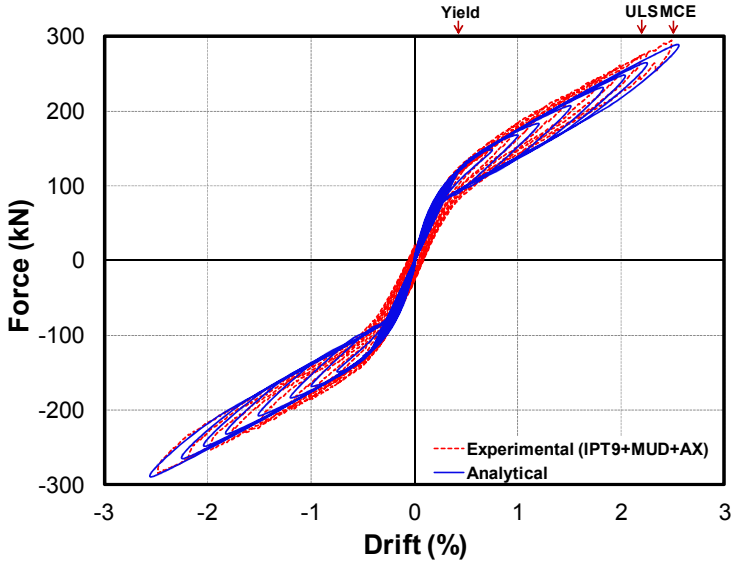

Figure 6.44. Force-drift hysteresis for LDB under IPT9+MUD+AX

6.4.2.4 ABC Low Damage with Combination of GDs and MUDs

In this part, analytical model to capture the response of LDB under IPT11.4+MUD+GD+AX (Section 5.4.6 in Chapter 5) is discussed. The model includes moment contributions from MUDs, GDs, post-tensioning, and gravity in the connection. Moment contribution from MUDs and GDs is combined into a single plot for energy dissipaters in the bent (Figure 6.45). The hysteretic response of the combined unbonded post-tensioning and gravity load is plotted in Figure 6.46.

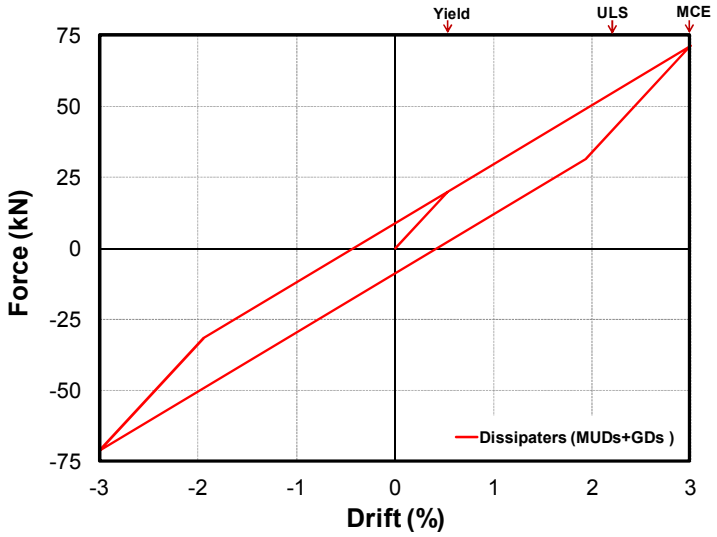

Figure 6.45. Force-drift hysteresis for MUDs in LDB under IPT11.4+MUD+GD+AX

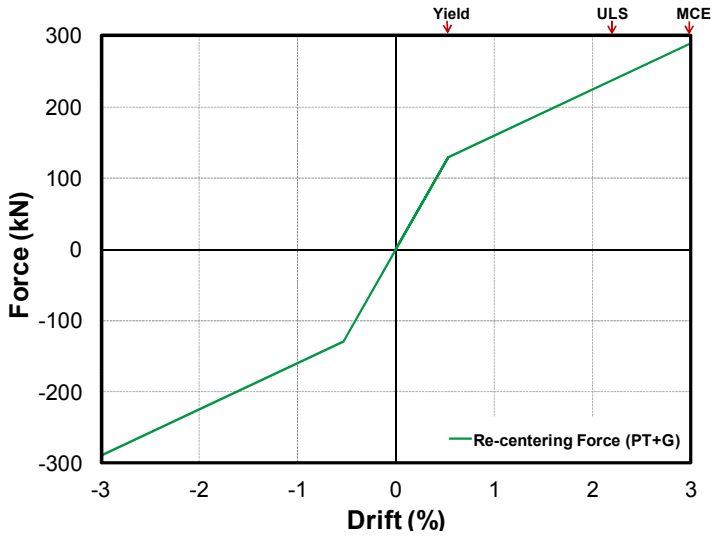

Figure 6.46. Force-drift hysteresis for post-tensioning and gravity in LDB under IPT11.4+MUD+GD+AX

Table 6.12 presents a summary of the calculated performance points for the combined flag-shaped response of LDB under IPT 11.4+MUD+GD+AX.

Table 6.12. Summary of parameters for LDB under IPT11.4+MUD+GD+AX

Test Name	Drift (%)			Force (kN)		
	Yielding	ULS	MCE	Yielding	ULS	MCE
IPT11.4+MUD+GD+AX	0.53	2.2	3.0	149	315	362

The moment rotation and backbone plots are shown in Figure 6.47a and Figure 6.47b, respectively. The analytical backbone plot is in good agreement with the experimental results. The force-drift hysteresis is plotted in Figure 6.48.

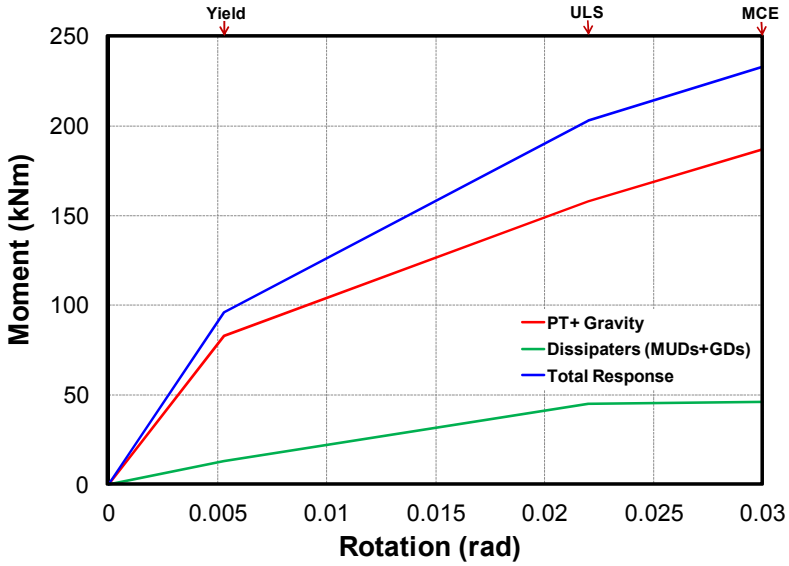

(a) Moment-rotation plot for a typical DCR connection

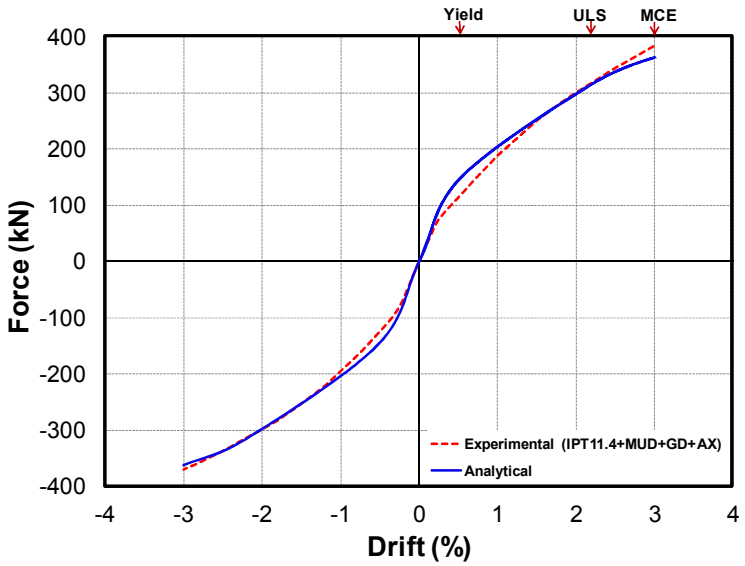

(b) backbone curves for the bent

Figure 6.47. Analytical response of LDB under IPT11.4+MUD+GD+AX

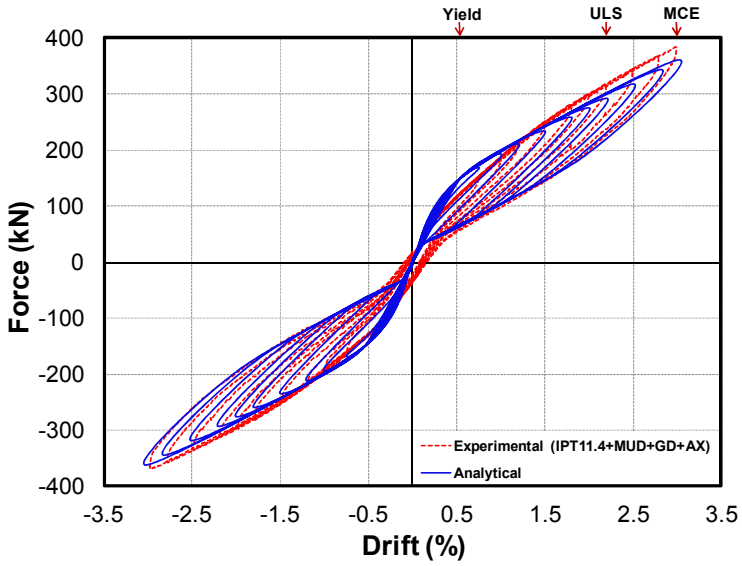

Figure 6.48. Force-drift hysteresis for LDB under IPT11.4+MUD+GD+AX

6.5 Conclusions

This Chapter presented simplified analytical modeling tools to validate and predict the response of ABC High Damage, Innovative Dissipaters, and ABC Low Damage under quasi-static cyclic loading. The macro-modeling technique aimed to capture an overall behavior of the system which included the backbone curve and the cyclic response. This type of modeling procedure is well suited for industry environment. It uses spreadsheets and commercial software packages such as SAP 2000 (Computers and Structures Inc., 2015) which requires development of less time consuming analytical model to predict the response of the system to a good level of accuracy. This type of modeling procedure has not been widely used in the academia. Therefore, the modeling procedure explained in this Chapter also aims to support a wider adoption of commercial software packages in research related activities.

In the first part of the Chapter, the response of cantilever and multi-column (bent) ABC High Damage systems was modeled using existing theoretical models for reinforced concrete. Idealized moment-curvature section analysis from Caltrans (2013) and the displacement-based design formulas from Priestley et al. (2007) were utilized to construct the elastic-perfectly plastic backbone curve of the columns with the grouted duct and member socket connection. The cyclic response of the connections was modeled using Takeda-Thin hysteretic rule.

For cantilever columns with grouted duct or member socket connection at the column to footing connection, the contribution for energy dissipation from the segment to segment connection can be neglected. The yield curvature and moment capacity can be obtained from the idealized moment-curvature plot. The unloading coefficient (α) for the cyclic response of the system can be taken as 0.4.

For the bent with a combination of grouted duct and member socket connections, the yield curvature was calculated using a general displacement based approach. This is possible by assuming each column in the bent as two short cantilever columns. The reason behind using a generic procedure for the bent was the fact that there were more than one type of connection in the structure compared to a simple cantilever column. The connections were shown to have slightly different seismic performance previously. By combining two types of connections in the structure, the overall behavior of the bent

could be influenced by the response of the individual connection and the interaction of between the connections to some extent. This means that a more complicated model would have to be developed if a generic displacement-based approach is not used.

In the generic procedure, the yield moment capacity should be taken from the connection interface with the lesser capacity. This can be obtained from a moment-curvature analysis of the section. If all connections incorporate similar reinforcing details, then the yield capacity should be identical in all connections. For the cyclic response, the unloading coefficient was taken as 0.3 for the bent. This is because there is a higher level of residual drift in the bent due to presence of more than one connection.

In the second part of the Chapter, two simplified analytical models, the Bilinear and Ramberg-Osgood, were used to model the behavior of the innovative dissipaters discussed in Chapter 4. Both models were able to capture the behavior of the dissipater to a good level of accuracy, with the Ramberg-Osgood model providing better results.

For the UFP Bracing Dissipater (UFP-BD) and Mini UFP Dissipater (MUD), the Ramberg-Osgood coefficient can be taken as $r = 5$. The yield drift and capacity were calculated using the expressions proposed by Kelly et al. (1972) and Baird et al. (2014). For the Bilinear model, the maximum capacity of the dissipater can be approximated to be 1.5 times the yield capacity in accordance with Kelly et al. (1972) and Baird et al. (2014).

For the Grooved Dissipaters (GDs), a methodology similar to that proposed by Sarti et al. (2013), which takes into account the elastic deformation over the non-yielding portions of the dissipater, can be adopted to calculate the yield point and initial stiffness. The Bilinear and Ramberg-Osgood models can then be utilized to capture the backbone curve and cyclic response of the dissipater. For the Bilinear model, the maximum capacity of GD under net positive deformation can be taken as 1.3 times the yield capacity. For the Ramberg-Osgood model the coefficient (r) can be taken as 15.

In the last part of the Chapter, the behavior of ABC Low Damage was modeled using lumped plasticity models as presented in the PRESSS Design Handbook (Pampanin et al. 2010). In this instance, similar to ABC High Damage, each column in the bent can be thought as two short cantilever columns. Each short column has DCR connection at the base. Given the fact that all connections in the bent incorporated similar DCR detailing,

the total capacity of the bent can be calculated by multiplying a factor (equals to the number of columns in the bent) to the computed capacity of the short cantilever column. The total displacement in the bent would be summation of the displacement from each short cantilever column.

A typical DCR connection can be modeled using two rotational springs for the unbonded post-tensioning and dissipaters which are positioned parallel to each other at the rocking interface. Results from the modeling of the innovative dissipaters in the previous part was utilized to construct the cyclic response of the dissipater rotational spring. The effect of gravity can also be considered and added to the post-tensioning rotational spring. The overall flag-shaped hysteresis can be obtained by summing the contributions from the two rotational springs. Using the procedure above, the analytical backbone curve and cyclic response showed good correlation with the experimental results.

6.6 Bibliography

1. Allen, M. and Kurama, Y. (2002). Design of Rectangular Openings in Precast Walls Under Combined Vertical and Lateral Loads. PCI Journal, 47(2):58-83.

2. Baird A., Smith, T., Palermo, A., and Pampanin, S. (2014). Experimental and Numerical Study of U-Shaped Flexural Plate (UFP) Dissipaters. Proceedings of New Zealand Society for Earthquake Engineering, Auckland, New Zealand.

3. Blandon, C. A. (2004). Equivalent Viscous Damping Equations for Direct Displacement Based Design. Master Thesis, European School of Advanced Studies in Reduction of Seismic Risk (ROSE School), Pavia, Italy.

4. California Department of Transportation (Caltrans) (2013). Seismic Design Criteria-Version 1.7. Caltrans, Sacramento, California, United States.

5. Carr, A. (2005). RUAUMOKO, Inelastic Dynamic Analysis. Christchurch, New Zealand. http://www.civil.canterbury.ac.nz/ruaumoko/

6. Conley, J., Sritharan, S. and Priestley, M. J. N. (1999). Precast Seismic Structural Systems PRESSS-3: The Five Story Precast Test Building Vol. 3-1: Wall Direction Response, Report No. SSRP-99/19. Department of Structural Engineering, University of California, San Diego, United States.

7. Computers and Structures Inc. (2015). Structural and Earthquake Engineering Software. Walnut Creek, United States. http://www.csiamerica.com/

8. Dassault Systemes (2015). ABAQUS, Finite Element Analysis Software. Vélizy-Villacoublay, France. http://www.3ds.com

9. El-Sheikh, M. T., Sause, R., Pessiki, S., Lu, L., and Kurama, Y. (1998). Seismic Analysis, Behavior and Design of Unbonded Post-Tensioned Precast Concrete Frames, PRESSS Report No 98/04. Lehigh University, Bethlehem, Pennsylvania, United States.

10. El-Sheikh, M. T., Sause, R., Pessiki, S., and Lu, L. (1999). Seismic Behavior and Design of Unbonded Post-Tensioned Precast Concrete Frames. PCI Journal, 44(3): 54- 71.

11. fib. (2003). Seismic Design of Precast Concrete Building Structures, International Federation for Structural Concrete, Lausanne, Switzerland.

12. Kelly, J. M., Skinner, R. I., and Heine, A. J. (1972). Mechanisms of Energy Absorption in Special Devices for use in Earthquake Resistant Structures. Bulletin of the New Zealand Society for Earthquake Engineering, 5(3).

13. Kim, J. (2002). Behavior of Hybrid Frames Under Seismic Loading. PhD Thesis, University of Washington, Seattle, United States.

14. Kowalsky, M. J. and Ayers, J. P. (2002). Investigation of Equivalent Viscous Damping for Direct Displacement-Based Design, PEER-2002/02. Pacific Earthquake Engineering Research Center, University of California, Berkeley, 173:185.

15. Kurama, Y. C. (2000). Seismic Design of Unbonded Post-Tensioned Precast Concrete Walls with Supplemental Viscous Damping. ACI Structural Journal, 97(4):648-658.

16. Kurama, Y. C., Pessiki, S., Sause, R., Lu, L., and El-Sheikh, M. T. (1998). Analytical Modeling and Lateral Load Behavior of Unbonded Post-Tensioned Precast Concrete Walls, PRESSS Report No. 98/02. Lehigh University, Bethlehem, Pennsylvania, United States.

17. Mander, J., Priestley, M. J. N., and Park, R. (1988). Theoretical Stress-Strain Model for Confined Concrete. Journal of Structural Engineering, 114(8):1804-1826.

18. MMPDS-01 (2003). Metallic Materials Properties Development and Standardization (MMPDS). Department of Transportation, Washington, D.C., United States.

19. Marriott, D. (2009). The Development of High-Performance Post-Tensioned Rocking Systems for the Seismic Design of Structures. PhD Thesis, University of Canterbury, Christchurch, New Zealand.

20. Naeim, F. and Kelly, J. M. (1999). Design of Seismic Isolated Structures: From Theory to Practice. John Wiley and Sons, New York, United States.

21. New Zealand Standards (NZS) (2006). The Design of Concrete Structures, NZS 3101. Wellington, New Zealand.

22. Palermo, A. (2004). The Use of Controlled Rocking In the Seismic Design of Bridges. PhD Thesis, Politecnico Di Milano (Technical University of Milan), Milan, Italy.

23. Palermo, A., Pampanin, S., and Calvi, G. M. (2005[1]). "Concept and Development of Hybrid Solutions for Seismic Resistant Bridge Systems. Journal of Earthquake Engineering, 9(6):899-921.

24. Palermo, A., Pampanin, S., and Carr, A. J. (2005[2]). Efficiency of Simplified Alternative Modeling Approaches to Predict the Seismic Response of Precast Concrete Hybrid Systems. fib symposium, Budapest, Hungary.

25. Palermo, A., Pampanin, S., and Calvi, G. M. (2005). Concept and Development of Hybrid Solutions for Seismic Resistant Bridge Systems. Journal of Earthquake Engineering, 9(6):899-921.

26. Pampanin, S., Marriot, D., and Palermo, A. (2010). PRESSS Design Handbook. New Zealand Concrete Society (NZCS) Incorporation, Auckland, New Zealand.

27. Pampanin, S., Priestley, M. J. N., and Sritharan, S. (2001). Analytical Modeling of the Seismic Behavior of Precast Concrete Frames Designed with Ductile Connections. Journal of Earthquake Engineering, 5(3):329-367.

28. Pampanin, S., Priestley, M. J. N., Sritharan, S. (2001). Analytical Modeling of the Seismic Behavior of Precast Concrete Frames Designed with Ductile Connections. Journal of Earthquake Engineering, 5(3):329-367.

29. Priestley, M. J. N., Calvi, G. M., and Kowalsky, M. J. (2007). Displacement-Based Seismic Design of Structures. IUSS Press, Pavia, Italy.

30. Ramberg, W., and Osgood, W. R. (1943). Description of Stress-Strain Curves By Three Parameters (Version Technical Note No. 902). Advisory Committee for Aeronautics, Washington D.C., United States.

31. Sarti, F., Smith, T., Palermo, A., Bonardi, D., and Carradine, D. M. (2013). Experimental And Analytical Study of Replaceable Buckling-Restrained Fuse-Type (BRF) Mild Steel Dissipaters. Proceedings of New Zealand Society for Earthquake Engineering Conference, Wellington, New Zealand.

32. Spieth, H. A., Carr, A. J., Pampanin, S., Murahidy, A. G., and Mander, J. B. (2004). Modeling of Precast Prestressed Concrete Frame Structures with Rocking Beam-Column Connections, University of Canterbury Research Report 2004-01. University of Canterbury, Christchurch, New Zealand.

33. Takeda, T., Sozen, M. A., and Nielsen, N. N. (1970). Reinforced Concrete Response to Simulated Earthquakes. Journal of Structural Division, American Society of Civil Engineers (ASCE), 96(12):2557-2573.

7. CONCLUSIONS AND RECOMMENDATIONS FOR FURTHER RESEARCH

7.1 Introduction

Over the last few decades, Accelerated Bridge Construction (ABC) is getting significant attention in countries such as the United States, Japan, Taiwan, New Zealand, and some European countries. ABC offers a number of advantages over the traditional monolithic construction of bridges. This includes, but not limited to:

1. Faster construction
2. Less traffic disruption
3. Higher construction quality
4. Robust material quality control
5. Improved work zone safety
6. Use of machineries and cranes on-site
7. Less environmental impacts

While offering great advantages over the traditional monolithic construction, however, ABC substructure systems have not been widely implemented in regions with moderate-to-high seismicity. This is due to concerns about the seismic performance of the precast connections during an earthquake. At the same time, there has been lack of extensive experimental investigation, design guidelines, detailing, and modeling of some of the proposed connections for ABC in high seismicity.

Over the last several years, a number of connections have been proposed for ABC in high seismicity. Past research studies investigated the suitability of some of these

connections. There has been a few examples of the implementation of these connections in prefabricated bridges in high seismicity. In general, the proposed connections can be classified under emulative "wet" and non-emulative "dry" cast-in-place connections, (Marsh et al., 2011).

Emulative cast-in-place connections aim to achieve similar performance for the bridge substructure system to that of traditional cast-in-place construction. This type of connections emulate the ductile seismic behavior of a cast-in-place construction through formation of plastic hinges in the pier. There have been many types of emulative connections proposed for ABC in high seismicity. The research here particularly emphasizes on the use of grouted duct and member socket connections for the cantilever and multi-column pier systems.

Emulative connections offer the advantage for prefabrication of the bridge substructure. However, given the extent of damage that can be expected from such detailing, the post-earthquake downtime, residual drift, and repairs, are the most undesirable aspects of this type of connections. Therefore, when emulative connections are used in the context for ABC, it is called "ABC High Damage" in this research.

Non-emulative cast-in-place connections target better seismic performance of the bridge substructure compared to emulative and cast-in-place. One type of the non-emulative connections is called "Hybrid" or "Dissipative Controlled Rocking" (DCR). This type of connection was primarily developed for precast buildings in seismic regions (Priestley et al., 1999). However, it was later extended to bridges by Palermo (2004).

In contrast to emulative cast-in-place connection, a typical DCR connection combines unbonded post-tensioned tendons with internally or externally attached dissipaters to form a dissipative rocking connection between the precast elements. The unbonded post-tensioned tendons provide self-centering for the connection while the energy dissipaters absorb the seismic energy. There have been several variations of DCR connections proposed for ABC. The research in this thesis emphasis on the use of DCR connection with externally attached mini plug and play dissipaters which can be easily installed or replaced. Given an enhanced performance of the DCR connection, it would eliminate the post-earthquake issues that are associated with the emulative cast-in-

place connections. Therefore, when DCR connections are used in the context of ABC, it is called "ABC Low Damage" here.

7.2 Development, Testing, and Modeling of ABC High Damage

In Chapter 3, two configurations of bridge substructure, the cantilever and multi-column, with grouted duct and member socket connections were investigated. A summary of each pier system is presented in the next sections.

7.2.1 Cantilever Pier System

In the first phase of testing, four half-scale precast cantilever segmental columns were developed and tested under uni and bi-directional quasi-static cyclic loading. Two columns were with square cross-section and featured grouted duct connection for the column to footing connection. The other two columns were with circular cross-section and member socket connection for the column to footing connection. The segment to segment connection in all four columns was grouted duct connection. A summary of the performance for each connection type is presented as follows.

7.2.1.1 Grouted Duct Connection

Experimental results suggested good ductility and strength of the column with grouted duct connection. The performance of this type of connection can be enhanced through debonding of the starter bars over a certain length at the column to footing interface. At the same time, providing simple armoring at the base of the column would prevent from spalling of concrete and strength degradation during lateral loading. This was shown to improve the behavior of the column significantly, and thus enhanced the ultimate displacement ductility of the column.

The debonded length of starter bar would distribute the total strain over a longer length of the bar, instead of a shorter length (concentrated crack) at the interface. This would also make the bar less susceptible to any low-cycle fatigue failure during larger drift ratios. The unbonded length of the starter bars can be calculated using the expressions provided in Paulay and Priestley (1992) and PRESSS Design Handbook (Pampanin et al., 2010). Similarly, an estimate of armoring thickness can be carried out using the concrete confinement model proposed by Mander et al. (1988).

The development length of the starter bars inside grouting ducts can be left equal to the what is required by the codes such as NZS 3101 (NZS, 2006) for typical cast-in-place concrete.

The plastic hinge length of the precast column with grouted duct connection can be taken as half diameter/height of the column cross-section. In accordance with NZS 3101 (NZS, 2006), this plastic hinge length would correspond to a reversing plastic hinge in conventional monolithic column.

Internal shear key can be used in grouted duct connection to provide shear resistance. In this instance, the dowel action of the starter bars to resist shear can be neglected.

In terms of construction, grouted duct connection carries a higher risk due to any misalignment of the starter bars inside the ducts. In order to overcome this, frequent inspection of the ducts during precasting process should be carried out to minimize the risk. A match casting for the precast elements would also eliminate the risk for the misalignment during assembly process. Another solution is to leave sufficient construction tolerance in the diameter of the grouting ducts. The research in this thesis showed that leaving 34 mm tolerance in the diameter of the grouting duct could eliminate the misalignment risk during assembly of the column.

To capture the response of the column with grouted duct connection, simplified macro-modeling procedure using existing theoretical models can be utilized. For the segmental column, the contribution for energy dissipation from the second plastic hinge at the segment to segment connection can be neglected. The yield curvature and moment capacity of the column can be calculated from an idealized bilinear moment-curvature cross-section analysis according to Caltrans Seismic Design Criteria (2013). Displacement-based formulas in accordance with Priestley et al. (2007) can be used to construct the monotonic response (backbone curve) of the column. Takeda-Thin model (Takeda et al., 1970, Kowalsky and Ayers, 2002) can be used to capture the cyclic response. Calibration of the analytical models with the experimental data showed that the unloading coefficient (α) can be taken as 0.4 for the cyclic response of the column.

7.2.1.2 Member Socket Connection

Experimental results showed good performance of the connection. Testing results showed higher ductility of the column with grouted duct connection compared to the column with member socket connection.

For the column with member socket connection, there was a wider distribution of the cracks at the plastic hinge. The observed plastic hinge length of the column was equal to the diameter of the column cross-section. This was almost twice longer than the observed plastic hinge length in the column with grouted duct connection. A longer plastic hinge would result in lesser strain concentration over the yielding portion of the rebars. Therefore, it improves the low-cycle fatigue performance of the bars. In accordance with NZS 3101 (NZS, 2006), similar plastic hinge length can be expected for a uni-directional plastic hinge in cast-in-place construction where inelastic rotation can develop on both sides of the critical section.

Some detailing considerations for the design and construction of the member socket connection are summarized as follows.

- The depth of the socket should be sufficient enough to prevent damage to the footing. Experimental results showed that keeping a ratio of one to one between the column diameter and thickness of the footing, the connection can be strong enough to push the plastic hinging in the column and limit the tearing stresses in the footing. Circular reinforcing bars can be provided around the socket on top and bottom of the footing to limit radial cracking.

- When selecting diameter of the socket, construction tolerance in placing the column inside the socket would have to be considered. The research showed that leaving 20 mm tolerance in the socket diameter was sufficient for assembly of the column with no issues. This gap was also observed to be adequate for the flow of the grout between the socket walls and the column stub.

- The socket walls and surface of the column stub can be roughened during precasting process. This would provide an improved bond for the grout.

- For the development length of the column longitudinal bars inside the socket, foot inserts (headed bars) can be used. This would eliminate the need for bent bars in the column. Another solution is to allow similar development length of the longitudinal bars inside the socket to that of cast-in-place concrete in accordance with NZS 3101. However, this may increase the depth of the socket if large-diameter bars are used in the column. Experimental results showed good performance for both solutions without any pull out of the column rebars.

In terms of construction, member socket connection offers simple assembly compared to grouted duct connection. Therefore, it carries a lower risk of misalignment during the on-site assembly process.

The analytical macro-modeling procedure for member socket connection was similar to that explained for the column with grouted duct connection in the previous section.

7.2.2 Multi-Column Pier System (Bent)

In the second phase of testing, a half-scale multi-column pier (bent) was developed and tested under uni-directional quasi-static cyclic loading. The bent featured grouted duct connection for the column to cap beam, and member socket connection for the column to footing connection.

Experimental results and observations from the testing showed good performance of the bent. The bent achieved good levels of ductility by forming plastic hinges at the top and bottom of the columns. The performance of the top grouted duct and bottom member socket connection was similar to that explained in Section 7.2.1 for the cantilever columns.

For macro-modeling of the bent with combination of grouted duct and member socket connections, the yield curvature can be calculated using a general displacement-based approach. Each column in the bent can be considered as two short cantilever columns. Similar to previous section, an idealized moment-curvature analysis for the column cross-section can be carried out. The yield moment capacity of the bent can be computed from the connection interface with the lesser moment capacity.

Similar to modeling of cantilever columns, Takeda-Thin hysteresis rule can be used to capture the cyclic response of the bent. A higher level of residual displacement can be expected in a bent due to the presence of more than one connection (plastic hinge). Therefore, when modeling the cyclic response of the bent using Takeda-Thin model, the unloading coefficient (α) can be taken lower than that for cantilever columns. Calibration of the numerical model against the experimental data showed that the unloading coefficient (α) can be taken as 0.3 for the bent with combination of grouted duct and member socket connections.

Table 7.1 presents a summary of the progressive collapse analysis for the bent according to Austroads Technical Report (2012).

Table 7.1. Summary of progressive collapse analysis for HDB

Limit States	**Yielding (YL)**		**Serviceability (SL)**		**Ultimate Limit State (ULS)**		**1.25 ULS (MCE)**	
Status	**Fully Operational**		**Delayed Operational**		**Delayed Operational**		**Delayed Operational**	
Drift (%)	0.82		1.5		2.7		3.4	
Ductility (μ)	1.0		1.8		3.3		4.1	
Moment Capacity	180 kNm		232 kNm		240 kNm		225 kNm	
Strain limits (ε)	ε_c	ε_s	ε_c	ε_s	ε_c	ε_s	ε_c	ε_s
	<0.004	0.00275	0.004	0.015	0.0176	0.0448	-	>0.05
Location	GDC	MSC	GDC	MSC	GDC	MSC	GDC	MSC
Crack size (mm)	0.5	1.5	1.5	3	7	Spall	9	Spall

In summary, for a real life bridge incorporating ABC High Damage technology, the expected seismic performance of the bridge is summarized as follows:

1. The bridge would not collapse during a Maximum Considered Earthquake (MCE) and would be derivable and open to traffic, but with delayed or limited functionality.

2. The bridge may have residual displacement following the earthquake.

3. Extensive repairs or possible replacement of the bridge might be needed after the earthquake for the long term resiliency.

7.3 Development, Testing, and Modeling of ABC Low Damage

In this phase of testing, a half-scale bent with Dissipative Controlled Rocking (DCR) or "Hybrid" connections was developed and tested under uni-directional quasi-static cyclic loading. The bent had identical dimensions and reinforcing detailing to that explained in Section 7.2.2 (ABC High Damage). The DCR connections replaced the plastic hinges in the bent. The design of a typical DCR connection was based on the Monolithic Beam Analogy (Palermo, 2004) in accordance with PRESSS Design Handbook (Pampanin et al., 2010).

Some detailing considerations for the design and construction of the DCR connection are summarized as follows.

- The rocking interface should be armored to prevent spalling and crushing of the concrete in the precast elements. For the column rocking section, steel armoring shell can be used. The shell can be connected through welded studs to the confined core. The armoring shoe thickness can be calculated using the concrete confinement model by Mander et al. (1988). The height of the armoring shoe can be taken equal to the diameter of the column or the plastic hinge length given in NZS 3101 for a cast-in-place ductile column. The armoring shoe should be placed in the column formwork before pouring concrete. Steel brackets can be welded around the outside face of the shell to provide anchoring points for one end of the dissipaters. Steel base plate can be used at the rocking interface to protect the concrete surface where the rocking motion occurs. The plate is normally located on top of the footing or bottom of the cap beam. It has to be designed as a capacity protected element. The base plate would also provide anchoring points for the other end of the dissipaters for the DCR connection.

- In order to prevent sliding and twisting of the columns at the rocking interfaces, internal or external shear keys can be used. Experimental results showed insufficiency of the internal circular shear keys to prevent sliding and twisting of the columns in the bent. External shear keys can be simply made of steel bars which are welded to the armoring shoe and the base plate. Observations from the testing showed great performance of the external shear keys which prevented sliding and twisting of the columns during rocking of the bent.

Grooved Dissipater (GD) and Mini UFP dissipater (MUD) were used to provide dissipation in the bent during testing. Several dissipater arrangements were tested in the bent. Testing results showed good performance of the Low Damage Bent (LDB) with mini plug and play dissipaters. Testing results showed that the bent achieved good levels of ductility and dissipation. At the same time, it had almost zero residual displacement.

GD offers the advantage for higher capacity in a compact package, however, testing results suggested strength degradation of the dissipater under cyclic loading. This would make GD susceptible to low-cycle fatigue failure. In contrast, MUD can undergo a large number of cycles before any noticeable strength degradation or low-cycle fatigue failure. Therefore, in order to optimize the seismic performance of the bent, MUD can be used in regions where maximum gap opening is expected when the bent start rocking. At the same time, GD can be used in regions where smaller gap opening occurs.

For a real life ABC Low Damage bridge which uses similar arrangement of the dissipaters as explained above, the external dissipaters would not have to be replaced following a big earthquake. This would further minimize the maintenance and the post-earthquake repair time and costs of the bridge.

For macro-modeling of the ABC Low Damage bent, a procedure similar to what discussed for ABC High Damage Bent (HDB) can be used. In this instance, each column can be considered as two short cantilever columns. Each short column has a DCR connection at the base. The Monolithic Beam Analogy can be used to construct the monotonic response of the column. To capture the cyclic response of the column, a lumped-plasticity model can be used. The column would have a DCR connection at the base. To model the connection, two rotational springs (one for the unbonded post-tensioning and one for the dissipaters) which are positioned parallel to each other, can be utilized. The summation of the contributions from the two springs would give the resultant cyclic response of the connection which is commonly known as "Flag-Shaped" hysteresis.

The total capacity of the bent can be obtained by multiplying a factor (equals to the number of columns in the bent) to the computed capacity of a short cantilever column.

The total displacement of the bent would be the summation of the displacement contributions from the two short cantilever columns.

In summary, for a real life bridge incorporating ABC Low Damage technology, the expected seismic performance of the bridge is summarized as follows:

1. The bridge would not suffer any substantial damage during a Maximum Considered Earthquake (MCE).
2. The bridge would remain immediately derivable and open to traffic without any delayed or limited functionality.
3. The bridge would self-center with minimal to no residual displacement.
4. Minor to no repairs of the bridge following the earthquake.

Table 7.2 provides a qualitative comparison between monolithic construction, ABC High Damage, and ABC Low Damage in high seismicity.

Table 7.2. Qualitative comparison of Monolithic, ABC High Damage, and ABC Low Damage

		Low	Moderate	High
Monolithic	Material / Fabrication Cost			
	Construction Time			
	Repair Cost and Time			
ABC High Damage	Material / Fabrication Cost			
	Construction Time			
	Repair Cost and Time			
ABC Low Damage	Material / Fabrication Cost			
	Construction Time			
	Repair Cost and Time			

7.4 Development, Testing, and Modeling of Innovative Dissipaters

In this part of testing, concepts for the innovative dissipaters were developed. The dissipaters incorporate metallic source of dissipation. The internal parts in the dissipater start yielding under axial displacement, and thus provide energy dissipation.

The dissipaters are in the shape of bracing and mini plug and play devices. They can be used in seismic, wind, and vibration protection of the buildings, bridges, and non-structural components.

The dissipaters provide advantages that are not integrated with the available dissipaters in the market such as Buckling Restrained Braces (BRBs) and Viscous Fluid Dampers. This includes, but not limited to the below:

1. Lower fabrication cost and use of readily available material (mild steel)
2. Higher capacity
3. Lightweight
4. Great compactness
5. Enhanced seismic performance and energy dissipation capacity
6. Multiple seismic/wind performance feature
7. Balanced hysteresis in tension and compression
8. Minimal strength degradation and low-cycle fatigue failure under a large number of cycles beyond the yield point
9. Option for self-centering
10. Rapid reinstatement with higher capacity after a major earthquake
11. Easy replaceability of the parts (if needed)
12. Lower life-cycle maintenance and total cost
13. Use of recycled material for the parts (environmentally friendly)

A number of concepts for using the bracing type and mini plug and play devices in ABC High Damage and ABC Low Damage, were proposed. Several prototypes were built to validate the concepts. Experimental results showed great performance and ductility of the dissipaters.

Out of all innovative dissipaters, the Mini UFP Dissipater (MUD) was implemented in the Low Damage Bent (LDB) and several quasi-static cyclic testing were carried out. In comparison to mini Buckling-Restrained Braces (BRBs) and GD, MUD offers enhanced low-cycle fatigue behavior with higher levels of hysteretic damping and displacement ductility. Experimental results showed great performance of the DCR connection with MUD. Similarly, a combination of MUD and GD in the DCR connection was also proven to result into an enhanced behavior. After dozens of testing, there was no damage to the bent including no hairline cracking to the columns.

The Bilinear (Kelly and Naeim, 1999) and Ramberg-Osgood (Ramberg and Osgood, 1943) analytical models were used to capture the response of the dissipaters. Numerical models were calibrated against the experimental data to accurately predict the monotonic and cyclic response of the dissipaters. It was shown that the Ramberg-Osgood model provides better accuracy and results compared to Bilinear.

The Ramberg-Osgood coefficient (r) for the UFP Bracing Dissipater (UFP-BD) and Mini UFP Dissipater (MUD) can be taken as $r = 5$. The yield drift and capacity of the UFPs can be calculated using the expressions proposed by Kelly et al. (1972) and Baird et al. (2013). For the Bilinear model, the maximum capacity of the UFP-BD and MUD can be taken as 1.5 times the yield capacity.

For the Grooved Dissipater (GD), the methodology proposed by Sarti et al. (2013) can be utilized. In this methodology, when calculating the yield point and initial stiffness of the dissipater, the elastic deformation over the non-yielding portions of the dissipater is taken into account. The Ramberg-Osgood coefficient (r) can be taken as 15 for GD. For Bilinear model, the maximum capacity of GD under net positive deformation can be taken as 1.3 times the yield capacity.

7.5 Recommendations for Further Research

Chapter 3 presented the development and testing of ABC High Damage with grouted duct and member socket connections. While several aspects of the two connections were investigated, however, further research is required in the following areas.

For column with member socket connection:

- Quantifying the appropriate socket depth for various column shapes and cross-section such as square, rectangle, octagonal etc.
- Quantifying the maximum gap width between the socket walls and the precast column that would not reduce the effectiveness of the connection for transferring gravity and lateral load.
- Quantifying the development length of the column longitudinal rebars in the socket, if headed bars or compliance with code requirements for cast-in-place construction are not used.
- Quantifying the roughness factor of the concrete surface for resisting vertical shear stresses in the socket.
- Durability of the connection.
- Effects of cracking in the grout on strength and durability.

For column with grouted duct connection:

- Use and effects of using shear key on reducing shear degradation under cyclic loading in the connection.
- Development of appropriate hand calculation methodologies for designing armoring shoe.
- Construction tolerances in the grouting ducts for a range of rebar sizes.

For modeling the response of ABC High Damage, the following areas are suggested for further research.

- Micro and Finite Element Modeling of ABC High Damage system.
- Calibration of the micro-models against experimental data.

Chapter 4 discussed the development of innovative dissipaters for a variety of structural and non-structural applications. The following areas are identified for further research.

- Experimental testing and validation of proposed concepts for the variations of the innovative dissipaters which were not tested in this thesis. This would require development and testing of full-scale prototypes under cyclic loading.
- Optimization of design and detailing for an enhanced performance of the bracing type dissipaters and mini plug and play devices.
- Finite Element Modeling (FEM) of the dissipaters and their components.
- Development of detailed analytical models for predicting the response of the innovative dissipaters.
- Evaluation of the seismic performance factors for each type of the innovative dissipaters in accordance with FEMA P695 (2009).

Chapter 5 presented the development of ABC Low Damage system. The following areas are recommended for further research.

- Experimental testing and validation of the proposed concepts in Chapter 4 for implementation of innovative dissipaters in ABC High Damage and ABC Low Damage that were not tested in this research.
- Finite Element and multi-spring modeling of ABC Low Damage system.
- Investigation of soil-structure interaction in ABC Low Damage system.

Other areas of further research are recommend as follows:

- A parametric study on self-centering ratio for a set of bridges (up to 30 m span) with cantilever and bent substructure configurations and incorporating ABC Low Damage technology.

- Preparation of a Design and Detailing Handbook for ABC High Damage and ABC Low Damage in moderate-to-high seismic regions in New Zealand.

In order to provide a detailed quantitative comparison between cast-in-place, ABC High Damage, and ABC Low Damage, loss modeling analysis can be used. This would require development of a set of bridges with different substructure configurations and short-to-medium spans for a variety of seismic hazard levels from NZS 1170.5 (2004).

Performance-Based Earthquake Engineering (PBEE) assessment can then be utilized to highlight and compare the relative performance of each system against the expected repair cost and downtime. After the recent earthquakes around the world, this type of assessment has been getting more popularity. Recent research studies on loss modeling were carried out by Christopoulos et al. (2003), Pampanin et al. (2003), Dhakal and Mander (2006), Uma et al. (2006,2010), Marriott et al. (2009), Solberg et al. (2008), Bradley et al. (2010), and Lee and Billington (2011).

The results from such an assessment would help infrastructure asset owners and managers to identity the probability of damage to a bridge for each structural system. It would confirm the overall cost benefit of ABC Low Damage over ABC High Damage and monolithic construction. At the same time, It would provide useful information on the expected downtime and repair cost of the bridge.

7.6 Bibliography

1. Austroads Technical Report (2012). Bridge Design Guidelines for Earthquakes. Austroads, Sydney, Australia.

2. Baird A., Smith, T., Palermo, A., and Pampanin, S. (2014). Experimental and Numerical Study of U-Shaped Flexural Plate (UFP) Dissipaters. Proceedings of New Zealand Society for Earthquake Engineering, Auckland, New Zealand.

3. Bradley, B., Cubrinovski, M., Dhakal, R., and MacRae, G. (2010). Probabilistic Seismic Performance and Loss Assessment of a Bridge-Foundation-Soil System. Soil Dynamics and Earthquake Engineering, 30(5):395-411.

4. California Department of Transportation (Caltrans) (2013). Seismic Design Criteria-Version 1.7. Caltrans, Sacramento, California, United States.

5. Christopoulos, C., Pampanin, S., and Priestley, M. J. N. (2003). Performance-Based Seismic Response of Frame Structures including Residual Deformations. Part I: Single-Degree of Freedom Systems. Journal of Earthquake Engineering, 7(1):97-118.

6. Dhakal, R. and Mander, J. (2006). Financial Risk Assessment Methodology for Natural Hazards. Bulletin of the New Zealand Society of Earthquake Engineering, 39(2):91-105.

7. FEMA P695 (2009). Quantification of Building Seismic Performance Factors. Federal Emergency Management Agency, Washington D.C., United States.

8. Kelly, J. M., Skinner, R. I., and Heine, A. J. (1972). Mechanisms of Energy Absorption in Special Devices for use in Earthquake Resistant Structures. Bulletin of the New Zealand Society for Earthquake Engineering, 5(3).

9. Kowalsky, M. J. and Ayers, J. P. (2002). Investigation of Equivalent Viscous Damping for Direct Displacement-Based Design, PEER-2002/02. Pacific Earthquake Engineering Research Center, University of California, Berkeley, 173:185.

10. Lee, W. K. and Billington, S. L. (2011). Performance-Based Earthquake Engineering Assessment of a Self-Centering, Post-Tensioned Concrete Bridge System. Earthquake Engineering and Structural Dynamics, 40(8):887-902.

11. Mander, J., Priestley, M. J. N., and Park, R. (1988). Theoretical Stress-Strain Model for Confined Concrete. Journal of Structural Engineering, 114(8):1804-1826.

12. Marriott, D. (2009). The Development of High-Performance Post-Tensioned Rocking Systems for the Seismic Design of Structures. PhD Thesis, University of Canterbury, Christchurch, New Zealand.

13. Marsh, M. L., Wenli, M., Garrett, B. E., Stanton, J. F., Eberhard, M. O., and Weinert, M. D. (2011). Application of Accelerated Bridge Construction Connections in Moderate-to-High Seismic Regions, NCHRP Report 698. TRB, National Research Council, Washington, D.C., United States.

14. Naeim, F. and Kelly, J. M. (1999). Design of Seismic Isolated Structures: From Theory to Practice. John Wiley and Sons, New York, United States.

15. New Zealand Standards (NZS) (2004). Structural Design Actions: Earthquake Actions, NZS 1170.5. Wellington, New Zealand.

16. New Zealand Standards (NZS) (2006). The Design of Concrete Structures, NZS 3101. Wellington, New Zealand.

17. Palermo, A. (2004). The Use of Controlled Rocking In the Seismic Design of Bridges. PhD Thesis, Politecnico Di Milano (Technical University of Milan), Milan, Italy.

18. Pampanin, S., Christopoulos, C., and Priestley, M. J. N. (2003). Performance-Based Seismic Response of Frame Structures Including Residual Deformations. Part II: Multi-Degree of Freedom Systems. Journal of Earthquake Engineering, 7(1):119-147.

19. Pampanin, S., Marriot, D., and Palermo, A. (2010). PRESSS Design Handbook. New Zealand Concrete Society (NZCS) Incorporation, Auckland, New Zealand.

20. Paulay, T., and Priestley, M. J. N. (1992). Seismic Design of Reinforced Concrete and Masonry Buildings. John Wiley & Sons, Inc., New Jersey, United States.

21. Priestley, M. J. N., Calvi, G. M., and Kowalsky, M. J. (2007). Displacement-Based Seismic Design of Structures. IUSS Press, Pavia, Italy.

22. Priestley, M. J. N., Sritharan, S., Conley, J. R., and Pampanin, S. (1999). Preliminary Results and Conclusions from the PRESSS Five-Story Precast Concrete Test Building. Precast/Prestressed Concrete Institute Journal, 44(6):42-67.

23. Ramberg, W., and Osgood, W. R. (1943). Description of Stress-Strain Curves By Three Parameters (Version Technical Note No. 902). Advisory Committee for Aeronautics, Washington D.C., United States.

24. Sarti, F., Smith, T., Palermo, A., Bonardi, D., and Carradine, D. M. (2013). Experimental And Analytical Study of Replaceable Buckling-Restrained Fuse-Type (BRF) Mild Steel Dissipaters. Proceedings of New Zealand Society for Earthquake Engineering Conference, Wellington, New Zealand.

25. Solberg, K., Dhakal, R., Mander, J., and Bradley, B. (2008). Computational and Rapid Expected Annual Loss Estimation Methodologies for Structures. Earthquake Engineering and Structural Dynamics, 37(1):81-101.

26. Takeda, T., Sozen, M. A., and Nielsen, N. N. (1970). Reinforced Concrete Response to Simulated Earthquakes. Journal of Structural Division, American Society of Civil Engineers (ASCE), 96(12):2557-2573.

27. Uma, S. R., Pampanin, S., and Christopoulos, C. (2006). A Probabalistic Framework for Performance-based Seismic Assessment of Structures Considering Residual Deformations. First European Conference on Earthquake Engineering and Seismology, Geneva, Switzerland.

28. Uma, S. R., Pampanin, S., and Christopoulos, C. (2010). Development of Probabilistic Framework for Performance-Based Seismic Assessment of Structures Considering Residual Deformations. Journal of Earthquake Engineering, 14:1092-1111.

APPENDIX A

A.1 Equivalent Static Method - (NZS 1170.5):

For Ultimate Limit State (ULS), the horizontal design action coefficient $C_d(T_1$, is given as follows:

$$C_d(T_1) = \frac{C(T_1)S_p}{k_\mu} \quad \text{(A. 1)}$$

$$\geq \left(\frac{Z}{20} + 0.02\right) R_u \text{but not less than } 0.03R_u \quad \text{(A. 2)}$$

Where,

$C(T_1)$ = Elastic site hazard spectrum ordinate, refer to Equation A.3

S_P = Structural performance factor, equals 0.7 for ULS except where $1.0 < \mu < 2.0$, then S_P is given by Equation A.4

R_u = Return period factor for ULS, refer to Table A.2

μ = Assumed value of displacement ductility

Z = Hazard factor, refer to Figure A.1 and Figure A.2

T_1 = Fundamental period of the structure in seconds

k_μ = Ductility factor, refer to Equation A.5 through Equation A.8

$$\mathrm{C}(T) = C_h(T)\, Z\, R\, N(T, D) \quad \text{(A. 3)}$$

Where in Equation A.3,

$C_h(T)$ = Spectral shape factor from Table A.1

R = Return Period factor (R_s or R_u) from Table A.2, ZR_u should not exceed 0.7

R_s = Return period factor for Serviceability Limit State (SLS), refer to Table A.2

$N(T, D)$ = Near-fault factor, equals 1.0 for locations with distance > 20 km from the nearest major fault listed in Table 3.6 of NZS 1170.5

where $1.0 < \mu < 2.0$, then S_P is calculated from Equation A.4.

$$S_P = 1.3 - 0.3\mu \tag{A.4}$$

For soil classes, A, B, C, and D and $T_1 \geq 0.7$ *sec:*

$$k_\mu = \mu \tag{A.5}$$

For soil classes, A, B, C, and D and $T_1 < 0.7$ *sec:*

$$k_\mu = \frac{(\mu - 1)T_1}{0.7} + 1 \tag{A.6}$$

For soil class E and $T_1 \geq 1$ *sec* or $\mu < 1.5$

$$k_\mu = \mu \tag{A.7}$$

For soil class E and $T_1 < 1$ *sec* and $\mu \geq 1.5$

$$k_\mu = (\mu - 1.5)T_1 + 1.5 \tag{A.8}$$

Table A.1. Spectral Shape Factor, C_h (T), in (g)

Period, T (seconds)	A Strong rock and B rock	C Shallow soil	D Deep or soft soil	E Very soft soil
0	1.89 (1.00)[1]	2.36 (1.33)[1]	3 (1.12)[1]	3 (1.12)[1]
0.1	1.89 (2.35)[1]	2.36 (2.93)[1]	3	3
0.2	1.89 (2.35)[1]	2.36 (2.93)[1]	3	3
0.3	1.89 (2.35)[1]	2.36 (2.93)[1]	3	3
0.4	1.89	2.36	3	3
0.5	1.6	2	3	3
0.6	1.4	1.74	2.84	3
0.7	1.24	1.55	2.53	3
0.8	1.12	1.41	2.29	3
0.9	1.03	1.29	2.09	3
1	0.95	1.19	1.93	3
1.5	0.7	0.88	1.43	2.21
2	0.53	0.66	1.07	1.66
2.5	0.42	0.53	0.86	1.33
3	0.35	0.44	0.71	1.11
3.5	0.26	0.32	0.52	0.81
4	0.2	0.25	0.4	0.62
4.5	0.16	0.2	0.32	0.49

Values in brackets in Table A.1 correspond to spectral values for the modal response spectrum and numerical integration time history methods.

Table A.2. Return Period Factor

Required annual probability of exceedance	R_s or R_u
1/2500	1.8
1/2000	1.7
1/1000	1.3
1/500	1.0
1/250	0.75
1/100	0.5
1/50	0.35
1/25	0.25
1/20	0.2

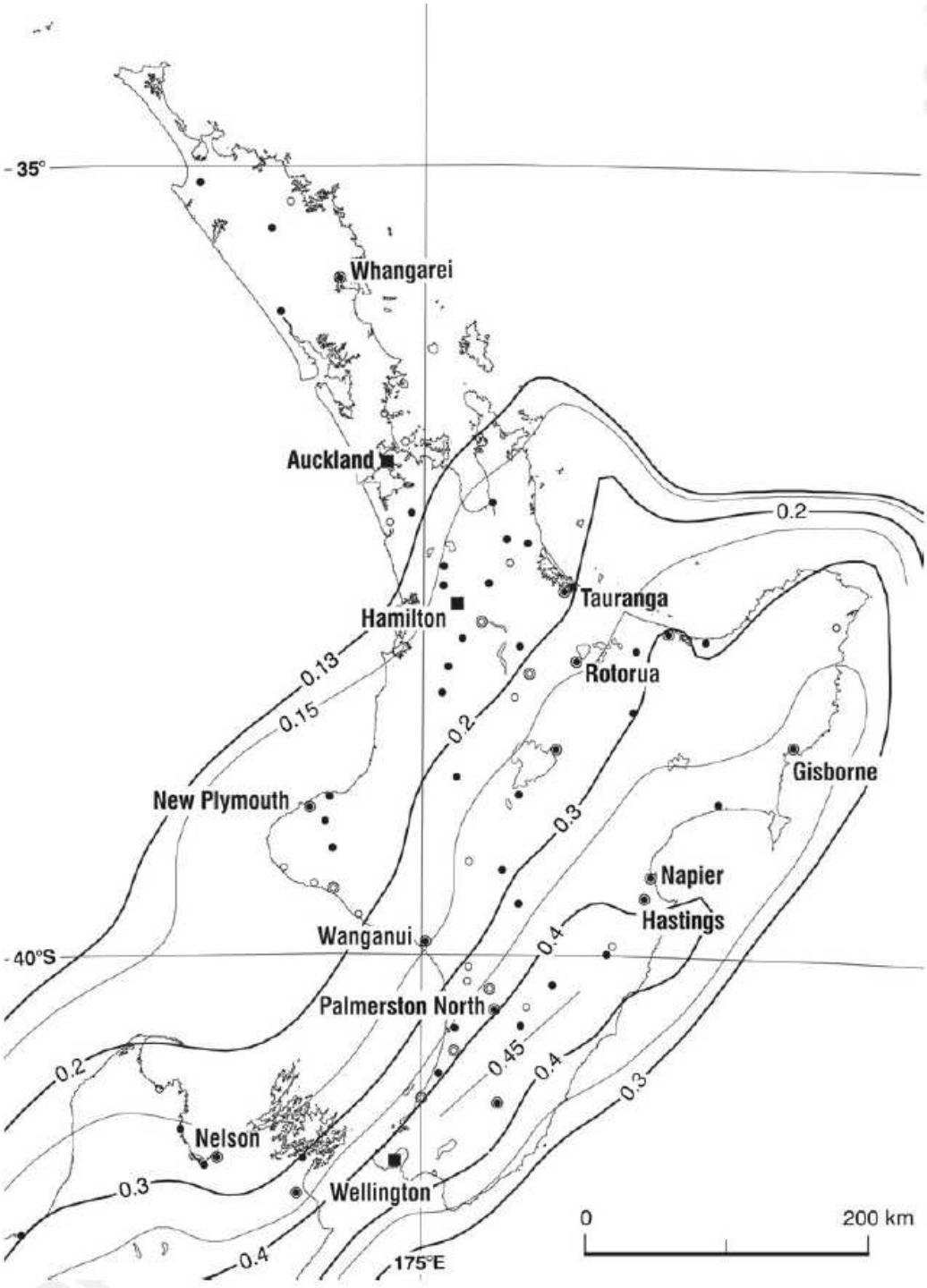

Figure A.1. Hazard Factor, *Z*, for the North Island of New Zealand

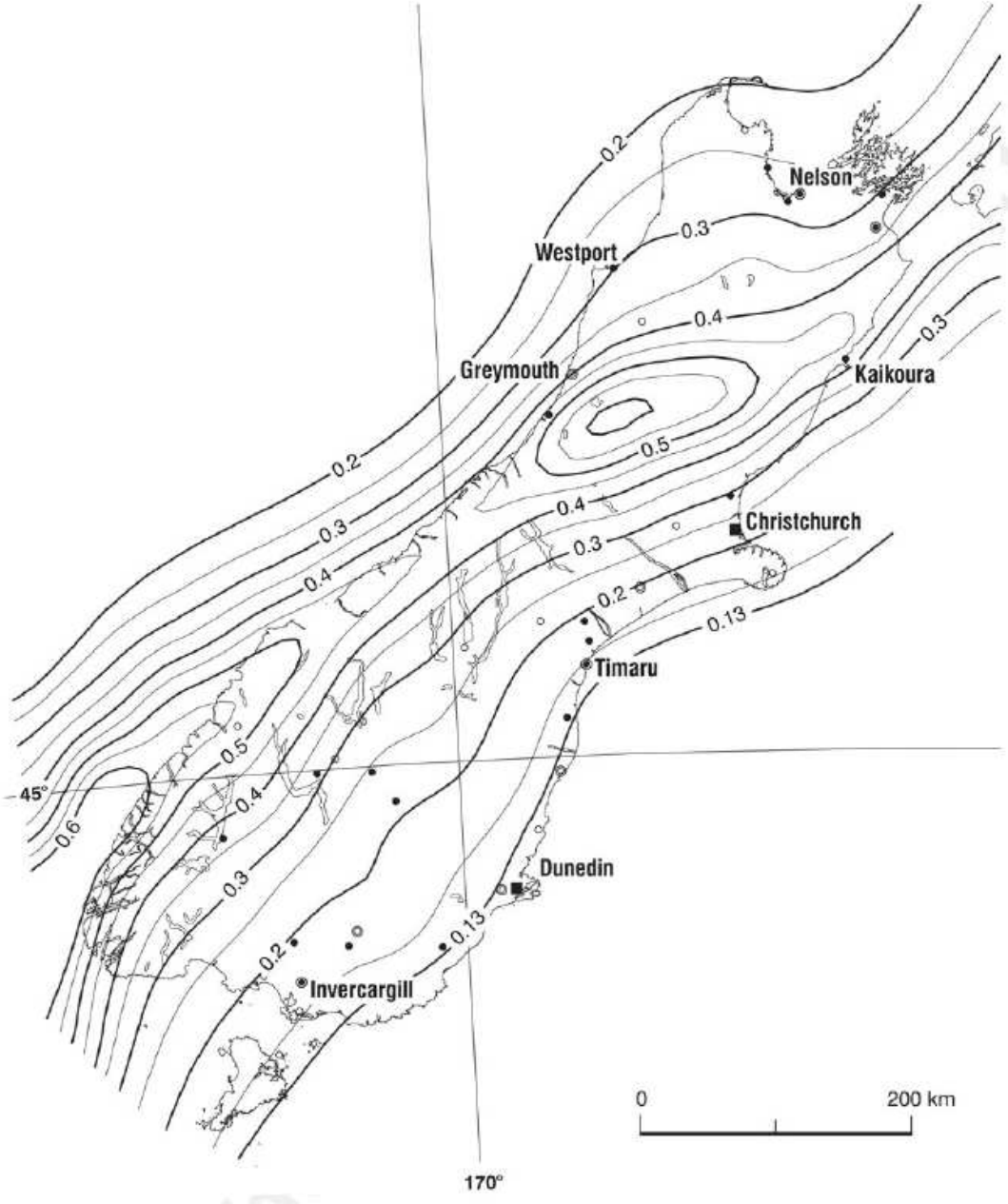

Figure A.2. Hazard Factor, *Z*, for the South Island of New Zealand

In Figure A.1 and Figure A.2, the circles and square correspond to towns and cities, respectively.

A.2 Nonlinear Static (Pushover) Analysis for HDB

In order to predict the maximum base shear and its corresponding drift ratio for the High Damage Bent (HDB), a simple nonlinear static (pushover) analysis was carried out in SAP 2000 (Computers and Structures Inc., 2015).

Lumped plasticity model was used to construct the nonlinear model of the bent in SAP 2000, as shown in Figure A.3. In this type of model, all nonlinear action in the bent is assumed to be concentrated in the plastic hinges. The regions of the column outside the plastic hinging zone and the entire cap beam were modeled to remain elastic (capacity protected elements).

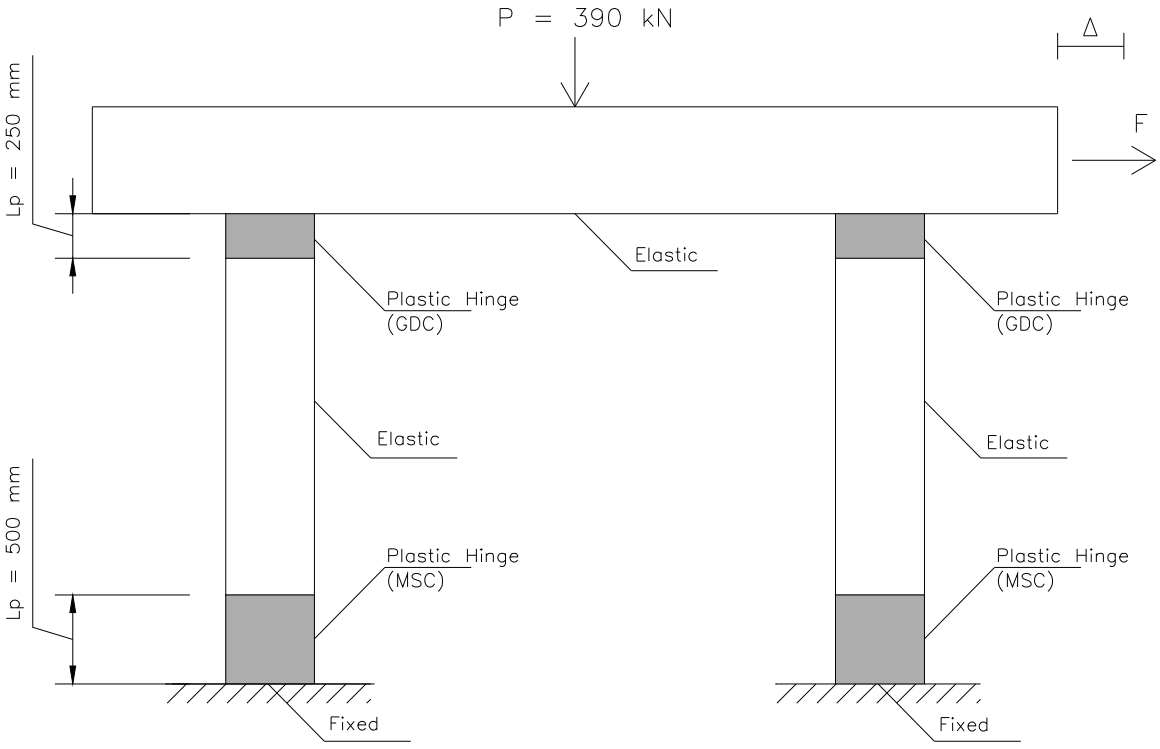

Figure A.3. Lumped plasticity model of HDB in SAP 2000

The plastic hinges were introduced in the software as rotational hinges. The moment-curvature relationship for the column section at the top Grouted Duct Connection (GDC) and bottom Member Socket Connection (MSC) was calculated from the SAP 2000 Section Designer Feature, refer to Figure A.4. It is important to note that the plots in Figure A.4 take into account a constant gravity (axial load) on the column section, depending on the location in the bent. In the SAP 2000 model of Figure A.3, the influence of the axial load when generating the moment-curvature relationship of the

column section was removed, and the hinges were introduced as Interacting Axial-Moment hinges in the software. This would eliminate the chance of having the axial load counted twice on the column section.

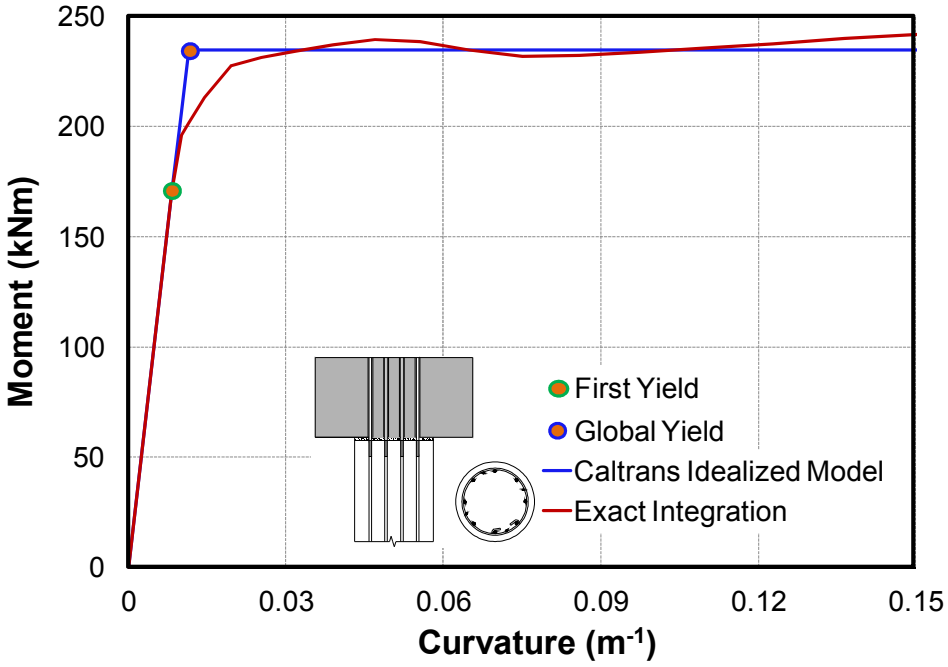

(a) Moment-curvature plot for the top GDC

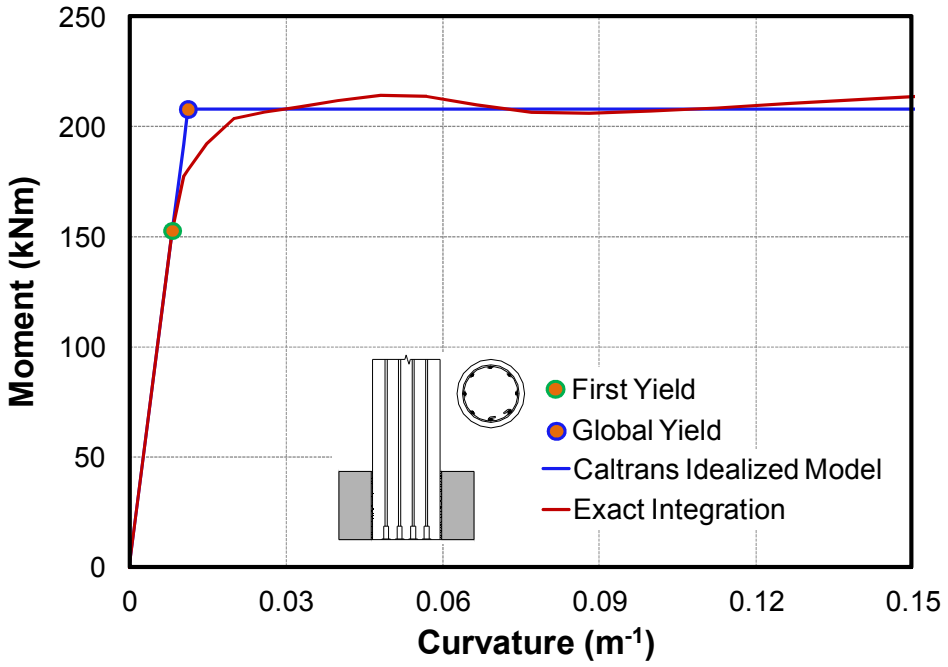

(a) Moment-curvature plot for the bottom MSC

Figure A.4. Lumped plasticity model of HDB in SAP 2000

Experimental observation and results from the first phase of testing on GDC and MSC (Section 3.2 in Chapter 3) was utilized to construct the moment-rotation relationship for each plastic hinge. In this instance, the plastic hinge length (L_p) for the top GDC was taken to be equal to half diameter of the column or 250 mm. For the bottom MSC, the plastic hinge length (L_p) was taken equal to the diameter of the column or 500 mm, as shown in Figure A.3. The self-weight of the bent is automatically considered by the software. The additional gravity from the superstructure weight (390 kN) was exerted as a point load acting on top of the cap beam.

The pushover curve of HDB is presented in Figure A.5. The bent is predicted to achieve maximum base shear capacity of 346.2 kN at the 2.2% drift ratio (ULS performance level). The Maximum Considered Earthquake (MCE) level was taken to be 1.5 times ULS or 3.4% drift ratio. It is also clear that the base shear from the equivalent static force method of NZS 1170.5 is slightly lower than the maximum capacity of the bent from a pushover analysis.

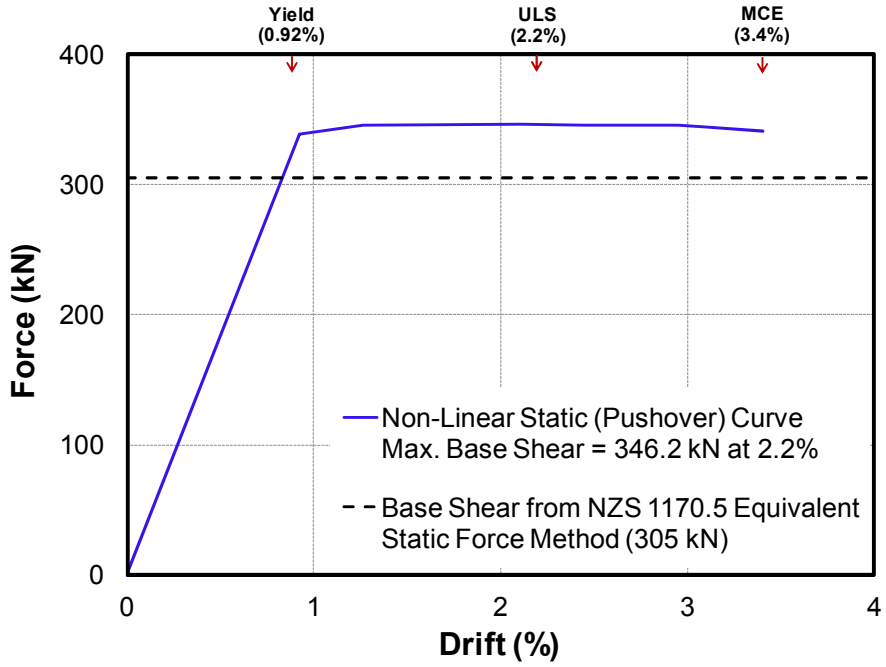

Figure A.5. Predicted pushover curve for HDB from SAP 2000

A.3 Bibliography

1. Computers and Structures Inc. (2015). Structural and Earthquake Engineering Software. Walnut Creek, United States. http://www.csiamerica.com/

2. New Zealand Standards (NZS) (2004). Structural Design Actions: Earthquake Actions, NZS 1170.5. Wellington, New Zealand.

APPENDIX B

B.1 HDS1 and HDS2 Technical Drawings

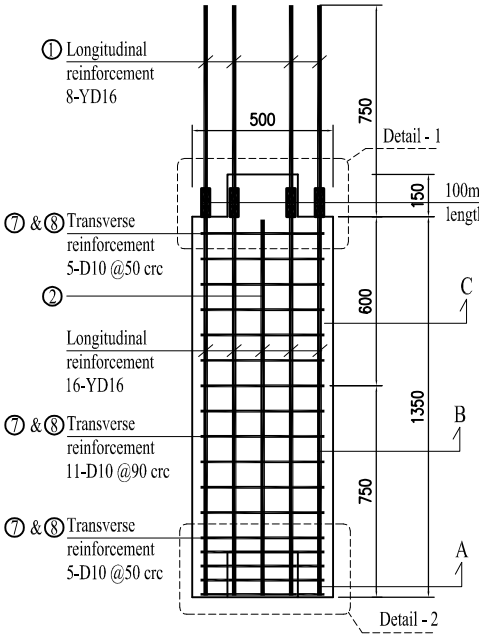

REINFORCMENT DETAILS OF THE BASE SEGMENT

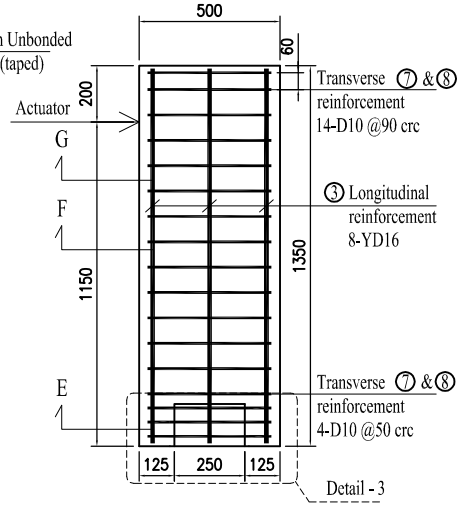

REINFORCMENT DETAILS OF THE TOP SEGMENT

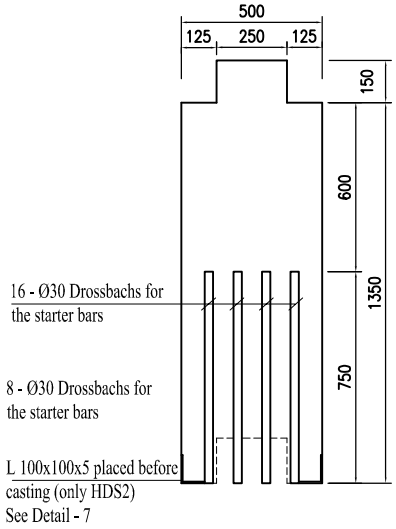

DROSSBACHS DETAIL OF THE BASE SEGMENT

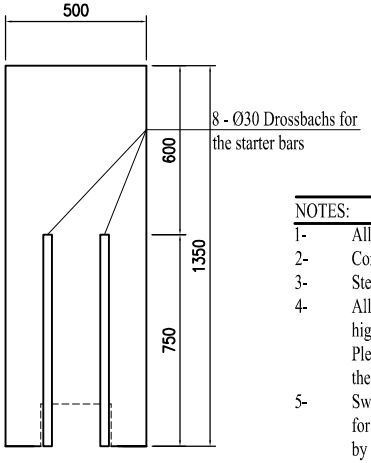

DROSSBACHS DETAIL OF THE TOP SEGMENT

NOTES:

1- All dimensions are in mm.
2- Concrete strength (f'c) is 40 MPa.
3- Steel grade is 500E seismic (fy = 500 MPa).
4- All starter bars are to be grouted inside the drossbachs with high strength mortar and hand pumped.
Please refer to unbonded length in drawings while assembling the segments for the specimen.
5- Swift lift anchors should be provided at appropriate locations for lifting purpose of each segment and the whole specimen by the crane.
6- The actuator will be connected at the cap part of the top column segment later in lab. In order to connect the steel plate on the face of the cap, appropriate anchor bolt should be placed during casting the segment so the steel plate can be attached later in lab.

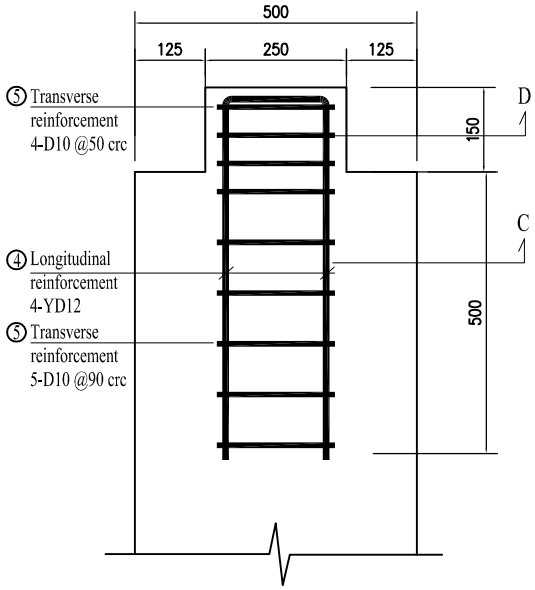

DETAIL - 1

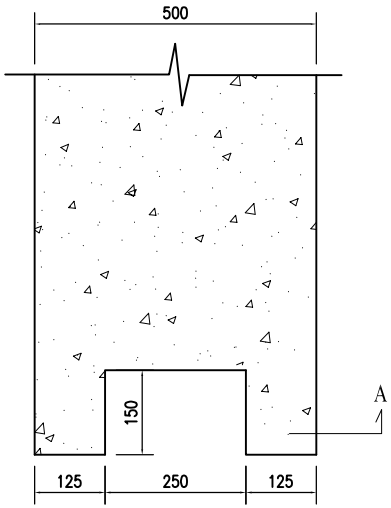

DETAIL - 2

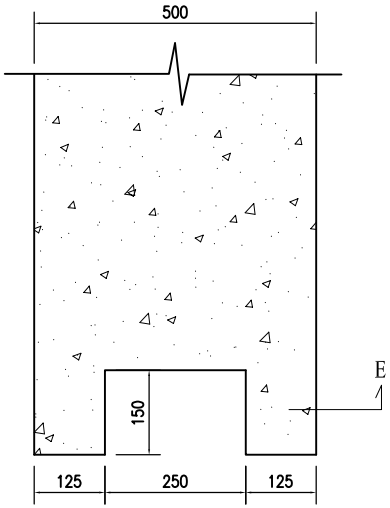

DETAIL - 3

Issue	Date	Description
1	03/09/2012	SPECIMEN NO - 1

UNIVERSITY OF CANTERBURY
Te Whare Wānanga o Waitaha
CHRISTCHURCH NEW ZEALAND

HDS1 and HDS2

Project Title

Advanced Bridge Construction and Design

(Natural Hazard Research Platform)

Drawing Name

PRECAST SQUARE COLUMN

Engineered by : **M.Mashal / S.White** Date : **09/2012**
Drawn by : **Mustafa Mashal** Date : **09/2012**

Drawing Scale 1:20 AT A3

Sheet No:

S-01

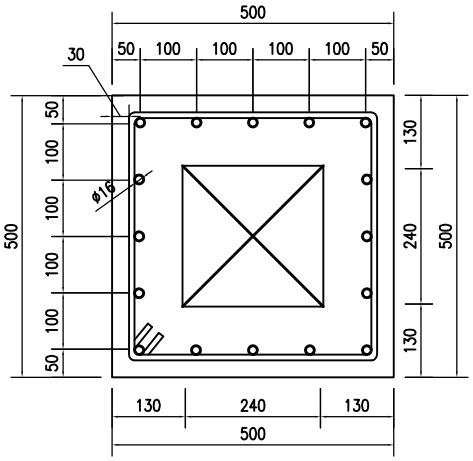

SECTION - A

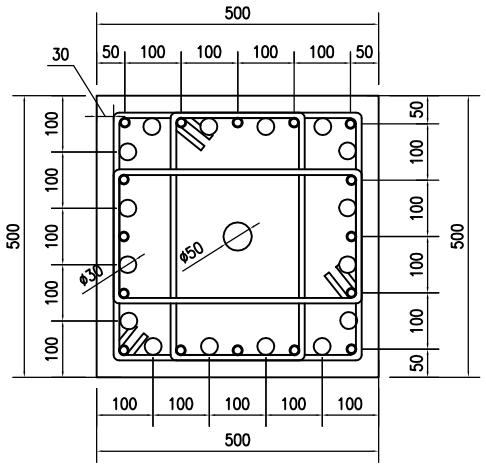

SECTION - B

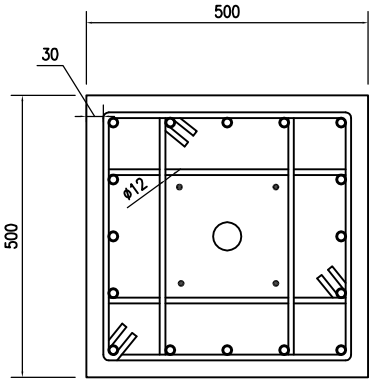

SECTION - C

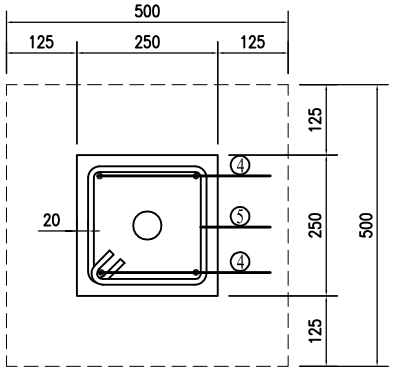

SECTION - D

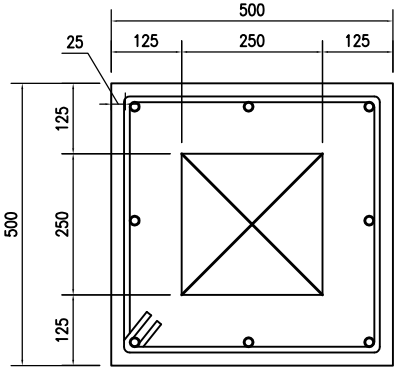

SECTION - E

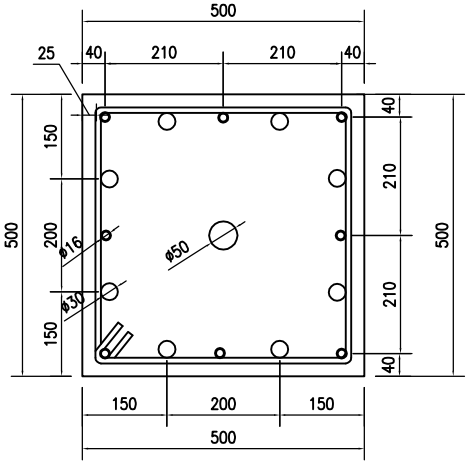

SECTION - F

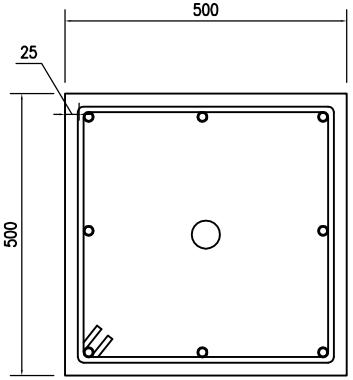

SECTION -G

LEGENDS

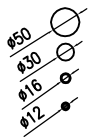

Ø50 drossbach
Ø30 Drossbachs
D16 Longitudinal rebars
D12 Longitudinal rebars

NOTES:

1- All dimensions are in mm.
2- Concrete strength (f'c) is 40 MPa.
3- Steel grade is 500E seismic (fy = 500 MPa).

Issue	Date	Description
1	03/09/2012	SPECIMEN NO - 1

UNIVERSITY OF CANTERBURY
Te Whare Wānanga o Waitaha
CHRISTCHURCH NEW ZEALAND

HDS1 and HDS2

Project Title

Advanced Bridge Construction and Design

(Natural Hazard Research Platform)

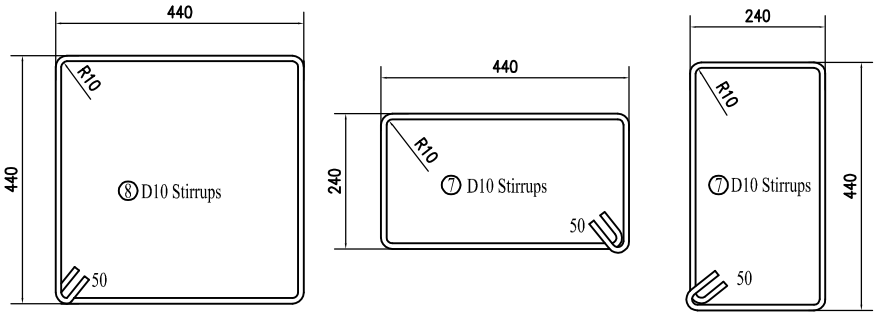

STIRRUPS DETAILS

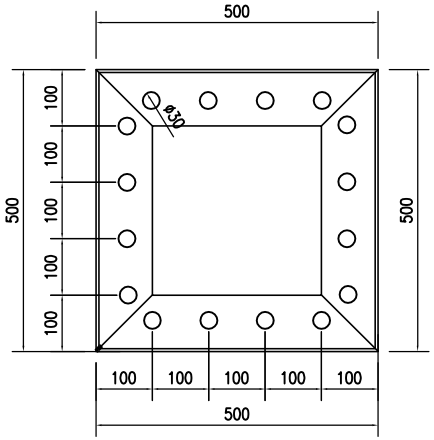

DETAIL - 7: ARMORING SHOE (HDS2 ONLY)

Drawing Name

SQUARE COLUMN SECTIONS

Engineered by : **M.Mashal / S.White** Date : **09/2012**
Drawn by : **Mustafa Mashal** Date : **09/2012**

Drawing Scale 1:10 AT A3

Sheet No:

S-02

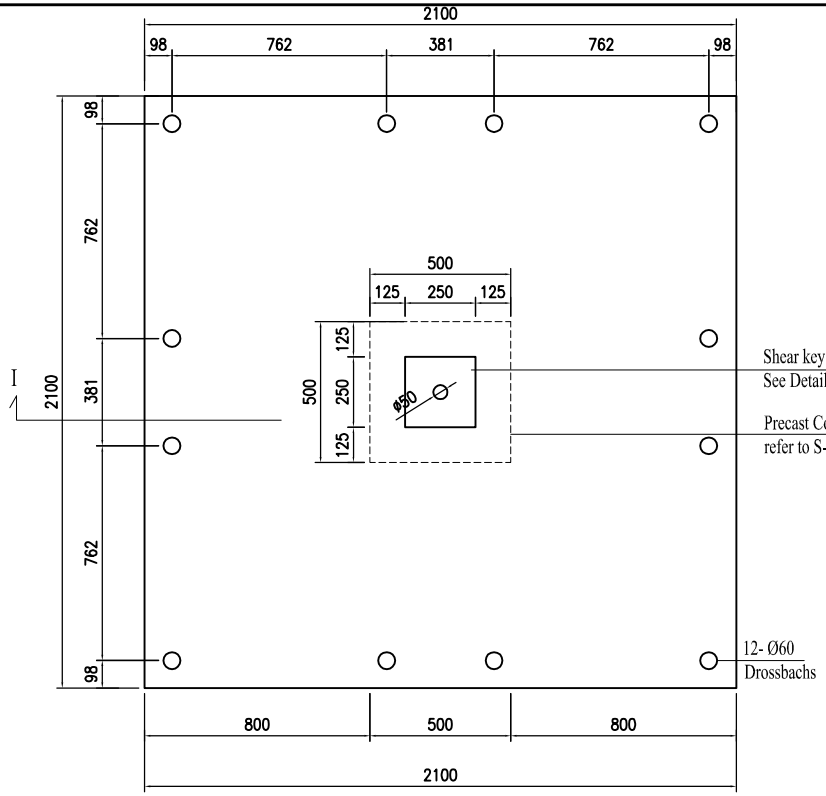

PRECAST FOUNDATION PLAN

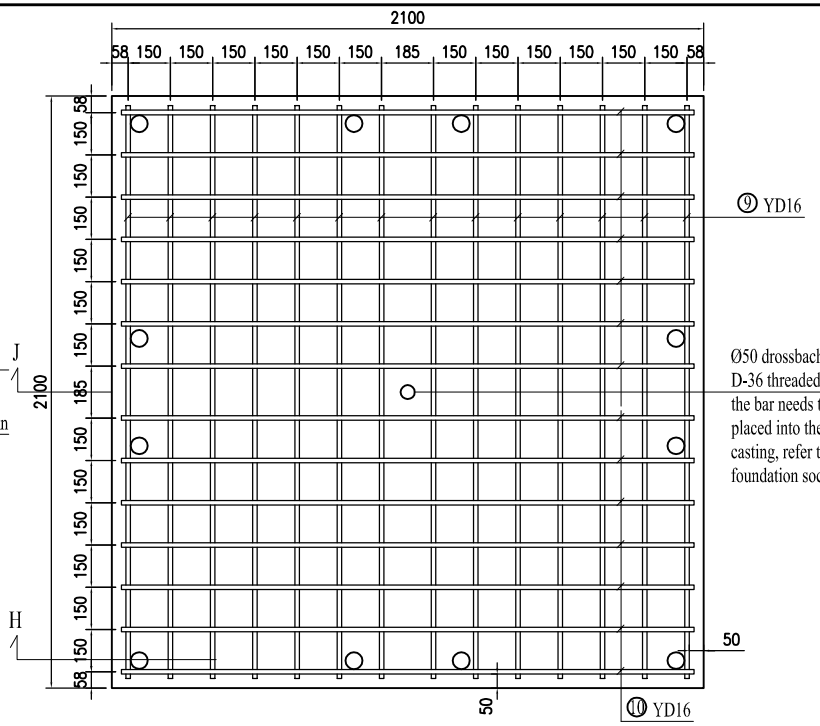

FOUNDATION REINFORCEMENT DETAILS

NOTES:

1- All dimensions are in mm.
2- Concrete strength (f'c) is 40 MPa.
3- Steel grade is 500E seismic (fy = 500 MPa).
4- All starter bars are to be grouted inside the drossbachs with high strength mortar and hand pumped. Please refer to unbonded length in drawings while assembling the segments for the specimen.
5- All reinforcement for the foundation are YD16, please refer to the reinforcement table for the dimensions.

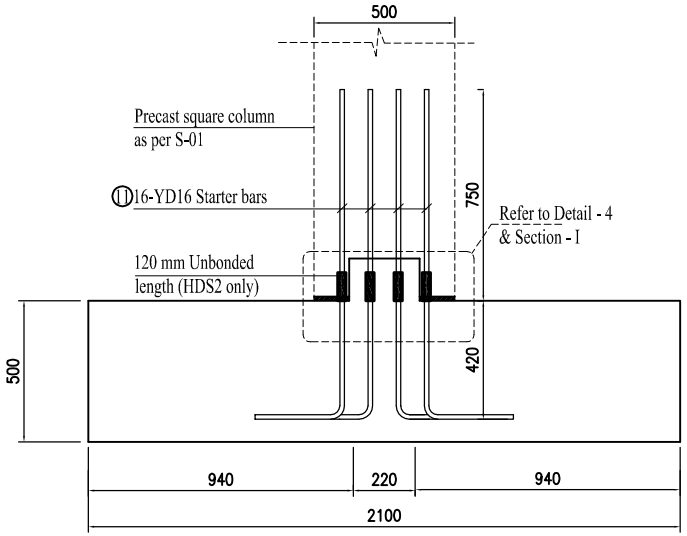

SECTION - I

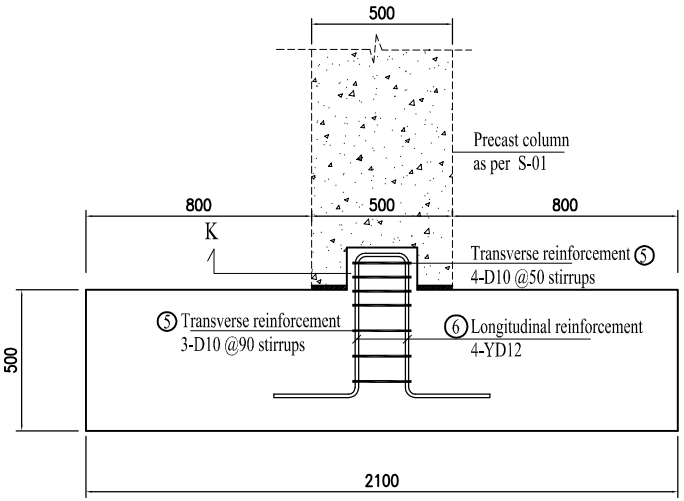

SECTION - J

Issue	Date	Description
1	03/09/2012	SPECIMEN NO - 1

UNIVERSITY OF CANTERBURY
Te Whare Wānanga o Waitaha
CHRISTCHURCH NEW ZEALAND

HDS1 and HDS2

Project Title

Advanced Bridge Construction and Design

(Natural Hazard Research Platform)

Drawing Name

PRECAST FOUNDATION PLANS

Engineered by : **M.Mashal / S.White** Date : **09/2012**
Drawn by : **Mustafa Mashal** Date : **09/2012**

Drawing Scale 1:20 AT A3

Sheet No:

S-03

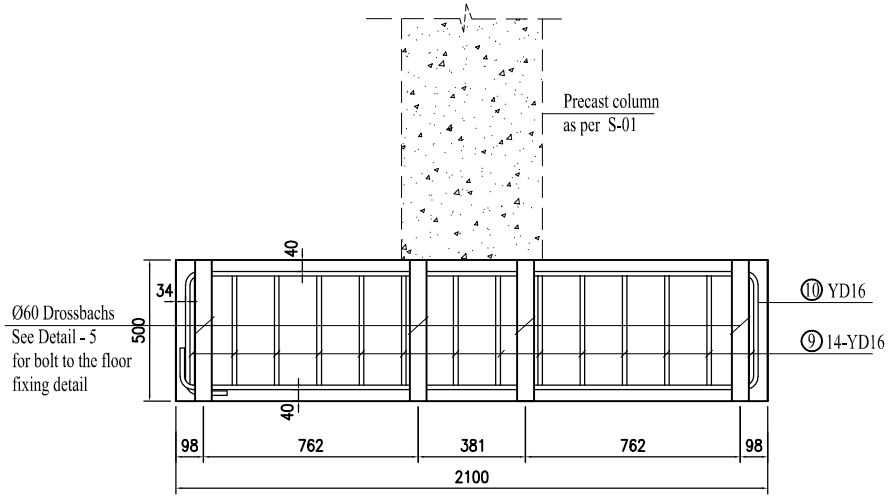

SECTION - H

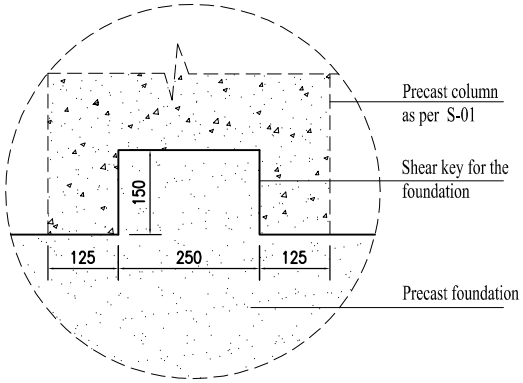

DETAIL - 4 Scale 1:10

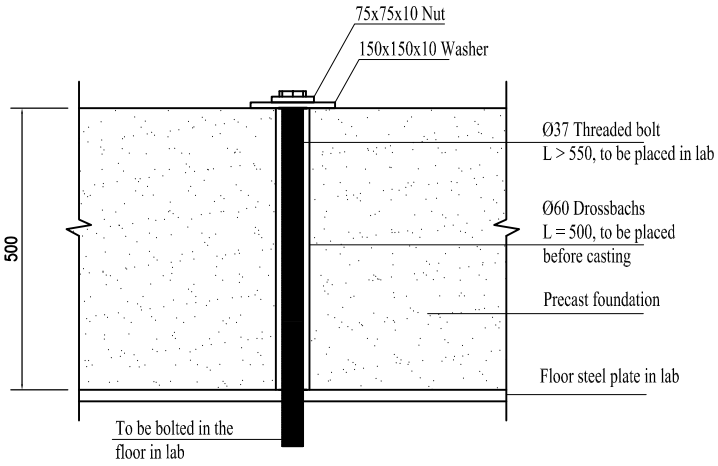

DETAIL - 5 Scale 1:10

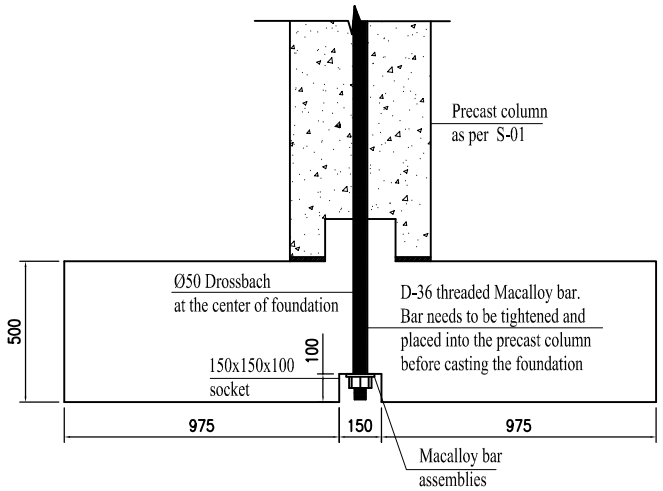

DETAIL - 6

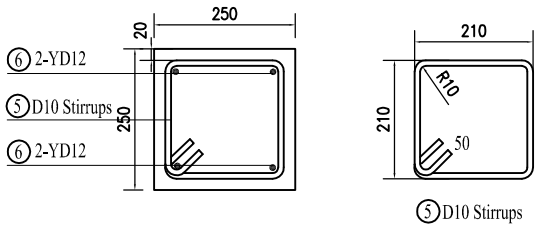

SECTION - K Scale 1:10

NOTES:

1- All dimensions are in mm.
2- Concrete strength (f'c) is 40 MPa.
3- Steel grade is 500E seismic (fy = 500 MPa).
4- All starter bars are to be grouted inside the drossbachs with high strength mortar and hand pumped.
Please refer to unbonded length in drawings while assembling the segments for the specimen.

Issue	Date	Description
3	08/10/2012	SPECIMEN NO - 1

UNIVERSITY OF CANTERBURY
Te Whare Wānanga o Waitaha
CHRISTCHURCH NEW ZEALAND

HDS1 and HDS2

Project Title

Advanced Bridge Construction and Design

(Natural Hazard Research Platform)

Drawing Name

SECTION & DETAILS

Engineered by : **M.Mashal / S.White** Date : **09/2012**
Drawn by : **Mustafa Mashal** Date : **09/2012**

Drawing Scale 1:20 AT A3

Sheet No:
S-04

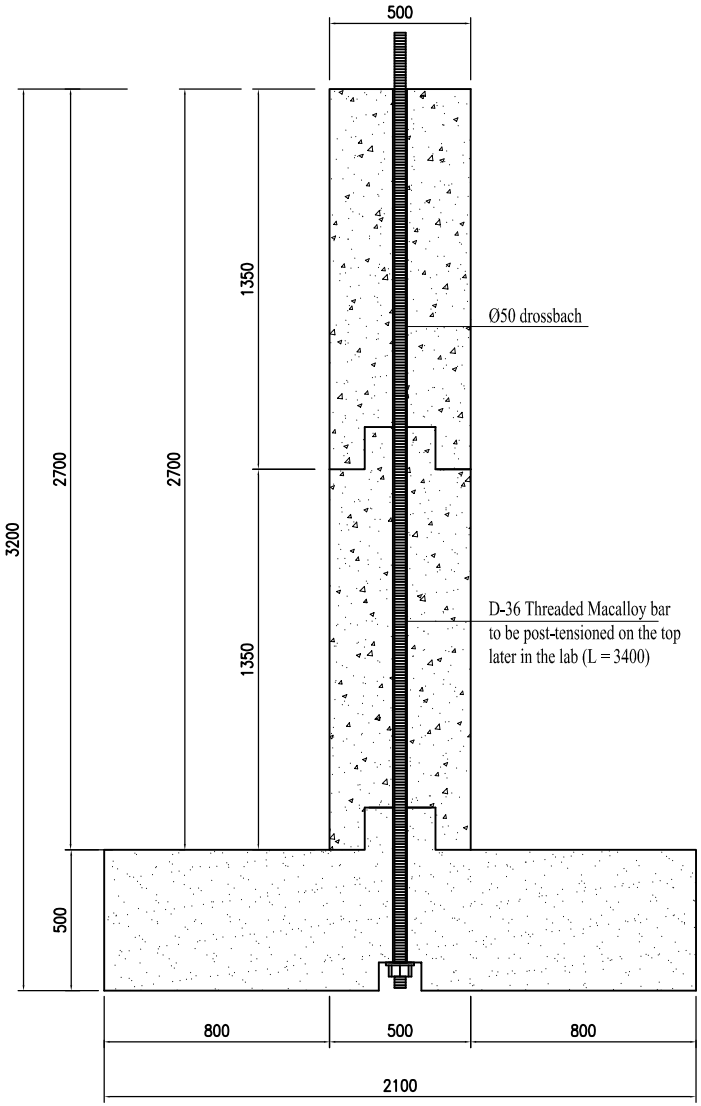

ASSEMBLED SPECIMEN TO BE DELIVERED
(SPECIMEN NO - 1)
QUANTITY NEEDED = 2

GENERAL NOTES:

1- All dimensions are in mm.
2- Concrete strength (f'c) is 40 MPa.
3- Steel grade is 500E seismic (fy = 500 MPa).
4- All starter bars are to be grouted inside the drossbachs with high strength mortar and hand pumped.
Please refer to unbonded length in drawings while assembling the segments for the specimen.
5- In order to have precise measurement of the fomwork for the segments and shear keys, match casting procedure is proposed.
6- The total weight of the specimen with the dimensions shown in these drawings is expected to be 6.91 Tons.
7- For quality control purposes, a minimum of five standard concrete cylinders per specimen are to be taken while casting the elements.
8- Swift lift anchors should be provided at appropriate locations for lifting purpose of each segment and the whole specimen by the crane.

Issue	Date	Description
1	03/09/2012	SPECIMEN NO - 1

UNIVERSITY OF CANTERBURY
Te Whare Wānanga o Waitaha
CHRISTCHURCH NEW ZEALAND

HDS1 and HDS2

Project Title

Advanced Bridge Construction and Design
(Natural Hazard Research Platform)

Drawing Name
ASSEMBLED SPECIMEN

Engineered by : **M.Mashal / S.White** Date : **09/2012**
Drawn by : **Mustafa Mashal** Date : **09/2012**

Drawing Scale 1:20 AT A3

Sheet No:
S-05

NO OF REBAR	DIAMETER	QUANTITY	DIMENSIONS	LENGTH	TOTAL LENGTH	TYPE
①	Ø16	8	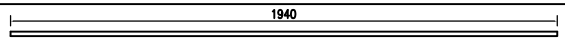	1940	15520	DEFORMED
②	Ø16	8	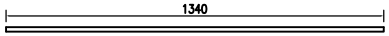	1340	10720	DEFORMED
③	Ø16	8	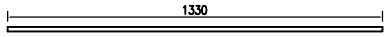	1330	10640	DEFORMED
④	Ø12	2	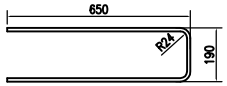	1460	2920	DEFORMED
⑤	Ø10	18		925	16650	PLAIN
⑪	Ø12	2	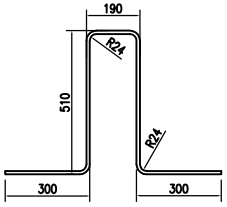	1640	3280	DEFORMED
⑦	Ø10	70	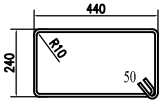	1470	102900	PLAIN
⑧	Ø10	36	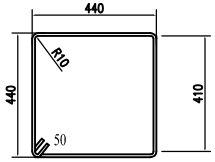	1900	68400	PLAIN
⑨	Ø16	14	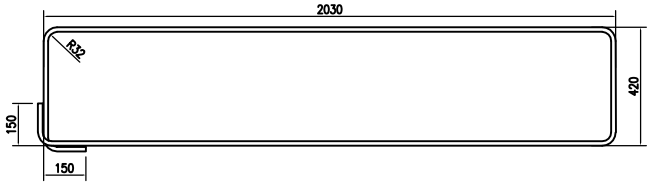	5120	71680	DEFORMED
⑩	Ø16	14	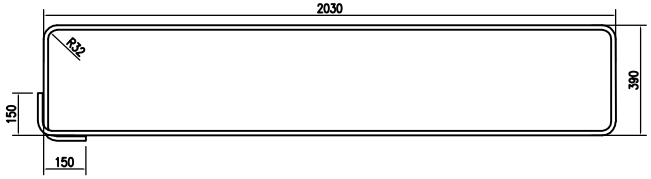	5060	70840	DEFORMED
⑪	Ø16	16	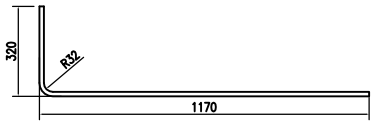	1470	23520	DEFORMED

SUMMARY CHART OF ANGLES FOR TWO SQUARE SPECIMENS

DETAIL	SECTION	QUANTITY	LENGTH (mm)
7	L 100x100x5	2	4000
8	L 100x100x5	2	4000
			TOTAL = 8000

SUMMARY CHART OF REINFORCEMENT FOR TWO SPECIMENS

DIAMETER	TOTAL LENGTH	TYPE
Ø10	375900	PLAIN
Ø12	12400	DEFORMED
Ø16	405840	DEFORMED

SUMMARY CHART OF CONCRETE FOR TWO SPECIMENS

ELEMENT	VOLUME (m^3)
FOUNDATION	4.43
COLUMN	1.33
TOTAL	5.76

SUMMARY CHART OF DROSSBACHS FOR TWO SPECIMENS

DIAMETER	TOTAL LENGTH
Ø30	36000
Ø50	6400
Ø60	12000

SPECIFIC NOTES:

1- All dimensions are in mm.
2- Concrete strength (f'c) is 40 MPa.
3- Steel grade is 500E seismic (fy = 500 MPa). All bars shown are deformed unless specified in the tables.
4- The summary charts show the amount of materials needed for both specimens with circular section.
5- Formwork, tying wire, spacer and amount of high strength mortar are not included in this bill of quantity.
6- For quality control purposes, a minimum of five standard concrete cylinders per specimen are to be taken while casting the elements.
7- A minimum length of 2000mm of reinforcement for the all three diameters shown in the table shall be added with the total amount. This will be used for testing of the bars in the lab to verify the strength.

Issue	Date	Description
1	03/09/2012	SPECIMEN NO - 1

UNIVERSITY OF CANTERBURY
Te Whare Wānanga o Waitaha
CHRISTCHURCH NEW ZEALAND

HDS1 and HDS2

Project Title

Advanced Bridge Construction and Design

(Natural Hazard Research Platform)

Drawing Name

BILL OF QUANTITY

Engineered by : **M.Mashal / S.White** Date : **09/2012**
Drawn by : **Mustafa Mashal** Date : **09/2012**

Drawing Scale 1:20 AT A3

Sheet No:

S-06

B.2 HDC1 and HDC2 Technical Drawings

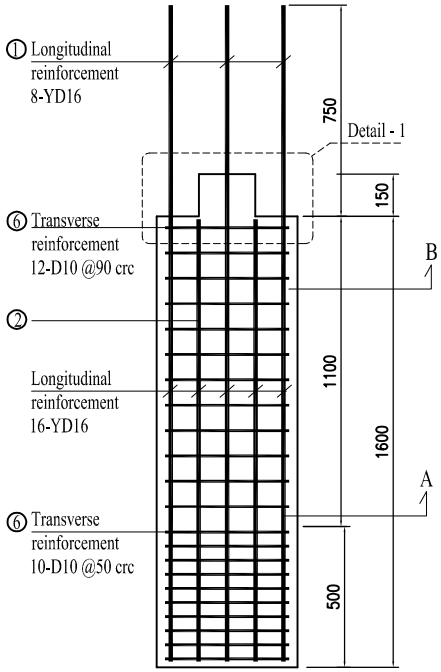

REINFORCMENT DETAILS OF THE BASE SEGMENT

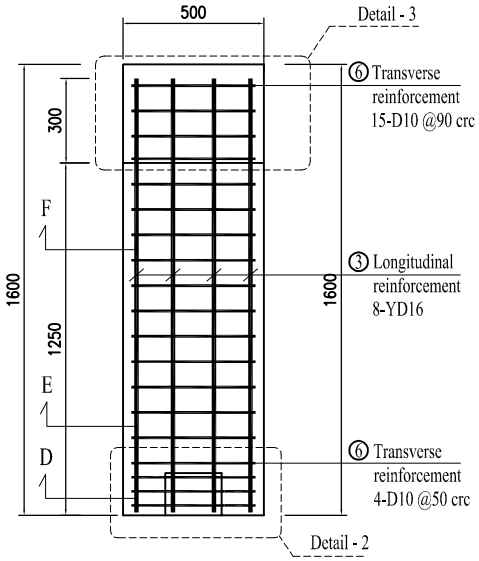

REINFORCMENT DETAILS OF THE TOP SEGMENT

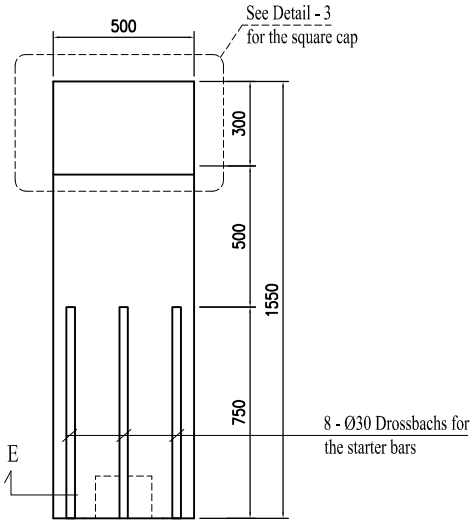

DROSSBACHS DETAIL OF THE TOP SEGMENT

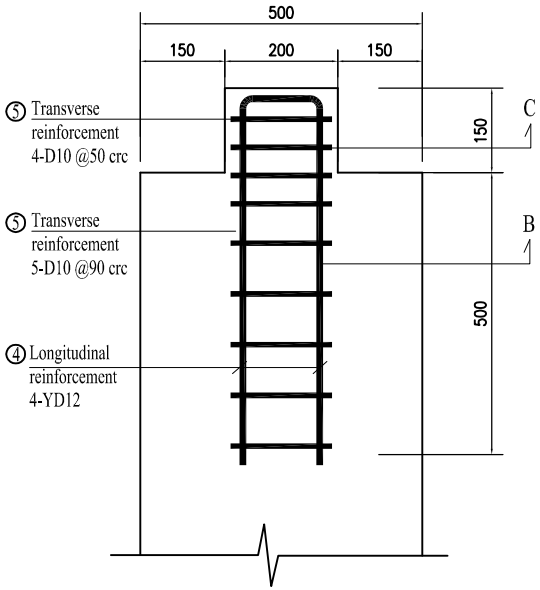

DETAIL - 1

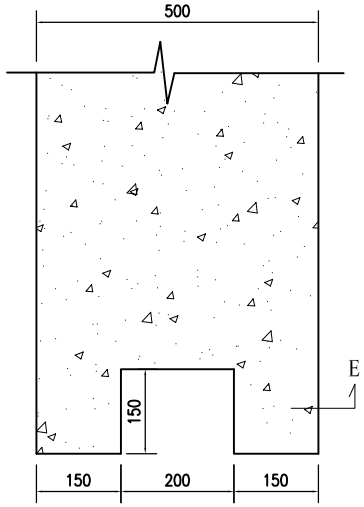

DETAIL - 2

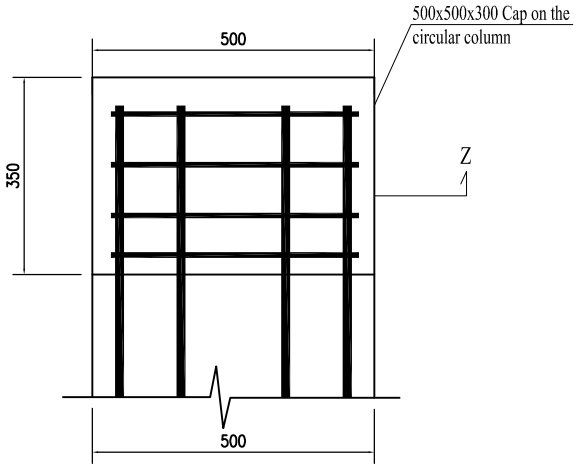

DETAIL - 3

NOTES:

1- All dimensions are in mm.
2- Concrete strength (f'c) is 40 MPa.
3- Steel grade is 500E seismic (fy = 500 MPa).
4- All starter bars are to be grouted inside the drossbachs with high strength mortar and hand pumped.
5- Swift lift anchors should be provided at appropriate locations for lifting purpose of each segment and the whole specimen by the crane.
6- The actuator will be connected at the cap part of the top column segment later in lab. In order to connect the steel plate on the face of the cap, appropriate anchor bolt should be placed during casting the segment so the steel plate can be attached later in lab.

Issue	Date	Description
1	03/09/2012	SPECIMEN NO - 2

UNIVERSITY OF CANTERBURY
Te Whare Wānanga o Waitaha
CHRISTCHURCH NEW ZEALAND

HDC1 and HDC2

Project Title

Advanced Bridge Construction and Design

(Natural Hazard Research Platform)

Drawing Name

PRECAST CIRCULAR COLUMN

Engineered by : **M.Mashal / S.White** Date : **09/2012**
Drawn by : **Mustafa Mashal** Date : **09/2012**

Drawing Scale 1:20 AT A3

Sheet No:

S-01

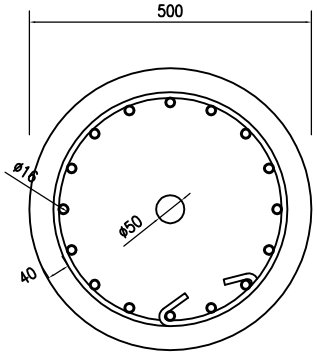

SECTION - A

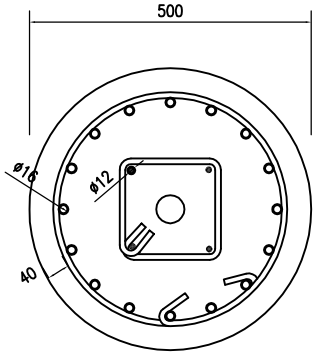

SECTION - B

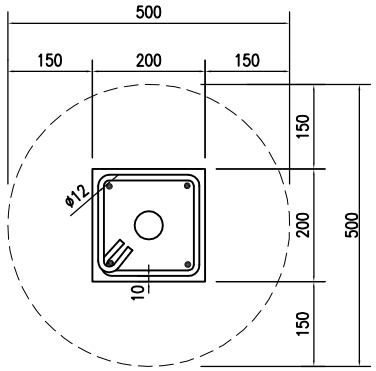

SECTION -C

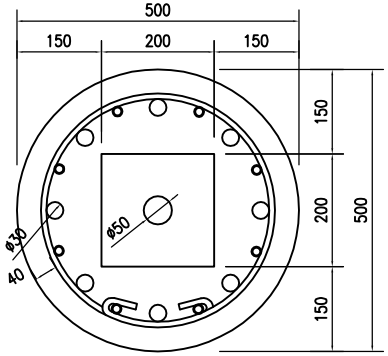

SECTION -D

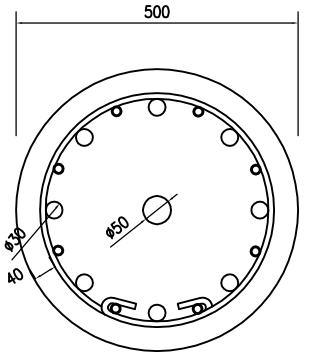

SECTION -E

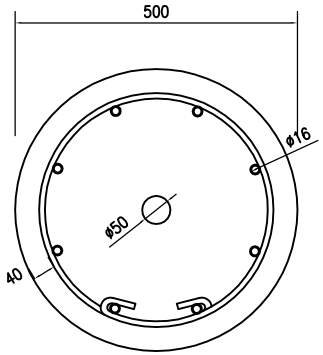

SECTION -F

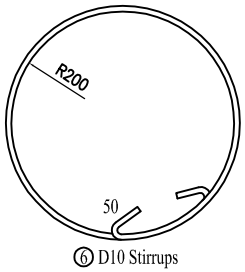

⑥ D10 Stirrups

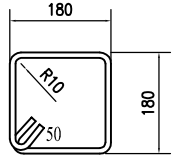

⑤ D10 Stirrups

STIRRUPS DETAILS

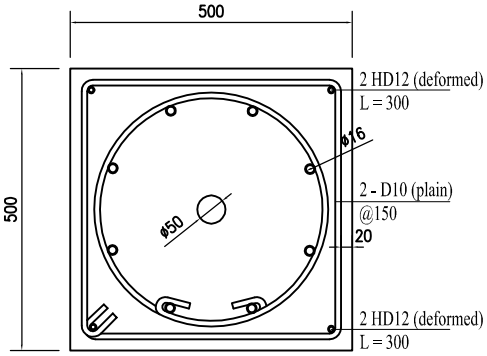

SECTION -Z

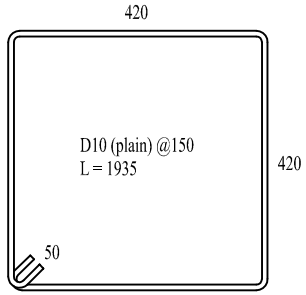

SPECIFIC NOTES:

1- All dimensions are in mm.
2- Concrete strength (f'c) is 40 MPa.
3- Steel grade is 500E seismic (fy = 500 MPa).
4- Slight change of 50mm for the top segment is detailed as shown.
5- Some extra reinforcement will be added to the bill of quantity for the materials as shown.

Issue	Date	Description
2	18/09/2012	SPECIMEN NO - 2

UNIVERSITY OF CANTERBURY
Te Whare Wānanga o Waitaha
CHRISTCHURCH NEW ZEALAND

HDC1 and HDC2

Project Title

Advanced Bridge Construction and Design

(Natural Hazard Research Platform)

Drawing Name

CIRCULAR COLUMN SECTIONS

Engineered by : **M.Mashal / S.White** Date : **09/2012**
Drawn by : **Mustafa Mashal** Date : **09/2012**

Drawing Scale 1:10 AT A3

Sheet No:

S-02

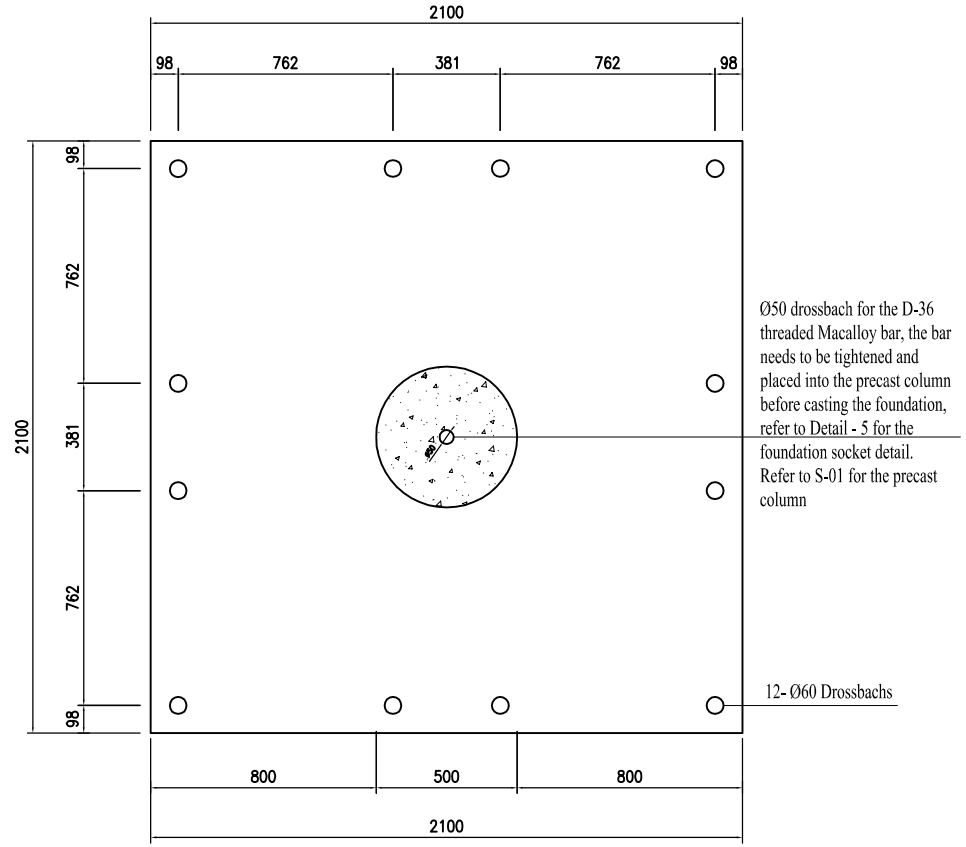

FOUNDATION PLAN

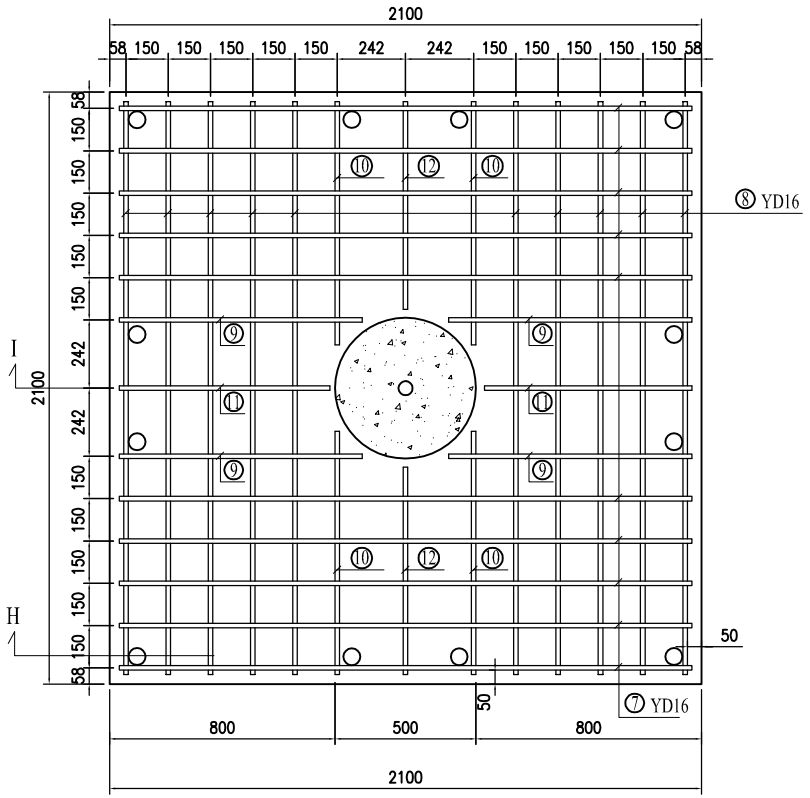

FOUNDATION REINFORCEMENT DETAILS

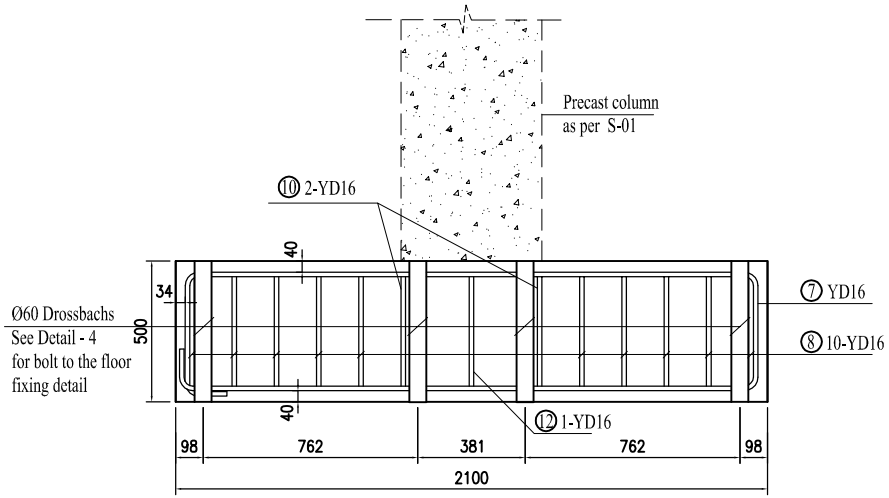

SECTION - H

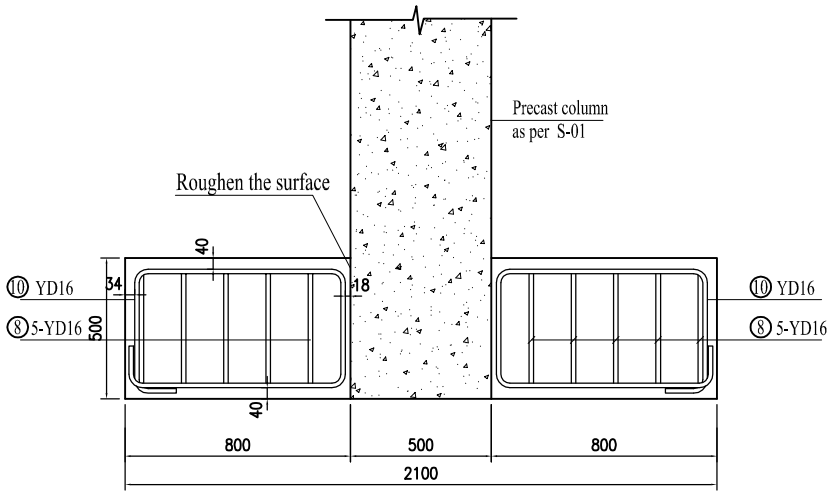

SECTION - I

NOTES:

1- All dimensions are in mm.
2- Concrete strength (f'c) is 40 MPa.
3- Steel grade is 500E seismic (fy = 500 MPa).
4- All starter bars are to be grouted inside the drossbachs with high strength mortar and hand pumped.
5- All reinforcement for the foundation are YD16, please refer to the reinforcement table for the dimensions.

Issue	Date	Description
1	03/09/2012	SPECIMEN NO - 2

UNIVERSITY OF CANTERBURY
Te Whare Wānanga o Waitaha
CHRISTCHURCH NEW ZEALAND

HDC1 and HDC2

Project Title

Advanced Bridge Construction and Design

(Natural Hazard Research Platform)

Drawing Name

FOUNDATION PLANS

Engineered by : **M.Mashal / S.White** Date : **09/2012**
Drawn by : **Mustafa Mashal** Date : **09/2012**

Drawing Scale 1:20 AT A3

Sheet No:

S-03

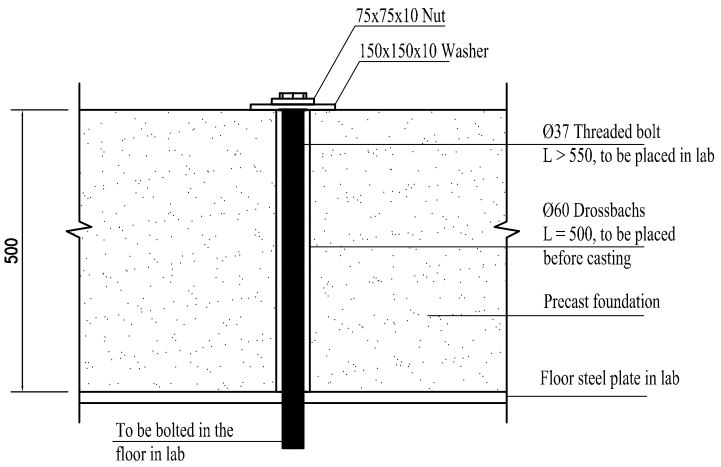

DETAIL - 4 Scale 1:10

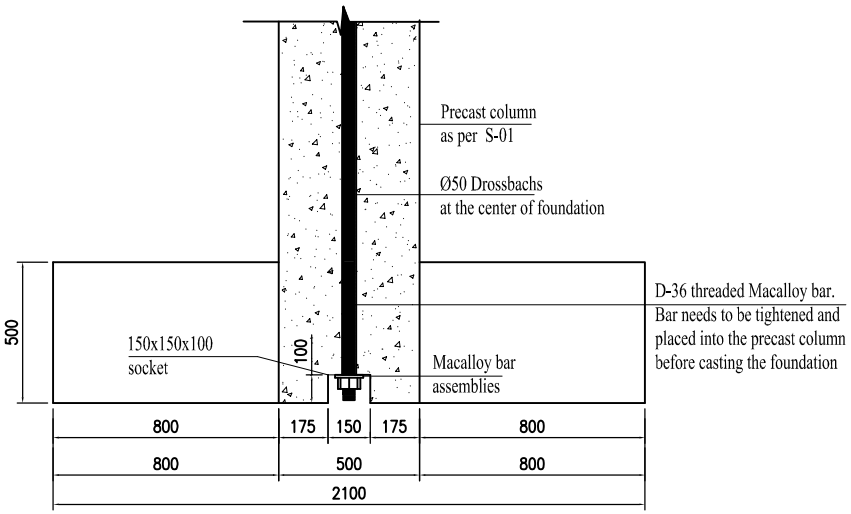

DETAIL - 5

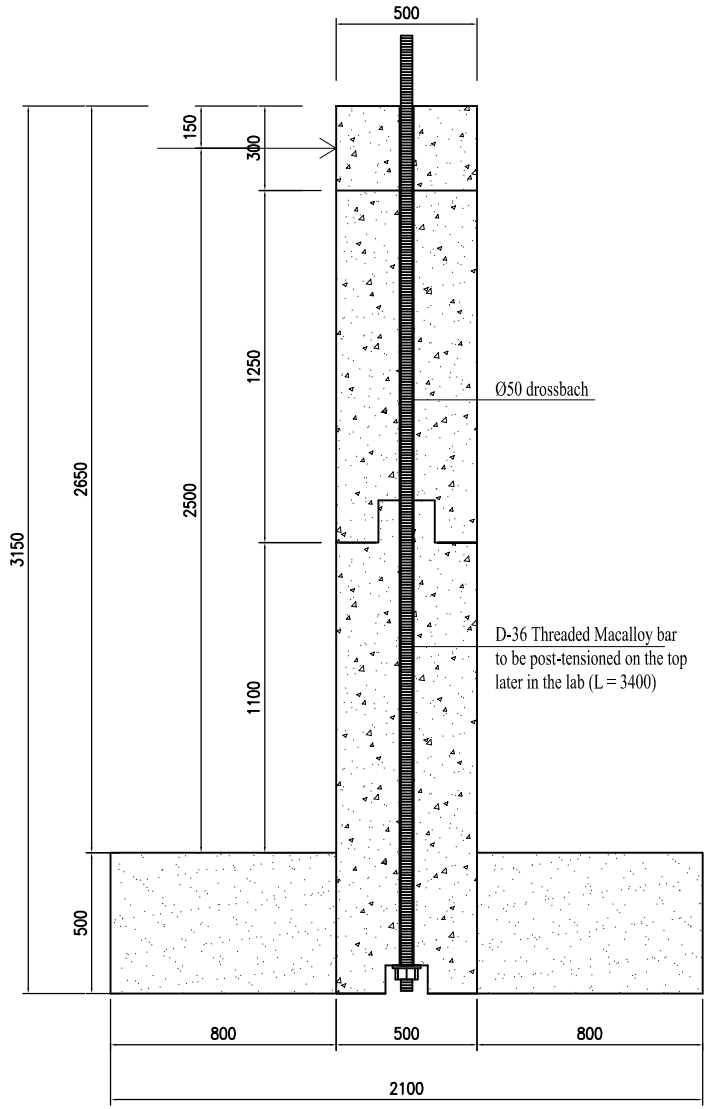

ASSEMBLED SPECIMEN TO BE DELIVERED
(SPECIMEN NO - 2)
QUANTITY NEEDED = 2

GENERAL NOTES:

1- All dimensions are in mm.
2- Concrete strength (f'c) is 40 MPa.
3- Steel grade is 500E seismic (fy = 500 MPa).
4- All starter bars are to be grouted inside the drossbachs with high strength mortar and hand pumped.
5- In order to have precise measurement of the fomwork for the segments and shear keys, match casting procedure is proposed.
6- The total weight of the specimen with the dimensions shown in these drawings is expected to be 6.5 Tons.
7- For quality control purposes, a minimum of five standard concrete cylinders per specimen are to be taken while casting the elements.
8- Swift lift anchors should be provided at appropriate locations for lifting purpose of each segment and the whole specimen by the crane.

Issue	Date	Description
1	03/09/2012	SPECIMEN NO - 2

UNIVERSITY OF CANTERBURY
Te Whare Wānanga o Waitaha
CHRISTCHURCH NEW ZEALAND

HDC1 and HDC2

Project Title

Advanced Bridge Construction and Design

(Natural Hazard Research Platform)

Drawing Name

DETAILS & ASSEMBLED SPECIMEN

Engineered by : **M.Mashal / S.White** Date : **09/2012**
Drawn by : **Mustafa Mashal** Date : **09/2012**

Drawing Scale 1:20 AT A3

Sheet No:

S-04

NO OF REBAR	DIAMETER	QUANTITY	DIMENSIONS	LENGTH	TOTAL LENGTH	TYPE
①	Ø16	8	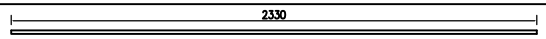	2330	18640	DEFORMED
②	Ø16	8	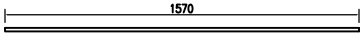	1570	12560	DEFORMED
③	Ø16	8	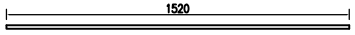	1520	12160	DEFORMED
④	Ø12	2	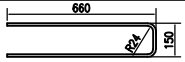	1440	2880	DEFORMED
⑤	Ø10	10		715	7150	PLAIN
⑥	Ø10	44		1530	67320	PLAIN
⑦	Ø16	10	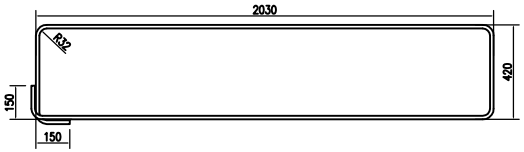	5120	51200	DEFORMED
⑧	Ø16	10	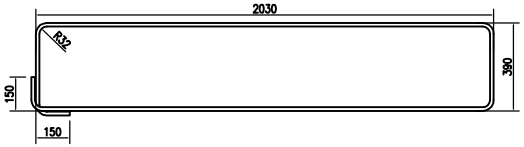	5060	50600	DEFORMED
⑨	Ø16	4	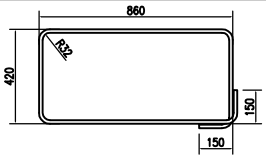	2750	11000	DEFORMED
⑩	Ø16	4	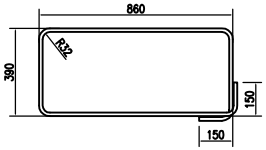	2690	10760	DEFORMED
⑪	Ø16	2	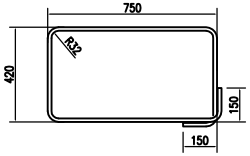	2530	5060	DEFORMED
⑫	Ø16	2	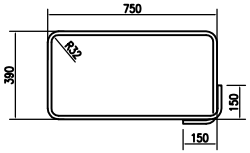	2470	4940	DEFORMED

SUMMARY CHART OF REINFORCEMENT FOR TWO SPECIMENS

DIAMETER	TOTAL LENGTH	TYPE
Ø10	148940	PLAIN
Ø12	5760	DEFORMED
Ø16	353840	DEFORMED

SUMMARY CHART OF CONCRETE FOR TWO SPECIMENS

ELEMENT	VOLUME (m^3)
FOUNDATION	4.21
COLUMN	1.21
TOTAL	5.42

SUMMARY CHART OF DROSSBACHS FOR TWO SPECIMENS

DIAMETER	TOTAL LENGTH
Ø30	12000
Ø50	6340
Ø60	12000

SUMMARY CHART OF REINFORCEMENTS FOR THE SQUARE CAPS (DETAIL-3)

DIAMETER	TOTAL LENGTH	TYPE
Ø10	7740	PLAIN
Ø12	2400	DEFORMED

SPECIFIC NOTES:

1- All dimensions are in mm.
2- Concrete strength (f'c) is 40 MPa.
3- Steel grade is 500E seismic (fy = 500 MPa). All bars shown are deformed unless specified in the tables.
4- The summary charts show the amount of materials needed for both specimens with circular section.
5- Formwork, tying wire, spacer and amount of high strength mortar are not included in this bill of quantity.
6- For quality control purposes, a minimum of five standard concrete cylinders per specimen are to be taken while casting the elements.
7- A minimum length of 2000mm of reinforcement for the all three diameters shown in the table shall be added with the total amount. This will be used for testing of the bars in the lab to verify the strength.

Issue	Date	Description
1	03/09/2012	SPECIMEN NO - 2

UNIVERSITY OF CANTERBURY
Te Whare Wānanga o Waitaha
CHRISTCHURCH NEW ZEALAND

HDC1 and HDC2

Project Title

Advanced Bridge Construction and Design

(Natural Hazard Research Platform)

Drawing Name

BILL OF QUANTITY

Engineered by : **M.Mashal / S.White** Date : **09/2012**
Drawn by : **Mustafa Mashal** Date : **09/2012**

Drawing Scale 1:20 AT A3

Sheet No:
S-05

APPENDIX C

C.1 HDB and LDB Technical Drawings

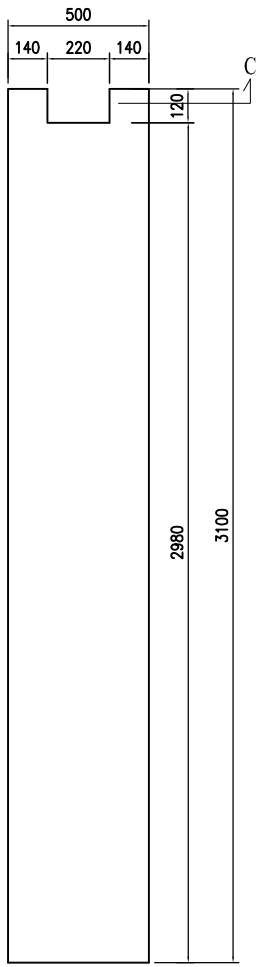

COLUMN 1: ELEVATION VIEW

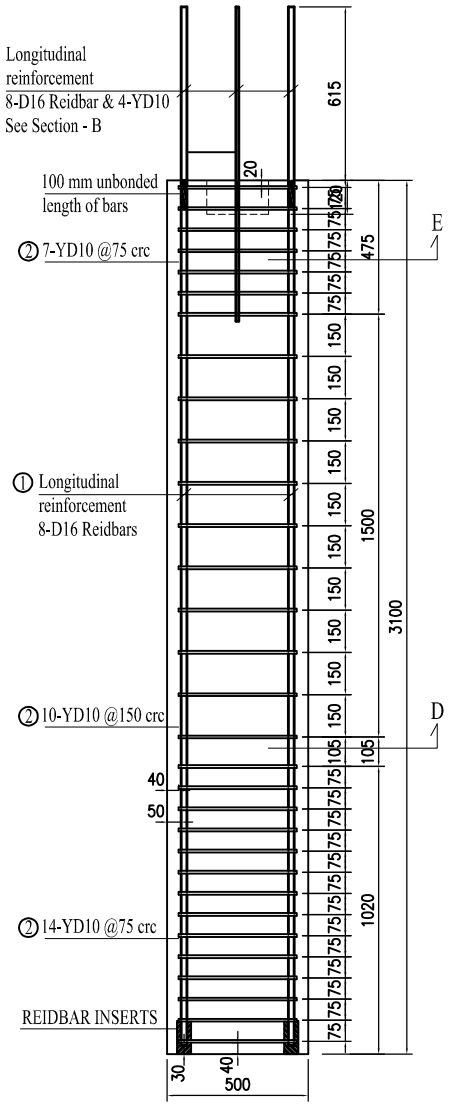

COLUMN 1: REINFORCMENT DETAILS

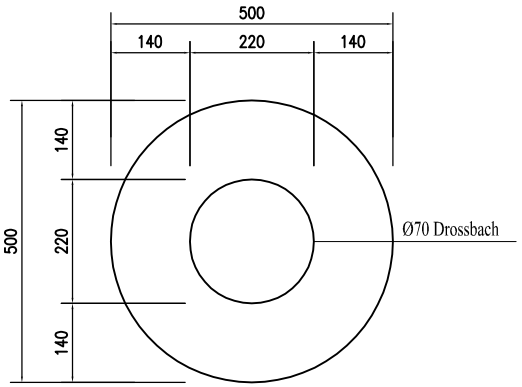

SECTION - C

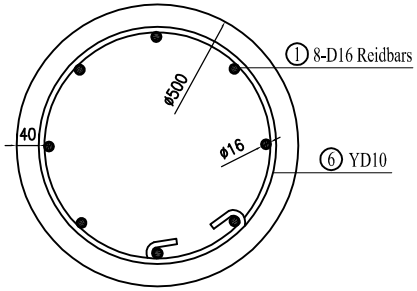

SECTION -D

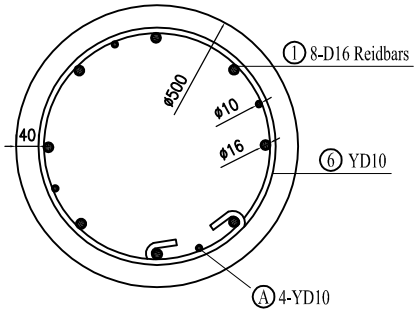

SECTION - E

NOTES:

1- All dimensions are in mm.
2- Concrete strength (f'c) is 40 MPa.
3- All drossbachs are corrugated steel ducts and must be tighten to the reinforcement bars before casting the cap beam.
4- Swift lift anchors should be provided at appropriate locations for lifting of each element.

Issue	Date	Description
3	22/05/2013	Phase II Specimens

UNIVERSITY OF CANTERBURY
Te Whare Wānanga o Waitaha
CHRISTCHURCH NEW ZEALAND

High Damage Bent Columns

Project Title

Advanced Bridge Construction and Design

(Natural Hazard Research Platform)

Drawing Name

COLUMN 1 SECTIONS & DETAILS

Engineered by : **Mustafa Mashal** Date : **05/2013**
Drawn by : **Mustafa Mashal** Date : **05/2013**

Drawing Scale 1:20 AT A3

Sheet No:
S-01

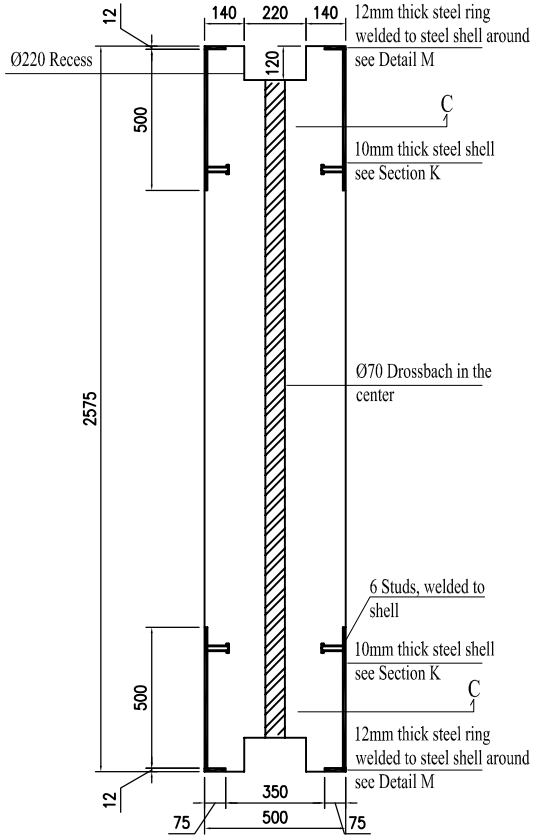

COLUMN 2: Elevation View/Armoring

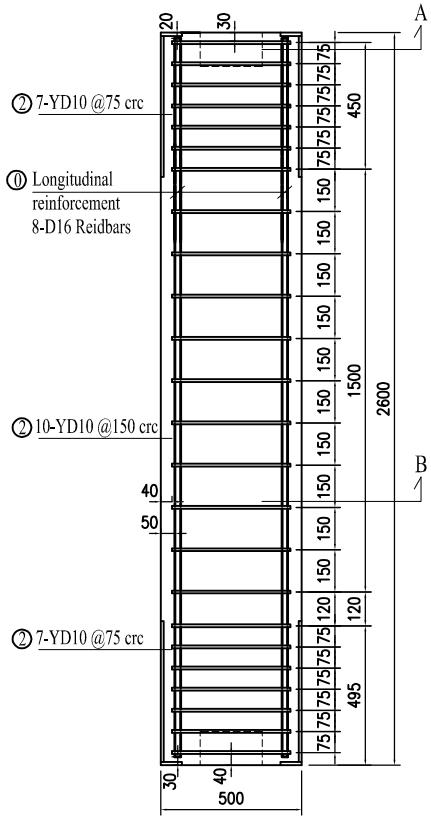

COLUMN 2: REINFORCMENT DETAILS

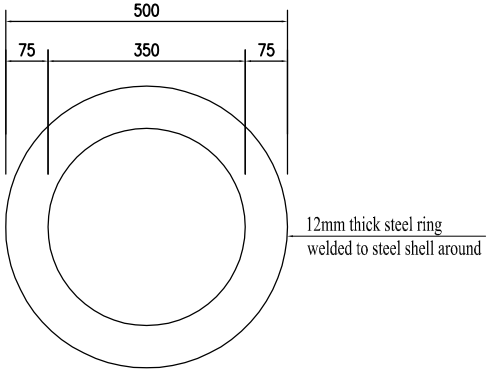

DETAIL M

BILL OF QUANTITY

Element	Quantity
Steel Shell	4
Base Plate Ring	4

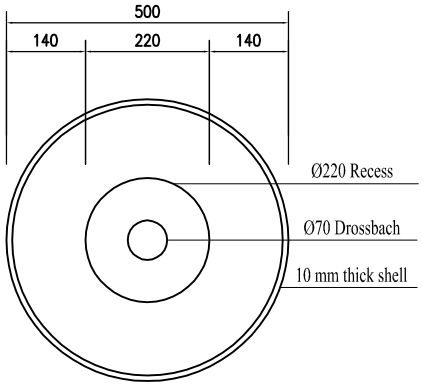

SECTION - A

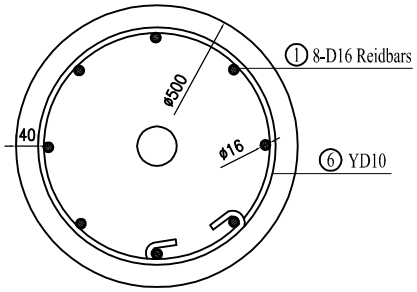

SECTION -B

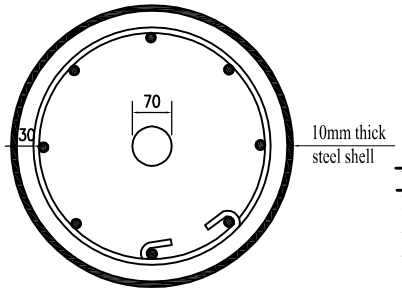

SECTION - C

NOTES:

1- All dimensions are in mm.
2- Concrete strength (f'c) is 40 MPa.
3- All drossbachs are corrugated steel ducts and must be tighten to the reinforcement bars before casting the cap beam.
4- Swift lift anchors should be provided at appropriate locations for lifting of each element.

Issue	Date	Description
3	22/05/2013	Phase II Specimens

UNIVERSITY OF CANTERBURY
Te Whare Wānanga o Waitaha
CHRISTCHURCH NEW ZEALAND

Low Damage Bent Columns

Project Title

Advanced Bridge Construction and Design
(Natural Hazard Research Platform)

Drawing Name
COLUMN 2 SECTIONS & DETAILS

Engineered by : **Mustafa Mashal** Date : **05/2013**
Drawn by : **Mustafa Mashal** Date : **05/2013**

Drawing Scale 1:20 AT A3

Sheet No:
S-02

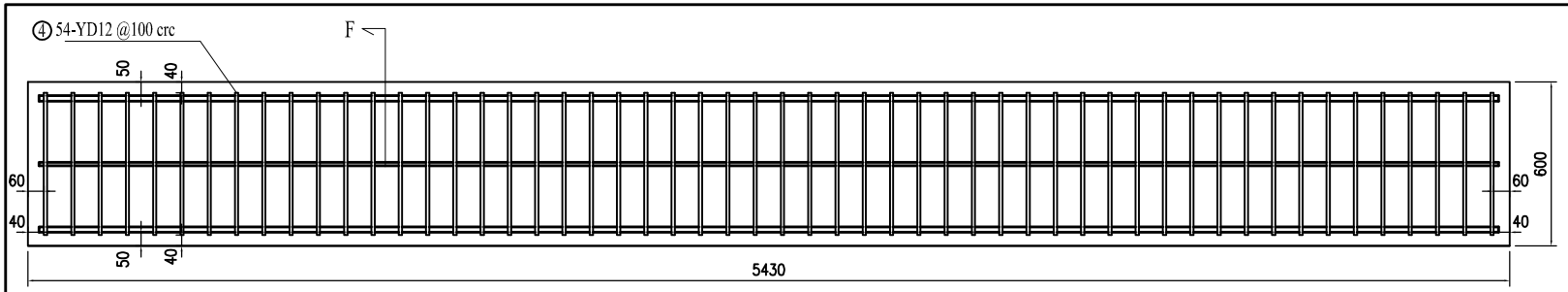

CAP BEAM: REINFORCMENT DETAILS

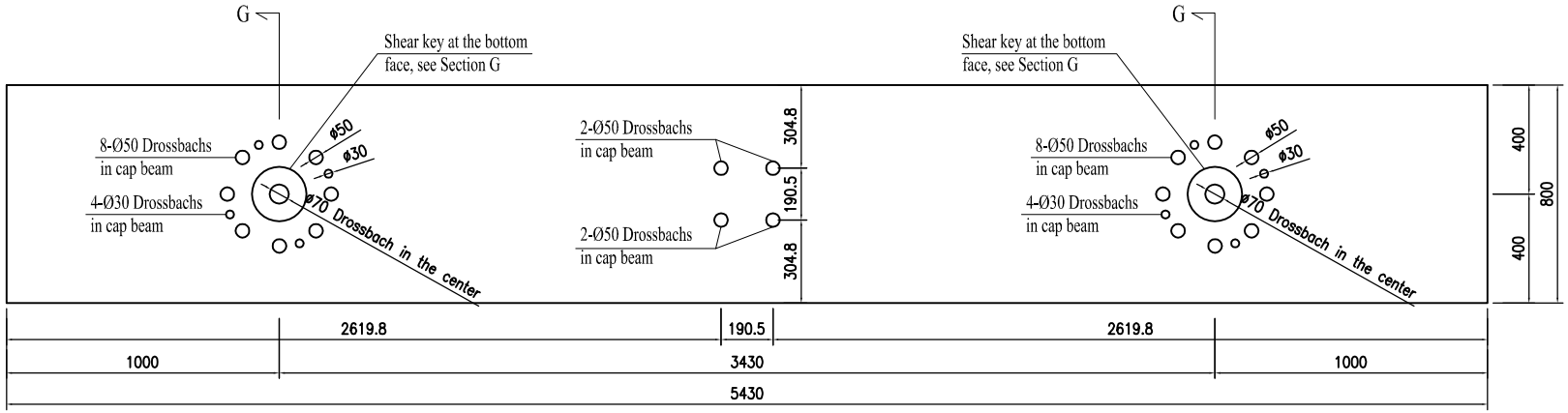

CAP BEAM: PLAN VIEW

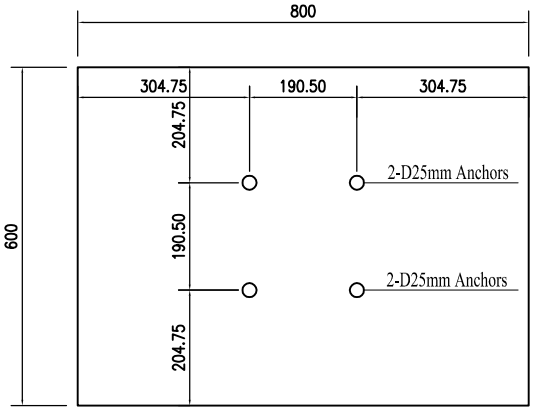

DETAIL - H: CAP BEAM FACE ANCHORS DETAIL
ONE FACE ONLY

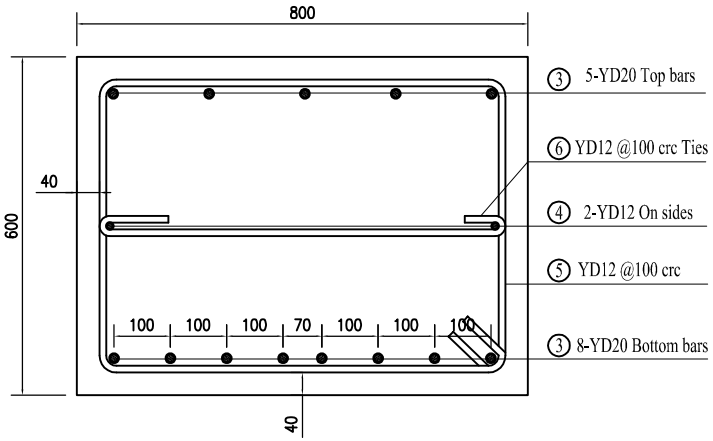

SECTION - F

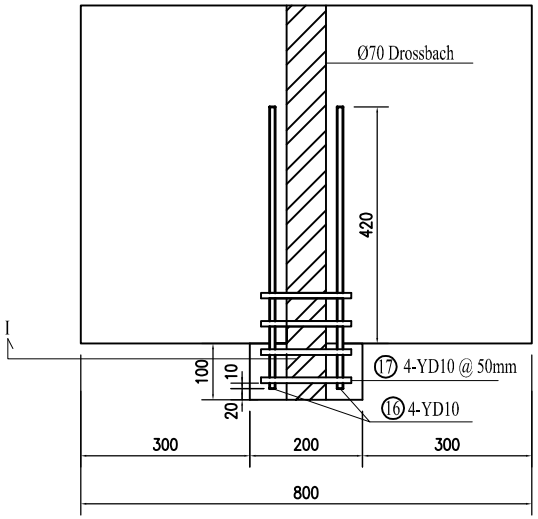

SECTION -G

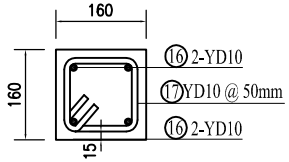

SECTION - I: SHEAR KEY DETAILS

NOTES:

1- All dimensions are in mm.
2- Concrete strength (f'c) is 40 MPa.
3- All drossbachs are corrugated steel ducts and must be tighten to the reinforcement bars before casting the cap beam.
4- Swift lift anchors should be provided at appropriate locations for lifting of each element.
5- Refer to Detail - H for cap beam anchor details on one face.

Issue	Date	Description
3	22/05/2013	Phase II Specimens

UNIVERSITY OF CANTERBURY
Te Whare Wānanga o Waitaha
CHRISTCHURCH NEW ZEALAND

High Damage Bent Cap Beam

Project Title

Advanced Bridge Construction and Design
(Natural Hazard Research Platform)

Drawing Name
CAP BEAM SECTIONS & DETAILS

Engineered by : **Mustafa Mashal** Date : **05/2013**
Drawn by : **Mustafa Mashal** Date : **05/2013**

Drawing Scale 1:20 AT A3

Sheet No:
S-03

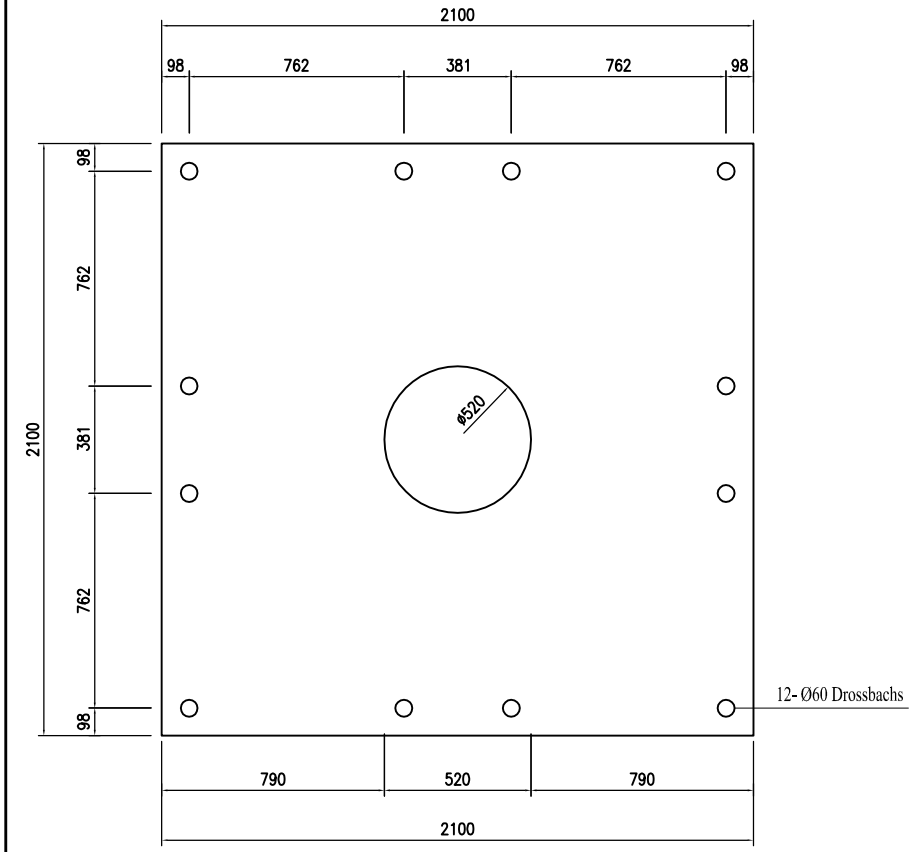

FOUNDATION PLAN

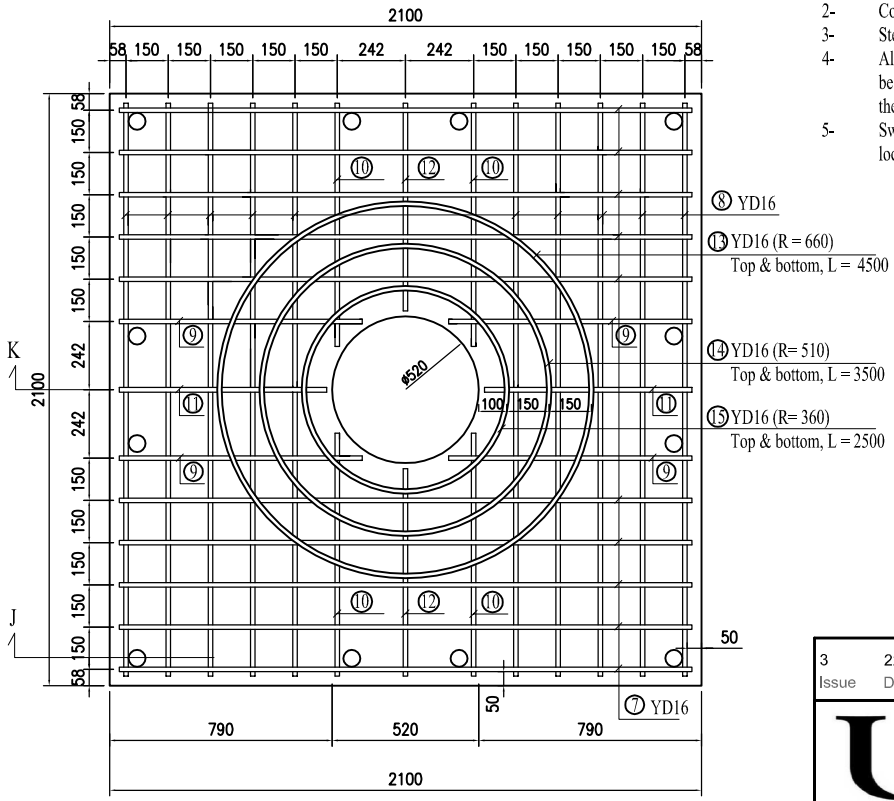

FOUNDATION REINFORCEMENT DETAILS

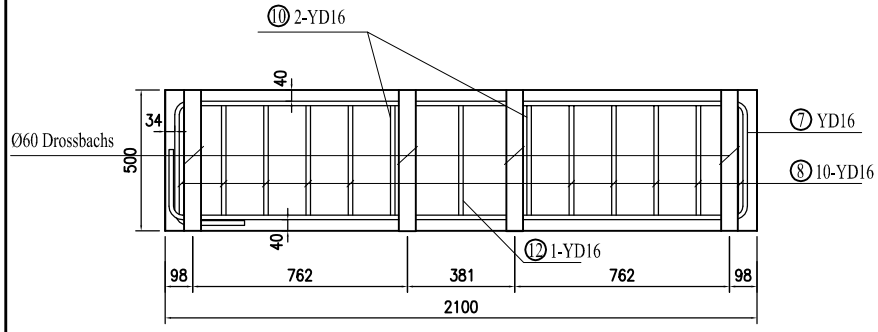

SECTION - J

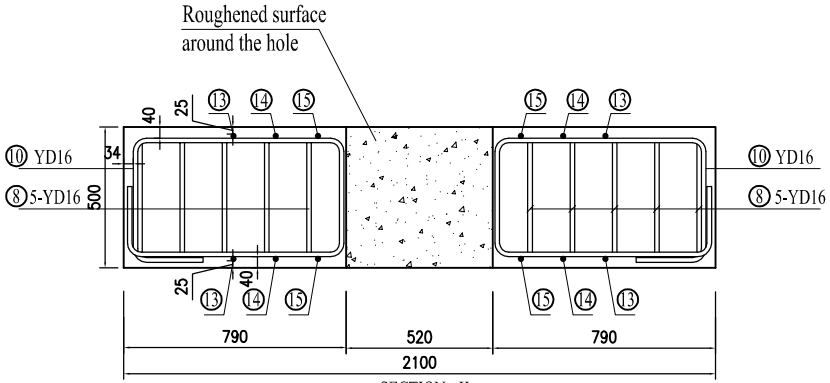

SECTION - K

NOTES:

1- All dimensions are in mm.
2- Concrete strength (f'c) is 40 MPa.
3- Steel grade is 500E seismic (fy = 500 MPa).
4- All drossbachs are corrugated steel ducts and must be tighten to the reinforcement bars before casting the footing.
5- Swift lift anchors should be provided at appropriate locations for lifting of each element.

Issue	Date	Description
3	22/05/2013	Phase II Specimens

UNIVERSITY OF CANTERBURY
Te Whare Wānanga o Waitaha
CHRISTCHURCH NEW ZEALAND

High Damage Bent Footings

Project Title

Advanced Bridge Construction and Design
(Natural Hazard Research Platform)

Drawing Name
FOUNDATION PLAN & DETAILS

Engineered by : **Mustafa Mashal** Date : **05/2013**
Drawn by : **Mustafa Mashal** Date : **05/2013**

Drawing Scale 1:20 AT A3

Sheet No:
S-04

TABLE 1: REBARS CHART

ELEMENT	NO OF REBAR	DIAMETER	QUANTITY	DIMENSIONS (mm)	LENGTH (mm)	TOTAL LENGTH (mm)	BAR TYPE
COLUMN	A	Ø10	8	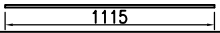	1115	8920	DEFORMED
	0	Ø16	16	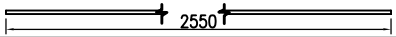	2550	40800	REIDBAR
	1	Ø16	16	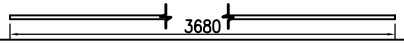	3680	58880	
	2	Ø10	110		1680	184800	PLAIN
CAP BEAM	3	Ø20	13	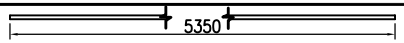	5350	69550	DEFORMED
	4	Ø12	2	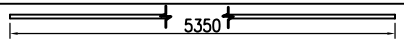	5350	10700	
	5	Ø12	54	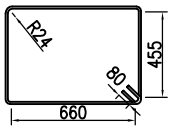	2680	144720	
	6	Ø12	54	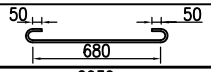	990	53460	
FOUNDATION	7	Ø16	10	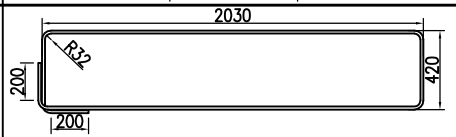	5320	53200	DEFORMED
	8	Ø16	10	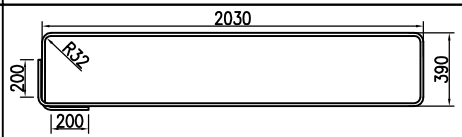	5260	52600	
	9	Ø16	4	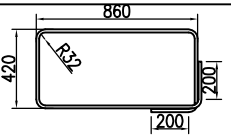	2950	11800	
	10	Ø16	4	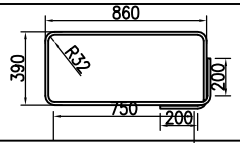	2890	11560	
	11	Ø16	2	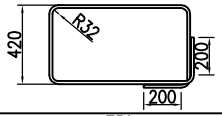	2730	5460	
	12	Ø16	2	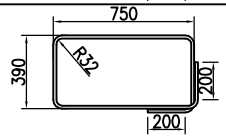	2670	5340	

TABLE 2: REBARS CHART FOR REINFORCEMENT TO BE BENT IN CIRCULAR SHAPE

ELEMENT	NO OF REBAR	QUANTITY	REBAR DIAMETER	BENT RADIUS (mm)	LENGTH (mm)	TOTAL LENGTH (mm)	BAR TYPE
FOUNDATION	13	2	Ø16	660	4500	9000	DEFORMED
	14	2	Ø16	510	3500	7000	
	15	2	Ø16	360	2500	5000	

TABLE 3: SUPPLEMENTARY REBARS CHART

ELEMENT	NO OF REBAR	DIAMETER	QUANTITY	DIMENSIONS (mm)	LENGTH (mm)	GRADE	BAR TYPE
Shear Key	16	Ø10	8	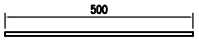	500	500E	DEFORMED
	17	Ø10	24	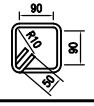	780	500E	PLAIN

TABLE 4: TOTAL AMOUNT OF REIDBAR INSERTS

SUIT TYPE	Foot Diameter (mm)	LENGTH (mm)	QUANTITY
RBA16	50	118	16

TABLE 5: SUMMARY OF CONCRETE CONSTRUCTION SCHEDULE

ELEMENT	DRAWING NO	QUANTITY	CASTING PIRORITY	CONCRETE POURING CRITERIA
COLUMN 1	S-01	2	1	BOTH COLUMNS SIMULTANEOUSLY
COLUMN 2	S-02	2	3	BOTH COLUMNS SIMULTANEOUSLY
CAP BEAM	S-03	1	2	NIL
FOUNDATION	S-04	2	2	NIL

SPECIFIC NOTES:

1- All dimensions are in mm unless noted.

Issue	Date	Description
3	22/05/2013	Phase II Specimens

UNIVERSITY OF CANTERBURY
Te Whare Wānanga o Waitaha
CHRISTCHURCH NEW ZEALAND

Project Title

Advanced Bridge Construction and Design
(Natural Hazard Research Platform)

Drawing Name

REBAR & CONSTRUCTION CHART

Engineered by : **Mustafa Mashal** Date : **05/2013**
Drawn by : **Mustafa Mashal** Date : **05/2013**

Drawing Scale 1:30 AT A3

Sheet No:

S-05

APPENDIX D

D.1 IPT15-EX Spreadsheet Calculations

IPT15-EX: ULS

Section Properties

Column Diameter	D	500	mm
Clear Cover	cover	0	mm

Member Properties

Column Height	H	1287.5	mm
Design Drift	θd	2.2%	

Concrete Properties

Core

Unconfined Compressive Strength	f'c	42.5	Mpa
Confined Compressive Strength	f'cc	55.3	Mpa
Unconfined Peak Strain	ε_o	0.003	
Peak Strain	εcc	0.007517647	
Ultimate Strain	εcu	0.016	

Outside Core

Unconfined Compressive Strength	f'c	42.5	Mpa
Confined Compressive Strength	f'cc	55.3	Mpa
Unconfined Peak Strain	ε_o	0.003	
Peak Strain	εcc	0.007517647	
Ultimate Strain	εcu	0.016	

Steel Properties

Modulus of Elasticity	E	200000	Mpa

Transverse

Stirrup Diamter	db_stirrup	10	mm
Stirrup Area	Ab_stirrup	78.53981634	mm2
Transverse Yield Strength	fy_stirrup	300	MPa
Transverse Yield Strain	εy_stirrup	0.0015	

Longitudinal

Longitudinal Bar Diamter	db_long	16	mm
Longitudinal Area	Ab_stirrup	201.0619298	mm2
Longitudinal Yield Strength	fy_long	364	MPa
Longitudinal Yield Strain	εy_long	0.00182	

Post-Tensioning

Bar Diameter	db_pt	40	mm
Bar Area	Ab_pt	1256.637061	mm2
0.1% Proof Strength	fy_pt	835	MPa
Ultimate Strength	fy_ult	1030	MPa

Detailed Design Check

Yield Displacement

Yield Curvature	ϕy	0.00000819	m-1
Strain Penetration Length	Lsp	128.128	mm
Yield Displacement	Δy	5.470927192	mm
Yield Drift	θy	0.42%	

Gap Opening	θ	1.78%	
Initial Post Tensioning	T_pt_i	165	kN
Neutral Axis Depth	c	66.14660236	mm
Force Equilibrium	ΣF	-2.067E-05	kN

Post Tensioning

Post Tensioning Location	d_PT	250	mm
Extension	Δ_pt	3.263533154	mm
Undonded Length	l_ub	2165	mm
Change in Strain	ε_pt	0.001507406	
Change in PT Force	ΔT_pt	378.8523522	kN
Total PT Force	T_pt	543.8523522	kN

Mild Steel

Unbonded Length	l'_ub	254	mm
Bi-linear Factor	r	0.80%	

	nbar	Abar mm2	As mm2	d mm	Δ_s mm	ε_s	f_s MPa	T_s kN	M-s kNm
Top	0	209	0	-46	-1.99068	-0.78%	-364	0	0
Mid1	0	209	0	128	1.097943	0.43%	364	0	0
Mid2	0	209	0	372	5.429123	2.14%	394.1293	0	0
Bottom	0	209	0	546	8.517751	3.35%	434.6206	0	0

Concrete

Cantilever Length	Lcant	1287.5	mm		
Plastic Hinge Length	Lp	231.128	mm	>	256.256 mm
Concrete Strain	ε_c	0.006122775			
Normalised Concrete Strain	ε_c/ε_co	2.04092499			
Confinement Ratio	f'cc/f'c	1.36			

Use table entry for confinement ratio of 1.3

Stress Block Factor	α	1.162565799	Interpolating between Table 16.3 and 16.4
Stress Block Factor	β	0.7811281	Interpolating between Table 16.3 and 16.4
radius	R	250	mm
	h	66.14660236	mm
	d	183.8533976	
angle	theta	1.489038978	
Compression Block Area	A	15386.85151	mm2
Concrete Compression	Cc	-593.8523729	kN
Column Weight	N	50	kN

Moment Capacity

Concrete Compression Depth	a/2	25.83448489	mm
PT Moment	M_pt	121.9129427	kNm
MS_Moment	M_ms	0	kNm
Weight Moment	M_N	11.20827576	kNm
Nominal Moment Capacity	Mn	133.1212184	kNm
Recentering Ratio	λ	∞	

IPT15-EX: Yielding

Section Properties

Column Diameter	D	500	mm
Clear Cover	cover	40	mm

Member Properties

Column Height	H	1287.5	mm

Concrete Properties

Core

Unconfined Compressive Strength	f'c	42.5	Mpa
Confined Compressive Strength	f'cc	55.3	Mpa
Unconfined Peak Strain	ε_o	0.003	
Peak Strain	εcc	0.007517647	
Ultimate Strain	εcu	0.016	

Outside Core

Unconfined Compressive Strength	f'c	42.5	Mpa
Confined Compressive Strength	f'cc	55.3	Mpa
Unconfined Peak Strain	ε_o	0.003	
Peak Strain	εcc	0.007517647	
Ultimate Strain	εcu	0.016	

Steel Properties

Modulus of Elasticity	E	200000	Mpa

Transverse

Stirrup Diamter	db_stirrup	10	mm
Stirrup Area	Ab_stirrup	78.53981634	mm2
Transverse Yield Strength	fy_stirrup	300	MPa
Transverse Yield Strain	εy_stirrup	0.0015	

Longitudinal

Longitudinal Bar Diamter	db_long	16	mm
Longitudinal Area	Ab_stirrup	201.0619298	mm2
Longitudinal Yield Strength	fy_long	364	MPa
Longitudinal Yield Strain	εy_long	0.00182	

Post-Tensioning

Bar Diameter	db_pt	40	mm
Bar Area	Ab_pt	1256.637061	mm2
0.1% Proof Strength	fy_pt	835	MPa
Ultimate Strength	fy_ult	1030	MPa

Detailed Design Check

Yield Displacement

Yield Curvature	ϕy	0.00000819	m-1
Strain Penetration Length	Lsp	128.128	mm
Yield Displacement	Δy	5.470927192	mm
Yield Drift	θy	0.42%	

Gap Opening	θ	0.10%	
Initial Post Tensioning	T_pt_i	165	kN
Neutral Axis Depth	c	83.17496415	mm
Force Equilibrium	ΣF	-2.96458E-05	kN

Yield Difference times 1000	
0.05%	
Total Yield θy	0.52%

Post Tensioning

Post Tensioning Location	d_PT	250	mm
Extension	Δ_pt	0.166675653	mm
Undonded Length	l_ub	2165	mm
Change in Strain	ε_pt	7.69864E-05	
Change in PT Force	ΔT_pt	19.34880395	kN
Total PT Force	T_pt	184.348804	kN

Mild Steel

Unbonded Length	l'_ub	254	mm
Bi-linear Factor	r	0.80%	

	nbar	Abar mm2	As mm2	d mm	Δ_s mm	ε_s	f_s MPa	T_s kN	M-s kNm
Top	0	209	0	-46	-0.12906	-0.05%	-101.621	0	0
Mid1	0	209	0	128	0.044785	0.02%	35.2637	0	0
Mid2	0	209	0	372	0.288566	0.11%	227.2176	0	0
Bottom	0	209	0	546	0.462411	0.18%	364	0	0

Concrete

Cantilever Length	Lcant	1287.5	mm		
Plastic Hinge Length	Lp	231.128	mm	>	256.256 mm
Concrete Strain	ε_c	0.0010762			
Normalised Concrete Strain	ε_c/ε_co	0.358733484			
Confinement Ratio	f'cc/f'c	1.36			

Use table entry for confinement ratio of 1.3

Stress Block Factor	α	0.378209475	Interpolating between Table 16.3 and 16.4
Stress Block Factor	β	0.679654141	Interpolating between Table 16.3 and 16.4
radius	R	250	mm
	h	83.17496415	mm
	d	166.8250359	
angle	theta	1.680436898	
Compression Block Area	A	21451.29396	mm2
Concrete Compression	Cc	-234.3488336	kN
Column Weight	N	50	kN

Moment Capacity

Concrete Compression Depth	a/2	28.26510441	mm
PT Moment	M_pt	40.8765628	kNm
MS_Moment	M_ms	0	kNm
Weight Moment	M_N	11.08674478	kNm
Nominal Moment Capacity	Mn	51.96330758	kNm
Recentering Ratio	λ	∞	

D.2 IPT30-EX Spreadsheet Calculations

IPT30-EX: ULS

Section Properties

Column Diameter	D	500	mm
Clear Cover	cover	0	mm

Member Properties

Column Height	H	1287.5	mm
Design Drift	θd	2.2%	

Concrete Properties

Core

Unconfined Compressive Strength	f'c	42.5	Mpa
Confined Compressive Strength	f'cc	55.3	Mpa
Unconfined Peak Strain	ε_o	0.003	
Peak Strain	εcc	0.007517647	
Ultimate Strain	εcu	0.016	

Outside Core

Unconfined Compressive Strength	f'c	42.5	Mpa
Confined Compressive Strength	f'cc	55.3	Mpa
Unconfined Peak Strain	ε_o	0.003	
Peak Strain	εcc	0.007517647	
Ultimate Strain	εcu	0.016	

Steel Properties

Modulus of Elasticity	E	200000	Mpa

Transverse

Stirrup Diamter	db_stirrup	10	mm
Stirrup Area	Ab_stirrup	78.53981634	mm2
Transverse Yield Strength	fy_stirrup	300	MPa
Transverse Yield Strain	εy_stirrup	0.0015	

Longitudinal

Longitudinal Bar Diamter	db_long	16	mm
Longitudinal Area	Ab_stirrup	201.0619298	mm2
Longitudinal Yield Strength	fy_long	364	MPa
Longitudinal Yield Strain	εy_long	0.00182	

Post-Tensioning

Bar Diameter	db_pt	40	mm
Bar Area	Ab_pt	1256.637061	mm2
0.1% Proof Strength	fy_pt	835	MPa
Ultimate Strength	fy_ult	1030	MPa

Detailed Design Check

Yield Displacement

Yield Curvature	ϕy	0.00000819	m-1
Strain Penetration Length	Lsp	128.128	mm
Yield Displacement	Δy	5.470927192	mm
Yield Drift	θy	0.42%	

Gap Opening	θ	1.78%	
Initial Post Tensioning	T_pt_i	330	kN
Neutral Axis Depth	c	74.65343433	mm
Force Equilibrium	ΣF	-0.000112533	kN

Post Tensioning

Post Tensioning Location	d_PT	250	mm
Extension	Δ_pt	3.112530624	mm
Undonded Length	l_ub	2165	mm
Change in Strain	ε_pt	0.001437658	
Change in PT Force	ΔT_pt	361.3229873	kN
Total PT Force	T_pt	691.3229873	kN

Mild Steel

Unbonded Length	l'_ub	254	mm
Bi-linear Factor	r	0.80%	

	nbar	Abar mm2	As mm2	d mm	Δ_s mm	ε_s	f_s MPa	T_s kN	M-s kNm
Top	0	209	0	-46	-2.14169	-0.84%	-364	0	0
Mid1	0	209	0	128	0.946941	0.37%	364	0	0
Mid2	0	209	0	372	5.27812	2.08%	391.8666	0	0
Bottom	0	209	0	546	8.366749	3.29%	432.8818	0	0

Concrete

Cantilever Length	Lcant	1287.5	mm		
Plastic Hinge Length	Lp	231.128	mm	>	256.256 mm
Concrete Strain	ε_c	0.006910199			
Normalised Concrete Strain	ε_c/ε_co	2.303399635			
Confinement Ratio	f'cc/f'c	1.36			

Use table entry for confinement ratio of 1.3

Stress Block Factor	α	1.196339964	Interpolating between Table 16.3 and 16.4
Stress Block Factor	β	0.794776781	Interpolating between Table 16.3 and 16.4
radius	R	250	mm
	h	74.65343433	mm
	d	175.3465657	
angle	theta	1.586911645	
Compression Block Area	A	18345.0467	mm2
Concrete Compression	Cc	-741.3230998	kN
Column Weight	N	50	kN

Moment Capacity

Concrete Compression Depth	a/2	29.66640811	mm
PT Moment	M_pt	152.3216769	kNm
MS_Moment	M_ms	0	kNm
Weight Moment	M_N	11.01667959	kNm
Nominal Moment Capacity	Mn	163.3383565	kNm
Recentering Ratio	λ	∞	

IPT30-EX: Yielding

Section Properties

Column Diameter	D	500	mm
Clear Cover	cover	0	mm

Member Properties

Column Height	H	1287.5	mm

Concrete Properties

Core

Unconfined Compressive Strength	f'c	42.5	Mpa
Confined Compressive Strength	f'cc	55.3	Mpa
Unconfined Peak Strain	ε_o	0.003	
Peak Strain	εcc	0.007517647	
Ultimate Strain	εcu	0.016	

Outside Core

Unconfined Compressive Strength	f'c	42.5	Mpa
Confined Compressive Strength	f'cc	55.3	Mpa
Unconfined Peak Strain	ε_o	0.003	
Peak Strain	εcc	0.007517647	
Ultimate Strain	εcu	0.016	

Steel Properties

Modulus of Elasticity	E	200000	Mpa

Transverse

Stirrup Diamter	db_stirrup	10	mm
Stirrup Area	Ab_stirrup	78.53981634	mm2
Transverse Yield Strength	fy_stirrup	300	MPa
Transverse Yield Strain	εy_stirrup	0.0015	

Longitudinal

Longitudinal Bar Diamter	db_long	16	mm
Longitudinal Area	Ab_stirrup	201.0619298	mm2
Longitudinal Yield Strength	fy_long	364	MPa
Longitudinal Yield Strain	εy_long	0.00182	

Post-Tensioning

Bar Diameter	db_pt	40	mm
Bar Area	Ab_pt	1256.637061	mm2
0.1% Proof Strength	fy_pt	835	MPa
Ultimate Strength	fy_ult	1030	MPa

Detailed Design Check

Yield Displacement

Yield Curvature	ϕy	0.00000819	m-1
Strain Penetration Length	Lsp	128.128	mm
Yield Displacement	Δy	5.470927192	mm
Yield Drift	θy	0.42%	

Gap Opening	θ	0.10%	

Yield Difference times 1000	
0.07%	
Total Yield θy	0.53%

Initial Post Tensioning	T_pt_i	330	kN
Neutral Axis Depth	c	103.3083114	mm
Force Equilibrium	ΣF	-4.44299E-05	kN

Post Tensioning

Post Tensioning Location	d_PT	250	mm
Extension	Δ_pt	0.153245582	mm
Undonded Length	l_ub	2165	mm
Change in Strain	ε_pt	7.07832E-05	
Change in PT Force	ΔT_pt	17.78975315	kN
Total PT Force	T_pt	347.7897532	kN

Mild Steel

Unbonded Length	l'_ub	254	mm
Bi-linear Factor	r	0.80%	

	nbar	Abar mm2	As mm2	d mm	Δ_s mm	ε_s	f_s MPa	T_s kN	M-s kNm
Top	0	209	0	-46	-0.15598	-0.06%	-122.818	0	0
Mid1	0	209	0	128	0.025795	0.01%	20.31092	0	0
Mid2	0	209	0	372	0.280696	0.11%	221.0207	0	0
Bottom	0	209	0	546	0.46247	0.18%	364	0	0

Concrete

Cantilever Length	Lcant	1287.5	mm		
Plastic Hinge Length	Lp	231.128	mm	>	256.256 mm
Concrete Strain	ε_c	0.001359085			
Normalised Concrete Strain	ε_c/ε_co	0.453028199			
Confinement Ratio	f'cc/f'c	1.36			

Use table entry for confinement ratio of 1.3

Stress Block Factor	α	0.466846507	Interpolating between Table 16.3 and 16.4
Stress Block Factor	β	0.684557466	Interpolating between Table 16.3 and 16.4
radius	R	250	mm
	h	103.3083114	mm
	d	146.6916886	
angle	theta	1.887472308	
Compression Block Area	A	29287.39095	mm2
Concrete Compression	Cc	-397.7897976	kN
Column Weight	N	50	kN

Moment Capacity

Concrete Compression Depth	a/2	35.36023796	mm
PT Moment	M_pt	74.64950986	kNm
MS_Moment	M_ms	0	kNm
Weight Moment	M_N	10.7319881	kNm
Nominal Moment Capacity	Mn	85.38149796	kNm
Recentering Ratio	λ	∞	

D.3 IPT45-EX Spreadsheet Calculations

IPT45-EX: ULS

Section Properties

Column Diameter	D	500	mm
Clear Cover	cover	0	mm

Member Properties

Column Height	H	1287.5	mm
Design Drift	θd	2.2%	

Concrete Properties

Core

Unconfined Compressive Strength	f'c	42.5	Mpa
Confined Compressive Strength	f'cc	55.3	Mpa
Unconfined Peak Strain	ε_o	0.003	
Peak Strain	εcc	0.007517647	
Ultimate Strain	εcu	0.016	

Outside Core

Unconfined Compressive Strength	f'c	42.5	Mpa
Confined Compressive Strength	f'cc	55.3	Mpa
Unconfined Peak Strain	ε_o	0.003	
Peak Strain	εcc	0.007517647	
Ultimate Strain	εcu	0.016	

Steel Properties

Modulus of Elasticity	E	200000	Mpa

Transverse

Stirrup Diamter	db_stirrup	10	mm
Stirrup Area	Ab_stirrup	78.53981634	mm2
Transverse Yield Strength	fy_stirrup	300	MPa
Transverse Yield Strain	εy_stirrup	0.0015	

Longitudinal

Longitudinal Bar Diamter	db_long	16	mm
Longitudinal Area	Ab_stirrup	201.0619298	mm2
Longitudinal Yield Strength	fy_long	364	MPa
Longitudinal Yield Strain	εy_long	0.00182	

Post-Tensioning

Bar Diameter	db_pt	40	mm
Bar Area	Ab_pt	1256.637061	mm2
0.1% Proof Strength	fy_pt	835	MPa
Ultimate Strength	fy_ult	1030	MPa

Detailed Design Check

Yield Displacement

Yield Curvature	ϕy	0.00000819	m-1
Strain Penetration Length	Lsp	128.128	mm
Yield Displacement	Δy	5.470927192	mm
Yield Drift	θy	0.42%	

Gap Opening	θ	1.78%	
Initial Post Tensioning	T_pt_i	495	kN
Neutral Axis Depth	c	82.65218249	mm
Force Equilibrium	ΣF	-0.000227594	kN

Post Tensioning

Post Tensioning Location	d_PT	250	mm
Extension	Δ_pt	2.970546956	mm
Undonded Length	l_ub	2165	mm
Change in Strain	ε_pt	0.001372077	
Change in PT Force	ΔT_pt	344.840591	kN
Total PT Force	T_pt	839.840591	kN

Mild Steel

Unbonded Length	l'_ub	254	mm
Bi-linear Factor	r	0.80%	

	nbar	Abar mm2	As mm2	d mm	Δ_s mm	ε_s	f_s MPa	T_s kN	M-s kNm
Top	0	209	0	-46	-2.28367	-0.90%	-364	0	0
Mid1	0	209	0	128	0.804957	0.32%	364	0	0
Mid2	0	209	0	372	5.136137	2.02%	389.7132	0	0
Bottom	0	209	0	546	8.224765	3.24%	431.2256	0	0

Concrete

Cantilever Length	Lcant	1287.5	mm		
Plastic Hinge Length	Lp	231.128	mm	>	256.256 mm
Concrete Strain	ε_c	0.007650593			
Normalised Concrete Strain	ε_c/ε_co	2.550197572			
Confinement Ratio	f'cc/f'c	1.36			

Use table entry for confinement ratio of 1.3

Stress Block Factor	α	1.219614225	Interpolating between Table 16.3 and 16.4
Stress Block Factor	β	0.807610274	Interpolating between Table 16.3 and 16.4
radius	R	250	mm
	h	82.65218249	mm
	d	167.3478175	
angle	theta	1.674814456	
Compression Block Area	A	21256.8583	mm2
Concrete Compression	Cc	-889.8408186	kN
Column Weight	N	50	kN

Moment Capacity

Concrete Compression Depth	a/2	33.37537586	mm
PT Moment	M_pt	181.9301524	kNm
MS_Moment	M_ms	0	kNm
Weight Moment	M_N	10.83123121	kNm
Nominal Moment Capacity	Mn	192.7613836	kNm
Recentering Ratio	λ	∞	

IPT45-EX: Yielding

Section Properties

Column Diameter	D	500	mm
Clear Cover	cover	0	mm

Member Properties

Column Height	H	1287.5	mm

Concrete Properties

Core

Unconfined Compressive Strength	f'c	42.5	Mpa
Confined Compressive Strength	f'cc	55.3	Mpa
Unconfined Peak Strain	ε_o	0.003	
Peak Strain	εcc	0.007517647	
Ultimate Strain	εcu	0.016	

Outside Core

Unconfined Compressive Strength	f'c	42.5	Mpa
Confined Compressive Strength	f'cc	55.3	Mpa
Unconfined Peak Strain	ε_o	0.003	
Peak Strain	εcc	0.007517647	
Ultimate Strain	εcu	0.016	

Steel Properties

Modulus of Elasticity	E	200000	Mpa

Transverse

Stirrup Diamter	db_stirrup	10	mm
Stirrup Area	Ab_stirrup	78.53981634	mm2
Transverse Yield Strength	fy_stirrup	300	MPa
Transverse Yield Strain	εy_stirrup	0.0015	

Longitudinal

Longitudinal Bar Diamter	db_long	16	mm
Longitudinal Area	Ab_stirrup	201.0619298	mm2
Longitudinal Yield Strength	fy_long	364	MPa
Longitudinal Yield Strain	εy_long	0.00182	

Post-Tensioning

Bar Diameter	db_pt	40	mm
Bar Area	Ab_pt	1256.637061	mm2
0.1% Proof Strength	fy_pt	835	MPa
Ultimate Strength	fy_ult	1030	MPa

Detailed Design Check

Yield Displacement

Yield Curvature	ϕy	0.00000819	m-1
Strain Penetration Length	Lsp	128.128	mm
Yield Displacement	Δy	5.470927192	mm
Yield Drift	θy	0.42%	

Gap Opening	θ	0.11%	
Initial Post Tensioning	T_pt_i	495	kN
Neutral Axis Depth	c	119.2567814	mm
Force Equilibrium	ΣF	-5.18773E-05	kN

Yield Difference times 1000	
0.07%	
Total Yield θy	0.53%

Post Tensioning

Post Tensioning Location	d_PT	250	mm
Extension	Δ_pt	0.141686184	mm
Undonded Length	l_ub	2165	mm
Change in Strain	ε_pt	6.5444E-05	
Change in PT Force	ΔT_pt	16.44786232	kN
Total PT Force	T_pt	511.4478623	kN

Mild Steel

Unbonded Length	l'_ub	254	mm
Bi-linear Factor	r	0.80%	

	nbar	Abar mm2	As mm2	d mm	Δ_s mm	ε_s	f_s MPa	T_s kN	M-s kNm	
Top	0	209	0	-46	-0.17909	-0.07%	-141.015	0	0	
Mid1	0	209	0	128	0.009475	0.00%	7.460638	0	0	
Mid2	0	209	0	372	0.273897	0.11%	215.6672	0	0	
Bottom	0	209	0	546	0.462461	0.18%	364	0	0	

Concrete

Cantilever Length	Lcant	1287.5	mm		
Plastic Hinge Length	Lp	231.128	mm	>	256.256 mm
Concrete Strain	ε_c	0.001591015			
Normalised Concrete Strain	ε_c/ε_co	0.530338472			
Confinement Ratio	f'cc/f'c	1.36			

Use table entry for confinement ratio of 1.3

Stress Block Factor	α	0.533935885	Interpolating between Table 16.3 and 16.4
Stress Block Factor	β	0.688820308	Interpolating between Table 16.3 and 16.4
radius	R	250	mm
	h	119.2567814	mm
	d	130.7432186	
angle	theta	2.040922468	
Compression Block Area	A	35919.10358	mm2
Concrete Compression	Cc	-561.4479142	kN
Column Weight	N	50	kN

Moment Capacity

Concrete Compression Depth	a/2	41.07324647	mm
PT Moment	M_pt	106.8551415	kNm
MS_Moment	M_ms	0	kNm
Weight Moment	M_N	10.44633768	kNm
Nominal Moment Capacity	Mn	117.3014791	kNm
Recentering Ratio	λ	∞	

D.4 IPT11.8+GD+AX Spreadsheet Calculations

IPT11.8+GD+AX: ULS

Section Properties

Column Diameter	D	500	mm
Clear Cover	cover	0	mm

Member Properties

Column Height	H	1287.5	mm
Design Drift	θd	2.2%	

Concrete Properties

Core

Unconfined Compressive Strength	f'c	42.5	Mpa
Confined Compressive Strength	f'cc	55.3	Mpa
Unconfined Peak Strain	ε_o	0.003	
Peak Strain	εcc	0.007517647	
Ultimate Strain	εcu	0.016	

Outside Core

Unconfined Compressive Strength	f'c	42.5	Mpa
Confined Compressive Strength	f'cc	55.3	Mpa
Unconfined Peak Strain	ε_o	0.003	
Peak Strain	εcc	0.007517647	
Ultimate Strain	εcu	0.016	

Steel Properties

Modulus of Elasticity	E	200000	Mpa

Transverse

Stirrup Diamter	db_stirrup	10	mm
Stirrup Area	Ab_stirrup	78.53981634	mm2
Transverse Yield Strength	fy_stirrup	300	MPa
Transverse Yield Strain	εy_stirrup	0.0015	

Longitudinal

Longitudinal Bar Diamter	db_long	16	mm
Longitudinal Area	Ab_stirrup	201.0619298	mm2
Longitudinal Yield Strength	fy_long	364	MPa
Longitudinal Yield Strain	εy_long	0.00182	

Post-Tensioning

Bar Diameter	db_pt	40	mm
Bar Area	Ab_pt	1256.637061	mm2
0.1% Proof Strength	fy_pt	835	MPa
Ultimate Strength	fy_ult	1030	MPa

Detailed Design Check

Yield Displacement

Yield Curvature	ϕy	0.00000819	m-1
Strain Penetration Length	Lsp	128.128	mm
Yield Displacement	Δy	5.470927192	mm
Yield Drift	θy	0.42%	

Gap Opening	θ	1.78%	
Initial Post Tensioning	T_pt_i	130	kN
Neutral Axis Depth	c	82.15850603	mm
Force Equilibrium	ΣF	-3.70461E-05	kN

Post Tensioning

Post Tensioning Location	d_PT	250	mm
Extension	Δ_pt	2.979310076	mm
Undonded Length	l_ub	2165	mm
Change in Strain	ε_pt	0.001376125	
Change in PT Force	ΔT_pt	345.8578716	kN
Total PT Force	T_pt	475.8578716	kN

Mild Steel

Unbonded Length	l'_ub	254	mm
Bi-linear Factor	r	0.80%	

	nbar	Abar mm2	As mm2	d mm	Δ_s mm	ε_s	f_s MPa	T_s kN	M-s kNm
Top	1	201.0619298	201.0619	-40	-2.1684	-0.85%	-364	-73.1865	5.353119
Mid1	1	201.0619298	201.0619	250	2.97931	1.17%	364	73.18654	15.87098
Mid2	1	201.0619298	201.0619	250	2.97931	1.17%	364	73.18654	15.87098
Bottom	1	201.0619298	201.0619	540	8.127024	3.20%	430.0734	86.4714	43.82859

Concrete

Cantilever Length	Lcant	1287.5	mm		
Plastic Hinge Length	Lp	231.128	mm	>	256.256 mm
Concrete Strain	ε_c	0.007604896			
Normalised Concrete Strain	ε_c/ε_co	2.534965397			
Confinement Ratio	f'cc/f'c	1.36			

Use table entry for confinement ratio of 1.3

Stress Block Factor	α	1.218517509	Interpolating between Table 16.3 and 16.4
Stress Block Factor	β	0.806818201	Interpolating between Table 16.3 and 16.4
radius	R	250	mm
	h	82.15850603	mm
	d	167.841494	
angle	theta	1.669491931	
Compression Block Area	A	21073.69969	mm2
Concrete Compression	Cc	-880.5158487	kN
Column Weight	N	245	kN

Moment Capacity

Concrete Compression Depth	a/2	33.143489	mm
PT Moment	M_pt	103.1928778	kNm
MS_Moment	M_ms	80.92366647	kNm
Weight Moment	M_N	53.12984519	kNm
Nominal Moment Capacity	Mn	237.2463894	kNm
Recentering Ratio	λ	1.931730602	

IPT11.8+GD+AX: Yielding

Section Properties

Column Diameter	D	500	mm
Clear Cover	cover	0	mm

Member Properties

Column Height	H	1287.5	mm

Concrete Properties

Core

Unconfined Compressive Strength	f'c	42.5	Mpa
Confined Compressive Strength	f'cc	55.3	Mpa
Unconfined Peak Strain	ε_o	0.003	
Peak Strain	εcc	0.007517647	
Ultimate Strain	εcu	0.016	

Outside Core

Unconfined Compressive Strength	f'c	42.5	Mpa
Confined Compressive Strength	f'cc	55.3	Mpa
Unconfined Peak Strain	ε_o	0.003	
Peak Strain	εcc	0.007517647	
Ultimate Strain	εcu	0.016	

Steel Properties

Modulus of Elasticity	E	200000	Mpa

Transverse

Stirrup Diamter	db_stirrup	10	mm
Stirrup Area	Ab_stirrup	78.53981634	mm2
Transverse Yield Strength	fy_stirrup	300	MPa
Transverse Yield Strain	εy_stirrup	0.0015	

Longitudinal

Longitudinal Bar Diamter	db_long	16	mm
Longitudinal Area	Ab_stirrup	201.0619298	mm2
Longitudinal Yield Strength	fy_long	364	MPa
Longitudinal Yield Strain	εy_long	0.00182	

Post-Tensioning

Bar Diameter	db_pt	40	mm
Bar Area	Ab_pt	1256.637061	mm2
0.1% Proof Strength	fy_pt	835	MPa
Ultimate Strength	fy_ult	1030	MPa

Detailed Design Check

Yield Displacement

Yield Curvature	ϕy	0.00000819	m-1
Strain Penetration Length	Lsp	128.128	mm
Yield Displacement	Δy	5.470927192	mm
Yield Drift	θy	0.42%	

Gap Opening	θ	0.11%	

Yield Difference times 1000	
0.09%	
Total Yield Dri θy	0.53%

Initial Post Tensioning	T_pt_i	130	kN
Neutral Axis Depth	c	111.8920139	mm
Force Equilibrium	ΣF	-6.49018E-05	kN

Post Tensioning

Post Tensioning Location	d_PT	250	mm
Extension	Δ_pt	0.149203667	mm
Undonded Length	l_ub	2165	mm
Change in Strain	ε_pt	6.89162E-05	
Change in PT Force	ΔT_pt	17.32054114	kN
Total PT Force	T_pt	147.3205411	kN

Mild Steel

Unbonded Length	l'_ub	254	mm
Bi-linear Factor	r	0.80%	

	nbar	Abar mm2	As mm2	d mm	Δ_s mm	ε_s	f_s MPa	T_s kN	M-s kNm
Top	1	201.0619298	201.0619	-40	-0.1641	-0.06%	-129.209	-25.979	2.03743
Mid1	1	201.0619298	201.0619	250	0.149204	0.06%	117.4832	23.6214	4.99767
Mid2	1	201.0619298	201.0619	250	0.149204	0.06%	117.4832	23.6214	4.99767
Bottom	1	201.0619298	201.0619	540	0.462502	0.18%	364	73.18654	36.70846

Concrete

Cantilever Length	Lcant	1287.5	mm		
Plastic Hinge Length	Lp	231.128	mm	>	256.256 mm
Concrete Strain	ε_c	0.001490976			
Normalised Concrete Strain	ε_c/ε_co	0.496991896			
Confinement Ratio	f'cc/f'c	1.36			

Use table entry for confinement ratio of 1.3

Stress Block Factor	α	0.508172383	Interpolating between Table 16.3 and 16.4
Stress Block Factor	β	0.686843579	Interpolating between Table 16.3 and 16.4
radius	R	250	mm
	h	111.8920139	mm
	d	138.1079861	
angle	theta	1.971034707	
Compression Block Area	A	32814.58026	mm2
Concrete Compression	Cc	-486.7709867	kN
Column Weight	N	245	kN

Moment Capacity

Concrete Compression Depth	a/2	38.42615563	mm
PT Moment	M_pt	31.16917325	kNm
MS_Moment	M_ms	48.74122603	kNm
Weight Moment	M_N	51.83559187	kNm
Nominal Moment Capacity	Mn	131.7459912	kNm
Recentering Ratio	λ	1.702968347	

D.5 IPT9+MUD+AX Spreadsheet Calculations

IPT9+MUD+AX: ULS

Section Properties

Column Diameter	D	500	mm
Clear Cover	cover	0	mm

Member Properties

Column Height	H	1287.5	mm
Design Drift	θd	2.2%	

Concrete Properties

Core

Unconfined Compressive Strength	f'c	42.5	Mpa
Confined Compressive Strength	f'cc	55.3	Mpa
Unconfined Peak Strain	ε_o	0.003	
Peak Strain	εcc	0.007517647	
Ultimate Strain	εcu	0.016	

Outside Core

Unconfined Compressive Strength	f'c	42.5	Mpa
Confined Compressive Strength	f'cc	55.3	Mpa
Unconfined Peak Strain	ε_o	0.003	
Peak Strain	εcc	0.007517647	
Ultimate Strain	εcu	0.016	

Steel Properties

Modulus of Elasticity	E	200000	Mpa

Transverse

Stirrup Diamter	db_stirrup	10	mm
Stirrup Area	Ab_stirrup	78.53981634	mm2
Transverse Yield Strength	fy_stirrup	300	MPa
Transverse Yield Strain	εy_stirrup	0.0015	

Longitudinal

Longitudinal Bar Diamter	db_long	16	mm
Longitudinal Area	Ab_stirrup	201.0619298	mm2
Longitudinal Yield Strength	fy_long	300	MPa
Longitudinal Yield Strain	εy_long	0.0015	

Post-Tensioning

Bar Diameter	db_pt	40	mm
Bar Area	Ab_pt	1256.637061	mm2
0.1% Proof Strength	fy_pt	835	MPa
Ultimate Strength	fy_ult	1030	MPa

Detailed Design Check

Yield Displacement

Yield Curvature	ϕy	0.00000675	m-1
Strain Penetration Length	Lsp	105.6	mm
Yield Displacement	Δy	4.366637123	mm
Yield Drift	θy	0.34%	

Gap Opening	θ	1.86%	
Initial Post Tensioning	T_pt_i	100	kN
Neutral Axis Depth	c	72.78307843	mm
Force Equilibrium	ΣF	1.8533E-05	kN

Post Tensioning

Post Tensioning Location	d_PT	250	mm
Extension	Δ_pt	3.297729953	mm
Undonded Length	l_ub	2165	mm
Change in Strain	ε_pt	0.001523201	
Change in PT Force	ΔT_pt	382.8221412	kN
Total PT Force	T_pt	482.8221412	kN

Mild Steel

Unbonded Length	l'_ub	254	mm
Bi-linear Factor	r	0.80%	

	nbar	Abar mm2	As mm2	d mm	Δ_s mm	ε_s	f_s MPa	T_s kN	M-s kNm
Top	1		0	-40	-2.09872			-13	0.901299
Mid1	0		0	250	3.29773			0	0
Mid2	0		0	250	3.29773			0	0
Bottom	1		0	540	8.694177			22.5	11.49006

Concrete

Cantilever Length	Lcant	1287.5	mm		
Plastic Hinge Length	Lp	208.6	mm	>	211.2 mm
Concrete Strain	ε_c	0.007556333			
Normalised Concrete Strain	ε_c/ε_co	2.518777803			
Confinement Ratio	f'cc/f'c	1.36			
Use table entry for confinement ratio of 1.3					
Stress Block Factor	α	1.217352002	Interpolating between Table 16.3 and 16.4		
Stress Block Factor	β	0.805976446	Interpolating between Table 16.3 and 16.4		
radius	R	250	mm		
	h	72.78307843	mm		
	d	177.2169216			
angle	theta	1.565809513			
Compression Block Area	A	17681.93584	mm2		
Concrete Compression	Cc	-737.3221226	kN		
Column Weight	N	245	kN		

Moment Capacity

Concrete Compression Depth	a/2	29.33072343	mm
PT Moment	M_pt	106.5440126	kNm
MS_Moment	M_ms	12.39135813	kNm
Weight Moment	M_N	54.06397276	kNm
Nominal Moment Capacity	Mn	172.9993435	kNm
Recentering Ratio	λ	12.96128993	

IPT9+MUD+AX: Yielding

Section Properties

Column Diameter	D	500	mm
Clear Cover	cover	0	mm

Member Properties

Column Height	H	1287.5	mm

Concrete Properties

Core

Unconfined Compressive Strength	f'c	42.5	Mpa
Confined Compressive Strength	f'cc	55.3	Mpa
Unconfined Peak Strain	ε_o	0.003	
Peak Strain	εcc	0.007517647	
Ultimate Strain	εcu	0.016	

Outside Core

Unconfined Compressive Strength	f'c	42.5	Mpa
Confined Compressive Strength	f'cc	55.3	Mpa
Unconfined Peak Strain	ε_o	0.003	
Peak Strain	εcc	0.007517647	
Ultimate Strain	εcu	0.016	

Steel Properties

Modulus of Elasticity	E	200000	Mpa

Transverse

Stirrup Diamter	db_stirrup	10	mm
Stirrup Area	Ab_stirrup	78.53981634	mm2
Transverse Yield Strength	fy_stirrup	300	MPa
Transverse Yield Strain	εy_stirrup	0.0015	

Longitudinal

Longitudinal Bar Diamter	db_long	16	mm
Longitudinal Area	Ab_stirrup	201.0619298	mm2
Longitudinal Yield Strength	fy_long	300	MPa
Longitudinal Yield Strain	εy_long	0.0015	

Post-Tensioning

Bar Diameter	db_pt	40	mm
Bar Area	Ab_pt	1256.637061	mm2
0.1% Proof Strength	fy_pt	835	MPa
Ultimate Strength	fy_ult	1030	MPa

Detailed Design Check

Yield Displacement

Yield Curvature	ϕy	0.00000675	m-1
Strain Penetration Length	Lsp	105.6	mm
Yield Displacement	Δy	4.366637123	mm
Yield Drift	θy	0.34%	

Gap Opening	θ	0.09%	
Initial Post Tensioning	T_pt_i	100	kN
Neutral Axis Depth	c	105.3310602	mm
Force Equilibrium	ΣF	4.08383E-05	kN

Yield Difference times 1000		
0.09%		
Total Yield Drift	θy	0.43%

Post Tensioning

Post Tensioning Location	d_PT	250	mm
Extension	Δ_pt	0.12680198	mm
Undonded Length	l_ub	2165	mm
Change in Strain	ε_pt	5.8569E-05	
Change in PT Force	ΔT_pt	14.72000625	kN
Total PT Force	T_pt	114.7200062	kN

Mild Steel

Unbonded Length	l'_ub	254	mm
Bi-linear Factor	r	0.80%	

	nbar	Abar mm2	As mm2	d mm	Δ_s mm	ε_s	f_s MPa	T_s kN	M-s kNm
Top	1			0	-40	-0.12738		-1	0.075901
Mid1	0			0	250	0.126802		0	0
Mid2	0			0	250	0.126802		0	0
Bottom	1			0	540	0.380986		3	1.512298

Concrete

Cantilever Length	Lcant	1287.5	mm		
Plastic Hinge Length	Lp	208.6	mm	>	211.2 mm
Concrete Strain	ε_c	0.00119258			
Normalised Concrete Strain	ε_c/ε_co	0.39752655			
Confinement Ratio	f'cc/f'c	1.36			

Use table entry for confinement ratio of 1.3

Stress Block Factor	α	0.414674957	Interpolating between Table 16.3 and 16.4
Stress Block Factor	β	0.681671381	Interpolating between Table 16.3 and 16.4
radius	R	250	mm
	h	105.3310602	mm
	d	144.6689398	
angle	theta	1.907384595	
Compression Block Area	A	30109.30155	mm2
Concrete Compression	Cc	-361.7199654	kN
Column Weight	N	245	kN

Moment Capacity

Concrete Compression Depth	a/2	35.9005846	mm
PT Moment	M_pt	24.56148627	kNm
MS_Moment	M_ms	1.588198831	kNm
Weight Moment	M_N	52.45435677	kNm
Nominal Moment Capacity	Mn	78.60404188	kNm
Recentering Ratio	λ	48.49257004	

D.6 IPT11.4+MUD+GD+AX Spreadsheet Calculations

IPT11.4+MUD+GD+AX: ULS

Section Properties

Column Diameter	D	500	mm
Clear Cover	cover	0	mm

Member Properties

Column Height	H	1287.5	mm
Design Drift	θd	2.2%	

Concrete Properties

Core

Unconfined Compressive Strength	f'c	45	Mpa
Confined Compressive Strength	f'cc	58.5	Mpa
Unconfined Peak Strain	ε_o	0.003	
Peak Strain	εcc	0.0075	
Ultimate Strain	εcu	0.016	

Outside Core

Unconfined Compressive Strength	f'c	45	Mpa
Confined Compressive Strength	f'cc	58.5	Mpa
Unconfined Peak Strain	ε_o	0.003	
Peak Strain	εcc	0.0075	
Ultimate Strain	εcu	0.016	

Steel Properties

Modulus of Elasticity	E	200000	Mpa

Transverse

Stirrup Diamter	db_stirrup	10	mm
Stirrup Area	Ab_stirrup	78.53981634	mm2
Transverse Yield Strength	fy_stirrup	364	MPa
Transverse Yield Strain	εy_stirrup	0.00182	

Longitudinal

Longitudinal Bar Diamter	db_long	16	mm
Longitudinal Area	Ab_stirrup	201.0619298	mm2
Longitudinal Yield Strength	fy_long	364	MPa
Longitudinal Yield Strain	εy_long	0.00182	

Post-Tensioning

Bar Diameter	db_pt	40	mm
Bar Area	Ab_pt	1256.637061	mm2
0.1% Proof Strength	fy_pt	835	MPa
Ultimate Strength	fy_ult	1030	MPa

Detailed Design Check

Yield Displacement

Yield Curvature	ϕy	0.00000819	m-1
Strain Penetration Length	Lsp	128.128	mm
Yield Displacement	Δy	5.470927192	mm
Yield Drift	θy	0.42%	

Gap Opening	θ	1.78%	
Initial Post Tensioning	T_pt_i	125	kN
Neutral Axis Depth	c	79.30198349	mm
Force Equilibrium	ΣF	0.000307341	kN

Post Tensioning

Post Tensioning Location	d_PT	250	mm
Extension	Δ_pt	3.030015454	mm
Undonded Length	l_ub	2165	mm
Change in Strain	ε_pt	0.001399545	
Change in PT Force	ΔT_pt	351.7440847	kN
Total PT Force	T_pt	476.7440847	kN

Mild Steel

Unbonded Length	l'_ub	254	mm
Bi-linear Factor	r	0.80%	

	nbar	Abar mm2	As mm2	d mm	Δ_s mm	ε_s	f_s MPa	T_s kN	M-s kNm
Top	1		0	-40	-2.1177			-17	1.22076
Mid1	1	201.0619298	201.0619	250	3.030015	1.19%	364	73.18654	15.96861
Mid2	1	201.0619298	201.0619	250	3.030015	1.19%	364	73.18654	15.96861
Bottom	1		0	540	8.177729			24	12.19657

Concrete

Cantilever Length	Lcant	1287.5	mm		
Plastic Hinge Length	Lp	231.128	mm	>	256.256 mm
Concrete Strain	ε_c	0.007340486			
Normalised Concrete Strain	ε_c/ε_co	2.446828622			
Confinement Ratio	f'cc/f'c	1.36			

Use table entry for confinement ratio of 1.3

Stress Block Factor	α	1.210682862	Interpolating between Table 16.3 and 16.4
Stress Block Factor	β	0.802235088	Interpolating between Table 16.3 and 16.4
radius	R	250	mm
	h	79.30198349	mm
	d	170.6980165	
angle	theta	1.638437885	
Compression Block Area	A	20022.64697	mm2
Concrete Compression	Cc	-875.1168623	kN
Column Weight	N	245	kN

Moment Capacity

Concrete Compression Depth	a/2	31.80941687	mm
PT Moment	M_pt	104.0210698	kNm
MS_Moment	M_ms	45.35456283	kNm
Weight Moment	M_N	53.45669287	kNm
Nominal Moment Capacity	Mn	202.8323255	kNm
Recentering Ratio	λ	3.472148178	

IPT11.4+MUD+GD+AX: Yielding

Section Properties

Column Diameter	D	500	mm
Clear Cover	cover	0	mm

Member Properties

Column Height	H	1287.5	mm

Concrete Properties

Core

Unconfined Compressive Strength	f'c	45	Mpa
Confined Compressive Strength	f'cc	58.5	Mpa
Unconfined Peak Strain	ε_o	0.003	
Peak Strain	εcc	0.0075	
Ultimate Strain	εcu	0.016	

Outside Core

Unconfined Compressive Strength	f'c	45	Mpa
Confined Compressive Strength	f'cc	58.5	Mpa
Unconfined Peak Strain	ε_o	0.003	
Peak Strain	εcc	0.0075	
Ultimate Strain	εcu	0.016	

Steel Properties

Modulus of Elasticity	E	200000	Mpa

Transverse

Stirrup Diamter	db_stirrup	10	mm
Stirrup Area	Ab_stirrup	78.53981634	mm2
Transverse Yield Strength	fy_stirrup	364	MPa
Transverse Yield Strain	εy_stirrup	0.00182	

Longitudinal

Longitudinal Bar Diamter	db_long	16	mm
Longitudinal Area	Ab_stirrup	201.0619298	mm2
Longitudinal Yield Strength	fy_long	364	MPa
Longitudinal Yield Strain	εy_long	0.00182	

Post-Tensioning

Bar Diameter	db_pt	40	mm
Bar Area	Ab_pt	1256.637061	mm2
0.1% Proof Strength	fy_pt	835	MPa
Ultimate Strength	fy_ult	1030	MPa

Detailed Design Check

Yield Displacement

Yield Curvature	ϕy	0.00000819	m-1
Strain Penetration Length	Lsp	128.128	mm
Yield Displacement	Δy	5.470927192	mm
Yield Drift	θy	0.42%	

Gap Opening	θ	0.11%	
Initial Post Tensioning	T_pt_i	125	kN
Neutral Axis Depth	c	104.9745718	mm
Force Equilibrium	ΣF	2.05234E-05	kN

Yield Difference times 1000		
0.01%		
Total Yield Drift	θy	0.53%

Post Tensioning

Post Tensioning Location	d_PT	250	mm
Extension	Δ_pt	0.15409367	mm
Undonded Length	l_ub	2165	mm
Change in Strain	ε_pt	7.11749E-05	
Change in PT Force	ΔT_pt	17.88820472	kN
Total PT Force	T_pt	142.8882047	kN

Mild Steel

Unbonded Length	l'_ub	254	mm
Bi-linear Factor	r	0.80%	

	nbar	Abar mm2	As mm2	d mm	Δ_s mm	ε_s		f_s MPa	T_s kN	M-s kNm
Top	1	0	0	-40	-0.15404				-1	0.075959
Mid1	1	201.0619298	201.0619	250	0.154094		0.06%	121.3336	24.39557	5.221661
Mid2	1	201.0619298	201.0619	250	0.154094		0.06%	121.3336	24.39557	5.221661
Bottom	1	0	0	540	0.462227				4.5	2.268186

Concrete

Cantilever Length	Lcant	1287.5	mm		
Plastic Hinge Length	Lp	231.128	mm	>	256.256 mm
Concrete Strain	ε_c	0.001389912			
Normalised Concrete Strain	ε_c/ε_co	0.463304071			
Confinement Ratio	f'cc/f'c	1.36			

Use table entry for confinement ratio of 1.3

Stress Block Factor	α	0.476505827	Interpolating between Table 16.3 and 16.4
Stress Block Factor	β	0.685091812	Interpolating between Table 16.3 and 16.4
radius	R	250	mm
	h	104.9745718	mm
	d	145.0254282	
angle	theta	1.903885542	
Compression Block Area	A	29964.02343	mm2
Concrete Compression	Cc	-440.179319	kN
Column Weight	N	245	kN

Moment Capacity

Concrete Compression Depth	a/2	35.9586098	mm
PT Moment	M_pt	30.58398998	kNm
MS_Moment	M_ms	12.78746718	kNm
Weight Moment	M_N	52.4401406	kNm
Nominal Moment Capacity	Mn	95.81159776	kNm
Recentering Ratio	λ	6.492617296	